ABSTRACT

Title of Dissertation: ENGINEERING OPTICAL LATTICES FOR ULTRACOLD ATOMS WITH SPATIAL FEATURES AND PERIODICITY BELOW THE DIFFRACTION LIMIT
and
DUAL-SPECIES OPTICAL TWEEZER ARRAYS FOR RUBIDIUM AND YTTERBIUM FOR RYDBERG-INTERACTION-MEDIATED QUANTUM SIMULATIONS
Sarthak Subhankar
Doctor of Philosophy, 2024

Dissertation Directed by: Professor Steven Rolston
Professor Trey Porto
Department of Physics
Joint Quantum Institute
National Institute of Standards and Technology
and
Department of Physics, University of Maryland

This dissertation is based on two independent projects and is therefore divided into two parts. The first half of this dissertation summarizes a series of investigations, both experimental and theoretical, that culminates in the realization of an optical lattice with a subwavelength spacing of $\lambda/4$, where λ is the wavelength of light used to create the lattice. The second half of this thesis presents details on the design and construction of an apparatus for dual-species optical tweezer arrays of Rb and Yb for Rydberg-interaction-mediated quantum computation and simulation.

Ultracold atoms trapped in optical lattices have proven to be a versatile, highly controllable, and pristine platform for studying quantum many-body physics. However, the characteristic single-particle energy scale in these systems is set by the recoil energy $E_R = h^2/(8md^2)$. Here, m is the mass of the atom, and d, the spatial period of the optical lattice, is limited by diffraction to $\lambda/2$, where λ is the wavelength of light used to create the optical lattice. Although the temperatures in these systems can be exceedingly low, the energy scales relevant for investigating many-body physics phenomena, such as superexchange or magnetic dipole interactions, can be lower yet. This limitation can be overcome by raising the relevant energy scales of the system ($E_R^{\text{eff}} = h^2/(8md_{\text{eff}}^2)$) by engineering optical lattices with spatial periodicities below the diffraction limit ($d_{\text{eff}} < \lambda/2$).

To realize this subwavelength-spaced lattice, we first generated a Kronig-Penney-like optical lattice using the nonlinear optical response of three-level atoms in spatially varying dark states. This conservative Kronig-Penney-like optical potential has strongly subwavelength barriers that can be less than 10 nm ($\equiv \lambda/50$) wide and are spaced $\lambda/2$ apart, where λ is the wavelength of light used to generate the optical lattice. Using the same nonlinear optical response, we developed a microscopy technique that allowed the probability density of atoms in optical lattices to be measured with a subwavelength resolution of $\lambda/50$. We theoretically investigated the feasibility of stroboscopically pulsing spatially shifted 1D Kronig-Penney-like optical lattices to create lattices with subwavelength spacings. We applied the lattice pulsing techniques developed in this theoretical investigation to realize a $\lambda/4$-spaced optical lattice. We used the subwavelength resolution microscopy technique to confirm the existence of this $\lambda/4$-spaced optical lattice by measuring the probability density of the atoms in the ground band of the $\lambda/4$-spaced optical lattice.

Single neutral atoms trapped in optical tweezer arrays with Rydberg interaction-mediated entangling gate operations have recently emerged as a promising platform for quantum computation and quantum simulation. These systems were first realized using atoms of a single species, with alkali atoms being the first to be trapped in optical tweezers, followed by alkaline-earth (like) atoms, and magnetic lanthanides. Recently, dual-species (alkali-alkali) optical tweezer arrays were also realized. Dual-species Rydberg arrays are a promising candidate for large-scale quantum computation due to their capability for multi-qubit gate operations and crosstalk-free measurements for mid-circuit readouts. However, a dual-species optical tweezer array of an alkali atom and an alkaline-earth (like) atom, which combines the beneficial properties of both types of atoms, has yet to be realized. In this half of the thesis, I present details on the design and construction of an apparatus for dual-species Rydberg tweezer arrays of Rb (alkali) and Yb (alkaline-earth like).

ENGINEERING OPTICAL LATTICES FOR ULTRACOLD ATOMS WITH SPATIAL FEATURES AND PERIODICITY BELOW THE DIFFRACTION LIMIT
and
DUAL-SPECIES OPTICAL TWEEZER ARRAYS FOR RUBIDIUM AND YTTERBIUM FOR RYDBERG-INTERACTION-MEDIATED QUANTUM SIMULATIONS

by

Sarthak Subhankar

Dissertation submitted to the Faculty of the Graduate School of the
University of Maryland, College Park in partial fulfillment
of the requirements for the degree of
Doctor of Philosophy
2024

Advisory Committee:
Professor Steven Rolston (chair/co-advisor)
Professor Trey Porto (chair/co-advisor)
Professor Ian Spielman
Professor Nathan Schine
Professor Ronald Walsworth (Dean's representative)

To my parents and my kittens

Acknowledgments

In many ways, I am a lucky man. Not many people can claim to have met so many amazing individuals and have had the opportunity to learn from them. My life is richer for having met them and I will now take this opportunity to express my gratitude.

First and foremost, I would like to thank my intellectual powerhouses of advisers, Prof. Trey Porto and Prof. Steve Rolston. I am the scientist I am today because of you. You have been infinitely patient with me. Thank you for being there to answer my questions about physics and life when I showed up at your office door. I thank you for how generous you were with your time when my "Do you have a minute?" conversations frequently turned into half-hour sessions. I am very grateful for the trust you have in me and in my abilities. You have given me the freedom to try new things and learn from the error of my ways. At the same time, you did not miss an opportunity to celebrate my victories. You were there to show me the path when I strayed too far. It has been an experience of a lifetime and I am truly grateful to have you both as mentors. I am also extremely grateful to Prof. Ian Spielman, who became my adviser on the tweezer apparatus. You are a fountain of knowledge and every time I talk to you, I learn something new. Your clarity of thought and brilliance have been awe-inspiring. I thank you for your patience, guidance, and the freedom you gave me. I thank Prof. Alexey Gorshkov and Prof. Jake Taylor, both intellectual powerhouses, for the amazing opportunities I have had to work with them on theory projects. I also thank Prof. Fredrik Fatemi, the adviser on the nanofiber project, for showing me the beautiful

and elegant world of nanofiber quantum optics. Witnessing your brilliance and depth and breadth of knowledge has been breathtaking. I thank Prof. Gretchen Campbell for the scientific and technical advice she has given me over the years. I thank Prof. Nathan Schine and Prof. Ronald Walsworth for serving on my dissertation committee.

I am grateful to Dan, Zach, Neal, Ben, Matt, Peter, Hiro, Dalia, Ana, Mingshu, Qiyu, Dimitrios, Junheng, Monica, Hector, Avinash, Paco, James, Martin, Thomas, Monica, Patrick, Deniz, Martin, Yaxin, Sean for their camaraderie and for their willingness to share equipment with me.

I would not have reached the finish line without the support of the many lab mates and collaborators I have had over the years. Thank you Varun for taking me under your wing when I first joined the lab, training me to be an experimentalist, and for your tough love. Your ability to explain difficult concepts in simple terms has always amazed me. Thank you Yang for also teaching me how to be an experimentalist. I have always been amazed by your problem-solving ability. Your "eyes on the prize" approach has played a crucial role in my growth as a scientist. Thank you Przemek for collaborating with us and for being the person I could talk to about theory-related topics. Thank you Joe for teaching me how to run the lab and its various ins and outs. I have taken your "Slow is smooth. Smooth is fast" attitude to heart. Thank you Creston for being there to answer my scientific inquiries, even though we overlapped for only a few months. Thank you Alessandro for teaching me electronics. I am very grateful for your mentorship over the years. Your passion for electronics and building cool new devices is contagious. Thank you Carlos for being a friend and collaborator. You are one of the smartest and kindest people I have met. Thank you Tsz-Chun for being my lab mate for many years. I have always been amazed by your knack for electronics and everything computer-related. You have been patient with me

and for that I am grateful. Thank you Ahreum and Hyok for teaching me about the world of nanofibers. Thank you Gayathrini for introducing me to the world of atom interferometry. I know you are going to achieve great things. Thank you Wance for helping me with PDH locks. I have seen very few people who are as systematic and meticulous in their approach to experimental science as you are. I am lucky to have worked with you.

Kevin, I don't think words can express how grateful I am to you, brother. You and I have gone through the toughest times and have come out on the other side. I thank you for introducing me to the Ravens and the after-effect of having to go through the roller coaster of emotions together. Thank you for introducing me to new music. Oliver, I have been impressed with how quickly you understand concepts and get things up and running. Kevin and Oliver, you are both assets to the lab and are going to achieve great things in life. I know that I have been demanding at times and I thank you for being patient with me. Madi, the second half of this thesis would not have ended on a high note had it not been for your efforts. For that, I am extremely grateful. Marissa, it has been a pleasure to have supervised you. I am amazed at the speed with which you get devices up and running. Yulong, it was also a pleasure to have supervised you. Thank you for all your hard work. Your careful documentation has made it easier for me to write this thesis.

I am very grateful for the company of my dear friends Sabyasachi, Nick, Shouvik, Proma, Tim, Avik, Rohini, Long, Anurag, Harjot, Sandy, Clarissa, Subhojit, Vikram, Natalia, and Swarnav. I cherish the many fun times we have had together. I thank you for giving me an ear when I needed one and for lifting me up when I was down. Thank you Sabyasachi for being an amazing friend. You have played a pivotal role in shaping me into who I am today. You are like a brother to me. Thank you Tim for all our lunches together. Thank you Nick for our many movie and coffee adventures. Thank you Shouvik and Proma for feeding me and loving me dearly. You are like

family to me. Thank you Avik and Rohini for all the fun evenings we have had together. Thank you Long for your friendship and company over the years. Our trip to Peru together is something I will never forget. Thank you Anurag, my childhood friend, for always being there for me. Your laughter is contagious, and somehow you managed to make everything fun. Thank you Sandy for being the best office mate anyone could ask for. Thank you for sharing the highs and lows of graduate school with me. Now everytime I am at a crossroads, I will remember to ask myself "Have you tried taking an FFT?" Thank you Swarnav for teaching me the art of lifting weights. Thank you Harjot and Subhojit for the pizza, barbecue and beer nights. Thank you Vikram and Natalia for the potluck nights. I would be remiss if I did not acknowledge the support of the great roommates I have had over the years. Thank you Gavin, Braden, Rajeev, Adi, Ari, Sayantan, Ananya for your company and for picking up my slack.

I want to thank my sweet Clara for her patience, dedication, gentleness, and love. Your smile brightens my day. You always found a way to take my mind away from work and encourage me to enjoy the finer and the simpler things in life. For that, I am very grateful. My gratitude also extends to her family for making me a part of their fun adventures. The stress of my days melt away at the sight of my kittens Mika and Nugget. From them greeting me at the door, to Nugget purring like a jet engine, to Mika checking on me throughout the night, I am very lucky to have them in my life. I thank my math teacher, Saroj sir, for helping me see the beauty in mathematics and for truly believing in my abilities. In many ways, I am who I am today because of you. Last but not least, I am forever grateful to my lovely parents for their many sacrifices, dedication, and love. They have been a constant pillar of strength my entire life, and I would not have made it this far without them cheering me on every step of the way. I thank you for always believing in me even when I did not. Thank you for giving me hope when I was without it. Although oceans

separate us, I always feel like you are right here. I will love you always.

Table of Contents

Dedication ii

Acknowledgements iii

Table of Contents viii

List of Tables xi

List of Figures xii

I Engineering optical lattices for ultracold atoms with spatial features and periodicity below the diffraction limit 1

Chapter 1: Introduction 2

Chapter 2: Dark State Optical Lattice with a Subwavelength Spatial Structure 4
2.1 Summary . . . 6
2.2 Hardware development . . . 9

Chapter 3: Nanoscale Atomic Density Microscopy 12
3.1 Summary . . . 13
3.2 Hardware and software development . . . 18

Chapter 4: Floquet engineering of optical lattices with spatial features and periodicity below the diffraction limit 21
4.1 Summary . . . 22

Chapter 5: Realization of a stroboscopic optical lattice for cold atoms with subwavelength spacing 28
5.1 Summary . . . 29

II Dual-species optical tweezer arrays for Rubidium and Ytterbium for Rydberg-interaction-mediated quantum simulations 33

Chapter 6: Introduction 34

Chapter 7: Design and construction of a dual-species Rydberg tweezer array apparatus **40**
7.1 Design and construction of the Ultra-High Vacuum (UHV) chamber assembly . . 42
7.1.1 The science chamber 42
7.1.2 The rest of the UHV chamber assembly 49
7.1.3 Atomic sources 56
7.1.4 Design and construction of electrodes for electric field control 62
7.2 Design and construction of the magnetic field coils and their housing 66
7.2.1 Mitigating coil heating 70
7.2.2 Driving the coils 73
7.3 Designing breadboards and UHV chamber carriage shaft assembly system 74
7.4 Ultra-Low Expansion (ULE) cavity design, installation, optics, and electronics . . 79
7.4.1 Design, installation, and optics 79
7.4.2 Electronics for generating the PDH error signal 85
7.4.3 Servo loop optimization for laser linewidth narrowing 88
7.5 Design and construction of low-NA optical systems 95
7.5.1 Rb MOT lasers and frequency-locking electronics 97
7.5.2 Yb MOT lasers and frequency-locking electronics 103
7.5.3 Design and construction of the optical layouts for the Rydberg lasers . . . 108
7.5.4 Launch optics for the AOD-based and SLM-based tweezer projection systems 120
7.5.5 Design and construction of the imaging launch 122
7.6 Design and construction of high-NA optical systems 122
7.6.1 Minimizing RMS $OPD_{fabrication}$ 132
7.6.2 Minimizing RMS OPD_{design} 138
7.6.3 Minimizing RMS $OPD_{alignment}$ 156
7.7 Towards trapping single atoms 175
7.7.1 3D MOTs of Rb and Yb 175
7.7.2 Optical tweezers of single ^{87}Rb atoms 179
7.8 Outlook 180

Appendix A: Dark State Optical Lattice with a Subwavelength Spatial Structure **182**

Appendix B: Microcontroller based scanning transfer cavity lock for long-term laser frequency stabilization **200**

Appendix C: Nanoscale Atomic Density Microscopy **207**

Appendix D: Floquet engineering of optical lattices with spatial features and periodicity below the diffraction limit **218**

Appendix E: Realization of a stroboscopic optical lattice for cold atoms with subwavelength spacing **236**

Appendix F: Cleaning machined parts for UHV assembly **243**

Appendix G: Drawings of the machined parts **247**

Appendix H: Glass cell cleaning and handling **273**
H.1 Glass cell handling instructions from Precision Glassblowing 273
H.2 Cleaning the RAR nanotextured windows of the glass cell 274

Appendix I: Aligning the tweezer projection systems **275**

Bibliography **280**

List of Tables

7.1 Electrical and mechanical specifications of our solenoid coils 69
7.2 Power supply and current settling time for each solenoid coil 74
7.3 Coherent illumination vs. Incoherent illumination 126
7.4 Specifications for the custom optics from Alluxa Inc. 133
7.5 Wavefront aberration polynomial coefficients expressed in terms of Seidel sums [ ] 142
7.6 Specifications of the spatial light modulators (SLM) from Meadowlark. The format for these SLMs is 1024×1024, the pixel pitch is 17.0μm$\times 17.0\mu$m, fill factor is 97.2 % 155

List of Figures

2.1 Level structures and experimental geometry. (a) The three levels in $^{171}\mathrm{Yb}$ used to realize the dark state are isolated from the fourth $^3P_1, m_F = +1/2$ state by a large magnetic field. They are coupled by a strong σ^-polarized control field Ω_c (green) and a weak π polarized probe field Ω_p (orange). The resulting dark state is a superposition of the ground states $|g_1\rangle$ and $|g_2\rangle$, with relative amplitudes determined by $\Omega_c(x)/\Omega_p$. (b) Spatial dependence of the dark state composition is created using a standing wave control field $\Omega_c(x)$ and a traveling wave probe field Ω_p. The geometric potential $V(x)$ (black) arises as the dark state rapidly changes its composition near the nodes of the standing wave. (c) The two counter-propagating σ^-beams creating the standing wave are aligned with a strong magnetic field along x, while the π beam travels along y. 5

3.1 Principle of a wavefunction microscope. (a) Configuration of the control field $\Omega_c(x)$ and probe field Ω_p. (b) Wavefunction $\psi(x)$ in $|g_1\rangle$ in the lattice of interest $V(x)$. (c) The spin state composition is transferred to $|g_2\rangle$ near the nodes of $\Omega_c(x - x_0)$ with probability density given by $f(x - x_0)$ (narrow red peaks), and $|g_1\rangle$ elsewhere. The width of $f(x - x_0)$ is determined by the relative strength of the two light fields $\epsilon = \Omega_p/\Omega_c$. (d) $f(x-x_0)$ maps $|\psi(x)|^2$ onto the population in $|g_2\rangle$, $n(x_0)$, which can be selectively measured via state-dependent imaging. By stepping through different positions x_0 and measuring $n(x_0)$, we can reconstruct $|\psi(x)|^2$ (indicated by the dashed curve). 14

3.2 Arbitrary waveform generator hardware schematic 17

3.3 A typical sequence for the Rabi frequencies of the different light fields and the relative phase ϕ between Ω_{c1} and Ω_{c2} for generating $\lambda/4$ subwavelength-spaced lattices. The stage III is when the wavefunction microscope is implemented. . . . 19

4.1 **(a)** An ideal Λ-system with inverse lifetime Γ and single-photon detuning Δ. One leg of the Λ-system is coupled by a spatially homogeneous and temporally varying probe light field $\Omega_p(t)$ and the other leg by a spatially inhomogeneous and temporally varying control light field $\Omega_c(x,t)$. **(b)** The geometry of the light fields with arbitrary control over the envelope, $\Omega_{c1}(t)$, $\Omega_{c2}(t)$, $\Omega_p(t)$ and phase, $\phi_1(t)$, $\phi_2(t)$ of each light field. **(c)** (i) The instantaneous (at $t = 0$) spatial dependence of the light fields $\Omega_c(t)|\cos(kx+\phi(t))|$ and $\Omega_p(t)$, (ii) the probability densities of the spin composition of the dark-state eigenfunction $|\psi(x,t)\rangle$ i.e. $|\langle 1|\psi(x,t)\rangle|^2$ and $|\langle 2|\psi(x,t)\rangle|^2$, and (iii) the instantaneous shape of $W_{DS}(x,t)$. **(d)** Typical pulse shapes considered here for the control beams $\Omega_{c(i)}(t) = 2\Omega_{c1(i)}(t) = 2\Omega_{c2(i)}(t)$, probe beam $\Omega_{p(i)}(t)$, and phase $\phi_i(t)$ for the ith sub-Floquet period where $-T_i/2 \leq t \leq T_i/2$ that determines the time-averaged potential $W_{\text{avg}}(x)$. . 23

4.2 The stroboscopic approach to creating a time-averaged effective potential with a lattice spacing of $\lambda/4$ by dynamically pulsing KP potentials with $\lambda/2$ spacing. . . 25

5.1 (a) The stroboscopically applied potential, shown here for $\Omega_{c0} = 500\Gamma$ and $\Omega_p = 50\Gamma$, is composed of KP barriers on top of a sinusoidal potential. The dotted line represents the potential shifted by $\lambda/4$. (b) The time-averaged effective potential $V_{\text{eff}}(x)$. (c) The black points are the measured $|\psi_{\text{avg}}(x)|^2$ of atoms in $V_{\text{eff}}(x)$. Number fluctuations between realizations result in number uncertainties of 5%. The black line is the calculation based on independently measured lattice parameters. The grey line is the calculated $|\psi_{\text{avg}}(x)|^2$ in the lattice before the relaxation during the measurement. (d) The micromotion dynamics at different time within a Floquet period. The blue(red)-shaded areas represent regions in which $|\psi(x,t)|^2$ is higher(lower) than $|\psi_{\text{avg}}(x)|^2$, which is shown as a solid black line. 32

6.1 Relevant electronic level structure for (a) Rb and (b) Yb 36

7.1 Evolution of the lab over the years. 41
7.2 Drawing of the dodecagonal glass cell from Precision Glassblowing. 43
7.3 Anti-reflection properties of the RAR nanotextured surfaces. 44
7.4 Aberrations induced in a perfectly spherical wavefront upon transmission through a glass plate [2, 3, 4]. Notice that the primary wavefront aberrations follow the typical wavefront aberration polynomial structure $\text{NA}^m\theta^{4-m}$. 46
7.5 50
7.6 CAD design of the UHV chamber assembly 52
7.7 (a) The UHV chamber assembly (b) The glass cell. 56
7.8 Rb dispensers modules: (a) CAD design (b) Assembling the modules. 57
7.9 CAD design for the Yb 2D MOT source 58
7.10 schematic of the optical layout for the Yb 2D MOT source 59
7.11 Yb 2D MOT cloud 61
7.12 Design, assembly, and installation of the electrode assembly 63

7.13 (a) CAD design for the housing for the magnetic field coils i.e. the coil housing (b) The fully assembled coil housing (c) Cross-section of the coil housing showing the shallow angle MOT beam paths . . . 67
7.14 (a) The coil winding jig for the rectangular/shim coils (b) The coil winding jig for the MOT coils (c) Using handscrew clamp to prevent the shim coils from bowing outward during winding (d) The potted MOT coils wound to their PEEK frames . 70
7.15 Manifold for cooling the MOT coils with pressurized and filtered dry nitrogen . . 71
7.16 Orthocyclically-wound unsupported potted coils . . . 72
7.17 The control voltage input of the BOPs driven with a 0-10 V Vpp 100 Hz square wave (yellow trace) and the measured voltage across the BOP output (cyan trace) (a) without damping circuits (b) with damping circuits. . . . 74
7.18 CAD design of the breadboard layout . . . 75
7.19 The assembled breadboards and carriage shaft assembly . . . 76
7.20 CAD design for the carriage shaft assembly for translating the mounted UHV chamber assembly. . . . 77
7.21 Solid aluminum glass cell mock-up . . . 79
7.22 (a) Installing the four-bored reference cavity block in its temperature-controlled high-vacuum housing (b) The arrangement of the reference cavity bores. . . . 81
7.23 . . . 82
7.24 (a) The vibration isolation boxing for the 420 nm laser (b) The vibration isolation boxing for the ULE cavity and its associated optics . . . 85
7.25 The ESB PDH error signals as a function of laser frequency detuning $\Delta\Omega$ where $\Delta\Omega = \Omega_0 + \Omega_c - 2\pi N \times$ FSR: we use laser light at 1112 nm, a high-finesse ULE reference cavity, and a fiber-coupled EOM driven by the high-quality phase-modulated rf signal from (a) the ADL5375-based design (b) and the ADALM-PLUTO-based design. . . . 88
7.26 The feedback control system for laser frequency stabilization in the presence of noise. . . . 90
7.27 Closed-loop transfer function measurement protocol/formalism. . . . 93
7.28 Layout of the low-NA optical systems around the glass cell as viewed from the front . . . 96
7.29 Layout of the low-NA optical systems around the glass cell as viewed from the top 97
7.30 Rb master laser optical layout and frequency locking feature . . . 98
7.31 The schematic of the optical layout for the (a) Rb repump laser (b) Rb cooling laser . . . 100
7.32 The layout of the optical phase locked loop electronics for stabilizing the frequency of the Rb cooling laser and Rb repump laser . . . 101
7.33 Single-mode PM fiber splitter/combiner with 2 inputs and 8 outputs for delivering Rb 3D MOT light . . . 103
7.34 Schematic of the optical layout for 399 nm laser system . . . 104
7.35 Schematic of the optical layout of the 556 nm laser system . . . 106
7.36 Two-photon Rydberg excitation . . . 109
7.37 Schematic of the optical layout of (a) the 420 nm laser system, (b) the 420 nm Rydberg excitation launch . . . 113
7.38 Schematic of the optical layout for the 1013 nm laser system. . . . 114

7.39 Schematic of the optical layout of the 556 nm Rydberg excitation launch 116
7.40 Schematic of the optical layout of the 308 nm laser system 118
7.41 Schematic of the optical layout for the launch side of the AOD-based and SLM-based tweezer projection systems. 119
7.42 General structure of an imaging system 124
7.43 My general strategy for creating diffraction-limited optical tweezers 131
7.44 Specifications of our 0.6 NA objectives from Special Optics. 136
7.45 CAD design of the V block mount for the objectives 137
7.46 Seidel diagram for the AOD-based tweezer projection system up to the entrance aperture of the objective for Yb 143
7.47 Schematic of the optical layout for the AOD-based tweezer projection system. The AOD is driven by a sum of three single tone sinusoidal waveforms, as an example. The optical layout for the SLM-based tweezer projection system is the same except it lacks the first $4f$ Keplerian f_1/f_0 magnification stage. 145
7.48 Schematic of the optical layout for the AOD-based tweezer projection systems. . 148
7.49 Schematic of the optical layout for the SLM-based tweezer projection systems. . 149
7.50 Zemax simulation of the optimized third-order layout for the AOD-based tweezer projection system for Rb: (a) Wavefront map at field angle of $0°$ (b) Wavefront map at the maximum field angle of $-1.5°$ (c) Spot diagrams at different field angles 151
7.51 Zemax simulation of the optimized third-order layout for the AOD-based tweezer projection system for Yb: (a) Wavefront map at field angle of $0°$ (b) Wavefront map at the maximum field angle of $-1.5°$ (c) Spot diagrams at different field angles 152
7.52 Zemax simulation of the optimized third-order layout for the SLM-based tweezer projection system for Rb: (a) Wavefront map at field angle of $0°$ (b) Wavefront map at the maximum field angle of $-0.4°$ (c) Spot diagrams at different field angles 153
7.53 Zemax simulation of the optimized third-order layout for the SLM-based tweezer projection system for Yb: (a) Wavefront map at field angle of $0°$ (b) Wavefront map at the maximum field angle of $-0.4°$ (c) Spot diagrams at different field angles 154
7.54 (a) AOD diffraction pattern (b) Beam profile of the input beam to the AOD (c) Beam profile of the diffracted beam at the output of the AOD 157
7.55 Schematic of the optical layouts for the Twyman-Green interferometer and the Fizeau interferometers 158
7.56 The schematic of the optical layout for the Twyman-Green-Fizeau interferometer: The Roman numerals represent the order in which the highlighted cyan sections of the interferometer are assembled. 160
7.57 The grid size is 1 mm. (a) Tip/tilt fringe (b) Newton's rings showing the bowing of the glass cell window with a decentered laser beam (c) Newton's rings showing the bowing of the glass cell window with a centered laser beam. 163
7.58 The interferogram for when the objectives are well aligned. This interferogram is representative of the minimum coma condition. The grid size is 1 mm. 165
7.59 The optical rail-based construction of (a) (b) the AOD-based tweezer projection systems, (c) (d) SLM-based tweezer projection systems 169
7.60 (a) The standard Gerchberg-Saxton (G-S) algorithm (b) My modification to the G-S algorithm for fast frame generation. 173

7.61 SLM generated image measured by the camera placed at an image plane in the SLM-based tweezer projection system . . . 175
7.62 A 3D MOT of ^{87}Rb atoms in the shallow-angle arm arrangement . . . 176
7.63 Absorption imaging of $\sim 100,000$ ^{87}Rb atoms sub-Doppler cooled to $\sim 30\mu$K in the shallow-angle arm arrangement . . . 176
7.64 A 3D MOT of ^{174}Yb atoms (a) in the blue shallow-angle arm arrangement (b) in the simultaneous blue plus green shallow-angle arm arrangement . . . 178
7.65 Absorption imaging of a cloud of $\sim 3\times10^6$ ^{174}Yb atoms cooled to $\sim 30-50\mu$K in the green 3D MOT shallow-angle arrangement. . . . 179
7.66 30 shot averaged image of ^{87}Rb atoms stochastically loaded into a 2x3 optical tweezer array. The $x-$ and $y-$ axes are in units of number of pixels. . . . 181

F.1 The workstation for cleaning machined parts for UHV operation. . . . 244
F.2 I am scrubbing the clamshell protectors . . . 246

G.1 Drawing of the clamshell protector for the glass cell . . . 248
G.2 Drawing of the base that supports the clamshell protectors . . . 249
G.3 Drawing of the custom post that prevents the UHV chamber from rotating about the mounting brackets . . . 250
G.4 Drawing of the sleeve for the Rb dispensing modules. The sleeve connects two dispensers together. . . . 251
G.5 Drawing of the adapter for the Rb dispensing modules. The adapter connects the dispenser to the conductors of the electrical feedthroughs. . . . 252
G.6 Drawing of the electrode holder . . . 253
G.7 Drawing of the electrode clamp . . . 254
G.8 Drawing of the small MACOR ring . . . 255
G.9 Drawing of the small MACOR ring . . . 256
G.10 Drawing of the long alumina rod . . . 257
G.11 Drawing of the short alumina rod . . . 258
G.12 Drawing of the MOT coil housing frame . . . 259
G.13 Drawing of the SLM breadboard . . . 260
G.14 Drawing of the objective breadboard . . . 261
G.15 Drawing of the upper vertical breadboard . . . 262
G.16 Drawing of the bottom vertical breadboard . . . 263
G.17 Drawing of the AOD breadboard . . . 264
G.18 Drawing of the machined shelf . . . 265
G.19 Drawing of the custom pillow block carriage assembly . . . 266
G.20 Drawing of the custom pre-aligned dual shaft assembly . . . 267
G.21 Drawing of the back holder . . . 268
G.22 Drawing of the front holder . . . 269
G.23 Drawing of the V block mount for the objectives . . . 270
G.24 Drawing of the custom mounting plate for translating the mounted objective . . . 271
G.25 Drawing of the PEI ULTEM 1/2-13 setscrews . . . 272

Part I

Engineering optical lattices for ultracold atoms with spatial features and periodicity below the diffraction limit

Chapter 1: Introduction

The first half of this dissertation summarizes a series of investigations, both experimental and theoretical, that culminate in the realization of an optical lattice with a subwavelength spacing of $\lambda/4$. To realize this lattice, we first generated a Kronig-Penney-like optical lattice using the nonlinear optical response of three-level atoms in spatially varying dark states. This conservative Kronig-Penney-like optical potential has strongly subwavelength barriers that can be less than 10 nm ($\equiv \lambda/50$) wide and are spaced $\lambda/2$ apart, where λ is the wavelength of light used to generate the optical lattice. Using the same nonlinear optical response, we developed a microscopy technique that allowed the probability density of atoms in optical lattices to be measured with a subwavelength resolution of $\lambda/50$. We theoretically investigated the feasibility of stroboscopically pulsing spatially shifted 1D Kronig-Penney-like optical lattices to create lattices with subwavelength spacings. We applied the lattice pulsing techniques developed in this theoretical investigation to realize a $\lambda/4$-spaced optical lattice. We used the subwavelength resolution microscopy technique to confirm the existence of this $\lambda/4$-spaced optical lattice by measuring the probability density of the atoms in the ground band of the $\lambda/4$-spaced optical lattice.

The first half of the thesis is organized around four published papers, each chapter summarizing the results of a paper:

- Chapter 2: Y. Wang, **S. Subhankar**, P. Bienias, and M. Łacki, T.-C. Tsui, M. A. Baranov, A. V. Gorshkov, P. Zoller, J. V. Porto, and S. L. Rolston, Dark State Optical Lattice with a Subwavelength Spatial Structure, Phys. Rev, Lett, 120, 083601 (2018).

- Chapter 3: **S. Subhankar**, Y. Wang, T.-C. Tsui, S. L. Rolston, and J. V. Porto, Nanoscale Atomic Density Microscopy, Phys. Rev. X 9, 021002 (2019).

- Chapter 4: **S. Subhankar**, P. Bienias, P. Titum, T.-C. Tsui, Y. Wang, A. V. Gorshkov, S. L. Rolston, and J. V. Porto, Floquet engineering of optical lattices with spatial features and periodicity below the diffraction limit, New J. Phys. 21, 113058 (2019).

- Chapter 5: T.-C. Tsui, Y. Wang, **S. Subhankar**, J. V. Porto, and S. L. Rolston, Realization of a stroboscopic optical lattice for cold atoms with subwavelength spacing, Phys. Rev. A 101,041603(2020).

Each chapter shares the title of the paper it summarizes. The published papers can be found in their entirety in the appendix. Other publications that did not make it to the first half of the dissertation:

- **S. Subhankar**, A. Restelli, Y. Wang, S. L. Rolston, J. V. Porto, Microcontroller based scanning transfer cavity lock for long-term laser frequency stabilization, Rev. Sci. Instrum. 90, 043115 (2019).

- P. Bienias, **S. Subhankar**, Y. Wang, T-C. Tsui, F. Jendrzejewski, T. Tiecke, G. Juzeliūnas, L. Jiang, S. L. Rolston, J. V. Porto, and A. V. Gorshkov, Coherent optical nanotweezers for ultracold atoms, Phys. Rev. A 102, 013306 (2020)

Chapter 2: Dark State Optical Lattice with a Subwavelength Spatial Structure

Coherent control of the position and motion of atoms with light has been a primary enabling technology in the physics of ultracold atoms. The paradigmatic examples of conservative optical potentials are the optical dipole trap and optical lattices, generated by far off-resonant laser fields, with the ac-Stark shift of atomic levels as the underlying mechanism. The spatial resolution for such optical potential landscapes is determined by the diffraction limit, which is of the order of the wavelength of light λ. This fundamentally limits optical manipulation of atoms. For example, in quantum simulation with atoms in optical lattices, the minimum lattice constant is $\lambda/2$, setting the energy scale for Hubbard models for both hopping (kinetic energy) and interaction of atoms, with challenging temperature requirements to observe quantum phases of interest [5]. Developing tools to overcome the diffraction limit, allowing coherent optical manipulation of atoms on the subwavelength scale, is thus an outstanding challenge.

In this chapter, I summarize the results of our paper, in which we report first experiments demonstrating coherent optical potentials with subwavelength spatial structure, by realizing a Kronig Penney-type optical lattice with barrier widths less than 10 nm $\equiv \lambda/50$, where λ is the wavelength of light used to create the potential. These strongly subwavelength spatial structures arise from the non-linear optical response of three-level atoms in dark states to spatially varying light fields. Even on resonance, the observed lifetimes of atoms trapped in the lattice are as long as

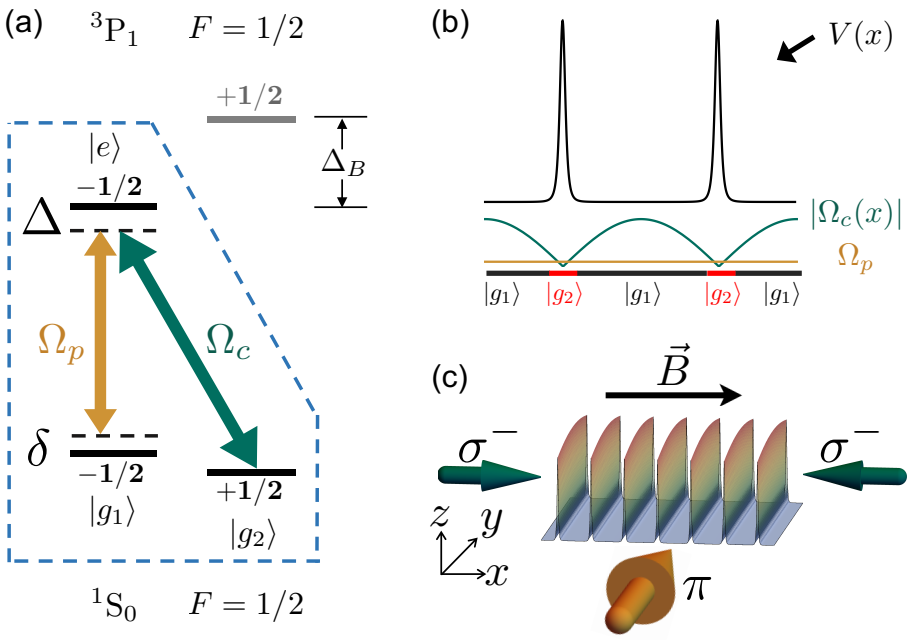

Figure 2.1: Level structures and experimental geometry. (a) The three levels in $^{171}\mathrm{Yb}$ used to realize the dark state are isolated from the fourth $^3P_1, m_F = +1/2$ state by a large magnetic field. They are coupled by a strong σ^-polarized control field Ω_c (green) and a weak π polarized probe field Ω_p (orange). The resulting dark state is a superposition of the ground states $|g_1\rangle$ and $|g_2\rangle$, with relative amplitudes determined by $\Omega_c(x)/\Omega_p$. (b) Spatial dependence of the dark state composition is created using a standing wave control field $\Omega_c(x)$ and a traveling wave probe field Ω_p. The geometric potential $V(x)$ (black) arises as the dark state rapidly changes its composition near the nodes of the standing wave. (c) The two counter-propagating σ^-beams creating the standing wave are aligned with a strong magnetic field along x, while the π beam travels along y.

$44\ \mathrm{ms}$, nearly 10^5 times the excited state lifetime, and could be further improved with more laser intensity. The potential is readily generalizable to higher dimensions and different geometries, allowing, for example, nearly perfect box traps, narrow tunnel junctions for atomtronics applications, and dynamically generated lattices with subwavelength spacings.

The paper can be found in its entirety in Appendix A. At the end of the chapter, I summarize the details on some of the hardware development that I did to help realize this project.

2.1 Summary

The main ingredient for realizing a Kronig-Penney-like optical lattice is a three-level system in a Λ configuration: two ground states $|g_1\rangle$, $|g_2\rangle$ and an excited state $|e\rangle$ (Fig. 2.1a). A spatially varying strong control field $\Omega_c(x) = \Omega_c \sin(kx)$ couples the $|g_2\rangle \leftrightarrow |e\rangle$ transition and a constant amplitude weak probe field Ω_p couples the $|g_2\rangle \leftrightarrow |e\rangle$ transition. Within the Born-Oppenheimer (BO) approximation, slowly moving atoms in the dark state $|E_0(x)\rangle$ are decoupled from the excited state $|e\rangle$, where $|E_0(x)\rangle = \sin(\alpha)\,|g_1\rangle - \cos(\alpha)\,|g_2\rangle$ and $\alpha(x) = \arctan\left(\Omega_c(x)/\Omega_p\right)$. The two bright states $E_\pm(x)$ have excited state component $|e\rangle$, leading to light scattering. Given this light field arrangement, the dark state changes composition over a narrow region, depending on the ratio $\epsilon = \Omega_p/\Omega_c$. The kinetic energy associated with this large gradient in the spin wave function gives rise to a conservative optical potential $V(x)$ for atoms in $|E_0(x)\rangle$ (Fig. 2.1b),

$$V(x) = \frac{\hbar^2}{2m}\left(\frac{d\alpha}{dx}\right)^2 = E_R \frac{\epsilon^2 \cos^2(kx)}{\left(\epsilon^2 + \sin^2(kx)\right)^2}, \tag{2.1}$$

where $k = 2\pi/\lambda, E_R = \hbar^2 k^2/2m$ is the recoil energy, and m is the mass of the atom. The potential $V(x)$ can be viewed as arising from nonadiabatic corrections to the BO potential or artificial scalar gauge potential. When $\epsilon \ll 1$, this creates a lattice of narrow barriers spaced by $\lambda/2$, with the barrier height scaling as $1/\epsilon^2$ and the full width at half maximum scaling as $0.2\lambda\epsilon$. Unlike ac-Stark shift potentials, this twist-induced potential is a quantum effect, with its magnitude proportional to $\hbar^2$.

We realize the Λ configuration using three states selected from the $|^1S_0, F = 1/2\rangle$ and $|^3P_1, F = 1/2\rangle$ hyperfine manifolds in ^{171}Yb cooled to a temperature of $\simeq 300$ nK ($T/T_F = 1.10$,

where T_F is the Fermi temperature). The two ${}^1S_0$ ground states $m_F = \pm 1/2$ comprise the lower two states $|g_1\rangle$ and $|g_2\rangle$ (see Fig. 2.1a). The $|{}^3P_1, \quad m_F = -1/2\rangle$ state, with inverse lifetime $\Gamma = 2\pi \times 182$ kHz, makes up the third state $|e\rangle$ in the Λ configuration. The $|g_i\rangle \rightarrow |e\rangle$ transitions are isolated from the transition to the other $|{}^3P_1, m_F = +1/2\rangle$ state by applying a 12 mT magnetic field $\vec{\boldsymbol{B}}$ to Zeeman split the two ${}^3P_1$ states by $\Delta_B = 1.8 \times 10^3 \Gamma$. The same field slightly splits the ${}^1S_0$ ground states by -0.5Γ due to the small nuclear magnetic moment. The standing-wave control field $\Omega_c(x)$, traveling along $\vec{\boldsymbol{B}}$, is produced by two counterpropagating σ^-laser beams that couple the $|g_2\rangle$ and $|e\rangle$ states with amplitudes $\Omega_{c1}e^{ikx}$ and $\Omega_{c2}e^{-ikx}$. A third beam, π polarized and traveling normal to $\vec{\boldsymbol{B}}$, couples the $|g_1\rangle$ and $|e\rangle$ states with amplitude $\Omega_p e^{iky}$ (see Fig. 2.1c). The frequency of the control and probe beams can be chosen to set the single and two-photon detunings, Δ and δ. We define $\delta = 0$ as the dark state condition for the isolated three-level system, accounting for the Zeeman splitting. Off-resonant couplings to other states can introduce light shifts, which require nonzero δ to maintain the dark state condition.

In order to confirm the creation of the dark state optical lattice, we probe its bandstructure. For small ϵ, this lattice maps to a ID KP model. One characteristic feature of the KP lattice is that the energy of the n th-band scales as $n^2 E_R$, such that the band spacing increases with n, which we confirm experimentally. In contrast, in a deep sinusoidal lattice, the band spacing decreases with n. To map out the bandstructure, we excite atoms from the ground (s) band into the higher bands by shaking the lattice by phase modulating of one of the σ^-beams. After band mapping, we measure the band populations, which become separated after time-of-flight (TOF).

Finally, we study dissipation in the dark state optical lattice. The nonadiabatic corrections to the BO potential that give rise to $V(x)$ also weakly couple the dark state with the bright states, which leads to light scattering, heating the atoms out of the trap. We measure the lifetime τ in

a dark state lattice for different Δ and find it significantly longer for $\Delta > 0$ than for $\Delta < 0$. This is in contrast to an optical lattice based on ac-Stark shifts, where heating is independent of the sign of Δ. To intuitively understand this asymmetry, we note that the coupling to the bright states takes place inside the barrier. An atom can scatter light by admixing with the bright states $E_{+}(x)$ (approximately Δ independent) or exiting into the energetically-allowed $E_{-}(x)$ state via nonadiabatic couplings (strongly Δ dependent). The $E_{-}(x)$ state contributes more to the loss, explaining the Δ asymmetry. The nonadiabatic bright state coupling also leads to a counterintuitive dependence of the dissipation on the laser power. Remarkably, the lifetime increases with Rabi frequency. In contrast, for a regular optical lattice at a fixed detuning, the lifetime does not improve with more laser power. For the dark state lattice, larger $\Omega_{c,p}$ increases the separations between BO potentials, resulting in decreased scattering. In general, the lifetime improves with more laser power and at blue detuning. With realistic increase in laser intensity, we can potentially improve the lifetime by an order of magnitude, while maintaining the ultranarrow barriers.

The conservative nanoscale optical potential demonstrated here adds to the toolbox of optical control of atoms, enabling experiments requiring subwavelength motional control of atoms. Such sharp potential barriers could be useful for the creation of narrow tunnel junctions for quantum gases or for building sharp-wall box-like traps. In addition, spin and motional localization on small length scales can enhance the energy scale of weak, long range interactions. The dark state lattice can be generalized to 2D and, for example, can be used to study Anderson localization with random strength in the barrier height. By stroboscopically shifting the lattice, the narrow barriers should enable optical lattices with spacings smaller than the $\lambda/2$ spacing set by the diffraction limit, which would significantly increase the characteristic energy scales

relevant for interacting many-body atomic systems.

2.2 Hardware development

I, along with the post-doc on the experiment, Yang Wang, built the hardware for all the experiments presented in the first half of this thesis. For example, we upgraded the high-current supply circuits. The current in the bias coils needed to be go as high as 300 A as large magnetic fields (as large as 360 G) were needed to create a well-isolated three-level system. We built the optics for the three 556 nm laser beams (Ω_{c1}, Ω_{c2}, and Ω_p) used in the experiments. I built the rf drivers for controlling the phase and amplitude pulsing of the 556 nm laser beams. Here are a few more things that were important in realizing the experiments in the first half of this thesis:

- **Building the fiber-based Yb 2D MOT source:** The original Yb 2D MOT source delivered $399\ \mathrm{nm}$ cooling light via free-space optics. The atom number was highly sensitive to drifts in the alignment of the free-space optics. We had to re-align the 2D MOT optics often, sometimes once or twice a week. We knew that a fiber-based 2D MOT source would be much more stable but did not have sufficient power to overcome the losses associated with fiber-coupling.

  In September 2016, we upgraded the TA chip on the 399 nm TA–DL SHG Pro system. This upgrade increased the 399 nm laser output power from 200 mW to 570 mW and made a fiber-based 2D MOT setup for Yb feasible. The new setup had much higher passive stability on the order of months in comparison to the free-space 2D MOT setup. I designed and built the fiber-based Yb 2D MOT setup.

- **Building the scanning transfer cavity lock setup for locking the frequency of the**

399 nm laser: Before I joined the lab, we used a DAVLL (Dichroic Atomic Vapour Laser Lock) [6, 7] in a hollow cathode cell for locking the frequency of the 399 nm laser frequency to the $(6s^2)^1S_0 \longrightarrow (6s6p)^1P_1$ atomic transition in Yb. However this lock was unstable. It would break every few hours. The error signal would randomly jitter up and down at amplitudes much greater than the capture range of the lock, despite using clean polarized light in the setup. We were never able to isolate the source of this jitter and hence efforts were made to lock the laser in different ways, specifically the scanning transfer cavity lock (STCL) (Appendix. B). I suggested using the 780 nm master laser [8, 9] that was locked to the $^{85}\mathrm{Rb}, F = 3 \leftrightarrow F' = 3-4$ crossover resonance via saturation-absorption spectroscopy as the frequency reference, and the 399 nm laser fundamental at 798 nm as the slave laser for the STCL lock. I designed and built the STCL setup, which we have used ever since. We wrote a paper about this setup and the details can be found in Appendix B.

- **Building the OPLL lock for the NKT seed**: Before I joined the lab, we had an OrangeOne laser operating at 1112 nm from Menlo Systems which pumped a periodically-poled lithium niobate (PPLN) wave-guided doubling crystal in order to generate 556 nm laser light. This laser system was locked to the $6s^2\ {}^1S_0 \leftrightarrow 6s6p^3\ P_1$ via saturation absorption spectroscopy [8, 9]. However, this laser system was the bane of my predecessors and malfunctioned multiple times, including one time after I joined the lab [8, 9]. Each repair took approximately two months as the laser or the doubling crystal had to be shipped back to Germany. We bought a second laser system (see 7.5.2.2) to serve as a back up. For the experiments presented in this thesis, this second laser system proved to be invaluable as it was used to generate all the three laser beams used in the experiments presented in the first half of the thesis: Ω_{c1}, Ω_{c2},

and Ω_p. In order to tune the frequency of the new 556 nm laser, I built a setup for optical phased-locked loop [10] locking of the frequency of the new laser to the old laser. We used Neal Pisenti's high voltage piezo-driver [11] for driving the piezoelectric transducer of the NKT seed. The OPLL circuit board—based on the design in Ref. [11]—was replicated here at JQI (https://github.com/JQIamo/beatnote-pll.git). We used 1112 nm light from the monitor port of both lasers for this beatnote lock.

- **Demagnetizing the chamber after each experimental shot:** Large magnetic fields in the range of 120 G to 360 G were needed to create the well isolated three-level system used in these experiments. However, this large magnetic field magnetized parts of the chamber at the end of every experimental sequence. The residual magnetization would then generate a weak bias field that shifted the position of the green Yb 3D MOT at the start of the subsequent sequence leading to fewer atoms in the Yb Fermi gas. Every subsequent experimental shot enhanced the strength of this residual magnetic field and eventually led to the complete annihilation of the Yb Fermi gas. I devised and implemented a simple protocol at the end of every experimental sequence where we would rapidly flip the orientation of the quadrupole magnetic field while ramping its amplitude down to zero. This oscillating and damped magnetic field removed the problematic magnetization.

Chapter 3: Nanoscale Atomic Density Microscopy

High spatial and temporal resolution microscopy can reveal the underlying physics, chemistry, and biology of a variety of systems. Examples range from the study of atoms on surfaces with atomic resolution scanning tunneling microscopy [12] to the use of superresolution microscopy to observe the dynamics of individual molecules within living cells [13]. The field of quantum simulation with ultracold atoms has emerged to study strongly correlated mAOMtems using precise control with light-atom interactions [5]. This entails confining atoms, engineering their interactions and potentials, and measuring their states with laser light. Based on fluorescence and absorption, the inherent imaging resolution is limited by diffraction. Bringing superresolution microscopy to the field of quantum simulation of condensed-matter systems with ultracold atoms will allow new direct probes of the wave function in a variety of many-body systems

In this chapter, I summarize the results of our paper on a technique that uses the nonlinear optical response of atoms to spatially and temporally varying laser fields introduced in the last chapter for superresolution imaging of the probability density of atoms with a spatial resolution of $\lambda/50$ and temporal resolution of $500\ \mathrm{ns}$. We characterize our microscope's performance by measuring the ensemble-averaged probability density of atoms within the unit cells of an optical lattice and observe the dynamics of atoms excited into motion.

The paper can be found in its entirety in Appendix C. At the end of this chapter, I elaborate

on the arbitrary waveform generator (AWG) that was critical in realizing the results presented in this chapter and chapter 5.

3.1 Summary

The basic principle of our approach is as follows (illustrated in Fig. 3.1). The dark state of a three-level atom in a Λ configuration (ground states $|g_1\rangle$, $|g_2\rangle$ and excited state $|e\rangle$) coupled by a standing-wave control field $\Omega_c(x) = \Omega_c \sin(kx)$ and homogeneous probe field Ω_p is:

$$|D(x)\rangle = \frac{1}{\sqrt{\Omega_c(x)^2 + \Omega_p^2}} \left[\Omega_c(x) |g_1\rangle - \Omega_p |g_2\rangle\right], \tag{3.1}$$

where $k = 2\pi/\lambda$, and λ is the wavelength of the light. For $\Omega_c \gg \Omega_p$, the resulting dark-state composition is predominantly $|g_1\rangle$ away from the nodes of $\Omega_c(x)$, and $|g_2\rangle$ near the nodes where $\Omega_p \gg |\Omega_c(x)|$. The probability density of $|g_2\rangle$ coming from this nonlinear dependence on the Rabi frequencies (Eq. 3.1) is periodic and has narrow peaks near the nodes

$$f(x) = \frac{\epsilon^2}{\epsilon^2 + \sin^2(kx)},$$

where $\epsilon = \Omega_p/\Omega_c$. The full width at half maximum (FWHM) σ of the peaks provides a good metric for the resolution within the unit cell $\lambda/2$. For $\Omega_c \gg \Omega_p$ (small ϵ), σ depends linearly on $\epsilon : \sigma \simeq \epsilon\lambda/\pi$, allowing resolution that greatly exceeds the diffraction limit. Starting with atoms in $|g_1\rangle$ with wave function $\psi(x)$, we can adiabatically transfer a narrow slice of atoms into $|g_2\rangle$. The wave-function probability density $|\psi(x)|^2$ can be determined by measuring the population

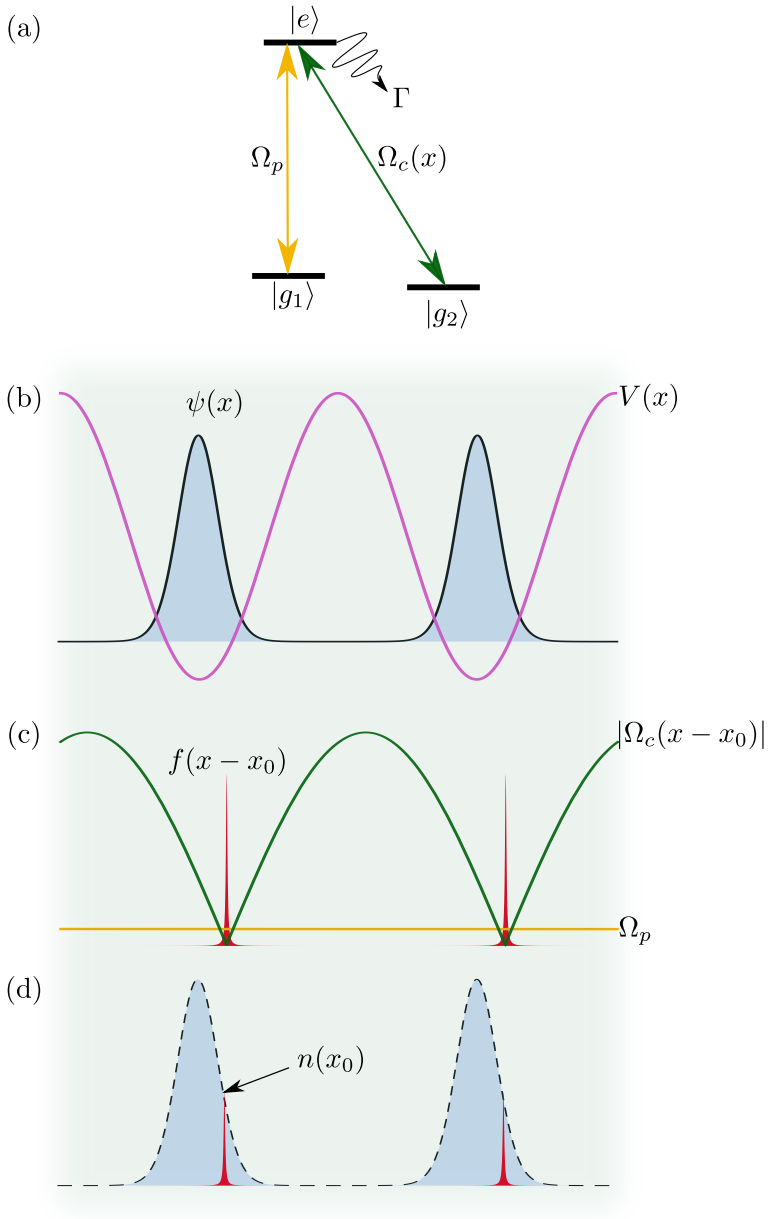

Figure 3.1: Principle of a wavefunction microscope. (a) Configuration of the control field $\Omega_c(x)$ and probe field Ω_p. (b) Wavefunction $\psi(x)$ in $|g_1\rangle$ in the lattice of interest $V(x)$. (c) The spin state composition is transferred to $|g_2\rangle$ near the nodes of $\Omega_c(x-x_0)$ with probability density given by $f(x-x_0)$ (narrow red peaks), and $|g_1\rangle$ elsewhere. The width of $f(x-x_0)$ is determined by the relative strength of the two light fields $\epsilon = \Omega_p/\Omega_c$. (d) $f(x-x_0)$ maps $|\psi(x)|^2$ onto the population in $|g_2\rangle$, $n(x_0)$, which can be selectively measured via state-dependent imaging. By stepping through different positions x_0 and measuring $n(x_0)$, we can reconstruct $|\psi(x)|^2$ (indicated by the dashed curve).

transferred to $|g_2\rangle$ at different locations x, yielding a signal

$$n(x) = \int |\psi(x')|^2 f(x' - x)\, dx'. \tag{3.2}$$

By deconvolving this signal with the probing function $f(x)$, we can reconstruct $|\psi(x)|^2$.

We use stimulated Raman adiabatic passage (STIRAP) to transfer the selected slices of the wave function from the state $|g_1\rangle$ into $|g_2\rangle$. In order to accurately measure the shape of the wave function, the STIRAP process must be adiabatic with respect to the spin degree of freedom (d.o.f.) (i.e., the dark-state composition given by Eq. 3.1) but diabatic with respect to the motional d.o.f. For small ϵ, the shortest duration of the STIRAP is inversely proportional to the Rabi frequencies. For typical trapped atoms experiments, Rabi frequencies can be tens of MHz, while the motional dynamics is on the order of tens of kHz.

We work with the three-level system in $^{171}\mathrm{Yb}$ cooled to a temperature of $\simeq 300\mathrm{nK}$ ($T/T_F = 1.10$, where T_F is the Fermi temperature), consisting of $|g_1\rangle = \left|^1S_0, F = \frac{1}{2}, m_F = -\frac{1}{2}\right\rangle$, $|g_2\rangle = |^1S_0, F = \frac{1}{2}, m_F = +\frac{1}{2}\rangle$, and $|e\rangle = \left|^3P_1, F = \frac{1}{2}, m_F = -\frac{1}{2}\right\rangle$, coupled by $\lambda = 556\,\mathrm{nm}$ light. The control field $\Omega_c(x)$ is formed by two counterpropagating σ^--polarized beams $\Omega_{c1}e^{ikx}$ and $\Omega_{c2}e^{-ikx}$ in the direction of the quantization axis defined by a magnetic field along $\hat{x}$, while the probe field Ω_p is a π-polarized traveling wave normal to the control beams. The Yb atoms are optically pumped into $|g_1\rangle$ with a final population approximately equal to 2×10^5. We measure $|\psi(x)|^2$ of spin-polarized Yb atoms loaded into either a Kronig-Penney- (KP) type lattice of thin barriers, or a regular sinusoidal lattice based on the ac Stark shift of $\Omega_{c1,2}$ off-resonantly coupled to the $|g_1\rangle \leftrightarrow \left|^3P_1, F = \frac{3}{2}, m_F = -\frac{3}{2}\right\rangle$ transition, which lies outside the three-level system making up the dark state.

Our microscope is implemented as follows. We first suddenly turn off the lattice potential $V(x)$ that supports the wave function to be probed by switching off the Ω_{c2} beam. Next, we ramp on Ω_p followed by Ω_{c2} with a different phase, which adiabatically flips the spin from $|g_1\rangle$ to $|g_2\rangle$ in the region tightly localized near the nodes of the shifted $\Omega_c\left(x'-x\right)=\Omega_c\sin\left(k\left(x'-x\right)\right)$. The intensity profiles for ramping these two beams are calculated to preserve adiabaticity, ensuring atoms follow the spatio-temporal dark state at all times. We then rapidly ramp off all beams simultaneously in order to preserve the dark-state composition. We measure the $|g_2\rangle$ population via state-selective absorption imaging. Scanning x in fine steps at small ϵ allows us to map out the $|\psi(x)|^2$ with high resolution.

We use our wave-function microscope to investigate atoms in sinusoidal and Kronig-Penney lattices. We measure the ground-state wave functions of these atoms within the unit cell of these optical lattices. We also study the dynamics of the wavefunction after a sudden quench in the position and depth of the sinusoidal optical lattices. The fast STIRAP slicing process allows for observing the wave-function dynamics. At our maximum Rabi frequency of $\Omega_c=2\pi\times 90\mathrm{MHz}$ and $\epsilon=0.05$, we can maintain the adiabaticity condition for a STIRAP time of $500\ \mathrm{ns}$, which sets the temporal resolution.

We estimate the spatial resolution of our microscope by measuring the narrowest wave function $|\psi(x)|^2$ that we can create with the breathing-mode excitation from quenching the depth of the sinusoidal optical lattice from 6 E_R to 140 E_R. This narrowest wave function $|\psi(x)|^2$ has a calculated FWHM of $w_0=26.2^{+1.6}_{-0.6}\ \mathrm{nm}$, where the uncertainty arises from the uncertainty in the Rabi-frequency calibrations used to determine the lattice depth for small ϵ. Following Eq. 3.2, by deconvolving the measured $n(x)$ with the calculated wave function ($|\psi(x)|^2$) and taking into account the $800\mathrm{ns}$ expansion time, we estimate the intrinsic resolution σ for different ϵ. The

smallest measured σ reaches $11.4^{+2.0}_{-4.4}$ nm.

The ultimate resolution is possibly limited by mechanical effects arising from the sharp potential associated with the dark state. As the slice width σ decreases, the total population in $|g_2\rangle$ also decreases, setting a practical limit on the usable resolution. Both the temporal and spatial could be improved with higher Rabi frequencies and signal-to-noise ratio.

The dark-state-based technique can be applied to image any atomic or molecular system as long as they host a three-level system, including the alkali atoms that are used in many experiments. Our subwavelength resolution already allows us to distinguish the different atomic wave functions trapped in lattices with different subwavelength structure. Such a resolution will be critical in the study of optical lattices with lattice constants $\lambda/2N$ created through stroboscopic techniques, which is the subject of the next two chapters. These subwavelength-spaced lattices are advantageous for studying many-body physics, since the energy scale is N^2 times larger than a typical $\lambda/2$ lattice.

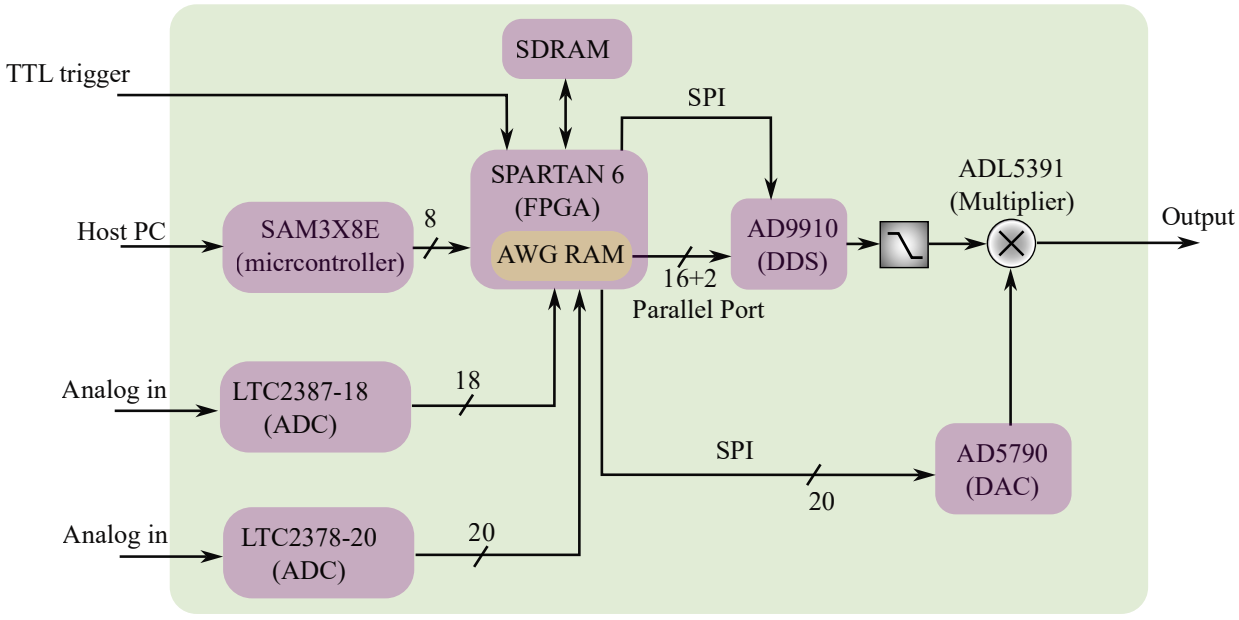

Figure 3.2: Arbitrary waveform generator hardware schematic

3.2 Hardware and software development

Here, I will elaborate on the arbitrary waveform generator (AWG), which was central to realizing the results presented in this chapter and chapter 5, particularly due to its ability to generate high-speed arbitrary waveforms. I was aware of the fact that Carlos (with help from Alessandro) had built an entire AWG from the ground up for Trey's Rb I experiment. He had designed and built the hardware as well as the associated firmware. I suggested modifying this AWG to fit our specific application and it turned out to be a success. The schematic of the modified device is shown in Fig. 3.2. I designed the fast AWG software architecture and Carlos and I made numerous modifications to the FPGA firmware to implement this architecture. The fast AWG software architecture was designed around the memory hierarchies and latencies inherent to the AWG hardware.

The AWG hardware is centered around the AD9910 Direct Digital Synthesizer controlled by a Xilinx Spartan 6 FPGA. The SAM3X8E interfaces the FPGA with the host PC via USB or ethernet. Slow amplitude, phase, and frequency profiles, as well as digital logic, are stored in the SDRAM as a table of values. The phase and frequency table of values—provided by SetList (`https://github.com/JQIamo/SetList.git`) on the host PC—are passed on to the DDS module over SPI upon receiving a trigger from the Pulseblaser (from SpinCore Technologies) every 2 μs, which would then update the relevant DDS parameter. As for the amplitude table of values stored on the SDRAM, the digital data is reconstructed as an analog signal (using an external DAC: AD5790 from Analog Devices) and is mixed with the waveform generated by the DDS using an analog multiplier (ADL5391 from Analog Devices) to adjust the amplitude of the waveform. A higher resolution and slower DAC at 20 bits is used instead of

the native 14-bit DAC on AD9910 as it helps better resolve small amplitudes at the start and end of amplitude ramps. However, this SDRAM-based arbitrary waveform generation is not fast. In order to boost the speed of the AWG, many modifications had to be made.

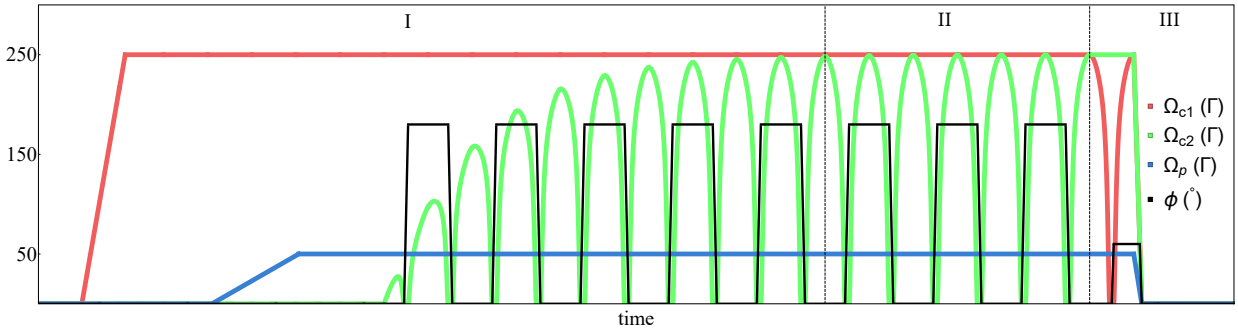

Figure 3.3: A typical sequence for the Rabi frequencies of the different light fields and the relative phase ϕ between Ω_{c1} and Ω_{c2} for generating $\lambda/4$ subwavelength-spaced lattices. The stage III is when the wavefunction microscope is implemented.

The fast software AWG architecture relies heavily on the concept of memory hierarchy in computer architecture [14]. For fast computations, the instructions and data must be spatially located close to the processor. The capacity and access time of a memory typically increases with decreasing proximity to the processor. Fast and small-capacity memory is therefore placed closer to the processor, and slow and large-capacity memory is placed further away. Only in the event of an instruction miss (or a data miss), does the processor search for the instruction (or data) in a memory lower in the memory hierarchy. Therefore, high-resolution slow ramps that are long and need larger storage space and do not require fast update rates are stored in the SDRAM. On the other hand, the fast rf amplitude modulation profile is stored in the RAM of the FPGA. This arrangement respects the memory hierarchy.

The table of values for the fast amplitude modulation profile is pre-generated on the host PC and subsequently saved in the FPGA RAM. The amplitude data is transmitted from this RAM to the DDS module by the FPGA using the parallel data port modulation mode on the AD9910,

where it is reconstructed as an analog signal by its native 14-bit DAC. This architecture allows arbitrary waveform data to be updated every 8 ns.The maximum length of the arbitrary waveform pulse is approximately 256 μs when updated every 8 ns. This fast AWG profile is then mixed with the slow amplitude profile saved in the SDRAM. The slow envelope is reconstructed by the AD5790 every Pulseblaster trigger. Note that the fast amplitude modulation table of values is clocked every 8 ns by the FPGA while the slow envelope table of values is clocked every 2 μs by the Pulseblaster trigger. A typical rf amplitude profile—green trace—that was used to generate a sub-wavelength spaced $\lambda/4$ lattice is shown in Fig. 3.3. This rf amplitude profile is imprinted on the laser electric field via an AOM. Stage III in Fig. 3.3 is when the wavefunction microscope is implemented.

The rf phase ramps are implemented by the digital ramp generator under the digital ramp modulation mode on the AD9910. The phase ramps are step functions with discrete phase values. The phase is intimately tied to the fast amplitude waveform. The phase of the rf is held constant when the amplitude of the rf is modulated. The transition between the phase steps is only performed when the amplitude of the waveform is 0 i.e. when the associated dark state is spatially homogeneous. The phase can be updated in 4 ns. The black trace in Fig. 3.3 shows the rf phase profile imprinted on the laser electric field via an AOM to generate a $\lambda/4$-spaced lattice.

Chapter 4: Floquet engineering of optical lattices with spatial features and periodicity below the diffraction limit

Time-periodic driving of quantum systems is ubiquitous in quantum mechanics. Small amplitude driving of a quantum system probes its linear response [15], while strong driving allows for Hamiltonian engineering [16, 17, 18, 19, 20]. Optical potentials and in particular optical lattices have proven to be a powerful tool for manipulating ultracold atomic systems and are used in a wide range of experiments [5, 21, 22]. However, the spatial features and periodicity of these potentials (generally arising from the second order ac-Stark shift) in the far field are constrained by the diffraction limit to be of order the wavelength of light used to create them. In particular, the Fourier decomposition of these far-field optical potentials cannot have components with wavelength less than $\lambda/2$, and thus the minimum lattice spacing is $\lambda/2$. As the lattice spacing determines many of the energy scales in cold-atom lattice systems, it has been of interest to produce optical lattices with smaller spacings in order to increase relevant energy scales [23, 24].

In this chapter, I summarize the results of a paper where I present a Floquet-based framework to stroboscopically engineer Hamiltonians with spatial features and periodicity below the diffraction limit of light used to create them by time-averaging over various configurations of a 1D optical Kronig-Penney (KP) lattice. Stroboscopic control over the strength and position of this lattice

requires time-dependent adiabatic manipulation of the dark-state spin composition. I investigate adiabaticity requirements and shape our time-dependent light fields to respect the requirements. I apply this framework to show that a $\lambda/4$-spaced lattice can be synthesized using realistic experimental parameters as an example, discuss mechanisms that limit lifetimes in these lattices.

The paper can be found in its entirety in Appendix D.

4.1 Summary

Time averaging a stroboscopically applied lattice potential with high spatial frequency Fourier components can give rise to an average potential with periodicity and spatial features smaller than $\lambda/2$. Since the dark-state KP lattice has high spatial frequency Fourier components, it is a candidate progenitor lattice with which to realize such a time-averaged, subwavelength-featured lattice. In the time-averaged approach, a time-periodic progenitor potential $W_0(x,t)$ is applied such that the atoms experience the time-averaged potential $W_{\text{avg}}(x)$:

$$W_{\text{avg}}(x) = \frac{1}{T}\int_{-T/2}^{T/2} W_0(x,t)\mathrm{d}t, \tag{4.1}$$

where $T = 2\pi/\omega_T$ is the period of $W_0(x,t)$ and ω_T is the Floquet frequency. In order to successfully realize $W_{\text{avg}}(x)$ while avoiding heating, ω_T must be much faster than the timescale associated with the motional degree of freedom in the lattice, which is set by the energy gaps between bands in the lattice. This requirement suggests that ω_T be as large as possible. The particular realization of $W_0(x,t)$ using a dark-state lattice has an additional requirement of spin adiabaticity that limits the maximum allowable ω_T.

The dark-state lattice is an artificial scalar gauge potential experienced by an atom in the

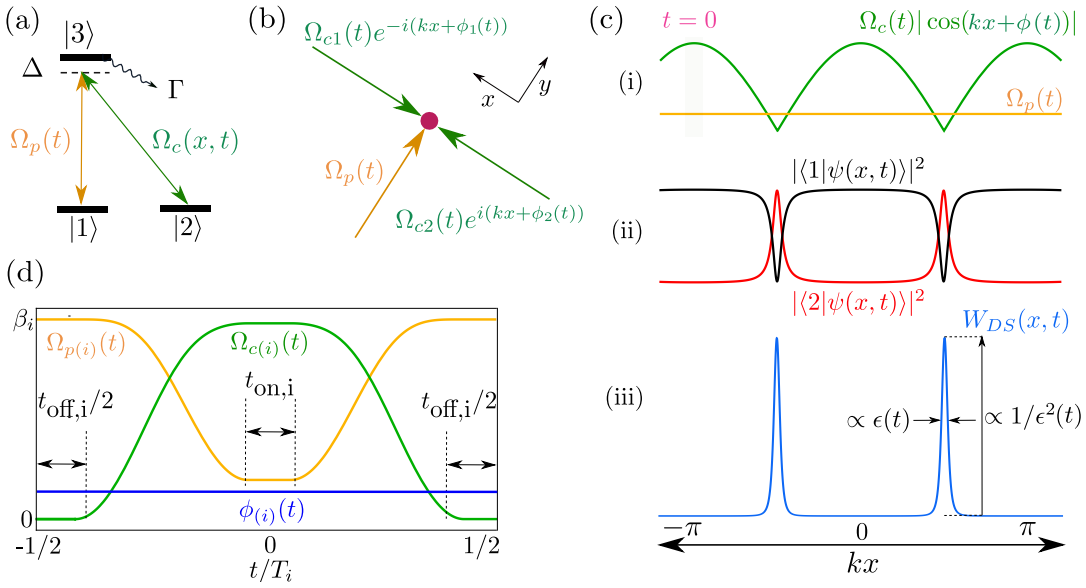

Figure 4.1: **(a)** An ideal Λ-system with inverse lifetime Γ and single-photon detuning Δ. One leg of the Λ-system is coupled by a spatially homogeneous and temporally varying probe light field $\Omega_p(t)$ and the other leg by a spatially inhomogeneous and temporally varying control light field $\Omega_c(x,t)$. **(b)** The geometry of the light fields with arbitrary control over the envelope, $\Omega_{c1}(t)$, $\Omega_{c2}(t)$, $\Omega_p(t)$ and phase, $\phi_1(t)$, $\phi_2(t)$ of each light field. **(c)** (i) The instantaneous (at $t=0$) spatial dependence of the light fields $\Omega_c(t)|\cos(kx+\phi(t))|$ and $\Omega_p(t)$, (ii) the probability densities of the spin composition of the dark-state eigenfunction $|\psi(x,t)\rangle$ i.e. $|\langle 1|\psi(x,t)\rangle|^2$ and $|\langle 2|\psi(x,t)\rangle|^2$, and (iii) the instantaneous shape of $W_{DS}(x,t)$. **(d)** Typical pulse shapes considered here for the control beams $\Omega_{c(i)}(t) = 2\Omega_{c1(i)}(t) = 2\Omega_{c2(i)}(t)$, probe beam $\Omega_{p(i)}(t)$, and phase $\phi_i(t)$ for the ith sub-Floquet period where $-T_i/2 \le t \le T_i/2$ that determines the time-averaged potential $W_{\text{avg}}(x)$.

dark-state eigenfunction of a three-level Λ-system with a spatially dependent spin composition. Dynamically manipulating the height, barrier width, and position of the lattice requires time-dependent manipulation of the spin composition of the dark-state eigenfunction. This spin manipulation can be seen as a stimulated Raman adiabatic passage (STIRAP) process and adiabaticity requirements set an upper bound on the window for usable ω_T within which the atoms are simultaneously motionally diabatic and spin adiabatic.

I consider the creation of time-periodic potentials for the dark-state channel, $W_{\text{DS}}(x,t)$ (which serves as $W_0(x,\,t\,)$ in Eq. 4.1), by coupling the three atomic levels in a Λ-system with a spatially homogeneous probe light field $\Omega_p(t)$, and a spatially inhomogeneous control light field.

The inhomogeneous control light field is composed of two counter propagating fields with equal magnitudes driven simultaneously, $\Omega_c(x,\, t) = \Omega_c(t)\cos(kx + \phi(t))$ where $k = 2\pi/\lambda$, as shown in Fig. 4.1a. The spin composition of the dark-state eigenfunction for the Λ-system in Fig. 4.1a is $|\mathrm{DS}(x,t)\rangle = -\cos\alpha(x,t)|1\rangle + \sin\alpha(x,t)|2\rangle$ where $\alpha(x,t) = \tan^{-1}\left[\Omega_p(t)/\Omega_c(x,t)\right]$. The non-adiabatic correction to the dark-state BO potential that gives rise to $W_{\mathrm{DS}}(x,t)$ is determined by the spatial gradient of the spin composition (Fig. 4.1c),

$$W_{\mathrm{DS}}(x,t) = \frac{\hbar^2}{2m}\left(\frac{\partial}{\partial x}\alpha(x,t)^2\right), \tag{4.2}$$

which for the light-field configuration considered here is a lattice of narrow repulsive barriers with temporally modulated strength and position. I take here a stroboscopic approach, where $W_{\mathrm{DS}}(x,t)$ is repeatedly pulsed on and off in magnitude at N different positions for time T_i with the position of $W_{\mathrm{DS}}(x,t)$ being shifted in between the lattice pulses (here $T = \sum T_i$). In addition, $W_{\mathrm{DS}}(x,t)$ can be held on and off for $t_{\mathrm{on},i}$ and $t_{\mathrm{off},i}$ (Fig. 4.1d). Time averaging over the N different pulsed KP lattice potentials with arbitrary strength and position can produce an arbitrary time-averaged potential $W_{\mathrm{avg}}(x)$. The stroboscopic approach to creating a time-averaged effective potential with a lattice spacing of $\lambda/4$ by dynamically pulsing KP potentials with $\lambda/2$ spacing is illustrated in Fig. 4.2.

The ability to paint potentials requires real-time control over the position, strength and width of the barriers (Eq. 4.2). The strength of the barriers can be controlled via the Rabi frequencies $\Omega_p(t)$ and $\Omega_c(t)$ (Figs. 4.1b, 4.1c) with the height and width of the barriers being proportional to $1/\epsilon^2(t)$ and $\epsilon(t)$ respectively where $\epsilon(t) = \Omega_p(t)/\Omega_c(t)$(for $\epsilon(t) \ll 1$). The barriers are located at the nodes/minimums of $\Omega_c(x,t)$ (Fig. 4.1c), and their positions can be

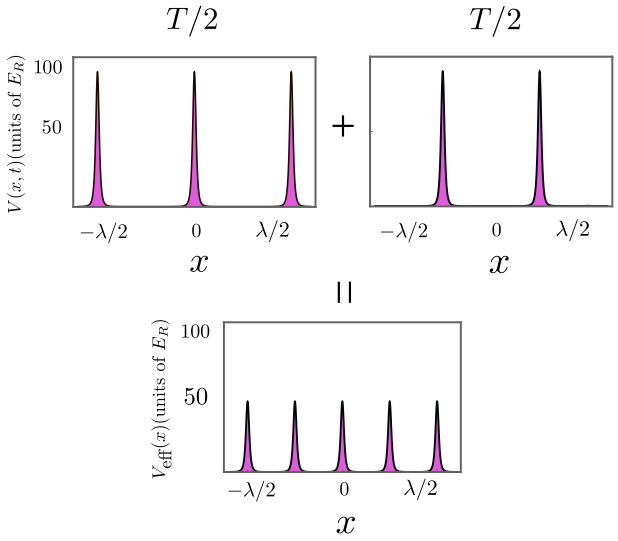

Figure 4.2: The stroboscopic approach to creating a time-averaged effective potential with a lattice spacing of $\lambda/4$ by dynamically pulsing KP potentials with $\lambda/2$ spacing.

controlled by the control beam phases $\phi_1(t)$ and $\phi_2(t)$ (Figs. 4.1b, 4.1c). Stitching N different sub-Floquet periods together (while ensuring continuity in the Rabi pulses between the sub-Floquet periods) into one Floquet period allows for the versatility in the time-averaged potential $W_{\text{avg}}(x)$ that can be generated. Each sub-Floquet period of duration T_i pulses a KP potential at a different position x_{0i} (determined by the phase ϕ_{0i}) with a strength and width determined by ϵ_i. Fig. 4.1d shows the pulses $\Omega_{p(i)}(t)$, $\Omega_{c(i)}(t)$ and $\phi_{(i)}(t)$ for the i th sub-Floquet period $-T_i/2 \leqslant t \leqslant T_i/2$.

My goal is to design the pulse shape for $\Omega_p(t)$ and $\Omega_c(x,t)$ for simultaneous motional diabaticity and spin adiabaticity. In order to design pulses that are spin adiabatic, I consider the three inequalities that quantify the sufficiency requirements for adiabaticity defined at single

photon resonance $\Delta = 0$:

$$\left|\frac{\partial}{\partial t}\alpha(x,t)\right| \ll \Omega_{\mathrm{rms}}(x,t) \tag{4.3}$$

$$\int_{-\pi/\omega_T}^{\pi/\omega_T}\left|\frac{\partial}{\partial t}\left(\frac{\partial\alpha(x,t)/\partial t}{\Omega_{\mathrm{rms}}(x,t)}\right)\right|\mathrm{d}t \ll 1, \tag{4.4}$$

$$\int_{-\pi/\omega_T}^{\pi/\omega_T}\frac{|\partial\alpha(x,t)/\partial t|^2}{\Omega_{\mathrm{rms}}(x,t)}\mathrm{d}t \ll 1 \tag{4.5}$$

where $\Omega_{\mathrm{rms}}(x,t) = \sqrt{|\Omega_c(x,t)|^2 + |\Omega_p(t)|^2}$. Eq. 4.3, called the local adiabatic criterion, states that to ensure adiabaticity during pulsing, the energy gap between the dark and bright eigenstates (set by $\Omega_{\mathrm{rms}}(x,t)$) must be much greater than the off-diagonal couplings between them ($|\partial\alpha(x,t)/\partial t$). Eq. 4.4 forces the pulses to be smooth while both equations 4.4 and 4.5 set bounds on their rise time and fall times.

I solve the Bloch-Floquet bandstructure for the full Hamiltonian using the engineered pulse shapes $\Omega_p(t)$ and $\Omega_c(x,t)$:

$$\hat{H}(x,t) = \frac{\hat{p}^2}{2m} + \frac{\hbar}{2}\underbrace{\begin{pmatrix} \delta_1(x,t) & 0 & \Omega_p(t) \\ 0 & \delta_2(x,t) & \Omega_c(x,t) \\ \Omega_p(t) & \Omega_c(x,t) & -(2\Delta(t) + \mathrm{i}\Gamma) \end{pmatrix}}_{\hat{\Omega}(x,t)}, \tag{4.6}$$

where $\hat{\Omega}(x+\lambda,t) = \hat{\Omega}(x,t+T) = \hat{\Omega}(x,t)$ with $\Delta(t) = 0$ and $\Gamma = 48.2\omega_R$ (for the $(6s^2)^1\,S_0 \leftrightarrow (6s6p)^3P_1$ transition in ^{171}Yb). $\delta_1(x,t)$ and $\delta_2(x,t)$ are complex-valued ac-Stark shifts of the ground states $|g_1\rangle$ and $|g_2\rangle$ that account for the effect of states outside the three-level system. These calculations helped us validate the choice of the calculated pulse shapes as well as identify

the range of Floquet frequencies over which the $\lambda/4$-spaced lattices would be feasible given the laser power available at our disposal. These calculations also showed that Rabi frequency requirements needed to generate $\lambda/2N$-spaced lattices increase dramatically with N.

While working with large Rabi frequencies reduces losses, a potential disadvantage is that the Λ-system approximation may break down. Perfect Λ-systems are rare in nature, and $\Omega_p(t)$ and $\Omega_c(t)$ can couple off resonantly to states outside of the Λ-system. These off-resonant couplings manifest as effective two-photon detunings $\delta_1(x,t)$ and $\delta_2(x,t)$ for the approximate Λ-system (see Eq. 4.6). Non-zero two-photon detunings are detrimental to STIRAP, although spatially homogeneous detuning could in principle be compensated with time-dependent laser detuning. Two-photon detunings originating from $\Omega_c(x,t)$, however, are temporally and spatially modulated and may not be completely compensated without the significant experimental overhead of adding more spatially dependent compensating laser fields. In addition to added two-photon detuning, the lifetime in the time-averaged lattices is further limited due to admixing of excited states outside the Λ-system. Hence, there are trade-offs when increasing the magnitude of the Rabi frequencies: while the dark-state evolution is more adiabatic with less bright-state admixture, the off-resonant scattering from states outside the Λ-system also increases.

The calculations ruled out the possibility of achieving $\lambda/6$-spaced (or smaller-spaced) lattices given our choice of atom and the laser power at our disposal. We experimentally verified the effect of the engineered pulses and found a multi-fold increase (at least $4\times$) in the lifetime of the atoms in the $\lambda/4$-spaced lattice generated by stitching together pulses that were used for the wavefunction microscope (Chap. 3 and Appendix C). I report on the realization of the $\lambda/4$-spaced lattice in the next chapter.

Chapter 5: Realization of a stroboscopic optical lattice for cold atoms with subwavelength spacing

Ultracold atoms trapped in periodic optical potentials provide wide-ranging opportunities to study many-body physics in highly controllable systems. In all cases, the characteristic single-particle energy scale is set by the recoil energy, $E_R = h^2/(8md^2)$, where m is the mass of the atom and d is the spatial period of the lattice. Although temperatures in such systems can be quite low, it is still challenging to reach temperatures well below the relevant many-body physics energy scales, which can be exceedingly small. Increasing the recoil energy can potentially increase both single-particle and many-body energy scales through tighter confinement, which may aid in creating systems well into the regime where many-body ground-state physics is observable. An inherent obstacle to smaller lattice spacing is the optical diffraction limit, which prevents lattice periodicities below $d = \lambda/2$, where λ is the wavelength of the light forming the lattice.

In this chapter, I summarize the results of our paper, where we demonstrate a $\lambda/4$-spaced lattice by stroboscopically applying optical Kronig-Penney-like potentials which are generated using spatially dependent dark states (see chapters 2 and 4). We directly probed the periodicity of the $\lambda/4$-spaced lattice by measuring the average probability density of the atoms loaded into the ground band of the lattice using the nanoscale atomic density microscopy technique presented in

chapter 3. We measure lifetimes of atoms in this lattice and discuss the mechanisms that limit the applicability of this stroboscopic approach.

The paper can can be found in its entirety in Appendix E.

5.1 Summary

To realize the $\lambda/4$-spaced lattice, KP potentials are stroboscopically applied to atoms to create potential landscapes with subwavelength spacings specifically $\lambda/4$. Atoms are subjected to a KP potential for half of the Floquet cycle $T/2$; the potential is then ramped down to zero and its position is shifted by half of the lattice spacing $\lambda/4$; the shifted potential is ramped on again and held for another half cycle, before being ramped off and its position is restored. It is important to note that time-averaging a dynamically applied lattice potential cannot create an effective potential landscape with higher spatial Fourier components than the underlying progenitor lattice. This implies that in order to create landscapes with subwavelength periodicity, one must time average a potential that itself has subwavelength features, and hence the choice for the KP lattice as the progenitor lattice.

Two more factors must be considered to ensure that time-averaging is an effective description of the system. First, motional diabaticity sets a lower bound on the Floquet frequency ω_F, beyond which the band structure becomes unstable and severe heating limits the lifetime. Second, the dark-state nature of the KP lattice sets an upper bound to ω_F. As the KP potential is a scalar gauge potential arising from a spatially varying dark state, switching on and off such a potential requires atoms to adiabatically follow the spatiotemporal dark state at all times. We ensure this adiabatic following by carefully designing the pulse shapes of our light fields (see chapter 4).

Losses occur at high ω_F, as the atom's dark-state spin composition fails to adiabatically follow the rapid changes in the light fields.

The spin adiabaticity condition significantly depends on the pulse shape and the Floquet frequency. Controlling the pulse shape within a Floquet period is critical. This was explored in the chapter 4. We use the arbitrary waveform generators discussed in chapter 3 to control the rf amplitude and phase with a resolution of 8 ns and 4 ns, respectively. However, we are limited by the bandwidth of the AOMs, which we measure to be 50 ns. This is a factor of 8 times smaller than the smallest half-period of 400 ns that we have used in this work.

Just like in the other chapters, we work with $\approx 2 \times 10^5$ $^{171}\mathrm{Yb}$ atoms that have a well-isolated Λ system, consisting of two ground states $|g_1\rangle, |g_2\rangle$ and an excited state $|e\rangle$ coupled by laser light with $\lambda = 556\,\mathrm{nm}$. The atoms have an initial temperature of $0.3\mu\mathrm{K}$. A control field $\Omega_c(x,t) = \Omega_{c1}e^{ikx} + \Omega_{c2}(t)e^{-i[kx+\phi(t)]}$, where $k = 2\pi/\lambda$ and $\phi(t)$ is the relative phase difference between the two fields, which couples $|g_2\rangle$ and $|e\rangle$, is composed of two counterpropagating lattice beams. The maximum value of $\Omega_{c2}(t)$ is constrained to be equal to $\Omega_{c1} = \Omega_{c0}/2$, in which case it gives rise to a standing wave $\Omega_{c0}e^{-i\phi(t)/2}\cos(kx + \phi(t)/2)$. We control the strength and position of the KP potential using $\Omega_{c2}(t)$ and $\phi(t)$. A homogeneous probe field $\Omega_p e^{iky}$, coupling $|g_1\rangle$ and $|e\rangle$, travels perpendicular to the control beams. The resulting spatially dependent dark state gives rise to a KP lattice of narrow subwavelength barriers, plus an additional sinusoidal potential owing to the light shifts caused by states outside the three-level system. For typical experimental values of $\Omega_{c0} = 500\Gamma$ and $\Omega_p = 50\Gamma$, where $\Gamma = 2\pi \times 182\mathrm{kHz}$ is the inverse lifetime of $|e\rangle$, the KP barrier has a minimum width of 0.02λ and a maximum height $\approx 100E_R$, where $E_R/h = h/(2m_{\mathrm{Yb}}\lambda^2) = 3.7\mathrm{kHz}, m_{\mathrm{Yb}}$ is the mass of a $^{171}\mathrm{Yb}$ atom, and the sinusoidal potential has a depth $\approx 145E_R$.

To load the atoms into the ground band of $V_{\text{eff}}(x)$, we adiabatically increase the depth of the stroboscopically applied lattices in 200μs (typically ~ 80 Floquet cycles) (see Fig. 3.3). To confirm the realization of the $\lambda/4$ subwavelength-spaced lattice, we measure the ensemble-averaged probability density $|\psi(x,t)|^2$ of atoms in the ground band of $V_{\text{eff}}(x)$ using the subwavelength resolution microscopy technique with FWHM resolution of 25 nm (see Fig. 5.1).

We also measure the momentum distribution of the atoms via absorption imaging after time of flight (TOF) to probe the momentum-dependent loss channels. A characteristic feature of a Bloch-Floquet band structure is the existence of avoided crossings at particular lattice momenta arising from coupling with high-lying states, which for large Floquet frequency are approximately plane waves with high momenta. We measure the momentum distribution of the atoms in $V_{\text{eff}}(x)$ at different ω_F by taking an absorption image after ramping down the lattice in 100μs followed by a TOF of 3 ms. In order to determine the range of usable Floquet frequencies for the stroboscopic scheme, we also study the lifetime at different ω_F under different Rabi frequency configurations. We measure the lifetime of the atoms in the $\lambda/4$-spaced lattice to be no more than 2 ms. The short lifetimes in the stroboscopically applied KP lattices are expected as a result of a few factors. First, couplings to the spatially and temporally dependent bright states reduce lifetimes in subwavelength-spaced lattices even for a perfect three-level system, through couplings with higher Floquet bands and off-resonant couplings with bright states. In principle, these couplings can be reduced by using larger Rabi frequencies. However, lifetimes are also limited by the breakdown of the three-level approximation at large Rabi frequencies due to admixing of states outside the three-level system. This manifests as a dynamically varying and spatially dependent two-photon detuning (arising from $\Omega_c(x,t)$), which reduces the fidelity of STIRAP. This competing requirement prevents us from benefiting from larger Rabi frequencies.

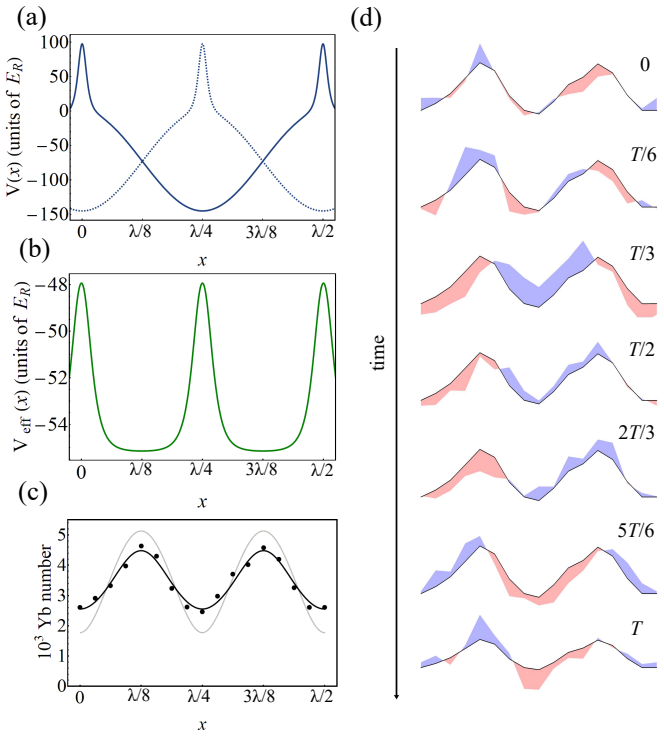

Figure 5.1: (a) The stroboscopically applied potential, shown here for $\Omega_{c0} = 500\Gamma$ and $\Omega_p = 50\Gamma$, is composed of KP barriers on top of a sinusoidal potential. The dotted line represents the potential shifted by $\lambda/4$. (b) The time-averaged effective potential $V_{\text{eff}}(x)$. (c) The black points are the measured $|\psi_{\text{avg}}(x)|^2$ of atoms in $V_{\text{eff}}(x)$. Number fluctuations between realizations result in number uncertainties of 5%. The black line is the calculation based on independently measured lattice parameters. The grey line is the calculated $|\psi_{\text{avg}}(x)|^2$ in the lattice before the relaxation during the measurement. (d) The micromotion dynamics at different time within a Floquet period. The blue(red)-shaded areas represent regions in which $|\psi(x,t)|^2$ is higher(lower) than $|\psi_{\text{avg}}(x)|^2$, which is shown as a solid black line.

In conclusion, we demonstrate the creation of a time-averaged $\lambda/4$-spaced lattice using a stroboscopic technique based on dynamically modulated dark states in a three-level system. The subwavelength structure of the lattice is confirmed by measuring the probability density of the atoms averaged over the ground band of the lattice. We measure the loss rate of atoms in the lattice and observe high-momentum excitation arising from Floquet-induced coupling to higher bands.The lifetime of the atoms in the $\lambda/4$-spaced lattice is $2\,\text{ms}$, which is not long enough compared to the tunneling time to allow for many-body studies in the current realization.

Part II

Dual-species optical tweezer arrays for Rubidium and Ytterbium for Rydberg-interaction-mediated quantum simulations

Chapter 6: Introduction

Individual neutral atoms trapped in optical tweezer arrays with controlled Rydberg interactions have recently emerged as a promising platform for quantum computation and quantum simulation [25, 26, 27, 28, 29, 30, 31, 32, 33]. Tweezer arrays of individually trapped atoms were first realized using alkali atoms, the workhorse for laser cooling and trapping experiments [34]. Single-species tweezer arrays were subsequently realized with alkaline-earth (like) atoms [35, 36, 37] and more recently with magnetic lanthanide atoms [38]. These single-species experiments have demonstrated an impressive level of control [39, 40], each species having its advantages and disadvantages. Dual-species arrays are an even more attractive platform for large-scale quantum computation and simulation, due to the flexibility they provide for controlled interaction and measurement. Recently, dual-species (alkali-alkali) optical tweezer arrays have been realized [41, 42]. However, a dual-species optical tweezer array of an alkali atom and an alkaline-earth (like) atom, which combines the beneficial properties of both types of atoms [32], has yet to be realized. In this half of the thesis, I present details on the design and construction of an apparatus for dual-species optical tweezer arrays of Rb and Yb for Rydberg-interaction-mediated quantum computation and simulation.

In addition to the capabilities of the single-species systems, dual-species Rydberg arrays are a promising candidate for large-scale quantum computation due to their increased capability

for *multi-qubit* gate operations [40, 43], and crosstalk-free measurements [30, 44, 45, 46] for mid-circuit readouts [40, 47, 48, 49, 50, 51]. Native multi-qubit gate operations can yield large improvements in efficiency and error tolerance over an equivalent set of single- and two-qubit gates [30, 52]. For example, CNOT^k fan-out gates can be implemented with heteronuclear Förster dipole-dipole interactions between the control atom of one atomic species and the target atoms of the other species, where the Förster enhanced heteronuclear interaction is much stronger than the van der Waals interactions between the target atoms. Similarly, C$_k$Z asymmetric blockade gates can be realized using asymmetric interactions with the role of control and target atoms reversed. [41, 44, 53, 54]. Multi-qubit gates can also be used to transfer quantum information from "computational" qubits of one atomic species to "measurement" qubits of the other atomic species. The measurement qubits can then be detected by resonance fluorescence, avoiding crosstalk errors since the scattered light of one atomic species is not resonant with the other atomic species [30, 44]. This crosstalk error mitigation is also enabled by the asymmetry in the strength of the heteronuclear Förster dipole-dipole interaction vs. the homonuclear van der Waals interaction. In particular, the Rb Yb combination of atoms is predicted to have anomalously weak van der Waals interaction between the Yb atoms in the $(6sns)^1S_0$ Rydberg series [55, 56], while the heteronuclear Förster dipole-dipole interaction is expected to be much stronger, which should allow for simple and efficient implementation of multi-qubit gates.

Building a dual-species Rydberg tweezer array—especially an alkali-alkaline earth (like)—is challenging. The complexity of the requirements for a single-species Rydberg array is at least doubled for a dual-species apparatus, which must now simultaneously satisfy the requirements for both species. Fig. 6.1 shows the broad range of required laser wavelengths (ultraviolet B to near infra-red) for our apparatus. To motivate and provide context for the following chapter, I

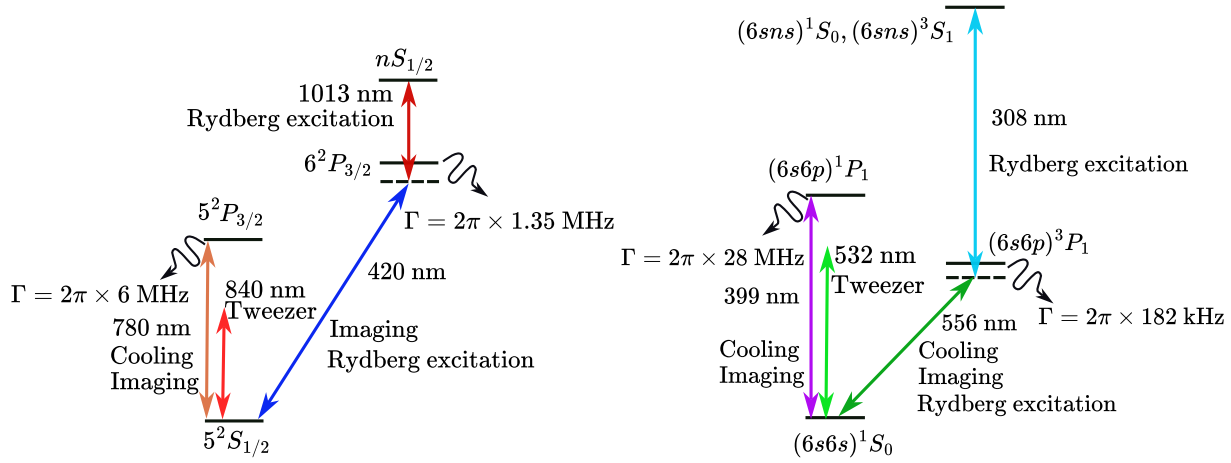

Figure 6.1: Relevant electronic level structure for (a) Rb and (b) Yb

.

outline the physical requirements for a dual-species tweezer array:

- *Cooling, trapping, and imaging single atoms*:

  Optical tweezers are tightly focused far-off resonant optical traps that use the dipole force to trap particles such as single atoms, molecules, nanoparticles, etc. [32, 57, 58]. Diffraction sets a lower limit to the smallest feature that can be created (or imaged), which is on the order of the wavelength of light used [59]. The size of the feature that can be created (or imaged) is inversely proportional to the numerical aperture (NA) of the optics used [59]. Therefore, creating optical tweezers and imaging single atoms confined in these tweezers requires high-NA optics [34, 60]. Diffraction-limited resolution can be degraded by aberrations in the optical system, which grow polynomially with the NA [2, 61]. In addition to the physical space required to deploy high NA objectives, great care must be taken to avoid adding aberrations to the system, and the optics must be diffraction limited at multiple wavelengths.

  In order to trap single atoms in optical tweezers, the atoms are laser cooled [62, 63] to

temperatures ranging from hundreds of nK to tens of μK. Cooling the atoms reduces the tweezer laser power requirements, which helps with system size scalability [28, 64]. It also helps mitigate the Doppler-induced decoherence process that limits ground-to-Rydberg excitation fidelity [28, 64]. Furthermore, the vacuum-limited lifetime of the atoms trapped in optical tweezers imposes a limitation to scaling up to large atom numbers [28, 64]. Ultra-high vacuum conditions are necessary for long vacuum-limited lifetimes. Recently, a vacuum-limited lifetime of up to 6000 s has been demonstrated for single atoms in tweezer arrays in a cryogenic environment [65].

Dual-species laser cooling of Rb and Yb in a UHV chamber with simultaneous high-NA optical access over a broad wavelength range is therefore necessary. We have designed and built such a room temperature UHV chamber. Rb and Yb atoms have been laser cooled to temperatures in the tens of μK range. We have also designed and built high-NA optics for projecting optical tweezers and imaging single Rb and Yb atoms.

- *Narrow linewidth high-power lasers for high-fidelity Rydberg excitation*:

  Two-photon transitions are typically used to excite atoms to Rydberg states, which induces the interactions needed for two-qubit and multi-qubit entangling gate operations [66]. Large two-photon Rabi frequencies allow for fast gates operations, necessitating the use of high-power lasers. The power requirements become especially stringent if one or both of the Rydberg excitation beams address atoms globally [41, 67, 68]. The power requirements are relaxed when the atoms are addressed locally [40], but this comes at the cost of increased complexity and sensitivity to beam alignment.

  The lifetime of atoms in Rydberg states is typically in the tens to hundreds μs regime [26,

66]. Therefore, narrow linewidth lasers are also required to address these transitions. The Pound-Drever-Hall (PDH) locking technique is typically used to spectrally narrow the linewidth of the lasers using an ultralow expansion (ULE) cavity as a reference [69, 70, 71].

We have implemented PDH locks for our four high-power Rydberg lasers (a pair of lasers for each species) with each laser locked to its own ULE reference cavity. The four cavities are built into a single cylinder of ULE glass. The frequency of each laser can be tuned by a large fraction of the free spectral range of its reference cavity while staying locked to it. We have built and aligned the optics for exciting both atoms to their Rydberg states via global addressing.

- *Dynamic control over the positions of trapped single atoms*:

  Due to the stochastic nature of the loading of a single atom in an optical tweezer [34, 72, 73, 74], rearrangement of the tweezers is typically performed to create a defect-free array of single atoms from larger, stochastically loaded arrays with defects [39, 75, 76]. Defect-free arrays are routinely used in quantum computation and quantum simulation [47, 77, 78, 79, 80, 81]. Controlled motion of the tweezers is also critical for parallel entangling gates with programmable non-local connectivity [82]. Therefore, we have integrated the capability for rapid real-time rearrangement/motion of the tweezers for both atomic species in our setup: an acousto-optic deflector [83] and a phase-only spatial light modulator designated for Rb, and another set of acousto-optic deflector and phase-only spatial light modulator for Yb.

- *Electric field control for high-fidelity Rydberg excitation and tuning Förster defects*:

  The polarizability of atoms in Rydberg states scales as n^7, where n is the principal quantum

number [26, 30]. Therefore, atoms in Rydberg states are extremely sensitive to electric fields. Stray electric fields shift the energy of the Rydberg state and introduce decoherence mechanisms that reduce gate fidelities, and electrodes are used to cancel out stray electric fields [40]. Ultraviolet light can also used to desorb charge build-up on the vacuum chamber surfaces during Rydberg excitation [84, 85]. Electric field control also allows for tuning the strength of Förster resonances [86, 87, 88, 89]. A challenge in electrode design is the requirement to preserve the high-NA performance of the objectives. We have implemented a high-NA compatible in-vacuum electrode solution in our apparatus.

- *Single qubit gates*:

  Typically, the states in the hyperfine ground state manifold are used to store quantum information [40, 47, 90, 91]. Single-qubit rotations between the two hyperfine ground states are performed using Raman transitions in Rb [40, 47, 92] and Yb [48, 49, 90, 91, 93]. At the time of writing this thesis, we are in the process of building these Raman laser setups and beam-delivery systems.

The electronic level structure for Rb and Yb atoms relevant to the experimental apparatus is shown in Fig. 6.1. The following chapter presents details on the design and construction of the RbYb Rydberg tweezer array apparatus, the first of its kind at JQI, for which we had no tried-and-tested recipe.

Chapter 7: Design and construction of a dual-species Rydberg tweezer array apparatus

This chapter describes the design and construction of a new apparatus to simultaneously control arrays of individually trapped Rb and Yb atoms, including controlled excitation of these atoms to Rydberg states. Although this new apparatus inherited components from the previous RbYb mixtures experiment (in particular, the Rb/Yb cooling lasers and the Yb 2D MOT cold atom source), meeting the challenging demands outlined in Chapter 6 required a completely new integrated design of essentially all other aspects of the apparatus. I designed the entire experimental apparatus and led its construction from the ground up. We started building the lab the week before the university entered lockdown in response to the COVID-19 pandemic (Fig. 7.1). I would like to thank Trey, Steve, and Ian immensely for their patience, guidance, and the freedom they gave me. I am also extremely grateful to Kevin for helping build this apparatus.

I used several software tools to integrate the vacuum, opto-mechanical and electrical aspects of the design with the physics requirements. For CAD design, I used Onshape, a cloud-based CAD design platform[1]. In addition, I regularly used the Design for Manufacturing (DFM) analysis available on the website of the machining vendor, Protolabs Network by Hubs. I used

[1]The links to the CAD designs can be found here: https://github.com/ssubhankar/Experiment-CAD-design.git.

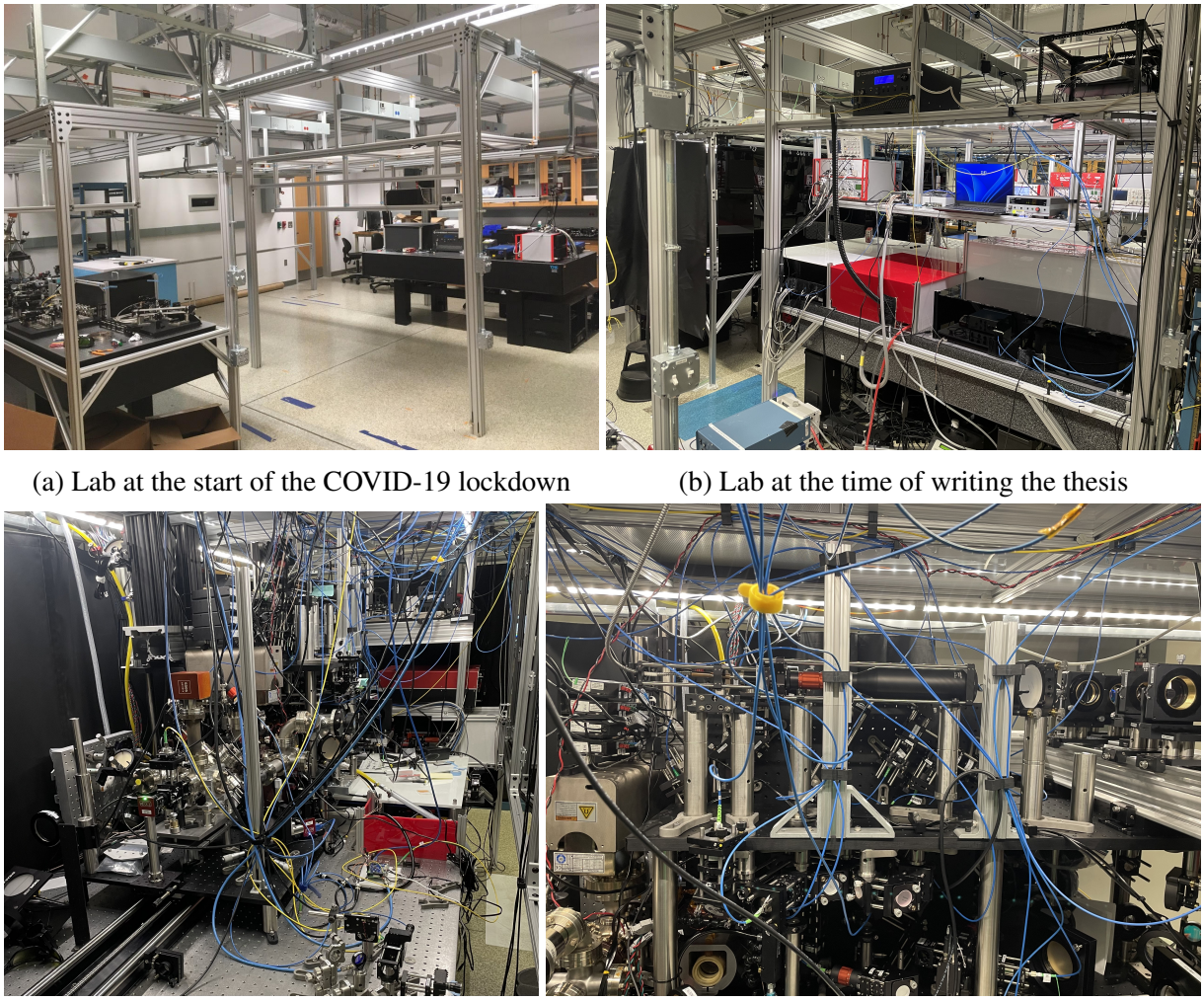

(a) Lab at the start of the COVID-19 lockdown

(b) Lab at the time of writing the thesis

(c) Science chamber optical table at the time of writing the thesis

(d) Optics around the science chamber at the time of writing the thesis

Figure 7.1: Evolution of the lab over the years.

Zemax to design the high-NA optical systems: the AOD-based tweezer projection systems, the SLM-based tweezer projection systems, and the single-atom imaging systems. All of my optical layouts can be found in this chapter.

7.1 Design and construction of the Ultra-High Vacuum (UHV) chamber assembly

7.1.1 The science chamber

At the heart of the experimental setup is the glass cell (see Fig. 7.2), and a pair of out-of-vacuum 0.6 NA infinity corrected objectives (see Fig. 7.44) that project the optical tweezers and image the single atoms. We chose this geometry over an in-vacuum objective lens in a stainless steel (SS) chamber because our objectives must be diffraction-limited for many colors: 399 nm, 420 nm, 532 nm, 556 nm, 780 nm, 840 nm (Fig. 6.1), and an in-vacuum objective lens of this caliber would be expensive. Additionally, housing and aligning such an objective under vacuum would be challenging. The wide range of high power lasers we need for our experiment—308 nm, 399 nm, 420 nm, 532 nm, 556 nm, 780 nm, 850 nm, 1013 nm (Fig. 6.1)— constrained the design of the vacuum chamber, which must in addition work well with the out-of-vacuum objectives.

The diffraction-limited Airy spot size ($1.22\lambda/\mathrm{NA}$) [94, 95, 96] at the focus of the objective lens is inversely proportional to its NA [97]. A high NA infinity-corrected objective with a large working distance implies a large collimated beam size at the entrance aperture of the objective. The large size of the beams forces the optical elements that constitute the objective lens assembly as well as the optics involved in light projection and collection to be large to accommodate such large beams. High-quality large optical elements (surface figure, flatness, parallelism, scratch-

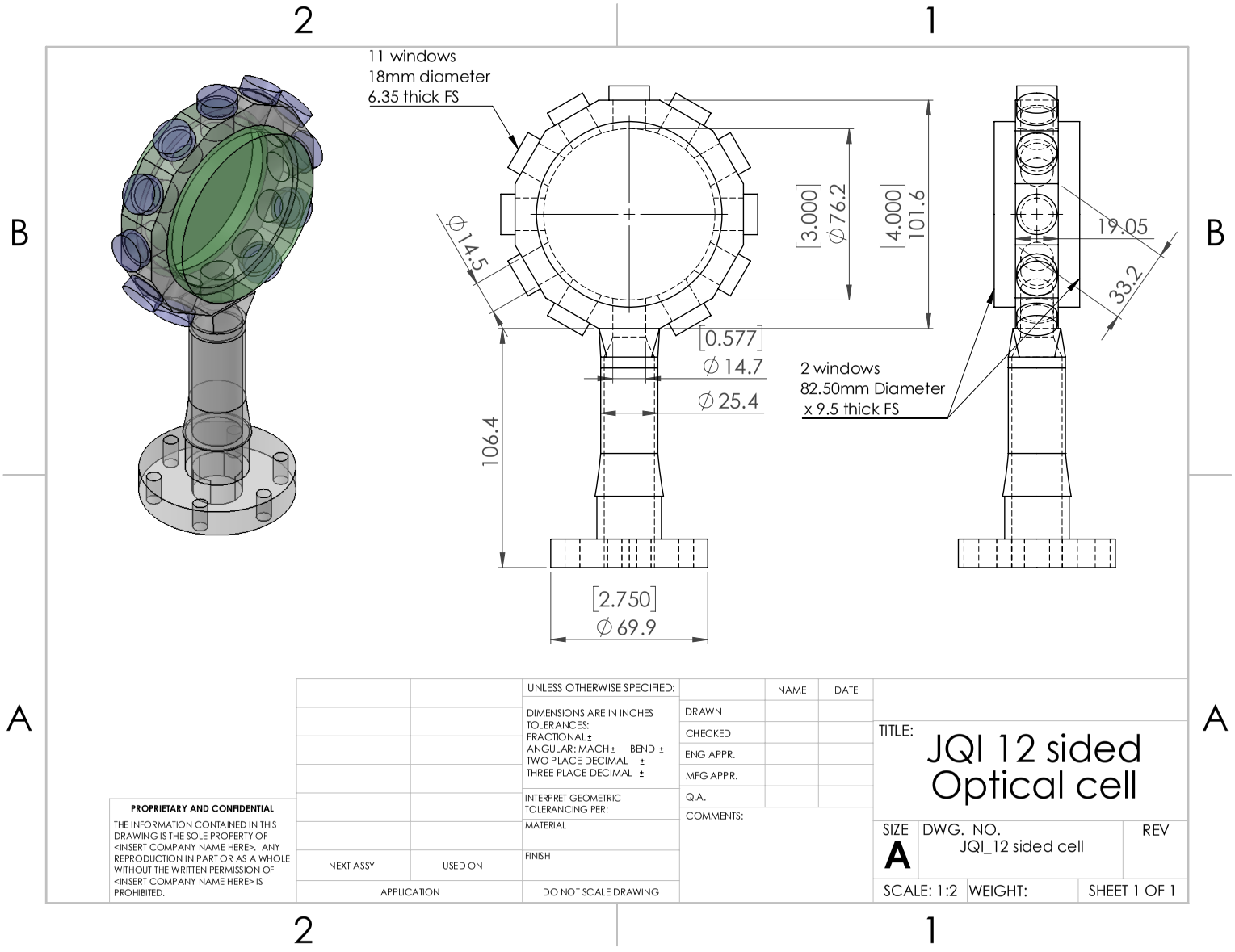

Figure 7.2: Drawing of the dodecagonal glass cell from Precision Glassblowing.

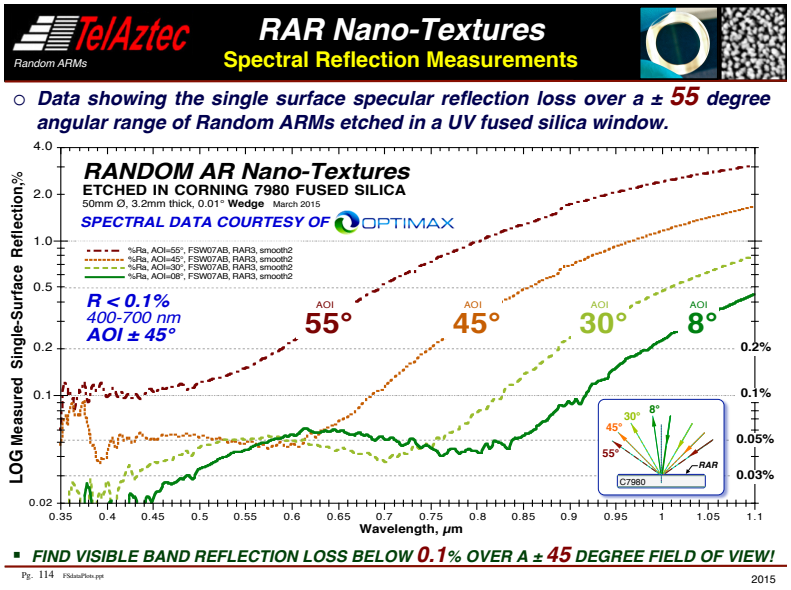

Figure 7.3: Anti-reflection properties of the RAR nanotextured surfaces.

dig, etc.) come with an increased price tag [98, 99]. Big beams also make it difficult to stay within the paraxial limit and therefore need careful optical design that adds minimal aberrations during beam shaping[2]. A small working distance is therefore highly desirable, which, for out-of-vacuum lens designs, favors a glass cell-based vacuum chamber instead of a SS chamber. Glass cells are typically smaller and provide more optical access than a SS chamber. Furthermore, we needed the flexibility to change the geometry of the paths of the optical beams to the atoms given the wide range of high-power laser light colors in our experiment: 308 nm to 1013 nm. For these reasons, we chose a dodecagonal glass cell with Random-type Anti-Reflective (RAR) plasma etched nanostructured windows [100, 101] from Precision Glassblowing (see Figs. 7.2 and 7.7b). The circular fused silica windows are glass-frit bonded [3] to circular counterbored holes in a

[2]The power of the lens will need to change with the beam size to preserve the NA. This makes optical paths long and can introduces drifts.

[3]Typically, glass vendors offer epoxy bonding or optically contact bonding. Epoxy bonding does not yield the best base pressure under UHV conditions.

fused silica frame. Our glass cell has 11 small windows with a clear aperture of 14.5 mm and two large high-quality objective windows with a clear aperture of 76.2 mm. The objective windows were held to typical high-NA optics standards: $\lambda/10$ surface flatness @ 633 nm, parallelism<1 arcmin, and 20:10 scratch-dig [102].

RAR nanostructures are similar in spirit to Moth-eye AR nanostructures [103, 104]. Moth-eye AR nanostrutures are a subwavelength-spaced periodic array of cone-like nanopillars etched onto a substrate. These Moth-eye nanostructures form an effective refractive index gradient at the substrate boundary for the impinging light, which suppresses Fresnel reflections via effective impedance matching[4]. This RAR nanotexturing leads to an optical performance (minimal reflection up to $\pm 60^\circ$ AOI) that is far superior to thin-film AR coatings that rely on interference effects, especially over the broad wavelength range in our experiment: $308 - 1013$ nm (see Fig. 7.3). RAR nanotexturing is not without its limitations as these nanopillars are fragile and touching the windows damages them, which degrades the AR properties. Therefore, I had to be extremely careful when handling and mounting the glass cell during assembly of the UHV chamber (see Appendix H for details on cleaning and handling the glass cell).

A primary reason for choosing a glass cell was so that we could use an out-of-vacuum objective. However, even a perfectly spherical wavefront gets aberrated upon transmission through a glass plate, i.e. the objective window [5] (see Fig. 7.4). The magnitude of these aberrations

[4] An alternate explanation for the anti-reflection behavior of the Moth-eye AR nanostrutures is that this periodic array acts like a zero-order grating where all the higher diffraction orders are evanescently suppressed due to the subwavelength grating period [103, 104]. Suppressing the higher order diffraction orders works better for light at longer wavelengths: it is easier to fabricate subwavelength arrays with large grating periods. However, randomizing the spacings between the nanopillars suppresses any constructive interference at lower wavelengths without the need to go to smaller lattice spacings [105]. The height of these nanopillars is typically 40% of the longest wavelength in the optical band of interest.

[5] This issue is non-existent for in-vacuum objectives as there are no aberrations imprinted on a flat wavefront upon transmission through a window with perfectly flat surfaces. However, actual windows do induce aberrations due to manufacturing defects.

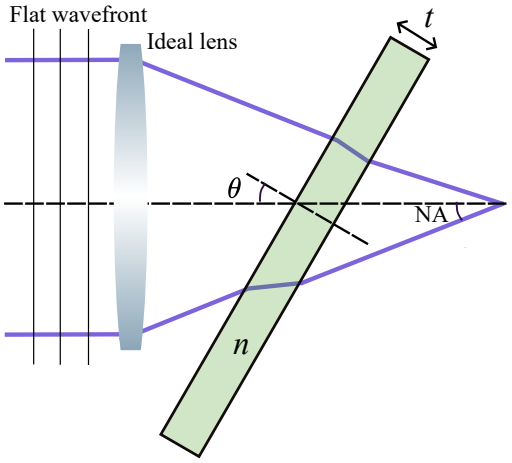

Primary wavefront aberration	Expression
Spherical	$-\frac{t\mathrm{NA}^4(n^2-1)}{8n^3}$
Coma	$-\frac{t\mathrm{NA}^3\theta(n^2-1)}{2n^3}\cos\phi$
Astigmatism	$-\frac{t\mathrm{NA}^2\theta^2(n^2-1)}{2n^3}\cos^2\phi$

Figure 7.4: Aberrations induced in a perfectly spherical wavefront upon transmission through a glass plate [2, 3, 4]. Notice that the primary wavefront aberrations follow the typical wavefront aberration polynomial structure $\mathrm{NA}^m\theta^{4-m}$.

depends on the thickness of the glass cell window, the NA of the objective lens, and the angle of the window with respect to the focused cone of light (θ). The objective lens needs to compensate for these intrinsic aberrations in order to guarantee diffraction-limited performance over a large field of view (FOV). Due to the higher-order polynomial dependence of wavefront aberrations on the NA [2, 102], poor tolerances associated with the objective window thickness can increase wavefront aberrations well beyond the diffraction-limited operation regime of the objective [106, 107, 108]. Therefore, the glass cell vendor (Precision Glassblowing), the objective lens vendor (Special Optics), and I worked closely together to ensure that the glass cell designs and the objective designs were compatible with each other.

In the final design, the working distance (WD) for our objective lenses is

$$\begin{aligned}\mathrm{WD} &= 21.025\ \mathrm{mm} \\ &= \underbrace{9.525\ \mathrm{mm}}_{d_{\mathrm{UHV}}} + \underbrace{9.5\ \mathrm{mm}}_{d_{\mathrm{window}}} + \underbrace{2\ \mathrm{mm}}_{d_{\mathrm{air}}},\end{aligned} \tag{7.1}$$

where d_{UHV} is the distance in UHV from the inner surface of the objective window to the center of the glass cell, d_{window} is the thickness of the fused silica objective windows, and d_{air} is the air space between the outer surface of the objective window and objective lip. Special Optics determined that the 9.5 mm thick fused silica objective window thickness needed to be held to a tolerance of ± 0.025 mm [106, 107, 108] (a very tight tolerance as stated by Precision Glassblowing), for diffraction-limited performance from the objectives. However, Precision Glassblowing's window vendor TelAztec managed to meet these tolerances. Most of the vendors offered windows that were 6 mm thick or less. From the previous paragraph, it might seem counterintuitive as to why we chose a thicker window. A few factors led us to this decision.

We needed objective windows with large enough clear apertures in order to accommodate shallow-angle MOT beams, since we did not want to project MOT beams through the objectives (see Fig. 7.29 and Fig. 7.13c). Projecting MOT beams through the objectives would lead to substantial background scattered light at the EMCCD camera. Additionally, generating a few mm collimated MOT beam through the objective is extremely challenging for high NA objectives (I know this from a failed attempt). The 0.6 NA requirement from our objectives and the fact that the glass cell frame cannot be made too thin pushed the OD of the Ultem (PEI Ultem 2300 30% glass filled) housing for the objectives to a large value of 50.8 mm OD. Unfortunately, the typical objective windows on Precision Glassblowing glass cells were also 50.8 mm OD and 6.35 mm thick. Therefore, in order to accommodate the MOT beams, we needed a larger objective window. However, keeping the window thickness at 6.35 mm would exacerbate the bowing of the windows because there is atmospheric pressure on one side and UHV on the other side[6].

[6]Bowing of circular windows is circularly symmetric, and the aberrations associated with this bowing can be compensated relatively easily. Typical glass cells on the market are cuboid in shape. This makes the bowing problem rectangular, which introduces cylindrical aberrations that are harder to compensate. In addition, vendors that offered cuboid cells did not offer RAR nanotexturing at the time.

The bowing problem is mathematically equivalent to the deflection of a circular plate that is subjected to a uniform load while being clamped at the circumference. The maximum stress and maximum deflection at the center of the circular plate scales as (clear aperture)^2/(plate thickness)^2 and (clear aperture)^4/(plate thickness)^3 respectively [7] [109]. To determine the required thickness for our 76.2 mm clear aperture objective window to match the performance of a standard 50.8 mm OD and 6.35 mm thick window, I computed the scaled thickness value that equalizes the maximum stress at the center of the objective windows: For a 76.2 mm clear aperture, the thickness must be 9.5 mm ($76.2\ \text{mm}/9.5\ \text{mm} = 50.8\ \text{mm}/6.35\ \text{mm} = 8.0$) [8].

While increasing the thickness of the objective windows lessens bowing, it increases the working distance of the objective (Eq. 7.1). To reduce the working distance, we decreased the thickness of the glass cell frame. However, there is a lower limit to the thickness of the glass frame, as thinner frames imply smaller holes in the frame body for connecting a glass-to-metal tube adapter. Since we wanted to not project the MOT beams through the objectives (see Fig. 7.29 and Fig. 7.13c), we needed enough clearance on the tube adapter side to fold the MOT beams out. A small hole in the frame with a long tube adapter reduces the UHV conductance to the glass cell, as the conductance scales as (tube adapter inner diameter)^3/(tube adapter length) in the molecular flow regime [110]. This limits the ultimate base pressure achievable in the glass cell, affecting the vacuum-limited lifetime of the atoms. The mechanical fragility of the tube adapter connection to the frame also increases with its length. Precision Glassblowing recommended against going below a frame hole size of 14.7 mm (Fig. 7.2). These requirements set the distance in UHV from the inner surface of the objective window to the center of the glass cell to 9.525

[7] https://www.engineersedge.com/material_science/circular_plate_uniform_load_13638.htm

[8] We have interferometrically measured the bowing of the objective windows (Sec. 7.6.3.1).

mm (Eq. 7.1).

7.1.2 The rest of the UHV chamber assembly

7.1.2.1 Vacuum firing parts of the UHV chamber assembly

A wide variety of custom-machined parts constitute the innards of our UHV chamber. I was very careful in verifying the UHV compatibility of the part materials using this reference [111]. All custom stainless steel parts (304L and 316L) for in-vacuum operation were brushed and electropolished to reduce outgassing [112]. We used UHV-compatible ceramics such as MACOR and alumina and metals such as tungsten. For the UHV-compatible plastics, we used machined PEEK and Kapton. We also used a UHV-compatible epoxy to bond the parts together. Special attention was paid to the threaded holes in the machined parts to avoid virtual leaks. We only used vented screws to connect the in-vacuum parts to minimize the chances of a virtual leak [112]. Usually, hydrogen trapped in the bulk of the austenitic stainless steel parts (we use 304L and 316L SS parts) limits the ultimate base pressure that can be achieved in a vacuum system.

Vacuum firing helps remove hydrogen from the bulk of the austenitic steel parts [112, 113, 114]. Vacuum firing is baking parts at elevated temperatures (typically at 950°C) in a furnace that is under vacuum. Elevated temperatures greatly increase the solubility of hydrogen (Arrhenius-type dependence on the temperature) in the bulk of steel parts, as given by the Sieverts law [112]. The vacuum environment of the furnace pumps out the hydrogen molecules desorbed from the surface of the SS part after diffusing to the surface from the bulk. Vacuum firing also reduces other contaminants such as hydrocarbons. Vacuum firing [112] of thoroughly cleaned (Appendix F) UHV metal and ceramic chamber components was performed in a furnace under

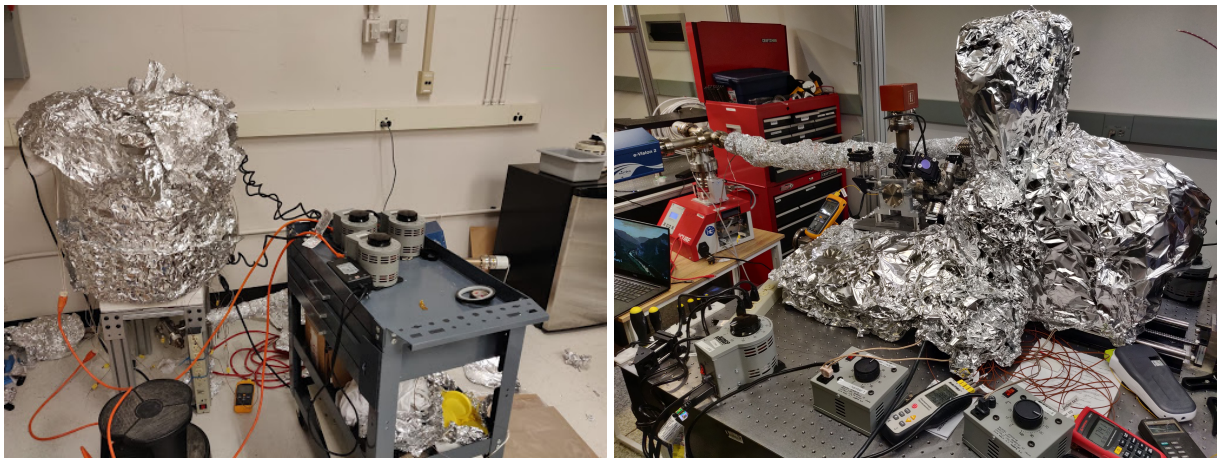

(a) Vacuum firing of the UHV parts. (b) In situ bake-out of the assembled UHV chamber.

Figure 7.5

vacuum for 2 weeks at 400°C (see Fig. 7.5a). After two weeks, the furnace pressure was at the base pressure of the turbomolecular pump (Pfeiffer HiCube). The heating of the furnace was accomplished by creating a support structure with chicken wire on the outer surface of the furnace. We draped fiber glass insulation on the outside of the support structure. Heater tapes were threaded on the chicken wire support structure and thermocouples were placed at random locations. The vacuum firing setup was based on these references [115, 116].

We did not vacuum fire any UHV chamber parts that weren't rated for 400 °C or had constituents that could differentially expand, like viewports or feedthroughs. These parts were later baked in situ after the chamber was assembled. Despite vacuum firing the stainless steel parts, they had an oxide layer on them, as evidenced by a yellowish sheen (a signature of air bake). The oxide layer on air-baked parts prevents the recombination of atomic hydrogen into hydrogen molecules and therefore suppresses the hydrogen desorption process [112]. Later, we will perform an in situ bake of the assembled UHV chamber (see Fig. 7.5b).

7.1.2.2 Assembling the UHV chamber assembly

After two weeks of vacuum firing, we assembled the UHV chamber. The entire chamber was assembled by strictly using the torque wrench values for the screws (tightened in a star-pattern) recommended for each flange size [117]. This helped us minimize leaks in the setup, which we verified quite frequently using a leak detector (Agilent VS PD031 Helium Leak Detector). We religiously followed and enforced on each other the UHV assembly guidelines I got from these references [118, 119]. I was the "clean" helper, and Tsz-Chun and Kevin were the "dirty" helpers according to the guidelines in this reference [118].

At the heart of the UHV chamber assembly (see Fig. 7.6) is a 2.75" multi-CF expanded spherical cube 316L stainless steel chamber (Kimball Physics, P/N: MCF275-ExpCube-C6A8). This miniature SS chamber has eight 1.33" CF sealing surfaces and six 2.75" CF sealing surfaces with one pair of grabber grooves per sealing surface. The SS chamber is supported by black anodized aluminum mounting brackets (Kimball physics, MCF275-ExtBrkt-R). The brackets clamp on to a double-sided mounting flange (Kimball physics, MCF275-MtgFlg-C2), which is hidden under the bracket in Fig 7.6. On one side of the chamber, the double-sided flange is sandwiched between a viewport (Kurt J. Lesker, P/N: VPZL-275DUNM) and a non-rotatable closed coupler (Kimball physics, P/N: MCF275-ClsCplr-C2-1400). On the other side of the chamber, the double-sided flange is sandwiched between another closed coupler and a five-way cross (Kurt J. Lesker, C5-0275). We used closed couplers to minimize the overall length of the chamber supports (and therefore the chamber cantilever between the two bracket locations). The mounting brackets are connected to large right-angle mounting brackets (Thorlabs AP90RL), which are then bolted to an anodized Thorlabs MB2424 breadboard. The top 2.75" sealing

(a)

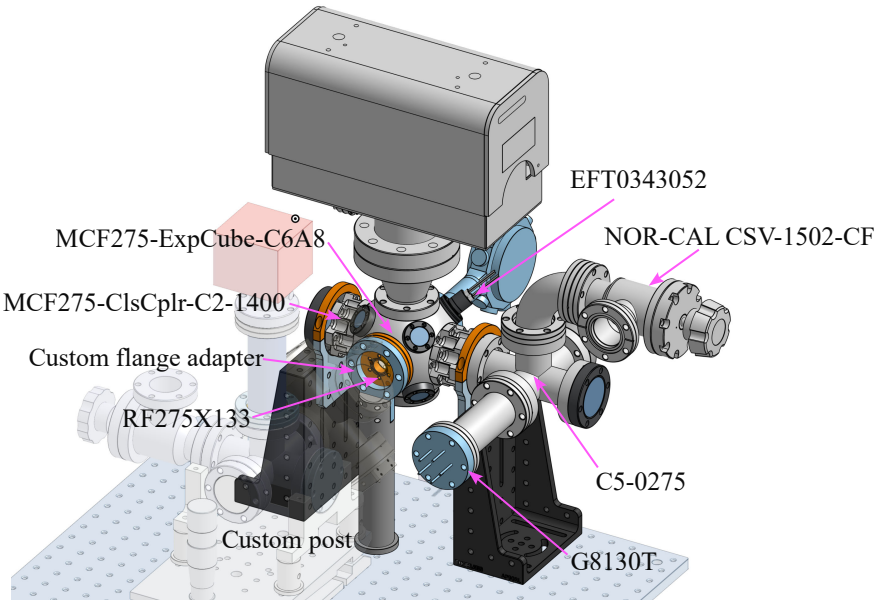

(b)

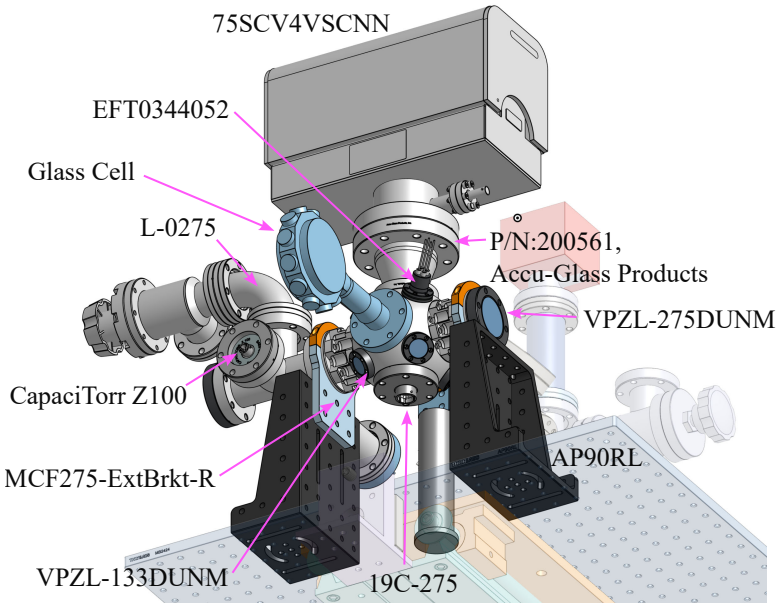

Figure 7.6: CAD design of the UHV chamber assembly

surface of the SS chamber is connected to an ion Pump (Kurt J. Lesker, P/N: 75SCV4VSCNN with a 75 l/s pumping speed and a 4.5" rotatable flange) via a 4.50" to 2.75" CF conical reducer flange (Accu-Glass Products, P/N:200561). On the bottom 2.75" sealing surface, we mount a 2.75" CF flange that hosts a 19 pin Mil-C-26482 circular feedthrough (Accu-Glass Products, 19C-275). This flange provides the electrical connections to the internal electrodes. The Yb 2D MOT source is connected to the rear 2.75" sealing surface of the SS chamber via a bellows (Kurt J. Lesker, P/N: MEW0750251C1) and a zero-length reducer flange (Kurt J. Lesker, P/N: RF275X133). The reducer flange was mounted to a 2.75" sealing surface using a custom adapter plate (made of stainless steel 304/304L). The adapter plate was connected to a custom post (made of aluminum 6061-T6) (see Fig. G.3), which was then bolted to the Thorlabs MB2424 breadboard. This adapter flange and custom post assembly prevents the entire vacuum chamber from rotating about the mounting brackets[9]. The glass cell was mounted to the front 2.75" sealing surface of the SS chamber[10]. The internal annular grabber grooves of the front sealing surface were also used to mount the electrode assembly (Sec. 7.1.4). Six of the 1.33" sealing surfaces were used to mount the viewports (Kurt J. Lesker, P/N: VPZL-133DUNM). The last two 1.33" sealing surfaces were used to mount Rb dispenser modules (Sec. 7.1.3.1) that are electrically connected to the air side through feedthroughs (Kurt J. Lesker, Part numbers: EFT0343052, EFT0344052)[11].

[9] Initially, the rear CF sealing surface had leaks when it was inspected with the leak detector. The standard torque values used for tightening the screws at this sealing surface was surprisingly inadequate. Using a higher torque value fixed the leaks.

[10] A 12 point head $1/4-28$ machine screw broke off on the glass cell side sealing surface of the steel chamber during the assembly. Fortunately, we were saved by the double density nature of the circumferential array of threaded holes on the sealing surfaces, as well as the fact that the glass cell flange was rotatable. We used a dremel tool with a mounted grinding wheel to grind down the screw head. This was done with extreme care to avoid contaminating the UHV chamber. As a rule of thumb, one should use silver-plated machine screws as the low friction associated with the silvered surface helps avoid these kinds of issues.

[11] I advise against using ball end hex heads to tighten $\#8-32$ screws (to their recommended torque value) despite their ease of use. We have a broken ball end lodged in the socket of an $\#8-32$ screw.

The five-way cross (Fig. 7.6) hosts a NEG pump (CapaciTorr Z100 from SAES Getter). The NEG pump was housed in the five-way cross, instead of the ion pump, because of its much higher pumping speed of 150 l/s (for some active gases). The effective pumping speed of the NEG pump, taking into account the conductance of the five-way cross, is similar to that of the ion pump. The five-way cross hosts a Bayard-Alpert nude UHV ionization gauge (G8130T from Kurt J. Lesker) to measure chamber pressure independently of the ion pump controller [112]. It also houses a NOR-CAL CSV-1502-CF gate valve, which we use to pump down the entire chamber using a turbomolecular pump.

After the UHV chamber was assembled (Fig. 7.7a), we performed a second bake of the chamber under vacuum at a lower temperature of $\lesssim$ 200°C (see Fig. 7.5b) to remove water vapor, nitrogen, and oxygen adsorbed on the surfaces of the vacuum parts from being exposed to air. I designed a clamshell protector (Figs. G.1, G.2, 7.7a, 7.7b) to protect the glass cell during baking. The clamshell protectors were vacuum fired to ensure clean inner surfaces so as not to dislodge impurities that could bond to the glass cell surfaces during the in situ bakeout. Fiberglass insulated heating tapes were wound around the clamshell protectors, the steel chamber, the mounting brackets, and the large right-angle brackets[12]. Thermocouples were inserted in strategic locations to monitor temperature during the bakeout.

Glass-to-metal seals in viewports are susceptible to leaks when the viewport temperature changes rapidly or if there is a large thermal gradient across the viewport. Therefore, we raised the temperature of the entire chamber assembly to $\lesssim$ 200° C (the maximum rated temperature for the viewports) at a rate much slower than the 2°C/min recommended by Kurt J. Lesker for

[12]We used silicone rubber heating tapes (instead of fiberglass insulated heating tapes as they flake fibers and can contaminate the glass cell surfaces) for the first bake. However, these silicone heater tapes burned at about 100°C due to local temperatures likely exceeding their rated temperature of 232°C.

temperature changes in viewports. Large thermal gradients were a particular concern for one 2.75" viewport that was located at a AP90RL aluminum mounting bracket. The two AP90RL mounting brackets were connected to the aluminum breadboard, a large heat sink. Therefore, we heated the AP90RL mounting brackets to provide a gradual temperature gradient from the hot chamber to the cold breadboard[13]. We baked the chamber at $\lesssim 200$°C for more than two weeks.

We achieved a UHV chamber pressure of 1×10^{-11} Torr, as measured at the ion pump, which is the base pressure of the ion pump[14]. The pressure is likely lower due to leakage currents that overestimate the pressure measurement [120, 121]. Such a low UHV pressure was achieved despite the many in-vacuum parts, some of which are epoxy-bonded and others that are made out of plastic like PEEK or Kapton. To protect the UHV conditions inside the chamber, the region between the closed gate valve and a copper pinch off adapter gasket (Ideal Vacuum Products LLC, P/N:P108190) was pumped down to the base pressure of the turbomolecular pump (1×10^{-9} Torr). We then pinched off the gasket.

One last thing to note, during the in situ bakeouts with the turbomolecular pump, we also conditioned the Rb dispensers at 3 A per dispenser for a day. The dispenser conditioning was performed every time we broke the vacuum. We also conditioned the NEG pump during the in situ bakeout with the turbomolecular pump. The ion pump was off during the dispenser and NEG pump conditioning and was only turned on after the conditioning was complete. We did not in situ bake the Yb 2D MOT source.

[13] One of the heater tapes on the mounting bracket failed mid-way during the bake. Fortunately, the vacuum was not compromised.

[14] Once we noticed a large spike in the measured ion pump pressure that we now attribute to an argon instability [112].

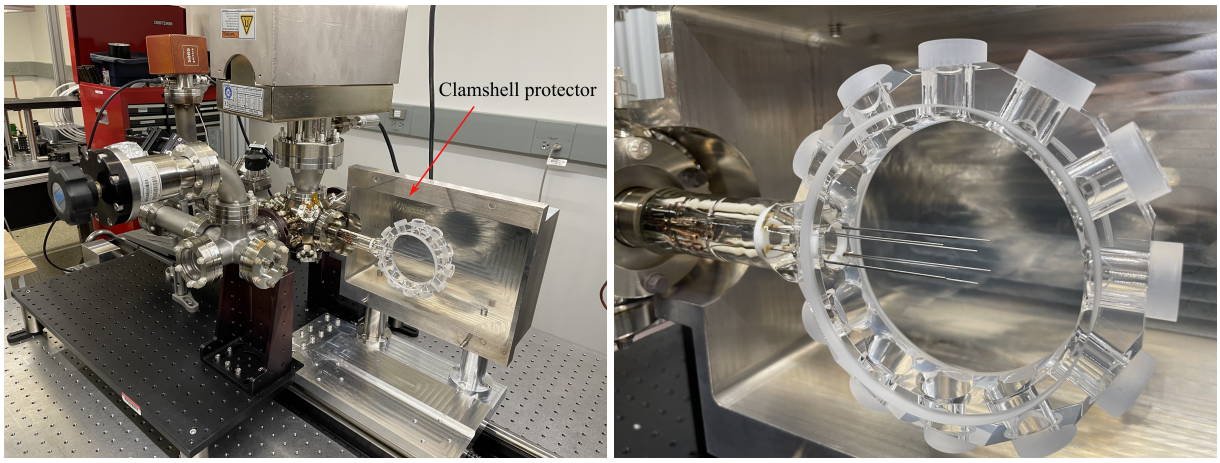

(a) (b)

Figure 7.7: (a) The UHV chamber assembly (b) The glass cell.

7.1.3 Atomic sources

7.1.3.1 Design and construction of the Rb dispensing modules

We use Rb getters (RB/NF/4.8/17) from SAES Getters to dispense Rb. The dispensers have an active length of 17 mm with a total nominal yield of 4.8 mg of Rb. Each dispenser has a 9.5 mm×2.7 mm×0.15 mm terminal connection tab on both ends for electrical connections. I designed (Fig. 7.8a) and assembled (Fig. 7.8b) two Rb dispensing modules. Each module consists of two pairs of dispensers in series that are connected in parallel to each other. These modules are then connected to two separate electrical feedthroughs with different conducting materials: Copper and Molybdenum (Kurt J. Lesker, Part numbers: EFT0343052, EFT0344052). The dispenser modules are installed in a way that the dispensing solid angle overlaps with the glass cell entrance.

For the purposes of designing the electrical connectors for the dispenser modules and a current supply for driving the module, it is imperative to consider the conductance (and thermal)

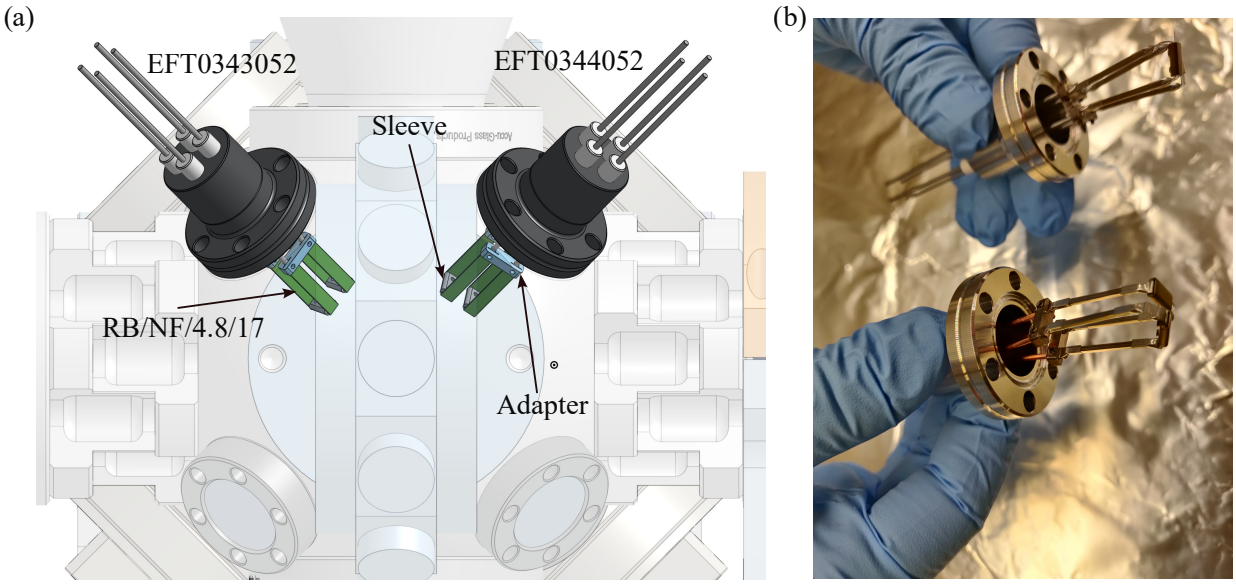

Figure 7.8: Rb dispensers modules: (a) CAD design (b) Assembling the modules.

properties of the dispensers. The power dissipated in each dispenser follows the typical $P = I^2R$ relation. The NiCr terminals have a resistance of 0.03 Ohm each. The resistance of the dispensing region is 0.0026 Ohm/mm. This gives a total resistance of 0.104 Ohms per dispenser. We measure a total resistance of 0.247 Ohms for our dispenser assembly setup, as measured from the Cu feedthrough ends. The extra resistance comes from the connectors used to construct the dispenser assembly. As the dispensers can reach temperatures between 550°C and 850°C when driven at currents from 4.5 Amps to 7.5 Amps, I used stainless steel connectors in the dispenser assembly for the electrical connections between the dispenser elements and the feedthroughs given its high melting point, high corrosion resistance, and low thermal expansion coefficient. An additional reason was that I used socket-head vented #0-80$\times$1/16 flat-tip stainless steel setscrews from Accu-Glass products for secure connections between dispenser flat terminals and electrical connections. Having the same material for the screws and electrical connections might mitigate the loosening of the screws from repeated thermal cycling. The connectors (Figs. G.4, G.5) were machined from stainless steel 304 / 304L, which were then brushed and electropolished for UHV

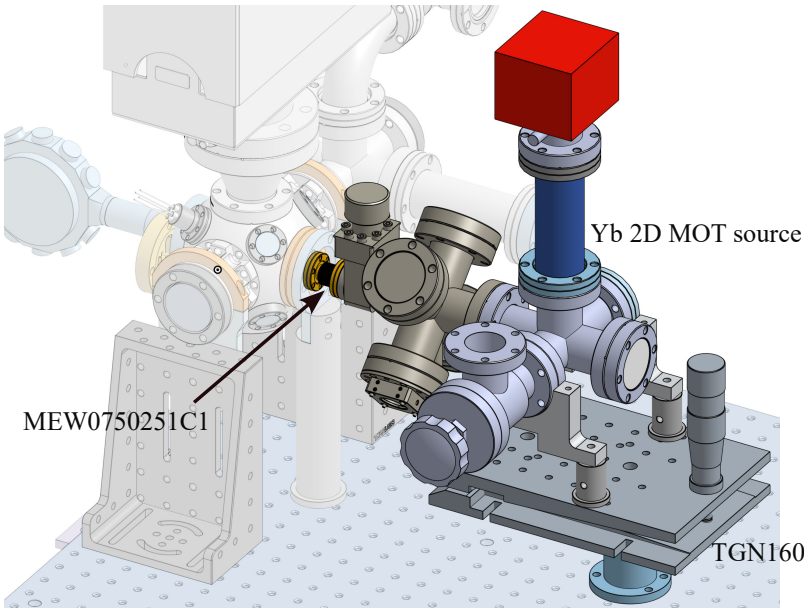

Figure 7.9: CAD design for the Yb 2D MOT source

operating conditions.

For the purposes of driving current through the dispensers, Alessandro and I came up with a MOSFET and microcontroller-based (Teensy 3.2) circuit design. This circuit was built, assembled, boxed, and debugged by Kevin. The link to the Github project folder is https://github.com/JQIamo/Rb-Dispenser-pwr-supp.git. We have added a few protections so as not to overdrive the dispensers: (a) Software current limits have been set by the Teensy and BLACS [122] at 8 A at the code level (b) Hardware current limit of 9A is set on the CSI3020X current supply (from Circuit Specialists) (c). Pulldown resistors were added to the PCB so that the current supply never turns on at the set/max current, but at 0 A.

7.1.3.2 Yb cold atom source

We recycled the Yb 2D MOT source from the previous experiment. More details on the source can be found in Creston's and Varun's thesis [8, 9]. In the new experiment, I decided

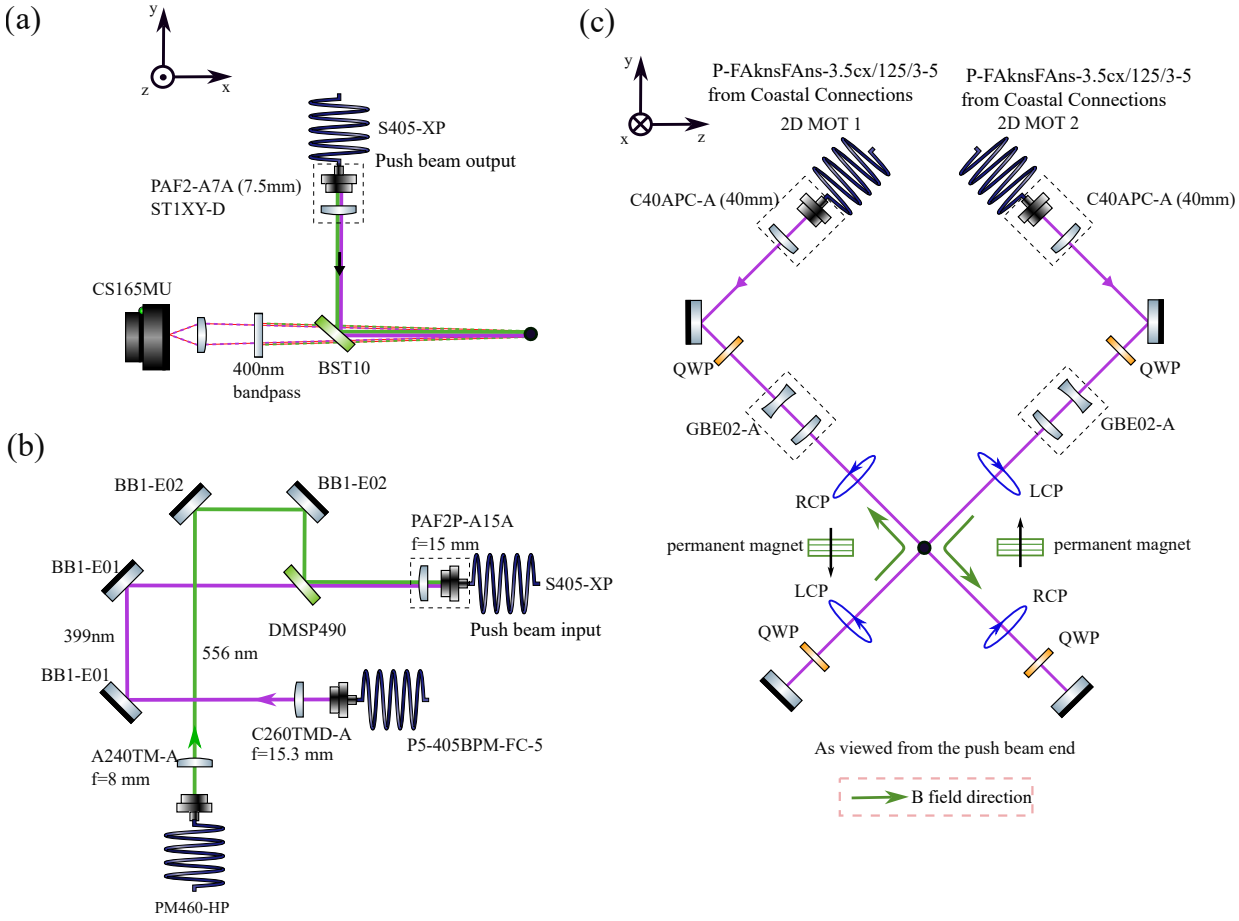

Figure 7.10: schematic of the optical layout for the Yb 2D MOT source

to mount the 2D MOT chamber on a tilt platform (Newport TGN160) and attach it to the steel chamber via a stainless steel bellows (Kurt J. Lesker MEW0750251C1) (see Fig. 7.9). Given the small diameter (2 mm) of the differential pumping tube hole, this tilt platform plus bellows arrangement would allow for additional flexibility in directing the Yb cold atomic beam to the science chamber. This tilt ability was useful in achieving the first Yb 3D MOT signal.

The optics for generating a Yb cold atomic beam in the previous setup is detailed in Creston's and Varun's thesis [8, 9]. While they took great care to minimize the coating of the 2D MOT windows with Yb, the windows have undergone some coating over the many years of operation. In the previous experiment, we used a green push beam and green 3D MOT beams to

capture Yb atoms [8, 9]. This method would fail in the new setup due to the increased distance of 380 mm between the center of the glass cell and the 2D MOT region, as well as a reduction in the size of the 3D MOT beams to $5.5 - 10.5$ mm range at the glass cell, which directly affected the loading rate of the atoms in the 3D MOT as well as their capture velocity [123]. Furthermore, the maximum total green light power was limited to 100 mW at the science chamber. Using a large green push beam power ($\sim$ 40 mW) accelerated atoms to velocities that exceeded the capture velocity of the 3D MOT. In contrast, lowering the push beam power resulted in the atomic beam drooping and blooming, preventing the atoms from ever reaching the 3D MOT region.

I realized that we needed to use a blue push beam paired with blue 3D MOT beams (see Figs. 7.34, 7.10, 7.28 and 7.29) at the science chamber to form a Yb 3D MOT in our setup. Atoms in this blue Yb 3D MOT would then be time-transferred to a green 3D MOT to realize a colder cloud of Yb atoms (Fog. 7.65). The required blue push beam power was less than 200 μW, which is significantly more power efficient than the 40 mW needed for the green push beam. The 2D MOT optics underwent a few rounds of revision before the setup was robust and low drift. In its final incarnation (see Fig. 7.10), we do not touch the 2D MOT optics for one year at a time. Here were my design choices:

- Improving the 2D MOT beam quality and uniformity: Thorlabs large beam collimators (C40APC-A) and Thorlabs Galilean beam expanders (GBE02-A) were used to collimate and shape the light from the fiber (see Fig. 7.10c). Using aberrated 2D MOT beams yielded serpentine-looking 2D MOT clouds. These 2D MOT clouds were especially sensitive to force imbalances at the edges of the 2D MOT beams as the atoms exit the trapping region.

- Boosting the passive structural stability: The size of the 2D MOT arms and the push beam

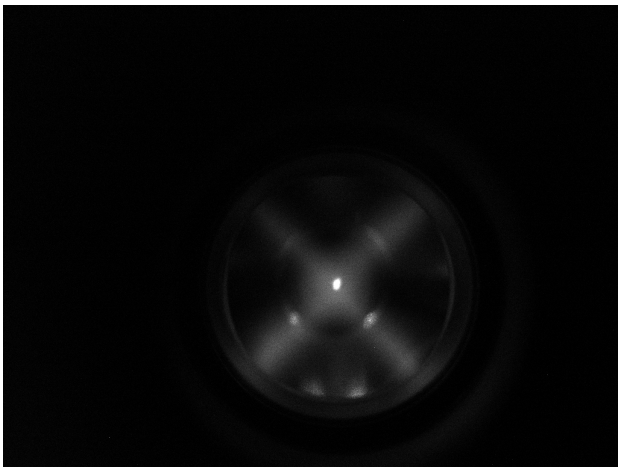

Figure 7.11: Yb 2D MOT cloud

launch arm was reduced. Reducing the mass of the optical mounts and optical elements, as well as their spatial extents, minimized the cantilever.

- Large push beam size: A large push beam helped reduce the sensitivity of its alignment to the Yb 2D MOT cloud. We used a Thorlabs achromatic fiber port (PAF2-A7A) that produced collimated beams for 556 nm and 399 nm with minimal chromatic shifts (see Fig. 7.10a). The $1/e^2$ beam diameter was slightly larger than 1 mm. When we used a green push beam (at maximum power) to get the initial signal for the 3D MOT, the blue push beam was automatically aligned.

- Continuous head-on visualization of the Yb 2D MOT cloud with a camera: A beam sampler was used as the last folding element in the push beam launch arm (see Fig. 7.10a) for head-on visualization of the Yb 2D MOT cloud.

My strategy to achieve the blue 3D MOT of Yb relied heavily on the ability to view the 2D MOT cloud of Yb head-on (see Fig. 7.10a). The differential pumping tube hole was used as a guide on the camera. The center of intensities of the 2D MOT beams fluorescing in the Yb

vapor were aligned to the differential pumping hole on the camera. This alignment led to tube-shaped Yb 2D MOT clouds that looked like bright circles when viewed head-on (see Fig. 7.11) (instead of serpentine-shaped clouds that extended transversely). Any residual offset between the 2D MOT cloud and the differential pumping tube hole was removed by moving the permanent magnets (see Fig. 7.10c). A 400 nm bandpass filter was mounted in front of the camera. The 40 mW green push beam was aligned to overlap with the Yb 2D MOT cloud (see Fig. 7.10a). The signature of this overlap and efficient pushing action was determined by slowly modulating the green laser frequency around the resonant frequency of the trapped Yb 2D MOT isotope. When the green push beam was well aligned, the integrated fluorescence from the Yb 2D MOT cloud would blink in and out. The effect of the push beam could not be discerned when the cloud was viewed from the side. Using this alignment method, we were able to achieve a Yb 3D MOT with a high-intensity green push beam, and consequently a blue push beam as well, due to the achromatic fiberport setup. Lastly, we noticed the robustness of the blue 3D MOT to alignment of the 2D MOT beams and the blue push beam. The blue push beam is far superior at overcoming the edge effects arising from 2D MOT force imbalances, which kick the atoms off axis, when compared with a green push beam of the same intensity.

7.1.4 Design and construction of electrodes for electric field control

Large electric dipole moments of atoms in Rydberg states makes them very sensitive to stray electric fields. It is therefore imperative to locally control the electric fields in the vicinity of the atoms. Eight tungsten rods mounted to a custom ceramic assembly (Fig. 7.12a) provide us with arbitrary 3D electric field control in the vicinity of the atoms at the center of the glass cell.

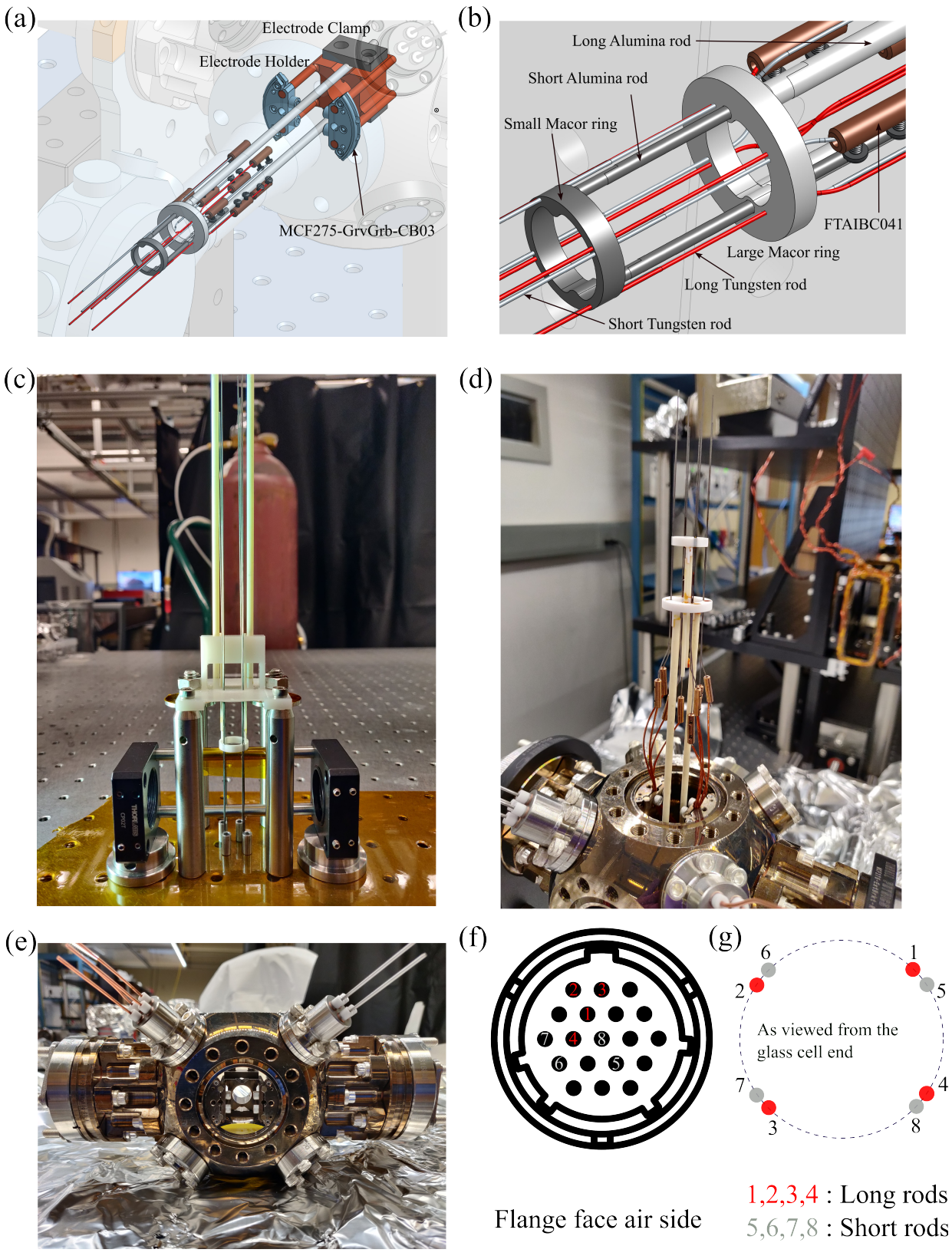

Figure 7.12: Design, assembly, and installation of the electrode assembly

The electrode assembly must satisfy a few constraints. Given that the dispensed Rb must flood the glass cell to create the Rb MOT, the electrode assembly, which extends all the way from the steel chamber and into the glass cell, must not obstruct this flooding. The assembly also must not obstruct the cold atomic Yb beam directed towards the center of the glass cell. Furthermore, the assembly must not hinder the vacuum pumps in our setup from continuously and efficiently pumping out the glass cell, to maintain good UHV conditions at the location of the atoms. Last but not least, the electrodes at the glass cell must not block optical access for high NA projection (0.6 NA for our objectives) of optical tweezers as well as imaging of the single fluorescing atoms. Therefore, the entire electrode assembly must be as compact as possible. To do this, we used 0.02 ” diameter Tungsten rods as the material for our electrodes. However, using such small diameter tungsten rods can cause cantilevering issues, which needs to be mitigated by appropriately designing the rest of the electrode assembly. A simple solution is to reduce the length of the rods that must cantilever.

Designing the electrode assembly (Fig. 7.12a and Fig. 7.12b) and assembling it using jigs (Fig. 7.12c and Fig. 7.12d) was one of my more complicated tasks. The frame of the electrode assembly is made up of ceramic parts (Fig. 7.12b), which were machined by Precision Ceramics. I worked closely with the ceramic vendor to machine these parts. Given the tight tolerances for these parts, machining them posed quite a challenge on the part of the vendor.

The tungsten electrode rods (from Midwest Tungsten Service) are guided by the holes in (and epoxied to) the small ring and the large ring (Fig. 7.12b). The rings were machined out of MACOR because they had many features (Fig. G.9 and Fig. G.8). The short rods (Fig. G.11) and the long rods (Fig. G.10) were machined from Alumina. The short alumina rods connect the small MACOR ring to the large MACOR ring (Fig. 7.12b). The long alumina rods connect to the

large MACOR ring. These long rods support the entire assembly. The long rods were clamped to the electrode holder (Fig. G.6) using electrode clamps (Fig. G.7).

The only feature on each of the Alumina rods was a lap joint. Given this simple feature and the need for large flexural strength and hardness to minimize the ceramic assembly cantilever, I chose to machine the rods out of Alumina instead of MACOR, despite Alumina's lesser machinability. The electrode holder contains two V grooves (included angle of 105 degrees) on its body (Fig. G.6). The long rods are placed in the V groove and pressed against the body of the electrode holder via electrode clamps (Fig. 7.12d). The electrode holder and electrode clamp were machined from 304/304L stainless steel and were brushed and electropolished. The electrode holder is held in place and connected to the steel chamber body via groove grabbers (MCF275-GrvGrb-CB03) (Fig. 7.12d and Fig. 7.12e). All connections between the ceramic parts and between the rings and the electrodes were made with UHV-compatible epoxy (Accu-Glass Products Inc., P/N: 111785). The rings were connected to their respective Alumina rods via lap joints. A heat lamp was used to cure the epoxy, which turned a deep amber color upon curing. I assembled the electrode assembly using a jig made out of HDPE (High Density Polyethylene) plastic as epoxy does not bond to it (Fig. 7.12c).

In the electrode assembly, four tungsten rods are longer (red rods) than the other four by 1 cm at the glass end (Fig. 7.12b and Fig. 7.12f). The ends of the shorter rods (gray rods) were aligned roughly with the center of the glass cell. Each pair of rods (red and gray) were bent away from each other in situ to avoid any electrical shorts. The electrodes were electrically connected to a 19-way UHV-compatible PEEK connector cable assembly (Accu-Glass Products, Inc., P/N: 110230) via Be/Cu inline barrel connectors (Kurt J. Lesker, P/N: FTAIBC041). The Kapton insulation on the wires was removed in order to make the connection. I compacted this electrical

connection by switching the standard slotted head screws in the inline barrel connectors with the vented $\#0-80$ setscrews. The 19-way UHV-compatible PEEK connector cable assembly was connected to a 19-pin feedthrough flange (Accu-Glass Products, Inc., P/N: 19C-275) (Fig. 7.12f and Fig. 7.12g).

Before mounting the actual glass cell, I ensured that the ceramic assembly was centered to the neck of the glass cell and would not snag on it when I installed the actual glass cell. I verified these centration and clearance requirements using an exact replica of just the neck and flange of the glass cell from Precision Glassblowing that was installed and removed a few times. Despite taking care to ensure that there were no shorts prior to the in situ chamber bakeout, we ended up with two pairs of rods that were shorted to each other after the bake.

7.2 Design and construction of the magnetic field coils and their housing

We wound our own magnetic field (solenoid) coils. There are 6 solenoid coils in total for arbitrary magnetic field control in 3D (see Figs. 7.13a, 7.13b). Each solenoid coil is helically [124] wound to the lip of a machined PEEK (polyetheretherketone) frame. PEEK is a high-performance machinable thermoplastic. It has high strength and is thermally resistant. The six coil frames are assembled into the coil housing. All PEEK frames are bolted to the housing frame (purple part in Fig. 7.13a) (see Figs. G.12). This design also facilitates easy future modifications. Winding solenoid coils on plastic frames immediately resolves any eddy current issues during rapid switching of currents in the coils. The downside to using PEEK frames is that the heat generated from the coils cannot be dissipated easily into the body of the frames as a result of PEEK's low thermal conductivity (0.24 - 0.26 W/(mK)).

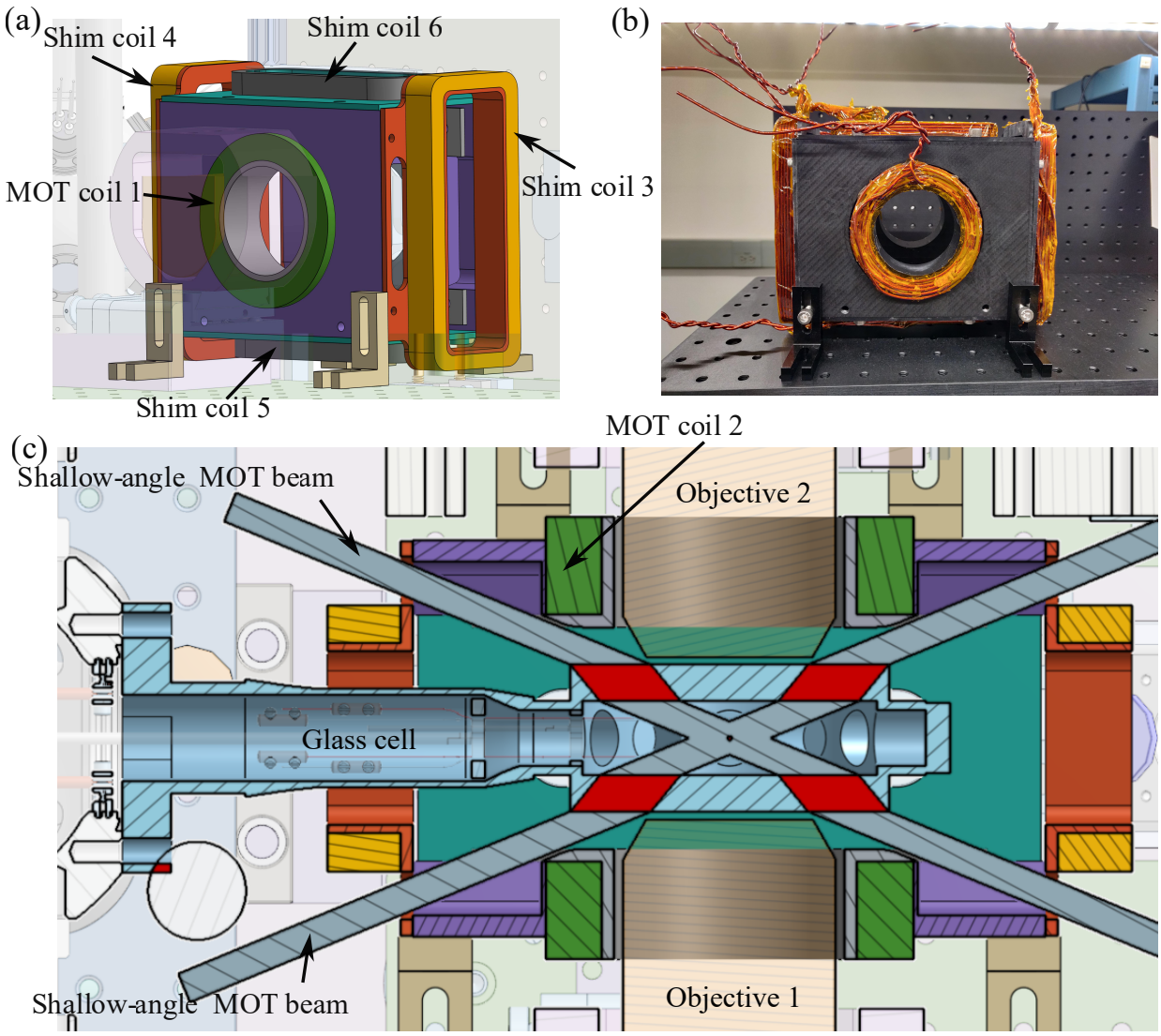

Figure 7.13: (a) CAD design for the housing for the magnetic field coils i.e. the coil housing (b) The fully assembled coil housing (c) Cross-section of the coil housing showing the shallow angle MOT beam paths

We did not want to form our MOTs with one pair of MOT beams being sent through the objectives. To do this, we made slots in the coil housing that would accommodate the shallow-angle MOT beams (Fig. 7.13c). However, a beam of light is displaced when it passes through a flat glass plate—the objective windows of the glass cell—at a non-zero angle of incidence. This displacement is 11.6 mm for a laser beam that passes through both glass cell objective windows at 67.5° angle of incidence. Given that the shallow-angle beam size is ~ 5 mm, determined by the

OD of the objective window, it was crucial that I considered this displacement when designing the coil housing. If the beam displacement is not considered, the shallow-angle beam will not exit the coil housing, which we have confirmed. Only when the vacuum chamber assembly was rolled in did the shallow-angle beam make its way out of the coil housing. The compactness of the coil housing and the need for considering the shallow-angle beam displacement was also driven by the fact that the MOT solenoid coils had to be placed at a certain distance from each other for optimal field gradient when driven in the anti-Helmholtz arrangement. The spacing between the coils is intimately related to the radius of the solenoid coils for the optimal field gradient [125].

In the case of thin solenoid coils, the gradient is maximal when the spacing between the coils is equal to the radius of the solenoid coils. The spacing is usually increased to $\sqrt{3}$ times the radius of the coil [125]. This increases the homogeneity of the field gradient as well as the volume between the coils. However, this comes at a cost of reduced magnitude for the field gradient. The field gradient is proportional to $(\text{current} \times \text{no. of solenoid turns})/(\text{radius})^2$. However, the inductance of the coils is proportional to $(\text{no. of solenoid turns})^2$, and high inductive loads are undesirable[15]. Therefore, it is important to strike a balance between the current [16], the number of turns, and the radius of the thin solenoid coils for optimal magnetic field gradient.

We construct our thick solenoid coils from enamel-coated 12 AWG magnet wire (Essex GP/MR-200®, Magnet Wire/ Winding Wire) (see Fig. 7.14d and 7.13b). We helically wind our coils onto the lip of each PEEK frame for good fill factor [124]. In order to maximize heat transfer in the coils (by removing air gaps) and to give the coils form, we applied a thermally conductive but electrically insulating epoxy (Cotronics Corp. DURAPOT 865) to each radial layer before

[15]For a thick solenoid coil, the inductance can be determined easily using this web calculator: https://www.66pacific.com/calculators/coil-inductance-calculator.aspx

[16]Heat dissipated in the coils scales as current^2 and low-noise high current supplies with fast switching are expensive.

Coil	Layers	Turns/layer	Total Turns	Measured inductance (mH)
MOT 1	5	9	45	0.33
MOT 2	5	9	45	0.33
Shim 3	3	8	24	0.08
Shim 4	3	8	24	0.08
Shim 5	4	5	20	0.04
Shim 6	4	5	20	0.05

Table 7.1: Electrical and mechanical specifications of our solenoid coils

winding a subsequent radial layer. This epoxy also binds the innermost radial layer of the solenoid coil to the PEEK frame lip. The jig I designed to wind the coils is based on a turntable where the PEEK frame is mounted to the turntable via a turntable adapter (see Figs. 7.14a and 7.14b). The height of the coils is defined by a 3D printed plastic that is also bolted to the turntable adapter. The 3D printed plastic presses onto the PEEK frame from the top, forming a tight seal. The coils are axially wound from the L notch in the 3D printed plastic (HP PA 12) down to the body of the PEEK frame by rotating the turntable, all the while maintaining tension in the wire. The inner surface of the 3D printed plastic was layered with Kapton tape to prevent the solenoid coil from bonding to its body. To wind the rectangular coils, we used an adjustable-angle handscrew clamp on the long rectangular sides of the coils (see Figs. 7.14c). If clamps were not used, the coils would bow outward and will not bond to the PEEK frame lip. Lastly, we apply layers of Kapton tape on the exposed surfaces of the coils to seal all the dry epoxy crumbs that may shed after the curing process (see Fig. 7.13b).

Tsz-Chun simulated the magnetic fields using a free Mathematica add-on (Radia) from European Synchrotron Radiation Facility (ESRF) and determined the number of axial and radial turns (Table 7.1) needed for optimal magnetic field gradient for Rb and Yb MOTs. He also

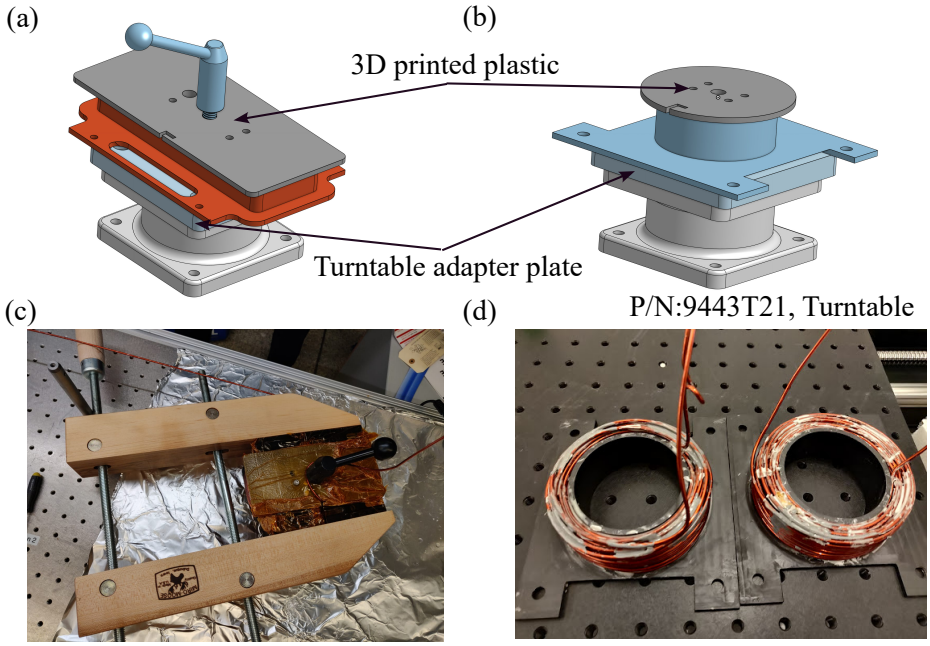

Figure 7.14: (a) The coil winding jig for the rectangular/shim coils (b) The coil winding jig for the MOT coils (c) Using handscrew clamp to prevent the shim coils from bowing outward during winding (d) The potted MOT coils wound to their PEEK frames

determined the number of axial and radial turns needed for the shim coils. The quadrupole magnetic field (for MOTs) is generated by the two MOT coils in an anti-Helmoholtz arrangement. 20 A current in each of the MOTs coils yields a 4.4 mT/cm magnetic field gradient at the center of the glass cell.

7.2.1 Mitigating coil heating

We noticed that during the steady state operation of the MOT coils at the typical MOT current values of $\pm 8 - 12$A, the temperature of the coils would increase enough to misalign the objectives. Steady-state operation of the MOT coils is needed for MOT optimization and debugging. Because the coils are epoxied to a PEEK frame, which has low thermal conductivity, the heat generated by the coils was not easily dissipated into the body of the PEEK frame. Furthermore, the spacing between the inner surface of the PEEK frame lip and the objective is 2

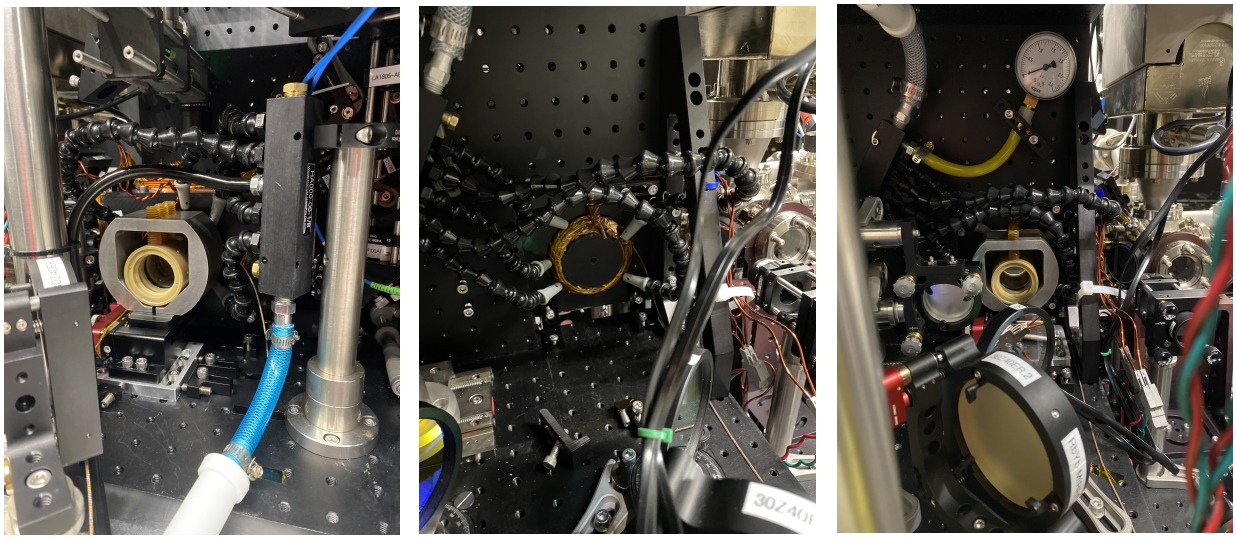

(a) (b) (c)

Figure 7.15: Manifold for cooling the MOT coils with pressurized and filtered dry nitrogen

mm. This meant that the heat generated by the MOT coil was being convectively transferred to the objective. This misalignment of the objectives due to heat from the steady-state operation of the MOT coils was interferometrically measured using the Twyman-Green-Fizeau interferometer (see Sec. 7.6.3.1). The collimated back-reflection from the objective was first aligned with a stable reference beam to yield one tilt fringe. Upon increasing the temperature of the coils, we would notice that the number of tilt fringes increases. When the coils were cooled down, the initial one-tilt fringe alignment would not recover.

The first change we made to mitigate this heating-induced misalignment was to lower the magnitude of the currents used to drive the MOT coils while still being able to form MOTs of both atomic species. The second thing I did was redesign the objective mount to improve recovery upon cool down after the objectives were misaligned by being exposed to heat (see Sec. 7.6.1.1). The last thing we did was air-cool the coils as suggested by Steve. I designed a filtered dry nitrogen delivery system that Kevin, Oliver, and I built together. Bend-and-Stay air nozzles (McMaster Carr part no. 3390K22) and anodized aluminum right-angle flow manifold

(McMaster Carr part no. 5469K121 and 5469K151) are used to deliver the filtered dry nitrogen to the coils (see Fig. 7.15). Thermocouples are also taped to the body of the MOT coils and connected to Raspberry Pis to monitor the temperature of the coils. With these changes, we were able to run the MOT coils for extended periods of time (30 mins and more) without fear of misaligning the objectives.

For a possible future iteration of this coil housing, I recommend using ceramics such as Boron Nitride instead of PEEK as its thermal conductivity is two orders of magnitude greater than that of PEEK. I also recommend manufacturing unsupported coils instead of winding the coils to the lip of the frame. In the case of a ceramic lip, the shear forces during coil winding may shatter the lip because ceramics are brittle. An unsupported coil helps with that. An unsupported coil also allows for the insertion of custom thermal insulation layers between the coil and the objective. Custom Coils, Inc. manufactured unsupported potted coils for us (see Fig. 7.16). These coils are orthocyclically wound instead of being helically wound for an even better fill factor [124]. The coil structure was held in place with DOWSIL™ 3-6752 thermally conductive adhesive.

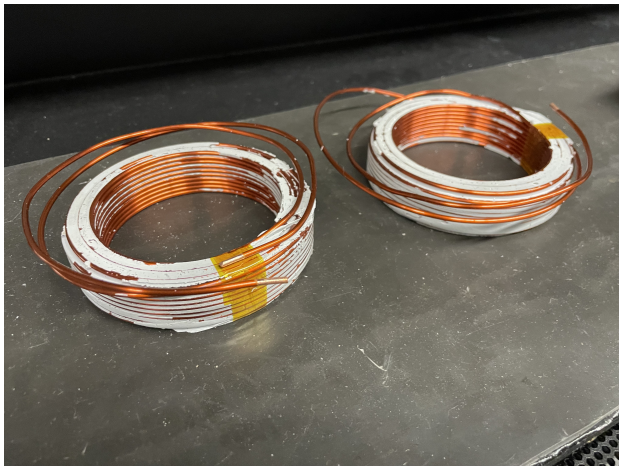

Figure 7.16: Orthocyclically-wound unsupported potted coils

7.2.2 Driving the coils

We use 6 independent bipolar power supplies (BOPs) from Kepco, Inc. to drive our 6 magnetic field coils for arbitrary magnetic field control at the atoms (Table 7.2). The BOPs are operated in current mode with the control voltage inputs provided by a National Instruments card (USB-6363). Given that our cycle times need to be short, we require fast switching of magnetic fields. However, due to the inductive nature of the load (0.32 mH for the MOT coils in table 7.1), oscillations in the current loop are to be expected when the current is rapidly turned on and off. Current oscillations (and therefore magnetic field oscillations), are especially detrimental during the sub-Doppler cooling stage of Rb and during the transfer of Yb atoms from the blue MOT to the green MOT.

We noticed jitters and wiggles in the positions of the Rb and Yb 3D MOTs that were partly due to these current oscillations. In order to diagnose (and remedy) the oscillatory behavior of the current in the coils, the control voltage input of the BOPs was driven with a 0-10 V Vpp 100 Hz square wave. The yellow trace is the control voltage signal and the clearly oscillating cyan trace is the voltage across the BOP output (Fig. 7.17a). To eliminate these oscillations (according to the vendor), we added a series-connected resistor-capacitor network (102 Ω and 390 nF) in parallel to the MOT coil at the BOP output ports, and a capacitor in the range of 10-100 nF was connected between pin 16 and pin 18 on the rear programming card connector, with the values for the capacitors and resistors empirically determined from within the vendor-specified range. These modifications strongly suppressed the current oscillations (see Fig. 7.17b). However, a balance between oscillation suppression and switching speed is necessary.

Coil	Power supply part no.	Settling time (ms)
MOT 1	KEPCO BOP 20-20M	1.3
MOT 2	KEPCO BOP 20-20M	0.82
Shim 3	KEPCO BOP 20-20D	0.3
Shim 4	KEPCO BOP 72-6M	0.57
Shim 5	KEPCO BOP 20-20M	0.27
Shim 6	KEPCO BOP 20-20M	0.128

Table 7.2: Power supply and current settling time for each solenoid coil

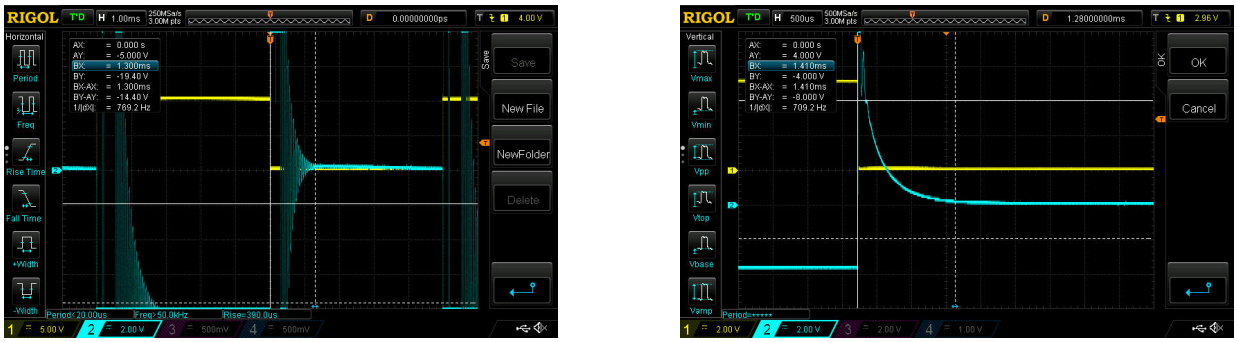

(a) (b)

Figure 7.17: The control voltage input of the BOPs driven with a 0-10 V Vpp 100 Hz square wave (yellow trace) and the measured voltage across the BOP output (cyan trace) (a) without damping circuits (b) with damping circuits.

7.3 Designing breadboards and UHV chamber carriage shaft assembly system

When I visited Harvard in 2019, I noticed some glass cell-based experiments that had their entire vacuum chamber side of the experiment mounted on translation stages. The chambers could be rolled in and out from the sensitive optical side of the experiment. We implemented this approach in our experiment. I had heard good things about this design at the time and on a personal note, we benefited from this design choice a few times.

I followed a few rules of thumb when designing the solid aluminum breadboards for our experiment (see Figs. 7.18 and 7.19). We got all of our breadboards manufactured from Baselab

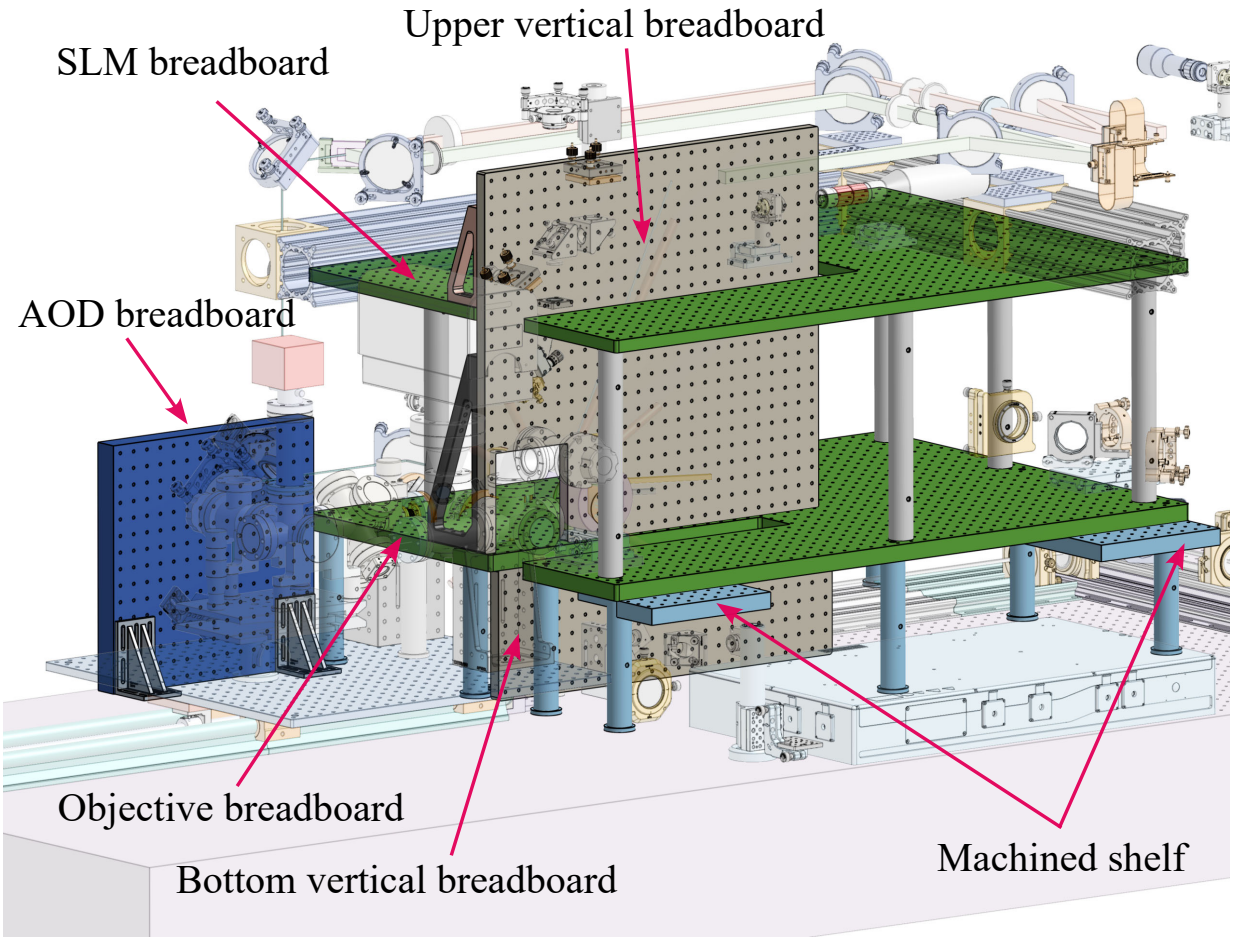

Figure 7.18: CAD design of the breadboard layout

Tools Inc. The most sensitive of optics need the thickest/heaviest of breadboards for high passive stability. However, one must balance this requirement against the additional machining and material costs associated with thicker breadboards. To that end, the AOD breadboard (Fig. 7.18) is the thickest at 1.5 ” because it folds the AOD tweezer beams up from the optical table up to the objective breadboard (and the SLM tweezer beams down from the SLM breadboard to the objective breadboard). The objective breadboard and machined shelves host the sensitive objective optics and are therefore 1 ” thick. The objective breadboard is the heaviest breadboard in our setup and is supported by ten 1.5 ” thick and 8 ” tall solid stainless steel posts, all secured to the optical table. All other breadboards are 0.75 ” thick. All breadboards are as monolithic

Figure 7.19: The assembled breadboards and carriage shaft assembly

as possible, given the cut-out requirements for our breadboards. The SLM breadboard hosts the SLM optics and is supported on the objective breadboard via seven 1.5 ” thick and 14 ” tall solid stainless steel posts. The upper vertical breadboard is connected to the SLM breadboard as well as the objective breadboard via vertical mounting brackets at 4 positions. The bottom vertical breadboard is secured to the optical table as well as the objective breadboard via mounting brackets at 5 positions. All breadboards have $1/4-20$ tapped through-holes (except the AOD breadboard, which is tapped only 1 ” deep) on a 1”$\times$1” grid. In order to minimize unwanted light scatter from the breadboards, we anodized as many breadboards as we could.

The above design choices served us well as drifts within a breadboard and between breadboards

were interferometrically measured to be less than 100 μrad, with little to no vibrations. Furthermore, tightening mounts to the breadboards do not lead to misalignment of already mounted optics[17]. The drawings for all the breadboards are shown in Figs G.13, G.14, G.15, G.17, G.16, and G.18.

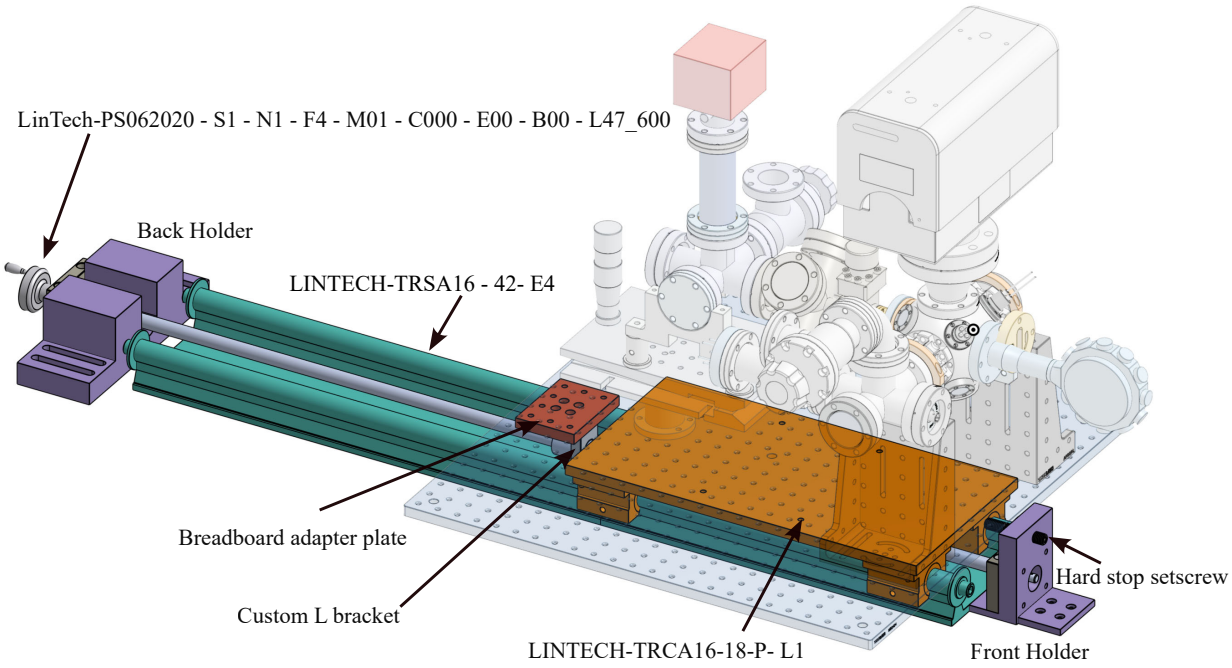

Figure 7.20: CAD design for the carriage shaft assembly for translating the mounted UHV chamber assembly.

The entire vacuum chamber was constructed on an anodized breadboard (Thorlabs MB2424) that was in turn mounted on carriage shaft assembly from Lintech Motion (see Fig. 7.20). The

[17]Commercially available 0.25" thick anodized Aluminum breadboards from Thorlabs mounted directly to an optical table at the counterbored holes distort when optics are mounted to them. Any time I tightened an optic on to a fastened breadboard flush with the optical table, it would distort the breadboard and misaligned the optics in its vicinity. This was especially apparent if there were fiber-coupling optics on that breadboard. The mode field diameter of the fibers is small, typically less than 5.5 μm. So breadboard distortions significantly affect fiber-coupling efficiencies. The obvious benefit of mounting optics to breadboards is that the optical setup is modular and movable. However, unfastening and fastening a breadboard to an optical table induces (or relieves) stresses that can misalign the already mounted optics. I found that never bolting the breadboard down to the optical table is the optimal solution. This is in addition to making sure that the length of the screws was smaller than the breadboard thickness. One can see how the screw length being longer than the breadboard thickness can be an even bigger issue for a fastened breadboard flush with optical table. Thorlabs mentions the distortion problem of 0.25" thick breadboards on their website.

breadboard was bolted to a custom pillow block carriage assembly (LINTECH-TRCA16-18-P-L1) (Fig. G.19). The carriage assembly can translate on a custom pre-aligned dual shaft assembly (LINTECH-TRSA16-42-E4) (Fig. G.20). The shaft assembly is bolted to the optical table. Controlled translation of the carriage assembly along the shaft assembly is provided by a ball screw assembly with mounted end supports (LinTech-PS062020-S1-N1-F4-M01-C000-E00-B00-L47_600). The end supports— Back holder (Fig. G.21) and Front holder (Fig. G.22)—are made of 304/304L stainless steel. The holders are both bolted to the optical table. The custom breadboard adapter plate connects the ball screw's custom L bracket to the breadboard (and therefore the carriage assembly). By turning the 4" hand wheel, ball screw L bracket translation is converted to the translation of the carriage on the shaft assembly. The front holder has a $1/2-13$ flat tip setscrew that acts as a hard stop (by pressing against the breadboard) and prevents the vacuum chamber from going too far in. Once the optimal position of the carriage assembly was found, we locked the position of the hard stop setscrew using a serrated flange locknut. This hard stop set screw now serves as a memory for when we pull the chamber out and in. This has been field tested and works well. During normal operation, the chamber breadboard is bolted to the optical table via posts at its counter-bore 1/4-20 through-holes. This locks the position of the breadboard (and the carriage assembly). We do not engage the hand lock on the ball screw assembly.

Due to the RAR nanotextured surfaces of the glass cell, caution was necessary when rolling the assembled vacuum chamber into the coil housing. We had to ascertain that there was enough clearance between the glass cell surfaces and the inner surfaces of the coil housing, and the glass cell was centered with respect to the coil housing cavity. To do that, we machined a solid aluminum glass cell mock-up (Fig. 7.21). We then mounted this mock-up to the front sealing

Figure 7.21: Solid aluminum glass cell mock-up

surface of the stainless steel chamber assembly. We rolled the mock-up chamber assembly in to the coil housing. Using laser levels mounted on translation stages, we adjusted the position of the coil housing with respect to the mock-up cell. We tried our best to center the coil housing cavity to the mock-up cell. This procedure ensured that when the vacuum chamber assembly with the actual glass cell was rolled in, the coil housing would not scratch the surface of the glass cell. It also ensured that the magnetic field zero would be close to the center of the glass cell when the MOT coils were run in an anti-Helmholtz configuration.

7.4 Ultra-Low Expansion (ULE) cavity design, installation, optics, and electronics

7.4.1 Design, installation, and optics

I worked closely with Stable Laser Systems (SLS) to choose the appropriate reference cavities for PDH locking our Rydberg lasers. A typical reference cavity consists of two ULE glass (or fused-silica glass) mirror substrates—one plano-plano and the other plano-concave—both of which are optically contacted to a cylindrical ULE glass spacer with a borehole concentric with

the cavity axis [126, 127, 128, 129]. In order to serve as a good reference, this cavity is typically housed in a high vacuum, temperature-controlled, vibrationally isolated environment. The ULE glass spacer typically has a thermal expansion zero-crossing temperature in the range $25 - 40°\mathrm{C}$ and the reference cavity housing is held at this temperature.

In our case, the seed of each Rydberg laser at 840 nm (2×420 nm), 1013 nm (1×1013 nm), 1112 nm (2×556 nm), 1232 nm (4×308 nm) is PDH locked to its own reference cavity (Fig. 6.1). As there are four Rydberg lasers (Fig. 6.1), we need four reference cavities. Instead of four independent reference cavities, SLS suggested an arrangement where the four reference cavities share the same ULE glass spacer i.e. there are four bored holes in the ULE glass spacer. The premium grade ULE glass cavity spacer is a $100\ \mathrm{mm}$ OD and $100\ \mathrm{mm}$ long cylinder with four $10\ \mathrm{mm}$ diameter bore holes centered on the corners of a 30 mm$\times$30 mm square. The thermal expansion zero-crossing temperature for the ULE glass is $33.77 \pm 1°\mathrm{C}$. Mirror pair (plano-plano and plano-concave) is constructed out of a premium grade ULE glass substrate that is 1" diameter $\times 0.25$" thick. The cavity mirrors coatings as shown in the table below:

Wavelength (nm)	Desired Finesse	S2 AR % 0 $0°$AOI
841 and 1013	30000 to 90000	< 0.2
1112 and 1232	30000 to 90000	< 0.2

Instead of building our own reference cavity housing, we bought the housing setup and accessories from SLS (Fig. 7.22a)

Tsz-Chun and I installed the reference cavity. The reference cavity vacuum housing pressure sits at $< 2.7 \times 10^{-7}$ Torr. Fig. 7.22a is a picture of me holding the four-bored reference cavity

block prior to installing it. The bore that serves as the reference cavity for the laser of choice is also depicted in Fig. 7.22b. In the actual setup, the bore 1 reference cavity is for the 1013 nm laser, the bore 3 reference cavity is for the 841 nm laser, the bore 2 reference cavity is for the 1232 nm laser, and the bore 4 reference cavity is for the 1112 nm laser (Fig. 7.22b).

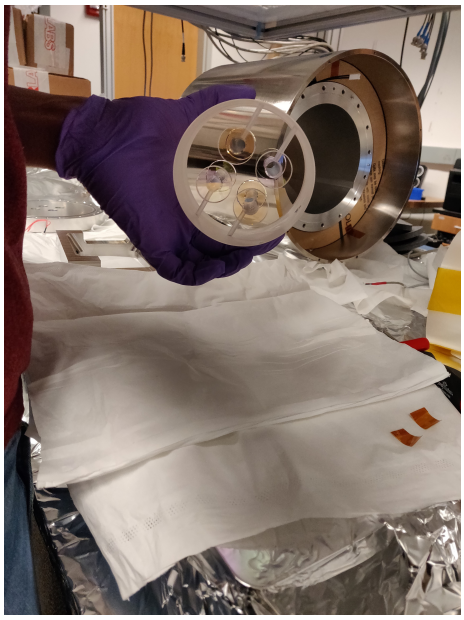

(a)

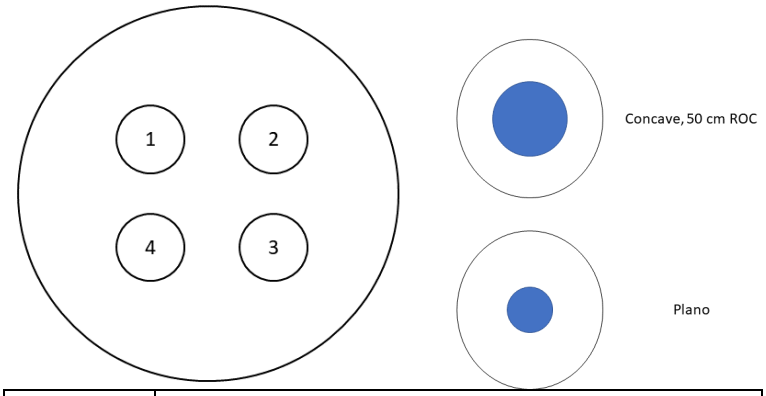

Bore 1	Plano in the front; 841, 1013 nm
Bore 2	Concave in the front; 1112, 1232 nm
Bore 3	Plano in the front; 841, 1013 nm
Bore 4	Concave in the front; 1112, 1232 nm

(b)

Figure 7.22: (a) Installing the four-bored reference cavity block in its temperature-controlled high-vacuum housing (b) The arrangement of the reference cavity bores.

After the four-bored reference cavity block was installed, I designed and built the optics for coupling light into ULE cavities. I devised the alignment strategy with help from Wance Wang from Joe Britton's group. I assembled the optics for each seed laser into a cage-system. The output of a fiber-coupled EOM serves as the input to the cage system. We use fiber EOMs for phase modulating the laser light: iXblue NIR-MPX-LN-05-00-P-P-FA-FA for 1112 nm, 1232 nm, and 1013 nm; and iXblue NIR-MPX800-LN-10-P-P-FA-FA for 840 nm (Fig. 7.23b). The schematic for each of the four cage systems is illustrated in Fig 7.23a and the parts used are listed in the table below.

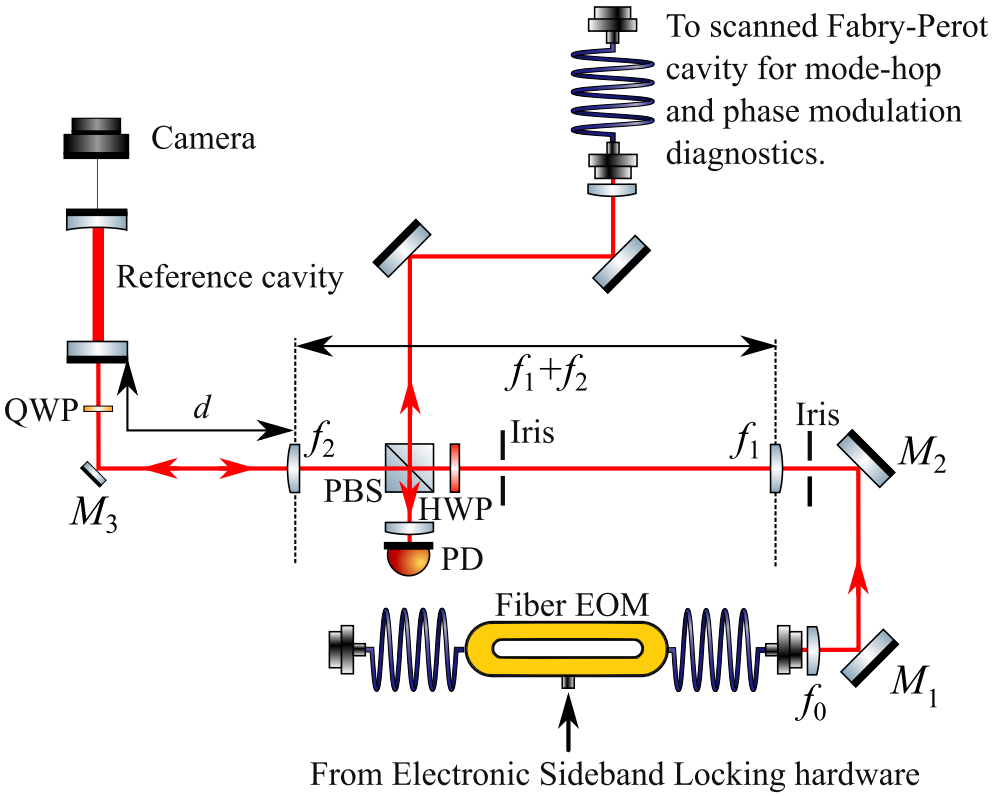

(a) Layout for the reference cavity mode-matching optics for PDH locking.

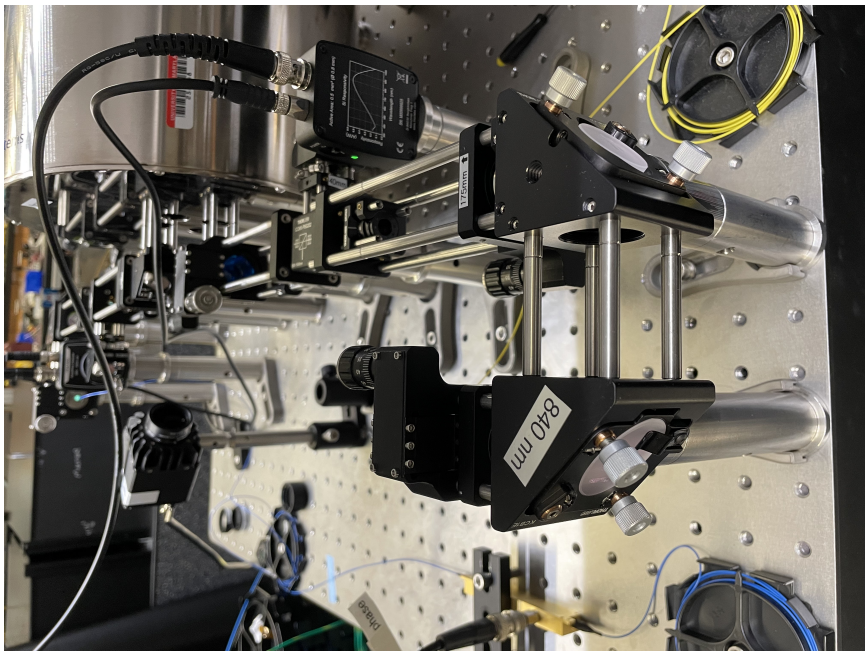

(b) A typical cage system to mode-match light into the reference cavity for PDH locking.

Figure 7.23

λ (nm)	f_0 (mm)	f_1 (mm)	f_2 (mm)	d(in)	PD
840	4.00 (C610TME-B)	175 (KPX103AR.400)	100 (KPX094AR.400)	6.19	PDA8A2
1013	4.51 (C230TMD-B)	175 (KPX103AR.18)	100 (KPX094AR.18)	6.19	PDA10D2
1112	3.10 (C330TMD-C)	125 (KPX097AR.18)	100 (KPX094AR.18)	7.08	PDA20C2
1232	3.10 (C330TMD-C)	125 (KPX097AR.18)	100 (KPX094AR.18)	7.08	PDA10D2

With the designed mode-matching optics [70, 130], I typically coupled 40% of the $\sim 200-400\mu$W of the seed light into the ULE cavity, measured as dips in the reflected intensity measured on the photodetector[18]. Part of the light is delivered to a separate scanning confocal Fabry-Perot for monitoring laser mode-hops and the status of the fiber EOM phase modulation. Apart from the 1013 nm laser, all the other lasers go through second harmonic generation stages. So the mode hop behavior of the seed laser can be monitored on its respective frequency-doubling cavity.

In order to monitor the spatial mode profile of the cavity, I used a Vanxse CCTV 1/3 CCD 1000TVL HD 3.6 mm mini bullet security camera. The laser transmission mode was monitored on an AUKUYEE 7 inch 1024X600 high-resolution IPS monitor. The camera provides information on the status of the PDH lock. Using the error signal to determine the status of the PDH lock is not easy, as a locked and unlocked laser yields zero error signal. However, the cavity spatial mode profile on the camera can be used to determine the laser lock status as we always lock to the TEM_{00} of the cavity.

I dedicate one power strip for powering the laser and its associated PDH lock electronics to prevent ground loops between the elements. Even the oscilloscopes are powered by the same

[18] An excellent guide for aligning into the ULE reference cavity can be found here: https://www.moglabs.com/support/appnotes/an002-pdh-r2.pdf

power strip. There are 4 power strips in total. I chose to use FALC 110 from Toptica as the servo for PDH locking the 420 nm, 308 nm, and 1013 nm Rydberg lasers to their respective reference cavities. For the 556 nm laser, I chose to use PID 110 from Toptica as the servo. The 1112 nm seed for the 556 nm laser is intrinsically narrow and does not need high-bandwidth feedback.

PDH locks are sensitive to noise in the acoustic frequency range. Therefore, I wanted to isolate the ULE cavity and the lasers that are locked to the ULE cavity from ambient vibrations. To that end, the ULE cavity and the associated optics for PDH locking are mounted on a B3036G Nexus breadboard from Thorlabs. The breadboard itself is placed on super-cushioning polyurethane rubber sheets (8514K68 and 8514K78 from McMaster Carr) to dampen vibrations from the optical table. All the diode laser heads that are locked to the ULE cavity were also built on breadboards that were placed atop polyurethane rubber sheets for vibration isolation from the optical table. Additionally, we built vibration isolation housing around the ULE cavity breadboard as well as the diode laser breadboards.

I designed the vibration isolation boxing (see Figs. 7.24a and 7.24b). Each piece or face of the vibration isolation boxing was built out of a hand-cut acrylic sheet (8505K759 from McMaster Carr) that was sandwiched between appropriately sized vinyl sound barrier sheets (9345T21 from McMaster Carr) or melamine foam sound barrier sheets (54995T24 and 54995T23 from McMaster Carr) or a mixture of both. The hard acrylic sheet reflects any sound that is damped by the sound barrier sheets. These faces are then assembled into a box around the ULE cavity breadboard and the laser breadboard using cut 80/20 Aluminum extrusions.

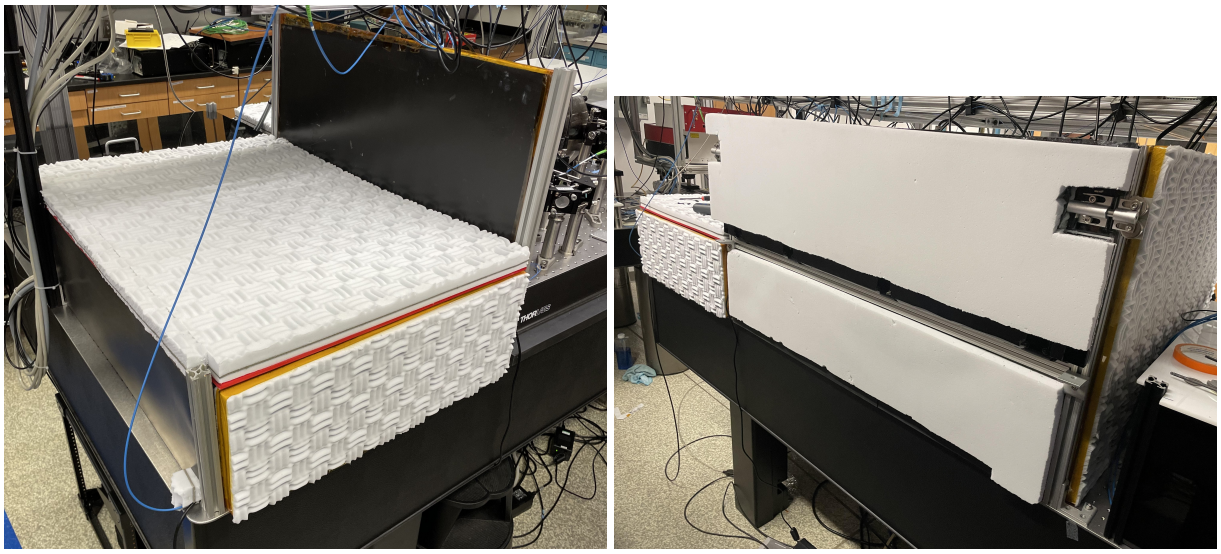

(a) (b)

Figure 7.24: (a) The vibration isolation boxing for the 420 nm laser (b) The vibration isolation boxing for the ULE cavity and its associated optics

7.4.2 Electronics for generating the PDH error signal

We used the electronic sideband (ESB) locking scheme [131, 132, 133]—a variant of the the standard PDH lock scheme—to stabilize our Rydberg excitation laser to its corresponding reference cavity. Using a dimensionally stable cavity as a frequency reference quantizes the locked laser frequency to integer multiples of the cavity free spectral range (FSR), which in our case is 1.5 GHz. The ESB PDH locking scheme is a method to bridge the frequency gap between the quantized cavity resonance frequency and the desired optical frequency.

The canonical optical electric field used in ESB locking is

$$E(t) = E_0 \exp\left\{ j\Omega_0 t + j \underbrace{\beta_c \sin[\Omega_c t + \beta_m \sin(\Omega_m t)]}_{\propto V_{\text{EOM}}(t)} \right\}, \tag{7.2}$$

$$= E_0 \sum_n J_n(\beta_c)\, e^{j\Omega_0 t + jn\Omega_c t} \times \sum_k J_k(n\beta_m)\, e^{jk\Omega_m t}, \tag{7.3}$$

$$= E_0 \sum_n \sum_k J_n(\beta_c)\, J_k(n\beta_m)\, e^{j(\Omega_0 + n\Omega_c + k\Omega_m)t}, \tag{7.4}$$

where E_0 is the amplitude of the laser electric field, Ω_0 is the bare laser frequency, J_n is the n$^{\text{th}}$ order Bessel function of the first kind, and $V_{\text{EOM}}(t) \propto \beta_c \sin[\Omega_c t + \beta_m \sin(\Omega_m t)]$ is the rf signal used to drive the EOM phase-modulating the laser electric field. The amplitude of the laser sideband at frequency $\Omega_0 + n\Omega_c + k\Omega_m$ is $E_0 J_n(\beta_c) J_k(n\beta_m)$. The rf signal $V_{\text{EOM}}(t)$ is parameterized by four parameters: β_c (the carrier modulation depth), Ω_c (the carrier rf frequency that lies in the ultra high frequency (UHF) band), Ω_m (the baseband rf frequency that lies in the medium frequency (MF) and high frequency (HF) bands), and β_m (is the phase-modulation index).

The carrier frequency Ω_c should be tunable by approximately the FSR of the cavity. In order to understand how changing the carrier wave frequency changes the bare laser frequency, we first approximate the expansion in Eq. 7.4 and consider only the set of three sidebands at frequencies $\Omega_0 + \Omega_c$, $\Omega_0 + \Omega_c + \Omega_m$, and $\Omega_0 + \Omega_c - \Omega_m$; or the set of three sidebands at frequencies $\Omega_0 - \Omega_c$, $\Omega_0 - \Omega_c - \Omega_m$ and $\Omega_0 - \Omega_c + \Omega_m$. Either set of sidebands can be used to generate a PDH error signal. When the lock is engaged, the laser sideband at $\Omega_0 \pm \Omega_c$ is resonant with the cavity i.e.

$$\Omega_0 \pm \Omega_c = 2\pi N \times \text{FSR} \tag{7.5}$$

where $2\pi N \times$ FSR is the frequency of the longitudinal mode of the reference cavity and N is the resonator mode number. Assuming now that the laser stays locked to the chosen reference cavity mode, a $\Delta\Omega_c$ change in the carrier wave frequency results in a $\Delta\Omega_0$ change in the base laser frequency, which can be mathematically expressed as follows:

$$\Delta\Omega_0 = \mp\Delta\Omega_c. \tag{7.6}$$

Generating the phase-modulated rf signal $V_{\text{EOM}}(t)$ is complex. We use quadrature amplitude modulation (QAM) [134, 135], employed extensively in digital signal communication, to generate the phase-modulated rf signal for ESB locking. Using the angle-sum identity on the rf signal $V_{\text{EOM}}(t)$, we get

$$\begin{aligned} V_{\text{EOM}}(t) &= \xi \sin[\Omega_c t + \beta_m \sin(\Omega_m t)] \\ &= \underbrace{\xi \sin[\beta_m \sin(\Omega_m t)]}_{I(t)} \cos(\Omega_c t) + \underbrace{\xi \cos[\beta_m \sin(\Omega_m t)]}_{Q(t)} \sin(\Omega_c t). \end{aligned}$$

Expressed in this form, one can see how QAM can be used to construct the rf signal $V_{\text{EOM}}(t)$. The in-phase baseband channel $I(t) = \xi \sin[\beta_m \sin(\Omega_m t)]$ amplitude modulates the carrier wave $\cos(\Omega_c t)$, and the quadrature-phase baseband channel $Q(t) = \xi \cos[\beta_m \sin(\Omega_m t)]$ amplitude modulates the quadrature carrier wave $\sin(\Omega_c t)$, which are then summed together to produce $V_{\text{EOM}}(t)$. The slope of an ideal ESB PDH error signal near cavity resonance [131] is proportional to $J_0(\beta_m)J_1(\beta_m)(J_1(\beta_c))^2$, where J_n is the n$^{\text{th}}$ order Bessel function of the first kind. This slope is maximal for rather large modulation depths $\beta_c = 1.84$ rad and $\beta_m = 1.01$ rad.

Tsz-Chun and Alessandro built our first version of the ESB locking hardware, which was

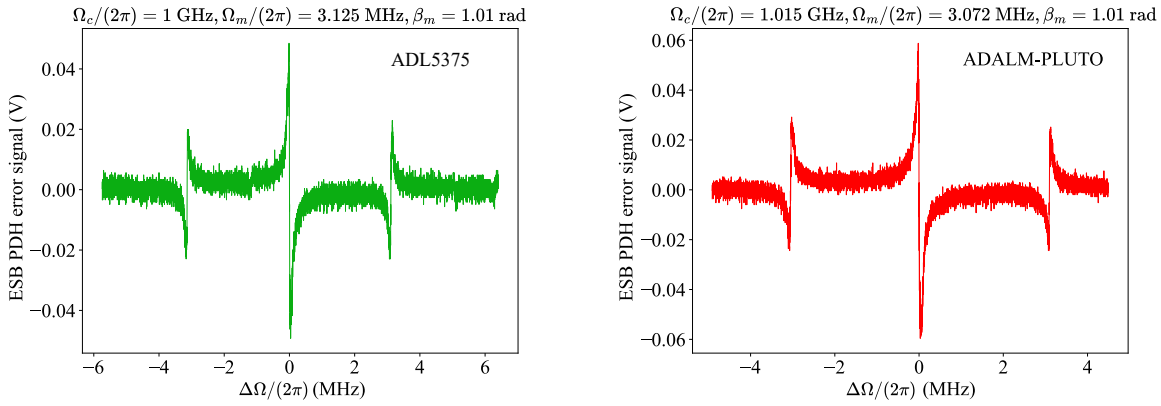

(a) (b)

Figure 7.25: The ESB PDH error signals as a function of laser frequency detuning $\Delta\Omega$ where $\Delta\Omega = \Omega_0 + \Omega_c - 2\pi N \times$ FSR: we use laser light at 1112 nm, a high-finesse ULE reference cavity, and a fiber-coupled EOM driven by the high-quality phase-modulated rf signal from (a) the ADL5375-based design (b) and the ADALM-PLUTO-based design.

centered around the ADL5375 chip from Analog devices. Later Alessandro would suggest a separate and more compact implementation using ADALM-PLUTO, a software-defined radio developed for hobbyists, students, and educators from Analog devices. Oliver helped Alessandro get that implementation up and running. The GitHub repositories for both system architectures can be found here: https://github.com/JQIamo/ESB_Signal_Generator and https://github.com/JQIamo/Electronic_Sideband_Locking_Pluto. Typical ESB PDH error signals generated using the phase-modulated rf signal from both system architectures are shown in Fig. 7.25. We are in the process of writing a manuscript on these system architectures.

7.4.3 Servo loop optimization for laser linewidth narrowing

The frequency of a laser is not a perfect sinusoid due to various noise processes that perturb its frequency. A widely used model for the spectral density of frequency noise in free-running

lasers $S_{f,\,\text{laser}}$ is [70, 136, 137]

$$S^2_{f,\,\text{laser}}\ \left[\,\text{Hz}^2/\text{Hz}\right] = \frac{\Delta\nu}{\pi} + \frac{k_f}{f} + \frac{k_r}{f^2}, \tag{7.7}$$

where f is the instantaneous frequency excursion, $\Delta\nu/\pi$ is the white frequency noise, k_f/f is the pink (or flicker) noise, and k_r/f^2 is the random-walk noise of the laser. Different lasers exhibit different amounts of the noise types listed in Eq. 7.7. The spectral density of the frequency noise determines the laser lineshape function [138, 139].

Schawlow and Townes calculated the fundamental lower limit to the linewidth of a laser [140]. The noise process that determines the Schawlow-Townes linewidth is quantum in nature as it arises from spontaneous emission that perturbs the phase of the laser electric field. The spectrum of this quantum noise process is white and the laser linewidth associated with Schawlow-Townes limit $\Delta\nu_{L,\text{ST}}$ is as follows:

$$\Delta\nu_{L,\text{ST}} = \pi S^2_{f,\text{ST}} = \frac{2\pi h\nu\delta\nu_L^2}{P}. \tag{7.8}$$

where $h\nu$ is the energy of the photon, $\delta\nu_L$ is the linewidth of the laser cavity linewidth and P is the output power of the laser. Note the quadratic scaling of the Schawlow-Townes linewidth on $\delta\nu_L$.

The lower limit is almost never achieved in a free-running laser as $(1/f)^a$-type noise sources dominate the spectral density of frequency noise at lower frequencies. The large spectral density of frequency noise in the low-frequency range (Eq. 7.7) determines the laser linewidth, while the spectral density of frequency noise is small in the high frequency range and contributes

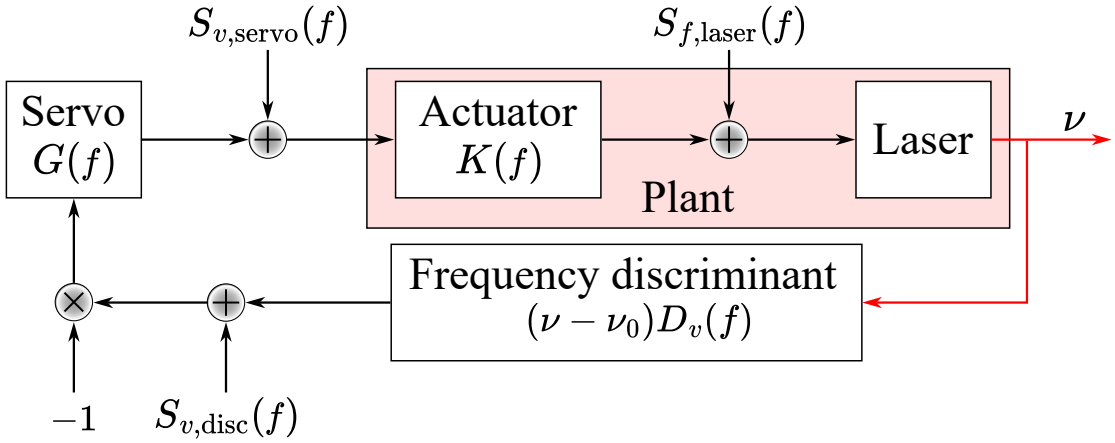

Figure 7.26: The feedback control system for laser frequency stabilization in the presence of noise.

to the wings of the laser lineshape [138]. However, low-frequency noise can be detected by a frequency discriminator and suppressed by implementing a high-bandwidth feedback control system. In fact, laser linewidths below the Schawlow-Townes limit can be achieved via active feedback [70, 137].

Figure 7.26 illustrates the layout of the closed-loop laser frequency stabilization system. In this system, the instantaneous optical frequency of the laser ν is tracked by a frequency discriminator. This discriminator transforms optical frequency deviations $\nu - \nu_0$ into voltage deviations via its transfer function $D_v(f)$ (has units of V/Hz), resulting in an error signal. The inverted error signal voltage is amplified and transformed by $G(f)$, the transfer function of the servo. The servo output voltage is transmitted to the actuator, which converts the voltage to a change in optical laser frequency through its transfer function $K(f)$.

$S_{f,\text{laser}}$ in units of $\text{Hz}/\sqrt{\text{Hz}}$ is the linear spectral density of frequency noise associated with the laser and is a measure of the RMS laser frequency fluctuation in a 1 Hz bandwidth. $S_{v,\text{disc}}$ and $S_{v,\text{servo}}$ in units of $\text{V}/\sqrt{\text{Hz}}$ are the spectral densities of voltage noise associated with the frequency discriminator and servo, respectively, and represent the RMS voltage fluctuation in a 1

Hz bandwidth. The steady-state optical frequency ν can be expressed as follows:

$$\nu = \Big(- \big((\nu - \nu_0) D_v(f) + S_{v,\text{disc}}(f)\big) \Big) G(f) + S_{v,\text{servo}} \Big) K(f) + S_{f,\text{laser}}(f) \tag{7.9}$$

$$\Rightarrow \nu = \frac{GKD_v}{1 + GKD_v} \nu_0 + \frac{S_{f,\text{laser}} + KS_{v,\text{servo}} - GKS_{v,\text{disc}}}{1 + GKD_v}, \tag{7.10}$$

where GKD_v is the open loop transfer function. The closed-loop spectral density of frequency noise $S_{f,\text{cl}}$ in units of Hz/$\sqrt{\text{Hz}}$ can therefore be expressed as follows:

$$S_{f,\text{cl}} = \frac{\sqrt{S_{f,\text{laser}}^2 + |KS_{v,\text{servo}}|^2 + |GKS_{v,\text{disc}}|^2}}{|1 + GKD_v|}, \tag{7.11}$$

where the contributions from the independent noise sources are added in quadrature. For a large servo loop gain G,

$$S_{f,\text{cl}} = \frac{S_{v,\text{disc}}}{|D_v|}. \tag{7.12}$$

Hence, the closed-loop spectral density of frequency noise should be limited by the property of the discriminator $D_A(f)$ (in units of A/Hz) and the shot-noise $S_{v,\text{disc}}$. The transfer function of a reference cavity frequency discriminator is as follows [70, 136]:

$$D_A(f) = \frac{D_0}{1 + i\frac{f}{\delta\nu_c/2}}, \tag{7.13}$$

where

$$D_0[A/\text{Hz}] = \frac{8J_0(\beta)J_1(\beta)}{\delta\nu_c} \frac{e\eta P_i}{h\nu} \tag{7.14}$$

is the discriminator low-frequency slope, η is the detector quantum efficiency, e is the charge of an electron, and $h\nu$ is the energy of the detected photons and P_i is the incident laser power [137]. Using Eqs. 7.12,7.13,7.14, the expression for the closed-loop laser linewidth is [137, 141]

$$\Delta\nu_{L,\text{cl}} = \frac{2\pi h\nu\delta\nu_c^2}{16\eta P_i J_0^2(\beta)}, \tag{7.15}$$

under that assumption that $S_{f,\text{cl}}$ is white.

The equations for the closed-loop shot-noise limited-laser linewidth (Eq. 7.15) and the Schawlow-Townes limited linewidth (Eq. 7.8) can be compared: $\delta\nu_c$ is equivalent to $\delta\nu_L$ and $16\eta P_i J_0^2(\beta)$ is equivalent to P. Therefore, a reference cavity with a narrow linewidth is desirable to suppress the closed-loop spectral density of frequency noise below the Schawlow-Townes limit (within the loop bandwidth).

In the case of a diode laser, the feedback is typically split into a fast branch that modulates the diode laser current and a slow branch that modulates the Piezoelectric Transducer (PZT) [70, 142]. For a fiber laser, the laser frequency feedback is facilitated by just a PZT. The PZT feedback branch suppresses frequency noise in the acoustic range. The transfer function of a PZT is $R_{\text{PZT}}(\omega) = {\Omega_{\text{PZT}}}^2/(\,{\Omega_{\text{PZT}}}^2 + 2\omega\eta\Omega_{\text{PZT}} + \omega^2\,)$, where Ω_{PZT} is 2π times the resonance frequency, $\eta = 1/2Q$ is the damping factor of the resonance, and $\omega = 2\pi f$ [70, 142]. Ω_{PZT} is typically in the range of $2\pi \times 1 - 20$ kHz. Therefore, a large unity gain frequency (ω_{slow}) for the PZT feedback branch requires careful engineering to handle the large phase lag introduced by the PZT transfer function close to Ω_{PZT}. Therefore, typically $\omega_{\text{slow}} \ll \Omega_{\text{PZT}}$ for simple[19] PZT servo loops, which deal only with the phase lag arising from the PZT transfer function and not the phase lag from the

[19]There are more complicated techniques like using a notch filter [70, 142].

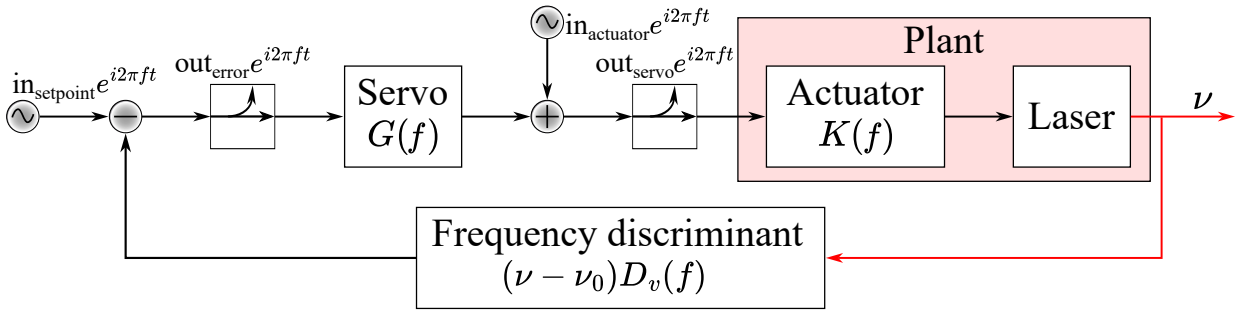

Figure 7.27: Closed-loop transfer function measurement protocol/formalism.

cavity pole at $\delta\nu_c/2$ (see Eq. 7.13). The cavity pole should therefore be much larger than ω_{slow}. A cavity linewidth in the 2-40 kHz range is therefore a reasonable choice (i.e. $\delta\nu_c/2 \sim \Omega_{\text{PZT}}/(2\pi)$).

Ignoring $S_{v,\text{disc}}$ and $S_{v,\text{servo}}$ in Eq. 7.11, the close-loop spectral density of frequency noise is

$$S_{f,\text{cl}} = \frac{S_{f,\text{laser}}}{|1 + GKD_v|}. \tag{7.16}$$

Eq. 7.16 suggests that a laser with a narrow free-running linewidth is desirable. It simplifies frequency locking and also reduces the need for a prestabilization cavity [143, 144]. It also reduces the complexity of tuning the high-bandwidth feedback control system for close-loop shot noise-limited performance (Eq. 7.15), as it requires expertise in control theory. To that end, we paid our laser vendors a surcharge for lasers with narrow free-running linewidths.

I used a Vector Network Analyzer (VNA) (Bode 100 from Omicron Lab) to tune our high-bandwidth feedback control systems [145]. I used the VNA to measure the transfer functions of many of the individual elements that make up the feedback control system. However, not all transfer functions are easily measurable. The transfer function of the reference cavity $D_v(f)$ (see Eq. 7.13) can be deduced by measuring the linewidth of the reference cavity $\delta\nu_c$ using the ring-down method [70], a non-trivial measurement. Determining the transfer function of the

laser actuator $K(f)$ can also be difficult [146]. Delays, which are especially detrimental to loop performance at high frequencies, can also be difficult to diagnose. In addition, there can be phase lags from unsuspecting elements in the loop. However, the behavior of these hard-to-measure transfer functions can be extracted by using the VNA to probe the closed-loop feedback control system. These measurements can then be used to optimize the feedback control system.

I developed a closed-loop transfer function measurement protocol/formalism illustrated in Fig. 7.27. Using the VNA, signals ($\text{in}_{\text{setpoint}}e^{i2\pi ft}$ and $\text{in}_{\text{actuator}}e^{i2\pi ft}$) are injected and their responses ($\text{out}_{\text{error}}e^{i2\pi ft}$ and $\text{out}_{\text{servo}}e^{i2\pi ft}$) measured at strategic positions in the loop. The relationships between the complex amplitudes of the injected and measured signals are as follows:

$$\begin{pmatrix} \frac{\text{out}_{\text{error}}}{\text{in}_{\text{setpoint}}} & \frac{\text{out}_{\text{error}}}{\text{in}_{\text{actuator}}} \\ \frac{\text{out}_{\text{servo}}}{\text{in}_{\text{setpoint}}} & \frac{\text{out}_{\text{servo}}}{\text{in}_{\text{actuator}}} \end{pmatrix} = \frac{1}{1+GKD_v} \begin{pmatrix} 1 & -KD_v \\ G & 1 \end{pmatrix}. \tag{7.17}$$

The VNA measures the quantities on the left hand side of Eq. 7.17. The gain and phase of the measured quantities are plotted as a function of f. These plots are referred to as Bode plots and are a great tool for understanding the behavior of transfer functions [70]. By performing these measurements, we can extract (and diagnose) the transfer function of interest. For example, the open-loop transfer function can be extracted by measuring $\text{out}_{\text{error}}/\text{in}_{\text{setpoint}}$:

$$GKD_v = \left(\frac{\text{out}_{\text{error}}}{\text{in}_{\text{setpoint}}}\right)^{-1} - 1. \tag{7.18}$$

The poles and zeros of the servo transfer function $G(f)$ can be tuned to push the unity gain frequency of the open-loop transfer function [70] to its highest possible value[20]. From the

[20]The phase margin ϕ_m of the open loop transfer function should be in the 30° to 60° range for closed-loop stability [70].

Kramers-Kronig relationship [147], a large unity gain frequency for the open-loop transfer function implies a large open-loop gain at low frequencies, essential for reducing the linewidth of the free-running laser (Eqs. 7.16, 7.12, 7.15).

The formalism laid out above (Eq. 7.17 and Fig. 7.27) measures the linear response of the closed-loop feedback control system. However, the reference cavity frequency discriminator is only linear for an optical frequency in the vicinity of the cavity resonance i.e. $|\nu - \nu_0| < \delta\nu_c/2$. Given that $\delta\nu_c$ is small, the laser must therefore be stabilized to the reference cavity before the quantities in the LHS of Eq. 7.17 can be measured [146] to optimize the servo loop.

Wance Wang from Joe Britton's group found this technique interesting and has used it to optimize the many PDH feedback control systems in the Britton lab. We are writing a paper together on this topic.

7.5 Design and construction of low-NA optical systems

In this section, I present details on the design and construction of the multiple laser systems used in our experiment. I elaborate on the optical layouts for the lasers for magneto-optical trapping (MOT) of Rb and Yb as well as the optical layouts for the lasers used for excitation of Rb and Yb to Rydberg states. I also elaborate on the frequency-locking hardware for these lasers. I designed all the optical layouts and built it with the help of Kevin.

I refer to these systems as low-NA optical systems because the NA of the laser light delivered to the atoms is quite small. The beams are either collimated as in the case of MOTs and imaging (NA $= 0$), or the beams are weakly focusing to a 100 μm spot size as in the case of Rydberg lasers. This classification helps to contrast the quality of optics and the degree of

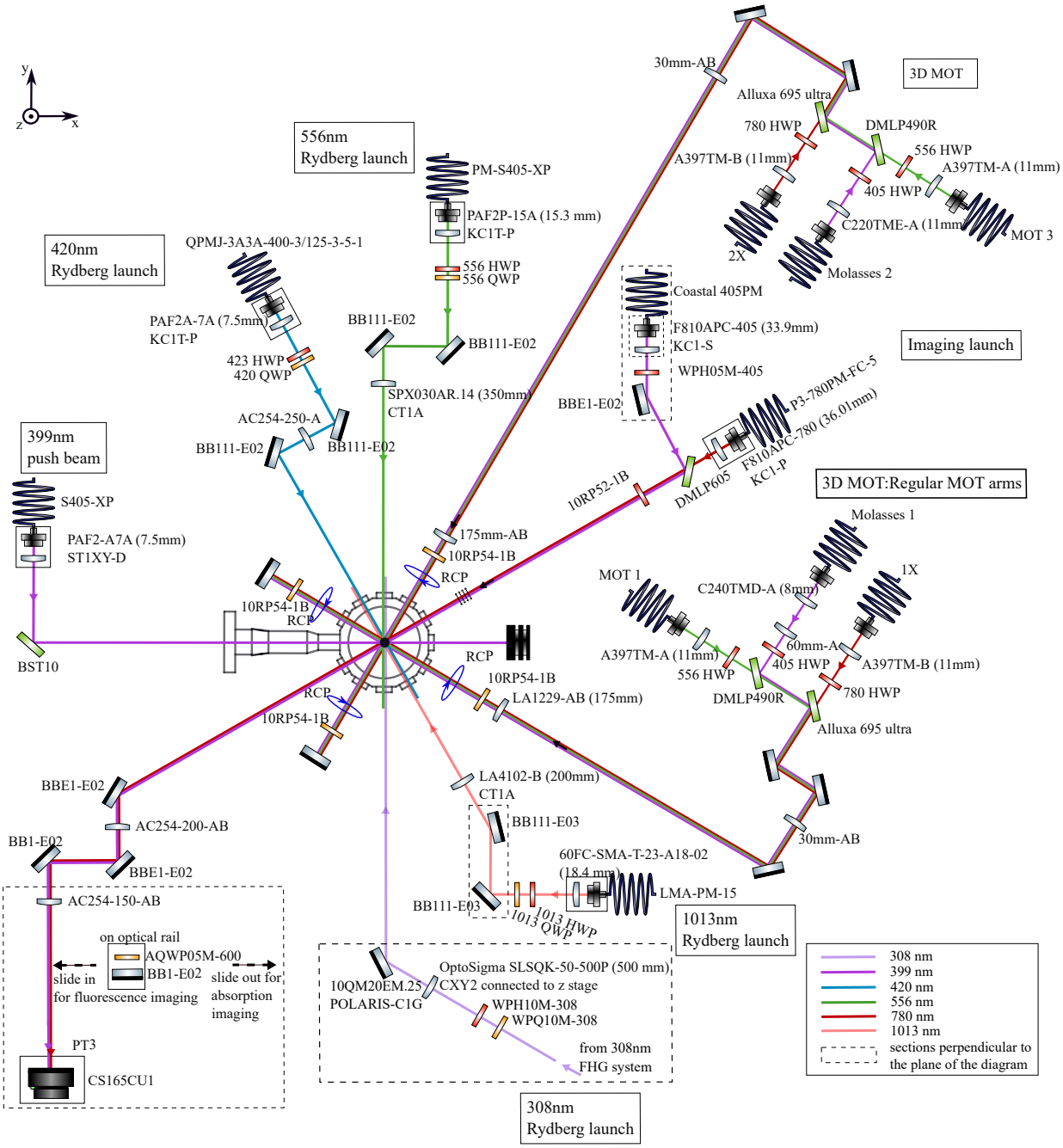

Figure 7.28: Layout of the low-NA optical systems around the glass cell as viewed from the front

alignment that will be needed when I introduce high-NA optical layouts for the optical tweezers (Sec. 7.6). The low-NA optical layouts around the glass cell to deliver light to the atoms are shown in Figs. 7.28 and 7.29.

We use Labscript suite [122] (https://github.com/labscript-suite) for computer

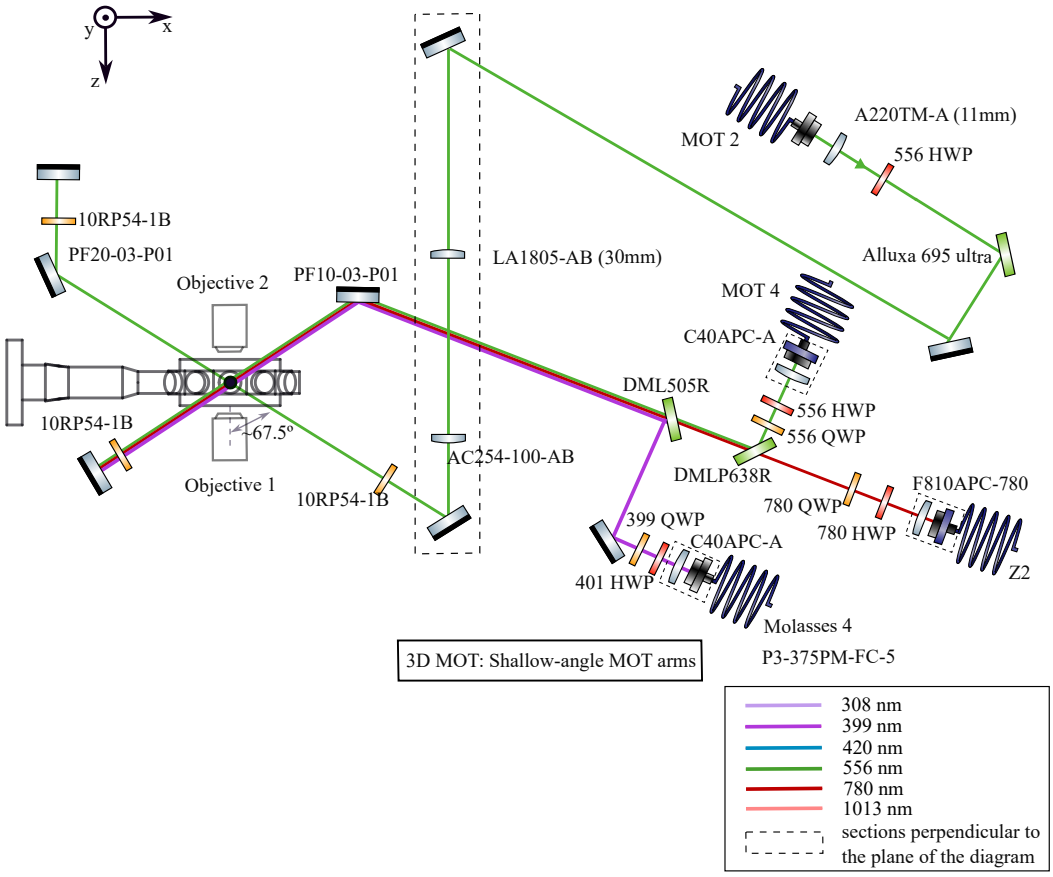

Figure 7.29: Layout of the low-NA optical systems around the glass cell as viewed from the top

control in our experiment.

7.5.1 Rb MOT lasers and frequency-locking electronics

We use the same lasers and frequency locking technique that were used in the old RbYb experiment [8, 9]. However, Kevin and I overhauled, redesigned, and rebuilt their optical layouts to boost the laser power efficiency and long-term stability of the setups (Figs. 7.30a, 7.31a, 7.31b). Kevin and Tsz-Chun upgraded the home-built frequency locking electronics [8, 9] so that the frequency locks remain engaged for multiple hours at a time.

The New Focus Vortex II TLB-6900 serves as the Rb master laser, which is locked 42.343 MHz red of the $^{85}\mathrm{Rb}, F = 3 \leftrightarrow F' = 3 - 4$ crossover resonance via saturation-absorption

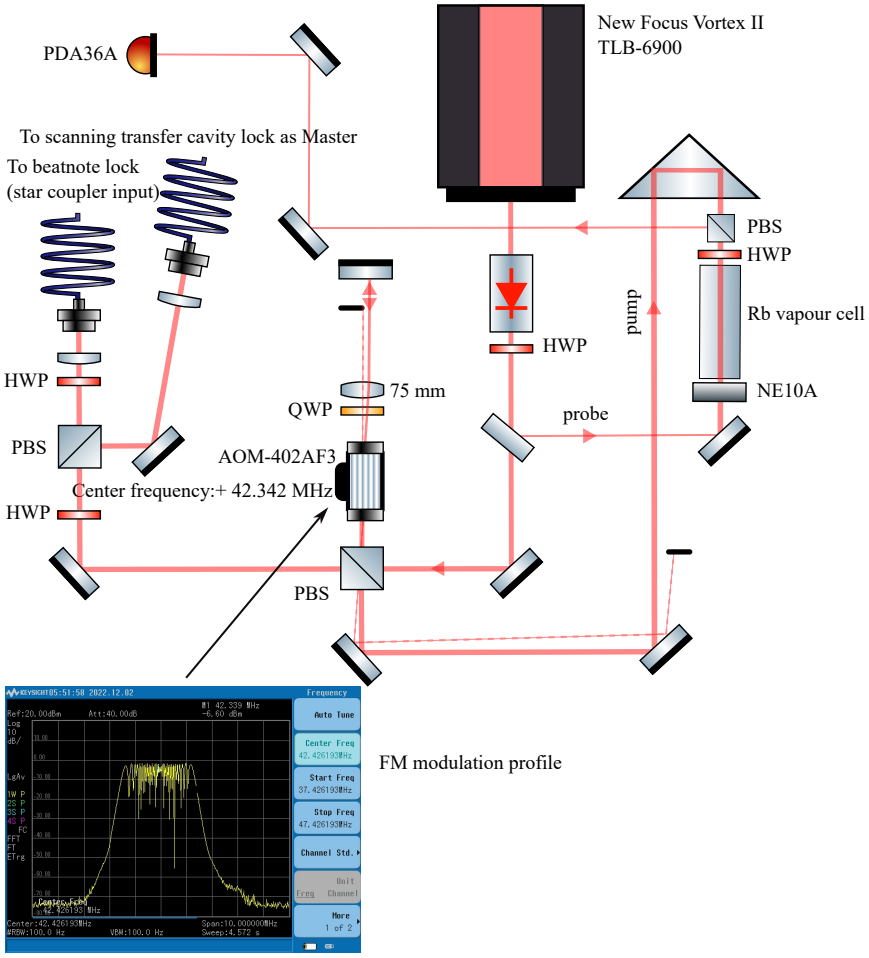

(a) Schematic of the optical layout for the Rb master laser

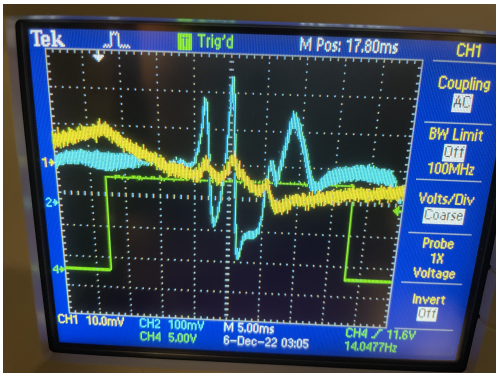

(b) Saturation-absorption crossover (^{85}Rb, $F = 3 \leftrightarrow F' = 3 - 4$) resonance feature (yellow trace) and its derivative (cyan trace)

Figure 7.30: Rb master laser optical layout and frequency locking feature

spectroscopy. The Rb cooling laser (Toptica DL Pro) frequency is locked $\sim$ 1.1 GHz red of the Rb master laser frequency. The Rb repump laser (Sharp diode in a Toptica DL Pro laser body) frequency is locked $\sim$ 5.5 GHz blue of the Rb master laser frequency [8, 9]. In Fig. 7.30a, I present the optical layout for the Rb master laser. Part of the optical layout constitutes the saturation-absorption spectroscopy setup for the Rb master laser. I added a path to direct some of the master light to the scanning transfer cavity lock (STCL) setup to lock the frequency of the seed of the 399 nm laser (Appendix B). Fig. 7.30b shows the zoomed-out cross-over resonance feature (yellow trace) and its derivative (cyan trace). Some of the Rb master laser light is also coupled into one of the input fiber ports of a single-mode, non-PM fiber optic star coupler. The other input fiber ports of the star coupler couple light from the Rb cooling and Rb repump setup. One of the output ports of the star coupler is used to monitor the mode-hop behavior as well as the lock status of the three Rb lasers on a scanning Fabry-Perot cavity. The other output port of the star coupler is fed to the beatnote electronics setup.

We use optical phase locked loops (OPLL) [148] to stabilize the frequency of the Rb cooling laser and the Rb repump laser. The reference for these OPLLs is the Rb master laser. The cooling-master beatnote signal is divided down by a factor of 16 and the repump-master beatnote is divided down by a factor of 64 by the EVAL-ADF4007 evaluation boards. The electronic schematic is shown in Fig. 7.32.

The optical layouts for the Rb repump laser and the Rb cooling laser are presented in Fig. 7.31a and Fig. 7.31b respectively. The Rb coolng and Rb repump MOT light are coupled into the input ports of a different single-mode PM fiber splitter/combiner with 2 inputs and 8 outputs from Evanescent Optics, Inc (Fig. 7.33). We use three of the six high-power output ports to deliver light to the 3D MOT arms in a retro-reflected geometry: two regular MOT arms and

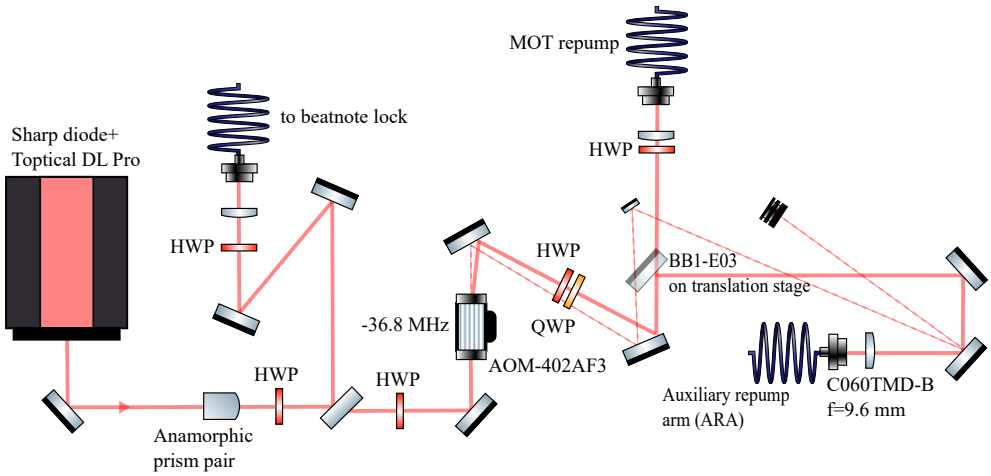

(a)

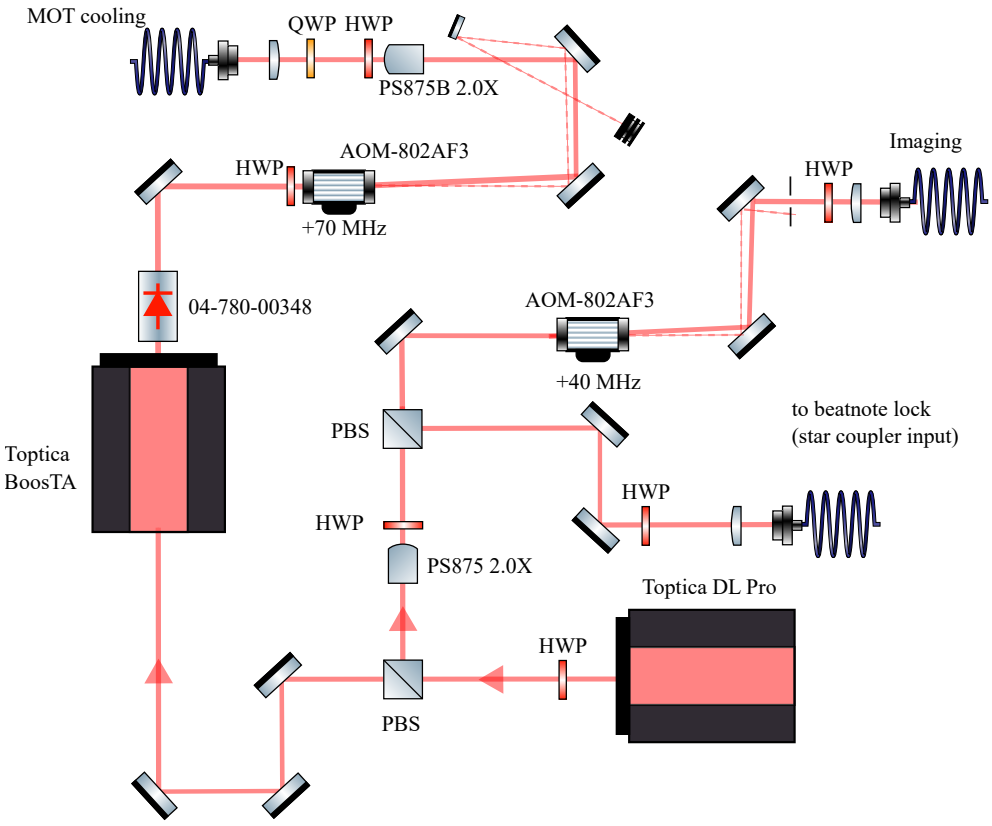

(b)

Figure 7.31: The schematic of the optical layout for the (a) Rb repump laser (b) Rb cooling laser

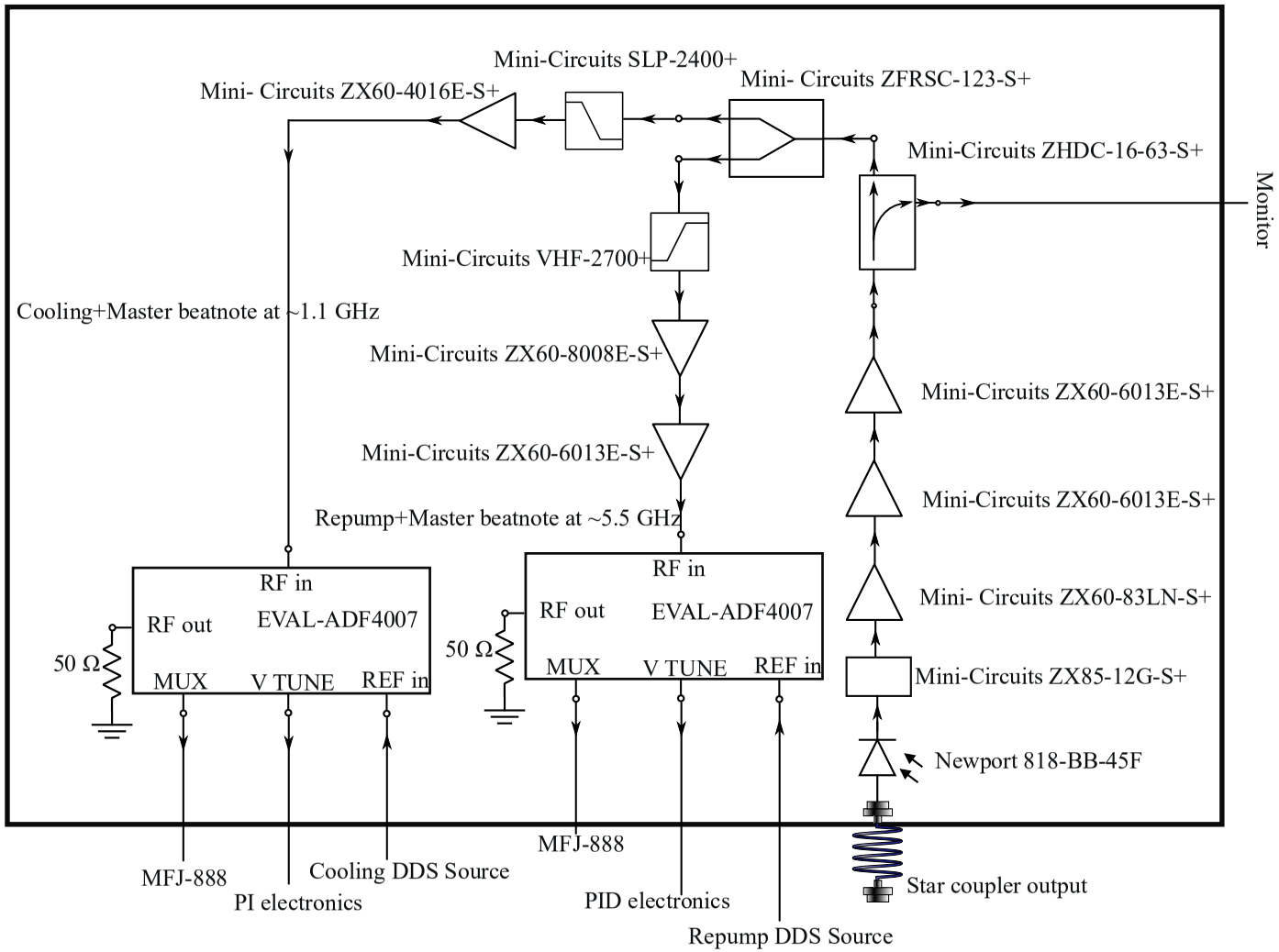

Figure 7.32: The layout of the optical phase locked loop electronics for stabilizing the frequency of the Rb cooling laser and Rb repump laser

one shallow-angle arm. The beam size of the regular MOT arms at the atoms is 10 mm and the beam size of the shallow-angle MOT arms is 5.7 mm. We maximally deliver 5.5 mW of cooling light and 2 mW of repump light to the atoms, as measured at one of the six high-power outputs of the star-coupler.

In the Rb repump laser setup, we added an additional beam-delivery arm called the Auxiliary Repump Arm (ARA). This arm delivers repump light over to the 1013 nm laser setup and was used to align the 1013 nm Rydberg arm to the atoms (Fig. 7.38). Instead of the 1013 nm laser light delivered via its 1013 nm Rydberg arm, we deliver 780 nm repump light to the atoms. When the unaligned ARA arm is engaged, the Rb MOT disappears as the atoms are pumped into the dark state when only the Rb cooling light is on. If the 1013 nm Rydberg arm, which now delivers the 780 nm repump light, is aligned appropriately to the Rb atoms, the Rb MOT will reappear as the atoms are pumped out of the dark state. Once we aligned the 1013 nm Rydberg arm using this method, we disengaged the ARA.

During typical Rb 3D MOT operation, the cooling DDS reference frequency is set to 137.827 MHz and the repump DDS reference frequency is set to 174.688 MHz. Previously, we used Novatech 409B to provide the reference rf frequencies for the beatnote locks. However, we now use home-built DDS boards built around AD9910 from Analog Devices (https://github.com/JQIamo/ad9910-dds.git) to provide these reference frequencies, as they have much faster update rates: 4 μs update rate for the home-built DDS board vs 100 μs update rate for Novatech 409B. We built a PCB for mounting these DDS boards into a Eurocard rack compatible module (https://github.com/JQIamo/Eurocard_DDS.git). I designed the topology of this PCB board. Oliver and Alessandro designed and built the PCB as well as the front panel. Currently, we use the Eurocard DDS module for providing the reference rf frequency

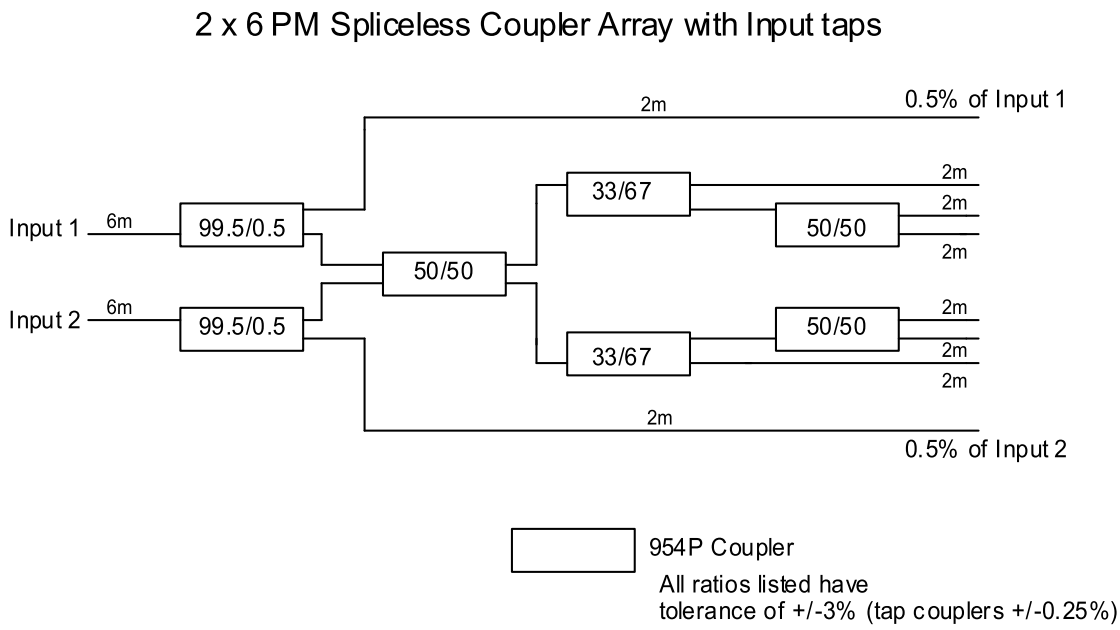

Figure 7.33: Single-mode PM fiber splitter/combiner with 2 inputs and 8 outputs for delivering Rb 3D MOT light

for only the cooling laser.

7.5.2 Yb MOT lasers and frequency-locking electronics

7.5.2.1 399 nm laser system: Optics and frequency-locking electronics

I designed the optical layout for the 399 nm laser light delivery system and built it with Kevin. The optical layout is presented in Fig. 7.34. The Toptica TA-DL-SHG Pro system for 399 nm light is something that we inherited from the old RbYb lab. The light from the 399 nm system is distributed between the two 2D MOT arms, the imaging arm, the 2D MOT push beam arm, and the three 3D molasses arms. The 399 nm power can be readily distributed between the various arms using half-wave plates and PBS cubes. All 399 nm light is delivered to the atoms via polarization-maintaining fibers (P3-375PM-FC series from Thorlabs). This is because the shallow-angle blue Yb 3D MOT is extremely sensitive to force imbalances arising

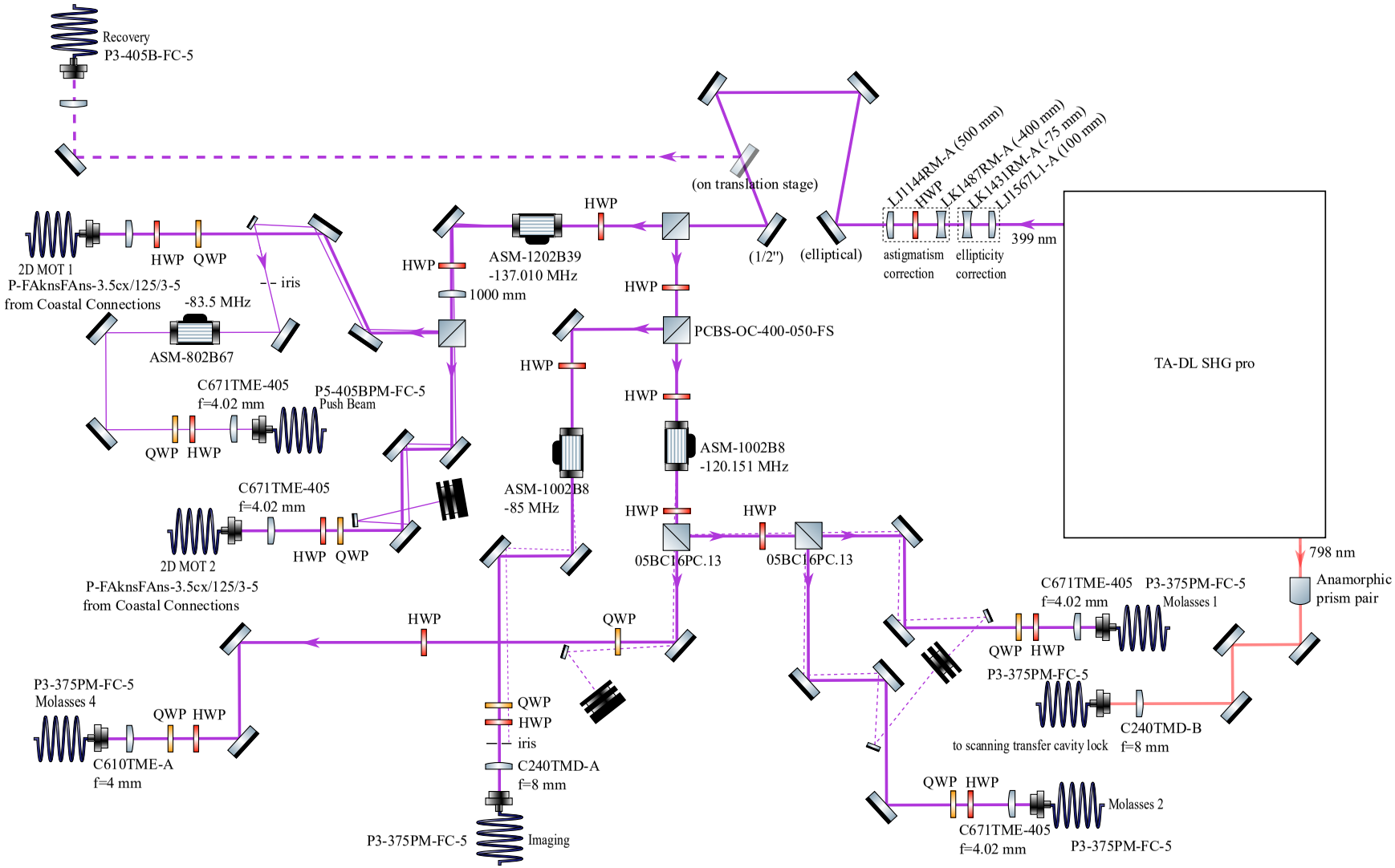

Figure 7.34: Schematic of the optical layout for 399 nm laser system

from polarization fluctuations.

The beam that exits the 399 nm laser head is elliptical despite there being an anamorphic prism pair right after the bow-tie SHG cavity inside the laser head. The beam is also astigmatic and is typical of laser light generated from a crystal pumped in a bow-tie cavity [70]. If the SHG from the cavity was optimized by tweaking the doubling-crystal alignment, it would change the astigmatic behavior of the output beam. We installed cylindrical beam-shaping optics to improve the beam ellipticity and astigmatism. After the beam-shaping optics, the spot size is ~ 1.2 mm. The 399 nm laser head can produce 340 mW of 399 nm light, measured after the beam-shaping optics. At the science chamber, we get ~ 13 mW in the 2D MOT arms, ~ 200 μW in the 2D MOT push beam arm, and 1.61 mW in the shallow-angle 3D molasses arm (beam size: 6.6 mm) and 18 mW in the other two regular molasses arms (beam size: 10.5 mm). One point to note, excess power in the push beam annihilates the blue 3D MOT,

We use the seed light at 798 nm to frequency stabilize the laser to the Rb master laser at 780 nm via the Scanning Transfer Cavity Lock (STCL) (Appendix B). Oliver later upgraded the software for easy interfacing with Labscript via the Bus Pirate(-v3.6a from Sparkfun). The Bus Pirate interfaces with the Arduino Due through its I^2C bus. Oliver also added blinking features to the LED to represent when the laser piezo control voltage and cavity piezo control voltage were close to the rails of the DAC or when the control voltages have railed. For example, solid LED light means that the control voltages are safely within the rails, slow blinking light implies that the control voltages are 500 DAC units away from the rails, and fast blinking light means that the control voltages have railed. This lock remains engaged for multiple hours at a time.

7.5.2.2 556 nm laser system: Optics and frequency-locking electronics

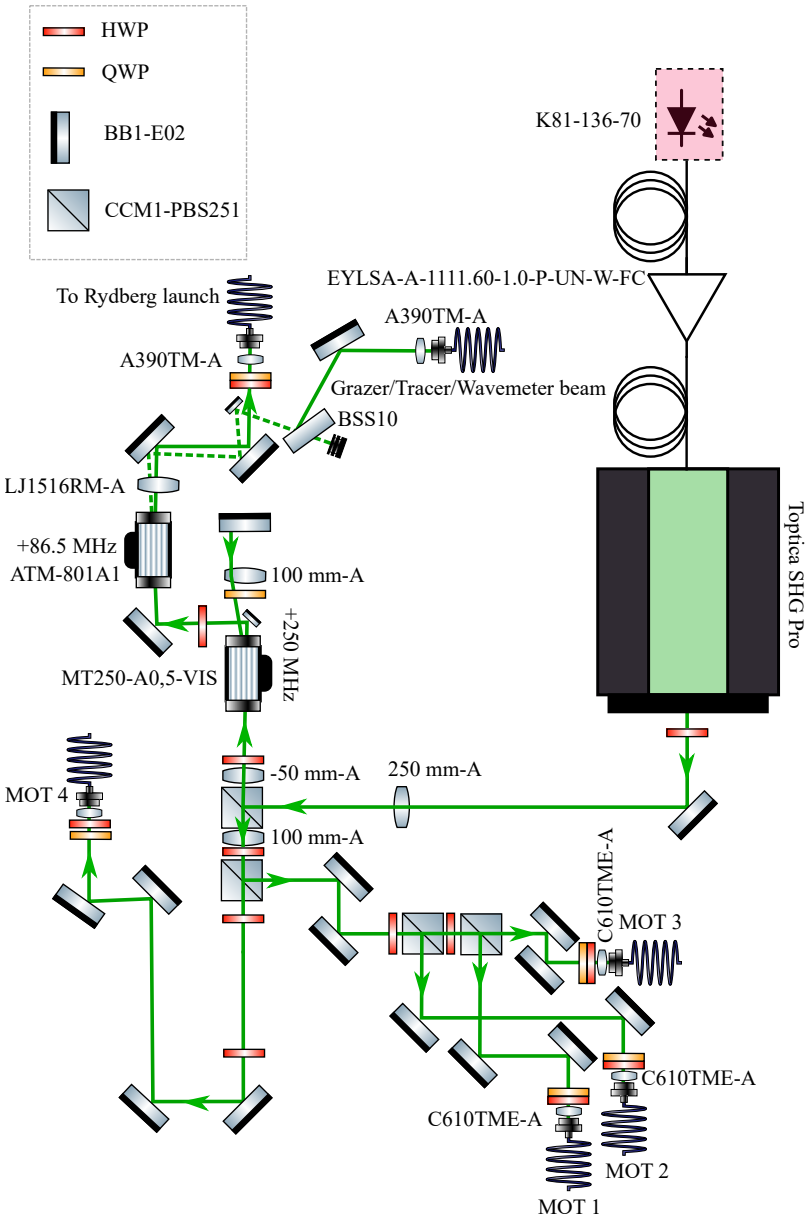

Figure 7.35: Schematic of the optical layout of the 556 nm laser system

We use a single-frequency distributed-feedback fiber laser (Koheras Adjustik Y10 System from NKT Photonics , P/N: K81-136-70) as the 1112 nm seed with an output power of $\sim$11 mW for the frequency doubled system. The output of this laser is amplified using a fiber laser amplifier system (Quantel EYLSA-A-1111.60-1.0-P-UN-W-FC) to a maximum power output of

1W of 1112 nm light. The amplified light is then frequency-doubled using the Toptica SHG-Pro system.

I designed and built the 556 nm optical layout shown in Fig. 7.35. We use the same laser to cool Yb atoms in a green Yb 3D MOT, and excite Yb atoms to the Rydberg states at different points in time in an experimental sequence. We use an AOM from AA Optoelectronics (MT250-A0,5-VIS) in a double-pass configuration to help us switch between these states of operation during the experimental sequence. When the AOM is on, the laser frequency is shifted up by 500 MHz and the light is directed to the 3D MOT arms. When the AOM is off, all the green power is directed to the Rydberg excitation arm. The ATM-801A1 AOM in the Rydberg excitation beam path provides control over the pulsing of the 556 nm Rydberg excitation light. We also sample some of the 0th order light in the Rydberg excitation beam path and couple it into a fiber. This fiber-coupled light is sometimes sent to the wavemeter to determine the wavelength of the unshifted frequency-doubled light.

We typically run the amplifier at 860 mW of 1112 nm light, which yields ~ 405mW of 556 nm light right before the MT250-A0,5-VIS AOM. After the MT250-A0,5-VIS AOM double-pass configuration (Fig. 7.35), we get approximately 210 mW of 556 nm light, which is then distributed to the four Yb 3D MOT arms in our setup: the two shallow-angle arms have typically 13 mW each (beam size: 5.7 mm), the other two standard MOT arms have 33 mW each (beam size: ~ 9 mm). The power between the MOT arms can be distributed appropriately using half-wave plates + PBSs. We use polarization-maintaining fibers to deliver the MOT light to the atoms. This is because shallow-angle MOTs are highly sensitive to force imbalances arising from polarization fluctuations.

We PDH lock the K81-136-70 1112 nm seed to the ULE reference cavity. A fiber-coupled

EOM (iXblue NIR-MPX-LN-05-00-P-P-FA-FA) is connected directly to the monitor port of the NKT photonics 1112 nm seed, which delivers the tapped seed light over to its ULE reference cavity for PDH locking. We need no more than 300 μW of 1112 nm light at the ULE cavity. I mounted a Toptica PID110 module, a Toptica SC110 module, and a low-noise high-voltage piezoelectric driver [11] Eurocard module to a Toptica rack. I made modifications to the PID110 and SC110 so that the modules can communicate via the backplane of the Toptica Eurocard rack.

The reason for choosing PID110 (the slower servo) over FALC110 (the faster servo) was multi-fold. The seed free-running linewidth is inherently narrow to begin with, i.e. < 2 kHz. We use the fiber laser's native piezoelectric actuator for laser frequency feedback. The modulation bandwidth is 20 kHz. However, there is an issue of FM to AM conversion in fiber lasers that can overdrive the ELSA laser amplifier. For all these reasons, slow feedback is preferred, and hence using PID110 as the servo. I chose to use a lower than normal modulation frequency of 625 kHz and a multipole low-pass filter (400 kHz from Kiwa electronics) to filter the demodulated error signal. This configuration helps increase the capture range of the lock and the laser stays locked for multiple hours at a time. However, reducing the modulation frequency to expand the lock capture range decreases the slope of the PDH error signal [69].

7.5.3 Design and construction of the optical layouts for the Rydberg lasers

In this section, I will present the optical layouts for all the Rydberg lasers we use in our experiment. While I designed the optical layouts, Kevin and Yulong helped me build them. Before that, I will motivate the choice of laser wavelengths used for Rydberg excitations in our experiment.

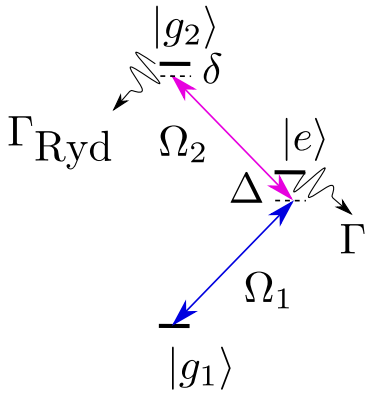

Figure 7.36: Two-photon Rydberg excitation

We intend to use a two-photon transitions to excite Rb and Yb atoms to Rydberg states. The general scheme is illustrated in Fig. 7.36. When $\Delta \gg \Omega_i, \delta, \Gamma, \Gamma_{\text{decoh.}}$, adiabatic elimination of the excited state can be performed and the scattering rate can be quantified as follows [149]:

$$\begin{aligned} R_{\text{sc}} &= \frac{\Gamma\Omega_1^2}{4\Delta^2}\rho_{\text{g}_1\text{g}_1} + \frac{\Gamma\Omega_2^2}{4\Delta^2}\rho_{\text{g}_2\text{g}_2} + 2\text{Re}\left[\frac{\Gamma\Omega_1\Omega_2}{4\Delta^2}e^{i(\mathbf{k}_2-\mathbf{k}_1)\cdot\mathbf{r}}\rho_{\text{g}_1\text{g}_2}\right] \\ &< \frac{\Gamma\Omega_1^2}{4\Delta^2} + \frac{\Gamma\Omega_2^2}{4\Delta^2} + \frac{\Gamma\Omega_1\Omega_2}{2\Delta^2} \\ &\leq \frac{\Gamma\Omega_1^2}{2\Delta^2} + \frac{\Gamma\Omega_2^2}{2\Delta^2} = R_T \end{aligned}$$

where Arithmetic mean$\geq$Geometric mean and $|\rho_{\alpha_i\beta}| \leq 1$. Furthermore, the two-photon Rabi frequency must be much greater than the decoherence of the Rydberg state ($\Gamma_{\text{decoh.}}$) which is greater than the linewidth of the Rydberg state (Γ_{Ryd}) [26]:

$$\Omega_R = \frac{\Omega_1\Omega_2}{2\Delta} = \kappa\Gamma_{\text{decoh.}}, \tag{7.19}$$

where $\kappa \gg 1$. The fidelity, f, of the π pulse of duration $\delta t = \pi/\Omega_R$ is given as follows:

$f =$ (prob. of not scattering a photon while in $|e\rangle$)$\times$(prob. of not scattering a photon while in $|g_2\rangle$)

(7.20)

$$= (1 - R_T \delta t)\left(1 - \frac{\Gamma_{\text{decoh.}}}{2}\delta t\right) \simeq 1 - R_T \delta t - \frac{\Gamma_{\text{decoh.}}}{2}\delta t \tag{7.21}$$

$$= 1 - \frac{\pi\Gamma(\Omega_1^2 + \Omega_2^2)}{\Delta\Omega_1\Omega_2} - \frac{\pi\Gamma_{\text{decoh.}}\Delta}{\Omega_1\Omega_2} \tag{7.22}$$

for $R_T\delta t \ll 1$ and $\Gamma_{\text{decoh.}}\delta t = \pi/\kappa \ll 1$. Now I will find the optimal Δ as follows:

$$\frac{\partial f}{\partial \Delta} = 0 \tag{7.23}$$

$$\implies \Delta = \sqrt{\frac{\Gamma}{\Gamma_{\text{decoh.}}}} \times \sqrt{\Omega_1^2 + \Omega_2^2}, \tag{7.24}$$

and the fidelity for this choice of optimal Δ,

$$f = (1 - \Gamma_{\text{decoh.}}\delta t/2)^2 = \left(1 - \frac{\pi}{2\kappa}\right)^2 \simeq \left(1 - \frac{\pi}{\kappa}\right). \tag{7.25}$$

The expressions for Ω_1 and Ω_2 are as follows:

$$\Omega_R = \frac{\Omega_1\Omega_2}{2\Delta} = \sqrt{\frac{\Gamma_{\text{decoh.}}}{\Gamma}}\frac{\eta}{2\sqrt{1+\eta^2}}\Omega_2 = \kappa\Gamma_{\text{decoh.}}$$

$$\implies \Omega_2 = \frac{2\kappa\sqrt{1+\eta^2}}{\eta}\sqrt{\Gamma_{\text{decoh.}}\Gamma} \tag{7.26}$$

where $\Omega_1 = \eta\Omega_2$. Few things to note:

1. The fidelity of the Rydberg excitation scales as $1/\kappa$ (Eq. 7.25), while the laser intensity

scales as κ^2 (Rabi frequency Ω_i scales as κ in Eq. 7.26). This is not a favorable scaling. One way to overcome this unfavorable scaling is to use the high NA objective to tightly focus the Rydberg excitation beam on to the atoms: intensity scales as the inverse squared of the spot size of the focused Rydberg excitation beam.

2. For a given κ, a longer intermediate state lifetime ($1/\Gamma$) helps relax laser power requirements (see Eq. 7.26).

For these reasons, we chose $6^2P_{3/2}$ ($\Gamma = 2\pi \times 1.35$ MHz) instead of $5^2P_{3/2}$ ($\Gamma = 2\pi \times 6$ MHz) as the intermediate state in Rb, and $(6s6p)^3P_1$ ($\Gamma = 2\pi \times 182$ kHz) instead of $(6s6p)^1P_1$ ($\Gamma = 2\pi \times 28$ MHz) as the intermediate state in Yb (Fig. 6.1). Furthermore, the transition from the intermediate state $6^2P_{3/2}$ ($\Gamma = 2\pi \times 1.35$ MHz) in Rb to the Rydberg state occurs at 1013 nm, a favorable wavelength where ample laser power is available. Last but not least, our high NA objectives are diffraction-limited for 420 nm ($5^2S_{1/2} \leftrightarrow 6^2P_{3/2}$ in Rb) and 556 nm ($(6s6p)^1S_0 \leftrightarrow (6s6p)^3P_1$ in Yb) Rydberg excitation light.

7.5.3.1 420 nm laser

The 420 nm laser system is a TA-DL SHG Pro system from Toptica that was inherited from the old RbYb experiment. Given that this is a Rydberg excitation laser, care must be taken to properly isolate it from vibrations (see Sec. 7.4.1). To that end, we mounted the laser on a honeycomb breadboard (Thorlabs PBG12105) and built the entire optical setup on the breadboard (Fig. 7.37a). We then placed this optical system in vibration isolation boxing (see Fig. 7.24a).

The laser used to operate at 423 nm on the old RbYb setup, which is one of the magic zero wavelengths for the $5s - 6p$ fine-structure manifold [150]. After the laser was moved downstairs,

I pulled the laser wavelength to the $5^2S_{1/2} \leftrightarrow 6^2P_{3/2}$ resonance in Rb at 420.29891 nm using the seed ECDL grating knob. The SHG crystal temperature was changed for good phase-matching in the doubling crystal followed by realigning the SHG cavity for an optimal power output of 250 mW.

The optical layout for delivering 420 nm Rydberg excitation light as well as the imaging light to the atoms is shown in Figs. 7.37a and 7.37b . The $1/e^2$ Gaussian beam diameter of the laser beam output is $\sim$2 mm. We use a passively stable achromatic fiber port (Thorlabs PAF2A-7A) mounted on a piezo-actuated cage-compatible kinematic mount (Thorlabs KC1T-P) for the Rydberg launch that yields a $1/e^2$ Gaussian beam diameter of 720 μm, which is then focused down to a 110 μm spot size at the atoms. We can deliver 95 mW of 420 nm to the atoms for Rydberg excitation. We also have an imaging arm that delivers 420 nm light for fluorescing the atoms on the $5^2S_{1/2} \leftrightarrow 6^2P_{3/2}$ transition.

We deliver the seed/fundamental light at 840 nm via a fiber-coupled EOM (iXblue NIR-MPX800-LN-10-P-P-FA-FA) to the ULE cavity (Sec. 7.4.1). A Toptica FALC 110 is used to PDH lock this laser to the ULE cavity. No more than 300 μW of 840 nm light is needed at the ULE cavity for PDH locking. A flipper mirror is placed in the path of the fundamental light to direct the light towards a wavemeter when necessary.

7.5.3.2 1013 nm laser

Fig. 7.38 shows the optical layout for the 1013 nm laser system. The 1013 nm seed laser is a Toptica DLC DL-Pro. For ease of PDH locking and subsequent laser linewidth narrowing, the free-running laser linewidth should be narrow (see Sec. 7.4.3 and Eq. 7.16). We asked Toptica

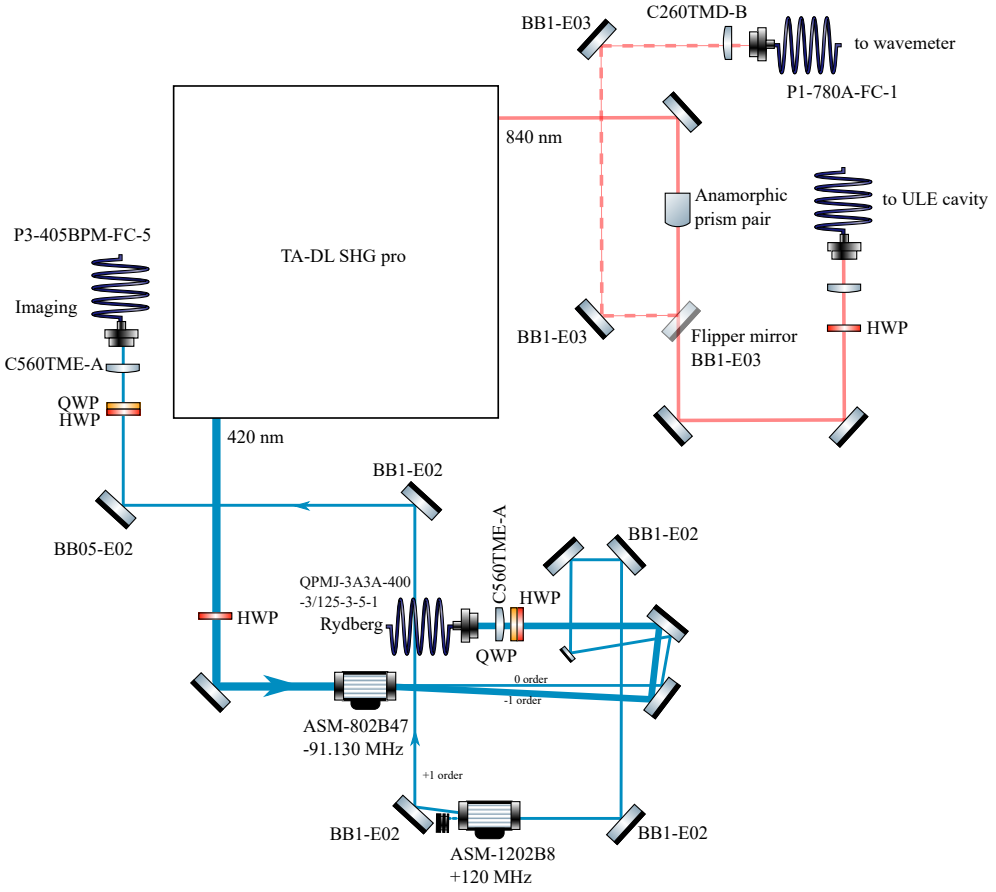

(a)

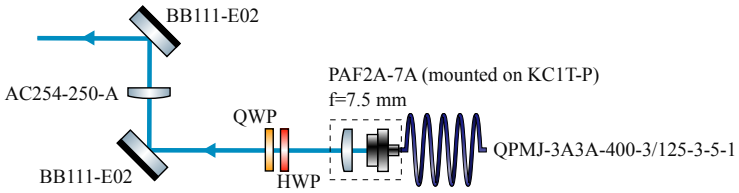

(b)

Figure 7.37: Schematic of the optical layout of (a) the 420 nm laser system, (b) the 420 nm Rydberg excitation launch

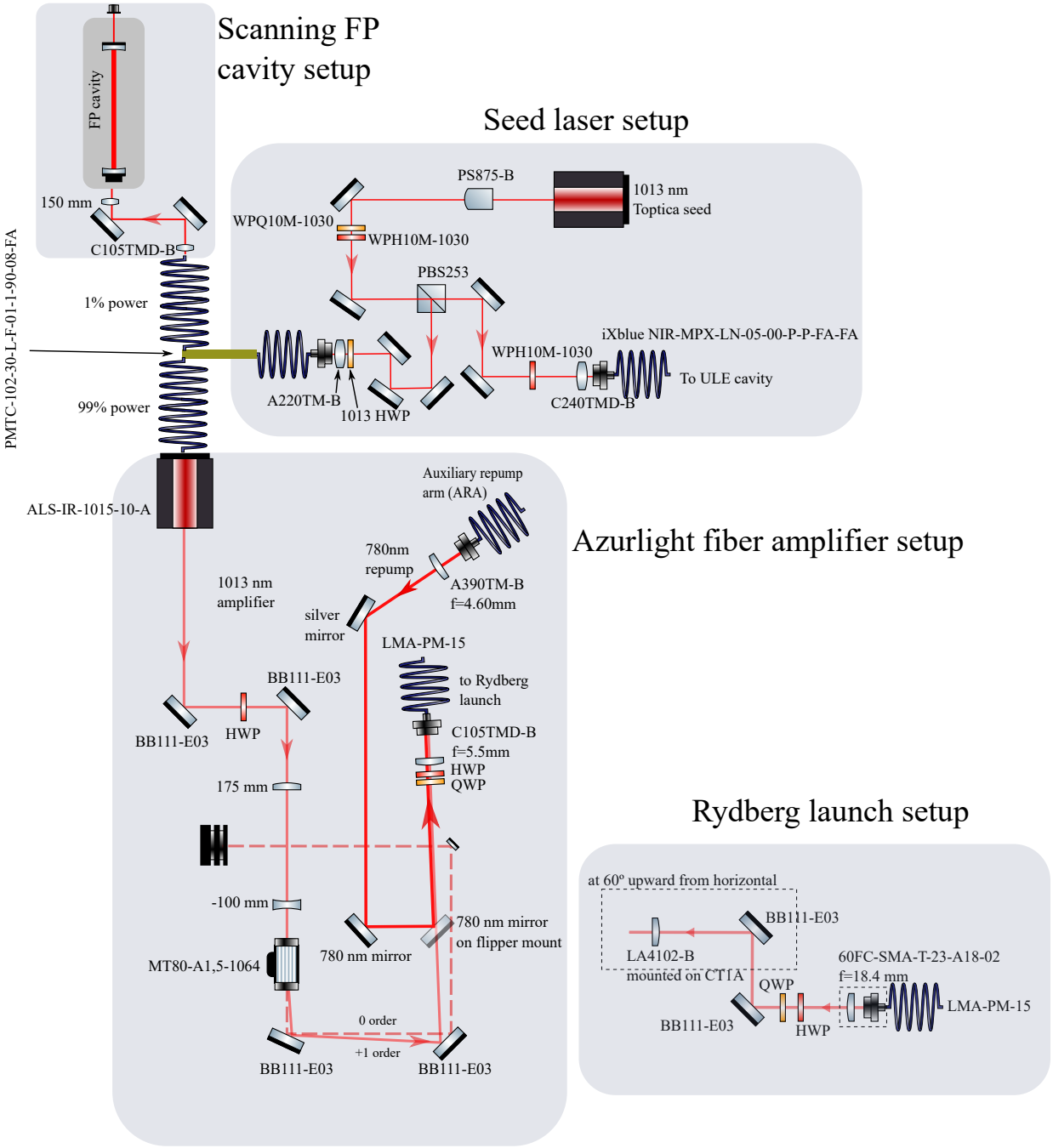

Figure 7.38: Schematic of the optical layout for the 1013 nm laser system.

for a special laser resonator that would yield a narrow free-running linewidth of <20 kHz at 5 μs (in comparison to the typical diode laser linewidths of 80 kHz or more).

The beam profile of the laser output is elliptical (2 mm major axis, 1.12 mm minor axis). We used a 2X anamorphic prism pair to shape the beam to a near Gaussian beam with a $1/e^2$

diameter of 2 mm. The laser yields 130 mW of 1013 nm light, which we distribute appropriately. We first sample a bit of this seed light and deliver it to the ULE cavity for PDH locking using a fiber-coupled EOM (iXblue NIR-MPX-LN-05-00-P-P-FA-FA). We need no more than 300 μW of laser light right at the ULE cavity. We couple the rest of the laser light into a 1030 nm polarization maintaining tap 1x2 coupler with a 1:99 coupling ratio from DK Photonics (PMTC-102-30-L-F-01-1-90-08-FA). The tapped light is coupled into a scanning FP-cavity (Thorlabs SA30-95) for mode-hop detection. Most of the light, 90 mW, is used to seed the Azurlight fiber amplifier (ALS-IR-1015-10-A-CP-SF).

The maximum output power is $8\ \mathrm{W}$ for seed laser wavelength between $1011\ \mathrm{nm}$ and $1012.8\ \mathrm{nm}$ for the Azurlight amplifier. Do not increase output power at the risk of damaging the system. Nominal output power is $10\ \mathrm{W}$ above $1012.8\ \mathrm{nm}$. The average $1/e^2$ diameter of the beam at the output of the Azurlight amplifier head at full power is 1.6 mm. We only use Zerodur mirrors (BB111-E03) to direct the high power laser light in the Azurlight fiber amplifier setup. An LMA-PM-15 Photonic Crystal Fiber (PCF) with SMA905 connectors (5° cut) is used to deliver the Rydberg laser light over to the science chamber. The fiber coupling efficiency and AOM diffraction efficiency are both progressively optimized with increasing power. From 7W of amplifier power output, we deliver 3.44 W of 1013 nm light to the atoms.

At the science chamber (Rydberg launch setup in Fig. 7.38), we use a collimator from Schäfter+Kirchhoff (60FC-SMA-T-23-A18-02) with a focal length of 18.4 mm to collimate the 1013 nm Rydberg excitation light exiting the photonic crystal fiber. Apart from the PCF's high power carrying capacity, the low fiber NA (due to a large mode field diameter of $\sim 12.6\ \mu$m) paired with the collimator yields a near Gaussian mode profile with a $1/e^2$ diameter of ~ 1.65 mm, which is then focused down to a spot size of $\sim 140\mu$m at the atoms. Zerodur mirrors

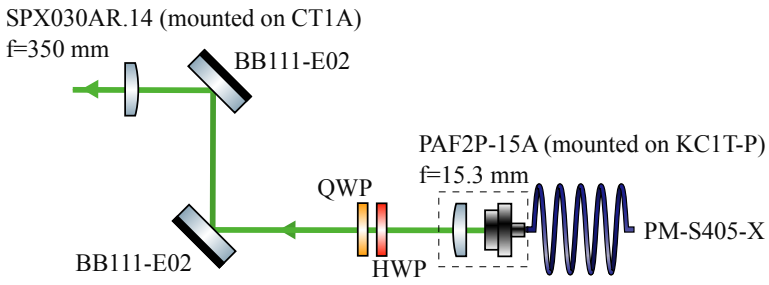

Figure 7.39: Schematic of the optical layout of the 556 nm Rydberg excitation launch

(BB111-E03) are used to direct the high power laser light. We used 780 nm repump light to align the 1013 Rydberg launch to the atoms via the ARA arm (Figs. 7.38 and 7.31a).

7.5.3.3 Setting up the 556 nm laser

The Rydberg excitation light and the 3D MOT light are derived from the same optical setup (see Sec. 7.5.2.2 and Fig. 7.35). The undiffracted beam from the MT250-A0,5-VIS AOM (in its off state) is utilized for Rydberg excitation, aiming to maximize the delivery of 556 nm light to the atoms. The ATM-801A1 AOM controls the pulsing of the 556 nm Rydberg excitation light. In order to ensure passive stability, the high power Rydberg light is collimated using a PAF2P-15A collimator mounted on a piezo-actuated cage-compatible kinematic mirror mount (KC1T-P). This light is guided using BB111-E02 Zerodur mirrors (see Fig. 7.39). The mean $1/e^2$ diameter of the collimated beam is ~ 1.6 mm, which is focused down to a mean spot size of 123 μm at the atoms. We can deliver more 150 mW of 556 nm Rydberg excitation light to the atoms.

7.5.3.4 308 nm laser

The 308 nm laser light is generated by a DLC FA-FHG Pro system. The 1232 nm seed light from the ECDL seeds a Raman Fiber Amplifier (RFA), which then amplifies the 1232 nm light. The amplified 1232 nm light undergoes two SHG stages. The first stage yields 616 nm light, which then seeds a second SHG stage to yield 500 mW of 308 nm light. Unlike the other Rydberg lasers, 500 mW of 308 nm light is directed to the atoms via free-space optics instead of fibre optics (see Fig. 7.40). The intrinsic laser linewidth (5 μs) is < 80 kHz. Leakage light after the first SHG atage at 616 nm is used to monitor the frequency of the laser on the wavemeter. I directed the leakage fundamental light at 1232 nm over to the ULE cavity for PDH locking via a P3-980PM-FC-5 fiber which is then butt-coupled to the fiber-coupled EOM (iXblue NIR-MPX-LN-05-00-P-P-FA-FA) using an FC/APC mating sleeve.

The 308 nm beam has a $1/e^2$ diameter of 1.6 mm, which is then focused down to a spot size of $\sim$ 122 μm at the atoms using excimer laser optics (Fig. 7.40). Two of the mirrors in the Rydberg excitation beam path are mounted on piezoelectric mirror mounts (8816-6 from Newport) to remove human alignment optimizations due to the hazardous nature of the light at this wavelength. To further reduce human involvement in laser power output optimizations, auto-alignment of the input light into the SHG cavity during each doubling stage can be performed via the TOPAS PC GUI from Toptica.

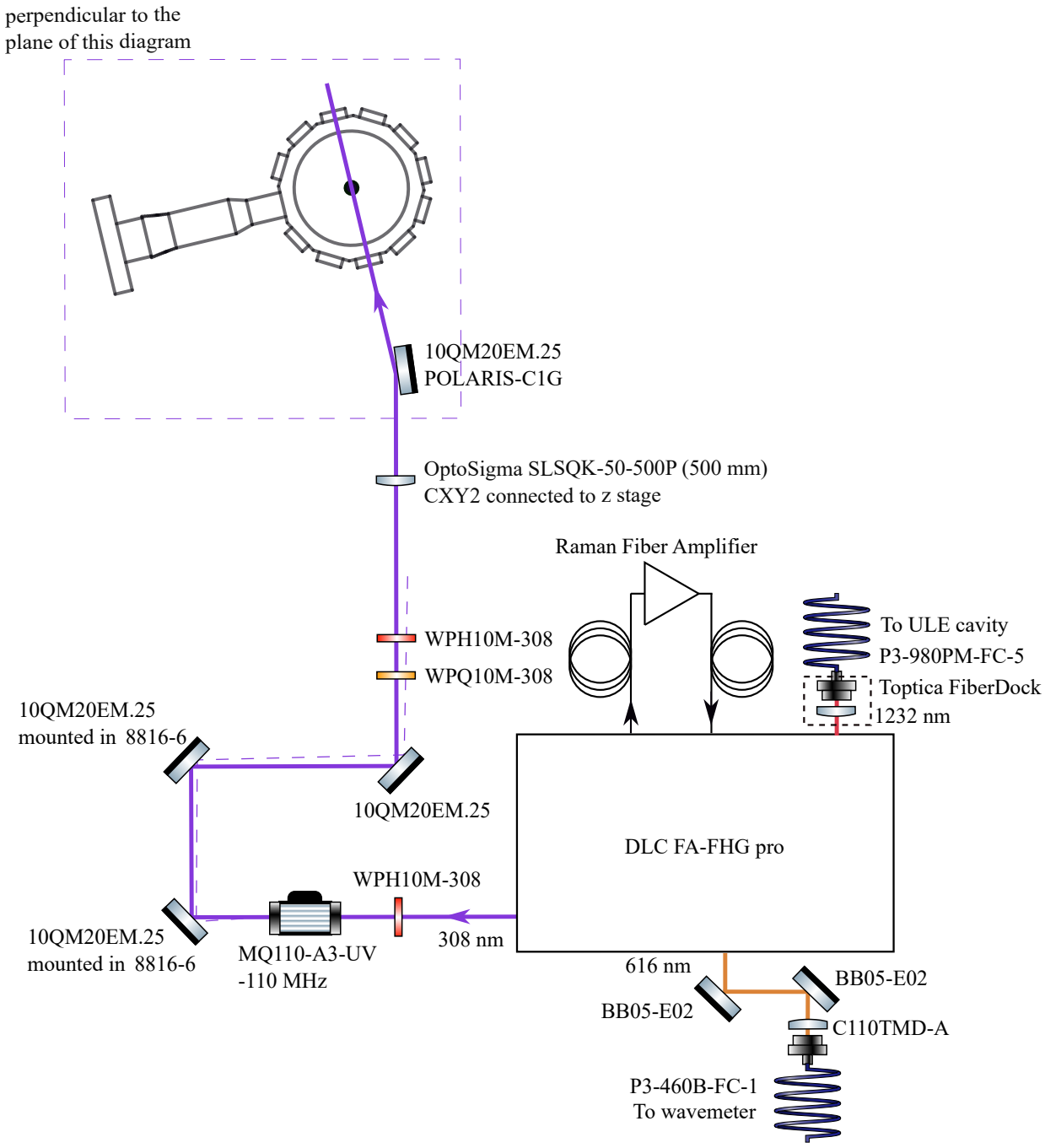

Figure 7.40: Schematic of the optical layout of the 308 nm laser system

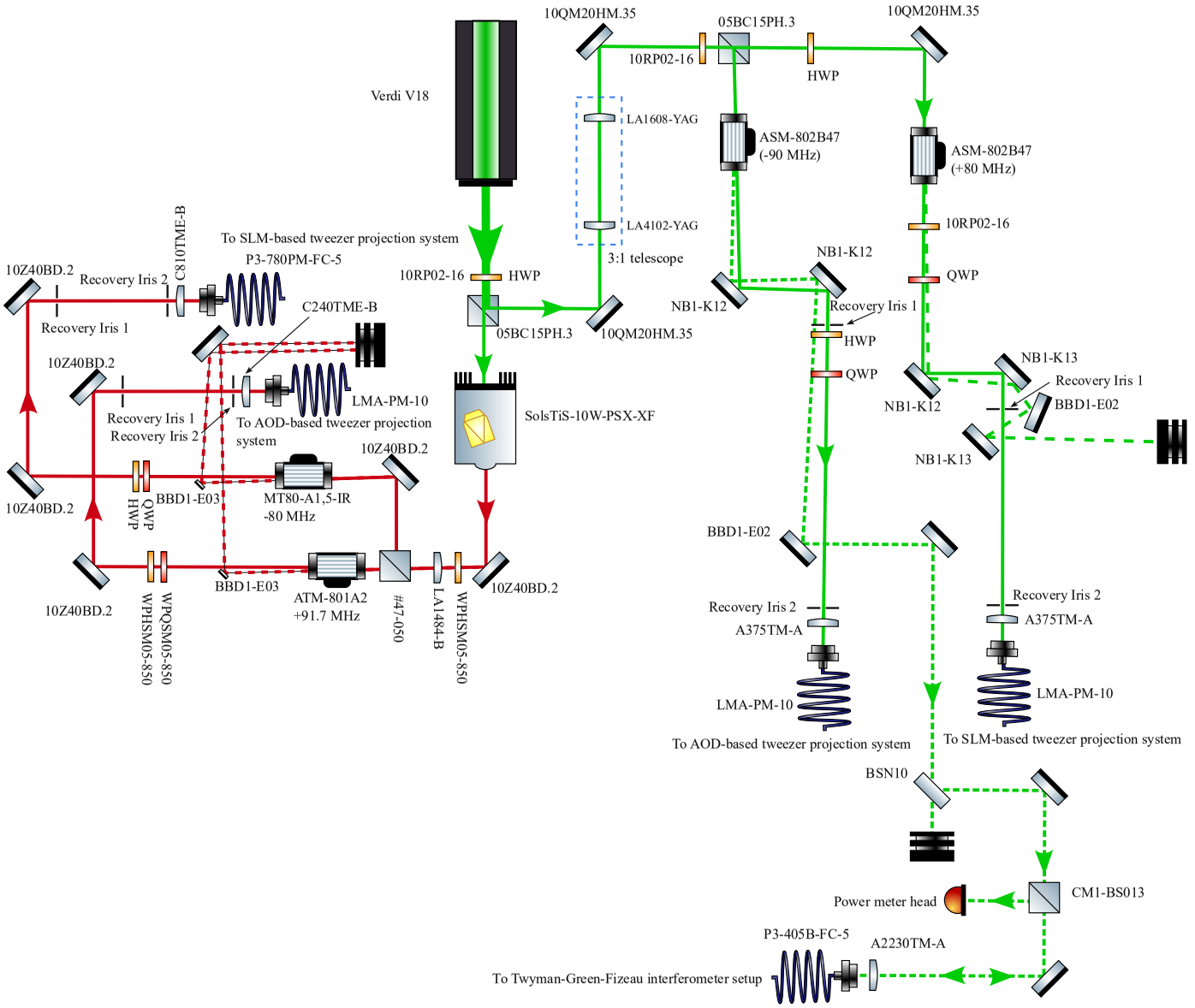

Figure 7.41: Schematic of the optical layout for the launch side of the AOD-based and SLM-based tweezer projection systems.

7.5.4 Launch optics for the AOD-based and SLM-based tweezer projection systems

We use a Coherent Verdi V18 laser, a diode-pumped solid-state laser [70], to generate the tweezer light for both species (see Fig. 7.41). The Verdi laser can generate 20 W of single-mode CW 532 nm light. A minimum of 5.5 W of 532 nm light is directed using a high-energy optically-contacted polarizing beamsplitter cube (Newport 05BC15PH.3) to seed the SolsTiS-10W-PSX-XF, a Ti:sapphire laser from M Squared Lasers. A high-energy V-coated HWP at 532 nm (Newport 10RP02-16) is used to control the power distribution between the Yb tweezer launch optics and the Rb tweezer launch optics. With 10 W of 532 nm seed light, we get 1.18 W of output 840 mW light from the Ti:sapphire laser.

7.5.4.1 Launch optics for the Yb tweezer projection systems

The 532 nm output beam (with an average $1/e^2$ Gaussian beam diameter of 2.8 mm at low power) is demagnified by 3X (using V-coated lenses at 532 nm) to match the AOM vendor suggested spot sizes for optimal diffraction efficiencies. The power in the demagnified beam is distributed between the AOD tweezer arm and the SLM arm using the Newport 05BC15PH.3 and 10RP02-16 combination from above. The SLM light and AOD light are frequency shifted with respect to each other (via their AOMs) to minimize optical interference. High energy mirrors (Newport 10QM20HM.35 and Thorlabs NB1-K12), V-coated at 532 nm, are used to direct the light to LMA-PM-10 Photonic Crystal Fibers (PCF) to deliver light to the AOD-based optical tweezer projection system and SLM-based optical tweezer projection system. The PCFs have

SMA-905 connectors (8° angle cut) to handle high power. Unfortunately, SMA-905 connectors do not have notches. This makes any form of mechanical recovery (and therefore alignment recovery) highly improbable when these PCFs are disconnected from their mounts and then later reconnected. The lack of a notch also precludes the recovery of any PM-matching into these fibers. Given the highly alignment-sensitive nature of the optical tweezer projection systems, recovery irises are placed just before the PCF launch. Aligning into these irises using the two mirrors should couple some 532 nm light into their respective PCFs. This topology mitigates the need to disconnect the fibers from their mounts in the most unfortunate of misalignment scenarios.

Some of the sampled undiffracted light from the AOM for the AOD-based optical tweezer system is coupled into an SM fiber (Thorlabs P3-405B-FC-5) for the Twyman-Green-Fizeau interferometer setup (see Sec. 7.6.3.1). The 50:50 non-polarizing beam splitter (Thorlabs CM2-BS013) is used to direct the light back-coupled into the fiber from the Twyman-Green-Fizeau interferometer setup, which is then measured using a power-meter head.

7.5.4.2 Launch optics for the Rb tweezer projection systems

The 840 nm light from the Ti:Sapphire laser is weakly expanding. It is collimated using a 300 mm lens to an average $1/e^2$ beam diameter of 860 μm. The light is distributed between the AOD arm and the SLM arm using a waveplate (Thorlabs WPHSM05-850) and a V-coated polarizing beam splitter (Edmund Optics #47-050). The SLM light and AOD light are frequency shifted with respect to each other (via their AOMs) to minimize optical interference. The high power 840 nm light is directed using broadband-coated Zerodur mirrors (Newport 10Z40BD.2)

for maximum passive stability. Recovery irises are placed in the AOD and SLM beam paths for the same reasons as the ones mentioned in the above section. While the 840 nm tweezer AOD light is delivered via an LMA-PM-10 PCF , the SLM light is delivered via a standard PM fiber patch cable (Thorlabs P3-780PM-FC-5).

7.5.5 Design and construction of the imaging launch

The imaging launch in Fig. 7.28 is used for absorption imaging [151, 152] of laser cooled atoms and for illuminating the atoms during fluorescence imaging via the high NA objectives. This setup was quite difficult to install because of the lack of space underneath the steel chamber. The imaging launch delivers polarized light at 399 nm for imaging Yb atoms and polarized light at 780 nm for imaging Rb atoms (Fig. 6.1). In the absorption imaging configuration, we use this setup to perform time-of-flight measurements [151, 152] to determine and optimize the temperature of laser-cooled Rb and Yb atoms (Fig. 7.63 and Fig. 7.65). The absorption imaging system is a $4f$ imaging system and has a magnification of 0.75. In the fluorescence imaging configuration, a mirror mounted in a kinematic mirror mount is installed right in front of the camera. This retroreflected illumination of the atoms helps balance out the photon recoil during fluorescence imaging.

7.6 Design and construction of high-NA optical systems

In order to fully appreciate the nuances of the high-NA optical system design and construction, I will approach this topic from the framework in Abbe's Theory of Image Formation [59, 153]. The Abbe Theory of Imaging treats the scattering of light from an object as scattering from a

superposition of gratings with different grating periods. By illuminating this superposition of gratings, light is diffracted into multiple orders. The imaging system captures some of these diffraction orders and directs them to the image plane where these orders interfere to create an image. The NA of any real imaging system spatially restricts the range of Bragg angles that can be sampled, serving as a low-pass amplitude filter for high spatial frequency components. Additionally, aberrations in the imaging system act as a phase filter that change the strict phase relationships between the sampled diffraction orders, which distorts the image formed from their interference. These physical effects therefore set a lower bound on the grating spacing—fine object details—that can be resolved by an imaging system.

Mathematically, an imaging system maps the object amplitude $u_o(\xi, \eta)$ to the image amplitude $u_i(x', y')$ using an impulse response function $h(x', y'; \xi, \eta)$ (Fig. 7.42). By imposing linearity on this mapping, the relationship between the object amplitude and image amplitude can be expressed as a superposition integral [154]

$$u_i(x', y') = \int_{-\infty}^{\infty} \int_{-\infty}^{\infty} h(x', y'; \xi, \eta) u_o(\xi, \eta) d\xi d\eta.$$

The impulse response function $h(x', y'; \xi, \eta)$ is typically referred to as a Point-Spread Function (PSF) in optical systems. In a well-corrected optical system, the PSF is shift invariant/uniform over a region of space called the isoplanatic patch [154, 155] and the imaging system is a linear shift invariant (LSI) system [154, 155]. Within an isoplanatic patch in the LSI imaging system, the image amplitude ($u_i(x', y')$) is the convolution of the amplitude PSF (h) of the imaging system (Fig. 7.42) with the amplitude of the object ($u_o(\xi, \eta)$) as given by the Fraunhofer diffraction

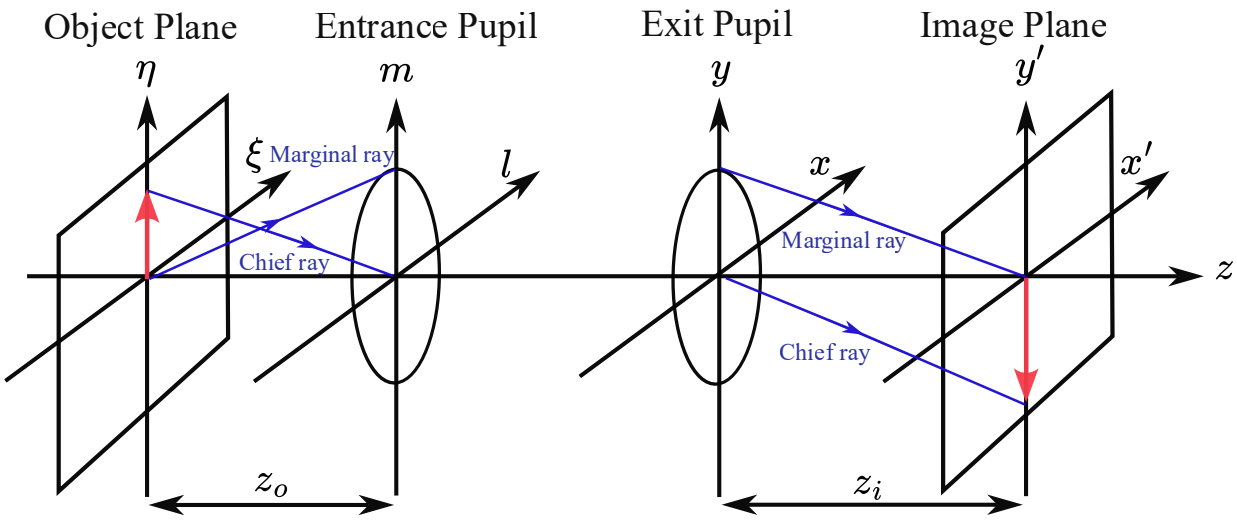

Figure 7.42: General structure of an imaging system

integral [154, 155, 156] and expressed as follows:

$$u_i(x', y') = \int_{-\infty}^{\infty} \int_{-\infty}^{\infty} h(x' - \xi', y' - \eta') u_g(\xi', \eta') d\xi' d\eta', \tag{7.27}$$

where

$$h(x', y') = \frac{A}{\lambda z_i} \int_{-\infty}^{\infty} \int_{-\infty}^{\infty} \underbrace{P(x, y) e^{ikW(x,y)}}_{\mathcal{P}(x,y)} e^{-i\frac{2\pi}{\lambda z_i}(x'x + y'y)} dx dy, \tag{7.28}$$

and

$$u_g(\xi', \eta') = \frac{1}{|M|} u_o(\xi, \eta), \tag{7.29}$$

where $\xi' = M\xi$, $\eta' = M\eta$, M is the magnification of the imaging system, A is a constant amplitude, $\mathcal{P}(x, y) = P(x, y)e^{ikW(x,y)}$ is the generalized pupil function that includes the effects of the aberration $W(x, y)$ across the pupil. The exit pupil and the entrance pupil are images of the aperture stop in the image space and object space respectively [96].

Complex exponential functions are the eigenfunctions of an LSI system and form the appropriate basis set for expressing the object and image fields [155]. With complex exponential

functions serving as the basis set, the action of optical elements and even their aberrations can be modeled as amplitude and/or phase filters in spatial frequency space. Therefore, an LSI imaging system allows the full applicability of the Transfer Function (TF) approach from Control Theory, which is highly convenient [70]. Taking the Fourier transform ($\mathcal{F}$) of the convolution integral (Eq. 7.27), we get the transfer function formulation for the imaging system:

$$\underbrace{U_i\left(f_X, f_Y\right)}_{\mathcal{F}(u_i)} = H\left(f_X, f_Y\right) \underbrace{U_g\left(f_X, f_Y\right)}_{\mathcal{F}(u_g)}, \tag{7.30}$$

where $H\left(f_X, f_Y\right)$ is referred to as the Amplitude Transfer Function (ATF) or Coherent Transfer Function (CTF). The expressions for $H\left(f_X, f_Y\right)$ are as follows [154]:

$$H\left(f_X, f_Y\right) = \mathcal{F}\left\{h(x', y')\right\} \tag{7.31}$$

$$= \mathcal{F}\left\{\frac{A}{\lambda z_i} \int_{-\infty}^{\infty} \int_{-\infty}^{\infty} \mathcal{P}(x, y) e^{-i\frac{2\pi}{\lambda z_i}(x'x + y'y)} dxdy\right\} \tag{7.32}$$

$$= A\lambda z_i \mathcal{P}\left(\lambda z_i f_X, \lambda z_i f_Y\right) \text{(for symmetrical pupils)} \tag{7.33}$$

$$= A\lambda z_i \underbrace{P\left(\lambda z_i f_X, \lambda z_i f_Y\right)}_{\text{Apodizing amplitude filter}} \times \underbrace{e^{ikW(\lambda z_i f_X, \lambda z_i f_Y)}}_{\text{Aberrations as a phase-only filter}} \tag{7.34}$$

The amplitude transfer function $H\left(f_X, f_Y\right)$ is basically the scaled generalized pupil function $\mathcal{P}\left(\lambda z_i f_X, \lambda z_i f_Y\right)$ (see Eq. 7.33). The unaberrated and unapodized ATF is therefore a simple low-pass filter as the pupil in a real imaging system always has a finite aperture size. This can be easily seen through the following coordinate transformation between the ATF spatial frequency

coordinates and the pupil physical coordinates [154, 157]:

$$f_X = \frac{x}{\lambda z_i} \leq \frac{\text{NA}}{\lambda}, \quad f_Y = \frac{y}{\lambda z_i} \leq \frac{\text{NA}}{\lambda}. \tag{7.35}$$

This transfer function approach helps differentiate the effects of diffraction from that of aberrations on the object field spectrum:

$$U_i\left(f_X, f_Y\right) = A\lambda z_i \underbrace{P\left(\lambda z_i f_X, \lambda z_i f_Y\right)}_{\text{diffraction}} \underbrace{e^{ikW(\lambda z_i f_X, \lambda z_i f_Y)} U_g\left(f_X, f_Y\right)}_{\text{Aberrated object spectrum}}. \tag{7.36}$$

Specifically, aberrations act as a phase-only filter that distorts the phase spectrum of $U_g\left(f_X, f_Y\right)$, while $P(x, y)$ acts as an amplitude-only filter [154, 157].

Although the expressions stated above are for electric field amplitudes, it is the object field intensity and image field intensity that are actually measured in practice. Depending on the type of illumination of the object (coherent or incoherent), the intensity of the image (and its spectrum) can be mapped to the intensity of the object (and its spectrum) using the relations in Table 7.3. As can be seen in Table 7.3, incoherently illuminated imaging systems are linear in irradiance, whereas coherently illuminated imaging systems are linear in electric field amplitude [154, 157].

Coherent Illumination	Incoherent Illumination
$\lvert u_i\rvert^2 = I_i = \lvert h * u_g\rvert^2$	$\lvert u_i\rvert^2 = I_i = \lvert h\rvert^2 * \lvert u_g\rvert^2$
Amplitude PSF (APSF): $h(x', y')$	Intensity PSF (IPSF): $\lvert h(x', y')\rvert^2$
TF: $H(f_X, f_Y) = \mathcal{F}\{h(x', y')\}$	TF: $H(f_X, f_Y) \star H(f_X, f_Y) = \mathcal{F}\{\lvert h(x', y')\rvert^2\}$
$f_{\text{cutoff, coherent}} = \text{NA}/\lambda$	$f_{\text{cutoff, incoherent}} = 2\text{NA}/\lambda$
$\mathcal{F}\left\{I_i\right\} = \left(HU_g\right) \star \left(HU_g\right)$	$\mathcal{F}\left\{I_i\right\} = \left(H \star H\right)\left(U_g \star U_g\right)$

Table 7.3: Coherent illumination vs. Incoherent illumination

Specifically, for incoherent illumination, the normalized incoherent transfer function is called the Optical Transfer Function (OTF), which is expressed as follows:

$$\mathrm{OTF}(f_X, f_Y) = \frac{H \star H}{\int_{-\infty}^{\infty}\int_{-\infty}^{\infty} |H(p', q')|^2 \, dp'dq'} \tag{7.37}$$

$$= \frac{\int_{-\infty}^{\infty}\int_{-\infty}^{\infty} H(p', q') \, H^*(p' - f_X, q' - f_Y) \, dp'dq'}{\int_{-\infty}^{\infty}\int_{-\infty}^{\infty} |H(p', q')|^2 \, dp'dq'} \tag{7.38}$$

$$= \frac{\mathcal{F}\{|h(x', y')|^2\}}{\int_{-\infty}^{\infty}\int_{-\infty}^{\infty} |h(x', y')|^2 dx'dy'} \tag{7.39}$$

$$= \mathrm{MTF}(f_X, f_Y) e^{i\mathrm{PTF}(f_X, f_Y)}, \tag{7.40}$$

where $\mathrm{MTF}(x, y)$ is referred to as the Modulation Transfer Function and $\mathrm{PTF}(x, y)$ is referred to as the Phase Transfer Function in literature [94, 158, 159]. For an unapodized pupil, the diffraction-limited OTF is [154, 160]

$$\mathrm{OTF}(f) = \frac{2}{\pi}\left[\cos^{-1}\frac{\lambda f}{2\mathrm{NA}} - \frac{\lambda f}{2\mathrm{NA}}\sqrt{1 - \left(\frac{\lambda f}{2\mathrm{NA}}\right)^2}\right], 0 \le f \le \frac{2\mathrm{NA}}{\lambda}.$$

A critical property of the OTF enforced by the Cauchy-Schwarz inequality is [154],

$$\mathrm{OTF}(f_X, f_Y)_u \le \mathrm{OTF}(f_X, f_Y)_a, \tag{7.41}$$

$$\implies \underbrace{\frac{\iint \mathrm{OTF}(f_X, f_Y)_a df_X df_Y}{\iint \mathrm{OTF}(f_X, f_Y)_u df_X df_Y}}_{\text{Strehl Ratio: } \mathcal{D}_S} \le 1. \tag{7.42}$$

The subscripts u and a stand for unaberrated/unapodized and aberrated/apodized respectively [155].

The inequality in Eq. 7.41 implies that the bandwidth (and cutoff frequency) of the transfer function for an imaging system decreases with increasing aberrations. This leads to increasing the size of the IPSF reducing the achievable resolution, as the OTF and IPSF are a Fourier transform pair. Eq. 7.42 shows the origins of the Strehl ratio ($\mathcal{D}_S$), an important metric of optical imaging quality, which can be derived directly from the OTF [59, 95, 159]. OTF is commonly switched out for MTF in Eq. 7.42 as the latter is measured in practice[21]. The Strehl ratio is also routinely expressed in other forms as [59, 155, 159]:

$$\mathcal{D}_S = \frac{|h(0,0)|_a^2}{|h(0,0)|_u^2} \tag{7.43}$$

$$\cong e^{-k^2(\langle W^2\rangle - \langle W\rangle^2)} \tag{7.44}$$

$$\cong \left(1 - \frac{k^2(\langle W^2\rangle - \langle W\rangle^2)}{2}\right)^2 \quad \text{(Maréchal formula)} \tag{7.45}$$

$$\cong 1 - k^2 \underbrace{(\langle W^2\rangle - \langle W\rangle^2)}_{\text{(RMS OPD)}^2\text{: } \sigma_W^2}, \tag{7.46}$$

where the subscripts u and a stand for unaberrated/unapodized and aberrated/apodized respectively, $\langle W^2\rangle = \frac{\iint PW^2 dxdy}{\iint P dxdy}$ and $\langle W\rangle = \frac{\iint PW dxdy}{\iint P dxdy}$. In the expression for the Strehl ratio (Eq. 7.46), the term σ_W^2 is representative of the amount of energy that is removed from the central peak and redistributed elsewhere in the point spread function. Having introduced the concepts of OTF, MTF, and $\mathcal{D}_S$, I can now comment on what it means to label an imaging system as diffraction-limited. In order to do that, I will introduce the concept of optical path difference (OPD).

OPD refers to the departure of an aberrated wavefront from an ideal reference wavefront. The reference wavefront is a plane wave for an afocal system or an ideal spherical wavefront

[21] The resultant MTF-based Strehl ratio is larger than the OTF-based Strehl ratio.

for a focusing system. OPD is typically quoted/measured in units of wavelength. Ideal imaging systems (unlike real imaging systems) have no aberrations and therefore have an OPD $= 0$. OPD is also called the wavefront error (WFE) [99]. Therefore, OPD can be (and is widely) used to determine the quality of a real imaging system [59, 95, 102, 158]:

- Lord Rayleigh's $\lambda/4$ criterion (P–V OPD$< \lambda/4$): Peak-to-valley (P–V) OPD is the maximum departure of the aberrated wavefront from the reference wavefront minimum over the aperture of the exit pupil. P-V OPD is a good measure of the image quality of an optical system if the wavefront error is smooth over most of the pupil aperture and is not greater than $\lambda/4$. Under these circumstances, the real imaging system is considered to perform at a level on par with an ideal imaging system with no aberrations. As the resolution of the ideal imaging system is limited only by diffraction, the real imaging system is classified as diffraction-limited if it satisfies Lord Rayleigh's $\lambda/4$ criterion.

- Maréchal's criterion (RMS OPD $< 0.071\lambda \implies \mathcal{D}_S > 0.82$) : The Rayleigh criterion is not airtight as different aberrations with the same P-V $\lambda/4$ OPD can have drastically different effects on the image quality [94, 102]. The Maréchal criterion states that the root-mean-squared OPD (RMS-OPD) calculated over the pupil aperture should be less than 0.071λ to yield an imaging system performance on par with an ideal system without aberrations. This RMS-OPD $< 0.071\lambda$ criterion when substituted into the expression for the Strehl ratio in Eq. 7.44 yields a $\mathcal{D}_S \geq 0.82$.

Using OPD as a metric to quantify the diffraction-limited performance of the imaging system is generally applicable for low P-V OPDs of λ or less. Typically, one starts off with geometrical ray tracing for evaluating the performance of an optical layout. The Geometrical PSF

(GPSF) is a handy tool to evaluate the performance of a highly aberrated imaging system [161]. In geometrical ray tracing, rays from a point source on the object plane are traced through the imaging system to generate a spot diagram at the image plane. The optical designer typically compares the geometric blur (distribution of the rays in the spot diagram) with the Airy disc size and tweaks the layout so that the geometric blur size is smaller than the Airy disc size. This is called the golden rule of optical design [160]. After the golden rule is satisfied, the optical designer typically moves on to the OPD metric to further refine the optical system. I used both of these metrics for evaluating the performance of our imaging/tweezer projection systems: spot diagrams and RMS OPD for focusing systems, and just the RMS OPD for afocal systems.

The RMS OPD metric when applied to a multi-element imaging system states that the total RMS OPD of the imaging system should be $< 0.071\lambda$ [102]. OPD errors can arise from the fabrication of the individual components of the multi-element imaging system, from the OPD residuals from the optical design itself, and from the relative mechanical alignment between the various elements of the optical system like tip/tilt, defocus/despace, and decenter. These OPD errors are added in quadrature to yield the RMS OPD error of the entire imaging system, which can be mathematically expressed as follows:

$$\text{RMS OPD}_{\text{imaging system}} = \sqrt{\text{RMS OPD}^2_{\text{fabrication}} + \text{RMS OPD}^2_{\text{design}} + \text{RMS OPD}^2_{\text{alignment}} + ...} \tag{7.47}$$

I individually addressed each term in Eq. 7.47 to minimize the RMS OPD of our optical systems for creating diffraction-limited optical tweezers and diffraction-limited imaging of single atoms. My general strategy to create diffraction-limited optical tweezers is illustrated in Fig. 7.43. This strategy also facilitates diffraction-limited imaging of single atoms. The next sections elaborate

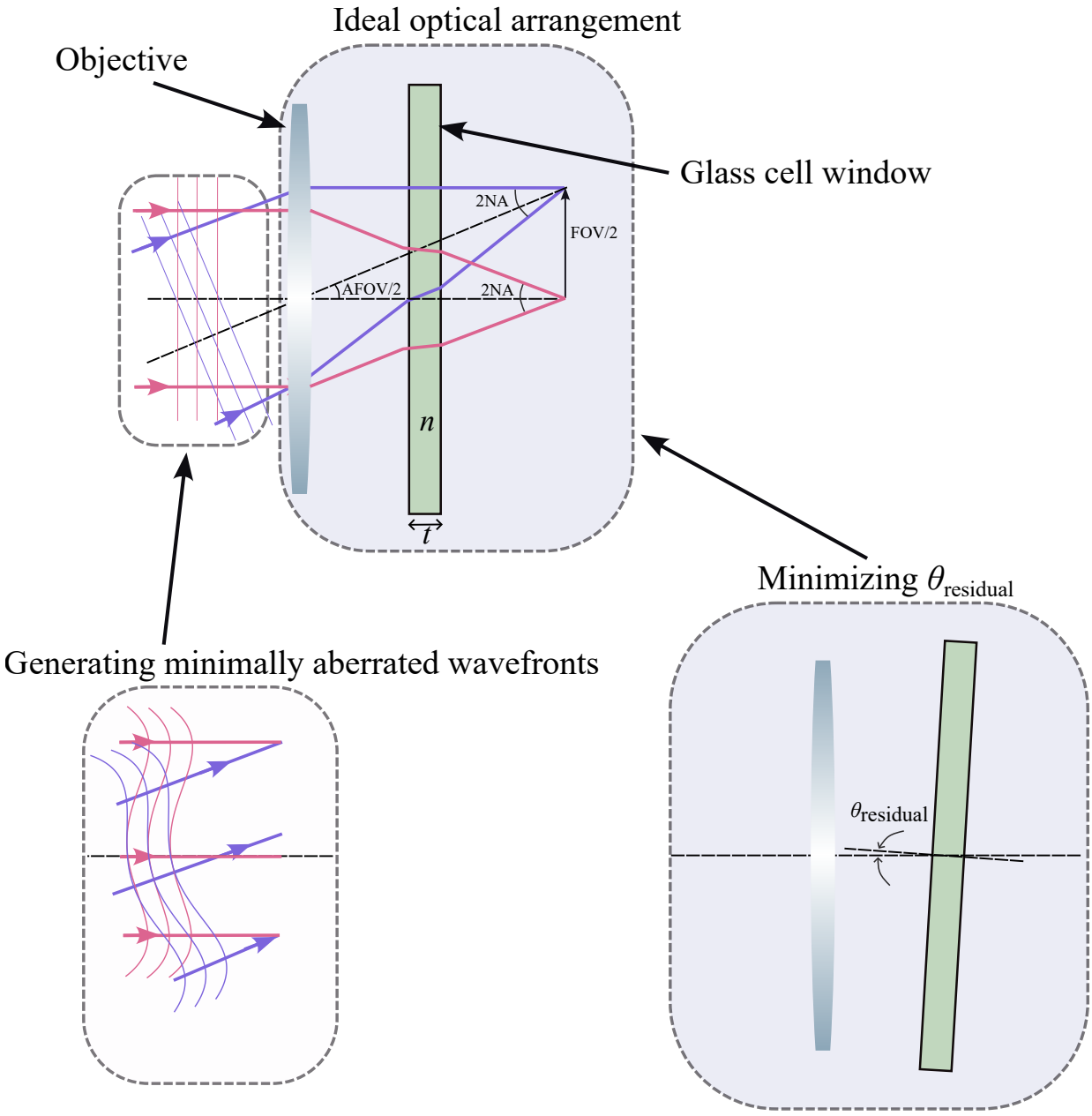

Figure 7.43: My general strategy for creating diffraction-limited optical tweezers

on how I addressed each term in Eq. 7.47.

Before I end this section, I will explore the question of what it means to be diffraction-limited by looking at the second moment width of the IPSF [159, 162], also known as the D4σ width. The IPSF is simply the image of an incoherently illuminated point source (Table 7.3). The

expression for the second moment of the IPSF is as follows:

$$\langle (x')^2 \rangle + \langle (y')^2 \rangle = \frac{\iint_{-\infty}^{+\infty} \left((x')^2 + (y')^2 \right) |h(x', y')|^2 dx' dy'}{\iint_{-\infty}^{+\infty} |h(x', y')|^2 dx' dy'}.$$

Invoking the Fourier moment theorem [159, 162], $\langle (x')^2 \rangle \propto \frac{\partial^2 \, \mathrm{OTF}(0,0)}{\partial x^2}$, one can derive the following expression for the second moment along one axis:

$$\langle (x')^2 \rangle \propto \underbrace{\iint \left(\frac{\partial P}{\partial x} \right)^2 dxdy}_{\propto (\text{Diffraction-limited spot size})^2} + \underbrace{k^2 \iint \left(P \frac{\partial W}{\partial x} \right)^2 dxdy}_{\propto (\text{RMS spot size from ray tracing data})^2}, \tag{7.48}$$

where x and y are the exit pupil coordinates (Fig. 7.42). This formulation for the second moment allows for the separation of the effects of the amplitude-only filtering effect of the pupil (first term) from the phase-only filtering effect of the wavefront aberrations (second term). The first term represents the effect of diffraction and defines the Airy disc size. The second term represents the purely geometrical effect of the wavefront aberrations, which manifests as transverse ray errors $\varepsilon_Y, \varepsilon_X$ in the image plane. (Eqs. 7.52, 7.53) [95, 96]. The RMS spot size, which is used to quantify the geometrical blur size in a spot diagram, is intimately related to these transverse ray errors $\varepsilon_Y, \varepsilon_X$ [96]. In order for a system to be considered diffraction-limited, the RMS spot size must be much smaller than the Airy disc size, which is at the heart of the golden rule of optical design.

7.6.1 Minimizing RMS $\mathrm{OPD}_{\mathrm{fabrication}}$

In my optical designs, I only used commercially available lens, mirrors, and waveplates. The surface quality of all these commercial parts was at worst 40-20 scratch-dig. The surface

flatness of the Zerodur mirrors and waveplates used in these layouts was typically $\lambda/20$ at 632.8 nm [102]. Care was taken to minimally distort the optics during mounting. For example, Delrin retaining rings (Newport LH2-T-RR) and retaining rings padded with Buna-N nitrile rubber O-rings (Thorlabs SM2LTRR, SM1LTRR; McMaster 4061T194, 4061T145) were used to secure lenses, dichroics, and plate PBS. The Zerodur mirrors were mounted in low-wavefront distortion mounts (ULTIMA low-wavefront distortion mirror mounts from Newport).

We used custom dichroics for our optical setups. To that end, Alluxa Inc. manufactured 3" OD dichroics and plate polarizing beam splitter (PPBS) for us. These parts were constructed from high-quality 5 mm thick fused silica substrates with 40-20 scratch-dig and $\sim 0.01\lambda$ RMS OPD flatness per inch. The specifications for the dichroics used in the optical layouts are in table 7.4. I carefully chose the transmission and reflection bands for the dichroics so as to be

Label	Transmits (nm)	Reflects (nm)	Surface Flatness & Scratch-Dig	OD
D1 (dichroic)	532, 830-870	399, 420, 556, 780	$\frac{\lambda}{100}$ RMS/in, 40-20	3"
D3 (dichroic)	780, 830-870	399, 420, 532, 556	$\frac{\lambda}{100}$ RMS/in, 40-20	3"
D4 (dichroic)	399	420, 556	$\frac{\lambda}{100}$ RMS/in, 40-20	3"
PPBS	532, 830-870	532, 830-870	$\frac{\lambda}{100}$ RMS/in, 40-20	3"

Table 7.4: Specifications for the custom optics from Alluxa Inc.

simultaneously cost-effective and maximize the number of the ways in which the many colors in our optical setup can be combined and separated (Fig. 6.1). D1 is the only multi-band dichroic in our setup. D3 and D4 are single-band dichroics. I preferred a PPBS over a cube polarizing beam splitter to minimize the number of surfaces, as each additional surface can add fabrication errors. Last but not least, the dichroics, waveplates, and PPBS were placed only at locations in the beam path where the beam is collimated to avoid aberrations (see Fig. 7.4).

7.6.1.1 Microscope objective

The defining characteristics of a microscope objective are its NA and FOV. However, the choice of NA and FOV for any lens (or lens assembly such as a microscope objective) is not arbitrary, although simultaneous large values for NA and FOV are desirable. In fact, NA and FOV are inversely related to each other [163]. This inverse relation originates from a very important principle in optical design called the Abbe sine condition, which can be readily derived from Fourier optics. The Abbe sine condition [164, 165] states that for off-axis and on-axis diffraction-limited performance

$$n_i r_i \sin\theta_i = n_o \text{FOV} \sin\theta_o = \text{FOV} \times \text{NA} = \text{constant}, \tag{7.49}$$

where $n_i \sin\theta_i$ is the image space NA, $n_o \sin\theta_o$ is the object space NA, and r_i is the size of the image. High NA microscope objectives are well-corrected for the offense against sine condition (OSC) over the FOV of the objective. An optical system that satisfies the Abbe sine condition conserves étendue [166] i.e. the optical throughput (denoted by the étendue G-value) between the object and image. The étendue G-value can be expressed in terms of FOV and NA as follows [163]:

$$G = \frac{\pi}{4} \text{FOV}^2 \text{NA}^2. \tag{7.50}$$

One can immediately see the relation between the Abbe sine condition and étendue G-value by squaring both sides of Eq. 7.49. The throughput of conventional microscope objectives usually lies between $G = 0.0243$ mm^2 and $G = 0.9503$ mm^2 [163]. Infographics classifying the various types of lenses as a function of their typical NA and FOV can be found in these references [95,

102]. Resources for designing microscope objectives can be found here [163, 167, 168, 169]. In our case, Special Optics designed and built two 0.6 NA infinity-corrected microscope objectives for us. The objectives have the following specifications (Fig. 7.44):

- Diffraction-limited performance at: 399 nm, 420 nm, 532 nm, 556 nm, 780 nm, 858 nm
- NA: 0.6
- Working distance: ~ 2 mm air $+ 9.5$ mm fused silica $+ 9.525$ mm vacuum
- Outer diameter (OD) and Length: < 50.8 mm, ~ 100 mm
- Aperture and Field of View (FOV): ~ 36 mm and ~ 0.2 mm
- Axial and lateral colors: < 10um
- Housing: We choose to use Ultem—a high-performance thermoplastic—so as to avoid eddy currents during magnetic field switching. The Ultem housing also provides resistance to thermally-induced alignment errors from having the magnetic field coils on for extended periods of time. Both of these features would be compromised if an Aluminum housing was chosen instead.

While the objective specifications are good, mounting the objectives turned out to be nontrivial. The mounting must be secure, long-term thermally stable, and should not introduce excess wavefront distortion. Special Optics told us to be wary of introducing aberrations during mounting. I conceived, manufactured, and interferometrically tested a few versions of the mounts before settling on a final version (Fig. 7.45). The collimated back-reflection from the mounted objective was interfered with a reference beam in the Twyman-Green-Fizeau interferometer setup

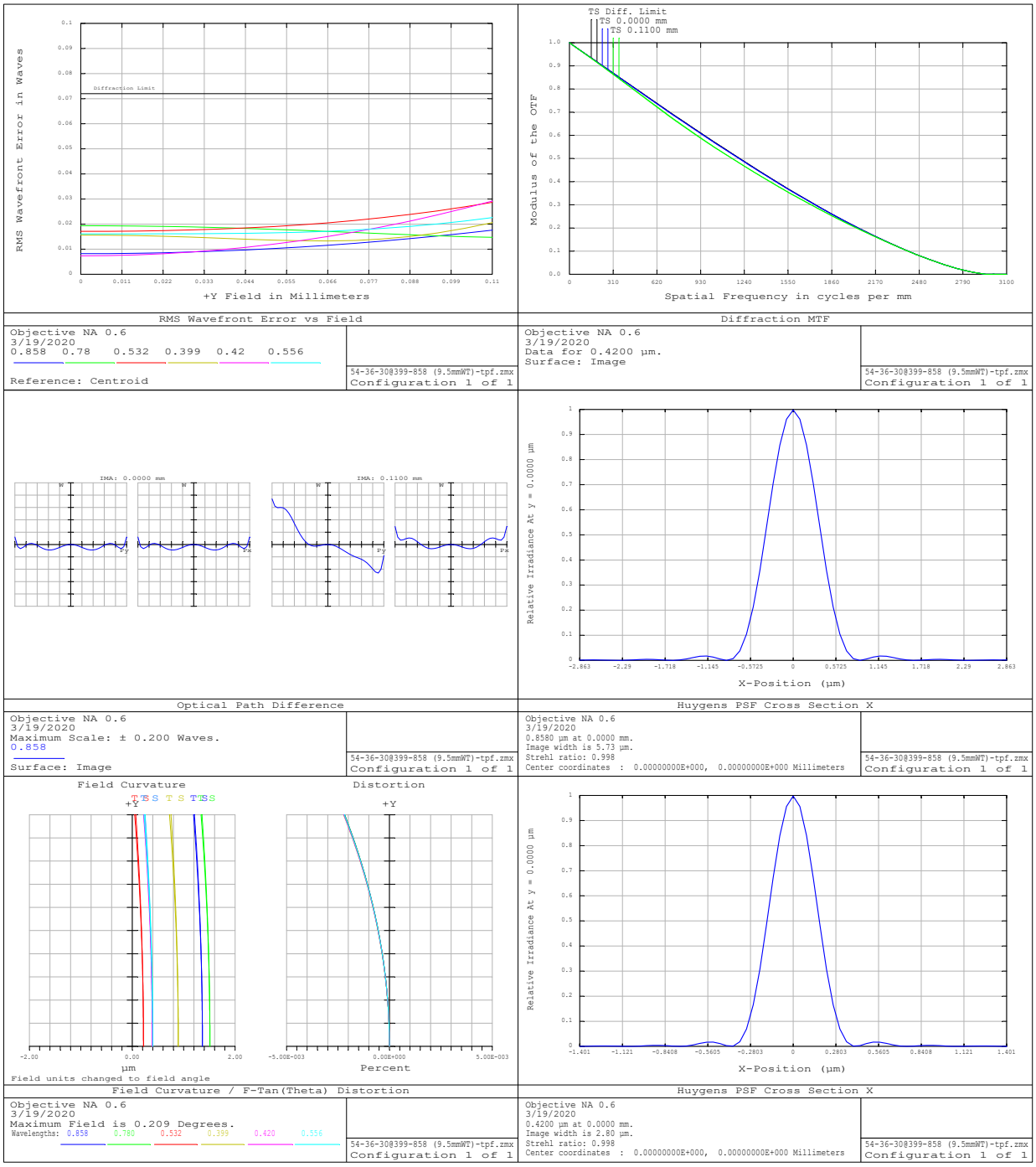

Figure 7.44: Specifications of our 0.6 NA objectives from Special Optics.

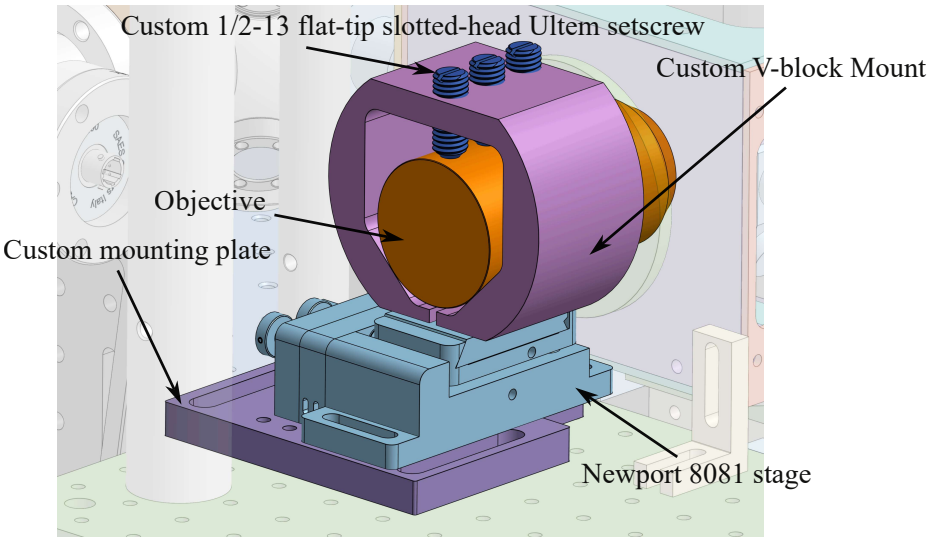

Figure 7.45: CAD design of the V block mount for the objectives

(see Sec. 7.6.3.1) for characterizing the recovery capabilities and drifts of the objective mount assemblies.

The final iteration of the mount was a V-block machined out of nonmagnetic 316 SS with a 90° angle for the V and Ultem 1/2-13 flat-tip slotted-head setscrews to secure the objective against the V-block (see Figs. G.23, G.25, G.24 and 7.45). The setscrews were tightened using a torque wrench to a torque of 0.6 lbf-in. The use of three flat-tip setscrews and the large surface area for each setcrew helps to evenly distribute the force over the objective body to minimize aberrations. Once secured, the objective was hard to remove from the V-block, but at the same time the setscrews could be unscrewed by hand. The Ultem material for the setscrews was determined interferometrically (see Sec. 7.6.3.1 and Sec. 7.2.1) by subjecting the objective V-block assembly to heat from the continuous operation of the MOT coils at currents appropriate for Rb MOT and Yb MOT. This is because debugging/recovering the highly sensitive shallow-angle MOTs (Sec. 7.7.1) requires steady-state operation of the MOT coils. The heat from the MOT coils during steady-state operation must not misalign the objectives. In its final iteration, the objective

mount assembly recovered to less than 70 μrads of tilt as measured on the Twyman-Green-Fizeau interferometer (see Sec. 7.6.3.1), when the coils were turned off after 30 mins of continuously operating the MOT coil at 12 A with air cooling of the coils applied.

The SS V-block is nonmagnetic, and has low conductivity that helps suppress eddy currents during magnetic field switching. This V-block objective assembly is mounted to a Newport 8081 stage, which is in turn mounted to a custom Aluminum base plate. As the SS V block significantly outweighs the objective, the center of mass of the V-block objective assembly is over the 8081 stage. This helps counteract the fact that the objective cantilevers quite a bit beyond the V-block. Furthermore, the 90° angle for the V improves the repeatability of the insertion and withdrawal of the objectives from the V block [170]. The importance of the angle for the V was born out of my discussions with Les Putnam. Repeated removal and reinstallation of the objective resulted in an interferometrically determined tilt alignment error of $\sim$ 70 μrad. The entrance aperture surface of the objective is flush with one vertical or end surface of the V block (Fig. 7.45). This helps in restoring the working distance between the objective and the glass cell surface to an acceptable degree upon reinstallation of the objective. In hindsight, it would have been easier to have asked the objective vendor to machine mount specific threads on the Ultem body. For example, the Newport LP-2A mount would have been an appropriate choice to mount the objective with a threaded body.

7.6.2 Minimizing RMS OPD_{design}

The design of any well-corrected optical system starts with a first-order optical layout [102]. First-order optics, Gaussian optics or paraxial optics [61, 96] is built on the first-order approximation

to Snell's law ($n \sin I = n' \sin I'$) i.e. $nI = n'I'$, where n and n' are the refractive indices of the two mediums, I and I' are the angle of incidence at the boundary between the two mediums. Gaussian optics represents the situation of perfect imaging, also known as stigmatic imaging [171].

Gaussian optics is a special case of a collinear transformation applied to a rotationally symmetric system that maps planes perpendicular to the optic axis in the object space to planes perpendicular to the optic axis in the image space without distortion [61]. In Gaussian optics, any "pencil" of lines from a single point in the object space maps to a unique "pencil" of lines directed towards a single point in the image space. The points in the object space are "conjugate" to points in the image space. A collinear transformation maps a point $P(x, y, z)$ in the object space to a point $P'(x', y', z')$ in the image space by a set of equations shown below [61] :

$$
\begin{aligned}
x' &= \frac{a_1 x + b_1 y + c_1 z + d_1}{a_0 x + b_0 y + c_0 z + d_0}, \\
y' &= \frac{a_2 x + b_2 y + c_2 z + d_2}{a_0 x + b_0 y + c_0 z + d_0}, \\
z' &= \frac{a_3 x + b_3 y + c_3 z + d_3}{a_0 x + b_0 y + c_0 z + d_0}.
\end{aligned}
$$

Collineation is very useful in determining the cardinal points and planes of a multi-element imaging system [61], which I used frequently for my first-order high-NA optical layouts. All object distances and image distances in the Gaussian and Newtonian imaging equations are referenced from these cardinal points and planes. The cardinal planes are defined by the specific transverse magnification (or lateral magnification) $m = \frac{h'}{h}$(= the image point height from the

optical axis/object point height from optical axis) as follows [96]:

$$m = \infty \rightarrow \text{Front Focal Plane (FFP)},$$

$$m = 0 \rightarrow \text{Back Focal Plane (BFP)},$$

$$m = 1 \rightarrow \text{Front Principal Plane (FPP)},$$

$$m = 1 \rightarrow \text{Back Principal Plane (BPP)}.$$

However, collineation cannot represent the imaging action of a lens (except in the case of afocal lens) as it does not take into account the equality of optical path lengths of the rays needed for stigmatic imaging. For example, for points on the optic axis, the transverse magnification according to collineation is $m \propto \tan\theta / \tan\theta'$ for ray angles θ and θ' relative to the axis in the object space and image space respectively. However, Abbe's sine condition, which considers optical path lengths, requires $m \propto \sin\theta / \sin\theta'$ [172]. The congruence exists in the afocal case and in the paraxial limit, where both magnifications reduce to $m \propto \theta/\theta'$. For desiging high-NA imaging systems, one needs to consider the higher-order terms in the expansion of the sine in Snell's law [102]:

$$\sin I = I - \underbrace{\frac{I^3}{3!}}_{\substack{\text{3rd order ray aberrations:} \\ \text{1) Spherical Aberration} \\ \text{2) Coma} \\ \text{3) Astigmatism} \\ \text{4) Petzval/Field curvature} \\ \text{5) Distortion}}} + \overbrace{\frac{I^5}{5!}}^{\text{5th order ray aberrations}} \quad \ldots \tag{7.51}$$

If the aberrations arising from higher-order terms are not corrected in an imaging system, stigmatic imaging breaks down; A point object is not mapped to a single point in the image plane via

collineation, but rather to a cluster of points around the ideal Gaussian image point. In fact, the transverse ray errors $\varepsilon_Y, \varepsilon_X$—the deviations of the ray intersections at the image plane from the ideal image point—are related to wavefront aberration $W(x, y)$ via the following relations [95, 96]:

$$\varepsilon_Y = -\frac{R}{r}\frac{\partial W(x,y)}{\partial y}, \tag{7.52}$$

$$\varepsilon_X = -\frac{R}{r}\frac{\partial W(x,y)}{\partial x}, \tag{7.53}$$

$$\frac{R}{r_P} = -\frac{1}{n'u'} \approx -\frac{1}{\mathrm{NA}}, \tag{7.54}$$

where $x = \rho\sin\theta,\ y = \rho\cos\theta$ are the normalized exit pupil coordinates, the physical pupil size is r , $0 \leq \rho \leq 1$, n' is the image space refractive index and u' is the marginal ray angle. Correcting these errors is at the heart of the third-order optical layout.

The wavefront aberration polynomial expansion picture pioneered by J.J. Hopkins is a very powerful tool. The wavefront aberrations at the exit pupil of an imaging system is a polynomial expansion [61, 173]:

$$W(\vec{H}, \vec{\rho}) = \sum_{j,m,n} W_{klm}(\vec{H}\cdot\vec{H})^j(\vec{H}\cdot\vec{\rho})^m(\vec{\rho}\cdot\vec{\rho})^n, \tag{7.55}$$

where $\vec{H}$ is the normalized field vector , $\vec{\rho}$ is the normalized aperture vector , ϕ is the cosine of the angle between the vectors, and W_{klm} are the coefficients of the aberrations in the polynomial expansion. The indices j, m, n represent integers and $k = 2j + m$ and $l = 2n + m$. The order of an aberration term is given by $2(j + m + n)$ and is always an even number. The indices k, l, m in each term represent the algebraic power of $\vec{H}$, $\vec{\rho}$, and $\cos\phi$ respectively. The aberration

coefficients, W_{klm} , can be expressed in terms of the contributions of the individual surfaces in the imaging system via the Seidel aberration coefficients (S_I,S_{II}, S_{III}, S_{IV},S_V). The goal is to minimize the aberration coefficients.

The Seidel aberration coefficients that encapsulate surface contributions (Seidel sums) can be evaluated using only first-order ray invariants determined from ray tracing data in an optical design software like Zemax (see Table 7.5). It is quite amazing how primary wavefront aberration coefficients can be calculated using just first-order ray quantities [61, 164].

Aberration	Term	Seidel aberration coefficients	Seidel sums
0^{th} Order			
Uniform piston	W_{000}	-	-
2^{nd}order			
Quadratic piston	$W_{200}H^2$	-	-
Tip/tilt	$W_{111}H\rho\cos(\phi)$	-	-
Focus	$W_{020}\rho^2$	-	-
4^{th}order			
Spherical aberration	$W_{040}\rho^4$	$W_{040} = \frac{1}{8}S_I$	$S_I = -\sum_{i=1}^{j}\left(A^2y\Delta\left(\frac{u}{n}\right)\right)_i$
Coma	$W_{131}H\rho^3\cos(\phi)$	$W_{131} = \frac{1}{2}S_{II}$	$S_{II} = -\sum_{i=1}^{j}\left(A\bar{A}y\Delta\left(\frac{u}{n}\right)\right)_i$
Astigmatism	$W_{222}H^2\rho^2\cos^2(\phi)$	$W_{222} = \frac{1}{2}S_{III}$	$S_{III} = -\sum_{i=1}^{j}\left(\bar{A}^2y\Delta\left(\frac{u}{n}\right)\right)_i$
Field curvature	$W_{220}H^2\rho^2$	$W_{220} = \frac{1}{4}\left(S_{IV} + S_{III}\right)$	$S_{IV} = -\text{Ж}^2\sum_{i=1}^{j}P_i$
Distortion	$W_{311}H^3\rho\cos(\phi)$	$W_{311} = \frac{1}{2}S_V$	$S_V = -\sum_{i=1}^{j}\left(\frac{\bar{A}}{A}\left[\text{Ж}^2P + \bar{A}^2y\Delta\left(\frac{u}{n}\right)\right]\right)_i$
Quartic piston	$W_{400}H^4$	-	-

Refraction invariant for the marginal ray	$A = ni = nu + nyc$
Refraction invariant for the chief ray	$\bar{A} = n\bar{i} = n\bar{u} + n\bar{y}c$
Lagrange invariant	$\text{Ж} = n\bar{u}y - nu\bar{y} = \bar{A}y - A\bar{y}$
Surface curvature	$c = \frac{1}{r}$
Petzval sum	$P = c\Delta\left(\frac{1}{n}\right)$

Table 7.5: Wavefront aberration polynomial coefficients expressed in terms of Seidel sums [1]

The Seidel sums of an optical system (see Table 7.5) do not intuitively inform optical design. To do that, one needs to factor out the structural aberration coefficients (σ_I,σ_{II}, σ_{III}, σ_{IV},σ_V) from the Seidel aberration coefficients (S_I,S_{II}, S_{III}, S_{IV},S_V) [61]. The Seidel coefficients of a component depend on its structural coefficients. For example, for a thin lens, these structural coefficients encapsulate its structural characteristics such as the shape factor, the conjugate / orientation factor, the refractive index of the lens material [61]. The reader is referred to the following reference for more details [174].

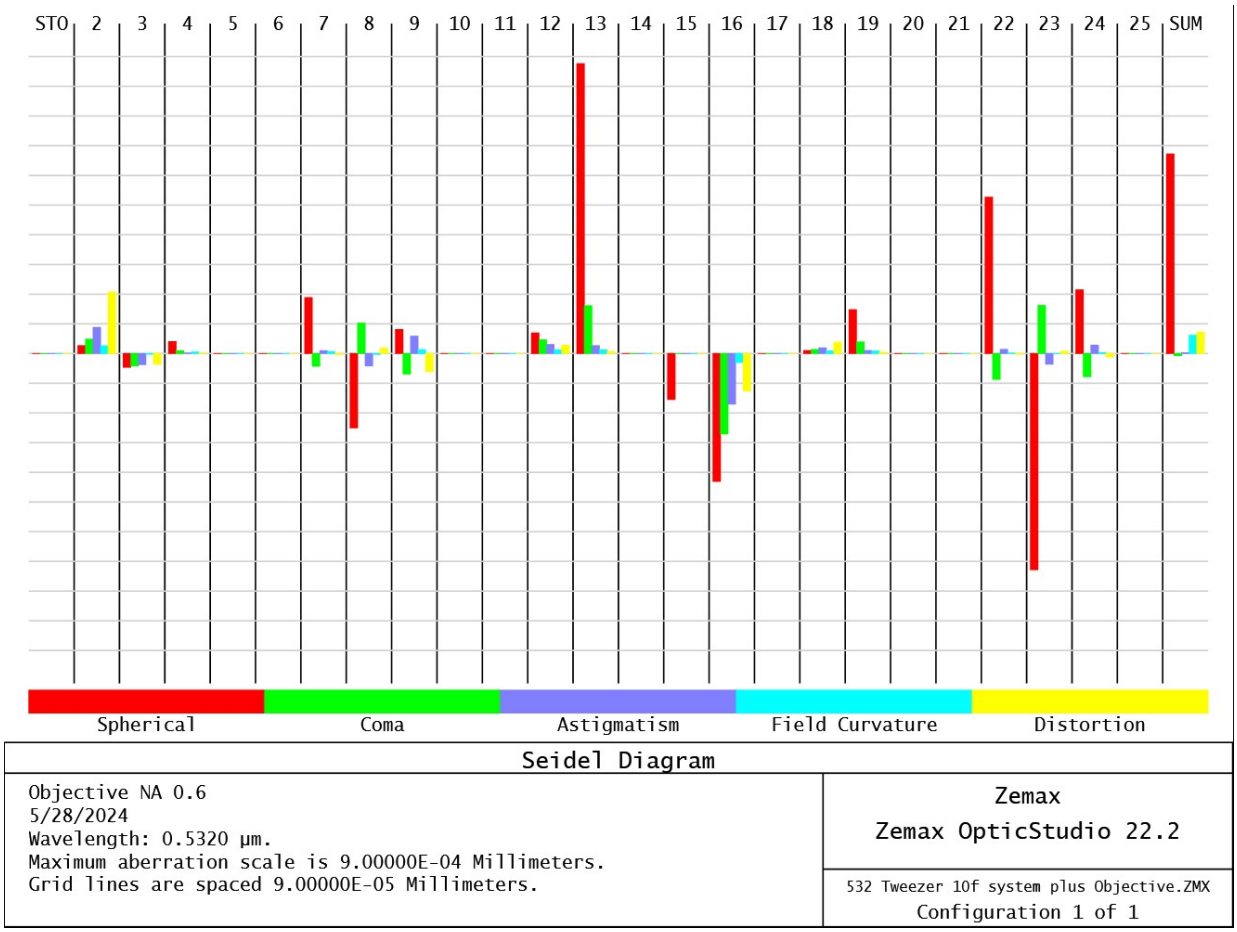

Figure 7.46: Seidel diagram for the AOD-based tweezer projection system up to the entrance aperture of the objective for Yb

One can immediately draw some insights from expressing the total Seidel surface contributions in terms of structural aberration coefficients of the components of the system [174]. I used these

insights to design my optical layouts, which are stated as follows:

- Try to always work with as low a lens power as possible [102].
- Split a high power lens into multiple low power lenses.
- Add negative lenses to counteract aberrations from positive lenses.
- Compound lenses into a doublet or a triplet.
- Play with the shape factor and the conjugate factor of the lenses. Sometimes, flipping the lens orientation can lead to lower total aberrations.
- Balancing of aberrations through the σ_W^2 in the expression for the Strehl ratio (Eq. 7.46): even aberrations like spherical aberration and astigmatism can be balanced with defocus; the odd aberrations like coma and distortion can be balanced with tip/tilt for a given field point.

The above design principles are by no means exhaustive. For a more exhaustive list, check out the following references [95, 159]. I routinely used the Seidel diagram feature on Zemax to optimize my third-order optical layouts. As an example, I show the Seidel diagram for the AOD-based tweezer projection system up to the entrance aperture of the objective for Yb in Fig. 7.46. The Seidel diagram shows the Seidel aberration coefficients of each surface and the Seidel sum.

7.6.2.1 First-order optical layout

All optimized third-order optical layouts start with a first-order optical layout. Here, I will only treat the optical layout for the AOD-based tweezer projection system (Fig. 7.47). The SLM-based tweezer projection system is very similar to the AOD-based tweezer projection system.

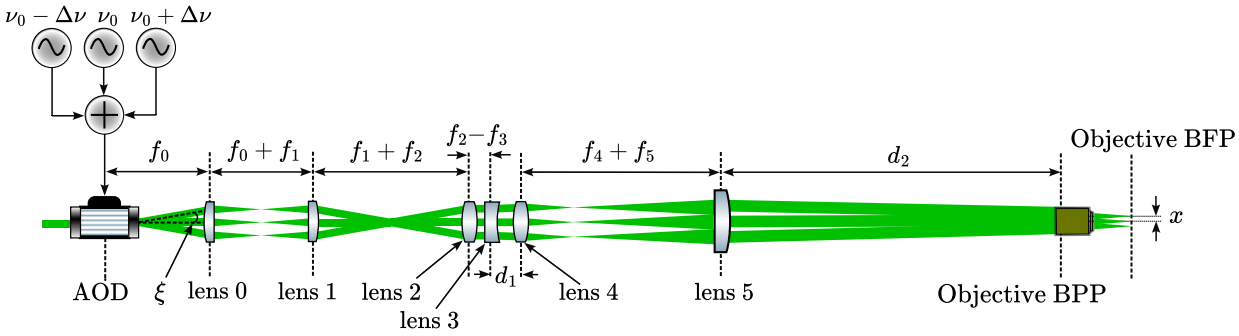

Figure 7.47: Schematic of the optical layout for the AOD-based tweezer projection system. The AOD is driven by a sum of three single tone sinusoidal waveforms, as an example. The optical layout for the SLM-based tweezer projection system is the same except it lacks the first $4f$ Keplerian f_1/f_0 magnification stage.

For the sake of simplicity, I will consider only one AOD axis as the optical system is symmetric about the optic axis.

Arbitrary motion of a tweezer in the back focal plane of the objective is facilitated by the radio-frequency (rf) waveform driving the AOD [83]. When the AOD is driven by a single-tone rf waveform at frequency ν, it deflects the beam by an angle ξ that is mapped to a tweezer position x by the optical system (Fig. 7.47). ξ and x are measured with respect to the optic axis of the tweezer projection system, which is defined by a single-tone rf waveform at frequency ν_0 driving the AOD (Fig. 7.47).

The ABCD matrix for the AOD-based tweezer projection system from the AOD plane to the objective BFP (Fig. 7.47) is

$$\mathrm{ABCD}_{\mathrm{tweezer}} = \begin{pmatrix} 0 & \frac{f_0 f_2 f_4 f_{\mathrm{objective}}}{f_1 f_3 f_5} \\ -\frac{f_1 f_3 f_5}{f_0 f_2 f_4 f_{\mathrm{objective}}} & \frac{f_0 f_2 \left(-d_2 f_4^2 - (d_1+f_3) f_5^2 + f_4 f_5^2 + f_4^2 \left(f_5 + f_{\mathrm{objective}}\right)\right)}{f_1 f_3 f_4 f_5 f_{\mathrm{objective}}} \end{pmatrix}, \tag{7.56}$$

where $f_{\mathrm{objective}}$ is the focal length of the objective. Setting the only on-diagonal component of this

ABCD matrix to 0 yields the following expression for d_2 as a function of d_1:

$$d_2 = f_5 \left(1 - \frac{f_5 f_3}{f_4^2} + \frac{f_5}{f_4}\right) - \frac{f_5^2}{f_4^2} d_1 + f_{\text{objective}}\,, \tag{7.57}$$

with a maximum value of

$$d_{2,\text{max}} = f_5 \left(1 - \frac{f_5 f_3}{f_4^2} + \frac{f_5}{f_4}\right) + f_{\text{objective}}\,. \tag{7.58}$$

With the on-diagonal term set to 0, this optical system facilitates the angle-to-position mapping expressed mathematically as follows:

$$x = \frac{f_{\text{objective}}}{M}\,\xi \tag{7.59}$$

where $M = (f_1 f_3 f_5)/(f_0 f_2 f_4)$ is the total magnification of the AOD-based tweezer projection system. The magnification should be chosen appropriately as Gaussian beams are used as input to the tweezer projection systems. This magnification determines the degree of truncation of the Gaussian beam by the entrance aperture of the objective given an input beam size to the tweezer projection system. The smallest spot size at the objective BFP is achieved when a plane wave is incident on the aperture of the objective, which implies an infinite magnification. This is obviously power-inefficient. Underfilling the entrance aperture of the objective leads to larger spot sizes. One thing to note is that Gaussian apodization broadens the central Airy disc, but reduces the power in the secondary rings. More details on the effect of Gaussian apodization on the PSF and the OTF can be found in Ref. [160].

I conceived of this atypical first-order layout because of its ability to implement a perfect

angle-to-position mapping. In a conventional $2nf$ ($2f$, $4f$, $6f$...) imaging system, the location of each lens is strictly defined by its focal length. For instance, in a $2f$ or a $6f$ imaging system that maps angle to position, deviations from these defined spacings lead to an imperfect angle-to-position mapping through the introduction of a non-zero angle-to-angle mapping. This angle-to-angle mapping has the same effect as θ_{residual} in Fig. 7.43 and Fig. 7.4, and can therefore decrease the FOV of the objective. This can happen, for example, when the objective is not $f_{\text{objective}} + f_{\text{last lens}}$ away from the last lens in a $2nf$ imaging system due to space constraints in the experiment. My design gets around these issues. By tuning d_1, the spacing d_2 between the last lens and the objective can be continuously adjusted to implement a perfect angle-to-position mapping (Eq. 7.57).

Another important feature of this layout is that lens 3 is negative and can therefore counteract aberrations from the positive lenses in the tweezer projection system. This cannot be easily done in a $2nf$ imaging system as the lenses are all positive. Lens 3 in my optical layout can also be positive and would yield a larger dynamic range for d_2. However, the system size would be larger and the aberrations from the positive lenses cannot be easily counteracted. As a comment, the combination of lens 2, lens 3, and lens 4 has the structure of a Cooke triplet anastigmat lens [164] with tunable power.

As we only control the frequency of the single-tone sinusoidal waveform (ν) driving the AOD (Fig. 7.47), it makes sense to derive an equation that maps ν to x. The relationship between ξ and ν in the Bragg regime is [175, 176]

$$\xi = \frac{\lambda(\nu - \nu_0)}{v_{\text{rf}}},$$

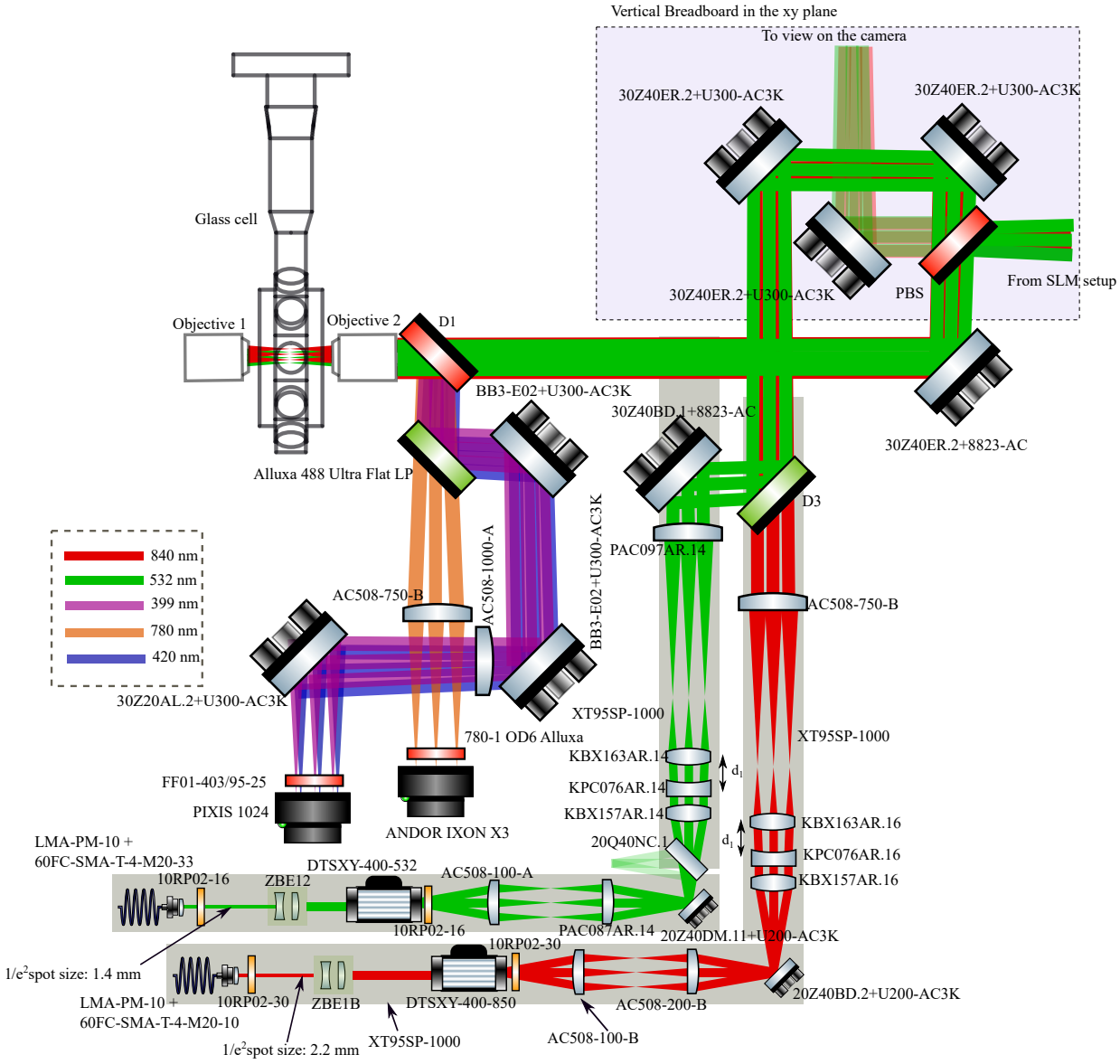

Figure 7.48: Schematic of the optical layout for the AOD-based tweezer projection systems.

where v_{rf} is the velocity of sound in the AOD crystal, λ is the wavelength of light in the AOD crystal. Substituting this expression for ξ in Eq. 7.59, one can get the following important mapping between x and ν [176]:

$$x = \frac{\lambda f_0}{M v_{\mathrm{rf}}}(\nu - \nu_0). \tag{7.60}$$

For our AOD-based tweezer projection systems with $M = 6.85$, $v_{\mathrm{rf}} = 650$ m/s, $f_0 = 30$ mm,

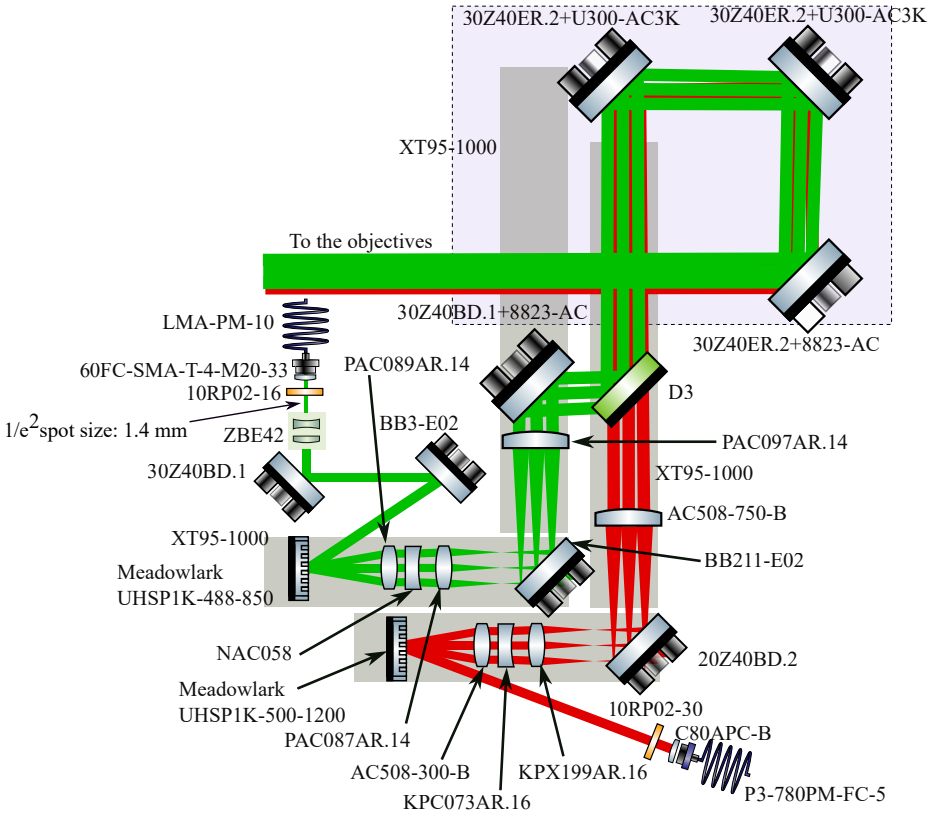

Figure 7.49: Schematic of the optical layout for the SLM-based tweezer projection systems.

a change in the frequency of the single tone rf drive by $\Delta\nu = 1$ MHz maps to a change in the position of the 532 nm (840 nm) tweezers Δx by 3.6 μm (5.7 μm) at the objective BFP.

The complete optical layout for the AOD-based tweezer projection system and the SLM-based tweezer projection system can be found in Fig. 7.48 and Fig. 7.49. The major difference in the optical layout for the SLM-based tweezer projection system and the AOD-based tweezer projection system is the lack of the first $4f$ Keplerian magnification stage (no lens 0 and lens 1 in Fig. 7.47) in the SLM layout. The SLM is placed f_2 away from lens 2 (see Figs. 7.47 and 7.49). The magnification of the SLM-based tweezer projection system is 1.875. In the AOD-based tweezer projection systems, we use DTSXY-400 from AAoptoelectronics as our AODs. In the SLM-based tweezer projection systems, we use ultra-high-speed SLMs from Meadowlark (see Table 7.6).

7.6.2.2 Third-order optical layout

The Zemax simulations of the optimized third-order layouts for the AOD- and SLM-based tweezer projection systems are presented in Figs. 7.50, 7.51, 7.52, 7.53. The maximum field angle [164, 177] ξ_{max} for the tweezer projection systems is (using Eq. 7.59)

$$\xi_{\text{max}} = \pm M \frac{\text{FOV}}{2 f_{\text{objective}}} = \pm M \frac{0.1 \text{ mm}}{30 \text{ mm}}, \tag{7.61}$$

where ξ_{max} is $\pm 1.31^\circ$ for the AOD-based tweezer projection system, and ξ_{max} is $\pm 0.36^\circ$ for the SLM-based tweezer projection system. I designed the tweezer projection systems to accommodate larger field angles: $\pm 1.5^\circ$ for the AOD-based tweezer projection systems and $\pm 0.4^\circ$ for the SLM-based tweezer projection systems. In other words, I built some overhead into the tweezer projection systems as aberrations grow polynomially with the field size/angle [164].

The tweezer projection systems are designed to be diffraction-limited over their entire range of field angles. I confirm this by looking at the spot diagrams and ensuring that the golden rule of optical design is satisfied. I also look at the wavefront map and ensure that RMS OPD $< 0.071\lambda$. Figs. 7.50a, 7.51a, 7.52a, 7.53a show the wavefront maps for a field angle of 0° for the AOD- and SLM-based tweezer projection systems. Figs.7.50b, 7.51b, 7.52b, 7.53b show the wavefront maps for the maximum field angles of the AOD- and SLM-based tweezer projection systems. Figs.7.50c, 7.51c, 7.52c, 7.53c show the spot diagrams for the AOD- and SLM-based tweezer projection systems.

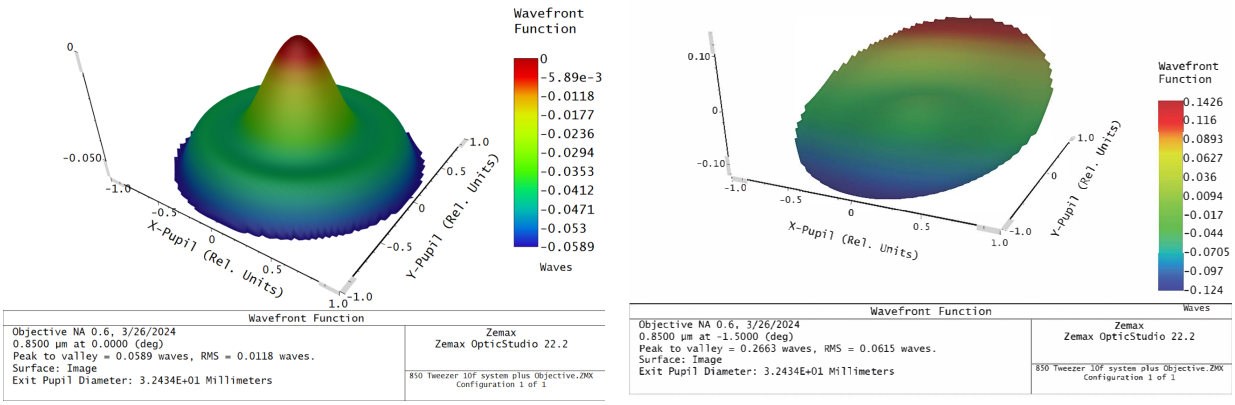

(a) (b)

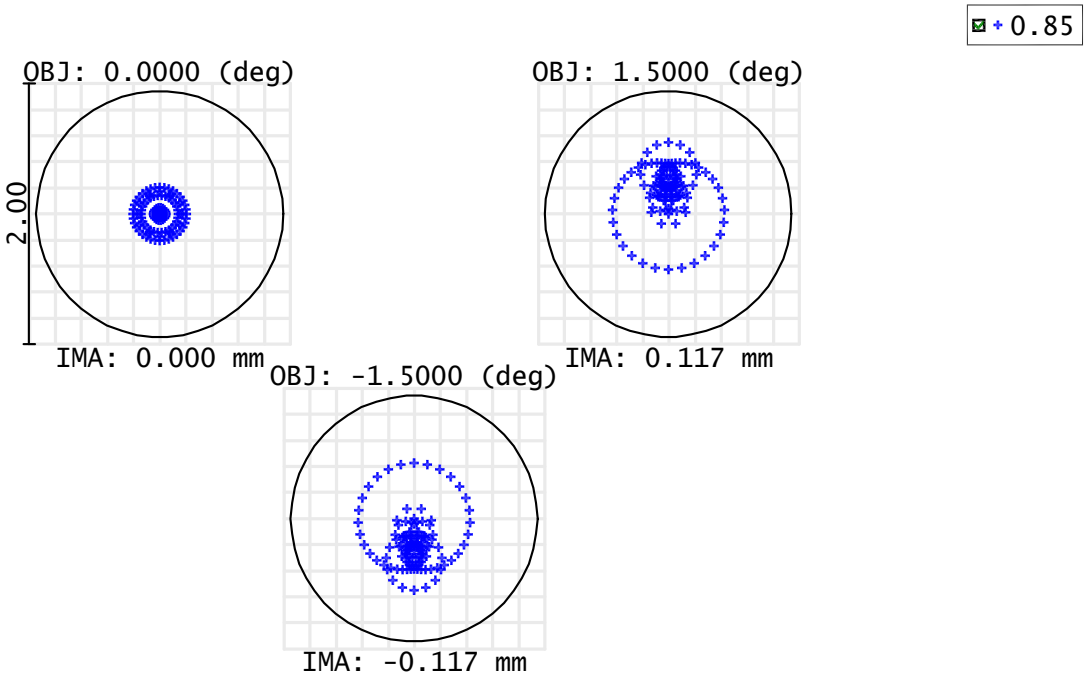

Surface: IMA

Spot Diagram	
Objective NA 0.6, 5/28/2024 Units are µm. Airy Radius: 0.9451 µm. Legend items refer to Wavelengths Field : 1 2 3 RMS radius : 0.146 0.314 0.314 GEO radius : 0.204 0.551 0.551 Scale bar : 2 Reference : Chief Ray	Zemax Zemax OpticStudio 22.2 850 Tweezer 10f system plus Objective.zmx Configuration 1 of 1

(c)

Figure 7.50: Zemax simulation of the optimized third-order layout for the AOD-based tweezer projection system for Rb: (a) Wavefront map at field angle of $0°$ (b) Wavefront map at the maximum field angle of $-1.5°$ (c) Spot diagrams at different field angles

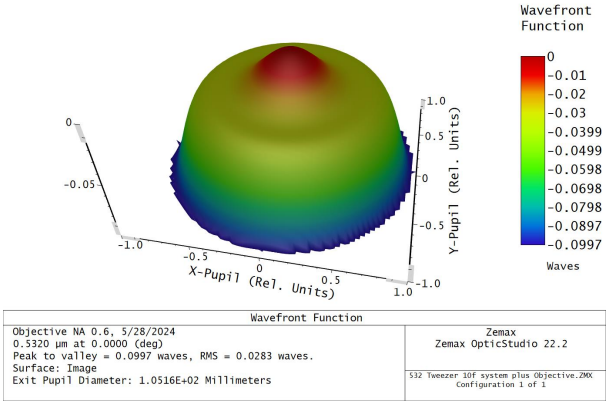

(a)

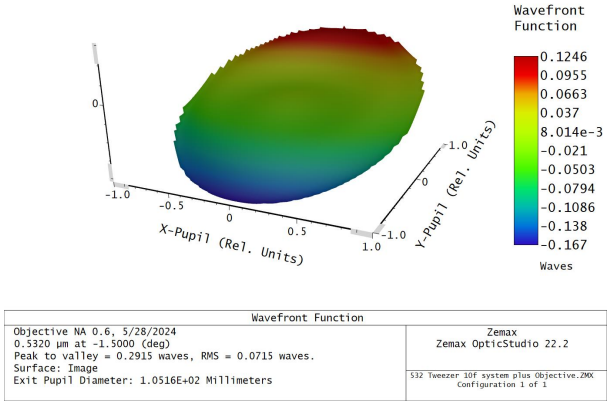

(b)

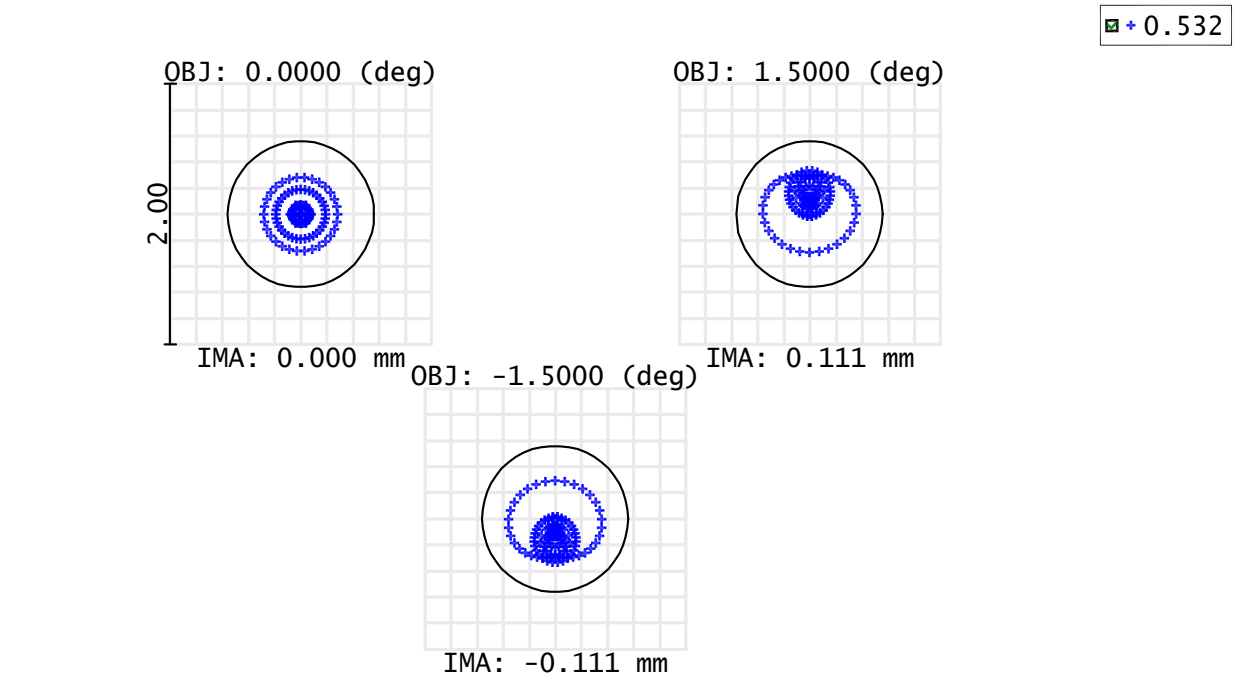

(c)

Figure 7.51: Zemax simulation of the optimized third-order layout for the AOD-based tweezer projection system for Yb: (a) Wavefront map at field angle of 0° (b) Wavefront map at the maximum field angle of -1.5° (c) Spot diagrams at different field angles

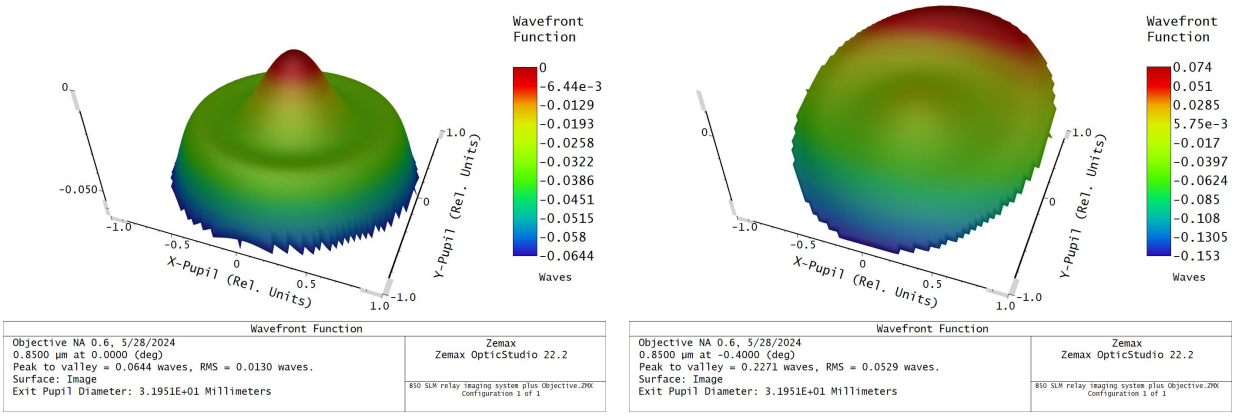

(a)

(b)

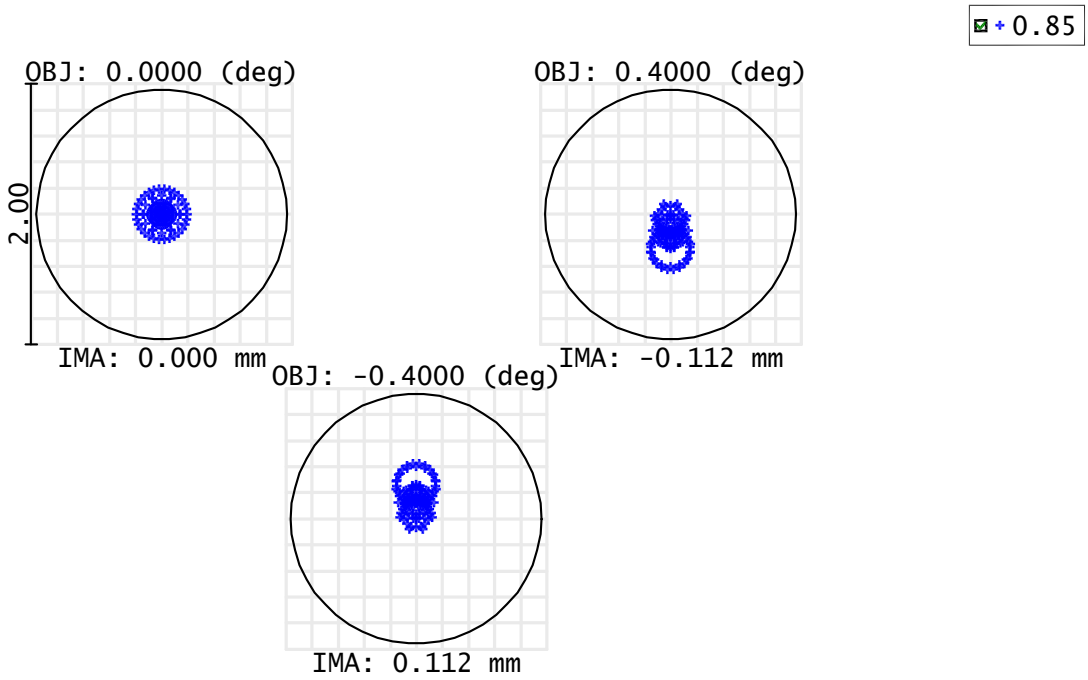

Surface: IMA

Spot Diagram	
Objective NA 0.6, 5/28/2024 Units are µm. Airy Radius: 0.9592 µm. Legend items refer to Wavelengths Field : 1 2 3 RMS radius : 0.118 0.209 0.209 GEO radius : 0.194 0.424 0.424 Scale bar : 2 Reference : Chief Ray	Zemax Zemax OpticStudio 22.2 850 SLM relay imaging system plus Objective.ZMX Configuration 1 of 1

(c)

Figure 7.52: Zemax simulation of the optimized third-order layout for the SLM-based tweezer projection system for Rb: (a) Wavefront map at field angle of 0° (b) Wavefront map at the maximum field angle of -0.4° (c) Spot diagrams at different field angles

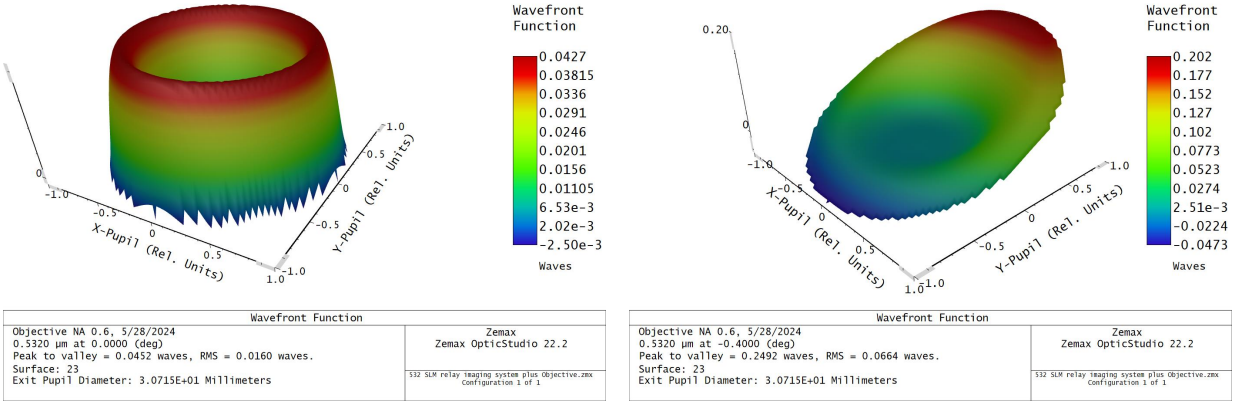

(a)

(b)

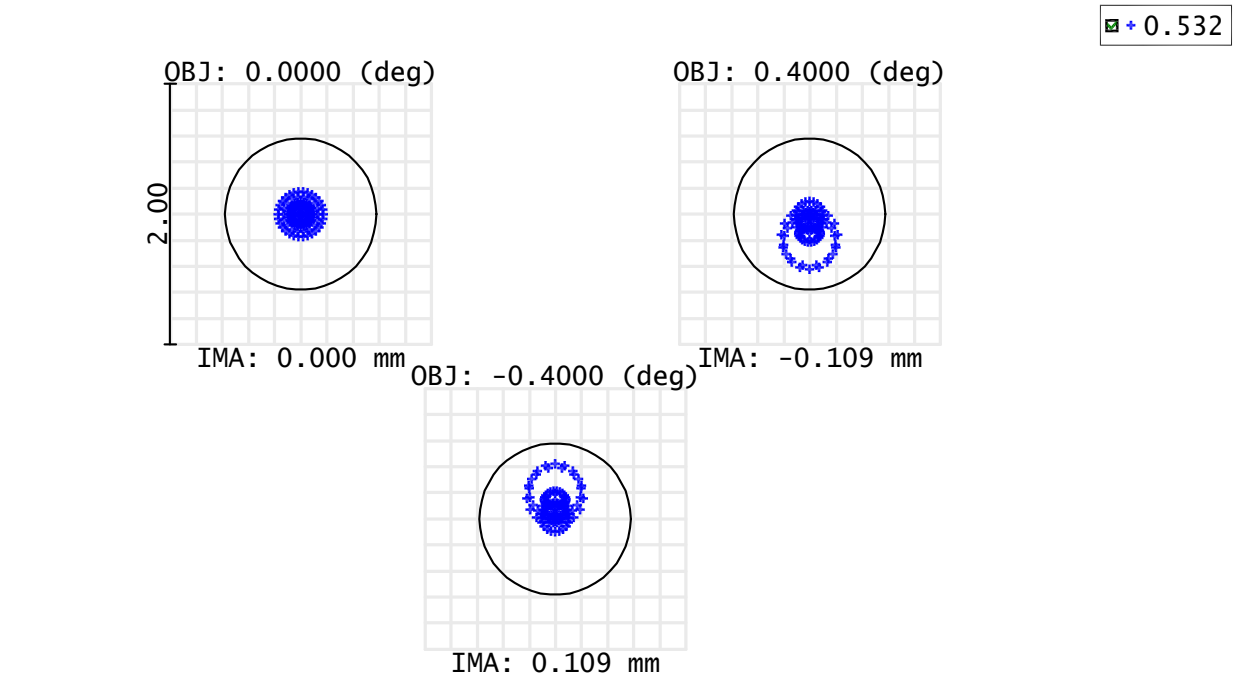

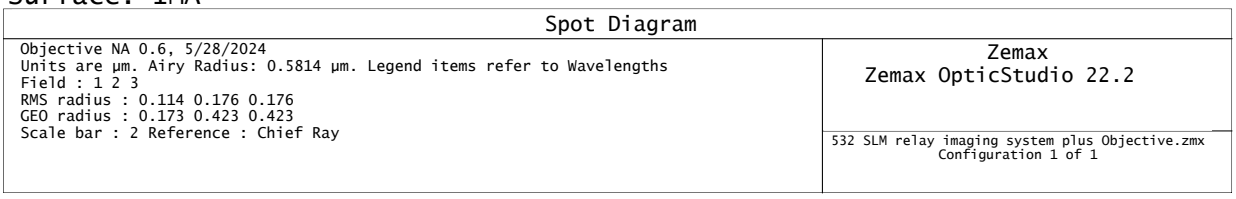

(c)

Figure 7.53: Zemax simulation of the optimized third-order layout for the SLM-based tweezer projection system for Yb: (a) Wavefront map at field angle of 0° (b) Wavefront map at the maximum field angle of -0.4° (c) Spot diagrams at different field angles

SLM Part number	Design wavelength	Liquid Crystal Response Time (10-90%):
UHSP1K-488-850	532 nm	≤ 0.6 ms
UHSP1K-500-1200	840 nm	≤ 1.2 ms

Table 7.6: Specifications of the spatial light modulators (SLM) from Meadowlark. The format for these SLMs is 1024×1024, the pixel pitch is 17.0μm$\times 17.0\mu$m, fill factor is 97.2 %

7.6.2.3 Remarks on the AODs and SLMs

When Kevin and I were playing with the AODs, we noticed a few things. First, the butterfly/floral pattern around the beam spots in the AOD diffraction pattern in Fig. 7.54a is normal. Our DTSXY-400 AOD vendor, AA-optoelectronics, told us that this diffraction pattern arises due to the low acoustic velocity in an anisotropic medium. We measured its effect on the beam profile: Fig. 7.54b is the beam profile of the input beam to the AOD, and Fig. 7.54c is the beam profile of the diffracted beam. Another thing to note is that the AOD crystals are typically cut such that the diffracted first-order light is collinear with the input beam to the AOD. The crystal is cut at an angle with respect to the input laser beam/optic axis. This implies that the undiffracted beam exiting the AOD is not collinear with the input beam to the AOD as it must refract at the angled-cut surface due to a large non-zero angle of incidence at this surface. However, the diffracted beam makes a small angle (i.e. is approximately orthogonal) with respect to the angled-cut surface. This is very convenient for axially symmetric optical systems as the diffracted light is approximately collinear with the optical axis without the need for any folding mirrors. This angled cut should not be confused with a different angled cut on the crystal that prevents standing acoustic waves. This cut is at an angle with respect to the piezoelectric transducer axis.

Regarding SLM-based tweezer projection systems, I suggested using ultrahigh-speed SLMs

i.e. SLMs with frame refresh rates in the few kHz range [178]. Typical SLMs have a refresh rate of 60 Hz or 120 Hz. Given these slow refresh rates, SLMs are used to generate the static background lattice into which the atoms are stochastically loaded. The AOD generated tweezers are then used to pick and place the single atoms in the stochastically loaded background lattice to create a defect-free array [39].

Using an SLM with a faster update rate may allow for a shorter rearrangement time. Many atoms in the background lattice may be moved simultaneously by updating the phase hologram on the SLM. This high-speed hologram update strategy can be paired with the pick-and-place strategy to shorten the rearrangement time. We procured two ultrahigh-speed SLMs from Meadowlark, one for 532 nm and the other for 840 nm. The specifications for these SLMs can be found in Table 7.6.

7.6.3 Minimizing RMS $\text{OPD}_{\text{alignment}}$

After minimizing the RMS $\text{OPD}_{\text{fabrication}}$ and RMS $\text{OPD}_{\text{design}}$ to the best of our abilities, we need to assemble the optical systems. During assembly, care must be taken to minimize RMS $\text{OPD}_{\text{alignment}}$ i.e. minimize alignment-induced aberrations. These aberrations arise from alignment errors like decentration, defocus/despace, and tip/tilt between the constituting elements of the optical system [102]. Diffraction-limited performance from the optical systems can only be ensured if these alignment-induced aberrations are low [102]. For example, θ_{residual}—the tilt between the glass cell and the objective—should be less than 0.02° for diffraction-limited performance from the objectives. In the following sections, I will elaborate on the techniques for aligning:

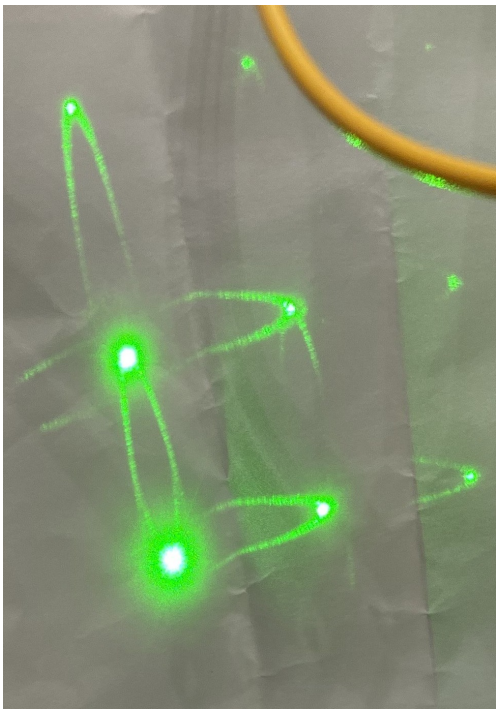

(a)

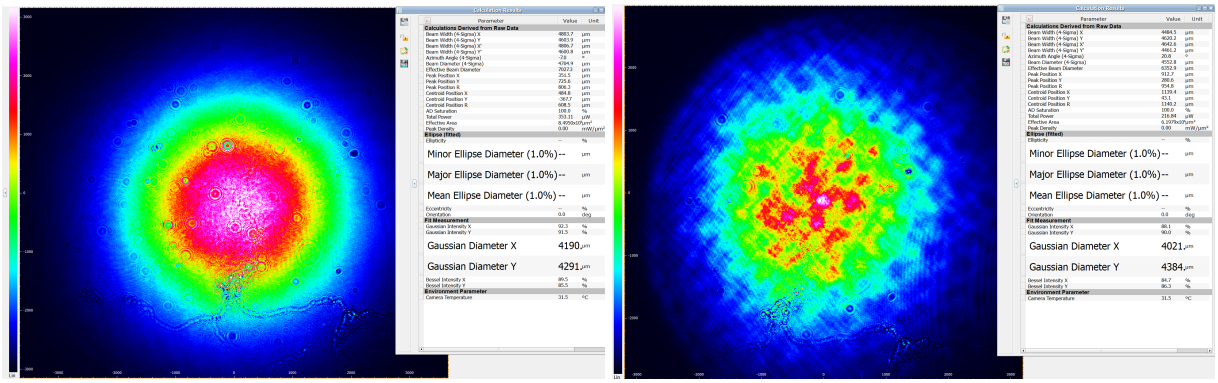

(b) (c)

Figure 7.54: (a) AOD diffraction pattern (b) Beam profile of the input beam to the AOD (c) Beam profile of the diffracted beam at the output of the AOD

1. The high NA objectives,

2. The imaging system,

3. The AOD-based tweezer projection systems,

4. The SLM-based tweezer projection systems.

7.6.3.1 Interferometric alignment of high NA objectives

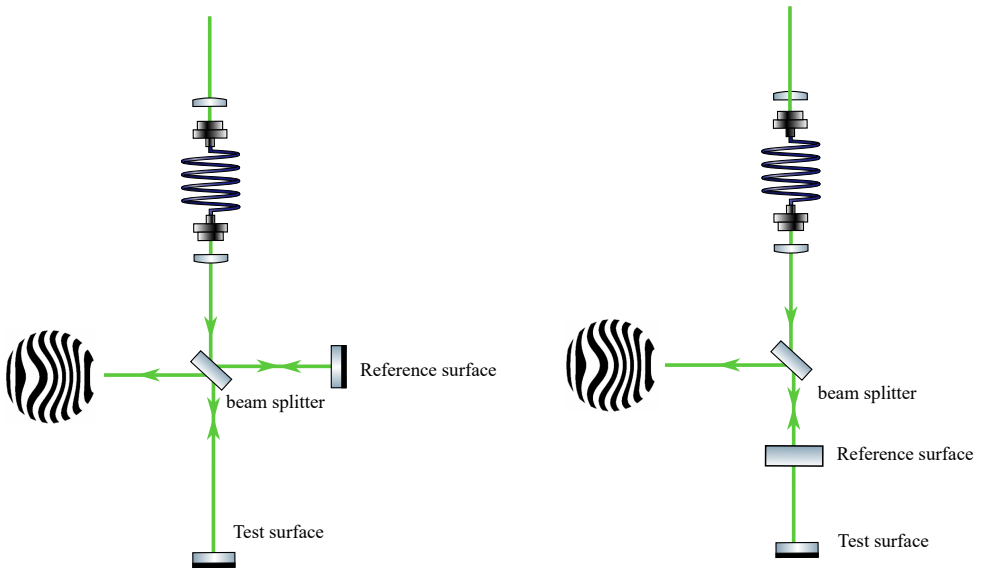

Twyman-Green interferometer Fizeau interferometer

Figure 7.55: Schematic of the optical layouts for the Twyman-Green interferometer and the Fizeau interferometers

I conceived and implemented an interferometric technique to align our two high NA objectives. I blended two amplitude-division interferometers—the Twyman-Green interferometer and the Fizeau interferometer—into an interferometer that I will name the Twyman-Green-Fizeau interferometer. The Twyman-Green interferometer and the Fizeau interferometer are typically used for testing the quality of the optics including microscope objectives [179, 180, 181, 182]. Schematics of the typical optical layouts for the Twyman-Green and the Fizeau interferometers are shown in Fig. 7.55. The interferogram at the exit port of the interferometers is used to determine the quality of the optics [183].

In the Fizeau interferometer—a type of common path interferometer [180]—the beamsplitter surface and the reference surface are one and the same, while these surfaces are separated in the Twyman-Green interferometer, which makes the latter more versatile. However, this versatility

comes at the cost of necessitating high quality optics [184, 185]. Fringe visibility in the interferogram is maximum when the reference beam and the beam returning from the test surface have a similar irradiance. The reflectivity of the reference (and beamsplitter) surface in the Fizeau interferometer is 4%, which is typical of Fresnel reflections. Therefore, a Fizeau interferometer is not well-suited for testing highly reflective optics. The Twyman-Green interferometer, on the other hand, is ideal for testing highly reflective optics.

The full Twyman-Green-Fizeau interferometer layout is shown in Fig. 7.56. One arm of the interferometer, which I refer to as the long arm, hosts the glass cell and the two objectives in a $1\times$ Keplerian telescope arrangement. The other interferometer arm, which I refer to as the short arm, provides the flat reference wavefront. By inspecting the interferograms at the exit port of the interferometer, we are able to determine the quality of the optics and the alignment precision of the various elements in the interferometer.

The alignment procedure makes use of the fact that in a system that is symmetric about the stop (i.e satisfies stop symmetry), the odd wavefront aberrations (such as coma) cancel out, whereas the even wavefront aberrations (such as spherical aberration and astigmatism) double in magnitude when light traverses the system [95]. The two well-corrected objectives in a $1\times$ Keplerian telescope arrangement form an afocal system and must be placed symmetrically on each side of the glass cell. The center of the glass cell is the position of the hypothetical stop and should coincide with the focal plane of each well-corrected objective. Therefore, by minimizing the coma [95, 186] in the interferogram measured at the exit port, optimal alignment can be achieved.

In order to observe interferograms with high fringe visibility, the interfering beams must be spatially coherent [179]. Therefore, the light source must approximate a point source. Hence, I

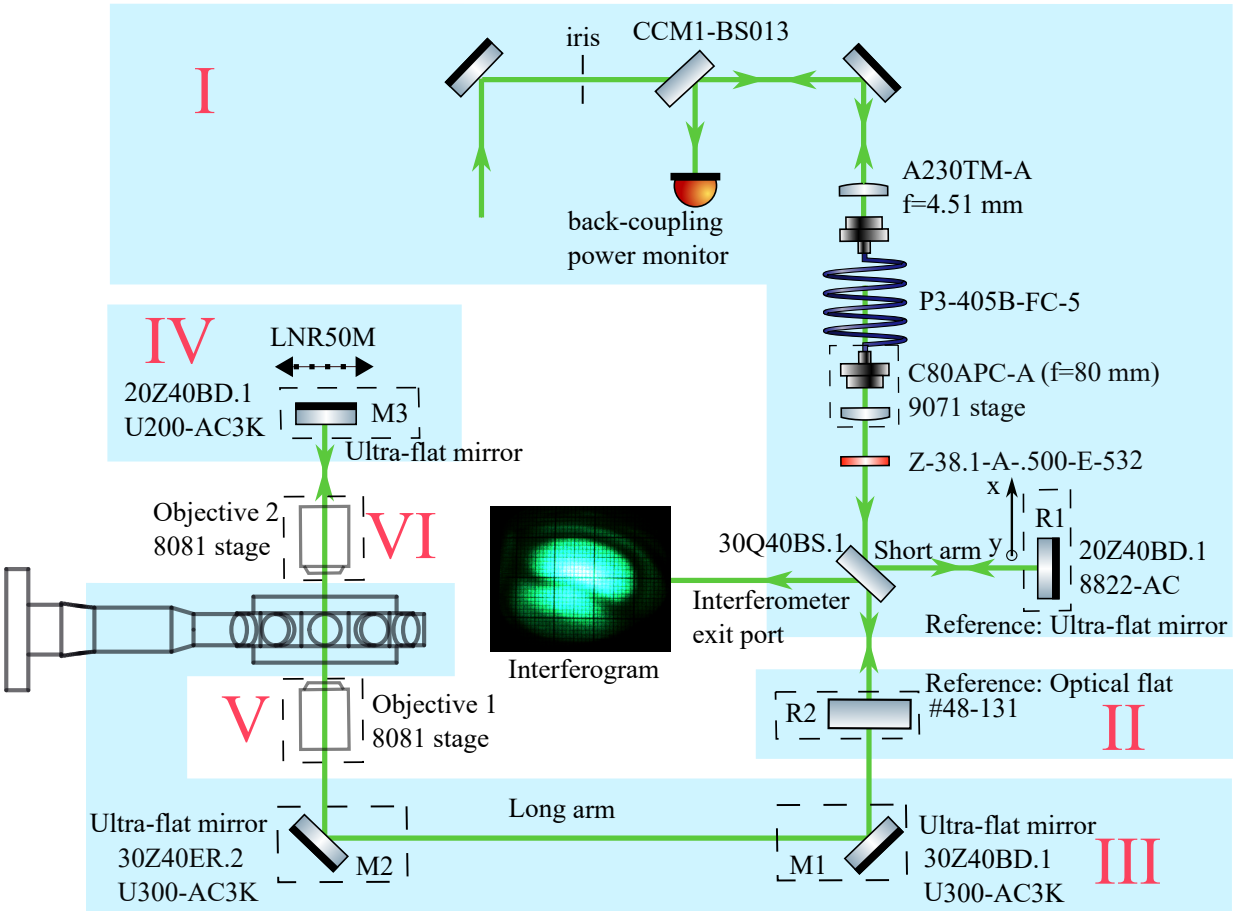

Figure 7.56: The schematic of the optical layout for the Twyman-Green-Fizeau interferometer: The Roman numerals represent the order in which the highlighted cyan sections of the interferometer are assembled.

used a single-mode fiber patch cable to deliver collimated light to the Twyman-Green-Fizeau interferometer. Although the Twyman-Green interferometer and Fizeau interferometer could have been implemented using light sources with short coherence lengths (superluminescent diodes), I chose to use highly coherent light from a laser to relax the requirements on matching the path lengths exactly. This allows for laser unequal path interferometry for optical shop testing [179, 187].

The mathematical form for an interferogram generated by an amplitude-division interferometer

is as follows [181, 188]:

$$I(x,y) = (I_{\text{test}} + I_{\text{ref}}) + 2\sqrt{I_{\text{ref}} I_{\text{test}}}\cos[k\underbrace{(W_{\text{test}}(x,y) - W_{\text{ref}}(x,y))}_{\text{OPD}}], \tag{7.62}$$

where I_{test} is the intensity of the beam reflected from the test surface, I_{ref} is the intensity of the reference beam, $W_{\text{test}}(x,y)$ is the wavefront of the laser beam reflected from the test surface, $W_{\text{ref}}(x,y)$ is the reference wavefront and is generated by a beam reflected from the reference surface, and (x,y) is the coordinate of a point in a plane parallel to the reference surface. The fringe visibility is maximum when $I_{\text{test}} = I_{\text{ref}}$. Aberrations introduced by the test surface can be inferred from the structure of the interference fringes [189]:

$$\text{OPD} = W_{\text{test}}(x,y) - W_{\text{ref}}(x,y) = n\lambda. \tag{7.63}$$

Let us now look at the important case of when the measured interferogram can be used to determine the tilt of the test surface with respect to $W_{\text{ref}}(x,y)$. For simplicity, I assume that the test surface does not introduce any higher-order aberrations and that the test surface is tilted along one axis. The location and spacing of the fringes can be used to infer the tilt from Eq. 7.63:

$$\text{OPD} = W_{\text{test}}(x,y) - W_{\text{ref}}(x,y) = 2\theta_x x = n\lambda \tag{7.64}$$

$$\implies \theta_x = \frac{\lambda}{2\Delta x}, \tag{7.65}$$

where θ_x is the relative wavefront tilt along the x axis, Δx is the measured spacing between the fringes and λ is the wavelength of light used in the interferometer. The minimum measurable tilt

(θ_{min}) is limited by the size of the laser beam i.e. when the fringe width is equal to the beam size. Large beams are therefore preferred. In our setup, $\theta_{\text{min}} = 532\text{ nm}/(2 \times 25\text{ mm}) = 10\ \mu\text{rad}$. A typical interferogram used to measure the amount of tip/tilt is shown in Fig. 7.57a. The grid lines are spaced by 1 mm.

When $W_{\text{ref}}(x, y)$ is a diffraction-limited plane wavefront and is normal to its flat reference surface, i.e. $\nabla W_{\text{ref}}(x, y) = 0$, the relative measured tilt θ_x is exactly equal to the angle of incidence (AOI) of the laser beam with respect to the test surface:

$$\nabla W_{\text{test}}(x, y) = 2\theta_x = 2\text{AOI}. \tag{7.66}$$

The FOV of the objective is greatly compromised by residual tilt θ_{residual} between the objective and the glass cell window (see Figs. 7.43 and 7.4). However, $\theta_{\text{residual}} = 0$ when the AOI of the laser beam is zero with respect to both the glass cell surface and the objective.

Now I will elaborate on how the interferograms can be used to assemble the Twyman-Green-Fizeau interferometer for the purposes of aligning the two high NA objectives (see Fig. 7.56). The Roman numerals in Fig. 7.56 in the following paragraphs represent the order in which the different highlighted cyan sections of the interferometer are assembled.

I: In order to realize $\nabla W_{\text{ref}}(x, y) = 0$, the light from the fiber must first be collimated using diffraction-limited optics. The collimation is performed using lateral shearing interferometry [180]. The reference beam wavefront must also be normal to the reference surface R1. This can be achieved by coupling the reflected light from R1 back into the fiber. This back-coupling can be challenging for large diameter collimated beams as the AFOV of the collimator plus single-mode fiber assembly is $2\arctan(\text{MFD}/(2f_{\text{collimator}})) \simeq \text{MFD}/(f_{\text{collimator}})$, where $f_{\text{collimator}}$ is the focal

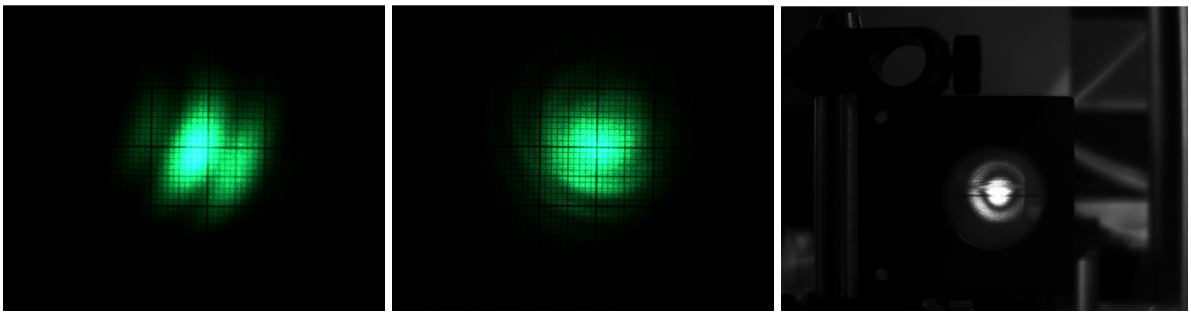

(a) (b) (c)

Figure 7.57: The grid size is 1 mm. (a) Tip/tilt fringe (b) Newton's rings showing the bowing of the glass cell window with a decentered laser beam (c) Newton's rings showing the bowing of the glass cell window with a centered laser beam.

length of the collimator and MFD is the mode field diameter of the single-mode fiber patch cable. The AFOV is in the range of 32 μrad to 43 μrad for a $f_{\text{collimator}} = 80$ mm (C80APC-A) and MFD in the range of $2.5-3.4$ μm (P3-405B-FC-5 single mode fiber patch cable). We have experimentally measured and verified this AFOV range by measuring the power of the light coupled back into the fiber as a function of the tilt of the reference $\lambda/20$ flat mirror R1 (20Z40BD.1 from Newport) mounted in a piezoelectric kinematic mirror mount (8822-AC from Newport which has an angular resolution of 0.7 μrad). We get close to the maximum expected fiber back-coupling from the short arm accounting for all losses in the optical chain. In the optimum back-coupling configuration, the uncertainty in the angle of incidence is less than 10 μrad.

II: Next we adjust the alignment of the $\lambda/20$ reference optical flat R2 (#48-131 from Edmund Optics) such that the interferogram between the back-reflection from this surface and the reference wavefront has a single tip/tilt fringe over the beam width i.e. $\theta = \theta_{\text{min}}$. In this arrangement, back-reflection from the reference optical flat R2 couples back into the fiber. When the alignment of R2 with respect to reference flat mirror R1 deteriorates to greater than 50 μrad i.e. 5 tilt fringes, we

measure no back-coupling into the fiber. This optical flat serves as the reference surface for the Fizeau interferometer. We block the light from the short arm to turn the Twyman-Green-Fizeau interferometer to just a Fizeau interferometer.

III: The utility of a Fizeau interferometer becomes apparent when the laser beam in the long arm must be made normal to the glass cell. Given that the glass cell has a small back-reflection due to the RAR nanotextured surface, it is important to match this back-reflected irradiance for maximum fringe visibility, justifying the use of the reference optical flat R2. While one can insert a neutral density filter in the short arm of the Twyman-Green interferometer and forego the optical flat R2 altogether, one must make sure that the neutral density filter does not introduce aberrations. We have experimentally verified the presence of large aberrations in a commercial neutral density filter from Thorlabs by measuring the interferogram using the back-reflection from the optical flat as the reference wavefront. When the back-reflection from the glass cell is aligned—using $\lambda/20$ flat mirrors M2 and M3 (30Z40BD.1 and 30Z40ER.2 from Newport)—to the back-reflection from R2, we can measure Newton's rings in the interferogram arising from the bowing of the objective window of the glass cell (see Figs. 7.57b and Fig. 7.57c). We can also identify the center of the objective windows by centering the Newton's rings (see Fig. 7.57c).

IV: To complete the skeleton of the Twyman-Green interferometer, the next step is to adjust the alignment of the last $\lambda/20$ flat mirror M3 (20Z40BD.1 froom Newport) in the long arm. Since Objective 2 is used for optical tweezer projection and single-atom imaging, this mirror must be retractable. To allow for removing M3 from the laser path while maintaining optical alignment,

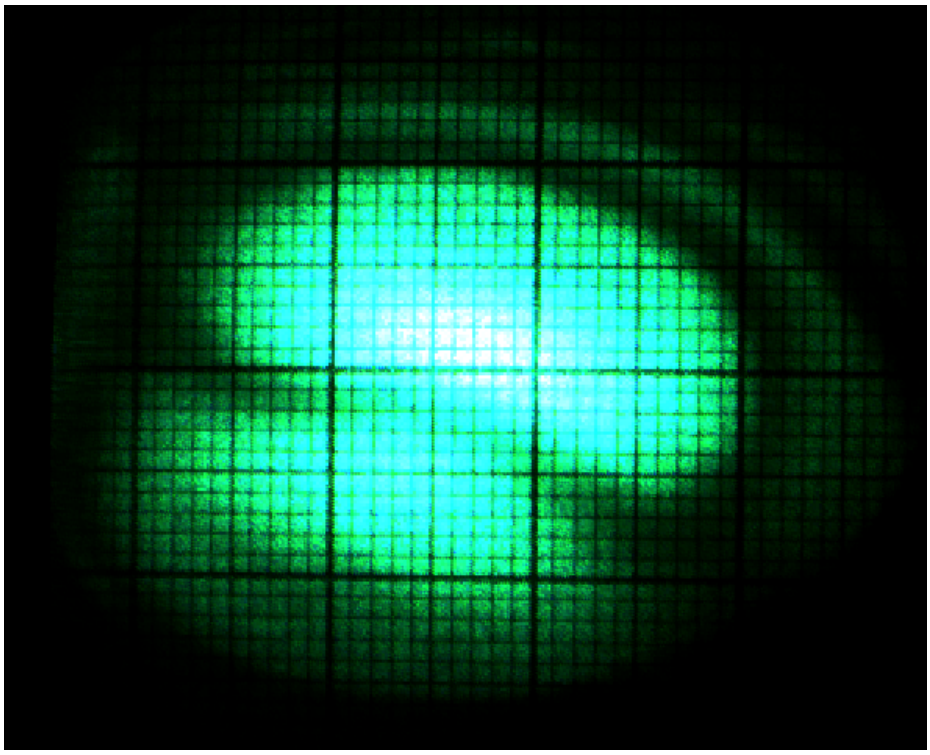

Figure 7.58: The interferogram for when the objectives are well aligned. This interferogram is representative of the minimum coma condition. The grid size is 1 mm.

we mount the mirror on a crossed-roller bearing translation stage (LNR50M from Thorlabs)[22]. To align M3, we unblock the light in the short arm and adjust the tip/tilt of M3 in the long arm until only one large tip/tilt fringe was observed on the interferogram. In this configuration, the retro-reflected long arm laser beam would also couple into the fiber. We get close to the maximum expected fiber back-coupling from the long arm cavity accounting for all losses in the chain. With M3 aligned, the skeleton for the Twyman-Green-Fizeau interferometer is complete and we are now in a position to start aligning the objectives.

[22]Crossed-roller bearing translation stages have the least angular deviation given the their travel range [190]. We removed the micrometer on this stage because we need only two discrete positions: fully retracted or fully inserted. We noticed that the tilt of the mirror changed when the micrometer was turned to move the stage. This problem disappeared when the stage had only two discrete positions. We would retract and insert the mirror using the stage multiple times and would not observe a discernible change in tilt greater than 10 μrad.

V: Objective 1 is aligned first. The objective is first centered on the optical axis of the laser beam in the long arm. The working distance for our objectives is 2 mm from the glass cell surface. The objective is mounted (Fig. 7.45) and translated, while its distance from the glass cell window is monitored using a camera. For this alignment, the back-reflection from the optical flat serves as the reference wavefront i.e. the Fizeau interferometer configuration. The dim collimated back-reflection from the first surface at the entrance aperture of objective 1 is interfered with the reference wavefront to generate an interferogram. The alignment of objective 1 is adjusted using a 5-axis piezoelectric motor-actuated stage from Newport (8081) until one tip/tilt fringe is measured on the interferogram.

VI: Objective 2 is aligned next. The FOV of each high NA objective is 200 μm with a depth of field of order λ [191]. Therefore, aligning the FOV of both objectives to each other is challenging. For this alignment, the Twyman-Green interferometer configuration is used i.e. the short arm is unblocked. The motion of the mounted objective 2 (Fig. 7.45) is controlled using another 5-axis piezoelectric motor-actuated stage from Newport (8081). The alignment of objective 2 is adjusted until the coma aberration as measured on the interferogram [180] is minimized (see Fig. 7.58). In the optimally aligned configuration, we even measure a third to a fourth of the maximum expected fiber back-coupling from the long arm cavity accounting for all losses in the chain with the objectives in place.

The residual coma in the interferogram arises from the decentration of the glass cell with respect to the optical axis of the laser beam in the long interferometer arm [192]. The objectives must be centered on the space between the electrodes in order to use their full NA. Unfortunately, the center of the space between the electrodes is offset from the center of the objective window

of the glass cell. We suspect that the electrode assembly must have drooped under gravity.

Apart from the high alignment precision, this alignment technique also allows for fast recovery/re-alignment of high NA objectives in the event of a misalignment. We have re-aligned our high NA objectives in less than 4 hours. Last but not least, this alignment technique yields laser beams that can now serve as reference beams for aligning the imaging system and the optical tweezer projection systems, which I will discuss next.

7.6.3.2 Aligning the tweezer projection systems

At the heart of the tweezer projection systems was the use of optical rails (see Fig. 7.59). Large-scale control over alignment errors between the constituent optics can be rectified by using optical rails and its compatible accessories. Finer control over the alignment errors can be performed by using lens mounts (LP-2A, 9081 alignment stage, and 9071 alignment stage from Newport) that have 5-axis capabilities: tip, tilt, defocus, decenter in x, and decenter in y. Defocus/despace errors between the lenses can be corrected by using shearing interferometry on the multiple afocal subsystems that make up the tweezer-projection system. I specifically chose the 95 mm optical construction rails from Thorlabs and all of its accessories like drop-on rail carriages and rail plates from Thorlabs and Newport. I designed my own long rail plates (red plates in Fig. 7.59) that were used in the tweezer-based projection systems. However, I eventually abandoned using these rail plates as they turned out to be less versatile than the drop-on rail carriages from Thorlabs and Newport. Using optical rails has multiple benefits, which I list below:

- Using the mechanical constraints of the rails and their accessories, it is straightforward to

approximately align the input beam to the tweezer-projection system and all the mounted optical components to the rails. For instance, the optical mounts mounted on rail carriages/plates can be readily centered transversely with respect to the rail. The input beam can be made level and centered transversely with respect to the rail using irises mounted on rail carriages that are tightened to the rail.

- The rails facilitate non-sequential alignment of the mounted optics, which was critical in the alignment of our tweezer-projection system. The optical elements can be removed for alignment or debugging purposes, and then reinstalled easily with no change in the alignment. We use additional rail plates to memorize the location of each optical element in the beam path when we remove it.

- The rails provide large dynamic range for defocus/despace corrections without compromising tip/tilt and decentration of the mounted optical elements in the process.

- The rail plates/carriages on which the optics are mounted have a large surface area overlap between the plates/carriages and the optical rails. This helps improve passive stability when the rail plates/carriages are tightened to the rails.

- The rails are heavy, monolithic machined pieces of aluminum. This feature, along with the fact that the large overlap area between the bottom surface of the rail and the optical table, helps increase passive stability when the rails are bolted down.

I built the tweezer projection systems (see Fig. 7.48 and Fig. 7.49) with help from Kevin. I detail my strategy for aligning the tweezer projection systems in Appendix I.

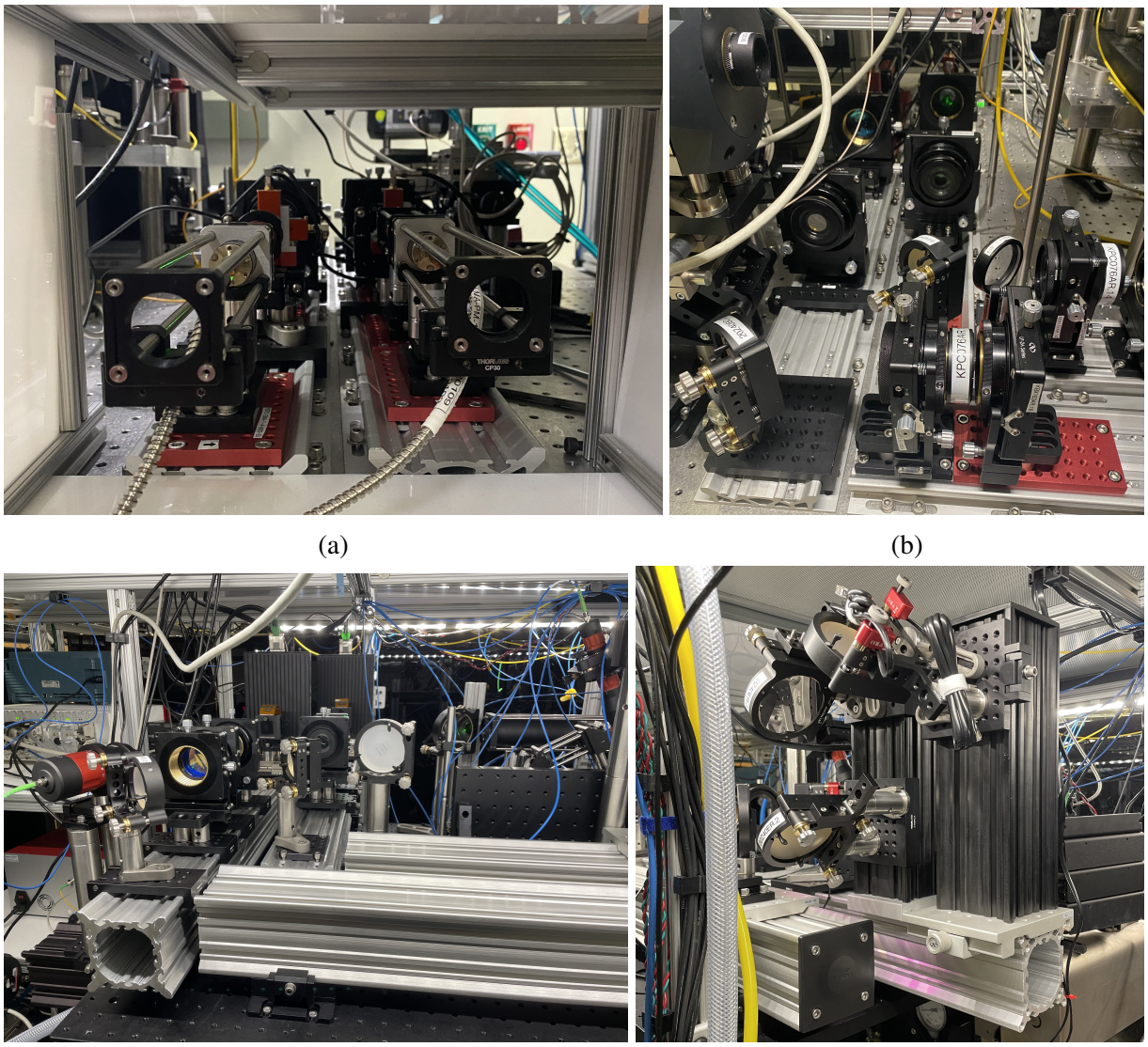

(a) (b)

(c) (d)

Figure 7.59: The optical rail-based construction of (a) (b) the AOD-based tweezer projection systems, (c) (d) SLM-based tweezer projection systems

7.6.3.3 Designing and aligning the imaging system

In order to align the imaging system, the mirror M3 in the long interferometer arm is retracted (see Fig. 7.56). The reference beam from the long interferometer is used to align the $4f$ imaging system (see Fig. 7.48). The imaging lens is centered on the interferometer beam. The camera is placed at the focus of the interferometer beam. The camera sensor area is also

centered on the focused interferometer beam. The magnification of the $4f$ imaging system is $M = f_{\text{imaging}}/f_{\text{objective}}$, where $f_{\text{objective}}$ is the focal length of the objective and f_{imaging} is the focal length of the imaging lens. The specifications of our imaging system for both species can be found in the table below.

Camera	M	Atom (Color)	Pixel size (μm)
Andor iXon X3 EMCCD, model number: DU-888D-c00-BV-9JO	25	Rb (780 nm)	16
Princeton 123 Instruments, model number: PIXIS 1024B DETECTOR EXCELON	33	Yb (399 nm), Rb (420 nm)	13

The transverse, axial, and angular magnification of a tweezer, with waist w_{tweezer} and Rayleigh range $z_{R,\text{tweezer}} = (\pi w_{\text{tweezer}}^2)/\lambda$, imaged by this $4f$ imaging system is as follows:

$$\text{Transverse magnification: } w_{\text{camera}} = M w_{\text{tweezer}} \tag{7.67}$$

$$\text{Axial magnification: } \underbrace{\text{DOF}}_{\text{depth of focus}} = M^2 z_{R,\text{tweezer}} = \frac{\pi M^2 w_{\text{tweezer}}^2}{\lambda}, \tag{7.68}$$

$$\text{Angular magnification: } \theta_{\text{camera}} \simeq \frac{\text{NA}}{M}. \tag{7.69}$$

The choice of magnification M depends on a few things. A small angular magnification θ_{camera} (large M) helps minimize aberrations when the focused imaging light passes through a plane-parallel plate (bandpass filter) installed right in front of the camera. In addition, the depth of focus [106, 193] of the imaging system increases quadratically with M. Therefore, a large M seems highly preferable. However, the Nyquist sampling theorem for digital imaging of a point

source sets an upper bound on M. The sampling theorem can be stated as follows [194, 195]:

$$\underbrace{M \times 1.22\lambda/\text{NA}}_{\text{Diameter of the Airy disc at the camera}} \geq 4 \times \text{camera pixel size}. \tag{7.70}$$

For a given SNR, oversampling the PSF of the imaging system—using more than four camera pixels to sample the diameter of the Airy disc—increases the camera acquisition time. This is not ideal, as we desire short cycle times. As the atoms in optical tweezers will be separated by 2 to 5 μm or more, we do not need to follow the 4 pixel rule. I designed the imaging system to undersample the PSF, dedicating 2 pixels to sample the Airy disc diameter. This choice also improves the accuracy in determining the position of the tweezer in the focal plane of the objective, when compared with using just one pixel for the Airy disc diameter.

Although the long arm interferometer beam at 532 nm was used to determine the position of the camera, the axial position of the camera is different for the imaging light due to chromatic aberrations induced by the imaging lens (The objective lens is corrected for chromatic aberrations). In order to determine the correct axial position of the camera, we need to image the atoms.

We first load atoms into a tweezer with a tunable waist. The waist size of the tweezer can be tuned using zoom beam expanders (ZBE1B and ZBE12 from Thorlabs in the AOD-based tweezer projection systems in Fig. 7.48). As the average number of atoms in the tweezer trap volume scales as w^2_{tweezer} [72], we start with a tweezer with a large waist. This arrangement yields a large fluorescence signal and the camera is comfortably in the depth of focus of the imaging system. The fluorescence signal measured on the camera reduces dramatically as the tweezer waist is reduced due to the w^4_{tweezer} trap volume scaling. At the same time, the depth of focus also decreases, but less dramatically, due to the w^2_{tweezer} scaling. The camera is mounted on two

translation stages (LNR50M from Thorlabs) and a lab jack (L490 from Thorlabs) for full x, y, z motion control. We adjusted the position of the camera so as to stay in the depth of focus of the imaging system as the tweezer waist (trap volume) is progressively reduced. This technique helped us image single atoms in tweezers (Fig. 7.66). I had originally devised this alignment technique but had abandoned it because I was afraid of beam steering issues with the zoom beam expander, which in the end was not as bad as I thought.

For pedagogical purposes, I will derive [72, 196] the scaling laws for the optical dipole trap volume $V_{\text{dipole trap}}$, the average number of atoms loaded into the dipole trap $\langle N \rangle$, and the dipole trap power $P_{\text{dipole trap}}$ as a function of the waist size of the dipole trap $w_{\text{dipole trap}}$. A tweezer is just a microscopic dipole trap. The rate equation for the number of atoms loaded into an optical dipole trap N is as follows [72, 196]:

$$\frac{dN}{dt} = R - \gamma N - \beta' N(N-1), \tag{7.71}$$

where R is the loading rate from the MOT, γ is the one-body decay rate due to collisions with fast background gas atoms, and β' is the two-body decay rate due to inelastic collisional mechanisms [72, 73, 196]. The steady-state average number of atoms in the dipole trap $\langle N \rangle$ under strong loading rate conditions is therefore [72, 196]:

$$\langle N \rangle \sim \sqrt{\frac{R}{\beta'}} \propto \underbrace{w_{\text{dipole trap}}^2 \sqrt{\frac{\pi^2}{\lambda_{\text{dipole trap}}} \ln\left(\frac{1}{1 - k_{\text{B}}T/|U_0|}\right)} \sqrt{\frac{k_{\text{B}}T/|U_0|}{1 - k_{\text{B}}T/|U_0|}}}_{\sqrt{V_{\text{dipole trap}}}}, \tag{7.72}$$

where $\lambda_{\text{dipole trap}}$ is the dipole trap wavelength, T is the temperature of the atoms in the dipole trap

and U_0 is the dipole trap depth. The ratio $k_B T/|U_0|$ in Eq. 7.72 was measured to be constant and equal to 0.4 in Ref. [196] for their range of trap parameters. Therefore, $\langle N \rangle$ scales as $w^2_{\text{dipole trap}}$, $V_{\text{dipole trap}}$ scales as $w^4_{\text{dipole trap}}$. $P_{\text{dipole trap}}$ scales as $w^2_{\text{dipole trap}}$ for a constant trap depth U_0.

Before using the zoom beam expander approach to adjust $w_{\text{dipole trap}}$, we used an iris screwed to the mount for the last lens in the AOD-based tweezer projection system (lens 5 in Fig. 7.47) to adjust $w_{\text{dipole trap}}$. This approach failed as we did not have enough tweezer laser power at our disposal as $P_{\text{dipole trap}}$ scales as $w^4_{\text{dipole trap}}$ for this approach.

7.6.3.4 Rearranging the optical tweezers

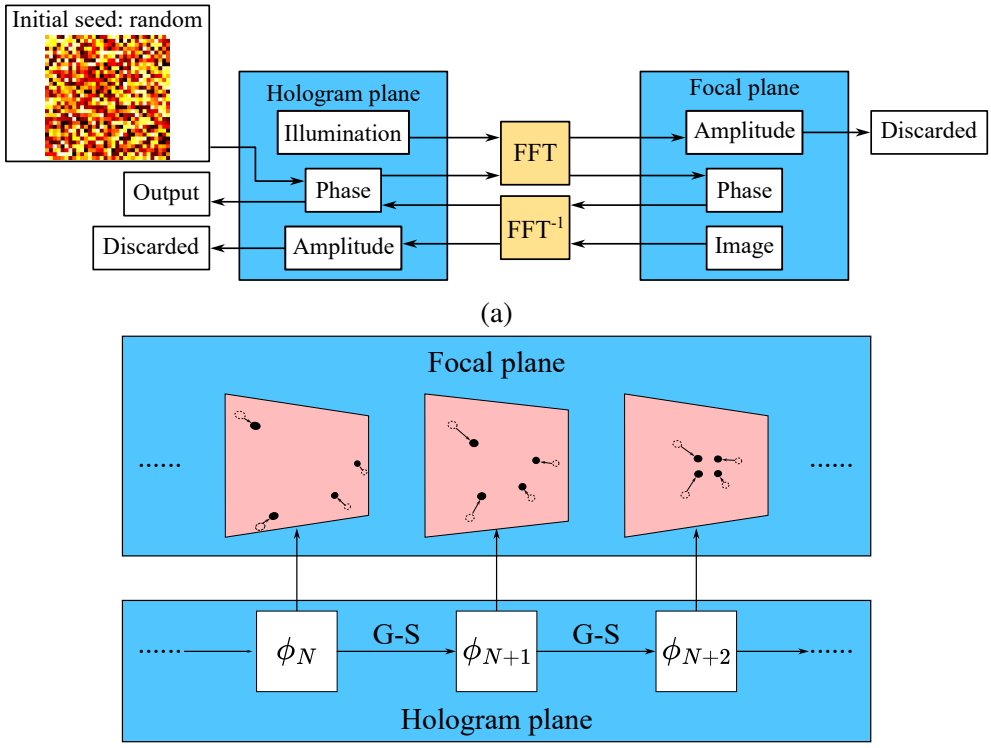

Figure 7.60: (a) The standard Gerchberg-Saxton (G-S) algorithm (b) My modification to the G-S algorithm for fast frame generation.

AOD-based optical tweezers are routinely used to create defect-free arrays of single neutral

atoms. Rearranging stochastically-loaded tweezer arrays requires dynamic arbitrary control over the amplitude, frequency, and phase of the single-frequency tones that comprise the multitone waveform driving the AOD. Some generate the multitone rf waveform using an FPGA-based signal generator or SDR [76, 197, 198]. Some use a PC to pre-compute and save the waveforms, and the rearrangement trajectories in memory [198, 199]. Others move an optical tweezer by controlling a voltage-controlled oscillator with a microcontroller [200].

I came up with an idea for fast real-time rf arbitrary waveform generation using graphic processing units for the purposes of rearranging/moving the AOD-based optical tweezers to create a defect-free array. This idea was implemented by Oliver. We wrote a paper about it [83].

The following work is preliminary, but seems promising. As we have ultrahigh speed SLMs on our system, we need to compute holograms at high speed to make good use of these SLMs. We use the Gerchberg-Saxton (G-S) algorithm to generate the phase-only holograms for the SLM. The standard G-S algorithm is illustrated in Fig 7.60a [178, 201, 202, 203]. It is an iterative algorithm that takes an initial random phase hologram as the seed. Typically, multiple iterations are needed to converge to the desired hologram. However, when we are rearranging the atoms using the SLM, we have intimate knowledge of the sequence of movements that must be made to generate a defect-free array. The motion of the traps from one frame to the next has to be small to minimize atom loss. Therefore, instead of seeding the G-S algorithm with the random phase hologram to generate a frame, I had the idea of seeding the G-S algorithm with the phase hologram of the frame that preceded it. This idea is illustrated in Fig. 7.60b.

Oliver implemented this idea on the Quadro RTX 6000 GPU using CUDA (Compute Unified Device Architecture). Typically, only one G-S iteration is needed to achieve fidelity of 96%. Fidelity is defined as the overlap integral between the target image electric field and

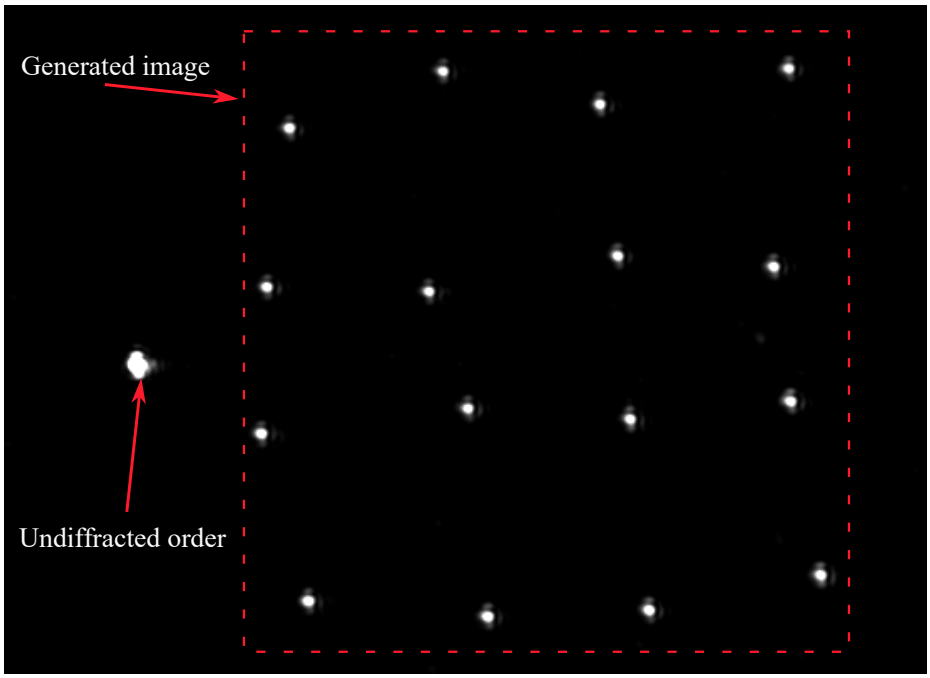

Figure 7.61: SLM generated image measured by the camera placed at an image plane in the SLM-based tweezer projection system

the generated image electric field in Ref. [204]. One iteration takes 220 μs on average. It takes $\sim$ 120 μs to transfer the data from the GPU to the CPU. Data transfer from the CPU to the SLM takes $\sim$ 200 μs. Oliver has been testing these computer-generated holograms on the actual SLM (Fig. 7.61).

7.7 Towards trapping single atoms

7.7.1 3D MOTs of Rb and Yb

The MOT arm arrangement in our experiment is as follows: two regular arms and one/two shallow-angle arms, which are at 67.5° from a regular third arm orientation (see 7.28 and Figs. 7.29). This arrangement for the arms was chosen to avoid forming the third MOT arm

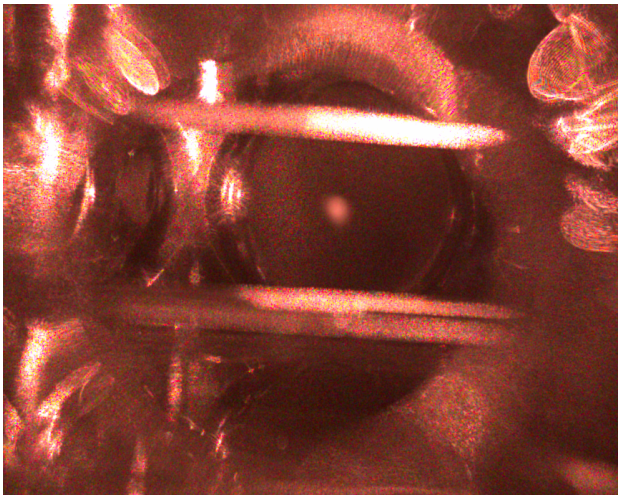

Figure 7.62: A 3D MOT of ^{87}Rb atoms in the shallow-angle arm arrangement

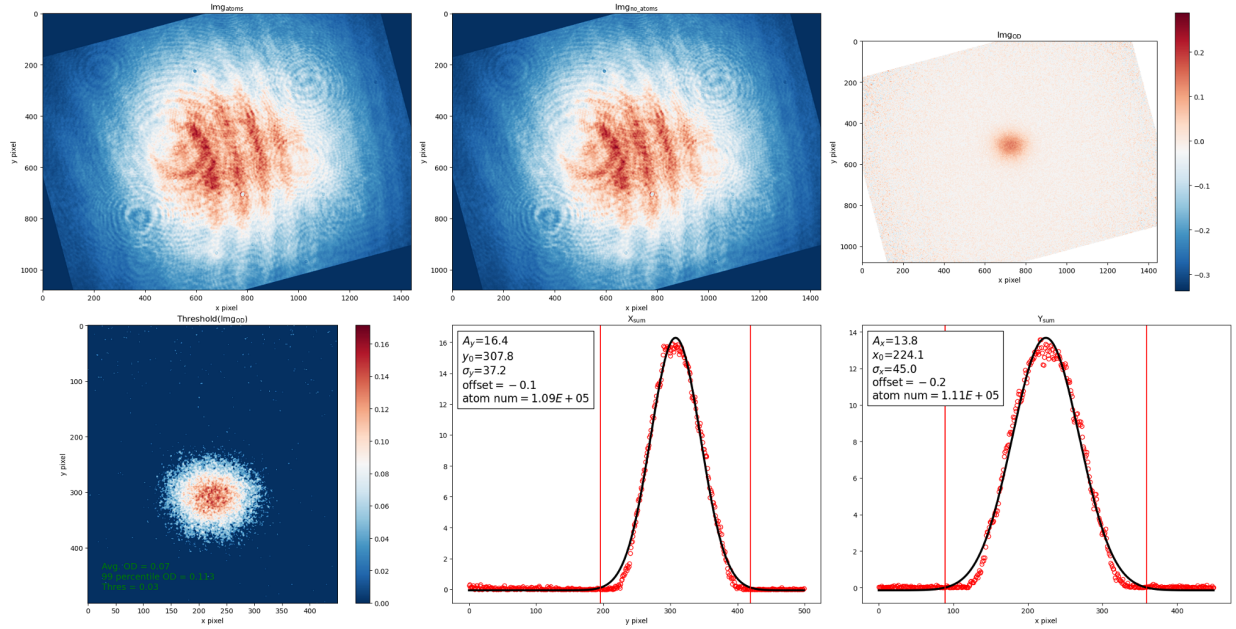

Figure 7.63: Absorption imaging of $\sim 100,000$ ^{87}Rb atoms sub-Doppler cooled to $\sim 30\mu$K in the shallow-angle arm arrangement

through the objectives. However, this design choice has delayed us by several months. Although we do not need a lot of atoms for experiments with atoms in optical tweezers, all the steps that lead up to it benefit from large atom numbers. For instance, debugging the MOTs and aligning laser beams to the MOTs is easy with large atom numbers.

Our MOT arrangement renders the capture and cooling of atoms highly sensitive to scattering force imbalances arising from power and polarization fluctuations in the MOT arms, especially the shallow-angle arms. These force imbalances lead to non-ideal MOT operations: higher ultimate temperatures and poor transfer of atoms between laser cooling stages. Force imbalances can be diagnosed when magnetic field gradients are lowered while all other parameters for the 3D MOT are kept constant. The 3D MOT cloud will move in the direction of the imbalance as the field gradient is lowered before it disappears [205]. The scattering force imbalances are overcome at large magnetic field gradients.

Force imbalances play an important role when Yb atoms are transferred from the Yb blue 3D MOT to the Yb green 3D MOT [205]. The maximum scattering force for the blue transition is ~ 230 times greater than the maximum scattering force for the green transition ((30 MHz/399 nm)/(0.182 MHz/ 556 nm)) (Fig. 6.1). Additionally, the optimal magnetic field gradient for a MOT is proportional to the linewidth of the cooling transition used: the optimal field gradient needed for the blue MOT is greater than that needed for the green MOT. The Doppler temperature of the MOT cloud is also proportional to the linewidth of the cooling transition. Due to the scattering force imbalances in the blue 3D MOT, the atoms can be accelerated to velocities beyond the capture velocity of the green 3D MOT. A green 3D MOT in a shallow-angle arm arrangement (two regular arms and one shallow-angle arm in a retro-reflected beam geometry) was unable to capture the atoms from the shallow-angle blue 3D MOT. I designed and installed

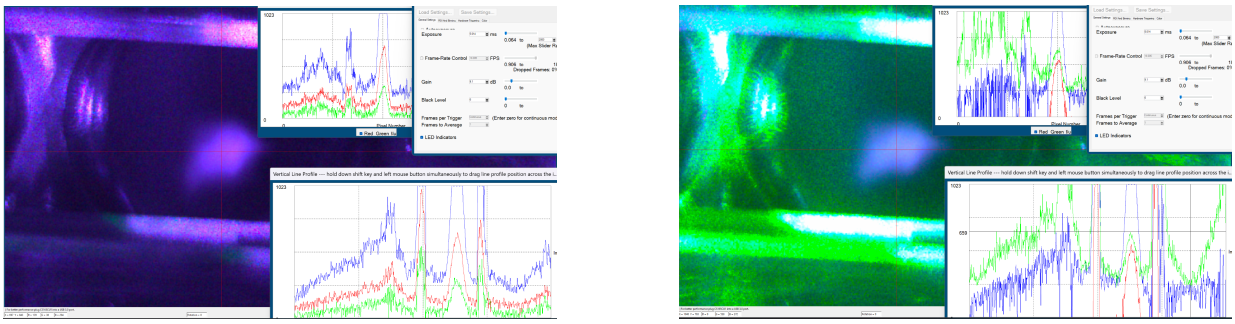

(a) (b)

Figure 7.64: A 3D MOT of ^{174}Yb atoms (a) in the blue shallow-angle arm arrangement (b) in the simultaneous blue plus green shallow-angle arm arrangement

(with Kevin) an additional shallow-angle arm for extra confinement, which made this a dual shallow-angle arm arrangement with two regular arms and two shallow-angle arms in a retro-reflected beam geometry (see Fig. 7.29).

We first achieved a 3D MOT of ^{87}Rb atoms in the shallow-angle arm arrangement (see Fig. 7.62). Subsequently, we sub-Doppler cooled $\sim 100,000$ ^{87} Rb atoms to $\sim 30\mu$K (see Fig. 7.63). The blue shallow-angle ^{174}Yb 3D MOT is shown in Fig 7.64a and the simultaneous blue plus green shallow-angle ^{174}Yb 3D MOT (aka hybrid Yb 3D MOT) is shown in Fig 7.64b. The hybrid 3D MOT is the starting point for transferring atoms to just the green 3D MOT. We use the same gradient for Yb as we do for Rb ($\pm 6 - 8$ A in the MOT coils). We shine a total ~ 100 mW of 556 nm light distributed over all the MOT arms, effectively power-broadening the MOT transition. Power broadening is a simple alternative to artificial broadening [8, 9]. We would then reduce the field gradients, while simultaneously decreasing the power in the green MOT beams and bringing the frequency of the green MOT closer to resonance. This would give us a cold ($\sim 30 - 50\mu$K) cloud of $3 - 5 \times 10^6$ ^{174}Yb atoms (see Fig. 7.65).

At some point, we tried to form the green 3D MOT of Yb with a third MOT arm through the objectives, but that turned out to be very challenging. Our setup was not designed for this

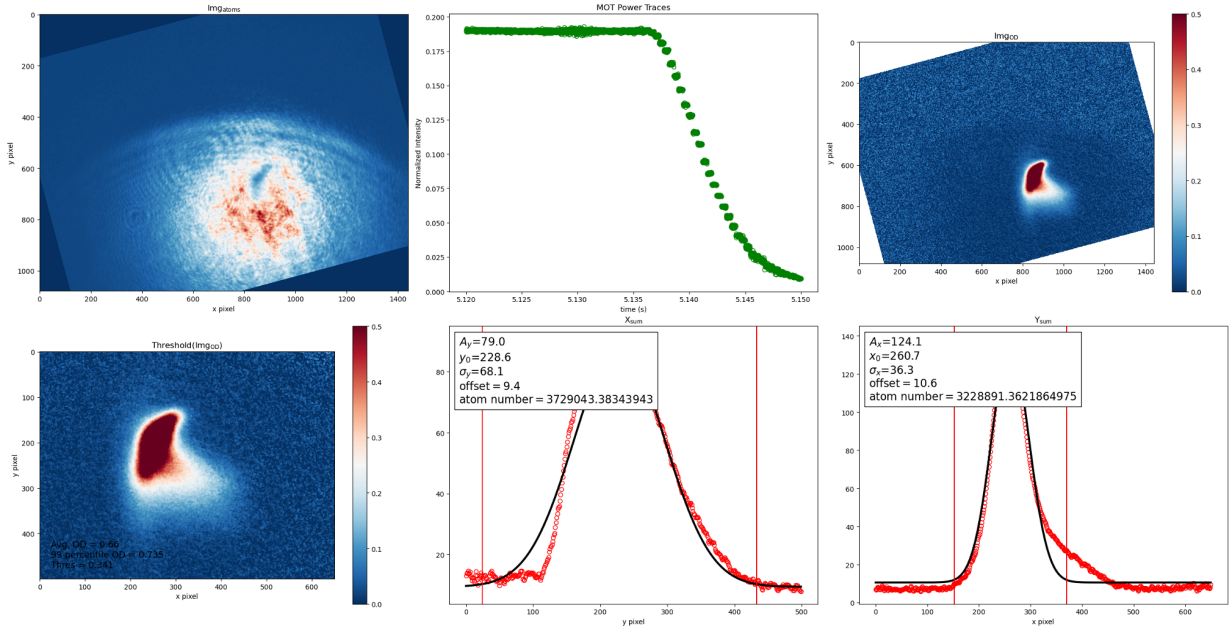

Figure 7.65: Absorption imaging of a cloud of $\sim 3 \times 10^6$ ^{174}Yb atoms cooled to $\sim 30 - 50\mu$K in the green 3D MOT shallow-angle arrangement.

particular arrangement, and the high-NA nature of the objectives did not make this alignment easy. In conclusion, my advice would be to simulate [206] an exotic MOT arrangement before implementing it. The difficulty of trapping and cooling atoms in exotic MOT arrangements should not be underestimated.

7.7.2 Optical tweezers of single ^{87}Rb atoms

Given that we are able to laser cool the Rb and Yb atoms to temperatures in the tens of μK range, the next step is to trap them in optical tweezers. We first tried to trap single ^{87} Rb atoms in optical tweezers because it is a simpler atom to work with.

One of the first things we did was to maximize the fluorescence from ^{87}Rb atoms in the MOT stage and the optical molasses stage on the Andor camera (Sec 7.6.3.3) by adjusting the values for the magnetic fields. However, the procedure laid out in Sec. 7.6.3.3 is what gave

us the first tweezer signal: The MOT and optical molasses were overlapped with a tweezer beam in a large waist configuration, and the fluorescence from the atoms was measured. By progressively reducing the tweezer waist using the zoom beam expander, we enter the single-atom tweezer loading regime where the atoms are stochastically loaded into the tweezer. To confirm the stochastic nature of the loading, we project a 2×3 optical tweezer array with the spacing between the rf tones set to 2.5 MHz, which maps to a 14.25 μm spacing at the objective BFP (Eq. 7.60). Fig. 7.66 shows the average image of 30 individual fluorescence images of the stochastically loaded 2×3 optical tweezer array. The $x-$ and $y-$ axes in this image are in units of the number of camera pixels. The exposure time on the Andor camera was set to 100 ms for these fluorescence measurements.

This signal (Fig. 7.66) was achieved just a few weeks before I finished writing this thesis. I would not have been able to present this image here without Madi's and Kevin's efforts during these past three months. For that, I am extremely grateful.

7.8 Outlook

Although the last few years of construction have been both fun and challenging, it is really good to see that we have gotten ever so close to doing real science. The immediate next step would be to trap single Yb atoms in optical tweezers followed by characterizing and optimizing the loading and trapping of both atoms in their respective optical tweezers. Given the ultrahigh-speed SLMs at our disposal, we can work towards accelerating the creation of simultaneous defect-free lattices of both species. Building the optical setups for implementing single-qubit gates for each species would also need to be done. Exciting both of these atoms to

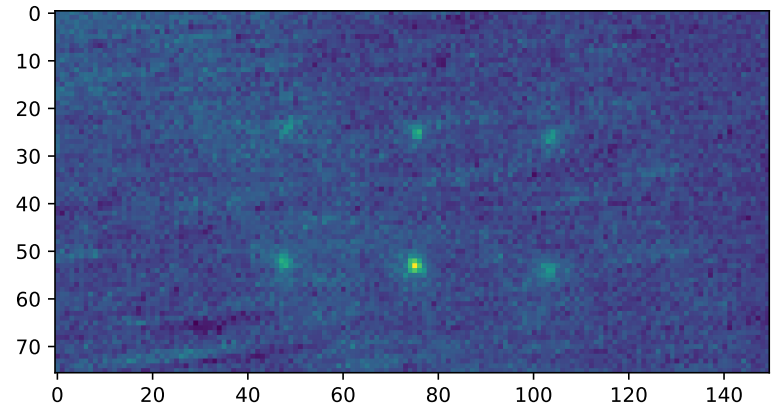

Figure 7.66: 30 shot averaged image of ^{87}Rb atoms stochastically loaded into a 2x3 optical tweezer array. The $x-$ and $y-$ axes are in units of number of pixels.

their Rydberg states to characterize the heteronuclear Förster resonances, in addition to measuring the anomalously weak van der Waals interaction between two Yb atoms in the $(6sns)^1S_0$ Rydberg states, are also on our scientific roadmap. These measurements would enable us to implement the multi-qubit gates needed for many of the proposals I have mentioned in Chapter 6. Some of these ideas include the transfer of quantum information between atoms of two species, and the creation of N-atom Greenberger–Horne–Zeilinger (GHZ) states [207, 208, 209].

Appendix A: Dark State Optical Lattice with a Subwavelength Spatial Structure

Editors' Suggestion | Featured in Physics

Dark State Optical Lattice with a Subwavelength Spatial Structure

Y. Wang (王扬),[1,*] S. Subhankar,[1] P. Bienias,[1] M. Łącki,[2,3,4] T-C. Tsui (崔子俊),[1]
M. A. Baranov,[3,4] A. V. Gorshkov,[1,5] P. Zoller,[3,4] J. V. Porto,[1] and S. L. Rolston[1]

[1]*Joint Quantum Institute, National Institute of Standards and Technology and the University of Maryland, College Park, Maryland 20742, USA*

[2]*Jagiellonian University, Institute of Physics, Łojasiewicza 11, 30-348 Kraków, Poland*

[3]*Institute for Quantum Optics and Quantum Information of the Austrian Academy of Sciences, A-6020 Innsbruck, Austria*

[4]*Institute for Theoretical Physics, University of Innsbruck, A-6020 Innsbruck, Austria*

[5]*Joint Center for Quantum Information and Computer Science, National Institute of Standards and Technology and the University of Maryland, College Park, Maryland 20742, USA*

(Received 1 December 2017; published 20 February 2018)

We report on the experimental realization of a conservative optical lattice for cold atoms with a subwavelength spatial structure. The potential is based on the nonlinear optical response of three-level atoms in laser-dressed dark states, which is not constrained by the diffraction limit of the light generating the potential. The lattice consists of a one-dimensional array of ultranarrow barriers with widths less than 10 nm, well below the wavelength of the lattice light, physically realizing a Kronig-Penney potential. We study the band structure and dissipation of this lattice and find good agreement with theoretical predictions. Even on resonance, the observed lifetimes of atoms trapped in the lattice are as long as 44 ms, nearly 10^5 times the excited state lifetime, and could be further improved with more laser intensity. The potential is readily generalizable to higher dimensions and different geometries, allowing, for example, nearly perfect box traps, narrow tunnel junctions for atomtronics applications, and dynamically generated lattices with subwavelength spacings.

DOI: 10.1103/PhysRevLett.120.083601

Coherent control of the position and motion of atoms with light has been a primary enabling technology in the physics of ultracold atoms. The paradigmatic examples of conservative optical potentials are the optical dipole trap and optical lattices, generated by far off-resonant laser fields, with the ac-Stark shift of atomic levels as the underlying mechanism. The spatial resolution for such optical potential landscapes is determined by the diffraction limit, which is of the order of the wavelength of light λ. This fundamentally limits optical manipulation of atoms. For example, in quantum simulation with atoms in optical lattices, the minimum lattice constant is $\lambda/2$, setting the energy scale for Hubbard models for both hopping (kinetic energy) and interaction of atoms, with challenging temperature requirements to observe quantum phases of interest [1]. Developing tools to overcome the diffraction limit, allowing coherent optical manipulation of atoms on the subwavelength scale, is thus an outstanding challenge. Following recent proposals [2–4], we report below first experiments demonstrating coherent optical potentials with subwavelength spatial structure, by realizing a Kronig-Penney–type optical lattice with barrier widths below $\lambda/50$.

In the quest to beat the diffraction limit, several ideas have been proposed to create coherent optical potentials with subwavelength structure. These include Fourier synthesis of lattices using multiphoton Raman transitions [5,6], optical or radio-frequency dressing of optical potentials [7,8], and trapping in near-field guided modes with nanophotonic systems [9,10] (although they suffer from decoherence induced by nearby surfaces). An alternative approach uses the spatial dependence of the nonlinear atomic response associated with the dark state of a three-level system [11–16] as a means to realize subwavelength atomic addressing and excitation. The subwavelength resolution arises when optical fields are arranged so that the internal dark state composition varies rapidly ("twists") over a short length scale.

As proposed in [3,4], such a subwavelength twist can also be used to create a conservative potential with narrow spatial extent, due to the energy cost of the kinetic energy term of the Hamiltonian [2,17,18]. Unlike ac-Stark shift potentials, this twist-induced potential is a quantum effect, with magnitude proportional to $\hbar$. Using this effect, we create 1D lattices with barrier widths less than $\lambda/50$. This potential realizes the Kronig-Penney (KP) lattice model [19]—a lattice of nearly δ-function potentials. We study the band structure and dissipation and find that the dark state nature of this potential results in suppressed scattering, in good agreement with theoretical models.

Our approach is illustrated in Fig. 1(a). A three-level system is coupled in a Λ configuration by two optical fields: a spatially varying strong control field $\Omega_c(x) = \Omega_c \sin(kx)$ and a constant weak probe field Ω_p. The excited

state $|e\rangle$ can decay to either ground state $|g_i\rangle$. Within the Born-Oppenheimer (BO) approximation, slowly moving atoms in the dark state $|E_0(x)\rangle$ are decoupled from $|e\rangle$, where $|E_0(x)\rangle = \sin(\alpha)|g_1\rangle - \cos(\alpha)|g_2\rangle$ and $\alpha(x) = \arctan[\Omega_c(x)/\Omega_p]$ [3]. The two bright states $E_\pm(x)$ have excited state component $|e\rangle$, leading to light scattering. As shown in Fig. 1(b), the fields are arranged in such a way that the dark state changes composition over a narrow region, depending on the ratio $\epsilon = \Omega_p/\Omega_c$. The kinetic energy associated with this large gradient in the spin wave function gives rise to a conservative optical potential $V(x)$ [3,4] for atoms in $|E_0(x)\rangle$,

$$V(x) = \frac{\hbar^2}{2m}\left(\frac{d\alpha}{dx}\right)^2 = E_R \frac{\epsilon^2 \cos^2(kx)}{[\epsilon^2 + \sin^2(kx)]^2}, \qquad (1)$$

where $k = 2\pi/\lambda$, $E_R = \hbar^2 k^2/2m$ is the recoil energy, and m is the mass of the atom. The potential $V(x)$ can be viewed as arising from nonadiabatic corrections to the BO potential [3,4] or artificial scalar gauge potential [18,20,21]. When $\epsilon \ll 1$, this creates a lattice of narrow barriers spaced by $\lambda/2$, with the barrier height scaling as $1/\epsilon^2$ and the full width at half maximum scaling as $0.2\lambda\epsilon$ [Fig. 1(b)].

The potential $V(x)$ exhibits several properties that distinguish it from optical potentials based on ac-Stark shifts: (1) The explicit dependence on $\hbar$, via the recoil energy E_R, reveals the quantum nature of $V(x)$ arising from the gradient in the wave function, whereas a typical optical potential can be described entirely classically as an induced dipole interacting with the electric field of the laser. (2) Since gradients in wave functions always cost energy, $V(x)$ is always repulsive. (3) The geometric nature of the potential results in it being only dependent on ϵ. By deriving both fields from the same laser, it is relatively insensitive to technical noise. (4) Unlike near-field guided modes [9,10], our scheme works in the far field, thus avoiding the decoherence associated with the proximity of surfaces.

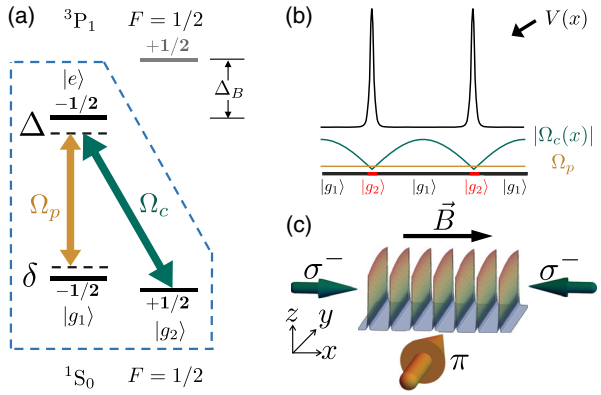

FIG. 1. Level structures and experimental geometry. (a) The three levels in ^{171}Yb used to realize the dark state are isolated from the fourth $^3P_1$, $m_F = +1/2$ state by a large magnetic field. They are coupled by a strong σ^- polarized control field Ω_c (green) and a weak π polarized probe field Ω_p (orange). The resulting dark state is a superposition of the ground states $|g_1\rangle$ and $|g_2\rangle$, with relative amplitudes determined by $\Omega_c(x)/\Omega_p$. (b) Spatial dependence of the dark state composition is created using a standing wave control field $\Omega_c(x)$ and a traveling wave probe field Ω_p. The geometric potential $V(x)$ (black) arises as the dark state rapidly changes its composition near the nodes of the standing wave. (c) The two counterpropagating σ^- beams creating the standing wave are aligned with a strong magnetic field along x, while the π beam travels along y.

We realize the Λ configuration using three states selected from the $^1S_0$, $F = 1/2$ and $^3P_1$, $F = 1/2$ hyperfine manifolds in ^{171}Yb. The two $^1S_0$ ground states $m_F = \pm 1/2$ comprise the lower two states $|g_1\rangle$ and $|g_2\rangle$ [see Fig. 1(a)]. The $^3P_1$, $m_F = -1/2$ state, with inverse lifetime $\Gamma = 2\pi \times 182$ kHz, makes up the third state $|e\rangle$ in the Λ configuration. The $|g_i\rangle \to |e\rangle$ transitions are isolated from the transition to the other $^3P_1$, $m_F = +1/2$ state by applying a 12 mT magnetic field $\vec{B}$ to Zeeman split the two $^3P_1$ states by $\Delta_B = 1.8 \times 10^3\ \Gamma$. The same field slightly splits the $^1S_0$ ground states by -0.5Γ due to the small nuclear magnetic moment. The standing-wave control field $\Omega_c(x)$, traveling along $\vec{B}$, is produced by two counterpropagating σ^- laser beams that couple the $|g_2\rangle$ and $|e\rangle$ states with amplitudes $\Omega_{c1}e^{ikx}$ and $\Omega_{c2}e^{-ikx}$. A third beam, π polarized and traveling normal to $\vec{B}$, couples the $|g_1\rangle$ and $|e\rangle$ states with amplitude $\Omega_p e^{iky}$. The frequency of the control and probe beams can be chosen to set the single- and two-photon detunings, Δ and δ. We define $\delta = 0$ as the dark state condition for the isolated three-level system, accounting for the Zeeman splitting. Off-resonant couplings to other states can introduce light shifts, which require nonzero δ to maintain the dark state condition.

We create an ultracold ^{171}Yb gas in a bichromatic crossed dipole trap by sympathetic cooling with Rb atoms that are also magnetically confined [22,23]. After Yb atoms are collected with a temperature of $\simeq$300 nK ($T/T_F = 1.10$, where T_F is the Fermi temperature), the magnetic field in the x direction is ramped up in 100 ms to 12 mT, removing Rb from the trap. The Yb atoms are then optically pumped into $|g_1\rangle$ using a 50 ms pulse from one of the control beams, resulting in $\simeq 1.5 \times 10^5$ Yb atoms polarized. The small ^{171}Yb scattering length ($-3a_0$ [24], with a_0 the Bohr radius), plus the lack of s-wave scattering in polarized fermions allow us to neglect interactions. The Rabi frequencies of each of the three beams are calibrated by measuring the two-photon Rabi frequencies from $|g_1\rangle \to |g_2\rangle$ at large Δ with different pairs of beams. The laser polarization purity and alignment to $\vec{B}$ are carefully optimized, such that the residual fraction of wrong polarization measured in Rabi frequency is less than 0.5%. To load Yb into the ground band of the dark state lattice, we first populate the spatially homogeneous dark state by ramping on Ω_{c1} followed by Ω_p and then adiabatically

ramp on Ω_{c2} in 1 ms, creating the lattice. We measure the momentum distribution using a band mapping sequence [25], by first ramping off Ω_{c2} in 0.5 ms and then suddenly turning off all the other light fields. We take absorption images after time-of-flight (TOF) along y to measure the momentum along x and z; see [26] for further details.

The existence of lattice structure of $V(x)$ leads to Brillouin zones (BZ), visible in TOF images taken after band mapping. Since $k_B T$ is less than the band gap, the population is predominantly in the first BZ and distinct band edges are visible [upper panel in Fig. 2(a)]. The lower panel shows the result with no probe beam, where we find a nearly Gaussian distribution in the lattice direction. We also see nearly Gaussian distributions for atoms loaded in the other two-beam configurations: Ω_{c1}, Ω_p and Ω_{c2}, Ω_p.

For small ϵ, this lattice maps to a 1D KP model. One characteristic feature of the KP lattice is that the energy of the nth-band scales as $n^2 E_R$, such that the band spacing increases with n. In contrast, in a deep sinusoidal lattice, the band spacing decreases with n. To map out the band structure, we excite atoms from the ground (s) band into the higher bands by shaking the lattice using phase modulation of one of the σ^- beams. After band mapping, we measure the band populations, which become separated after TOF [see Fig. 2(c)]. Figure 2(b) plots the frequency-dependent

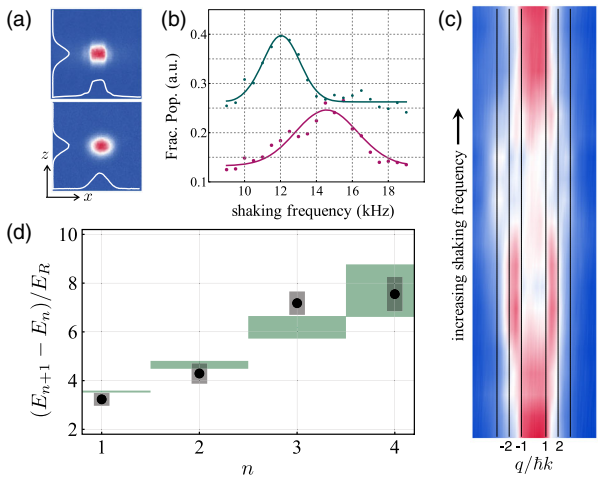

FIG. 2. (a) Band mapping results for atoms loaded into the dark state lattice with three beams (upper) and with only Ω_c beams (lower). The white traces show the integrated momentum distribution in each direction (x is the lattice direction). (b),(c) Band spectroscopy: in (c), we plot the TOF column density integrated over z after shaking the lattice vs the shaking frequency; in (b), we plot the fraction of the population (frac. pop.) excited to the p band (dark green) and d band (magenta) Brillouin zones [see (c)] vs shaking frequency. Gaussian fits [colored lines in (b)] are used to determine the center frequency and the width of the transition. (d) Band spacing scaling: $E_{n+1} - E_n$ is plotted vs the band index n of a dark state lattice with $\Omega_c = 70\ \Gamma$, $\Omega_p = 10\ \Gamma$, $\Delta = 22\ \Gamma$, and $\delta = 0$. The gray vertical bars indicate the transition width inferred from the measurements, while the green rectangles are predictions of the expected band spacings and widths [26].

excitation into the first (p) and second (d) excited bands for $\epsilon = 0.14$, extracted from the data in Fig. 2(c). The $s \to d$ excitation arises from a two-step process involving the p band. We map out the band structure up to the g band and plot the energy differences for adjacent bands [see Fig. 2(d)], which increase monotonically with n. The green rectangles show the theoretical band spacings and widths, calculated from a model that includes both the light shifts from states outside the three-level system [26] and mixing with the bright states.

Another property of a KP lattice is that, in the deep lattice limit, its band structure is almost independent of the barrier strength (the area under the potential for a single barrier), which scales with $1/\epsilon$. The band spacings for different ϵ are plotted in Fig. 3(a) for fixed $\Omega_c = 100\ \Gamma$ and Ω_p varied from 5 to 20 Γ. As expected, the band spacings are almost independent of ϵ, even though the probe power varies by an order of magnitude. The upper panels of Fig. 3(a) show the potentials of the upper bright state (blue) and dark state (green) for three ϵ. For $\epsilon \leq 0.1$, mixing between $E_0(x)$ and $E_\pm(x)$ states modifies the band structure, reducing the band spacing. For $\epsilon \simeq 0.1$, we realize a barrier width of 10 nm with minimal coupling to the bright state. The shaded regions are predictions based on a model that takes bright state couplings into account, which are in better agreement with the measured spacings, compared to the model that has no couplings (dashed line). We attribute the discrepancy between theory and experiment to the residual polarization imperfections, calibration errors in the optical intensity, and limitations of band spectroscopy. We note that the theory predicts a vanishing band width near $\epsilon \simeq 0.125$ and the growth of the bandwidth at even smaller ϵ, due to the interference of dark state and bright state mediated tunneling [26].

Away from $\delta = 0$, the state is no longer completely dark and it experiences an additional periodic potential with amplitude δ [26,30] [Fig. 3(b)]. This additional potential perturbs the KP lattice and the band structure. We verify this by measuring the band spacings as a function of δ [Fig. 3(b)] and find it agrees with the prediction (shaded area), with the systematic deviation likely coming from the same factors as in Fig. 3(a).

Finally, we study dissipation. The nonadiabatic corrections to the BO potential that give rise to $V(x)$ also weakly couple the dark state with the bright states, which leads to light scattering, heating the atoms out of the trap. We measure the lifetime τ in a dark state lattice [Fig. 4(a)] for different Δ and find it significantly longer for $\Delta > 0$ than for $\Delta < 0$. This is in contrast to an optical lattice based on ac-Stark shifts, where heating is independent of the sign of Δ [31,32]. To intuitively understand this asymmetry, we use the model described in [4] and note that the coupling to the bright states takes place inside the barrier. An atom can scatter light by admixing with the bright states $E_\pm(x)$ (approximately Δ independent) or exiting into the energy-allowed $E_-(x)$ state via nonadiabatic couplings (strongly Δ

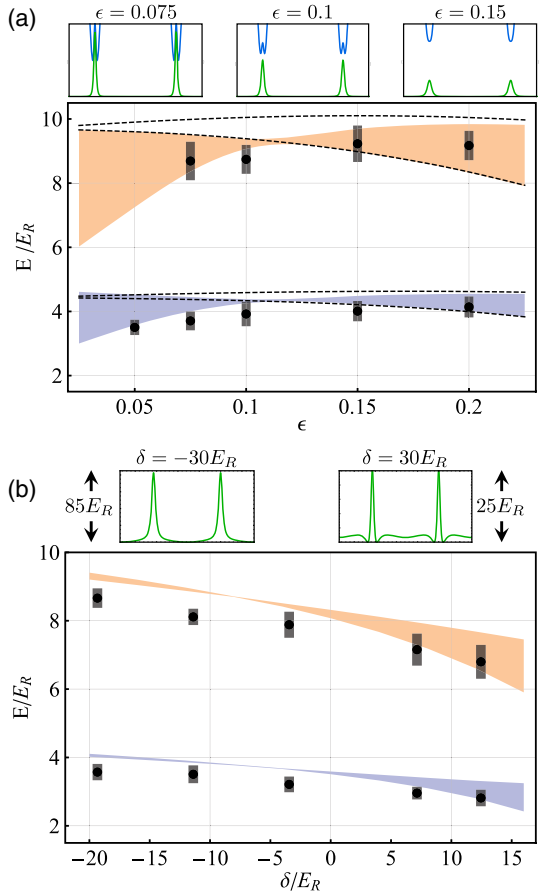

FIG. 3. Band structure scalings. Energies of the p and the d bands with respect to the s band are plotted. (a) Vary ϵ: $\Omega_c = 100\ \Gamma$, $\Omega_p = 5$–$20\ \Gamma$, $\Delta = 22\ \Gamma$, and $\delta = 0$. Dashed lines indicate the allowed transition energies predicted from modeling $V(x)$ alone, while the shaded regions are from a model including couplings to the bright states. (Upper) Representative potentials for the dark state (green) and bright state (blue). At $\epsilon = 0.075$, the bright and dark states are no longer good basis states because of the strong coupling between them. (b) Vary δ: $\Omega_c = 70\ \Gamma$, $\Omega_p = 10\ \Gamma$, $\Delta = 22\ \Gamma$. (Upper) Calculated dark state potentials for positive and negative δ.

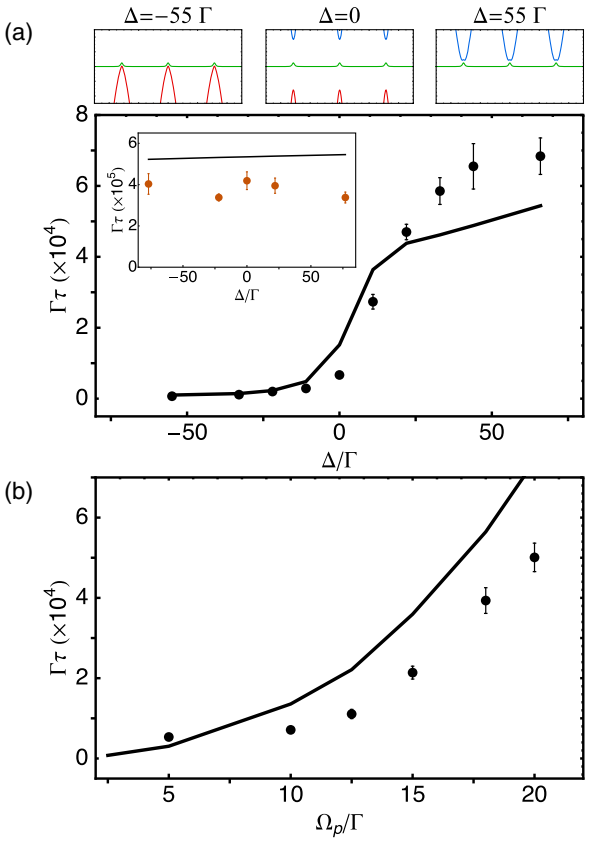

FIG. 4. (a) Lifetime of dark state lattice τ scaled by the excited state lifetime Γ^{-1} vs Δ, with $\Omega_c = 70\ \Gamma$, $\Omega_p = 10\ \Gamma$, and $\delta = 0$. (Inset) Lifetime of the dark state in spatially homogeneous control fields, with $\Omega_{c1} = 35\ \Gamma$, $\Omega_{c2} = 0$, $\Omega_p = 10\ \Gamma$, and $\delta = 0$. (Upper three panels) The two bright state potentials $E_-(x)$ (red) and $E_+(x)$ (blue), and the dark state potential (green), at different Δ. (b) Lifetime vs Ω_p in a dark state lattice where $\epsilon = 0.2$ and $\Delta = 0$. The solid black lines are predictions scaled with a factor 2.2 [except for (a) inset, where no scaling is applied]. The error bars represent 1 standard deviation uncertainty from fitting the population decay data.

dependent). The $E_-(x)$ state [red, Fig. 4(a), upper panels] contributes more to the loss, explaining the Δ asymmetry. The result of the model [26] is depicted as the black line, with an empirical scale factor of 2.2 applied to the theory to account for the unknown relationship between the scattering rate and loss rate ($1/\tau$). The lifetime in a homogeneous control field when one of the Ω_c beams is blocked is shown in Fig. 4(a) (inset). The $\tau \simeq 4 \times 10^5/\Gamma$ lifetime is almost independent of Δ, as theory would predict, and is 70% of the expected lifetime due to nonadiabatic coupling to the bright states and off-resonant scattering from states outside the three-level system.

The nonadiabatic bright state coupling also leads to a counterintuitive dependence of the dissipation on the laser power. Figure 4(b) shows the lifetime at constant ϵ as a function of Rabi frequencies. Remarkably, the lifetime increases with Rabi frequency. In contrast, for a regular optical lattice at a fixed detuning, the lifetime does not improve with more laser power. For the dark state lattice, larger $\Omega_{c,p}$ increases the separations between BO potentials, resulting in decreased scattering. In general, the lifetime improves with more laser power and at blue detuning. However, couplings to $E_+(x)$ adversely affects the barrier height [similar to the case with $\epsilon \ll 1$ in Fig. 3(a)]. With realistic increase in laser intensity, we can potentially improve the lifetime by an order of magnitude, while maintaining the ultranarrow barriers.

The conservative nanoscale optical potential demonstrated here adds to the toolbox of optical control of atoms, enabling experiments requiring subwavelength motional control of atoms. Such sharp potential barriers could be useful for the creation of narrow tunnel junctions for

quantum gases [33] or for building sharp-wall box-like traps [34]. In addition, spin and motional localization on small length scales can enhance the energy scale of weak, long range interactions [3]. The dark state lattice is generalizable to 2D and, for example, can be used to study Anderson localization with random strength in the barrier height [35]. By stroboscopically shifting the lattice [36], the narrow barriers should enable optical lattices with spacings much smaller than the $\lambda/2$ spacing set by the diffraction limit, which would significantly increase the characteristic energy scales relevant for interacting many-body atomic systems.

We thank Victor M. Galitski and Luis A. Orozco for stimulating discussions. Y. W., S. S., T-C. T., J. V. P., and S. L. R. acknowledge support by NSF PFC at JQI and ONR Grant No. N000141712411. P. B. and A. V. G. acknowledge support by NSF PFC at JQI, AFOSR, ARL CDQI, ARO, ARO MURI, and NSF QIS. M. Ł. acknowledges support of the National Science Centre, Poland via Project 2016/23/D/ST2/00721. M. Ł., M. A. B., and P. Z. acknowledge support from the ERC Synergy Grant UQUAM, the Austrian Science Fund through SFB FOQUS (FWF Project No. F4016-N23), and EU FET Proactive Initiative SIQS.

P. B. and M. Ł. contributed equally to this work.

*yuw127@umd.edu

[1] C. Gross and I. Bloch, Science **357**, 995 (2017).
[2] R. Dum and M. Olshanii, Phys. Rev. Lett. **76**, 1788 (1996).
[3] M. Łącki, M. A. Baranov, H. Pichler, and P. Zoller, Phys. Rev. Lett. **117**, 233001 (2016).
[4] F. Jendrzejewski, S. Eckel, T. G. Tiecke, G. Juzeliūnas, G. K. Campbell, L. Jiang, and A. V. Gorshkov, Phys. Rev. A **94**, 063422 (2016).
[5] G. Ritt, C. Geckeler, T. Salger, G. Cennini, and M. Weitz, Phys. Rev. A **74**, 063622 (2006).
[6] T. Salger, C. Geckeler, S. Kling, and M. Weitz, Phys. Rev. Lett. **99**, 190405 (2007).
[7] W. Yi, A. J. Daley, G. Pupillo, and P. Zoller, New J. Phys. **10**, 073015 (2008).
[8] N. Lundblad, P. J. Lee, I. B. Spielman, B. L. Brown, W. D. Phillips, and J. V. Porto, Phys. Rev. Lett. **100**, 150401 (2008).
[9] A. González-Tudela, C. L. Hung, D. E. Chang, J. I. Cirac, and H. J. Kimble, Nat. Photonics **9**, 320 (2015).
[10] M. Gullans, T. G. Tiecke, D. E. Chang, J. Feist, J. D. Thompson, J. I. Cirac, P. Zoller, and M. D. Lukin, Phys. Rev. Lett. **109**, 235309 (2012).
[11] A. V. Gorshkov, L. Jiang, M. Greiner, P. Zoller, and M. D. Lukin, Phys. Rev. Lett. **100**, 093005 (2008).
[12] M. Kiffner, J. Evers, and M. S. Zubairy, Phys. Rev. Lett. **100**, 073602 (2008).
[13] J. A. Miles, Z. J. Simmons, and D. D. Yavuz, Phys. Rev. X **3**, 031014 (2013).
[14] M. Sahrai, H. Tajalli, K. T. Kapale, and M. S. Zubairy, Phys. Rev. A **72**, 013820 (2005).
[15] J. Cho, Phys. Rev. Lett. **99**, 020502 (2007).
[16] K. T. Kapale and M. S. Zubairy, Phys. Rev. A **73**, 023813 (2006).
[17] S. K. Dutta, B. K. Teo, and G. Raithel, Phys. Rev. Lett. **83**, 1934 (1999).
[18] M. Cheneau, S. P. Rath, T. Yefsah, K. J. Günter, G. Juzeliūnas, and J. Dalibard, Europhys. Lett. **83**, 60001 (2008).
[19] R. de L. Kronig and W. G. Penney, Proc. R. Soc. A **130**, 499 (1931).
[20] J. Dalibard, F. Gerbier, G. Juzeliūnas, and P. Öhberg, Rev. Mod. Phys. **83**, 1523 (2011).
[21] N. Goldman, G. Juzeliūnas, P. Öhberg, and I. B. Spielman, Rep. Prog. Phys. **77**, 126401 (2014).
[22] V. D. Vaidya, J. Tiamsuphat, S. L. Rolston, and J. V. Porto, Phys. Rev. A **92**, 043604 (2015).
[23] C. D. Herold, V. D. Vaidya, X. Li, S. L. Rolston, J. V. Porto, and M. S. Safronova, Phys. Rev. Lett. **109**, 243003 (2012).
[24] M. Kitagawa, K. Enomoto, K. Kasa, Y. Takahashi, R. Ciurylo, P. Naidon, and P. S. Julienne, Phys. Rev. A **77**, 012719 (2008).
[25] A. Kastberg, W. D. Phillips, S. L. Rolston, R. J. C. Spreeuw, and P. S. Jessen, Phys. Rev. Lett. **74**, 1542 (1995).
[26] See Supplemental Material at http://link.aps.org/supplemental/10.1103/PhysRevLett.120.083601 for details of experimental setup and calculations on the band structure and lifetime, which includes Refs. [27–29].
[27] S. Subhankar, Y. Wang, A. Restelli, S. L. Rolston, and J. V. Porto (to be published).
[28] J. H. T. Burke, O. Garcia, K. J. Hughes, B. Livedalen, and C. A. Sackett, Rev. Sci. Instrum. **76**, 116105 (2005).
[29] D. Steck, Quantum and Atom Optics, available online at http://steck.us/teaching.
[30] P. Bienias *et al.* (to be published).
[31] J. P. Gordon and A. Ashkin, Phys. Rev. A **21**, 1606 (1980).
[32] F. Gerbier and Y. Castin, Phys. Rev. A **82**, 013615 (2010).
[33] S. Eckel, J. G. Lee, F. Jendrzejewski, N. Murray, C. W. Clark, C. J. Lobb, W. D. Phillips, M. Edwards, and G. K. Campbell, Nature (London) **506**, 200 (2014).
[34] A. L. Gaunt, T. F. Schmidutz, I. Gotlibovych, R. P. Smith, and Z. Hadzibabic, Phys. Rev. Lett. **110**, 200406 (2013).
[35] W. Morong and B. DeMarco, Phys. Rev. A **92**, 023625 (2015).
[36] S. Nascimbene, N. Goldman, N. R. Cooper, and J. Dalibard, Phys. Rev. Lett. **115**, 140401 (2015).

Supplementary Material: Dark state optical lattice with sub-wavelength spatial structure

Y. Wang,[1] S. Subhankar,[1] P. Bienias,[1] M. Łącki,[2,3,4] T-C. Tsui,[1] M. A. Baranov,[3,4] A. V. Gorshkov,[1,5] P. Zoller,[3,4] J. V. Porto,[1] and S. L. Rolston[1]

[1] *Joint Quantum Institute, National Institute of Standards and Technology and the University of Maryland, College Park, Maryland 20742 USA*
[2] *Jagiellonian University, Institute of Physics, Łojasiewicza 11, 30-348 Kraków, Poland*
[3] *Institute for Quantum Optics and Quantum Information of the Austrian Academy of Sciences, A-6020 Innsbruck, Austria*
[4] *Institute for Theoretical Physics, University of Innsbruck, A-6020 Innsbruck, Austria*
[5] *Joint Center for Quantum Information and Computer Science, National Institute of Standards and Technology and the University of Maryland, College Park, Maryland 20742 USA*

(Dated: January 3, 2018)

I. EXPERIMENTAL TECHNIQUES

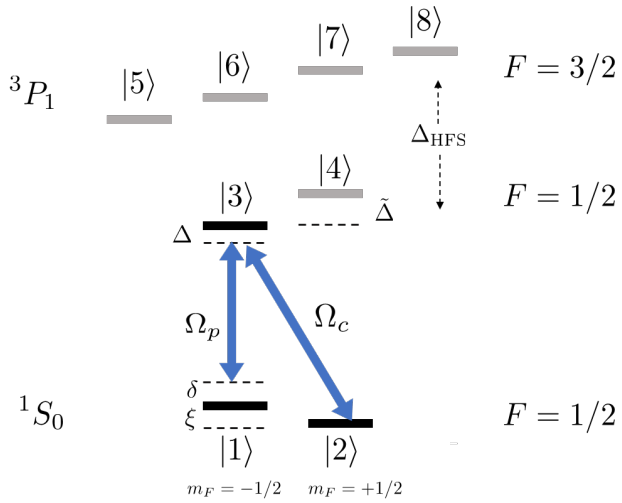

FIG. S1. Level structure of the $^1S_1$ and $^3P_1$ manifolds of ^{171}Yb: δ is the two photon detuning; Δ is the single photon detuning; ξ is the ground state Zeeman splitting and $\tilde{\Delta}$ is the Zeeman splitting in the excited state due to the external magnetic field; and Δ_{HFS} is the $^3P_1$ hyperfine splitting.

We use forced evaporation of co-trapped ^{87}Rb to sympathetically cool $\sim 3\times10^5$ atoms of ^{171}Yb to a temperature of 1.1 T_F. The ^{87}Rb -^{171}Yb mixture is produced in a combined magnetic and multi-wavelength optical dipole trap [S1]. After reaching the final temperature, the Rb atoms are removed by ramping on the magnetic field to 12 mT. The lifetime of Yb atoms in the trap after removal of the Rb atoms is 3 s. Referring to Fig. 1c. in the main text, the final Yb trap frequencies are $\omega_x \simeq 2\pi \times 164$ Hz, $\omega_{z+y} \simeq 2\pi \times 50$ Hz, and $\omega_{z-y} \simeq 2\pi \times 155$ Hz.

The σ_i^- and π coupling beams at 556 nm are generated from the same laser, which is beat-note (BN) locked to a separate laser (used for laser cooling on the $^1S_0 - {}^3P_1$ transition), which itself is locked to an Yb atomic saturation absorption signal. The dynamic control of the BN allows for rapid tuning of the single-photon detuning Δ of the beams. Separate acousto-optic modulators (AOM) allow for independent intensity control of all three coupling beams, as well as control over the two photon detuning δ and the phase offset between the two σ_i^- beams ($i = 1, 2$) used for shaking the lattice. The three beams are delivered to the atoms through independent optical fibers, and have beam waists of $\sim$ 1mm at the atoms.

We image the atoms using the Yb $^1S_0 - {}^1P_1$ transition at 399 nm, with light generated by a frequency doubled laser system. We stabilize the seed of the imaging laser (at 800 nm) via a scanning transfer cavity lock [S2, S3] with light locked to the $5^2S_{1/2} - 5^2P_{3/2}$ transition at 780 nm in Rb as the reference. State-selectivity is achieved by imaging in a large magnetic field of 12 mT along $\hat{x}$, such that the resulting 116 MHz spacing between the Zeeman states of $^1P_1$ is sufficient to resolve the spin-dependent transitions with linewidth $\Gamma_{1P1} = 2\pi\times30$ MHz. The imaging beam propagates along $\hat{y}$ with linear polarization along $\hat{z}$, such that it has an equal superposition of $\hat{\sigma}_+$ and $\hat{\sigma}_-$ relative to the B-field.

We measure the population in each hyperfine ground state by making the laser resonant with its respective stretched state ($^1S_0\,|F=1/2, m_F=\pm 1/2\rangle \leftrightarrow {}^1P_1\,|F=3/2, m_F=\pm 3/2\rangle$) during imaging.

II. RABI FREQUENCY CALIBRATION

We calibrate the Rabi frequencies of σ_i^- (Ω_{ci}) and π (Ω_p) by measuring two-photon Raman Rabi frequencies and light-shift induced Raman detuning of the $\sigma_i^- - \pi$ pairs of beams as a function of their beam powers. When $\Delta \gg \Gamma, \Omega$, one can adiabatically eliminate the excited state, $|3\rangle$, and reduce the three-level system to an effective two-level system with states $|\vec{p}\rangle\,|1\rangle$ and $\left|\vec{p}+2\hbar\delta\vec{k}\right\rangle|2\rangle$, resulting in the following expressions for the two-photon Rabi frequency (Ω_R) and Raman detuning (δ_R) [S4]

$$\Omega_R = \frac{\Omega_p \Omega_{ci}}{2\Delta} \tag{S1}$$

$$\delta_R = \delta + \frac{4\omega_R(\vec{p}\cdot\delta\vec{k} + \left|\delta\vec{k}\right|)}{\left|\delta\vec{k}\right|} + \xi - \frac{\Omega_{ci}^2}{4\Delta} + \frac{\Omega_p^2}{4\Delta} \tag{S2}$$

where $\delta\vec{k} = \vec{k}_c - \vec{k}_p$, and $\omega_R = \frac{\hbar\left|\delta\vec{k}\right|^2}{2m}$ is the Raman recoil energy. $\vec{k}_c$ and $\vec{k}_p$ are the k-vectors for one of the pump beams and probe beam respectively. For a stationary gas, the second term in (S2) averages to 0.

We extract Ω_R and δ_R by measuring the oscillation of the center of mass (COM) position of the cloud as a function of the Raman pulse time, after a 12 ms time-of-flight (TOF). In addition to transferring population between ground states, stimulated Raman transitions provide a momentum kick i.e. $|\vec{p}\rangle\,|1\rangle \leftrightarrow \left|\vec{p}+2\hbar\delta\vec{k}\right\rangle|2\rangle$. This momentum kick manifests itself in TOF measurements as spatially separated momentum peaks, and the COM position of the cloud provides a measure of the ground state populations. Fig. S2(a) shows typical Rabi oscillation data, which we fit to a damped sinusoid to determine Ω_R. The damping arises from the spread in the momentum distribution of the atoms.

Ω_R gives us information about the product of Ω_{ci} and Ω_p, but not their absolute magnitudes. For fixed Δ, Ω_R and $\delta_R = 0$, Eqs. (S1) and (S2) can be used to determine the two Rabi frequencies Ω_{ci} and Ω_p as a function of laser power. Defining $\Omega_p^2 = A_p P_p$ and replacing $\Omega_{ci} = 2\Omega_R\Delta/\Omega_p$ in Eq. (S2), we get

$$\delta = \xi - \frac{A_p P_p}{4\Delta} + \frac{\Delta\Omega_R^2}{A_p P_p} \tag{S3}$$

where P_p is the power of the probe beam and A_p is the constant that connects Ω_p to P_p.

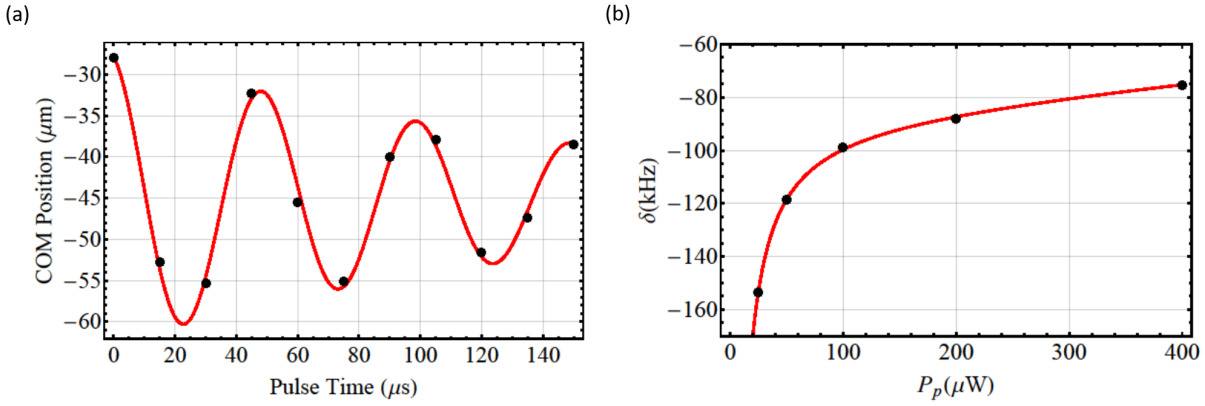

FIG. S2. (a) Example center of mass oscillation of the cloud as a function of Raman pulse time, used to calibrate Rabi frequencies. (b) Change in two-photon detuning (δ) as function of the probe power, P_p.

Experimentally, we fix $\Delta = 40$ MHz and vary P_{ci} (the power of σ_i^- beam) and P_p so as to keep Ω_R constant. We tune δ to satisfy $\delta_R = 0$, determined by maximizing the COM shift after a $\pi/2$ Raman pulse. We fit the measured

values for δ as a function P_p using Eq. (S3) as the fit function with A_p and ξ as fit parameters. Fig. S2(b) shows the fit to data. Defining $\Omega_{ci}^2 = A_{ci}P_{ci}$ just as for the probe beam, we extract A_{ci} using Eq. (S1). Given the uncertainty in the measurement of Ω_R for the two cases, we can determine the balanced condition $\Omega_{c1} = \Omega_{c2}$ to within 2%.

III. IMBALANCED LATTICE BEAMS

To determine the potential $V(x)$ for imbalanced control beams, $\Omega_{c1} \neq \Omega_{c2}$, we consider the spatially dependent control Rabi frequency of the form

$$\Omega_c(x) = \frac{\Omega_{c1}\mathrm{e}^{ikx} - \Omega_{c2}\mathrm{e}^{-ikx}}{i} \tag{S4}$$

When $\Omega_{c1} = \Omega_{c2} = \Omega_c$, we recover $\Omega_c(x) = 2\Omega_c \sin(kx)$. The resulting Hamiltonian in the bare state basis has the form

$$H = \frac{\hbar\Omega_p}{2}\begin{pmatrix} 0 & 0 & 1 \\ 0 & 0 & s\sin(kx) + i\eta\cos(kx) \\ 1 & s\sin(kx) - i\eta\cos(kx) & 0 \end{pmatrix} \tag{S5}$$

where $s = \frac{1}{\epsilon} = \frac{\Omega_{c1}+\Omega_{c2}}{\Omega_p}$ and $\eta = \frac{\Omega_{c1}-\Omega_{c2}}{\Omega_p}$, and $\Delta = \Gamma = \delta = 0$. Diagonalizing H gives the following normalized eigenvectors:

$$|E_0(x)\rangle = -\frac{i\eta\cos(kx) + s\sin(kx)}{\sqrt{(1+\eta^2\cos^2(kx) + s^2\sin^2(kx))}}|1\rangle + \frac{1}{\sqrt{(1+\eta^2\cos^2(kx) + s^2\sin^2(kx))}}|2\rangle$$

$$|E_-(x)\rangle = -\frac{1}{\sqrt{2(1+\eta^2\cos^2(kx) + s^2\sin^2(kx)}}|1\rangle + \frac{(i\eta\cos(kx) - s\sin(kx))}{\sqrt{2(1+\eta^2\cos^2(kx) + s^2\sin^2(kx))}}|2\rangle + \frac{1}{\sqrt{2}}|3\rangle$$

$$|E_+(x)\rangle = \frac{1}{\sqrt{2(1+\eta^2\cos^2(kx) + s^2\sin^2(kx)}}|1\rangle + \frac{(-i\eta\cos(kx) + s\sin(kx))}{\sqrt{2(1+\eta^2\cos^2(kx) + s^2\sin^2(kx))}}|2\rangle + \frac{1}{\sqrt{2}}|3\rangle$$

The resulting scalar potential for the dark state $|E_0(x)\rangle$ [S5] is

$$V(x) = \frac{\hbar^2}{2M}\sum_{j=\pm}|\langle E_j(x)|\nabla|E_0(x)\rangle|^2 = E_R\frac{s^2\cos^2(kx) + \eta^2\sin^2(kx)}{(1+\eta^2\cos^2(kx) + s^2\sin^2(kx))^2} \tag{S6}$$

When there is no imbalance, $\eta = 0$, we recover Eq. (1) from the main text,

$$V(x;\eta=0) = E_R\frac{s^2\cos^2(kx)}{(1+s^2\sin^2(kx))^2} \tag{S7}$$

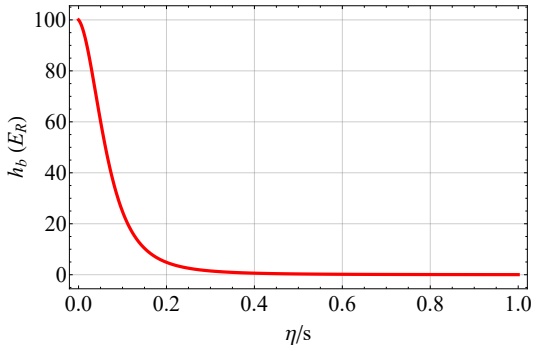

FIG. S3. Growth of the barrier with decrease in η/s.

The barrier height is given by $h_b = V(x=0) = E_R s^2/(1+\eta^2)^2$. In Fig. S3, we show how h_b grows as the imbalance η/s is reduced from 1 to 0 (adiabatically loading into a $100E_R$ lattice). When one of the control beams is turned off, $s^2 = \eta^2$, the potential $V(x)$ is small and spatially homogeneous. Given that our Rabi frequencies $(\Omega_{c1}, \Omega_{c2})$ are balanced to within 2%, the uncertainty in η has negligible effect on the barrier height as $h_b \simeq E_R s^2(1-2\eta^2)$ for $\eta \ll 1$. We also note that the FWHM of the sub-wavelength barriers in the dark state lattice is well approximated by $0.2\lambda\epsilon$ below $\epsilon = 0.3$.

IV. LOADING ATOMS INTO DARK STATE LATTICE AND BANDMAPPING

To adiabatically load atoms into the ground band of the lattice, we first prepare the atoms in $|1\rangle$ by optically pumping using the σ_1^- beam with $\Delta = 12$ MHz. We then change Δ to the final desired value using the BN lock. We ramp on the power of the σ_1^- beam in 0.1 ms and hold for 0.1 ms, followed by ramping on the π beam in 0.3 ms and holding for 0.1 ms. This adiabatically transfers the atoms in $|1\rangle$ into the dark state of the $\sigma_1^- - \pi$ beam configuration. Finally, we ramp on the σ_2^- beam in 1 ms. As discussed in the previous section, this final step ramps the lattice imbalance from $\eta = 1$ to $\eta = 0$, smoothly transforming the potential into the lattice potential.

To find the quasimomentum distribution of the atoms in the dark lattice we perform bandmapping at the end of the experiment by adiabatically ramping down σ_2^- in 0.5 ms (ramping down the barrier height), and then snapping off the σ_1^- beam, the π beam and the optical dipole trap. This maps atoms with given quasimomentum in the lattice to real momentum in free space. We then take an absorption image of this momentum distribution after 12 ms TOF.

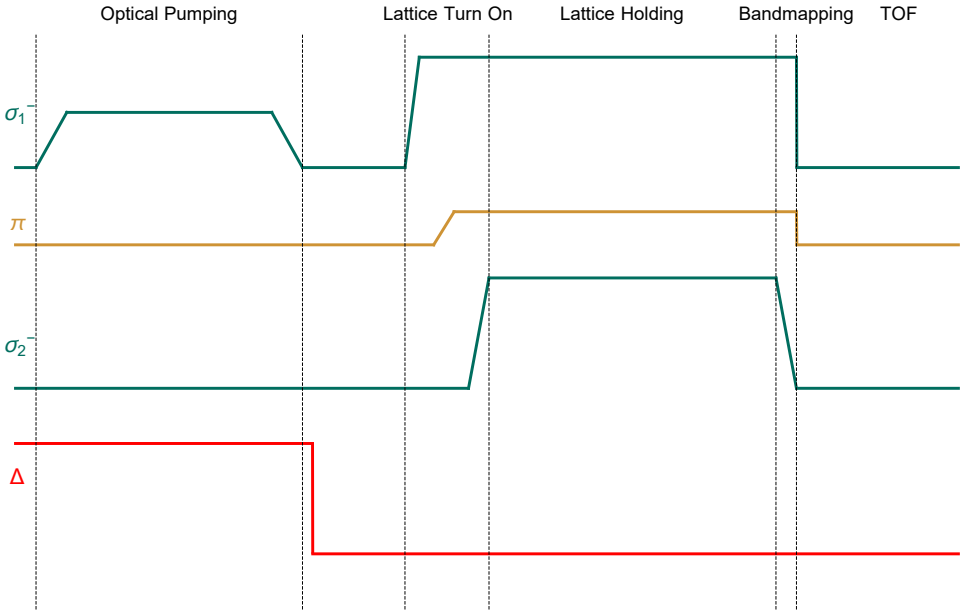

FIG. S4. Procedure to adiabatically load atoms into the ground band of the dark state lattice and performing bandmapping at the end of the sequence.

V. POLARIZATION OPTIMIZATION

The polarization purity of the beams is sensitive to the alignment of the beams, $\vec{k}_p$ and $\vec{k}_{ci}$, with the magnetic field $\vec{B}$. When $\vec{k}_{ci}$ of the circularly polarized control beams is well aligned with $\vec{B}$, the atoms are optically pumped into the trivial dark state, $|1\rangle$. But when the magnetic field is misaligned by an angle θ from $\vec{k}_{ci}$, the resulting π component intensity scales as $\sin^2(\theta)$. The effect of the π component can be investigated in the context of off-resonant EIT. Due to the non-zero ground state Zeeman splitting (89 kHz), the π component and the σ^- component of the control beam are not on two-photon resonance which leads to photon scattering. This causes loss of atoms from the trap. By measuring atom loss as function of the strength of the transverse magnetic field component$(\vec{B}_\perp)$, we adjust $\vec{B}$ such that $\vec{B} \parallel \vec{k}_{c1}$. We then align $\vec{k}_{c2}$ to $\vec{k}_{c1}$ by coupling the σ_2^- beam into the optical fiber that delivers the σ_1^- beam to the atoms with over 50% coupling efficiency.

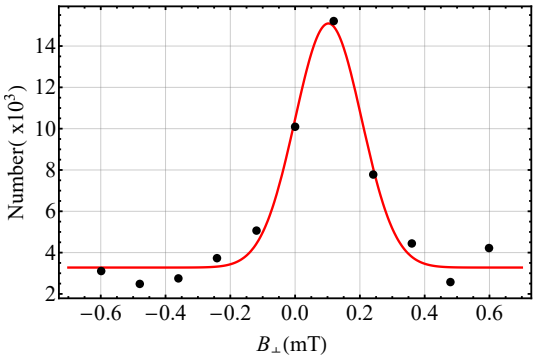

FIG. S5. Atom loss measurement to optimize polarization of σ_1^- beam by scanning the transverse component of magnetic field, $\vec{B}_\perp$.

The polarization of the π beam is optimized by aligning its polarization $\vec{\epsilon_\pi}$ along $\vec{B}$, $\vec{\epsilon_\pi} \times \vec{B} = 0$. This also implies $\vec{k}_p \cdot \vec{B} = 0$ where $\vec{B}$ is the magnetic field that also satisfies $\vec{B} \parallel \vec{k}_{c1}$. We use a Glan-Taylor polarizer to define $\vec{\epsilon}_\pi$. The optimal setting for the polarizer is determined by minimizing loss of atoms from the trap. To satisfy $\vec{k}_p \cdot \vec{B} = 0$, we adjust $\vec{k}_p$ such that the same $\vec{B}_\perp$ satisfies both $\vec{k}_p \cdot \vec{B} = 0$ and $\vec{B} \parallel \vec{k}_{c1}$. We do this via a scheme where we first adjust $\vec{k}_p$ and then perform the measurement we did to make $\vec{B} \parallel \vec{k}_{c1}$ (Fig.S5), but now with the π beam. We iterate this scheme until the $\vec{B}_\perp$ we measure coincides with the $\vec{B}_\perp$ needed to satisfy $\vec{B} \parallel \vec{k}_{c1}$. When the polarization of the π beam is not well aligned with $\vec{B}$, undesired σ component from the π beam causes increased atom loss from the trap. Just as in the case for σ_1^-, this atom loss can be understood in the context of off-resonant EIT. With these techniques, we accurately make $\vec{B} \parallel \vec{k}_{c1}$, $\vec{k}_p \cdot \vec{B} = 0$ and $\vec{\epsilon}_\pi \times \vec{B} = 0$ to within ~ 5 mrad.

VI. LATTICE MODULATION SPECTROSCOPY

We probe the bandstructure of the dark lattice by modulating the phase of the σ_2^- beam with respect to the σ_1^- beam using an analog RF phase-shifter on the RF drive to the AOM for the σ_2^- beam. We transfer atoms from the ground band to the first excited band by shaking the lattice at the appropriate frequency for 200 μs and an amplitude of $\lambda/8$. We then perform bandmapping by ramping down one of the lattice beams in 0.5 ms. We measure the population in each band as a function of modulation frequency and fit a Gaussian to the excited population to extract the transition frequencies.

Since the short lattice shaking pulse is Fourier broadened, we are unable to resolve the quasimomentum dependence of the band excitations when we scan the frequency. We also notice that in order to significantly populate excited bands, a lattice shaking pulse with large amplitude is needed, in contrast to standard sinusoidal lattices where the curvature of band dispersion can be easily resolved with small shaking amplitudes and longer pulse times. In standard sinusoidal optical lattices, the Rabi frequency between a pair of bands is proportional to the shaking amplitude and the lattice depth, and a small shaking amplitude in deep lattices can significantly populate the excited bands. This is in contrast with the KP lattice, where the Rabi frequency is proportional to shaking amplitude, but independent of the barrier height. Larger shaking amplitudes are required to transfer substantial population to the excited bands. In addition, since the wavefunction in the dark state lattice goes to zero at the barriers and the potential is flat elsewhere (where most of the wavefunction lives), the barrier excursion during a lattice shaking pulse needs to be large to diabatically distort the wavefunction between the barriers and hence cause band excitations.

In Figs. 3(a) and 3(b) of the main text, we note that the frequencies of the transitions ($s \to p$ and $s \to p \to d$) measured are slightly lower than the shaded regions. The dipole nature of the coupling due to lattice shaking allows only transitions between bands of opposite parity i.e. $s \leftrightarrow p$ and $p \leftrightarrow d$. The population in the d band arises after some population has been transferred into the p band from the s band, which may affect the resonance spectrum. To better understand this potential systematic redshift of the measured transition frequencies, we employ a model where we map the first three bands (s, p, d) of the dark-lattice to an ensemble of discrete three-level ladder-type systems where the energy spacings trace the curvatures of the bands sampled at various values of q. We solve the full time-dependent Hamiltonian with an appropriate scaling factor for the drive strength and fit the ensemble average of the population in the excited states as a function of lattice shaking frequency to estimate the transition frequencies. These estimated transition frequencies are systematically lower by $\sim E_R/3$ than the average transition frequency between the bands

which, has the same sign as the redshifts observed but is too small to account for all of the shift.

VII. MULTI-LEVEL MODEL

Fig. S1 depicts the three hyperfine states that constitute the Λ-system consisting of $|1\rangle, |2\rangle$, and $|3\rangle$ (black) along with five hyperfine states (grey) that the Λ system is coupled to off-resonantly. Couplings to these off-resonant states affect the bandstructure of the Λ-system. We account for the effect of these off-resonant couplings by adiabatically eliminating the five far off-resonant hyperfine states, which to second ordeer shifts the energies of the ground states of the Λ-system, $|1\rangle$ and $|2\rangle$, by $\delta_1(x)$ and $\delta_2(x)$ respectively.

The Hamiltonian for our effective Λ-system is as follows.

$$H = -\frac{\hbar^2\partial_x^2}{2m} + \hbar \begin{pmatrix} \delta_1(x) & 0 & \frac{\Omega_p}{2} \\ 0 & \delta_2(x) & \frac{\Omega_c(x)}{2} \\ \frac{\Omega_p}{2} & \frac{\Omega_c(x)}{2} & -(\Delta + i\frac{\Gamma}{2}) \end{pmatrix} \tag{S8}$$

Here we use the same treatment to solve this non-hermitian Hamiltonian, as explained in [S6]. As H has the periodicity of λ, we use Bloch's theorem to define the wavefunction that solves H as $\vec{\Phi}(x) = (u_1(x), u_2(x), u_3(x))^T$, where $u_j(x) = \sum_{n=-N}^{n=N} C_{j,q,n} e^{i(q+\frac{2n\pi}{\lambda})x}$ for $j = 1, 2, 3$. Here $u_1(x), u_2(x)$, and $u_3(x)$ represent the atomic wavefunctions for states $|1\rangle, |2\rangle$ and $|3\rangle$ respectively, and q is the quasimomentum such that $q \in [-\pi/\lambda, \pi/\lambda]$. The basis truncation at N must be chosen large enough to correctly capture the non-adiabatic couplings between bright and dark Born-Oppenheimer states at high momenta, and for the typical values of the parameters used in the experiment (e.g. $\Omega_p = 5 - 30\Gamma$, $\Omega_c = 70 - 100\Gamma$, and $\Delta = 2\pi \times 4$MHz), we find $N = 105$ to be sufficient to simulate the bandstructure.

The expressions for the ac-Stark shifts, $\delta_1(x)$ and $\delta_2(x)$, due to off-resonant Rabi couplings are as follows.

$$\delta_1(x) = \delta - \frac{\Omega_p^2}{2\Delta_{\text{HFS}}} - \frac{3\Omega_c(x)^2}{8\Delta_{\text{HFS}}} \tag{S9}$$

$$\delta_2(x) = -\frac{\Omega_p^2}{4\tilde{\Delta}} - \frac{\Omega_p^2}{2\Delta_{\text{HFS}}} - \frac{\Omega_c(x)^2}{8\Delta_{\text{HFS}}} \tag{S10}$$

Substituting the expressions for $\delta_1(x)$ and $\delta_2(x)$ in Eq. (S8) and using the Bloch ansatz we calculate the bandstructure for the Λ system.

The effects of the off-resonant couplings on the dark state ($|E_0(x)\rangle$) can also be understood in the context of perturbation theory. With the perturbing Hamiltonian given by

$$H_{\text{pert.}} = \hbar \begin{pmatrix} \delta_1(x) & 0 & 0 \\ 0 & \delta_2(x) & 0 \\ 0 & 0 & 0 \end{pmatrix} \tag{S11}$$

the first order correction to $V(x)$ is:

$$V_{\text{pert.}}(x) = \langle E_0(x)| H_{\text{pert.}} |E_0(x)\rangle = \hbar \left(\frac{\delta_2 \Omega_p^2}{\Omega_p^2 + \Omega_c^2(x)} + \frac{\delta_1 \Omega_c^2(x)}{\Omega_c^2(x) + \Omega_p^2} \right) \tag{S12}$$

where $|E_0(x)\rangle = \frac{-\Omega_c(x)|1\rangle + \Omega_p|2\rangle}{\sqrt{\Omega_c^2(x) + \Omega_p^2}}$. With independent control over the two-photon detuning (δ), we are able to engineer sub-wavelength traps as depicted in the upper panel of Fig. 3(b) in the main text.

We also note an interesting feature upon simulating the bandstructure for various values of ϵ. As ϵ is decreased from 0.2 to 0.05, we observe that the curvature of the band inverts as shown in Fig. S6. For reference, we also present the bandstructure calculated for just the potential $H = \frac{p^2}{2m} + V(x) + V_{\text{pert.}}(x)$ for each ϵ, represented as black dashed lines. At a particular value of ϵ, which in this case is $\simeq 0.125$, the bandwidth vanishes due to destructive interference between the normal hopping within dark state and the upper bright state assisted hopping implying no tunneling despite barriers having finite width and height.

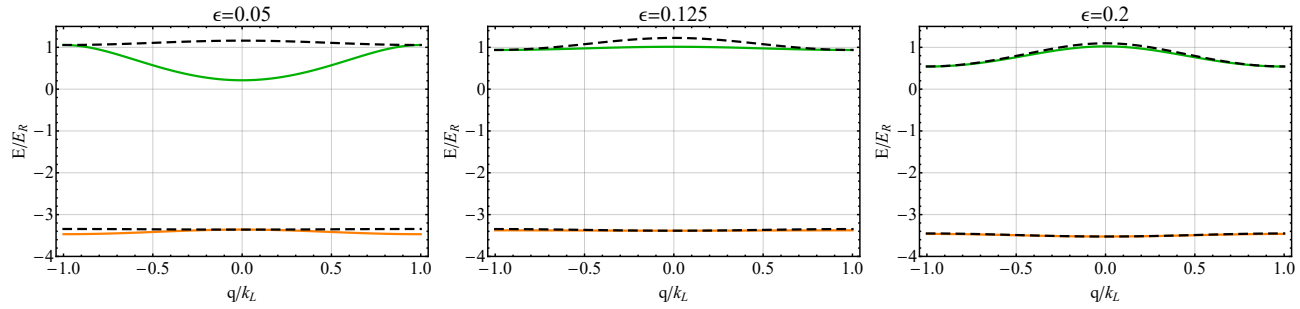

FIG. S6. Change in curvatures of the first two bands of the dark state lattice for different ϵ. Colored lines represent bands for the H given by Eq. (S8) and black dashed lines represent bands for $H = \frac{p^2}{2m} + V(x) + V_{\text{pert.}}(x)$.

VIII. ESTIMATE OF LOSSES BASED ON TRANSMISSION THROUGH A SINGLE BARRIER

In this section, we provide estimates of losses present in our system, based on the analysis of scattering from a single barrier created by $\Omega_c = \Omega_p x/w$, where $w = \epsilon\lambda/(2\pi)$ [S7]. The advantage of this approach is that we can analytically calculate P_{NA}, the probability to lose an atom into state $|E_-\rangle$ from state $|E_0\rangle$ due to non-adiabatic coupling between the states, as well as provide intuitive explanations for P_{sc}, the probability of scattering a photon from state $|3\rangle$. This approach is discussed in Ref. [S7], where P_{NA} and P_{sc} are calculated for $\Delta = 0$. An alternative complementary approach for the estimation of losses is discussed in section IX.

First, we estimate P_{sc} for the case when the detuning $\Delta = 0$. We follow the physical argument from Ref. [S7] to estimate the probability P_e of being in the excited state $|3\rangle$: the dark state probability at $x = 0$ is $\sim |t|^2 \sim E/E_w$, where $E_w = \hbar^2/(2mw^2)$ is the barrier height as well as the strength of the non-adiabatic coupling. The admixture of $|E_-\rangle$ and $|E_+\rangle$ (and hence of $|3\rangle$) is simply $\sim (E_w/(\Omega_p/2))^2$, where E_w plays the role of an effective Rabi frequency and $\Omega_p/2$ plays the role of detuning. Multiplying the two together we obtain $P_e \sim \frac{4EE_w}{\Omega_p^2}$. Then the probability of scattering a photon in a single pass is $P_{\text{sc}} \sim \Gamma P_e 2w/v$, where $2w/v$ is the approximate crossing time for atoms having velocity $v = \sqrt{2E/m}$. In order to estimate the impact of these losses on dark-state lifetime in the lattice, we multiply P_{sc} by the rate $R_{\lambda/2} = v/(\lambda/2)$ with which atoms scatter from the barriers separated by $\lambda/2$. This leads to photon scattering rate $\gamma_{\text{sc}} = c_{\text{sc}} P_{\text{sc}} R_{\lambda/2}$, where the prefactor c_{sc} is on the order of unity. We have confirmed the validity of this expression by numerically calculating the photon scattering rate γ_{sc} from a single barrier as

$$\gamma_{\text{sc}} = \Gamma \frac{\int_{-2w}^{2w} |\psi_e(x)|^2}{\int_0^{\lambda/2} |\psi_{E_0}(x)|^2}, \tag{S13}$$

where $\psi_e(x)$ and $\psi_{E_0}(x)$ are the amplitudes to be in states $|3\rangle$ and $|E_0\rangle$, respectively, for and incoming dark-state plan wave. From comparison with numerical results, we find that the prefactor c_{sc} is approximately 0.9. The second imperfection comes from the nonzero probability P_{NA} of losing the atom into the open $|E_-\rangle$ channel due to the nonadiabatic coupling between $|E_0\rangle$ and $|E_-\rangle$. Based on Ref. [S7], we know that $P_{\text{NA}} \approx 1.37\sqrt{E/E_w} e^{-1.75\sqrt{\Omega_p/(2E_w)}}$. In order to estimate the impact of these losses on dark-state lifetime in the lattice, we multiply P_{NA} by the rate $R_{\lambda/2}$, which leads to the rate $\gamma_{\text{NA}} = 2P_{\text{NA}}\sqrt{2E/m}/\lambda$ of losing atoms into state $|E_-\rangle$.

Using the expressions for γ_{sc} and γ_{NA} found above, we can estimate the decay rate γ_n of the n-th Bloch band dark state by evaluating $\gamma_{\text{sc}} + \gamma_{\text{NA}}$ at $E = E_n$. In order to test the relation between our barrier-based results and the results from a direct lattice calculation more quantitatively, we consider $\gamma_1 = \gamma_{1,\text{sc}} + \gamma_{1,\text{NA}}$ for the lowest Bloch band (subscript 1 indicates the number of the band) for the parameters as in Fig. 3(left) from the supplement of Ref. [S6]. We find good agreement between the lattice-based calculation and the barrier-based calculation, see Fig. S7. Moreover, we see that $\gamma_{1,\text{NA}}$ is much smaller than $\gamma_{1,\text{sc}}$ for the parameters considered; therefore the scaling with Ω_p is given by the scaling of $\gamma_{1,\text{sc}}$. Since, for fixed n, all terms except P_e are Ω_p-independent, the scaling of γ_1 with Ω_p is governed by the scaling of P_e with Ω_p. This gives us a physical explanation for the numerically observed scaling in Fig. 3(left) in the supplement of Ref. [S6], as well as for the scaling of our experimental results, which we comment on below.

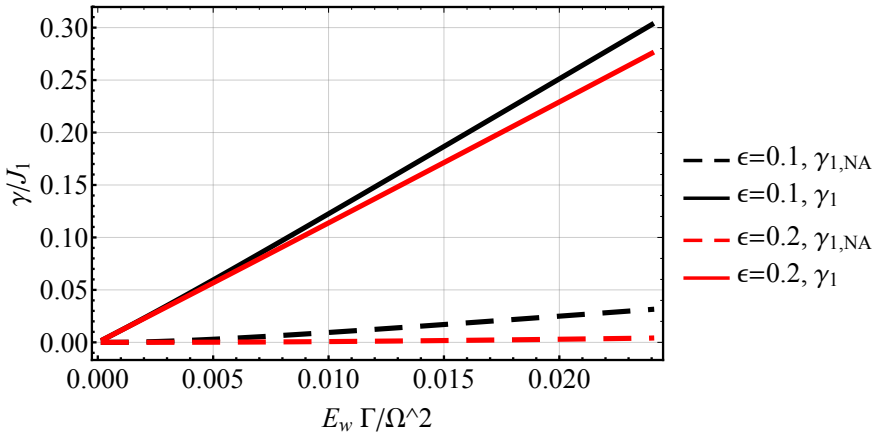

FIG. S7. We plot analytical results for the total decay rate $\gamma_1 = \gamma_{1,\mathrm{NA}} + \gamma_{1,\mathrm{sc}}$ and the non-adiabatic decay rate $\gamma_{1,\mathrm{NA}}$ for the first Bloch band in units of $J_1 = 2\epsilon E_R/\pi^2$ as a function of $E_w\Gamma/\Omega_p^2$ for $\Delta = 0$, $\Gamma = 600E_R$, and two different values of ϵ. Note that the prefactor c_{sc} is fixed using the numerics for a single barrier. For comparison with analogous results for a direct lattice calculation, see Fig. 3(left) in the Supplementary materials for Ref. [S6]. The numerics for a barrier gives the decay rate γ_1 approximately two times greater than the decay from lattice calculations. Note that, for $\epsilon = 0.1$, losses due to P_{NA} become non-negligible.

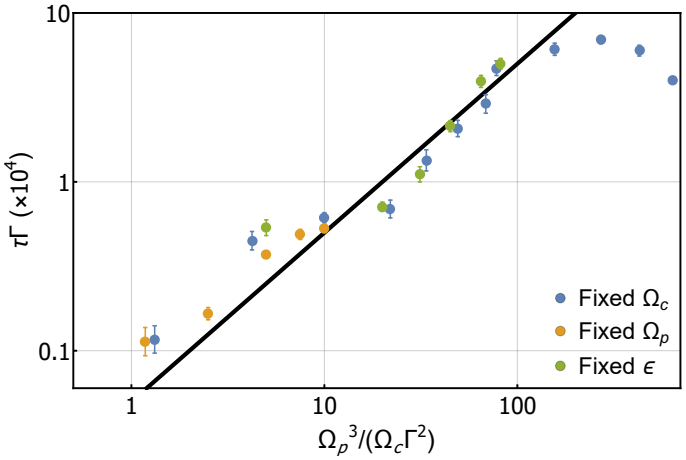

FIG. S8. Lifetime plotted on a log-log scale against the parameter $\Omega_p^3/(\Omega_c\Gamma^2)$ under three conditions: keep $\Omega_c = 100\Gamma$ and scan Ω_p from 5 to 40 Γ (blue); keep $\Omega_p = 5\Gamma$ and scan Ω_c from 12.5 to 100 Γ (orange); and keep $\epsilon = 0.2$ fixed and scan Ω_p from 2.5 to 20 Γ (green). A linear fit $\tau\Gamma \propto \Omega_p^3/(\Omega_c\Gamma^2)$ is also shown (black line).

In Fig. S8, we plot the experimentally observed lifetime as a function of the parameter $\Omega_p^3/(\Omega_c\Gamma^2)$ for different cases where we vary ϵ, Ω_p, and Ω_c. We checked based on barrier numerics for the complete data set that τ has a greater or equal contribution from γ_{sc} than from γ_{NA}. This explains the observed linear scaling over orders of magnitudes of $\tau\Gamma$ with $\Omega_p^3/(\Omega_c\Gamma^2)$. This linear scaling is plotted as a black line in Fig. S8.

Finally, we comment on the dependence of $\gamma_{\mathrm{sc}} + \gamma_{\mathrm{NA}}$ on Δ. In this case, both P_{sc} and P_{NA} are relevant, and the interplay between them describes the results shown in Fig. 4(a) in the main text. For $\Delta < 0$, P_{NA} gives a leading contribution to τ, whereas, for $\Delta > 0$, P_{NA} is negligible and the leading contribution comes from P_{sc}. P_{NA} strongly depends on Δ, whereas P_{sc} is only very weakly dependent on Δ. This explains the observed asymmetry in the dependence of losses on Δ, as explained in the main text. Finally, we numerically confirmed that the results (not shown) based on barrier calculations describe well the quantitative behavior of the losses as a function of Δ and quantitatively agree with the full lattice calculations. The full lattice analysis is presented in the next section.

IX. THEORY FOR LIFETIME MEASUREMENTS BASED ON PERTURBATIONS TO THE DARK STATE

Here we use a direct lattice-based calculation to explain the lifetime in the context of perturbations to the dark state eigenfunction induced by couplings to the bright channels and off-resonant couplings to states outside the Λ-system (Fig. S1). The imaginary part of the dark state eigenenergy determines the scattering rate of the atoms which determine their lifetime in the trap up to a scaling factor. The couplings between the dark and bright channels are small when the energy separations between them are large. As we change Δ, Ω_p, and Ω_c, we alter the admixture of $|3\rangle$ into the dark state and hence the amount of photon scattering. First we discuss the measured lifetime in the context of two beam EIT (inset of Fig. 4(a) in the main text) and then explain the lifetime measurements in the dark state lattice when we scan Δ and Rabi frequencies Ω_p and Ω_c (Fig. 4(a) and Fig. 4(b) in the main text).

When the off-resonant couplings to the Λ-system are neglected the Hamiltonian is given by:

$$H = -\frac{\hbar^2}{2m}\left(\frac{\partial^2}{\partial x^2}+\frac{\partial^2}{\partial y^2}+\frac{\partial^2}{\partial z^2}\right)+\hbar\begin{pmatrix} 0 & 0 & \Omega_p e^{iky}/2 \\ 0 & 0 & \Omega_c(x)/2 \\ \Omega_p e^{-iky}/2 & \Omega_c^*(x)/2 & -\Delta' \end{pmatrix} \tag{S14}$$

with $\Delta' = \Delta + \frac{i\Gamma}{2}$. In the experiment $\Omega_c(x)$ can be either $\Omega_c(x) = \Omega_c e^{ikx}$ with lasers in the homogeneous EIT configuration, or $\Omega_c(x) = \Omega_c \sin kx$ for standing wave case.

A. Homogenous EIT configuration

We first consider the two-beam EIT configuration. In this configuration the non-hermitian Hamiltonian (S14) can be exactly diagonalized by finding a proper biorthogonal basis. The right eigenvectors are indexed by the 3D momentum $\vec{q}$, and are of the form:

$$e^{i\vec{q}\cdot\vec{r}}(ae^{iky}|1\rangle + be^{ikx}|2\rangle + c|3\rangle) \tag{S15}$$

where $(a,b,c)^\dagger$ is a right eigenvector of the matrix:

$$H_{\vec{q},k} = \begin{pmatrix} \frac{\hbar^2}{2m}(q^2+2kq_y+k^2) & 0 & \hbar\Omega_p/2 \\ 0 & \frac{\hbar^2}{2m}(q^2+2kq_x+k^2) & \hbar\Omega_c/2 \\ \hbar\Omega_p/2 & \hbar\Omega_c/2 & -\hbar\Delta'+\frac{\hbar^2 q^2}{2m} \end{pmatrix} \tag{S16}$$

with $q^2 = q_x^2+q_y^2+q_z^2$.

The Hamiltonian $H_{\vec{q},k}$ can be diagonalized analytically, however the resulting expressions are complicated. For the experimental parameters, both $\hbar^2q^2/2m$ and the recoil energy $\hbar^2k^2/2m$ are much smaller than $\hbar\Omega_c$ and $\hbar\Omega_p$, defining small parameters with respect to which one can expand. Expanding up to the second order we get the following expression for the energy of the dark state:

$$E_0 \approx \frac{\hbar^2q^2}{2m}+\frac{\hbar^2}{2m}\left(k^2+\frac{2kq_y\Omega_c^2}{\Omega_c^2+\Omega_p^2}+\frac{2kq_x\Omega_p^2}{\Omega_c^2+\Omega_p^2}\right)-\left(\frac{\hbar^3}{m^2}\right)\frac{4\Delta\Omega_c^2\Omega_p^2k^2\left(q_y-q_x\right)^2}{\left(\Omega_c^2+\Omega_p^2\right)^3}-\left(\frac{\hbar^3}{m^2}\right)\frac{2i\Gamma\Omega_c^2\Omega_p^2k^2\left(q_y-q_x\right)^2}{\left(\Omega_c^2+\Omega_p^2\right)^3}, \tag{S17}$$

with imaginary part $\mathrm{Im}E_0$ Δ-independent. The last two terms in (S17) appear then as a second order correction. It should be mentioned that the imaginary term in Eq. (S17) is a sum of Δ-dependent contributions from the upper and from the lower bright states. In their sum, however, the Δ-dependence disappears.

The other loss mechanism results from off-resonant couplings to the states beyond the Λ-system ($|4\rangle, |5\rangle, |6\rangle$, and $|7\rangle$ in Fig. S1). This additional loss rate is given by

$$\Gamma_{\text{offres.}} = \Gamma\frac{\Omega_p^4}{4\tilde{\Delta}^2\left(\Omega_c^2+\Omega_p^2\right)}+\Gamma\frac{5\Omega_c^2\Omega_p^2+3\Omega_c^4+4\Omega_p^4}{8\Delta_{\text{HFS}}^2\left(\Omega_c^2+\Omega_p^2\right)}, \tag{S18}$$

and is approximately Δ-independent. For the parameters used in the experiment for the EIT configuration we find $\Gamma_{\text{offres.}}$ to be approximately a factor of two smaller than the loss rate from Eq. (S17). We conclude that the combined loss rate in the homogeneous EIT configuration is approximately Δ-independent, in agreement with the results shown in the inset of Fig. 4(a).

B. Standing wave case

We now consider the standing-wave case. In contrast to the homogeneous EIT configuration, the standing wave case does not admit an exact analytic treatment. Although the Hamiltonian (S14) can be diagonalized numerically, to support our numerical results and to get an insight into underlying loss mechanisms, we present below the analysis based on the Born-Oppenheimer (BO) approach (as in Ref. [S6]).

We first diagonalize the atomic part of the non-Hermitian Hamiltonian (S14) (the last term) to find its BO eigenstates: The dark state right eigenvector

$$|E_0(y,x)\rangle = \frac{1}{N_0}\left[(-\Omega_p)\,|2\rangle + \Omega_c(x)e^{iky}|1\rangle\right], \quad N_0 = \sqrt{\Omega_c^2(x)+\Omega_p^2}$$

and the two bright states

$$|E_\pm(y,x)\rangle = \frac{1}{N_\pm}\left[\Omega_c(x)|2\rangle + \left(\Delta' \pm \sqrt{\Omega_c^2(x)+\Omega_p^2+\Delta'^2}\right)|3\rangle + \Omega_p e^{iky}|1\rangle\right],$$

where $N_\pm = \sqrt{2}\sqrt{\Omega_c^2(x)+\Omega_p^2+\Delta'\left(\Delta' \mp \sqrt{\Omega_c^2(x)+\Omega_p^2+\Delta'^2}\right)}$.

The eigenfunctions of the Hamiltonian (S14) can be written as

$$\psi(x,y,z) = e^{iq_z z + iq_y y}\left(f_0(x)|E_0(y,x)\rangle + f_+(x)|E_+(y,x)\rangle + f_-(x)|E_-(y,x)\rangle\right),$$

and the Hamiltonian for the wave functions $f_0(x)$ and $f_\pm(x)$ in the BO basis takes the form (see Ref. [S6])

$$\begin{aligned}
\mathcal{H} = &-\frac{\hbar^2\partial_x^2}{2m} + \frac{\hbar^2 q_y^2}{2m} + \frac{\hbar^2 q_z^2}{2m} + \begin{pmatrix} 0 & 0 & 0 \\ 0 & E_+ & 0 \\ 0 & 0 & E_- \end{pmatrix} \\
&+\frac{\hbar^2}{2m}\frac{\Omega_c'^2(x)\Omega_p^2}{\left(\Omega_c^2(x)+\Omega_p^2\right)^2}\begin{pmatrix} 1 & 0 & 0 \\ 0 & M_+^2+C^2 & 0 \\ 0 & 0 & M_-^2+C^2 \end{pmatrix} \\
&-\frac{i\hbar}{2m}\left(\partial_x\hat{A} + \hat{A}\partial_x\right) \\
&-\frac{\hbar^2}{2m}\frac{\Omega_c'^2(x)\Omega_p^2}{\left(\Omega_c^2(x)+\Omega_p^2\right)^2}\begin{pmatrix} 0 & CM_- & -CM_+ \\ CM_- & 0 & -M_+M_- \\ -CM_+ & -M_+M_- & 0 \end{pmatrix} \\
&+\frac{\hbar^2}{2m}\begin{pmatrix} D_{00} & D_{0-} & D_{0+} \\ D_{0-} & D_{--} & D_{+-} \\ D_{0+} & D_{-+} & D_{++} \end{pmatrix},
\end{aligned} \tag{S19}$$

where

$$E_\pm = \frac{1}{2}\left(-\Delta' \pm \sqrt{\Omega_c^2(x)+\Omega_p^2+\Delta'^2}\right) \tag{S20}$$

and the matrix $\hat{A}$ has the form

$$\hat{A} = -i\hbar\frac{\Omega_c'(x)\Omega_p}{\Omega_c^2(x)+\Omega_p^2}\begin{pmatrix} 0 & -M_+ & -M_- \\ M_+ & 0 & -C \\ M_- & C & 0 \end{pmatrix}.$$

The coefficients

$$C = \Delta'\frac{\Omega_c(x)}{2\Omega_p}\frac{\Omega_c^2(x)+\Omega_p^2}{\Omega_c^2(x)+\Omega_p^2+\Delta'^2}$$

and

$$M_\pm = \left[1 + \frac{2E_\pm(x)}{\Omega_c^2(x) + \Omega_p^2}\right]^{-1/2}.$$

determine couplings between the dark and the bright state manifold, which takes place in the region of subwavelength peaks. They also result in the energy corrections to the bright states [second line, Eq (S19)], which are typically much smaller than $E_\pm$. The matrix in the last line of (S19) originates from the y-dependent phase of Ω_p and has elements

$$D_{00} = \frac{\Omega_c^2(x)k(k+2q_y)}{N_0^2},$$

$$D_{0\pm} = \frac{\Omega_c(x)\Omega_p k(k+2q_y)}{N_0 N_\pm},$$

$$D_{\pm\pm} = \frac{\Omega_p^2 k(k+2q_y)}{N_\pm^2},$$

$$D_{\mp\pm} = \frac{\Omega_p^2 k(k+2q_y)}{N_\pm N_\mp}.$$

Note that D_{00} gives a correction to the dark state non-adiabatic potential, Eq. (1) in the main text, which is small under the conditions of the experiment.

Considering the first two terms in (S19) as a zero-order Hamiltonian (where the dark- and bright state BO channels are decoupled), we define the dark state eigenfunctions $\psi^{E_0}_{(\vec{q},n)}(x,y,z)$ and bright states ones $\psi^{E_\pm}_{(\vec{q},n)}(x,y,z)$, where q_z and q_y are the transverse momenta, $q_x \in [-\pi/\lambda, \pi/\lambda]$ is the lattice quasimomentum, and n being the band index. The corresponding energies are $E_{0,(\vec{q},n)}$ and (complex) $E_{\pm,(\vec{q},n)}$, respectively. Note that q_x, q_y, and q_z are conserved quantum numbers even when the couplings between the BO channels are taken into account, in contrary to n.

We can now consider the couplings between the BO channels [other terms in the Hamiltonian (S19)] perturbatively assuming the gaps between the BO states being much larger than the coupling matrix elements. The finite lifetime of the dark state $\psi^{E_0}_{(\vec{q},n)}$ is given by the imaginary part of the corresponding eigenenergy, which appears in the second order contribution

$$\delta^{(2)}E_{0,(\vec{q},n)} = \sum_{\sigma=\pm}\sum_m \frac{{}_L\langle\psi^{E_0}_{(\vec{q},n)}|\mathcal{H}|\psi^{E_\sigma}_{(\vec{q},m)}\rangle_R\, {}_L\langle\psi^{E_\sigma}_{(\vec{q},m)}|\mathcal{H}|\psi^{E_0}_{(\vec{q},n)}\rangle_R}{E_{0,(\vec{q},n)} - E_{\sigma,(\vec{q},m)}}. \tag{S21}$$

To analyze the Δ-dependence of the imaginary part of $\delta^{(2)}E_{0,(\vec{q},n)}$, we first notice that the largest contributions to the matrix elements $\langle\psi^{E_\sigma}_{(\vec{q},m)}|\mathcal{H}|\psi^{E_0}_{(\vec{q},n)}\rangle$ from the spacial integrals come from the states with eigenenergies close to $\min \mathrm{Re}\epsilon_+$ for the upper bright states, and close to $\max \mathrm{Re}\epsilon_-$for the lower ones. Matrix elements with other states are small because their spatial wave functions are either rapidly oscillating or exponentially suppressed in the coupling regions.

In the red detuned case $\Delta < 0$, the upper bright states are pushed away from the dark ones. This leads to the decrease of the coupling matrix elements with the relevant states because the amplitudes of the internal states $|1\rangle$ and $|2\rangle$ in the upper bright state decrease in favor of $|3\rangle$. On the other hand, the relevant lower bright states are pushed towards the dark ones, with increasing amplitudes of $|1\rangle$ and $|2\rangle$ in its internal structure. In the experiment we have $|\Delta| \lessapprox \Omega_c$ and, as a result, Im $E_{-,\vec{q},n}$ remains approximately unchanged and close to $-\Gamma/4$ for the states close to $\max \mathrm{Re}\epsilon_-$. Therefore, the dominant contribution to $\mathrm{Im}\delta^{(2)}E_{0,(\vec{q},n)}$ comes from the lower bright states and increases with $|\Delta|$, resulting in the decrease of the life-time observed in the experiment, see Fig. 4(a).

In the opposite case $\Delta > 0$, the contribution of the lower dark states decreases, while the contribution of the upper bright states increases and becomes dominant. Here, however, the decrease of imaginary part of $E_{+,(\vec{q},m)}$ dominates over the growth of its real part and over weak increase of the coupling matrix elements, such that $\mathrm{Im}\delta^{(2)}E_{0,(\vec{q},n)}$ decreases with increasing Δ in agreement with the experimental observations.

Finally, we mention that the life-time is an increasing function of Rabi frequencies Ω_c, Ω_p, see Fig. 4(b). This is due to the increase of the gaps to the bright states, while the couplings matrix elements remain practically unchanged.

Connecting Eq. (S21) to the population decay rate is done in the following way: we assume a homogeneous trapped gas with a Fermi-Dirac distribution, where the chemical potential is chosen to fit the total number of particles. For each band index n and quasimomentum $\vec{q}$ the decay rate $\Gamma_{(\vec{q},n)}$ is evaluated by finding the imaginary part of the eigenenergy in Eq. (S21). Since most of the atoms occupy the lowest band of the lattice, we average $\Gamma_{(\vec{q},n)}$ over the lowest three bands to find the average decay rate, which is justified by the fact that the third band almost gives no contribution ($<5\%$). We use the experimentally measured atom number, temperature, and trapping frequencies as the inputs for each data point of Fig. 4, which explains why the theory curve is not smooth in Fig. 4.

[S1] V. D. Vaidya, J. Tiamsuphat, S. L. Rolston, and J. V. Porto, Phys. Rev. A **92**, 043604 (2015).

[S2] S. Subhankar, Y. Wang, A. Restelli, S. L. Rolston, and J. V. Porto, (2018), in preparation.

[S3] J. H. T. Burke, O. Garcia, K. J. Hughes, B. Livedalen, and C. A. Sackett, Review of Scientific Instruments **76**, 11 (2005).

[S4] D. Steck, "Quantum and Atom Optics", available online at http://steck.us/teaching.

[S5] M. Cheneau, S. P. Rath, T. Yefsah, K. J. Günter, G. Juzeliūnas, and J. Dalibard, EPL (Europhysics Letters) **83**, 60001 (2008).

[S6] M. Łącki, M. A. Baranov, H. Pichler, and P. Zoller, Phys. Rev. Lett. **117**, 233001 (2016).

[S7] F. Jendrzejewski, S. Eckel, T. G. Tiecke, G. Juzeliūnas, G. K. Campbell, L. Jiang, and A. V. Gorshkov, Phys. Rev. A **94**, 063422 (2016).

Appendix B: Microcontroller based scanning transfer cavity lock for long-term laser frequency stabilization

Review of Scientific Instruments ARTICLE scitation.org/journal/rsi

Microcontroller based scanning transfer cavity lock for long-term laser frequency stabilization

Cite as: Rev. Sci. Instrum. 90, 043115 (2019); doi: 10.1063/1.5067266
Submitted: 16 October 2018 • Accepted: 30 March 2019 •
Published Online: 22 April 2019

S. Subhankar,[a] A. Restelli, Y. Wang, S. L. Rolston, and J. V. Porto

AFFILIATIONS

Joint Quantum Institute, National Institute of Standards and Technology and the University of Maryland, College Park, Maryland 20742, USA

[a]Electronic mail: sarthaks@umd.edu.

ABSTRACT

We present a compact all-digital implementation of a scanning transfer cavity lock (STCL) for long-term laser frequency stabilization. An interrupt-driven state machine is employed to realize the STCL with the capability to correct for frequency drifts in the slave laser frequency due to measured changes in the lab environmental conditions. We demonstrate an accuracy of 0.9 MHz for master laser and slave laser wavelengths of 556 nm and 798 nm as an example. The slave laser is also demonstrated to dynamically scan over a wide frequency range while retaining its lock, allowing us to accurately interrogate atomic transitions.

I. INTRODUCTION

Many applications require stabilizing the frequency of a laser, and various methods have been developed to lock a laser frequency to a desired value. One of the simplest locking techniques is the scanning transfer cavity lock (STCL),[1–6] in which the stability of a master laser frequency (for example, locked to an atomic transition) is transferred to a scanned Fabry-Pérot cavity, which plays the role of a frequency discriminator, and the slave laser frequency is then stabilized to the cavity. In addition to its simplicity, STCL has a wide capture range and the difference in wavelength between the slave and master lasers can be multiple nanometers. Scanned Fabry-Pérot cavities are common in atomic physics labs, and the optical hardware for STCL is typically readily available.

In this paper, we present an all-digital and cost-effective approach for implementing the STCL. The signal acquisition and processing, detailed in Sec. III, is done digitally in a low-cost Arduino Due development board[7] mounted on a custom shield. This is in contrast to the implementations that use analog circuitry for peak detection[1,3,4] and a dedicated computer for signal acquisition and/or processing.[4–6] We also investigate the effect of the environment on the slave laser frequency[8,9] and present a method that can compensate for this effect to within an accuracy of 0.9 MHz for master and slave laser wavelengths of 556 nm and 798 nm, respectively. We monitor the environment using a low-cost commercially available BME280 sensor breakout board[7] that measures the temperature, pressure, and humidity with an accuracy and precision sufficient for the measurements we present in Sec. V C. This sensor can be integrated to the current hardware design with relevant updates to the current software protocol to provide a compact all-digital STCL with long-term laser frequency stability and accuracy. The particulars of our STCL implementation are detailed in Sec. IV. The GitHub link for the project is https://github.com/JQIamo/Scanning-Transfer-Cavity-Lock.

II. SCANNING TRANSFER CAVITY LOCK TECHNIQUE

The transmission resonances of light through a Fabry-Pérot cavity relate the frequency of the light to the length of the cavity. For a confocal cavity, the resonance frequencies are given by

$$\nu = \frac{Nc}{4nd}, \tag{1}$$

where ν is the laser frequency, N is the longitudinal mode number of the resonance, c is the speed of light, n is the refractive index of the medium inside the cavity, and d is the length of the cavity. For a fixed cavity length, the transmission peaks are spaced by the free spectral range (FSR): $\Delta_{\mathrm{FSR}} = c/4nd$. In our implementation, the length of the cavity is scanned with an amplitude large enough such that the resonant frequency is scanned over a range slightly larger than its FSR. The average cavity length is adjusted to provide three peaks arranged in a Master-Slave-Master ($M - S - M'$) configuration, as shown in

Fig. 1(b). For a linear scan of d with speed α, the arrival time of the peak t_i is given by

$$t_i = (d_i - d_0)/\alpha,$$

where $i = M$, S, or M', d_i is the resonant cavity length, and d_0 is the (arbitrary) cavity length at $t = 0$. Using Eq. (1), we relate the frequencies of the lasers to the arrival times of the peaks and provide signals that can be used to stabilize the average cavity length and the frequency of the slave laser. Drifts in the average cavity length are measured by the position of the first peak of the master laser, t_M, which is used to stabilize d_0. With the average cavity length locked, t_S is then used to stabilize the desired slave laser frequency ν_S to the cavity. In order to remove dependence on the ramp speed α, we use the second peak position of the master laser, $t_{M'}$, forming the ratio

$$r = \frac{t_M - t_S}{t_{M'} - t_M} = \frac{d_M - d_S}{d_{M'} - d_M} = N_M - N_S \frac{n_M \nu_M}{n_S \nu_S}, \tag{2}$$

where n_i is the refractive index of air for light at frequency ν_i and $i = M$, S. The slave mode number N_S is the largest integer smaller than $N_M(n_S\nu_S)/(n_M\nu_M)$ so that $0 < r < 1$. If we define a reference frequency $\nu_{S0} = (\nu_M n_M N_S)/(n_S N_M)$, then the slave frequency $\delta\nu_S = \nu_S - \nu_{S0}$ is given by

$$\delta\nu_S = \nu_M \frac{N_S}{N_M} \frac{n_M}{n_S} \left(\frac{r/N_M}{1 - r/N_M} \right) \simeq \frac{N_S}{N_M} \Delta_{\mathrm{FSR}}\, r, \tag{3}$$

up to order $r/N_M \ll 1$ and n_M, $n_S \simeq 1$. Deviations of r from a chosen lock point r_0 generate the error signal that can be used to feedback to the slave laser.

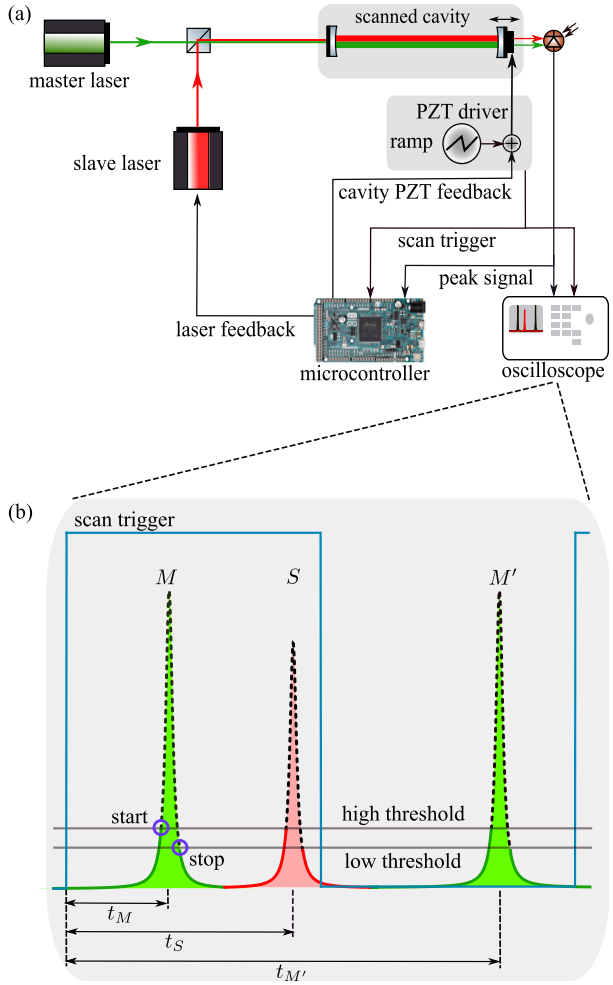

FIG. 1. (a) Schematic of the STCL hardware. (b) Schematic of the STCL peak finding algorithm. The dashed segments of the peaks represent the relevant peak data that are acquired and processed by the μC to determine the arrival times of the peaks, t_M, t_S, and $t_{M'}$. All the arrival times are measured with respect to the rising edge of the scan trigger. The circles pinpoint the start timestamp at high threshold and low timestamp at low threshold, between which peak data of interest (dashed segments) are acquired.

III. SOFTWARE IMPLEMENTATION

In order to lock both the cavity to the master laser and the slave laser to the cavity via t_M and r, the arrival times (t_M, t_S, $t_{M'}$) of the peaks need to be determined during each scan of the cavity length, the respective error signals calculated, and feedback performed via the changes in control voltages to the piezoelectric transducers (PZT) that sets the DC offset for the cavity spacing d_0 and the slave laser frequency. We use an interrupt-driven[10,11] state machine to achieve these tasks.

A. State machine

The flow structure of the interrupt-driven state machine is shown in Fig. 2. It is designed to respond to a series of interrupts generated by hardware (peripherals) or software (software triggered interrupts) which changes the control flow of execution in the program.[10,11]

The functionalities of each state and the conditions for transitions between states are described below:

0. State 0 is the open-loop state. This is the default state of the device upon start-up. In this state, the device output is at the middle of the dynamic range of the feedback voltages. When the lock is engaged, the device transitions into state 1 and the loop is closed engaging feedback. It then returns to this state only when the lock is disengaged.
1. State 1 is the feedback and reset timer state. It is triggered by an interrupt on the rising edge of the scan trigger [Fig. 1(b)] provided by the cavity driver. It updates the control voltages to the slave laser and the Fabry-Pérot cavity that were calculated in the previous cycle, and the system timer is reset. All timestamps are referred to the rising edge of the scan trigger [Fig. 1(b)]. Upon completion, it returns to state 2.
2. State 2 is the data processing and wait state. If returning from state 1, it waits until a peak signal is ready to be sampled. When the signal exceeds the high threshold of the programmed comparison window [Fig. 1(b)], the Analog to Digital Converter (ADC) asserts an interrupt to change the state to state 3. If returning from state 3, it processes the acquired data and waits. Processing involves finding the arrival time of the peak (t_M/t_S/$t_{M'}$) and calculating the new control signals for the cavity and the slave laser feedback. Upon completion, it waits.

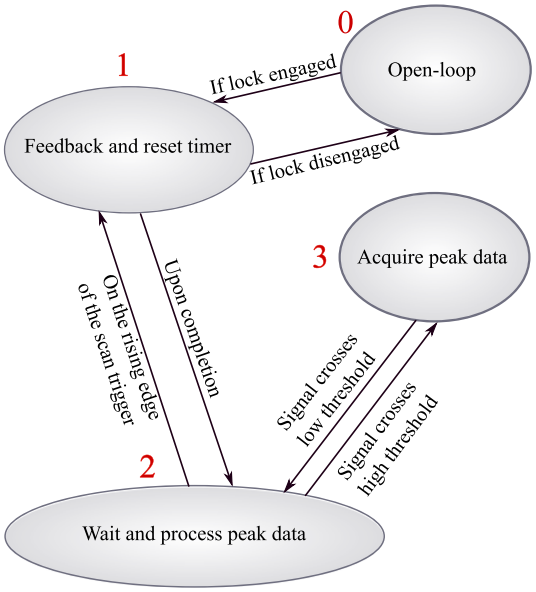

FIG. 2. State machine schematic. The arrows indicate the transitions between states and their directions upon meeting the stated requirements.

3. State 3 is the data acquisition state. The start timestamp is saved, and the data acquisition is initiated. When the peak data crosses the low threshold, the ADC asserts an interrupt which saves the stop timestamp and terminates the data acquisition and returns to state 2. The sampled data are saved in the μC Random Access Memory (RAM) for subsequent processing [dashed segments in Fig. 1(b)].

B. Data acquisition

The transmission peaks are sampled by a 12-bit ADC native to the SAM3x8E μC[7] at 1 Megasamples per second. In order to optimize RAM usage and reduce the need for data filtering of irrelevant data, we only save sampled data near the peak via signal threshold based interrupts in our state machine. We use the direct memory access functionality to rapidly transfer the data of interest directly into a buffer in the μC RAM without any processor intervention. We found that a comparison-window based interrupt [high threshold-low threshold as shown in Fig. 1(b)][11,12] is superior to a single-valued level-triggered interrupt since fluctuations in the peak signal near the threshold spuriously triggered interrupts. This is resolved by setting a sufficient difference between high threshold and low threshold. Depending on the alignment into the cavity, the intensity of the master and slave lasers, and the choice of thresholds, we sample 70–125 points for each peak, approximately 2–3 cavity linewidths.

C. Peak detection algorithm

The position of the maximum of the transmission peak is given by the zero-crossing of the 1st derivative determined by a 5-point digital Savitzky-Golay (SG) filter.[13,14] This filter is an efficient method to smooth the acquired data without significantly distorting the signal while improving the signal-to-noise ratio, which has the following form:

$$Y'_j = \frac{-2y_{j-2} - y_{j-1} + y_{j+1} + 2y_{j+2}}{10}, \tag{4}$$

where y_j = value of the buffer at index j and Y'_j = derivative at buffer position j. This filter can be efficiently implemented using shift operators in the program. Using the zero-crossing timestamps to tag the peaks makes the STCL robust to laser power fluctuations. Upon finding a zero-crossing timestamp (t_M, t_S, or $t_{M'}$), the state machine calculates the error signals and control voltages for the servo loop.

D. Servo loop

The servo loop feeds back on the slave laser and to the cavity PZT to stabilize the cavity length. The zero-crossing timestamps t_M, t_S, and $t_{M'}$ are used to compute the error signal for the cavity and slave laser, which are $t_{M,\mathrm{lock}} - t_M$ and $r_{\mathrm{lock}} - \Delta t_{MS}/\Delta t_{MM'}$, respectively. The control signal ($u(t_y)$) at discrete time t_y is given by the discrete PI filter[15]

$$u(t_y) = u(t_{y-1}) + K_{\mathrm{P}}(e(t_y) - e(t_{y-1})) + K_{\mathrm{I}}e(t_y)\Delta t, \tag{5}$$

where $e(t_y)$ is the error signal at t_y, K_{P} is the proportional gain, K_{I} is the integral gain, Δt is the time it takes to scan the cavity, and $t_y = y\Delta t$, where y is an integer. Updates are performed at the rising edge of the next scan trigger using two 12-bit DACs native to the SAM3x8E μC. Windup is prevented by not updating the value of $u(t_y)$ if $u(t_y) - u(t_{y-1})$ causes the DAC output to fall outside an adjustable range of voltages (the rails).[15]

IV. EXPERIMENTAL SETUP

In our implementation, we use a Thorlabs scanning confocal Fabry-Pérot Cavity, SA200-5B,[7] that has an FSR of 1.5 GHz. The cavity PZT is scanned in a sawtooth fashion with a period of 100 Hz and with an amplitude that scans the resonant frequency of the cavity by 1.2 FSR. The cavity is neither temperature controlled nor sealed or evacuated.

For the master, we demonstrate the lock with two different lasers, one at 780 nm and the other at 556 nm, and for the slave, we use a laser at 798 nm. The λ_M = 780 nm master laser is locked to a saturated absorption feature on the ^{85}Rb $5^2S_{1/2}|F = 3\rangle \leftrightarrow 5^2P_{3/2}|F' = 3\text{–}4\rangle$ crossover signal with a precision of 1 MHz, and the other λ_M = 556 nm master laser is stabilized to the $^1S_0|F = 1/2\rangle \leftrightarrow {}^3P_1|F = 3/2\rangle$ transition in ^{171}Yb with a linewidth of 1 MHz. Once the cavity is stabilized to either of the two master lasers, the slave laser is locked to the cavity, using the ratio r. The locked slave laser at λ_S = 798 nm is the seed input for a Toptica TA-DL SHG pro laser system[7] that generates frequency-doubled light at 399 nm that we use to interrogate the $^1S_0 \leftrightarrow {}^1P_1$ transition in Yb.

V. PERFORMANCE

A. Lock bandwidth

In our implementation, the bandwidth of the lock is limited by the frequency of the cavity PZT scan to 100 Hz. The state machine on the Arduino Due development board can acquire peak data, process the data, and update the feedback output voltages for each ramp of the cavity at a maximum rate of 2 kHz, which is much faster than

the 100 Hz cavity PZT scan. The cavity and the slave laser typically stay locked for a day's operation. The laser lock is robust against acoustic noise in the lab, and when it does unlock, it is due to drifts in the slave laser and not the cavity.

Pound-Drever-Hall locking[16] to a cavity has a much higher bandwidth allowing one to narrow the linewidth of a laser but is more involved as it requires modulating the laser frequency and demodulating the photodiode signal. The STCL is simpler to implement and is intended for stabilization against long-term laser frequency drifts and does not narrow the slave laser (the slave laser in our experiment has an intrinsic short-term laser linewidth of ~100 kHz). The ultimate limit on the bandwidth of the STCL will likely be determined by the speed of the cavity PZT scan.

B. Dynamic setpoint change

The STCL allows us to scan the frequency of the slave laser by changing r. We translate a change in r, Δr, to a corresponding change in frequency of the slave laser, $\Delta\nu_S$, through a scale factor, β. The value of β can be calibrated using atomic transitions or calculated via first principle as follows:

$$r + \Delta r = N_M - N_S \frac{\nu_M}{(\nu_S + \Delta\nu_S)} \tag{6}$$

$$\Longrightarrow \Delta r \simeq \frac{N_S \nu_M}{\nu_S^2}\Delta\nu_S = \frac{4d\lambda_S}{c\lambda_M}\Delta\nu_S = \beta^{-1}\Delta\nu_S, \tag{7}$$

where n_M, $n_S \simeq 1$. With $d = 50$ mm, $\lambda_M = 780$ nm, and $\lambda_S = 798$ nm, $\beta = 1.465$ GHz. In our implementation, it takes 40 ms for the STCL to lock after a sudden jump in its slave laser setpoint r. In principle, since the slave laser response time is much faster than the 10 ms cavity sweep time, by feed-forwarding on the slave laser control voltage, it should be possible to change the slave laser frequency in one cavity sweep.

In Fig. 3, we show the absorption spectrum of the $^1S_0 \leftrightarrow {}^1P_1$ transition in ^{171}Yb obtained by scanning the frequency of the slave laser using the STCL. The linewidth extracted from the fit matches well with the natural linewidth of the transition, indicating that the magnitude of β has been accurately determined.

C. Effect of the environment on the accuracy of the slave laser

The expression for the slave laser setpoint r [Eq. (2)] can be simplified to

$$\begin{aligned} r &= N_M - N_S \frac{n_M \nu_M}{n_S \nu_S} \\ &\simeq N_M - N_S \frac{\nu_M}{\nu_S}[1 + n_M - n_S] \end{aligned} \tag{8}$$

since n_M, $n_S \simeq 1$. Differentiating both sides of the equation yields,

$$\Delta r = N_S \frac{\nu_M}{\nu_S}\left(\frac{1 + n_M - n_S}{\nu_S}\Delta\nu_S - \Delta(n_M - n_S)\right). \tag{9}$$

When the feedback loop is engaged ($\Delta r = 0$), accuracy of the slave laser frequency ($\Delta\nu_S = 0$) is only guaranteed when $\Delta(n_M - n_S) = 0$. The magnitudes of n_i depend on environmental factors like temperature (T), pressure (P), humidity (H), and CO_2 content of air.

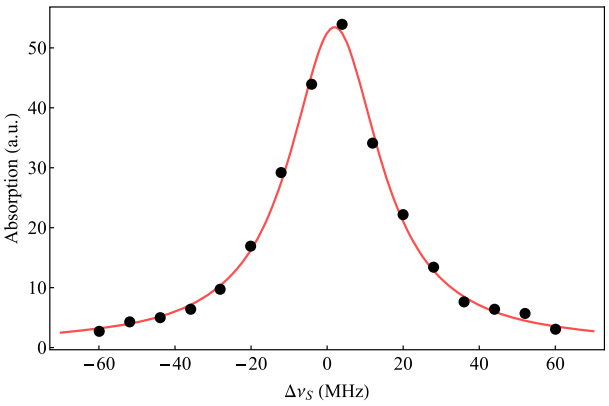

FIG. 3. Absorption spectrum of the $^1S_0 \leftrightarrow {}^1P_1$ transition in Yb as the slave laser frequency is stepped through a chosen frequency range in every experimental realization. The Lorentzian fit to the distribution gives a linewidth $\Gamma = 2\pi \times (28.74 \pm 1.16)$ MHz which is close to the natural linewidth of $2\pi \times 28$ MHz.

Analytic expressions for this dependence of n_i of air on T, P, H, and CO_2 content are presented in Refs. 17–20. Equation (9) indicates that implementation of STCL in a cavity exposed to ambient air, long-term laser frequency stability and accuracy ($\Delta\nu_S = 0$) requires that the setpoint is dynamically changed via feed-forward to account for variations in the lab environment, i.e.,

$$\Delta r = -\frac{N_S \nu_M}{\nu_S}\Delta(n_M - n_S). \tag{10}$$

Feed-forward is ideal for this application since changes in the ambient environmental parameters occur on a timescale of a few minutes, which is much slower than the bandwidth of the lock (10 ms). Along the lines of the work presented in Refs. 8 and 9, we investigate the effect of environmental parameters T, P, and H on the slave laser frequency. The sensitivity of the slave laser frequency's dependence on T, P, or H increases with increasing dissimilarity between the master and slave laser wavelengths.

We use the line center of the $^1S_0|F = 1/2, m_F = 1/2\rangle \leftrightarrow {}^1P_1|F = 3/2, m_F = 3/2\rangle$ transition in ^{171}Yb as an absolute frequency reference (Fig. 3) to determine the value of $\nu_S = \nu_S^0$, where $\nu_S^0 = 751\,527\,368.68(39)/2$ MHz[21] is half the reference transition frequency since we frequency-double our slave laser for the atomic spectroscopy. We measure the effect of the environment [Eq. (10)] by experimentally determining the r that brings the doubled slave laser into resonance with the atomic transition. We quantify drifts in the required r by comparing it to an arbitrary reference r_{ref},

$$\Delta r = -\frac{N_S \nu_M}{\nu_S^0}\Delta(n_M - n_S)$$

$$\Longrightarrow \beta(r - r_{\text{ref}}) = -\nu_S^0[(n_M - n_S) - (n_M - n_S)_{\text{ref}}], \tag{11}$$

$$\Longrightarrow \Delta\nu_{\text{env}} = -\nu_S^0 \Delta n_{\text{diff.}}, \tag{12}$$

where $r_{\text{ref}} = N_M - N_S\nu_M/\nu_S^0[1 + (n_M - n_S)_{\text{ref}}]$ serves as a reference position of the atomic line center under the environmental conditions on an arbitrarily chosen day. In this paper, we have used

the method according to Ciddor[18] (applicable over a wavelength range of 230 nm–1690 nm) to perform all calculations related to the differential refractive index.

The sensitivity of $\Delta\nu_{\text{env}}$ depends strongly on the difference between λ_M and λ_S. From Eqs. (11) and (12), the expected environmentally induced change $\Delta\nu_{\text{env}}$ is given by

$$\Delta\nu_{\text{env}} = -\nu_S^0\Delta(n_M - n_S) = \sum_i -\nu_S^0\frac{\partial(n_M - n_S)}{\partial X_i}\Delta X_i,$$

where X_i is T, P, or H and $-\nu_S^0\partial(n_M - n_S)/\partial X_i$ is the sensitivity coefficient[22] for the parameter X_i. For a given change, ΔX_i,

$$\Delta\nu_{X_i} = -\nu_S^0\frac{\partial(n_M - n_S)}{\partial X_i}\Delta X_i, \tag{13}$$

with the partial derivatives evaluated at T = 22 °C, P = 101 168 Pa, and H = 43.3%, which are the mean values of the environmental parameters we explore in our measurements. In Fig. 4, we plot the frequency shift $|\Delta\nu_{X_i}|$[18] resulting from a specific change of the parameter X_i as a function of λ_M/λ_S. The values of $|\Delta\nu_{X_i}|$ decreases as λ_M/λ_S approaches 1, implying that the closer the wavelengths λ_M and λ_S are to each other, the less sensitive is the accuracy of the slave laser frequency to variations in environmental parameters.

The local lab environment is monitored using a BME280 sensor breakout board placed near the cavity. The sensor board measures the temperature, pressure, and humidity of air which we average over the 8 min it takes to acquire a complete spectrum measurement. Spectrum measurements were taken over the course of a few weeks, during which the lab experienced a range of ambient environmental conditions. The largest contribution to changes in differential refractive index came from weather-related atmospheric pressure changes ranging from 100 323 Pa to 102 224 Pa. Figures 5(a) and 5(b) show the measured change in the lock point r (scaled in frequency units) as a function of the change in the differential refractive index, $\Delta n_{\text{diff.}}$, calculated using the method according to Ciddor[18] with the measured environmental conditions. The solid line in both plots has a slope given by the known resonance frequency ν_S^0 = 751.5/2 THz and is offset vertically in each case to minimize the mean deviation of the points from the line predicted from the environmental conditions. Histograms of the deviations, y_i, from the theory are shown in the insets of Figs. 5(a) and 5(b). The standard deviations are 1.0 MHz and 0.3 MHz, respectively, for the λ_M = 556 nm and λ_M = 780 nm data, suggesting that by using feed-forward based on the environmental measurements, drifts in the slave laser frequency (which typically occurs on the timescale of a few minutes) can be corrected in real time to that level of precision.

For λ_M = 780 nm and λ_S = 798 nm, the values of $|\Delta X_i|$ that induce a $\Delta\nu_{\text{env}}$ = 1 MHz are ΔT = 7.4 °C, ΔP = 2390 Pa, or ΔH = 311%. Such changes in temperature, pressure, or humidity are never observed during the course of any one measurement shown in Fig. 5(b), suggesting that the 0.3 MHz scatter in the 780 nm data is due to the error inherent to our experimental measurement, e.g., the error in fitting to the line center (that is typically 250 kHz for ν_S^0) is due to number fluctuations between successive experimental realizations.

For λ_M = 556 nm and λ_S = 798 nm, the values of $|\Delta X_i|$ that induce a $\Delta\nu_{\text{env}}$ = 1 MHz are ΔT = 0.3 °C, ΔP = 104 Pa, or ΔH = 14.6%. We attribute the increased error of 1.0 MHz in the λ_M = 556 nm measurements to the facts that we do not control the atmospheric pressure in our lab (which can drift during the 8 min spectrum measurement time) and that we do not possess the level of precision in our temperature control needed to correct for

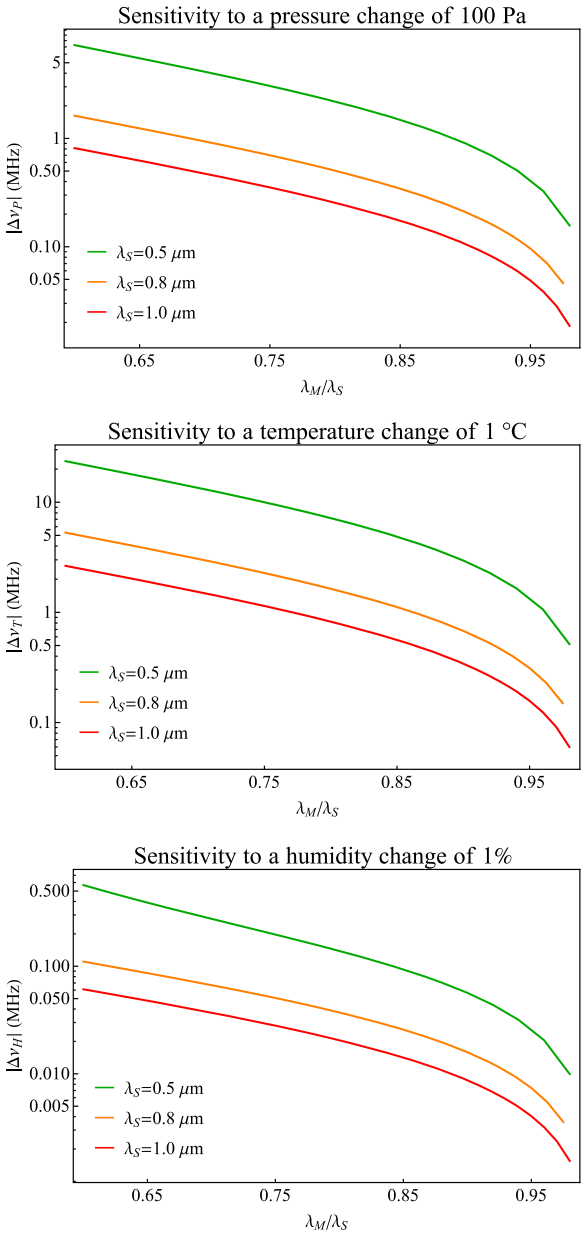

FIG. 4. Calculations of the sensitivity of the slave laser frequency, $\Delta\nu_{X_i}$, to changes in environmental parameters ΔX_i (ΔT = 1 °C, ΔP = 100 Pa, or ΔH = 1%) as a function of master and slave laser wavelengths. The absolute values of the sensitivity coefficients monotonically decrease as λ_M/λ_S approaches 1, implying that the closer the wavelengths λ_M and λ_S are to each other, the less sensitive is the accuracy of the slave laser frequency to variations in environmental parameters.

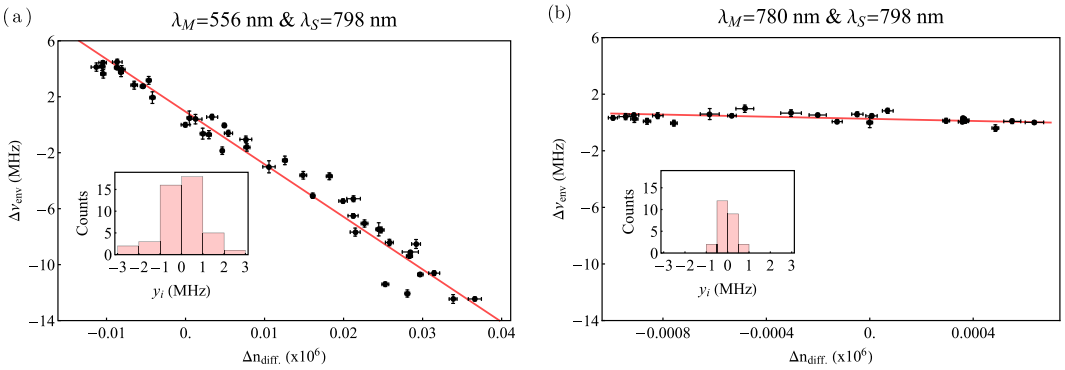

FIG. 5. Measurements of the shifts in the locked slave laser frequency, $\Delta\nu_{env}$, due to changes in the lab environmental conditions: (a) Measurement of the change in setpoint r such that the doubled slave laser is in resonance with the absolute frequency reference (the atomic line center of the $^1S_0|F = 1/2, m_F = 1/2\rangle \leftrightarrow {}^1P_1|F = 3/2, m_F = 3/2\rangle$ transition in ^{171}Yb), as a function of change in differential refractive index, $\Delta n_{diff.}$, determined from measurements of pressure, temperature, and humidity. In this measurement, we use λ_M = 556 nm. The solid line has a slope given by the known value $\nu_S^0 = 751.5/2$ THz. (The offset of the line was chosen to minimize the mean deviation of the measured points from the predicted line.) Error bars along the y axis are given by the fit error in the line center from Fig. 3 and along the x axis by the propagated uncertainty in $\Delta n_{diff.}$ from random fluctuations in measurements from the BME280 sensor breakout board. Inset: Histogram of the deviations of the slave laser frequency, y_i, from the prediction for the λ_M = 556 nm measurements. The deviations are normally distributed with 65% probability and with the standard deviation of 1.0 MHz. (b) The same measurement as in (a), but with λ_M = 780 nm. The range of environmental conditions in this plot correspond to a drift of 13 MHz in (a). Inset: For the λ_M = 780 nm measurements, the deviations, y_i, are normally distributed with 69% probability and with the standard deviation of 0.3 MHz.

fluctuations less than 0.3 °C. In addition, the cavity is susceptible to air currents, and we do not measure the temperature, pressure, and humidity inside the cavity. Subtracting the environment insensitive measurement error of 0.3 MHz in quadrature, we estimate our error due to uncontrolled environmental parameters to be 0.9 MHz.

VI. SUMMARY AND OUTLOOK

We have implemented an all-digital μC-based STCL with environmental monitoring of pressure, temperature, and humidity. The environmental measurements have the precision to compensate for environmental drifts, with appropriate feed-forward to the slave laser setpoint. We demonstrate the capability to compensate for environmentally induced frequency drifts at the 0.9 MHz level for master and slave laser wavelengths of 556 nm and 798 nm as an example. Integration of the environmental sensors into the cavity could improve this performance. Currently, the bandwidth of the STCL is limited by the frequency of the cavity PZT scan (100 Hz). Future implementations of the STCL may include designing custom cavities with PZT scan speeds in the kHz range, thereby increasing the bandwidth.

ACKNOWLEDGMENTS

We would like to thank Tsz-Chun Tsui for his help in data acquisition. This work was supported by NSF PFC at JQI (Grant No. PHY1430094) and ONR (Grant No. N000141712411).

REFERENCES

[1] J. H. T. Burke, O. Garcia, K. J. Hughes, B. Livedalen, and C. A. Sackett, Rev. Sci. Instrum. **76**, 116105 (2005).
[2] B. G. Lindsay, K. A. Smith, and F. B. Dunning, Rev. Sci. Instrum. **62**, 1656 (1991).
[3] S. Wang, J. Zhang, Z. Wang, B. Wang, W. Liu, Y. Zhao, and L. Wang, Chin. Opt. Lett. **11**, 031401 (2013).
[4] N. Seymour-Smith, P. Blythe, M. Keller, and W. Lange, Rev. Sci. Instrum. **81**, 075109 (2010).
[5] A. Rossi, V. Biancalana, B. Mai, and L. Tomassetti, Rev. Sci. Instrum. **73**, 2544 (2002); e-print arXiv:1006.3242.
[6] W. Z. Zhao, J. E. Simsarian, L. A. Orozco, and G. D. Sprouse, Rev. Sci. Instrum. **69**, 3737 (1998).
[7] The identification of commercial products is for information only and does not imply recommendation or endorsement by the Joint Quantum Institute or the National Institute of Standards and Technology.
[8] S. Uetake, K. Matsubara, H. Ito, K. Hayasaka, and M. Hosokawa, Appl. Phys. B: Lasers Opt. **97**, 413 (2009).
[9] K. Matsubara, S. Uetake, H. Ito, Y. Li, K. Hayasaka, and M. Hosokawa, Jpn. J. Appl. Phys., Part 1 **44**, 229 (2005).
[10] E. White, *Making Embedded Systems: Design Patterns for Great Software* (O'Reilly, 2011), Vol. 2011.
[11] J. Yiu, *The Definitive Guide to ARM® Cortex®-M3 and Cortex®-M4 Processors*, 3rd ed. (Newnes, Elsevier, 2013).
[12] See http://www.atmel.com/Images/Atmel-11057-32-bit-Cortex-M3-Microcontroller-SAM3X-SAM3A_Datasheet.pdf for SAM3X/SAM3A Series Atmel—SMART ARM-based MCU; accessed 2015.
[13] H. Mark and J. Workman, "Derivatives in Spectroscopy: Part 4 - Calibrating with Derivatives" in *Chemometrics in Spectroscopy* (Academic Press, 2007), Chap. LVII, pp. 371–378.
[14] R. W. Schafer, IEEE Signal Process. Mag. **28**, 111 (2011).
[15] K. J. Åström and R. M. Murray, *Feedback Systems: An Introduction for Scientists and Engineers* (Princeton University Press, 2008).
[16] R. W. P. Drever, J. L. Hall, F. V. Kowalski, J. Hough, G. M. Ford, A. J. Munley, and H. Ward, Appl. Phys. B **31**, 97 (1983).
[17] B. Edlén, Metrologia **2**, 71 (1966).
[18] P. E. Ciddor, Appl. Opt. **35**, 1566 (1996).
[19] G. Bonsch and E. Potulski, Metrologia **35**, 133 (1998).
[20] K. P. Birch and M. J. Downs, Metrologia **30**, 155 (1993).
[21] M. Kleinert, M. E. Gold Dahl, and S. Bergeson, Phys. Rev. A **94**, 052511 (2016).
[22] D. M. Hamby, Environ. Monit. Assess. **32**, 135 (1994); e-print arXiv:1404.2405.

Appendix C: Nanoscale Atomic Density Microscopy

Featured in Physics

Nanoscale Atomic Density Microscopy

S. Subhankar, Y. Wang,* T-C. Tsui, S. L. Rolston, and J. V. Porto

Joint Quantum Institute, National Institute of Standards and Technology and the University of Maryland, College Park, Maryland 20742 USA

(Received 10 October 2018; revised manuscript received 14 December 2018; published 1 April 2019)

Quantum simulations with ultracold atoms typically create atomic wave functions with structures at optical length scales, where direct imaging suffers from the diffraction limit. In analogy to advances in optical microscopy for biological applications, we use a nonlinear atomic response to surpass the diffraction limit. Exploiting quantum interference, we demonstrate imaging with superresolution of $\lambda/50$ and excellent temporal resolution of 500 ns. We characterize our microscope's performance by measuring the ensemble-averaged probability density of atoms within the unit cells of an optical lattice and observe the dynamics of atoms excited into motion. This approach can be readily applied to image any atomic or molecular system, as long as it hosts a three-level system.

DOI: 10.1103/PhysRevX.9.021002

Subject Areas: Atomic and Molecular Physics, Optics, Quantum Physics

I. INTRODUCTION

High spatial and temporal resolution microscopy can reveal the underlying physics, chemistry, and biology of a variety of systems. Examples range from the study of atoms on surfaces with atomic resolution scanning tunneling microscopy [1] to the use of superresolution microscopy to observe individual molecule dynamics within living cells [2]. The field of quantum simulation with ultracold atoms has emerged to study strongly correlated many-body systems using precise control with light-atom interactions [3]. This entails confining atoms, engineering their interactions and potentials, and measuring their states with laser light. Based on fluorescence and absorption, the inherent imaging resolution is limited by diffraction. Bringing superresolution microscopy to the field of quantum simulation of condensed-matter systems with ultracold atoms will allow new direct probes of the wave function in a variety of many-body systems.

We demonstrate here the imaging of atoms with unprecedented spatial resolution approximately equal to 11 nm that is well below the diffraction limit. Our approach is based on a technique to localize atomic excitation on a subwavelength scale, first proposed by Agarwal and Kapale [4] and first demonstrated by Miles *et al.* [5]. We can directly measure the atomic probability density optically within the unit cell of a 1D optical lattice (scanning electron microscopy has been used to measure such quantities with 150-nm resolution [6]), in contrast to measuring site occupancies [3,7,8]. Far-field microscopy at the nanoscale based on nonlinear optical response is well established [2] to resolve molecular dynamics inside biological samples. Using similar ideas, subwavelength addressing [9] and localized excitation have been proposed [10–16] and observed in atomic systems [5,17]. Based on the dark state associated with a three-level system [5,9–14,16], we coherently shelve narrow slices of the wave function in every unit cell of the lattice into one of the spin states dictated by the local dark state. We selectively read out the total population in that spin state, which is proportional to the local probability density of the lattice wave function. The working resolution (width of the slice) can be adjusted by changing the dark-state composition. The coherent nature of this approach allows us to measure on a timescale much faster than the evolution of the wave function. Our setup can be readily applied to current quantum gas experiments [3]. By dispersively coupling the readout state to a cavity, as suggested by Refs. [16,18], one could perform subwavelength quantum nondemolition measurements.

The principle of our approach is illustrated in Fig. 1 and is similar to Refs. [4,5,16,18]. Assuming adiabaticity, a three-level atom [Fig. 1(a)] coupled by two spatially varying light fields will stay in a dark state, which is decoupled from the excited state $|e\rangle$. This dark state is a superposition of the two ground states with spatially varying amplitudes:

$$|D(x)\rangle = \frac{1}{\sqrt{\Omega_c(x)^2 + \Omega_p^2}}[\Omega_c(x)|g_1\rangle - \Omega_p|g_2\rangle]. \quad (1)$$

*Corresponding author.
wang.yang.phy@gmail.com

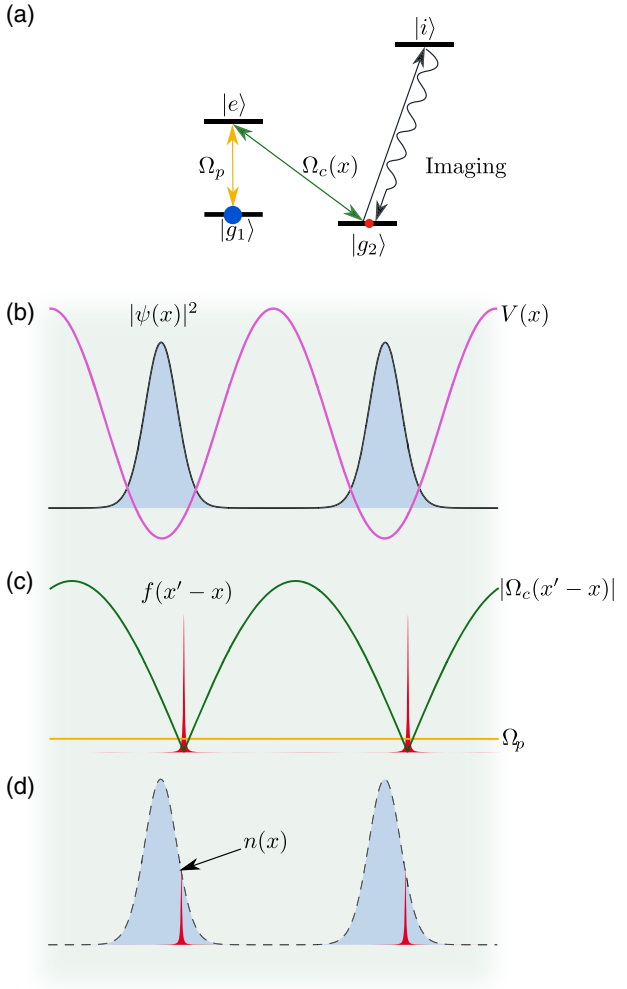

FIG. 1. Principle of our nanoscale atomic density microscope. (a) Configuration of the control field $\Omega_c(x)$ and probe field Ω_p coupling a Λ system composed of $|g_1\rangle$, $|g_2\rangle$, and $|e\rangle$. Population in $|g_2\rangle$ is measured via a cycling transition connecting the imaging state $|i\rangle$. (b) Wave function density $|\psi(x)|^2$ in $|g_1\rangle$ in the lattice of interest $V(x)$. (c) The spin-state composition is transferred to $|g_2\rangle$ near the nodes of $\Omega_c(x'-x)$ with probability given by $f(x'-x)$ (narrow red peaks) and $|g_1\rangle$ elsewhere. The width of $f(x'-x)$ is determined by the relative strength of the two light fields $\epsilon = \Omega_p/\Omega_c$ [see Eq. (2)]. (d) $f(x'-x)$ maps $|\psi(x)|^2$ onto the population in $|g_2\rangle$, $n(x)$, which can be selectively measured via state-dependent imaging. By stepping through different positions x and measuring $n(x)$, we can reconstruct $|\psi(x)|^2$.

Here, we use a standing-wave control field $\Omega_c(x) = \Omega_c \sin(kx)$ and homogeneous probe field Ω_p, where $k = 2\pi/\lambda$, and λ is the wavelength of the light. For $\Omega_c \gg \Omega_p$, the resulting dark-state composition is predominantly $|g_1\rangle$ away from the nodes of $\Omega_c(x)$, and $|g_2\rangle$ near the nodes where $\Omega_p \gg |\Omega_c(x)|$. The probability density of $|g_2\rangle$ [Fig. 1(c)] coming from this nonlinear dependence on the Rabi frequencies [Eq. (1)] is periodic and has narrow peaks near the nodes

$$f(x) = \frac{\epsilon^2}{\epsilon^2 + \sin^2(kx)}, \tag{2}$$

where $\epsilon = \Omega_p/\Omega_c$. The full width at half maximum (FWHM) σ of the peaks provides a good metric for the resolution within the unit cell $\lambda/2$. For $\Omega_c \gg \Omega_p$ (small ϵ), σ depends linearly on ϵ: $\sigma \simeq \epsilon\lambda/\pi$, allowing resolution greatly exceeding the diffraction limit. Starting with atoms in $|g_1\rangle$ with wave function $\psi(x)$, we can adiabatically transfer a narrow slice of atoms into $|g_2\rangle$. The wave-function probability density $|\psi(x)|^2$ [Fig. 1(b)] can be determined by measuring the population transferred to $|g_2\rangle$ at different locations x [Fig. 1(d)], yielding a signal

$$n(x) = \int |\psi(x')|^2 f(x'-x)dx'. \tag{3}$$

By deconvolving this signal with the probing function $f(x)$, we can reconstruct $|\psi(x)|^2$.

We use stimulated Raman adiabatic passage (STIRAP) [19] to transfer the selected slices of the wave function from the state $|g_1\rangle$ into $|g_2\rangle$. In order to accurately measure the shape of the wave function, the STIRAP process must be adiabatic with respect to the spin degree of freedom (d.o.f.) [i.e., the dark-state composition given by Eq. (1)] but diabatic with respect to the motional d.o.f. For small ϵ, the shortest duration of the STIRAP is inversely proportional to the Rabi frequencies. For typical trapped atoms experiments, Rabi frequencies can be tens of megahertz, while the motional dynamics is on the order of tens of kilohertz.

II. EXPERIMENTAL METHOD

We work with the three-level system in ^{171}Yb consisting of $|g_1\rangle = |^1S_0, F = \frac{1}{2}, m_F = -\frac{1}{2}\rangle$, $|g_2\rangle = |^1S_0, F = \frac{1}{2}, m_F = +\frac{1}{2}\rangle$, and $|e\rangle = |^3P_1, F = \frac{1}{2}, m_F = -\frac{1}{2}\rangle$ (see Appendix A), coupled by $\lambda = 556$ nm light. The control field $\Omega_c(x)$ is formed by two counterpropagating σ^--polarized beams $\Omega_{c1}e^{ikx}$ and $\Omega_{c2}e^{-ikx}$ in the direction of the quantization axis defined by a magnetic field along $\hat{x}$, while the probe field Ω_p is a π-polarized traveling wave normal to the control beams [20]. We prepare ^{171}Yb atoms by sympathetically cooling them with ^{87}Rb atoms [21]. After ramping up the magnetic field to 36 mT and removing the Rb atoms, the Yb atoms are optically pumped into $|g_1\rangle$ with a final population approximately equal to 2×10^5. We measure $|\psi(x)|^2$ of spin-polarized Yb atoms loaded into either a Kronig-Penney- (KP) type lattice of thin barriers, as described in Ref. [20], or a regular sinusoidal lattice based on the ac Stark shift of $\Omega_{c1,2}$ off-resonantly coupled to the $|g_1\rangle \leftrightarrow |^3P_1, F = \frac{3}{2}, m_F = -\frac{3}{2}\rangle$ transition, which lies outside the three-level system making up the dark state.

Our microscope is implemented as follows. We first suddenly turn off the lattice potential $V(x)$ that supports the wave function to be probed by switching off the Ω_{c2} beam.

Next, we ramp on Ω_p followed by Ω_{c2} with a different phase, which adiabatically flips the spin from $|g_1\rangle$ to $|g_2\rangle$ in the region tightly localized near the nodes of the shifted $\Omega_c(x'-x)=\Omega_c\sin[k(x'-x)]$. The intensity profiles for ramping these two beams are calculated to preserve adiabaticity, ensuring atoms follow the spatiotemporal dark state at all times. We then rapidly ramp off all beams simultaneously in order to preserve the dark-state composition. We measure the $|g_2\rangle$ population via state-selective absorption imaging. Scanning x in fine steps at small ϵ allows us to map out the $|\psi(x)|^2$ with high resolution.

III. RESULTS

We use our wave-function microscope to investigate atoms in sinusoidal and KP lattices. We start by preparing the atoms in the ground band of the lattice of interest, as described in Appendix B. Figure 2(a) shows $n(x)$ measured in a $140E_R$ sinusoidal lattice using a calculated resolution of 8.8 nm, along with $n(x)$ in a KP lattice with $50E_R$ barriers using a calculated resolution of 17.6 nm. Here, $E_R=\hbar^2k^2/2m$ is the recoil energy, and m is the mass of the atom. The different lattice potentials (sinusoidal vs boxlike KP) give rise to different functional forms of the wave function in the lattice [inset of Fig. 2(a)]. The expected $|\psi(x)|^2$ is Gaussian for a deep sinusoidal lattice and cosine for a KP lattice. The solid lines are the calculated $|\psi(x)|^2$ using independently measured Rabi frequencies including both the resolution due to finite slice width as well as wave-function expansion over the 800-ns measurement time. In Fig. 2(b), we show the FWHM w of the ground-band $|\psi(x)|^2$ of the sinusoidal lattice as a function of the lattice depth. The blue curve represents the calculated width, which is in good agreement with the data. The remaining discrepancy may result from trap inhomogeneities, the uncertainty of the Rabi frequencies, and mechanical effects arising from the nonadiabatic potentials due to the spatially varying dark state [20,22,23].

The fast STIRAP slicing process allows for observing the wave-function dynamics. At our maximum Rabi frequency of $\Omega_c=2\pi\times 90$ MHz and $\epsilon=0.05$, we can maintain the adiabaticity condition for a STIRAP time of 500 ns. Figure 3(a) shows the dynamics of the wave function in a sinusoidal lattice after a sudden shift in the lattice position. The atoms are first adiabatically loaded into a $140E_R$ lattice. Then, the lattice position is diabatically changed in 100 ns by 1/4 of the lattice spacing via the phase of the Ω_{c1} lattice beam, which excites a "sloshing" motion. We map out the evolution of the wave function within the unit cell by holding the atoms in the shifted lattice for incremental periods of time before probing. In Fig. 3(a), we show the measured $|\psi(x)|^2$, which are in agreement with the calculations.

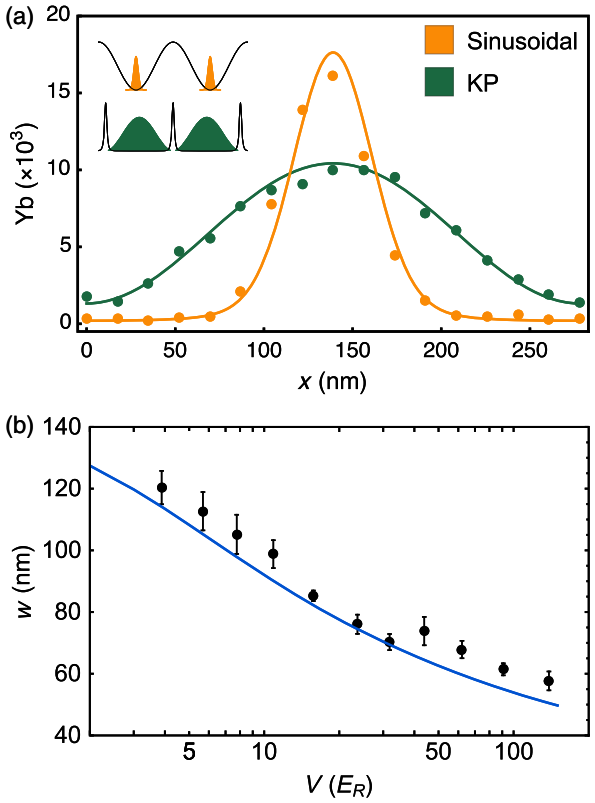

FIG. 2. Measurements of the ground-state wave function within the unit cell of an optical lattice with different shapes. (a) The orange points show $n(x)$ for atoms in a sinusoidal lattice measured with $\epsilon=0.05$. The green points represent $n(x)$ in a Kronig-Penney lattice measured with $\epsilon=0.1$. Number fluctuations between realizations result in number uncertainties of 5%. The solid lines are calculations using measured Rabi frequencies to determine the lattice depth normalized to the same atom number. Inset: Schematic of different lattice potentials and corresponding $|\psi(x)|^2$. (b) FWHM w of $n(x)$ in a sinusoidal lattice as a function of the lattice depth. Black points show experimental data with $\epsilon=0.05$, and the blue line is a calculation including the 800-ns measurement time. The error bars are 1 standard deviation from the Gaussian fits.

The dynamics of the wave function after a sudden change in the lattice depth is shown in Fig. 3(b). The atoms are first adiabatically loaded into the ground band of a shallow lattice ($6E_R$). The depth of the lattice is then suddenly increased to $140E_R$, which excites a "breathing" motion of the atoms inside a unit cell. As time increases, we see that the $|\psi(x)|^2$ breathes at a frequency characterized by the band energies. At $t=3.5$ μs and $t=9.5$ μs, $|\psi(x)|^2$ is focused to calculated $w_0\simeq 26$ nm.

We estimate the spatial resolution of our microscope by measuring the narrowest wave function $|\psi(x)|^2$ that we create with the breathing-mode excitation. This condition occurs at 9.5 μs where the calculated $|\psi(x)|^2$ has

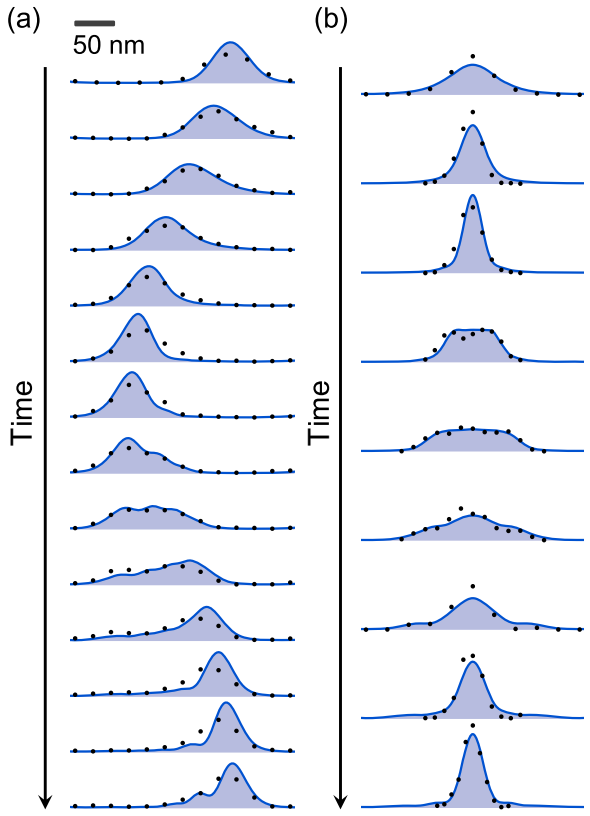

FIG. 3. Wave-function dynamics within the unit cell of an optical lattice. We excite the (a) sloshing motion and (b) breathing motion of $|\psi(x)|^2$ appears to have a wrong scale in a $140E_R$-deep sinusoidal lattice by suddenly changing either the position or the depth of the lattice potential. $n(x)$ is plotted at different hold times [1 to 14 μs in steps of 1 μs for (a) and 1.5 to 9.5 μs in steps of 1 μs for (b)] after the sudden change. The points are experimental data with $\epsilon = 0.05$, and the blue curves represent calculations of $n(x)$ based on the independently measured lattice parameters. Typical number uncertainties are 5% due to fluctuations from shot to shot.

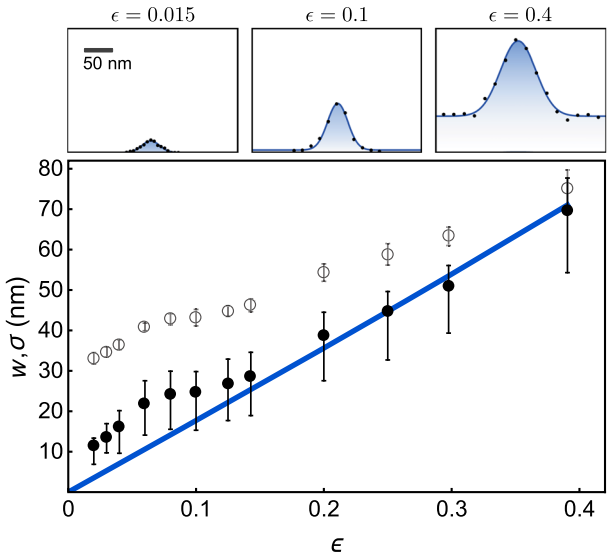

FIG. 4. Spatial resolution of the microscope. We create a narrow wave function $|\psi(x)|^2$ (FWHM 26 nm) by exciting the breathing motion of atoms in a deep sinusoidal lattice and measure $n(x)$ at the focus point [see Fig. 3(b)] as a function of ϵ. The measured w from a Gaussian fit with a vertical offset to the $n(x)$ (see upper panel for typical wave-function measurements) is plotted against ϵ as the gray open circles, with the error bars showing 1 standard deviation from the fitting. These data are then deconvolved with the calculated wave function $|\psi(x)|^2$ to find the intrinsic resolution σ and plotted as the black closed circles. The error bars are dominated by the systematic uncertainties in the width of $|\psi(x)|^2$. The blue curve is the calculated width of $f(x)$ at different ϵ.

$w_0 = 26.2^{+1.6}_{-0.6}$ nm, where the uncertainty arises from the uncertainty in the Rabi-frequency calibrations used to determine the lattice depth. We measure $n(x)$ at this time with different resolution by varying ϵ, as shown in Fig. 4. The measured width w of $n(x)$ is plotted as the gray open circles, which decrease and approach the expected value for small ϵ. Following Eq. (3), by deconvolving the results $[n(x)]$ with the calculated wave function $(|\psi(x)|^2)$ and taking into account the 800-ns expansion time, we estimate the intrinsic resolution σ for different ϵ, which is plotted as the black closed circles. The blue solid line is the calculated width of $f(x)$. The ultimate resolution is possibly limited by mechanical effects arising from the sharp potential associated with the dark state [20,22,23]. As the slice width σ decreases, the total population in $|g_2\rangle$ also decreases, setting a practical limit on the usable resolution, as illustrated by the wave-function measurements shown in the Fig. 4 upper panel. The smallest measured σ reaches $11.4^{+2.0}_{-4.4}$ nm, which could be improved with higher signal-to-noise ratio and Rabi frequencies.

IV. CONCLUSION

We demonstrate superresolution imaging of atomic wave-function probability density with a spatial resolution of $\lambda/50$ and a temporal resolution of 500 ns. This imaging technique (demonstrated here on an ensemble of atoms) can be extended to single atoms by averaging over multiple realizations. The dark-state-based technique can be applied to image any atomic or molecular system as long as they host a three-level system, including the alkali atoms that are used in many experiments. Such high spatial and temporal resolution microscopy provides a new tool to address ultracold atom simulations of condensed-matter systems, especially phenomena associated with higher momenta and energies. For instance, the temporal resolution will allow us to measure the rapid dynamic evolution of the wave functions in periodically driven Floquet systems [24]. The spatial resolution of the technique could allow one to probe density fluctuations due to phonon and vortex excitations in a nonlattice cold atom system, which can be the size of the healing length (typically submicron) [25,26]. It is also useful

in probing lattice systems with higher band population either intentionally populated to exploit the orbital d.o.f. [27,28] or due to band mixing from strong interactions [29]. As demonstrated in Fig. 3, our subwavelength resolution already allows us to distinguish the different atomic wave functions trapped in lattices with different subwavelength structure. Such a resolution will be critical in the study of optical lattices with lattice constants $\lambda/2N$ created through stroboscopic techniques [30], which is advantageous for studying many-body physics since the energy scale is N^2 times larger than a typical $\lambda/2$ lattice. Finally, while the imaging technique demonstrated here measures the wave-function probability density, the coherence of the dark-state selection process could allow for measurement of the local wave-function phase as well.

ACKNOWLEDGMENTS

We thank Victor M. Galitski, Alexey V. Gorshkov, and Przemyslaw Bienias for fruitful discussions. We also want to thank Carlos Bracamontes Palma for DDS/FPGA hardware development. This work is supported by NSF Physics Frontier Center, PFC@JQI (PHY1430094) and ONR (Grant No. N000141712411).

S. S. and Y. W. contributed equally to this work.

Note added.—Recently, we became aware of similar work from Cheng Chin's group [34].

APPENDIX A: ^{171}YB ATOM LEVEL STRUCTURE

We measure the Yb atoms by absorption imaging on the $^1S_0 - {}^1P_1$ transition with light at 399 nm generated by a frequency-doubled laser system. We stabilize the seed of the imaging laser (at 800 nm) via a scanning transfer cavity lock [31,32] with the master laser locked to a saturated absorption feature on the ^{85}Rb $|5^2S_{1/2}, F = 3\rangle \leftrightarrow |5^2P_{3/2}, F' = 3\text{–}4\rangle$ crossover signal. State selectivity is achieved by imaging in a large magnetic field of 36 mT along $\hat{x}$, such that the resulting 440-MHz separation between the $|6\rangle$ and $|7\rangle$ Zeeman sublevels of $^1P_1$ is much larger than the linewidth $\Gamma_{^1P_1} = 2\pi \times 27.9$ MHz. The imaging beam propagates along $\hat{x}$ with σ^+ polarization relative to $\vec{B}$. We measure the population in the $|g_2\rangle$ hyperfine ground state by making the laser resonant with its respective stretched state, $|g_2\rangle \leftrightarrow |6\rangle$ for 10 μs. Optical pumping of atoms in $|g_1\rangle$ into $|g_2\rangle$ via $|7\rangle$ is suppressed by a factor of over 3000 due to the 440-MHz detuning and the short imaging time.

Figure 5 depicts the three hyperfine states that constitute the Λ system consisting of $|g_1\rangle, |g_2\rangle$, and $|e\rangle$ that we use to generate the KP lattice and to probe the wave function of arbitrary lattices. We create the off-resonant sinusoidal ac-Stark-shift lattices using the $|g_1\rangle \leftrightarrow |5\rangle$ transition with the lattice depth given by $3\Omega_c^2(x)/8\Delta_{\mathrm{HFS}}$. The effect of this off-resonant lattice is negligible when the atoms are in the KP

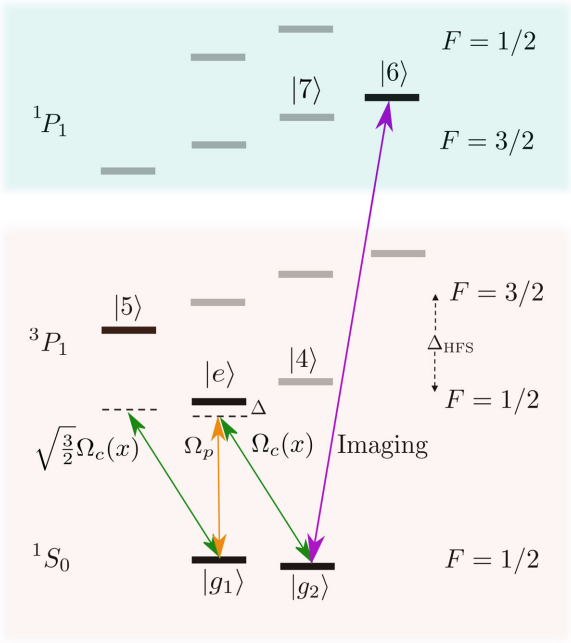

FIG. 5. Level structure of the $^1S_0$, $^3P_1$, and $^1P_1$ manifolds of ^{171}Yb: Δ is the single-photon detuning and $\Delta_{\mathrm{HFS}} \sim 6$ GHz is the $^3P_1$ hyperfine splitting.

lattice with $\Omega_c = 70\ \Gamma$ and $\Omega_p = 10\ \Gamma$, where $\Gamma = 2\pi \times 182$ kHz is the inverse lifetime of $^3P_1$. The method we use to calibrate our Rabi frequencies is detailed in Ref. [20].

APPENDIX B: EXPERIMENTAL SEQUENCE

Preparation and experimental sequence: Before the start of each experimental sequence, the atoms are optically pumped into $|g_1\rangle$.

Stage I: To simplify the study of the static and dynamics properties of wave functions in lattices, we prepare our atom cloud to fill only the ground band of the lattice of interest. Since the Fermi energy of our atomic cloud is approximately $3E_R$, adiabatic loading into the lattice will have some population in the first excited band. We resolve this issue by first loading atoms into a KP lattice with $\epsilon = 0.14$ ($\Omega_{c1} = \Omega_{c2} = 35\ \Gamma$, $\Omega_p = 10\ \Gamma$, and $\Delta = 4$ MHz) [20] and then holding for 5 ms. Atoms in higher bands of the KP lattice have a shorter lifetime and are lost from the trap, effectively removing atoms in the higher bands.

Stage II: In this stage, we adiabatically transfer atoms from the ground band of the KP lattice into the ground band of an ac-Stark-shift lattice in 10 ms. Δ is ramped down to 0, which is important in achieving the maximum speed while adiabatically following the dynamic dark state in stage IV.

Stage III: In this stage, we excite dynamics in the lattice. In Fig. 6(c), the phase of the Ω_{c1} beam is ramped to 90° in 100 ns, so as to diabatically shift the position of the lattice by $\lambda/8$ which induces sloshing dynamics. In Fig. 6(d), the lattice depth is suddenly increased from $6E_R$ to $140E_R$,

and the atoms are held in the deep lattice for different times (1.5 to 9.5 μs) to study the breathing motion.

Stage IV: In this stage, we measure the wave function. First, Ω_{c2} is suddenly turned off to 0, while Ω_{c1} is set to 250 Γ. Then, the Ω_p beam is suddenly turned on to its desired value. Because of the large energy separation of 125 Γ ($\Omega_{c1} = 250\ \Gamma$ and $\Omega_p = \Omega_{c2} = 0$) between the dark and bright states, the adiabatic following of the dark state is guaranteed during the turn-on of the Ω_p beam. Then Ω_{c2} beam is turned on with a different phase ϕ_{c2} implemented by changing the phase of the rf drive to the acousto-optic modulator (AOM), with the amplitude being ramped up to 250 Γ with the optimal waveform so as to preserve the adiabaticity during the ramp. By scanning ϕ_{c2} from 0° to 360°, we change the position of the node of $\Omega_c(x) = 500\Gamma\cos(kx)$, thereby mapping out the probability amplitude of atoms in each spatial slice of the wave function.

Stage V: Finally, the lattice beams are ramped off simultaneously in 100 ns by switching off the rf drive to the AOMs. Since the dark-state composition depends only on the ratio $(\Omega_{c1} + \Omega_{c2})/\Omega_p$ and not on the absolute magnitude of the Rabi frequencies, simultaneous ramp-off of the lattice beams preserves the dark-state composition until the atoms are imaged.

APPENDIX C: HARDWARE CONTROL

In order to generate the experimental sequences described earlier, we need to have fine, high-bandwidth control over the amplitude and phase of the light fields Ω_{c1}, Ω_{c2}, and Ω_p. This control is achieved by using a home-built field-programmable-gate-array- (FPGA; Spartan 6) controlled direct-digital-synthesis- (DDS; AD9910) based rf signal generator. We use three such devices to drive three AOMs for the light fields. Phase coherence between the light fields is ensured by having the devices be clocked by the same 10-MHz clock source and having the light fields be derived from the same laser. Each device generates an 80-MHz rf carrier signal with arbitrary amplitude and phase and imprints that onto the light via its respective AOM. The DDS can update the phase of the rf signal every 4 ns. The desired amplitude waveform (AW) is loaded into the local RAM of the FPGA of the device and is updated at a maximum update rate of 8 ns. The maximum length of the AW pulse is approximately 256 μs when updated every 8 ns.

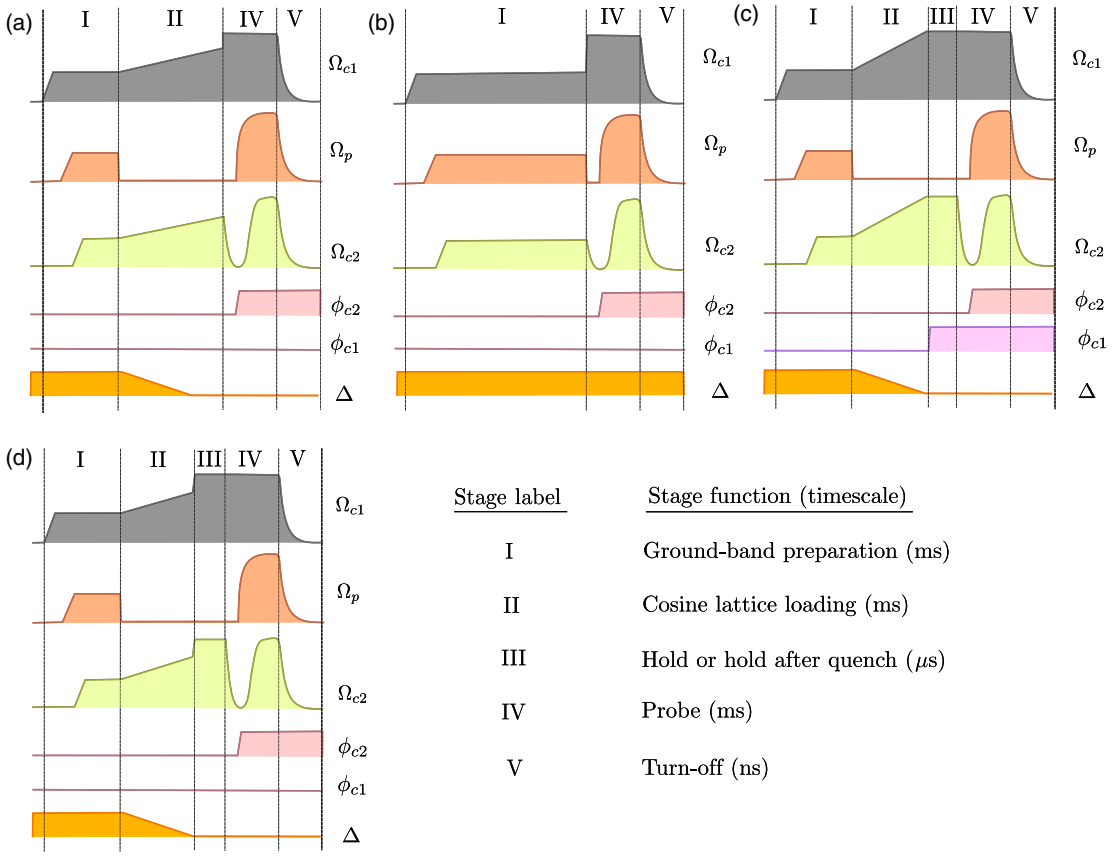

FIG. 6. Experimental sequences. (a) Probing the ground-state wave function of a sinusoidal lattice. (b) Probing the ground-state wave function of a KP lattice. (c) Probing the dynamics after a sudden change in the lattice position. (d) Probing the dynamics after a sudden change in lattice depth. The drawings are not to scale.

APPENDIX D: OPTIMAL AMPLITUDE WAVEFORM FOR STIRAP

During stage IV, we adiabatically transfer atoms from $|1\rangle$ to $|2\rangle$ near the node of $\Omega_c(x)$ via STIRAP [19]. For an ideal Λ system, the local adiabatic criterion is given by Ref. [19] as $\Omega_{\rm rms} \gg |\Omega_c\dot{\Omega}_p - \dot{\Omega}_c\Omega_p|/\Omega_{\rm rms}^2$, where $\Omega_{\rm rms}=\sqrt{\Omega_c^2+\Omega_p^2}$ (at $\Delta=0$) is the energy gap between the dark and bright eigenstates and the rhs is the off-diagonal coupling between them. We define an adiabaticity parameter r,

$$\Omega_{\rm rms} = r\frac{|\Omega_c\dot{\Omega}_p - \dot{\Omega}_c\Omega_p|}{\Omega_{\rm rms}^2}. \tag{D1}$$

A larger value of r implies a more adiabatic but slower transfer. The equation is solved to give an optimal shape of Ω_{c2} near the node of $\Omega_c(x)$ (Ω_{c1} and Ω_p are kept constant here) for stage IV:

$$\Omega_{c2}(t) = \Omega_{c1} - \Omega_p\frac{\left(\frac{\Omega_{c1}}{\sqrt{\Omega_{c1}^2+\Omega_p^2}} - \frac{\Omega_p t}{r}\right)}{\sqrt{1-\left(\frac{\Omega_{c1}}{\sqrt{\Omega_{c1}^2+\Omega_p^2}} - \frac{\Omega_p t}{r}\right)^2}}. \tag{D2}$$

The time it takes to finish the $\Omega_{c2}(t)$ ramp is

$$T_r = \frac{r}{\Omega_p}\frac{1}{\sqrt{1+4\epsilon^2}}. \tag{D3}$$

For a typical value of $r=15$, $\Omega_{c1}=250\ \Gamma$, and $\Omega_p = 25\ \Gamma$, T_r is 0.52 μs; see Fig. 7. For a given spatial resolution determined by ϵ, more available laser power will reduce T_r and increase the temporal resolution.

We experimentally investigate the minimum r required to ensure adiabatic following of the dynamic dark state. We do this by keeping r fixed and measuring the temperature of the cloud after STIRAP pulses. If the adiabaticity is not well satisfied, the nonzero probability of atoms being in the excited state $|e\rangle$ leads to scattering which increases the temperature of the atoms. To increase the sensitivity of the measurement, we apply ten successive STIRAP pulses. This study is performed with only one control beam Ω_{c2} and the probe beam Ω_p. In each pulse, Ω_{c2} is ramped up from 0 to 250 Γ and then ramped down to 0 following the optimal waveform described by Eq. (D1). After ten cycles, the temperature of the cloud is measured, and the results are shown in Fig. 8(a). One can see that beyond a certain value of r, the STIRAP process becomes adiabatic; i.e., the temperature is independent of r, which occurs at about $r=15$ for $\Omega_p = 50\ \Gamma, 25\ \Gamma$. Below $r=15$, the local adiabaticity criterion breaks down. During the probe stage in Fig. 6, we use $r=15$ in Eq. (D2) to calculate the optimal AWs.

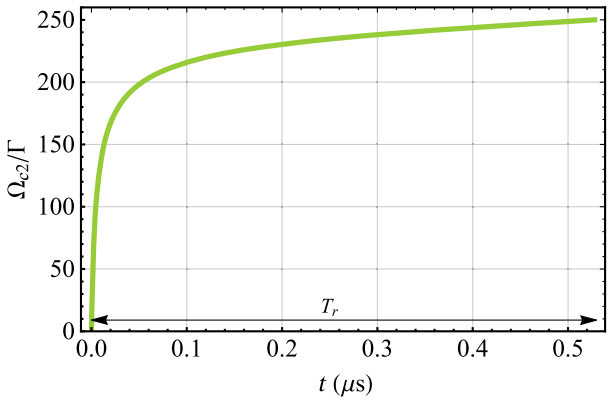

FIG. 7. The optimal amplitude waveform for $\Omega_{c2}(t)$ for $\Omega_{c1}=250\ \Gamma$, $\Omega_p = 25\ \Gamma$.

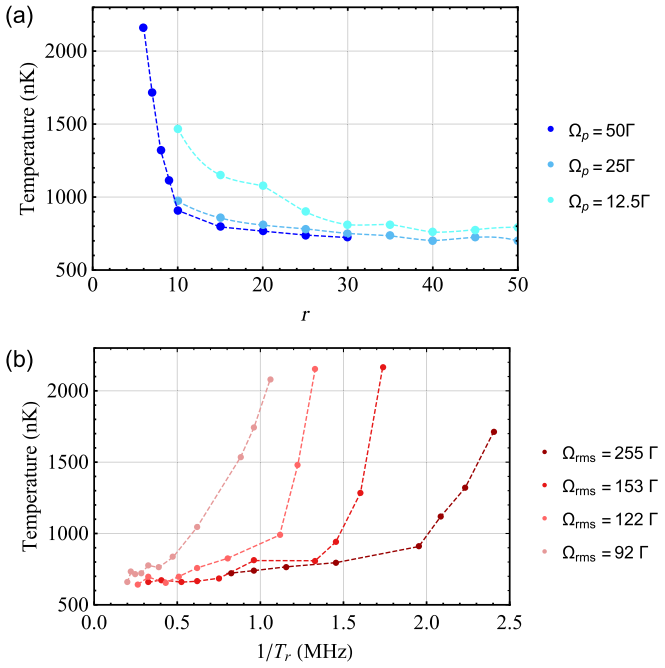

FIG. 8. (a) The temperature of the atoms after ten complete STIRAP pulses for different values of r and Ω_p and (b) different values of $\Omega_{\rm rms}$ and T_r

The energy gap between the dark and bright eigenstates increases with increasing $\Omega_{\rm rms}$, which reduces T_r needed to ensure adiabaticity. We study this effect by keeping the ratio of $\Omega_p/\Omega_{c2}=0.2$ constant while $\Omega_{\rm rms}$ is varied. As shown in Fig. 8(b), with larger $\Omega_{\rm rms}$, faster ramp speed can be achieved while still being adiabatic.

APPENDIX E: PRESERVING THE DARK-STATE COMPOSITION DURING RAMP-OFF

The ramp-off stage of the lattice beams is crucial for our measurement since it must preserve the dark-state composition generated during the probing stage. We achieve this requirement by ramping down the light fields simultaneously while maintaining a fixed ratio between the Rabi frequencies $\Omega_{ci}(t)/\Omega_p(t)$, where $i=1, 2$. The dark-state composition is thus preserved, as it depends only on the ratio and not on the absolute magnitudes of the Rabi frequencies. For the typical Rabi frequencies we use in the experiments, the relative delay between the light fields

needs to be less than 20 ns to preserve the dark-state composition. The ramp-off must be diabatic with respect to the mechanical d.o.f. of the wave function. This is guaranteed by turning off the rf drive to the AOMs simultaneously in 100 ns.

Experimentally, simultaneous turn-off of the light fields between different AOMs is not guaranteed, as delays may exist due to the laser light hitting the AOM crystals at different distances from their respective piezoelectric transducers. With our best alignment of the AOMs, we reduce the delay of the light fields to within 60 ns of each other. This remnant delay at the atoms is compensated by delaying the digital trigger that turns off the rf drive to an AOM. We accurately measure the turn-off delays between the light fields at the atoms using the method shown in Fig. 9(a). Sweeping t_{shift} of the digital trigger, thereby changing $\Delta t = t_{\text{shift}} - t_{\text{delay}}$, we measure the atom number in $|g_2\rangle$ using state-selective imaging. We are able to change t_{shift} at picosecond timescales using a delayed-pulse generator (SRS DG535). When $\Delta t < 0$, the spin composition of the dark-state wave function is $|g_1\rangle$. But as $\Delta t \geq 0$, the dark-state composition starts to become predominantly $|g_2\rangle$ with increase in Δt as shown in Fig. 8(b). By fitting a line to the data, we get the time at which the dark-state spin composition just starts to change from $|g_1\rangle$ to $|g_2\rangle$. The $|g_2\rangle$ component of the dark state is close to 0 for the Rabi frequencies used in the measurement when $\Delta t = 0$. By measuring these delays for each pair of beams Ω_{c1} and Ω_p, Ω_{c2} and Ω_p, we can compensate them via adjusting the lengths of the BNC cables of the digital trigger to the rf sources.

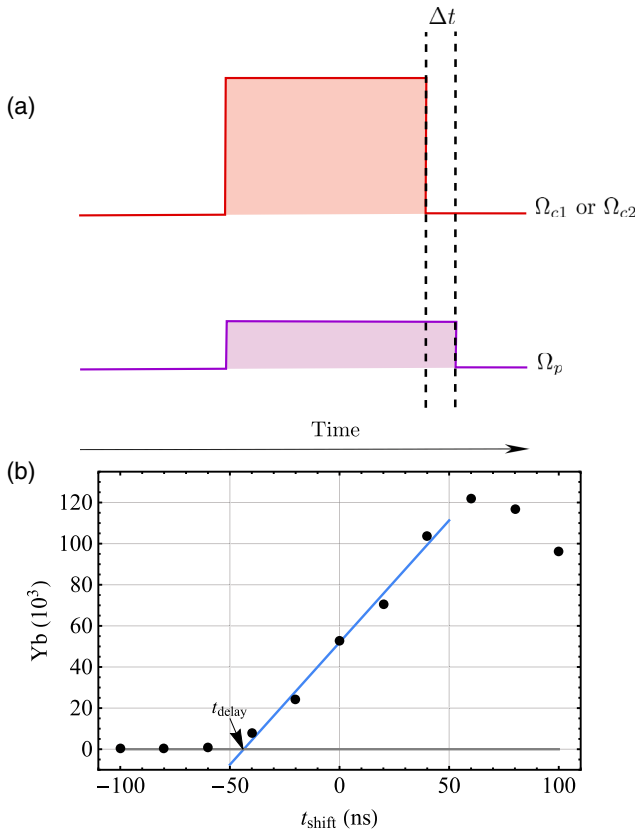

FIG. 9. (a) Optical pulse sequence used to optimize the temporal overlap between the Ω_{ci} and Ω_p light fields. (b) The population of the atoms in the $|g_2\rangle$ state as a function of t_{shift} with $\Omega_{c1} = 250\ \Gamma$ and $\Omega_p = 50\ \Gamma$.

Another approach to ensure that the dark-state composition does not change is to turn off the light fields *diabatically* with respect to the spin d.o.f. of the dark-state wave function. As the Rabi frequencies of the light fields are in the range of hundreds of megahertz, the turn-off time must be less than 10 ns. It is challenging to achieve such turn-off times with AOMs, but one could use electro-optical modulators instead.

APPENDIX F: THEORY AND CALCULATION

The eigenfunctions of atoms in an optical lattice are given by the Bloch ansatz as $\phi_q(x) = e^{iqx}u_q(x)$, where $u_q(x) = u_q(x+a), q \in [-k, k]$ is the quasimomentum, and a is the periodicity of the lattice. The field operator for a spin $|\sigma\rangle, \Psi^\dagger_\sigma(x)$, and the total field operator for a spin-1/2 particle in a lattice $\Psi^\dagger_S(x)$ is given as [33]

$$\Psi^\dagger_\sigma(x) = \sum_{q=-k}^{q=k} \phi^*_q(x) c^\dagger_{q\sigma},$$

$$\Psi^\dagger_S(x) = [\Psi^\dagger_{|g_1\rangle}(x), \Psi^\dagger_{|g_2\rangle}(x)]^T,$$

where $\{c_{q\sigma}, c^\dagger_{q'\sigma'}\} = \delta_{qq'}\delta_{\sigma\sigma'}$.

Before stage IV, all atoms are in $|g_1\rangle$ as the trivial dark state which is represented by the total field operator $\Psi^\dagger_S(x) = \Psi^\dagger_{|g_1\rangle}(x)(1,0)^T$. During stage IV, the adiabatic preparation of the dark-state wave function is given as

$$\Psi^\dagger_S(x) = \Psi^\dagger_{|g_1\rangle}(x)\left(\frac{s\sin(kx)}{\sqrt{s^2\sin^2(kx)+1}}, \frac{1}{\sqrt{s^2\sin^2(kx)+1}}\right)^T,$$

where $s = \frac{1}{\epsilon} = (\Omega_{c1} + \Omega_{c2})/\Omega_p$.

The measurement involves probing the probability density of atoms in $|g_2\rangle$ averaged over the filled ground band of the optical lattice ($|\text{GB}\rangle$) using state-selective imaging. The observable that we measure is therefore,

$$\begin{aligned}
&\langle g_2|\langle \text{GB}|\Psi^\dagger_S(x)\Psi_S(x)|\text{GB}\rangle|g_2\rangle \\
&= \left(\frac{1}{s^2\sin^2(kx)+1}\right)\sum_{q=-k}^{q=k}\sum_{q'=-k}^{q'=k}\phi^*_q(x)\phi_{q'}(x) \\
&\quad\times\langle \text{GB}|c^\dagger_{q|g_1\rangle}c_{q'|g_1\rangle}|\text{GB}\rangle \\
&= \left(\frac{1}{s^2\sin^2(kx)+1}\right)\sum_{q=-k}^{q=k}|\phi_q(x)|^2 \\
&= f(x)\sum_{q=-k}^{q=k}|\phi_q(x)|^2.
\end{aligned}$$

Therefore, the measured density distribution within a unit cell is the convolution of the actual density distribution $\sum_{q=-k}^{q=k} |\phi_q(x)|^2$ and the probing function $f(x)$.

We solve for the band structure of two types of lattices: the KP lattice and the sinusoidal ac-Stark-shift lattice. Using the Bloch ansatz, the Schrödinger equation can be written as

$$\left(\frac{\hbar^2}{2m}(-i\hbar\partial_x + q)^2 + V(x)\right)u_q(x) = \epsilon(q)u_q(x).$$

The Schrödinger equation can be solved numerically by Fourier expansion of $u_q(x)$ into plane waves

$$u_q(x) = \sum_{n=-N}^{N} c_{n,q}e^{inkx},$$

where $n \in (0, 1, 2, \ldots)$ is the band index and diagonalizing the matrix equation resulting in this basis. Similarly, the time dependence of the wave function after suddenly changing the lattice can be calculated by solving the time-dependent Schrödinger equation with appropriate initial conditions.

[1] G. Binnig and H. Rohrer, *Scanning Tunneling Microscopy*, Surf. Sci. **126**, 236 (1983).

[2] S. W. Hell, *Far-Field Optical Nanoscopy*, Science **316**, 1153 (2007).

[3] C. Gross and I. Bloch, *Quantum Simulations with Ultracold Atoms in Optical Lattices*, Science **357**, 995 (2017).

[4] G. S. Agarwal and K. T. Kapale, *Subwavelength Atom Localization via Coherent Population Trapping*, J. Phys. B **39**, 3437 (2006).

[5] J. A. Miles, Z. J. Simmons, and D. D. Yavuz, *Subwavelength Localization of Atomic Excitation Using Electromagnetically Induced Transparency*, Phys. Rev. X **3**, 031014 (2013).

[6] T. Gericke, P. Würtz, D. Reitz, T. Langen, and H. Ott, *High-Resolution Scanning Electron Microscopy of an Ultracold Quantum Gas*, Nat. Phys. **4**, 949 (2008).

[7] A. Alberti, C. Robens, W. Alt, S. Brakhane, M. Karski, R. Reimann, A. Widera, and D. Meschede, *Super-Resolution Microscopy of Single Atoms in Optical Lattices*, New J. Phys. **18**, 053010 (2016).

[8] K. D. Nelson, X. Li, and D. S. Weiss, *Imaging Single Atoms in a Three-Dimensional Array*, Nat. Phys. **3**, 556 (2007).

[9] A. V. Gorshkov, L. Jiang, M. Greiner, P. Zoller, and M. D. Lukin, *Coherent Quantum Optical Control with Subwavelength Resolution*, Phys. Rev. Lett. **100**, 093005 (2008).

[10] E. Paspalakis and P. L. Knight, *Localizing an Atom via Quantum Interference*, Phys. Rev. A **63**, 065802 (2001).

[11] J.-T. Chang, J. Evers, M. O. Scully, and M. S. Zubairy, *Measurement of the Separation between Atoms beyond Diffraction Limit*, Phys. Rev. A **73**, 031803 (2006).

[12] J. Cho, *Addressing Individual Atoms in Optical Lattices with Standing-Wave Driving Fields*, Phys. Rev. Lett. **99**, 020502 (2007).

[13] D. D. Yavuz and N. A. Proite, *Nanoscale Resolution Fluorescence Microscopy Using Electromagnetically Induced Transparency*, Phys. Rev. A **76**, 041802 (2007).

[14] H. Li, V. A. Sautenkov, M. M. Kash, A. V. Sokolov, G. R. Welch, Y. V. Rostovtsev, M. S. Zubairy, and M. O. Scully, *Optical Imaging beyond the Diffraction Limit via Dark States*, Phys. Rev. A **78**, 013803 (2008).

[15] Y. Ashida and M. Ueda, *Diffraction-Unlimited Position Measurement of Ultracold Atoms in an Optical Lattice*, Phys. Rev. Lett. **115**, 095301 (2015).

[16] D. Yang, C. Laflamme, D. V. Vasilyev, M. A. Baranov, and P. Zoller, *Theory of a Quantum Scanning Microscope for Cold Atoms*, Phys. Rev. Lett. **120**, 133601 (2018).

[17] P. C. Maurer, J. R. Maze, P. L. Stanwix, L. Jiang, A. V. Gorshkov, A. A. Zibrov, B. Harke, J. S. Hodges, A. S. Zibrov, A. Yacoby, D. Twitchen, S. W. Hell, R. L. Walsworth, and M. D. Lukin, *Far-Field Optical Imaging and Manipulation of Individual Spins with Nanoscale Resolution*, Nat. Phys. **6**, 912 (2010).

[18] D. Yang, D. V. Vasilyev, C. Laflamme, M. A. Baranov, and P. Zoller, *Quantum Scanning Microscope for Cold Atoms*, Phys. Rev. A **98**, 023852 (2018).

[19] N. V. Vitanov, A. A. Rangelov, B. W. Shore, and K. Bergmann, *Stimulated Raman Adiabatic Passage in Physics, Chemistry, and Beyond*, Rev. Mod. Phys. **89**, 015006 (2017).

[20] Y. Wang, S. Subhankar, P. Bienias, and M. Łącki, T.-C. Tsui, M. A. Baranov, A. V. Gorshkov, P. Zoller, J. V. Porto, and S. L. Rolston, *Dark State Optical Lattice with a Subwavelength Spatial Structure*, Phys. Rev. Lett. **120**, 083601 (2018).

[21] V. D. Vaidya, J. Tiamsuphat, S. L. Rolston, and J. V. Porto, *Degenerate Bose-Fermi Mixtures of Rubidium and Ytterbium*, Phys. Rev. A **92**, 043604 (2015).

[22] F. Jendrzejewski, S. Eckel, T. G. Tiecke, and G. Juzeliūnas, G. K. Campbell, Liang Jiang, and A. V. Gorshkov, *Subwavelength-Width Optical Tunnel Junctions for Ultracold Atoms*, Phys. Rev. A **94**, 063422 (2016).

[23] M. Łącki, M. A. Baranov, H. Pichler, and P. Zoller, *Nanoscale "Dark State" Optical Potentials for Cold Atoms*, Phys. Rev. Lett. **117**, 233001 (2016).

[24] N. Goldman and J. Dalibard, *Periodically Driven Quantum Systems: Effective Hamiltonians and Engineered Gauge Fields*, Phys. Rev. X **4**, 031027 (2014).

[25] K. W. Madison, F. Chevy, W. Wohlleben, and J. Dalibard, *Vortex Formation in a Stirred Bose-Einstein Condensate*, Phys. Rev. Lett. **84**, 806 (2000).

[26] S. Krönke, M. Pyzh, C. Weitenberg, and P. Schmelcher, *Quantum Point Spread Function for Imaging Trapped Few-Body Systems with a Quantum Gas Microscope*, arXiv:1806.08982.

[27] G. Wirth, M. Ölschläger, and A. Hemmerich, *Evidence for Orbital Superfluidity in the p-Band of a Bipartite Optical Square Lattice*, Nat. Phys. **7**, 147 (2011).

[28] X. Li and W. V. Liu, *Physics of Higher Orbital Bands in Optical Lattices: A Review*, Rep. Prog. Phys. **79**, 116401 (2016).

[29] A. Goban, R. B. Hutson, G. E. Marti, S. L. Campbell, M. A. Perlin, P. S. Julienne, J. P. D'Incao, A. M. Rey, and J. Ye, *Emergence of Multi-Body Interactions in a Fermionic Lattice Clock*, Nature (London) **563**, 369 (2018).

[30] S. Nascimbene, N. Goldman, N. R. Cooper, and J. Dalibard, *Dynamic Optical Lattices of Subwavelength Spacing for Ultracold Atoms*, Phys. Rev. Lett. **115**, 140401 (2015).

[31] S. Subhankar, A. Restelli, Y. Wang, S. L. Rolston, and J. V. Porto, *Microcontroller Based Scanning Transfer Cavity Lock for Long-Term Laser Frequency Stabilization*, arXiv:1810.07256.

[32] J. H. T. Burke, O. Garcia, K. J. Hughes, B. Livedalen, and C. A. Sackett, *Compact Implementation of a Scanning Transfer Cavity Lock*, Rev. Sci. Instrum. **76**, 116105 (2005).

[33] R. A. Jishi, *Feynman Diagram Techniques in Condensed Matter Physics* (Cambridge University Press, Cambridge, England, 2013).

[34] M. McDonald, J. Trisnadi, K.-X. Yao, and C. Chin, preceding paper, *Super-Resolution Microscopy of Cold Atoms in an Optical Lattice*, Phys. Rev. X **9** 021001 (2018).

Appendix D: Floquet engineering of optical lattices with spatial features and periodicity below the diffraction limit

New Journal of Physics
The open access journal at the forefront of physics

Deutsche Physikalische Gesellschaft DPG
IOP Institute of Physics

Published in partnership with: Deutsche Physikalische Gesellschaft and the Institute of Physics

OPEN ACCESS

RECEIVED
19 June 2019

REVISED
19 September 2019

ACCEPTED FOR PUBLICATION
22 October 2019

PUBLISHED
28 November 2019

PAPER

Floquet engineering of optical lattices with spatial features and periodicity below the diffraction limit

S Subhankar[1], P Bienias[1,2], P Titum[1,2,3], T-C Tsui[1], Y Wang[1], A V Gorshkov[1,2], S L Rolston[1] and J V Porto[1]

[1] Joint Quantum Institute, National Institute of Standards and Technology and the University of Maryland, College Park, MD 20742, United States of America
[2] Joint Center for Quantum Information and Computer Science, NIST/University of Maryland, College Park, MD 20742, United States of America
[3] Johns Hopkins University Applied Physics Laboratory, Laurel, MD 20723, United States of America

E-mail: subhankarsarthak1@gmail.com

Keywords: Floquet, Hamiltonian engineering, subwavelength, stimulated Raman adiabatic passage (STIRAP), adiabaticity, pulse shaping, Kronig–Penney lattice

Abstract

Floquet engineering or coherent time-periodic driving of quantum systems has been successfully used to synthesize Hamiltonians with novel properties. In ultracold atomic systems, this has led to experimental realizations of artificial gauge fields, topological bandstructures, and observation of dynamical localization, to name a few. Here we present a Floquet-based framework to stroboscopically engineer Hamiltonians with spatial features and periodicity below the diffraction limit of light used to create them by time-averaging over various configurations of a 1D optical Kronig–Penney (KP) lattice. The KP potential is a lattice of narrow subwavelength barriers spaced by half the optical wavelength ($\lambda/2$) and arises from the nonlinear optical response of the atomic dark state. Stroboscopic control over the strength and position of this lattice requires time-dependent adiabatic manipulation of the dark-state spin composition. We investigate adiabaticity requirements and shape our time-dependent light fields to respect the requirements. We apply this framework to show that a $\lambda/4$-spaced lattice can be synthesized using realistic experimental parameters as an example, discuss mechanisms that limit lifetimes in these lattices, explore candidate systems and their limitations, and treat adiabatic loading into the ground band of these lattices.

1. Introduction

Time-periodic driving of quantum systems is ubiquitous in quantum mechanics. Small amplitude driving of a quantum system probes its linear response [1], while strong driving allows for Hamiltonian engineering [2–6]. Optical potentials and in particular optical lattices have proven to be a powerful tool for manipulating ultracold atomic systems and are used in a wide range of experiments [7–9]. However, the spatial features and periodicity of these potentials (generally arising from the second order ac-Stark shift) in the far field are constrained by the diffraction limit to be of order the wavelength of light used to create them. In particular, the Fourier decomposition of these far-field optical potentials cannot have components with wavelength less than $\lambda/2$, and thus the minimum lattice spacing is $\lambda/2$. As the lattice spacing determines many of the energy scales in cold-atom lattice systems, it has been of interest to produce optical lattices with smaller spacings in order to increase relevant energy scales [10, 11]. Approaches to making subwavelength-spaced optical lattices have been proposed [12] and realized [13, 14] based on multiphoton effects, and on adiabatic dressing of different spin dependent lattices [15, 16].

Recently, optical lattices based on the nonlinear optical response of dark states [17, 18] were realized [19] with $\lambda/2$ periodicity but strongly subwavelength structure within a unit cell, consisting of a Kronig–Penney-like (KP) lattice of narrow repulsive barriers of width $\simeq\lambda/50$. Time averaging a stroboscopically applied lattice potential with high spatial frequency Fourier components can give rise to an average potential with periodicity and spatial features smaller than $\lambda/2$ [10]. Since the dark-state KP lattice has high spatial frequency Fourier components, it is a candidate progenitor lattice with which to realize such a time-averaged, subwavelength-featured lattice. Here, we explore the

implementation of a time-averaged dark-state KP lattice, taking into account realistic imperfections in the dark-state system. After careful consideration of the adiabaticity requirements, we show that lattices with $\lambda/4$ period can be realized as an example, and discuss the prospects for lattices with smaller spacings and features. Reference [20] explores related ideas about painting arbitrary subwavelength optical potentials.

In the time-averaged approach, a time-periodic progenitor potential $W_0(x, t)$ is applied such that the atoms experience the time-averaged potential $W_{\rm avg}(x)$:

$$W_{\rm avg}(x) = \frac{1}{T}\int_{-T/2}^{T/2} W_0(x,\, t)\,{\rm d}t, \tag{1}$$

where $T = 2\pi/\omega_T$ is the period of $W_0(x, t)$ and ω_T is the Floquet frequency. In order to successfully realize $W_{\rm avg}(x)$ while avoiding heating, ω_T must be much faster than the timescale associated with the motional degree of freedom in the lattice, which is set by the energy gaps between bands in the lattice [10, 21]. This requirement suggests that ω_T be as large as possible. As we discuss below, the particular realization of $W_0(x, t)$ using a dark-state lattice [19] has an additional requirement of spin adiabaticity that limits the maximum allowable ω_T.

The dark-state lattice is an artificial scalar gauge potential [17–19, 22, 23] experienced by an atom in the dark-state eigenfunction of a three-level Λ-system with a spatially dependent spin composition. Dynamically manipulating the height, barrier width, and position of the lattice requires time-dependent manipulation of the spin composition of the dark-state eigenfunction. This spin manipulation can be seen as a stimulated Raman adiabatic passage (STIRAP) process [24] and adiabaticity requirements set an upper bound on the window for usable ω_T within which the atoms are simultaneously motionally diabatic and spin adiabatic. Understanding the practical limits of these constraints requires a detailed consideration of the system dynamics, which we apply to the specific ^{171}Yb system previously used to demonstrate the dark-state lattice [19].

2. Time-dependent dark-state potentials

We consider the creation of time-periodic potentials for the dark-state channel, $W_{\rm DS}(x, t)$ (which serves as $W_0(x, t)$ in equation (1)), by coupling the three atomic levels in a Λ-system with a spatially homogeneous probe light field $\Omega_p(t)$, and a spatially inhomogeneous control light field. The inhomogeneous control light field is composed of two counter propagating fields with equal magnitudes driven simultaneously, $\Omega_c(x, t) = \Omega_c(t)\cos(kx+\phi(t))$ where $k = 2\pi/\lambda$, as shown in figure 1(a). Working in the spatially and temporally local dressed state basis of the Λ-system determined by the coupling fields $\Omega_p(t)$ and $\Omega_c(x, t)$, the Hamiltonian is given by (equation (A.5))

$$\hat{H}_{\rm rot}(x,\, t) = \frac{\hat{p}^2}{2m} + \begin{pmatrix} W_{\rm DS}(x) & 0 & 0 \\ 0 & W_{-}(x) & 0 \\ 0 & 0 & W_{+}(x) \end{pmatrix} + \hat{H}_{\rm od}(x,\, p,\, t), \tag{2}$$

where $W_{\rm DS}(x, t)$ and $W_{\pm}(x, t)$ are the dark-state and bright-state potentials in the three Born–Oppenheimer (BO) channels and $\hat{H}_{\rm od}(x,\, p,\, t)$ represents the off-diagonal couplings between these channels (see appendix A). $W_{\rm DS}(x, t)$ and $W_{\pm}(x, t)$ include the BO potentials as well as the non-adiabatic corrections to these potentials. The dressed state coupling induced by $\hat{H}_{\rm od}(x,\, p,\, t)$ is detrimental, since it mixes bare excited state $|3\rangle$ into the dark-state channel through the bright-state channels, inducing photon scattering in the otherwise lossless dark state.

The spin composition of the dark-state eigenfunction for the Λ-system in figure 1(a) is $|{\rm DS}(x,\, t)\rangle = -\cos\alpha(x,\, t)|1\rangle + \sin\alpha(x,\, t)|2\rangle$ where $\alpha(x,\, t) = \tan^{-1}[\Omega_p(t)/\Omega_c(x,\, t)]$. The non-adiabatic correction to the dark-state BO potential that gives rise to $W_{\rm DS}(x, t)$ is determined by the spatial gradient of the spin composition [17, 18] (appendix A.1) (figure 1(c)),

$$W_{\rm DS}(x,\, t) = \frac{\hbar^2}{2m}\left(\frac{\partial}{\partial x}\alpha(x,\, t\right)^2, \tag{3}$$

which for the light-field configuration considered here is a lattice of narrow repulsive barriers with temporally modulated strength and position. We take here a stroboscopic approach, where $W_{\rm DS}(x, t)$ is repeatedly pulsed on and off in magnitude at N different positions for time T_i with the position of $W_{\rm DS}(x, t)$ being shifted in between the lattice pulses (here $T = \sum T_i$). In addition, $W_{\rm DS}(x, t)$ can be held on and off for $t_{{\rm on},i}$ and $t_{{\rm off},i}$ (figure 1(d)). Time averaging over the N different pulsed KP lattice potentials with arbitrary strength and position can produce an arbitrary time-averaged potential $W_{\rm avg}(x)$ [20].

The ability to paint potentials requires real-time control over the position, strength and width of the barriers (equation (3)). The strength of the barriers can be controlled via the Rabi frequencies $\Omega_p(t)$ and $\Omega_c(t)$ (figures 1(b), (c)) with the height and width of the barriers being proportional to $1/\epsilon^2(t)$ and $\epsilon(t)$ respectively [17–19] where $\epsilon(t) = \Omega_p(t)/\Omega_c(t)$ (for $\epsilon(t) \ll 1$). The barriers are located at the nodes/minimums of $\Omega_c(x, t)$

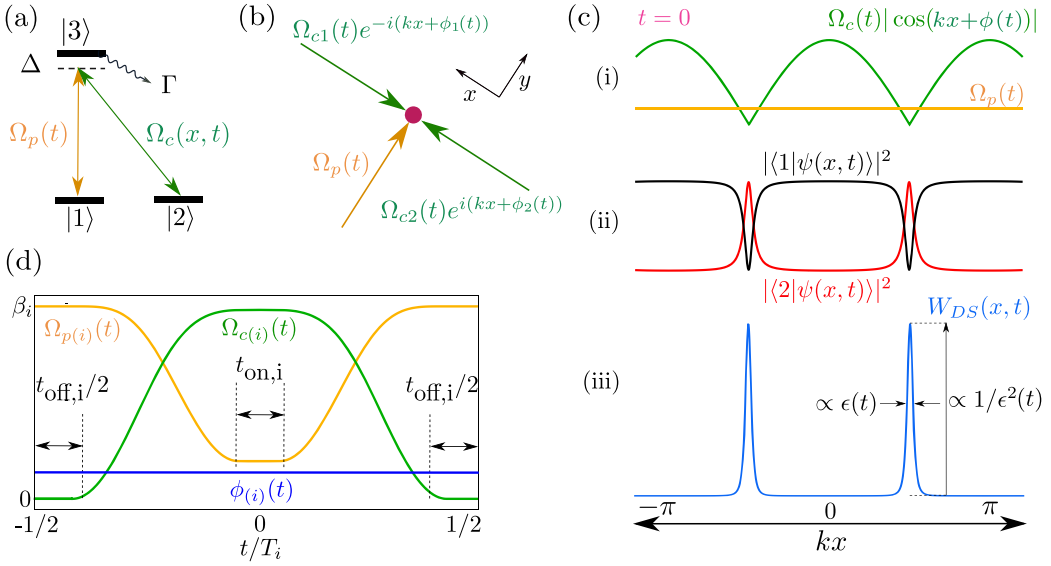

Figure 1. (a) An ideal Λ-system with inverse lifetime Γ and single-photon detuning Δ. One leg of the Λ-system is coupled by a spatially homogeneous and temporally varying probe light field $\Omega_p(t)$ and the other leg by a spatially inhomogeneous and temporally varying control light field $\Omega_c(x, t)$. (b) The geometry of the light fields with arbitrary control over the envelope, $\Omega_{c1}(t)$, $\Omega_{c2}(t)$, $\Omega_p(t)$ and phase, $\phi_1(t)$, $\phi_2(t)$ of each light field. (c) (i) The instantaneous (at $t = 0$) spatial dependence of the light fields $\Omega_c(t)|\cos(kx + \phi(t))|$ and $\Omega_p(t)$ where $\phi(t) = \phi_1(t) = \phi_2(t)$, (ii) the probability densities of the spin composition of the dark-state eigenfunction $|\psi(x, t)\rangle$ i.e. $|\langle 1|\psi(x, t)\rangle|^2$ and $|\langle 2|\psi(x, t)\rangle|^2$, and (iii) the instantaneous shape of $W_{DS}(x, t)$. (d) Typical pulse shapes considered here for the control beams $\Omega_{c(i)}(t) = 2\Omega_{c1(i)}(t) = 2\Omega_{c2(i)}(t)$, probe beam $\Omega_{p(i)}(t)$, and phase $\phi_i(t)$ for the ith sub-Floquet period where $-T_i/2 \leqslant t \leqslant T_i/2$ that determines the time-averaged potential $W_{avg}(x)$.

(figure 1(c)), and their positions can be controlled by the control beam phases $\phi_1(t)$ and $\phi_2(t)$ (figures 1(b), (c)). Stitching N different sub-Floquet periods together (while ensuring continuity in the Rabi pulses between the sub-Floquet periods) into one Floquet period allows for the versatility in the time-averaged potential $W_{avg}(x)$ that can be generated. Each sub-Floquet period of duration T_i pulses a KP potential at a different position x_{0i} (determined by the phase ϕ_{0i}) with a strength and width determined by ϵ_i. Figure 1(d) shows the pulses $\Omega_{p(i)}(t)$, $\Omega_{c(i)}(t)$ and $\phi_{(i)}(t)$ for the ith sub-Floquet period $-T_i/2 \leqslant t \leqslant T_i/2$.

3. Adiabaticity considerations

Without explicit time-dependence, $\hat{H}_{od}(x, p, t)$ has static, off-diagonal terms depending on the spatial gradient of the dark-state spin composition that couple the dark-state channel to the lossy bright-state channels. This loss mechanism was theoretically [17, 18] and experimentally [19] shown to limit lifetimes in the KP lattice. Large energy gaps between the BO channels via large Rabi frequencies Ω_c and Ω_p generally aid in suppressing this loss [19]. When explicit time dependence to the Rabi frequencies is included i.e. $\Omega_c(x, t)$ and $\Omega_p(t)$, the spatially dependent loss mechanism has a trivial time dependence due to the temporally periodic nature of the changing dressed states, and the loss is quantified by averaging over one Floquet period. There is, however, an additional loss mechanism mediated via an explicitly time-dependent term in $\hat{H}_{od}(x, p, t)$ (see appendix A). This term mediates non-adiabatic couplings between the dark-state channel and the bright-state channels, but can be suppressed by careful pulse shaping.

Our goal is to design $\Omega_p(t)$ and $\Omega_c(x, t)$ to be simultaneously motionally diabatic and spin adiabatic. In order to design pulses that are spin adiabatic, we consider the three inequalities that quantify the sufficiency requirements for adiabaticity [25] defined at single photon resonance $\Delta = 0$ (see appendices A.2, B.2):

$$\left|\frac{\partial}{\partial t}\alpha(x, t)\right| \ll \Omega_{rms}(x, t), \tag{4a}$$

$$\int_{-\pi/\omega_T}^{\pi/\omega_T} \left|\frac{\partial}{\partial t}\left(\frac{\partial\alpha(x, t)/\partial t}{\Omega_{rms}(x, t)}\right)\right| dt \ll 1, \tag{4b}$$

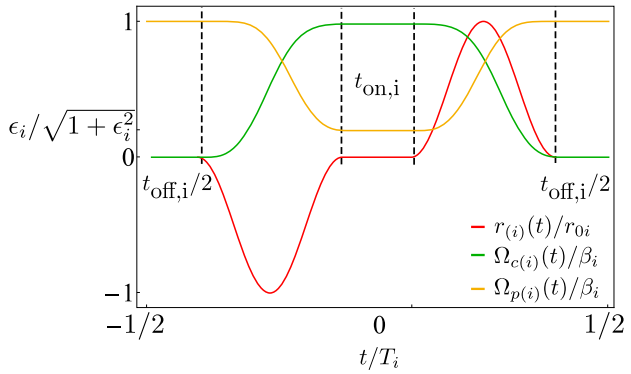

Figure 2. The functional forms for $\Omega_{c(i)}(t)$, $\Omega_{p(i)}(t)$, and $r_{(i)}(t)$ for the ith sub-Floquet period $-T_i/2 \leqslant t \leqslant T_i/2$. Control over the duty cycle of $W_{\mathrm{DS}}(x, t)$ is provided by the hold times $t_{\mathrm{off},i}$ and $t_{\mathrm{on},i}$.

$$\int_{-\pi/\omega_T}^{\pi/\omega_T} \frac{|\partial\alpha(x,\,t)/\partial t|^2}{\Omega_{\mathrm{rms}}(x,\,t)}\mathrm{d}t \ll 1, \tag{4c}$$

where $\Omega_{\mathrm{rms}}(x,\,t) = \sqrt{|\Omega_c(x,\,t)|^2 + |\Omega_p(t)|^2}$. Equation (4*a*), called the local adiabatic criterion [24], states that to ensure adiabaticity during pulsing, the energy gap between the dark and bright eigenstates (set by $\Omega_{\mathrm{rms}}(x, t)$) must be much greater than the off-diagonal couplings between them ($|\partial\alpha(x,\,t)/\partial t|$). Equation (4*b*) forces the pulses to be smooth while both equations (4*b*) and (4*c*) set bounds on their rise time and fall times.

To design pulse shapes that satisfy equations (4*a*)–(4*c*), we parameterize the condition equation 4(a) through a parameter $r(t)$:

$$r(t) = \frac{\partial\alpha(x_h,\,t)/\partial t}{\Omega_{\mathrm{rms}}(x_h,\,t)}, \tag{5}$$

evaluated at $x = x_h$, the position where the inequality is the hardest to satisfy. The role of $r(t)$ is to quantify the spin adiabaticity during the rising and falling segments of the $\Omega_{c1}(t)$, $\Omega_{c2}(t)$ and $\Omega_p(t)$ pulses (figure 1(d)). Specifying $r(t)$ determines the functional form for the Rabi frequencies and the Floquet frequency. To satisfy equation (4) during the switching between the on ($t_{\mathrm{on},i}$) and off times ($t_{\mathrm{off},i}$), $|r_{(i)}(t)|$ should satisfy the condition $|r_{(i)}(t)| \ll 1$ (see appendix B.2) and smoothly change from 0. We consider a convenient analytic form for $r_{(i)}(t)$ that has a continuous first derivative (figure 2):

$$r_{(i)}(t) = \begin{cases} 0 & -T_i/2 \leqslant t \leqslant -T_i/2 + t_{\mathrm{off},i}/2 \\ -r_{0i}\sin^2\left(\dfrac{2\pi(t + t_{\mathrm{on},i}/2)}{t_{Si}}\right) & -T_i/2 + t_{\mathrm{off},i}/2 \leqslant t \leqslant -t_{\mathrm{on},i}/2 \\ 0 & -t_{\mathrm{on},i}/2 \leqslant t \leqslant t_{\mathrm{on},i}/2 \\ r_{0i}\sin^2\left(\dfrac{2\pi(t - t_{\mathrm{on},i}/2)}{t_{Si}}\right) & t_{\mathrm{on},i}/2 \leqslant t \leqslant T_i/2 - t_{\mathrm{off},i}/2 \\ 0 & T_i/2 - t_{\mathrm{off},i}/2 \leqslant t \leqslant T_i/2 \end{cases}, \tag{6}$$

where $T_i = t_{Si}+t_{\mathrm{off},i}+t_{\mathrm{on},i}$ and $t_{Si}/2$ is the rise or fall time.

Generally, it is easiest to be spin adiabatic for large energy separation between the dark and bright-state channels. However at the nodes of $\Omega_c(x, t)$, this energy gap is the smallest with a value of $\hbar\Omega_p(t)/2$ for $\Delta = 0$. Therefore, we consider pulse schemes that change the positions of the nodes only when the energy gap at the nodes is large and the spin composition is essentially homogeneous ($\epsilon(t) \gg 1$). We consider two ways to achieve the homogeneous condition in between pulses:

(1) $\Omega_p(t) \gg \Omega_c(x, t)$ achieved by turning up Ω_p while turning off both control beams,

(2) $\Omega_{c1} \gg \Omega_p \gg \Omega_{c2}(t)$ achieved by turning off $\Omega_{c2}(t)$ while Ω_p and Ω_{c1} are kept constant.

We note that the pulsing schemes considered here are not unique. Control over $\Omega_{c1}(t)$, $\Omega_{c2}(t)$, $\Omega_p(t)$, $\phi_1(t)$, and $\phi_2(t)$ allows for multiple ways by which arbitrary potentials can be painted, and we refer the reader to [20] for other variants.

For pulse scheme (1), the position where the local adiabatic criterion is the hardest to satisfy, x_h, occurs between the nodes. (Pulse scheme (2), for which only one of the two control beams is driven, is treated in the appendix). We choose

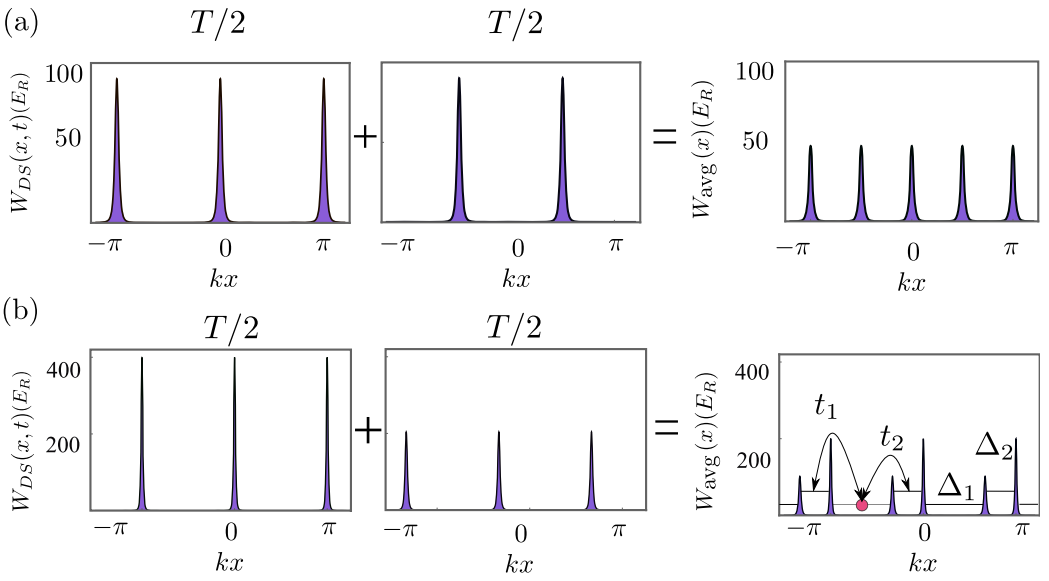

Figure 3. (a) Recipe to stroboscopically realize a $W_{\rm avg}(x)$ that is a $\lambda/4$-spaced lattice: Pulse $W_{\rm DS}(x, t)$ with $\phi_{(i)}(t) = 0$ for $-T/2 \leqslant t \leqslant 0$ and $\phi_{(i)}(t) = \pi/2$ for $0 \leqslant t \leqslant T/2$. For realistic dark-state lattices, spin adiabaticity requires that the lattice cannot be turned on or off instantaneously. (b) Stroboscopic realization of the Rice–Mele model.

the rms average of the Rabi frequencies to be constant at x_h, $\Omega_{\rm rms} = \Omega^2_{p(i)}(t) + \Omega^2_{c(i)}(t) = \beta_i^2 = (\Omega^0_{ci})^2 + (\Omega^0_{pi})^2 = (\Omega^0_{ci})^2(1 + \epsilon_i^2)$ where β_i is a constant and $\Omega_{c(i)}(t) = 2\Omega_{c1(i)}(t) = 2\Omega_{c2(i)}(t)$. Solving equations (5) and (6) simultaneously, the expressions for t_{Si}, $\Omega_{c(i)}(t)$ are as follows (figure 2):

$$\Omega_{c(i)}(t) = \begin{cases} 0 & -T_i/2 \leqslant t \leqslant -T_i/2 + t_{{\rm off},i}/2 \\ \beta_i \sin[\arctan(1/\epsilon_i)\mathcal{G}(t + t_{{\rm on},i}/2)/(2\pi)] & -T_i/2 + t_{{\rm off},i}/2 \leqslant t \leqslant -t_{{\rm on},i}/2 \\ \Omega^0_{ci} & -t_{{\rm on},i}/2 \leqslant t \leqslant t_{{\rm on},i}/2 \\ \beta_i \sin[\arctan(1/\epsilon_i)\mathcal{G}(t - t_{{\rm on},i}/2)/(2\pi)] & t_{{\rm on},i}/2 \leqslant t \leqslant T_i/2 - t_{{\rm off},i}/2 \\ 0 & T_i/2 - t_{{\rm off},i}/2 \leqslant t \leqslant T_i/2 \end{cases}, \tag{7}$$

where $\mathcal{G}(t) = |4\pi t/t_{Si} - \sin(4\pi t/t_{Si}) - 2\pi|t|/t\,|$ and

$$t_{Si} = 4\arctan(1/\epsilon_i)/(r_{0i}\beta_i). \tag{8}$$

As a specific example, we explore creation of $\lambda/(2N)$-spaced lattices where $N = 2, 3, 4\ldots$. These lattices are created by time-averaging N $\lambda/2$-spaced progenitor KP lattice potentials, each shifted in position by $i\lambda/(2N)$ for $(i - 1)T/N \leqslant t \leqslant iT/N$ and pulsed for a period of $T_i = T/N$ [10], where $i = 0, 1, \ldots, N - 1$ (figure 3(a)). More flexibility is possible by pulsing the progenitor lattice with different strengths and relative positions, realizing for example the Rice–Mele model [26, 27] as shown in figure 3(b).

The goal to create $\lambda/(2N)$-spaced lattices that significantly confines the ground band sets constraints on the lattice parameters. Without requirements of spin adiabaticity, time-averaging the KP potential creates $\lambda/(2N)$-spaced lattices with barriers of maximum average height of $(1/N)E_R/\epsilon^2$. Due to the reduction in the size of the unit cell by N, the characteristic energy increases to N^2E_R, which is also approximately the energy of the lowest band in a KP lattice. Hence for the $\lambda/(2N)$-spaced lattice to provide significant confinement,

$$N^2E_R < \frac{E_R}{N\epsilon^2} \Rightarrow \epsilon < \frac{1}{N^{3/2}}. \tag{9}$$

The barrier height for the $\lambda/(2N)$-spaced lattice is $W_{\rm avg}(x_{0i}) = \int_{-T/2}^{T/2} W_{\rm DS}(x_{0i}, t)/T\,{\rm d}t$, which can be controlled by choosing ϵ (limited by requirements on spin adiabaticity) and $t_{{\rm off},i}$ and $t_{{\rm on},i}$. Of course, non-zero values for $t_{{\rm off},i}$ and $t_{{\rm on},i}$ decrease the Floquet frequency (ω_T) as

$$\frac{1}{\omega_T} = \frac{N}{2\pi}(t_{Si} + t_{{\rm off},i} + t_{{\rm on},i}). \tag{10}$$

Reducing ω_T makes it more difficult to be fully motionally diabatic, so that the operational window between the two constraints rapidly decreases with increasing N.

4. Solving for the Bloch–Floquet bandstructure

We solve the Bloch–Floquet bandstructure for our Hamiltonian

$$\hat{H}(x,\,t) = \frac{\hat{p}^2}{2m} + \underbrace{\frac{\hbar}{2}\begin{pmatrix} 0 & 0 & \Omega_p(t) \\ 0 & 0 & \Omega_c(x,\,t) \\ \Omega_p(t) & \Omega_c(x,\,t) & -(2\Delta(t) + \mathrm{i}\Gamma) \end{pmatrix}}_{\hat{\Omega}(x,t)}, \tag{11}$$

where $\hat{\Omega}(x+\lambda,\,t) = \hat{\Omega}(x,\,t+T) = \hat{\Omega}(x,\,t)$ with $\Delta(t) = 0$ and $\Gamma = 48.2\omega_R$ (for the $(6s^2)^1S_0 \leftrightarrow (6s6p)^3P_1$ transition in ^{171}Yb). We substitute the Bloch–Floquet ansatz, $|\psi(x,\,t)\rangle = \mathrm{e}^{\mathrm{i}qx - \mathrm{i}E_q t/\hbar}|u_{q,E_q}(x,\,t)\rangle\rangle$ [2, 3, 5, 28–31] into the time-dependent Schrödinger equation $\hat{H}(x,\,t)|\psi(x,\,t)\rangle = \mathrm{i}\hbar\frac{\partial}{\partial t}|\psi(x,\,t)\rangle$ to yield

$$\hat{K}_q|u_{q,E_q}(x,\,t)\rangle\rangle = E_q|u_{q,E_q}(x,\,t)\rangle\rangle, \tag{12}$$

where q is the quasimomentum, E_q is the quasienergy, $|u_{q,E_q}(x,\,t)\rangle\rangle$ is the Bloch–Floquet mode, and

$$\hat{K}_q = \frac{(\hat{p} + \hbar q)^2}{2m} - \mathrm{i}\hbar\frac{\partial}{\partial t} + \hat{\Omega}(x,\,t),$$

is the quasienergy operator defined in an extended Hilbert space where time is treated as a coordinate with periodic boundary conditions [2, 3, 5]. The extension of the Hilbert space is symbolically represented by the double ket notation for the Bloch–Floquet mode $|u_{q,E_q}(x,\,t)\rangle\rangle$ [2, 3]. We solve the eigenvalue problem in equation (12) to calculate the Bloch–Floquet bandstructure (appendix C.1).

5. Results

The loss due to the off-diagonal coupling terms in $\hat{H}_{\mathrm{od}}(x,\,t)$ that arises from the spatial gradient of the dark-state spin composition increases with smaller ϵ [17–19]. This suggests that in order to generate potentials that have reasonable lifetimes with realistic values for Rabi frequencies, it is desirable to work at large ϵ, as allowed by equation (9). In figure 4, we investigate the creation of a $\lambda/4$-spaced lattice potential that significantly confines the ground band. With a choice of $\epsilon_i = 0.2$, $r_{0i} = 0.01$, $\Omega_{ci}^0 = 600\Gamma$, and $t_{Si} = 0.36T_i$ (equation (10)) we use the pulse shape in equation (7) to create this potential (figure 4(a)). The green trace is the pulse profile for $\Omega_c(t)$ (and therefore $\Omega_p(t) = \sqrt{\beta^2 - \Omega_c^2(t)}$) while the blue trace is the phase profile $\phi(t)$ during one Floquet period. The numbered red dots enumerate the different time slices during the pulse. One Floquet period of pulsing involves stitching together two sub-Floquet periods that have a relative phase $\phi_{(i)}(t)$ differing by $\pi/2$. Note that the phase is suddenly switched during an off period when there is no spatial variation to the dark state. The sub-Floquet periods are color coded and labeled as I and II. This pulse yields an effective $\lambda/4$-spaced $W_{\mathrm{avg}}(x)$ potential with $\sim 8E_R$ barriers as shown in figure 4(b) where $W_{\mathrm{avg}}(x)$ is plotted.

In figure 4(c), we search for the window of operational ω_T within which the bands of an effective $\lambda/4$-spaced lattice Hamiltonian are clearly defined by monitoring the Floquet spectrum E_q at $q = 0$ as a function of ω_T/ω_R. As ω_T is increased, the pulsing becomes more motionally diabatic, but at the cost of increased r_{0i} (equation (8)). The increased r_{0i} results in stronger admixing of the dark-state channel with the bright-state channels. The loss rate $-\mathrm{Im}(E_q)$ is encoded in the color of the points in figure 4(c). The gray dots have loss ($-\mathrm{Im}(E_q)$) much larger than the highest value in the color bar.

In figure 4(d), we plot the bandstructure in the Brillouin zone of $\hat{H}(x,\,t)$ for the time-averaged Hamiltonian $\hat{p}^2/(2m) + W_{\mathrm{avg}}(x)$ where $W_{\mathrm{avg}}(x)$ is evaluated using equation (1) (figure 4(b)) for the chosen pulse shape (figure 4(a)). The folded bandstructure is indicative of a $\lambda/4$-spaced lattice. The Bloch–Floquet bandstructure for the dark-state channel (figure 4(e)) is obtained by solving the Hamiltonian $\hat{H}_{\mathrm{DS}}(x,\,t) = \hat{p}^2/(2m) + W_{\mathrm{DS}}(x,\,t)$ for $\omega_T = 150\omega_R$ (equation (3) and see appendix C.2). The avoided crossings enclosed in the red circles in figure 4(e) arise from couplings with high-lying dark-state eigenfunctions. The bandstructures shown in figures 4(d) and (e) ignore $\hat{H}_{\mathrm{od}}(x,\,t)$ and therefore exclude loss due to non-adiabatic couplings with the bright states. In figure 4(f), we show the Bloch–Floquet bandstructure of $\hat{H}(x,\,t)$ (equation (11)), which includes the non-adiabatic bright-state couplings. The avoided crossings exist in the Bloch–Floquet bandstructure at the same place (q, E_q) for the same parameters in figures 4(e) and (f), suggesting that these crossings arise from couplings with high-lying dark-state eigenfunctions. The ground Bloch–Floquet band for $\hat{H}(x,\,t)$ has the same shape as the static $\lambda/4$-spaced lattice (except near the avoided crossings). The calculated average lifetime in the time-averaged potential for the ground band in figure 4(f) is 1 ms, which can be substantially improved with a lower ω_T. In general, lifetimes can be increased and the avoided crossings can be removed by operating at larger Rabi frequencies.

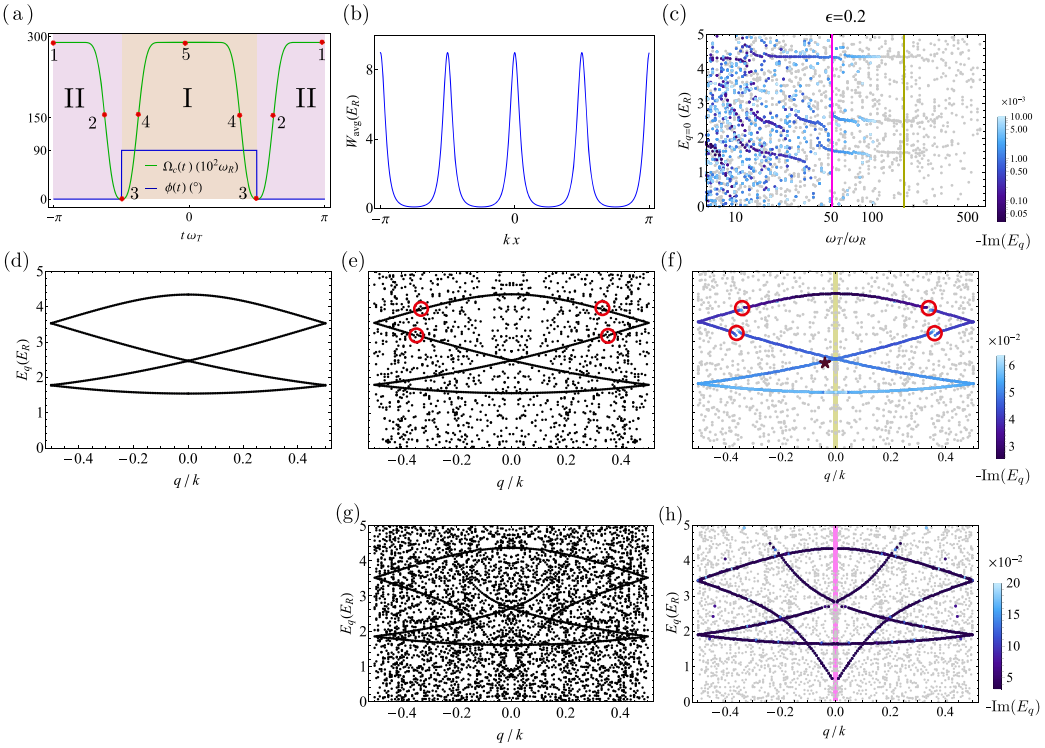

Figure 4. Stroboscopic creation of a $\lambda/4$-spaced lattice potential: (a) one Floquet period constituting the $\Omega_c(t)$ pulse (green trace) and phase pulse $\phi(t)$ (blue trace) for $\epsilon_i = 0.2$, $r_{0i} = 0.01$, $\Omega_{ci}^0 = 600\Gamma$, and $t_{Si} = 0.36T_i$. The numbered red dots enumerate the different time slices shown in figure 5. The two sub-Floquet periods are labeled as I and II. (b) The time-averaged potential $W_{\text{avg}}(x)$. (c) The Floquet spectrum E_q at $q = 0$ as a function of ω_T/ω_R. The background of seemingly random points represent Floquet states whose quasienergies are only defined up to modulo $\hbar\omega_T$. The loss rate $-\text{Im}(E_q)$ is given by the colors of the points. (d) The ground band of the time-averaged Hamiltonian $\hat{p}^2/2m + W_{\text{avg}}(x)$. (e) The Bloch–Floquet ground band of the dark-state channel Hamiltonian $\hat{H}_{\text{DS}}(x,\,t) = \hat{p}^2/2m + W_{\text{DS}}(x,\,t)$ at $\omega_T/\omega_R = 150$. (f) The Bloch–Floquet ground band of $\hat{H}(x,\,t)$ at $\omega_T/\omega_R = 150$. The yellow region at $q = 0$ represents the yellow vertical cut in subfigure (c). In (d)–(f) the bottom edge of the first excited band is at $\sim 8E_R$. (g) The Bloch–Floquet ground band of the dark-state channel Hamiltonian $\hat{H}_{\text{DS}}(x,\,t) = \hat{p}^2/2m + W_{\text{DS}}(x,\,t)$ at $\omega_T/\omega_R = 50$. (h) The Bloch–Floquet ground band of $\hat{H}(x,\,t)$ at $\omega_T/\omega_R = 50$. The pink region at $q = 0$ represents the pink vertical cut in subfigure (c).

We also calculate the Bloch–Floquet bandstructures at a lower Floquet frequency of $\omega_T = 50\ \omega_R$ (pink vertical line in figure 4(c)). The Bloch–Floquet bandstructure of the dark-state channel Hamiltonian $\hat{H}_{\text{DS}}(x,\,t)$ is shown in figure 4(g), and of $\hat{H}(x,\,t)$ in figure 4(h). The average lifetime of the ground band is 32 ms (the colored regions in figure 4(h)) and is much longer than the lifetime of 1 ms for the Bloch–Floquet bandstructure obtained at $\omega_T = 150\ \omega_R$ in figure 4(f). The avoided crossings due to coupling to high-lying dark states, however, are larger for the same Rabi frequencies.

In figure 5, we show the dynamics of the spatial probability densities of the dark-state Bloch–Floquet mode and its spin composition at time slices 1–5 (figure 4(a)) in the (q, E_q) configuration labeled by the brown star in figure 4(f). The purple trace is the scaled probability density of the Bloch–Floquet dark-state mode and it has $\lambda/4$ periodicity. It is roughly stationary except for the small wiggles that correspond to micromotion. Meanwhile, the spin composition (the black and red traces) of the Bloch–Floquet mode changes dramatically as a function of time during the Floquet period. The population in $|3\rangle$ (yellow trace) remains quite small.

To create subwavelength-spaced lattices with larger N, the window of operational ω_T will be smaller by N (equation (10)). In addition, since larger N requires working with smaller ϵ (equation (9)), the loss mechanisms limiting lifetime in these lattices become more significant. However, higher Rabi frequencies can combat both these limitations. Using larger Rabi frequencies, we show an example demonstrating the feasibility of a $\lambda/6$-spaced lattice.

With increased Rabi frequency of $\Omega_{ci}^0 = 1800\Gamma$, we use the pulse shape in equation (7) to design a composite pulsing profile (figure 6(a)) to create a time-averaged $\lambda/6$-spaced lattice potential $W_{\text{avg}}(x)$ that has $\sim 9E_R$ tall barriers (figure 6(b)). Here $\epsilon_i = 0.135$, $r_{0i} = 0.01$, and $t_{Si} = 0.59T_i$. One Floquet period of pulsing involves stitching together three sub-Floquet periods with the relative phase $\phi_{(i)}(t)$ differing by $\pi/3$ between adjacent sub-Floquet periods. For $\omega_T = 280\ \omega_R$ (yellow vertical line in figure 6(c)), we plot the bandstructure of the time-averaged Hamiltonian $\hat{p}^2/(2m) + W_{\text{avg}}(x)$ in figure 6(d), the Bloch–Floquet bandstructure of the dark-state

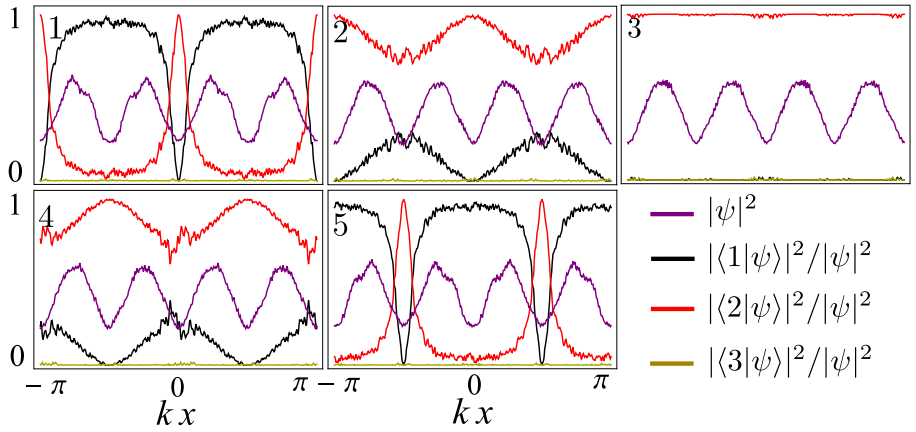

Figure 5. The dynamics of the wavefunction $|\psi\rangle = \langle x,\ t|u_{q,E_q}(x,\ t)\rangle\rangle$ of the (q, E_q) state indicated by the brown star in figure 4(f) within one Floquet period, sampled at the times indicated by the red dots in figure 4(a).

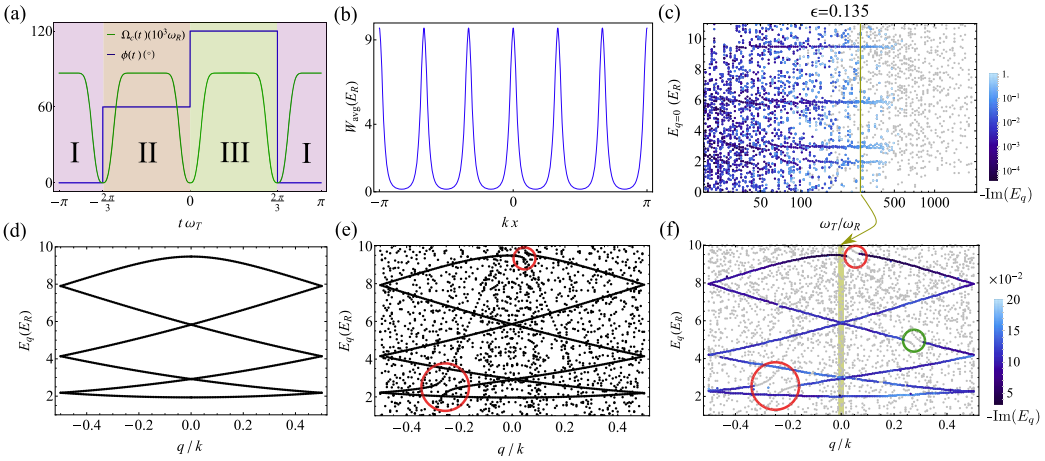

Figure 6. Stroboscopic creation of a $\lambda/6$-spaced lattice potential: (a) one Floquet period constituting the $\Omega_c(t)$ pulse (green trace) and phase pulse $\phi(t)$ (blue trace) for $\epsilon_i = 0.135$, $r_{0i} = 0.01$, $\Omega_{ci}^0 = 1800\Gamma$, and $t_{Si} = 0.59T_i$. The three sub-Floquet periods are labeled as I, II, and III. (b) The time-averaged potential $W_{\mathrm{avg}}(x)$. (c) The Floquet spectrum E_q at $q = 0$ as a function of ω_T/ω_R. The loss rate $-\mathrm{Im}(E_q)$ is given by the colors of the points. (d) The ground band of the time-averaged Hamiltonian $\hat{p}^2/2m + W_{\mathrm{avg}}(x)$. (e) The Bloch–Floquet ground band of the dark-state channel Hamiltonian $\hat{H}_{\mathrm{DS}}(x,\ t) = \hat{p}^2/2m + W_{\mathrm{DS}}(x,\ t)$ at $\omega_T/\omega_R = 280$. (f) The Bloch–Floquet ground band of $\hat{H}(x,\ t)$ at $\omega_T/\omega_R = 280$. The yellow region at $q = 0$ represents the yellow vertical cut in subfigure (c).

channel Hamiltonian $\hat{H}_{\mathrm{DS}}(x,\ t)$ in figure 6(e), and the Bloch–Floquet bandstructure of $\hat{H}(x,\ t)$ in figure 6(f). The folded bandstructures are indicative of a $\lambda/6$-spaced lattice. The particular phase sequence in figure 6(a) used to create the $\lambda/6$-spaced lattice breaks time-reversal symmetry: the Bloch–Floquet bandstructures are therefore asymmetric about $q = 0$. The avoided crossings enclosed in the red circles exist in both Bloch–Floquet bandstructures at the same place (q, E_q) for the same parameters in figures 6(e) and (f), suggesting that these particular crossings arise from couplings with high-lying dark-state eigenfunctions. The avoided crossing enclosed in the green circle in figure 6(f) arises due to couplings with bright-state eigenfunctions.

6. Experimental considerations and limitations

While working with large Rabi frequencies reduces losses, a potential disadvantage is that the Λ-system approximation may break down. Perfect Λ-systems are rare in nature, and $\Omega_p(t)$ and $\Omega_c(t)$ can couple off-resonantly to states outside of the Λ-system. These off-resonant couplings manifest as effective two-photon detunings for the approximate Λ-system. Non-zero two-photon detunings are detrimental to STIRAP [24, 32], although spatially homogeneous detuning could in principle be compensated with time-dependent laser detuning. Two-photon detunings originating from $\Omega_c(x, t)$, however, are temporally and spatially modulated

and may not be completely compensated without the significant experimental overhead of adding more spatially dependent compensating laser fields. In addition to added two-photon detuning, the lifetime in the time-averaged lattices is further limited due to admixing of excited states outside the Λ-system. Hence, there are trade-offs when increasing the magnitude of the Rabi frequencies: while the dark-state evolution is more adiabatic with less bright-state admixture, the off-resonant scattering from states outside the Λ-system also increases. Appendix D presents calculations for a realistic system consisting of ^{171}Yb atoms, which was used to create KP lattices [19].

A number of techniques can be used to verify the creation of these subwavelength lattices. For example, nanoresolution microscopy [33] can be used to directly map out the ensemble-averaged probability density of atoms in the ground band of the $\lambda/(2N)$-spaced lattices. In addition, Bloch oscillations [20, 34] or time-of-flight measurements of the momentum distributions [35] could be used to measure the N times larger Brillouin zones. In fact, $\lambda/4$-spaced lattices were recently realized using the techniques explored in this paper with ^{171}Yb atoms [36].

To adiabatically load into the ground band of the time-averaged $\lambda/(2N)$-spaced lattice potential, the stroboscopic lattice should be turned on slower than the motional timescale set by $\hbar/(N^2E_R)$, while maintaining a large gap to the bright states at all times. For pulse scheme (1) this can be achieved by slowly adjusting the envelope of the pulsed control beam $\tilde{\Omega}_c(t) = f(t)\Omega_c(t)$ while maintaining constant $\Omega_{\rm rms}$ (see appendix E).

7. Summary and outlook

In this paper, we evaluate the idea of stroboscopically generating potentials using the repulsive barriers of a dark-state KP potential. We analyzed the competing requirements of maintaining dark-state spin adiabaticity and simultaneous motional diabaticity during pulsing of the KP potentials in the presence of realistic imperfections. We showed that it is possible to create such potentials in an experimental system of ^{171}Yb atoms by calculating the Floquet spectrum of atoms in a stroboscopically generated $\lambda/4$-spaced lattice. This approach is applicable to any three-level system, although it needs to be well isolated from coupling to other levels in order to ensure good lifetimes. While we have treated 1D systems here, this method can be readily generalized to 2D. Using progenitor lattices of subwavelength attractive traps [37] in conjunction with barriers can allow for flexibility in tailoring arbitrary time-averaged potential landscapes not limited by diffraction.

Acknowledgments

We would like to thank Jean Dalibard for stimulating discussions. SS, YW, T-CT, SLR, and JVP acknowledge support from NSF PFC at JQI (Grant No. PHY1430094) and ONR (Grant No. N000141712411). PB and AVG acknowledge funding by AFOSR, ARL CDQI, NSF PFC at JQI, DoE ASCR Quantum Testbed Pathfinder program (award No. DE-SC0019040), ARO MURI, NSF PFCQC program, and the DoE BES QIS program (award No. DE-SC0019449). PT acknowledges support from the NRC postdoctoral fellowship.

Note-We note that related and complementary work is being pursued by Łacki *et al* [20].

Appendix A. Sufficiency conditions for adiabaticity

We start with the time-dependent Hamiltonian

$$\hat{H}(x,\,t) = \frac{\hat{p}^2}{2m} + \frac{\hbar}{2}\begin{pmatrix} 0 & 0 & \Omega_p(t) \\ 0 & 0 & \Omega_c^*(x,\,t) \\ \Omega_p(t) & \Omega_c(x,\,t) & -(2\Delta(t) + \mathrm{i}\Gamma) \end{pmatrix}. \tag{A.1}$$

$\hat{H}(x,\,t)$ is non-Hermitian due to the $\mathrm{i}\Gamma/2$ term and requires a biorthogonal set of eigenvectors to diagonalize it [38]. Due to the non-Hermitian nature of $\hat{H}(x,\,t)$, the eigenvectors are not guaranteed to be orthogonal to each other, but still form a linearly independent set that spans the Hilbert space [38]. To derive the artificial gauge potentials and for quantifying the sufficiency conditions for adiabaticity, we transform $\hat{H}(x,\,t)$ using a rotation transform $\hat{R}(x,\,t)$ composed of the right eigenvectors [38] of the spin-light field coupling part of $\hat{H}(x,\,t)$. The expression for $\hat{R}(x,\,t)$ is:

$$\hat{R}(x,\,t)=\begin{pmatrix}-\cos\alpha e^{i\theta} & \sin\alpha\dfrac{1}{\sqrt{1+l^2}} & \sin\alpha\dfrac{1}{\sqrt{1+u^2}}\\ \sin\alpha & \cos\alpha\dfrac{e^{-i\theta}}{\sqrt{1+l^2}} & \cos\alpha\dfrac{e^{-i\theta}}{\sqrt{1+u^2}}\\ 0 & \dfrac{l}{\sqrt{1+l^2}} & \dfrac{u}{\sqrt{1+u^2}}\end{pmatrix}, \tag{A.2}$$

where

$$\alpha=\tan^{-1}\left|\frac{\Omega_p(t)}{\Omega_c(x,\,t)}\right|,\ \zeta=\sqrt{|\Omega_c(x,\,t)|^2+\Omega_p^2(t)},$$
$$\theta=\mathrm{Arg}\,\Omega_c(x,\,t),\ l=\frac{2E_-(x,\,t)}{\zeta},\ u=\frac{2E_+(x,\,t)}{\zeta}. \tag{A.3}$$

For pulse scheme (1) where both control beams are changed simultaneously with equal magnitude: $\Omega_c(x,t)=\Omega_c(t)\sin(kx+\phi(t))$ resulting in $\theta(x,t)=0$. For pulse scheme (2) where only one control beam is pulsed: $\Omega_c(x,\,t)=\Omega_{c2}(t)e^{i(\phi_2(t)+kx)}/i-\Omega_c^0e^{-ikx}/2i$ resulting in $\theta(x,t)\neq$ constant.

The transformation $\hat{H}_{\rm rot}(x,\,t)=\hat{R}^{-1}\hat{H}\hat{R}-i\hbar\hat{R}^{-1}\partial\hat{R}/\partial t$ rotates $\hat{H}(x,\,t)$ into the dressed-atom picture of the Λ-system. The effective Hamiltonian after the transformation is [22, 24, 32, 39–41]

$$\hat{H}_{\rm rot}(x,\,t)=\frac{(\hat{p}-\hat{A})^2}{2m}-\hat{B}+\underbrace{\hbar\begin{pmatrix}0 & 0 & 0\\ 0 & E_-(x,\,t) & 0\\ 0 & 0 & E_+(x,\,t)\end{pmatrix}}_{\hat{E}_{\rm BO}(x,t)}, \tag{A.4}$$

where $\hat{A}=i\hbar\hat{R}^{-1}\nabla\hat{R}$, $\hat{B}=i\hbar\hat{R}^{-1}\partial\hat{R}/\partial t$, $\Delta_\Gamma(t)=\Delta(t)+i\Gamma/2$, and $E_\pm=(-\Delta_\Gamma(t)\pm\sqrt{\Delta_\Gamma^2(t)+\Omega_p^2(t)+|\Omega_c(x,\,t)|^2})/2$ are the energies of the upper and lower bright states.

We rearrange the terms in equation (A.4) to separate the motion of atoms in the three BO channels (dark state, upper-bright state, and lower-bright state) [17, 18, 22] from the off-diagonal couplings ($\hat{H}_{\rm od}(x,\,p,\,t)$). For pulse scheme (1) ($\theta(x,t)=0$), this gives

$$\hat{H}_{\rm rot}(x,\,t)=\overbrace{\frac{\hat{p}^2}{2m}+\frac{\hbar^2}{2m}\begin{pmatrix}(\alpha')^2 & 0 & 0\\ 0 & \dfrac{l'u'}{(l-u)^2}-\dfrac{u}{(l-u)}(\alpha')^2 & 0\\ 0 & 0 & \dfrac{l'u'}{(l-u)^2}+\dfrac{l}{(l-u)}(\alpha')^2\end{pmatrix}+\hat{E}_{\rm BO}(x,\,t)}^{\text{Born}-\text{Oppenheimer channels}}$$
$$\underbrace{-\hat{B}(x,\,t)-\frac{\hat{p}.\hat{A}(x,\,t)}{2m}-\frac{\hat{A}(x,\,t).\hat{p}}{2m}+\hat{N}(x,\,t)}_{\hat{H}_{\rm od}(x,p,t)}, \tag{A.5}$$

where $f'=\partial f/\partial x$ and $\dot{f}=\partial f/\partial t$. The term $\hat{B}(x,\,t)$ arises from the explicit time dependence of $\hat{H}(x,\,t)$. Careful pulse shaping can help suppress the terms in $\hat{B}(x,\,t)$ that couple the dark-state channel with the bright-state channels. The coupling terms in $\hat{H}_{\rm od}(x,\,p,\,t)$ depend only on the ratio of the Rabi frequencies (α', $\dot{\alpha}$) and not on their absolute magnitudes, while the energy separation between the channels ($\hat{E}_{\rm BO}(x,\,t)$) depend on absolute magnitudes of the Rabi frequencies. Thus at higher Rabi frequencies the BO channels become increasingly decoupled. In addition, $\Delta\ll\Omega_p^0$, Ω_c^0 ensures that the bright-state channels are well separated from the dark-state channel.

A.1. Floquet scalar gauge potentials

Here we derive the expression for the Floquet scalar gauge potential for the dark-state channel. The expression for $\hat{A}$ when both control beams are driven simultaneously as in pulse scheme (1) is

$$\hat{A} = \mathrm{i}\hbar \begin{pmatrix} 0 & -\frac{1}{\sqrt{l^2+1}}\alpha' & -\frac{1}{\sqrt{u^2+1}}\alpha' \\ -\frac{\sqrt{l^2+1}\,u}{(l-u)}\alpha' & 0 & -\frac{u'\sqrt{l^2+1}}{(u-l)\sqrt{u^2+1}} \\ -\frac{l\sqrt{u^2+1}}{(u-l)}\alpha' & -\frac{l'\sqrt{u^2+1}}{\sqrt{l^2+1}\,(l-u)} & 0 \end{pmatrix}. \tag{A.6}$$

The expression for the scalar gauge potentials for the BO channels is [23, 40]:

$$\frac{\hat{A}^2 - \mathrm{Diag}(\hat{A})^2}{2m} = \frac{\hbar^2}{2m}\begin{pmatrix} (\alpha')^2 & 0 & 0 \\ 0 & \frac{l'u'}{(l-u)^2} - \frac{u}{(l-u)}(\alpha')^2 & 0 \\ 0 & 0 & \frac{l'u'}{(l-u)^2} + \frac{l}{(l-u)}(\alpha')^2 \end{pmatrix} + \overbrace{\frac{\hbar^2}{2m}\begin{pmatrix} 0 & -\frac{ll'\alpha'}{(l^2+1)^{3/2}} & -\frac{uu'\alpha'}{(u^2+1)^{3/2}} \\ -\frac{l\sqrt{l^2+1}\,u'\alpha'}{(l-u)^2} & 0 & \frac{\sqrt{l^2+1}\,u(\alpha')^2}{\sqrt{u^2+1}\,(u-l)} \\ -\frac{u\sqrt{u^2+1}\,l'\alpha'}{(l-u)^2} & \frac{l\sqrt{u^2+1}\,(\alpha')^2}{\sqrt{l^2+1}\,(l-u)} & 0 \end{pmatrix}}^{\hat{N}(x,t)}, \tag{A.7}$$

where the first matrix contains the scalar gauge potentials for each of the BO channels. The scalar gauge potential for the dark-state channel is

$$W_{\mathrm{DS}}(x,\,t) = \frac{\hbar^2}{2m}\left(\frac{\partial}{\partial x}\alpha(x,\,t)\right)^2. \tag{A.8}$$

The expressions for $\hat{A}(x,\,t)$ and $W_{\mathrm{DS}}(x,t)$ for pulse scheme (2) ($\theta(x,t) \neq$ constant), are

$$\hat{A} = \mathrm{i}\hbar \begin{pmatrix} \mathrm{i}\theta'\cos^2\alpha & -\frac{\mathrm{e}^{-\mathrm{i}\theta}(\mathrm{i}\sin(2\alpha)\theta' + 2\alpha')}{2\sqrt{l^2+1}} & -\frac{\mathrm{e}^{-\mathrm{i}\theta}(\mathrm{i}\sin(2\alpha)\theta' + 2\alpha')}{2\sqrt{u^2+1}} \\ \frac{\mathrm{e}^{\mathrm{i}\theta}\sqrt{l^2+1}\,u(\mathrm{i}\sin(2\alpha)\theta' - 2\alpha')}{2(l-u)} & \frac{\mathrm{i}u\theta'\cos^2\alpha}{(l-u)} & -\frac{\sqrt{l^2+1}\,(\mathrm{i}u\theta'\cos^2\alpha + u')}{(u-l)\sqrt{u^2+1}} \\ \frac{\mathrm{e}^{\mathrm{i}\theta}l\sqrt{u^2+1}\,(\mathrm{i}\sin(2\alpha)\theta' - 2\alpha')}{2(u-l)} & -\frac{\sqrt{u^2+1}\,(\mathrm{i}l\theta'\cos^2\alpha + l')}{\sqrt{l^2+1}\,(l-u)} & -\frac{\mathrm{i}l\theta'\cos^2\alpha}{(l-u)} \end{pmatrix}, \tag{A.9}$$

and

$$W_{\mathrm{DS}}(x,\,t) = \frac{\hbar^2}{2m}\left[\frac{1}{4}\left(\sin(2\alpha(x,\,t))\frac{\partial}{\partial x}\theta(x,\,t)\right)^2 + \left(\frac{\partial}{\partial x}\alpha(x,\,t)\right)^2\right]. \tag{A.10}$$

A.2. Formulating the sufficiency conditions for adiabaticity

The general expression for $\hat{B}$ is analogous to $\hat{A}$, except that the derivatives are with respect to x in $\hat{A}$ and with respect to t in $\hat{B}$, which for pulse scheme (1) is:

$$\hat{B} = \mathrm{i}\hbar \begin{pmatrix} 0 & -\frac{1}{\sqrt{l^2+1}}\dot{\alpha} & -\frac{1}{\sqrt{u^2+1}}\dot{\alpha} \\ -\frac{\sqrt{l^2+1}\,u}{(l-u)}\dot{\alpha} & 0 & -\frac{\sqrt{l^2+1}}{(u-l)\sqrt{u^2+1}}\dot{u} \\ -\frac{l\sqrt{u^2+1}}{(u-l)}\dot{\alpha} & -\frac{\sqrt{u^2+1}}{\sqrt{l^2+1}\,(l-u)}\dot{l} & 0 \end{pmatrix}. \tag{A.11}$$

The local adiabatic criterion (equation (4*a*)) for the instantaneous dark state requires that the minimum of the spatially and temporally varying energy gap between the dark and bright states must be much larger than the largest off-diagonal couplings between them, which we quantify as

$$\min(|E_{-}(x_h,\,t)|,\,|E_{+}(x_h,\,t)|) \gg \left|\frac{\partial}{\partial t}\alpha(x_h,\,t)\right|. \tag{A.12}$$

For $\Delta = 0$, where fastest STIRAP pulses are guaranteed [24, 32, 42, 43]

$$\Omega_{\rm rms}(x_h,\,t) \gg \left|\frac{\partial}{\partial t}\alpha(x_h,\,t)\right|, \tag{A.13}$$

where $\Omega_{\rm rms}(x,\,t) = \sqrt{|\Omega_c(x,\,t)|^2 + \Omega_p^2(t)}$.

The expression for pulse scheme (2) ($\theta(x,t) \neq$ constant) is:

$$\hat{B} = \mathrm{i}\hbar\begin{pmatrix} \mathrm{i}\dot{\theta}\cos^2\alpha & -\dfrac{\mathrm{e}^{-\mathrm{i}\theta}(\mathrm{i}\sin(2\alpha)\dot{\theta} + 2\dot{\alpha})}{2\sqrt{l^2+1}} & -\dfrac{\mathrm{e}^{-\mathrm{i}\theta}(\mathrm{i}\sin(2\alpha)\dot{\theta} + 2\dot{\alpha})}{2\sqrt{u^2+1}} \\ \dfrac{\mathrm{e}^{\mathrm{i}\theta}\sqrt{l^2+1}\,u(\mathrm{i}\sin(2\alpha)\dot{\theta} - 2\dot{\alpha})}{2(l-u)} & \dfrac{\mathrm{i}u\dot{\theta}\cos^2\alpha}{(l-u)} & -\dfrac{\sqrt{l^2+1}\,(\mathrm{i}u\dot{\theta}\cos^2\alpha + \dot{u})}{(u-l)\sqrt{u^2+1}} \\ \dfrac{\mathrm{e}^{\mathrm{i}\theta}l\sqrt{u^2+1}\,(\mathrm{i}\sin(2\alpha)\dot{\theta} - 2\dot{\alpha})}{2(u-l)} & -\dfrac{\sqrt{u^2+1}\,(\mathrm{i}l\dot{\theta}\cos^2\alpha + \dot{l})}{\sqrt{l^2+1}\,(l-u)} & -\dfrac{\mathrm{i}l\dot{\theta}\cos^2\alpha}{(l-u)} \end{pmatrix}, \tag{A.14}$$

which in addition to $\dot{\alpha}$ and α depends on $\dot{\theta}$ and θ.

Appendix B. Pulse shaping

B.1. Pulse scheme (2)

In the main text, we consider pulse scheme (1) with the constraint $\Omega_{p(i)}^2(t) + \Omega_{c(i)}^2(t) = \beta_i^2$. For pulse scheme (2), in which only one control beam is pulsed, $\Omega_{p(i)}(t) = \Omega_{pi}^0$ and $\Omega_{c1(i)}(t) = \Omega_{ci}^0/2$, the pulse shape $\Omega_{c2(i)}(t)$ and t_{Si} are determined by $r_{(i)}(t)$ (equation (6)) and ϵ_i as follows:

$$\Omega_{c2(i)}(t) = \begin{cases} 0 & -T_i/2 \leqslant t \leqslant -T_i/2 + t_{\mathrm{off},i}/2 \\ \dfrac{\Omega_{ci}^0}{2} - \dfrac{\Omega_{pi}^0\mathcal{G}(t + t_{\mathrm{on},i}/2)}{\sqrt{16\pi^2\epsilon_i^2 + 4\pi^2 - \mathcal{G}^2(t + t_{\mathrm{on},i}/2)}} & -T_i/2 + t_{\mathrm{off},i}/2 \leqslant t \leqslant -t_{\mathrm{on},i}/2 \\ \dfrac{\Omega_{ci}^0}{2} & -t_{\mathrm{on},i}/2 \leqslant t \leqslant t_{\mathrm{on},i}/2 \\ \dfrac{\Omega_{ci}^0}{2} - \dfrac{\Omega_{pi}^0\mathcal{G}(t - t_{\mathrm{on},i}/2)}{\sqrt{16\pi^2\epsilon_i^2 + 4\pi^2 - \mathcal{G}^2(t - t_{\mathrm{on},i}/2)}} & t_{\mathrm{on},i}/2 \leqslant t \leqslant T_i/2 - t_{\mathrm{off},i}/2 \\ 0 & T_i/2 - t_{\mathrm{off},i}/2 \leqslant t \leqslant T_i/2 \end{cases}, \tag{B.1}$$

where $\mathcal{G}(t) = |4\pi t/t_{Si} - \sin(4\pi t/t_{Si})|$ and

$$t_{Si} = \frac{4}{r_{0i}\Omega_{pi}^0\sqrt{4\epsilon_i^2 + 1}}. \tag{B.2}$$

For this scheme, x_h is at the nodes of $\Omega_c(x,t)$ since the energy gap between the dark-state and bright-state channels is the smallest at the nodes and the spin at the node must completely flip from $|2\rangle$ to $|1\rangle$ (figure 1(a)) at the end of the pulse.

B.2. Verifying the spin-adiabaticity requirements and choice for r_{0i}

We use the off-diagonal coupling terms in equation (A.11) and set $\Delta = 0$ to recast the sufficiency conditions in [25] (the inequalities equations (4*a*)–(4*c*)). The first condition equation (4*a*) implies

$$\left|\frac{\partial}{\partial t}\alpha(x_h,\,t)\right| \ll \Omega_{\rm rms}(x_h,\,t), \tag{B.3}$$

$$\Rightarrow r_{0i} \ll 1, \tag{B.4}$$

where we have used equations (5) and (6). For $r_{0i} = 0.01$, this inequality is well satisfied. The stronger version [25] of the second inequality equation (4*b*) states:

$$\left|\frac{\partial}{\partial t}\left(\frac{\partial\alpha(x_h,\,t)/\partial t}{\Omega_{\rm rms}(x_h,\,t)}\right)\right|_{\max} t_{Si} \ll 1 \tag{B.5}$$

$$\Rightarrow r_{0i} \ll \frac{1}{2\pi} \simeq 0.16. \tag{B.6}$$

For $r_{0i} = 0.01$, this inequality is also well satisfied. We note that equation (B.5) also enforces that $r(t)$ must be differentiable. The stronger version of the third inequality equation (4*c*) is [25]

$$|\Omega_{\rm rms}(x_h, t) r^2(t)|_{\max} t_{Si} \ll 1 \tag{B.7}$$

$$\Rightarrow t_{Si}\beta_i r_{0i}^2 \ll 1 \Rightarrow 4\arctan(1/\epsilon_i) \ll 1/r_{0i} \text{ for pulse scheme (1)}, \tag{B.8}$$

where we have substituted equation (8). Again, this inequality is well satisfied for $r_{0i} = 0.01$.

Appendix C. Bloch–Floquet bandstructure

C.1. Bandstructure of $\hat{H}(x, t)$

We evaluate the matrix elements of the quasienergy operator $\hat{K}_q$ derived in section 4. $\hat{K}_q$ is expressed in dimensionless units $\tilde{x}$ and $\tilde{t}$ where $\tilde{x} = (2\pi/\lambda)x = kx, \tilde{t} = (2\pi/T)t = \omega_T t$, $E_R = \hbar^2k^2/(2m) = \hbar\omega_R$, and the tildes over x and t are dropped for convenience, as follows:

$$\left[(-\mathrm{i}\partial_x + q)^2 + \hat{\Omega}(x, t) - \mathrm{i}\omega_T \frac{\partial}{\partial t}\right]|u_{q,E_q}(x, t)\rangle\rangle = E_q|u_{q,E_q}(x, t)\rangle\rangle \tag{C.1}$$

$$\Rightarrow \hat{K}_q|u_{q,E_q}(x, t)\rangle\rangle = E_q|u_{q,E_q}(x, t)\rangle\rangle. \tag{C.2}$$

We expand the Hilbert space of the Bloch–Floquet modes in a plane wave basis: $|u_{q,E_q}(x, t)\rangle\rangle = \sum_{lmj} c_{lmj}|lmj\rangle$ where $\langle xt|lmj\rangle = \mathrm{e}^{\mathrm{i}lx}\mathrm{e}^{\mathrm{i}mt}|j\rangle$. Here $l \in [-L, L]$, $m \in [-M, M]$, $j \in [1, 2, 3]$ representing the three spins, and L and M are integers. The Hilbert space spanned by the basis set is composed of plane waves with the property $\sum_{lmj}|lmj\rangle\langle lmj| = I^{(2L+1)} \otimes I^{(2M+1)} \otimes I^3$. We solve equation (C.2) by diagonalizing $\hat{K}_q$. The matrix elements of the spin-independent components of $\hat{K}_q$ ($\langle\langle l'm'j'|\hat{K}_q|lmj\rangle\rangle$) are:

$$\left\langle l'm'j'\left|-\mathrm{i}\frac{\partial}{\partial t}\right|lmj\right\rangle = \delta_{ll'} \otimes (m\delta_{mm'}) \otimes \delta_{jj'}, \tag{C.3}$$

$$\langle l'm'j'|(-\mathrm{i}\partial_x + q)^2|lmj\rangle = [(l + q)^2\delta_{ll'}] \otimes \delta_{mm'} \otimes \delta_{jj'}. \tag{C.4}$$

The spin-dependent component of $\hat{K}_q$ is $\hat{\Omega}(x, t)$:

$$\hat{\Omega}(x, t) = \frac{1}{2}\begin{pmatrix} 0 & 0 & \Omega_p(t) \\ 0 & 0 & \Omega_c^*(x, t) \\ \Omega_p(t) & \Omega_c(x, t) & -(2\Delta(t) + \mathrm{i}\Gamma) \end{pmatrix} \tag{C.5}$$

$$= \frac{1}{2}(\underbrace{\Omega_p(t)(|1\rangle\langle 3| + |3\rangle\langle 1|)}_{\mathrm{A}} + \underbrace{-(2\Delta(t) + \mathrm{i}\Gamma)|3\rangle\langle 3|}_{\mathrm{B}} + \underbrace{\Omega_c^*(x, t)|2\rangle\langle 3| + \Omega_c(x, t)|3\rangle\langle 2|}_{\mathrm{C}}), \tag{C.6}$$

where the matrix elements of A and B are

$$\langle l'm'j'|\mathrm{A}|lmj\rangle = \delta_{ll'} \otimes \langle m'|\Omega_p(t)|m\rangle \otimes (\delta_{j'1}\delta_{j3} + \delta_{j'3}\delta_{j1}), \tag{C.7}$$

$$\langle l'm'j'|\mathrm{B}|lmj\rangle = -\mathrm{i}\Gamma\delta_{ll'} \otimes \delta_{mm'} \otimes \delta_{j'3}\delta_{j3} - 2\delta_{ll'} \otimes \langle m'|\Delta(t)|m\rangle \otimes \delta_{j'3}\delta_{j3}. \tag{C.8}$$

Depending on the pulse scheme, $\langle l'm'j'|\mathrm{C}|lmj\rangle$ has different forms. For pulse scheme (1) i.e. $\Omega_c(x, t) = \Omega_c(t)\sin(x + \phi(t))$:

$$\langle l'm'j'|\mathrm{C}|lmj\rangle = \left\{\tfrac{1}{2}(\delta_{l',l-1} + \delta_{l',l+1}) \otimes \langle m'|\Omega_c(t)\sin\phi(t)|m\rangle + \tfrac{1}{2\mathrm{i}}(\delta_{l',l+1} - \delta_{l',l-1}) \otimes \langle m'|\Omega_c(t)\cos\phi(t)|m\rangle\right\} \otimes (\delta_{j'2}\delta_{j3} + \delta_{j'3}\delta_{j2}). \tag{C.9}$$

For pulse scheme (2) i.e. $\Omega_c(x, t) = \Omega_{c2}(t)\mathrm{e}^{\mathrm{i}(\phi_2(t)+x)}/\mathrm{i} - \Omega_c^0\mathrm{e}^{-\mathrm{i}x}/2\mathrm{i}$:

$$\langle l'm'j'|\mathrm{C}|lmj\rangle = \left\{\frac{1}{\mathrm{i}}\delta_{l',l+1} \otimes \langle m'|\Omega_{c2}(t)\mathrm{e}^{\mathrm{i}\phi_2(t)}|m\rangle - \frac{\Omega_c^0}{2\mathrm{i}}\delta_{l',l-1} \otimes \delta_{m'm}\right\} \otimes \delta_{j'3}\delta_{j2} + \left\{-\frac{1}{\mathrm{i}}\delta_{l',l-1} \otimes \langle m'|\Omega_{c2}(t)\mathrm{e}^{-\mathrm{i}\phi_2(t)}|m\rangle + \frac{\Omega_c^0}{2\mathrm{i}}\delta_{l',l+1} \otimes \delta_{m'm}\right\} \otimes \delta_{j'2}\delta_{j3}. \tag{C.10}$$

The spatio-temporal probability distribution of a Bloch–Floquet mode is

$$|\psi|^2 = \sum_{l'm'lmj} c_{l'm'j}c_{lmj}\mathrm{e}^{\mathrm{i}(l-l')x+\mathrm{i}(m-m')t}, \tag{C.11}$$

where $|\psi\rangle = \langle x,\ t|u_{q,E_q}(x,\ t)\rangle\rangle$ with the fractional probability of being in spin $|i\rangle$ at x and t ($x \in [-\pi, \pi]$, $t \in [-\pi, \pi]$) given by

$$\frac{|\langle j|\psi\rangle|^2}{|\psi|^2} = \frac{\sum_{l'm'lm} c_{l'm'j} c_{lmj} e^{i(l-l')x+i(m-m')t}}{\sum_{l'm'lmj} c_{l'm'j} c_{lmj} e^{i(l-l')x+i(m-m')t}}. \tag{C.12}$$

It is important [17] to appropriately choose the number of plane waves L and M to be large enough to accurately represent the couplings between the dark-state channel and bright-state channels. We solve for the lowest few dozen eigenstates near zero energy of these sparse matrices with dimensions $3(2L+1)(2M+1) \times 3(2L+1)(2M+1) \sim 10^5 \times 10^5$ using the Arnoldi algorithm. We find that the solution converges with M as low as 25, however for all our calculations we use $M \simeq 210$.

C.2. Bandstructure of $\hat{H}_{\rm DS}(x,\ t)$

In this subsection, we outline the method used to numerically solve for the Bloch–Floquet bandstructure of the dark-state channel ignoring non-adiabatic couplings to the bright-state channels:

$$\hat{H}_{\rm DS}(x,\ t) = \frac{\hat{p}^2}{2m} + W_{\rm DS}(x,\ t) \tag{C.13}$$

where $\hat{H}_{\rm DS}(x + \lambda/2,\ t) = \hat{H}_{\rm DS}(x,\ t)$ and $\hat{H}_{\rm DS}(x,\ t + T) = \hat{H}_{\rm DS}(x,\ t)$. Due to the nonlinear nature of $W_{\rm DS}(x, t)$ solving for the bandstructure in the extended Hilbert space approach requires a 2D Fourier transform of $W_{\rm DS}(x, t)$. Instead, we solve for the bandstructure using the approach outlined in [2, 3, 5, 29] where we evaluate the time evolution operator over one Floquet period, $\hat{U}(T,\ 0)$, and then diagonalize it.

Making the Bloch ansatz, $|\psi_{\rm DS}(x,\ t)\rangle = e^{iqx}|u_{q,\rm DS}(x,\ t)\rangle$, the time-dependent Schrödinger equation in dimensionless units is

$$\frac{\partial}{\partial t}|u_{q,\rm DS}(x,\ t)\rangle = -\frac{i}{\omega_T}\overbrace{((-i\partial_x + q)^2 + W_{\rm DS}(x,\ t))}^{\hat{H}_{q,\rm DS}}|u_{q,\rm DS}(x,\ t)\rangle. \tag{C.14}$$

We determine the time evolution operator for one Floquet period $\hat{U}_{q,\rm DS}(2\pi + t_0,\ t_0)$ [2, 3, 5] and equate that to the time evolution operator of an effective Floquet Hamiltonian $e^{-i\hat{H}^{\rm F}_{q,\rm DS}[t_0]T/\hbar}$, where $\hat{H}^{\rm F}_{q,\rm DS}[t_0]$ is defined at a Floquet gauge t_0 [4].

The expression for $\hat{U}_{q,\rm DS}(2\pi,\ 0)$ for $t_0 = 0$ is derived as follows:

$$\begin{aligned}
|u_{q,\rm DS}(x,\ 2\pi)\rangle &= \hat{U}_{q,\rm DS}(2\pi,\ 0)|u_{q,\rm DS}(x,\ 0)\rangle \\
&= \mathcal{T}\left(e^{-i\int_0^{2\pi}\hat{H}_{q,\rm DS}(x,t)dt/\omega_T}\right)|u_{q,\rm DS}(x,\ 0)\rangle \\
&= \left(\prod_{l=0}^{L} e^{-i\hat{H}_{q,\rm DS}(x,l\Delta t)\Delta t/\omega_T}\right)|u_{q,\rm DS}(x,\ 0)\rangle \\
&= \left(\prod_{l=0}^{L} \hat{S}_{q,l} e^{-i\hat{E}_q(l\Delta t)\Delta t/\omega_T}\hat{S}^{-1}_{q,l}\right)|u_{q,\rm DS}(x,\ 0)\rangle \\
\Rightarrow\ \hat{U}_{q,\rm DS}(2\pi,\ 0) &= \left(\prod_{l=0}^{L} \hat{S}_{q,l} e^{-i\hat{E}_q(l\Delta t)\Delta t/\omega_T}\hat{S}^{-1}_{q,l}\right) = e^{-\hat{H}^{\rm F}_{q,\rm DS}[0]T/\hbar},
\end{aligned} \tag{C.15}$$

where $\mathcal{T}$ is the time-ordering operator, $L\Delta t = 2\pi$ and L is an integer number of time-steps. $\hat{S}_{q,l}$ is chosen to diagonalize $\hat{H}_{q,\rm DS}(x,\ l\Delta t)$ at time $l\Delta t$: $\hat{S}^{-1}_{q,l}\hat{H}_{q,\rm DS}(x,\ l\Delta t)\hat{S}_{q,l} = \hat{E}_q(l\Delta t)$ where $\hat{S}^{-1}_{q,l}\hat{S}_{q,l} = I^{2L+1}$. Finally, we diagonalize $\hat{U}_{q,\rm DS}(2\pi,\ 0)$ in equation (C.15) to evaluate the Floquet eigenvalues and the eigenvectors [2, 3, 5]:

$$\hat{U}_{q,\rm DS}(2\pi,\ 0) = e^{-i\hat{H}^{\rm F}_{q,\rm DS}[0]T/\hbar} = \sum_{j=1}^{2L+1} e^{-iE^j_q T/\hbar}|u^j_{q,\rm DS}(x,\ 0)\rangle\langle u^j_{q,\rm DS}(x,\ 0)|. \tag{C.16}$$

The Floquet eigenvalues E^j_q are time-independent. For $\lambda/(2N)$-spaced lattices, the Rabi pulses are the same for each T/N sub-Floquet period and symmetry arguments were used to speed up the creation of the one-period Floquet evolution operator, $\hat{U}_{q,\rm DS}(2\pi,\ 0)$ [5].

Appendix D. Effect of two-photon detuning

In this section, we discuss the detrimental effect of the states outside the Λ-system in realizing $\lambda/(2N)$-spaced lattices for the specific case of ^{171}Yb. In addition to the Λ-system composed of the states $|1\rangle$, $|2\rangle$ and $|3\rangle$, the $(6s6p)^3P_1$ manifold has 5 additional states $|4\rangle$ to $|8\rangle$ that can couple to states $|1\rangle$ and $|2\rangle$ (figure D1). When the

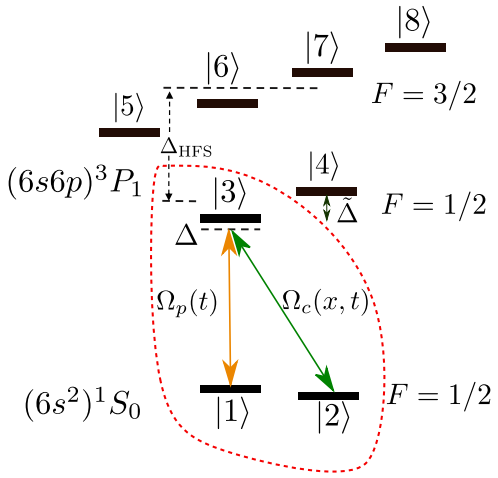

Figure D1. Level structure of the $(6s^2)^1S_0$ and $(6s6p)^3P_1$ manifolds of ^{171}Yb: Δ is the single photon detuning, $\tilde{\Delta}$ is the Zeeman splitting in the excited state due to an external magnetic field, and $\Delta_{\rm HFS}$ is the $(6s6p)^3P_1$ hyperfine splitting.

effective Rabi frequencies are much smaller than their respective detunings to the off-resonant excited states $|4\rangle$ to $|8\rangle$, we can adiabatically eliminate the excited states and quantify their effect on the ground states $|1\rangle$ and $|2\rangle$ of the Λ-system in dimensionless units as follows:

$$\begin{aligned}\hat{\Omega}_{\rm OR}(x,\,t) \simeq &\left(\delta_1(t) + \frac{\Omega_p^2(t)}{2(\Delta_{\rm HFS} + {\rm i}\Gamma/2)} + \frac{3|\Omega_c(x,\,t)|^2}{8(\Delta_{\rm HFS} + {\rm i}\Gamma/2)}\right)|1\rangle\langle 1| \\ &+ \left(\delta_2(t) + \frac{\Omega_p^2(t)}{4(\tilde{\Delta} + {\rm i}\Gamma/2)} + \frac{\Omega_p^2(t)}{2(\Delta_{\rm HFS} + {\rm i}\Gamma/2)} + \frac{|\Omega_c(x,\,t)|^2}{8(\Delta_{\rm HFS} + {\rm i}\Gamma/2)}\right)|2\rangle\langle 2| \qquad \text{(D.1)} \\ \simeq &\left(\delta_1(t) + \frac{\Omega_p^2(t)}{2\Delta_{\rm HFS}} + \frac{3|\Omega_c(x,\,t)|^2}{8\Delta_{\rm HFS}} - {\rm i}\frac{\Gamma_1(x,\,t)}{2}\right)|1\rangle\langle 1| \\ &+ \left(\delta_2(t) + \frac{\Omega_p^2(t)}{4\tilde{\Delta}} + \frac{\Omega_p^2(t)}{2\Delta_{\rm HFS}} + \frac{|\Omega_c(x,\,t)|^2}{8\Delta_{\rm HFS}} - {\rm i}\frac{\Gamma_2(x,\,t)}{2}\right)|2\rangle\langle 2|, \qquad \text{(D.2)}\end{aligned}$$

where

$$\Gamma_1(x,\,t) = \Gamma\left(\frac{\Omega_p^2(t)}{2\Delta_{\rm HFS}^2} + \frac{3|\Omega_c(x,\,t)|^2}{8\Delta_{\rm HFS}^2}\right), \qquad \text{(D.3)}$$

$$\Gamma_2(x,\,t) = \Gamma\left(\frac{\Omega_p^2(t)}{4\tilde{\Delta}^2} + \frac{\Omega_p^2(t)}{2\Delta_{\rm HFS}^2} + \frac{|\Omega_c(x,\,t)|^2}{8\Delta_{\rm HFS}^2}\right), \qquad \text{(D.4)}$$

when $\Gamma \ll \tilde{\Delta},\ \Delta_{\rm HFS}$. By dynamically modulating $\delta_1(t)$ and $\delta_2(t)$, we compensate for the spatially homogeneous but temporally modulated real parts in equation (D.2). The compensated $\hat{\Omega}_{\rm OR}(x,\,t)$ is added to $\hat{H}(x,\,t)$ and solved for using the method outlined in section 4 and appendix C.1 to calculate the Bloch–Floquet bandstructure of $\lambda/(2N)$-spaced lattices in the presence of two-photon detunings and photon scattering loss due to states outside the Λ-system. The non-Hermitian terms in equation (D.2) (equations (D.3) and (D.4)) account for loss from photon scattering due to admixing of the adiabatically eliminated excited states with the bare stable ground states $|1\rangle$ and $|2\rangle$. For a $\lambda/4$-spaced lattice created by pulse scheme (1), equation (D.2) is

$$\begin{aligned}\langle l'm'j'|\hat{\Omega}_{\rm OR}(x,\,t)|lmj\rangle = &-{\rm i}\frac{\Gamma}{4\Delta_{\rm HFS}^2}\delta_{l',l} \otimes \langle m'|\Omega_p^2(t)|m\rangle \otimes (\delta_{j'1}\delta_{j1} + \delta_{j'2}\delta_{j2}) \\ &- {\rm i}\frac{\Gamma}{8\tilde{\Delta}^2}\delta_{l',l} \otimes \langle m'|\Omega_p^2(t)|m\rangle \otimes \delta_{j'2}\delta_{j2} - {\rm i}\frac{\Gamma}{2\Delta_{\rm HFS}^2}\delta_{l',l} \otimes \langle m'|\Omega_c^2(t)|m\rangle \otimes \left(\frac{3}{16}\delta_{j'1}\delta_{j1} + \frac{1}{16}\delta_{j'2}\delta_{j2}\right) \\ &- \left(\frac{1}{\Delta_{\rm HFS}} - {\rm i}\frac{\Gamma}{2\Delta_{\rm HFS}^2}\right)\left\{\frac{1}{2}(\delta_{l',l-2} + \delta_{l',l+2}) \otimes \langle m'|\Omega_c^2(t)\cos 2\phi(t)|m\rangle\right\} \otimes \left(\frac{3}{16}\delta_{j'1}\delta_{j1} + \frac{1}{16}\delta_{j'2}\delta_{j2}\right), \qquad \text{(D.5)}\end{aligned}$$

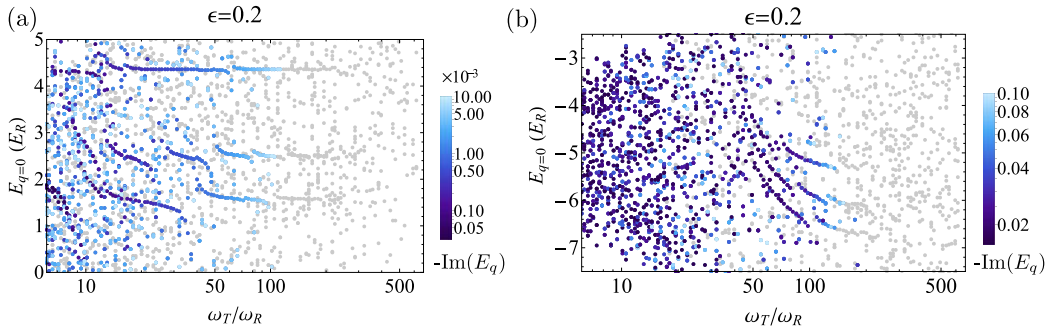

Figure D2. The Floquet spectrum E_q at $q = 0$ as a function of ω_T/ω_R for a $\lambda/4$-spaced lattice: all calculations are performed for $\Omega_{ci}^0 = 600\Gamma$, $r_{0i} = 0.01$, $\epsilon_i = 0.2$, $\Delta = 0$, and $t_{Si} = 0.36T_r$. (a) For the ideal Λ-system. (b) For the Λ-system with the spatio-temporally modulated ac-Stark shifts and losses due to the excited states $|4\rangle$–$|8\rangle$.

where $\Delta_{\rm HFS} \simeq -33,\ 000\ \Gamma$ and $\tilde{\Delta} \simeq -5500\ \Gamma$ (figure D1). The real spatio-temporally modulated terms in equation (D.5) originate from $\Omega_c(x, t)$ and may only be compensated with the experimental overhead of adding more laser fields.

In figure D2(b), we show the effect of $\hat{\Omega}_{\rm OR}(x,\ t)$ and contrast it with an ideal Λ-system (figure D2(a)). In figure D2(b), the window of operational ω_T is smaller and the losses are higher, as expected. At lower ω_T, the sinusoidal two-photon detunings are not time-averaged out. The ground band is also red shifted due to the ac-Stark shifts being red detuned. Large Rabi frequencies with uncompensated spatio-temporally modulated two-photon detuning destroy the fidelity of the STIRAP pulses and make it harder to create $\lambda/(2N)$-spaced lattices. Losses from excited states admixing further shorten lifetimes.

Another possible candidate system that uses fine-structure states instead of hyperfine states for the Λ-system consists of the metastable states $(6s6p)^3{\rm P}_2$ and $(6s6p)^3{\rm P}_0$ of Yb as the long-lived states $|1\rangle$ and $|2\rangle$, and $(6s7s)\,^3{\rm S}_1$ as the excited state $|3\rangle$. This Λ-system is well isolated, and $|1\rangle$ and $|2\rangle$ are separated in energy by multiple THz. In this configuration, $\lambda/(2N)$-spaced lattices can be realized for both bosonic and fermionic species of Yb. The large matrix elements for the $(6s6p)^3P_2 \leftrightarrow (6s7s)\,^3S_1$ and $(6s6p)^3P_0 \leftrightarrow (6s7s)\,^3S_1$ transitions ensure that higher Rabi frequencies can be achieved in these systems without the detrimental effect of states outside the Λ-system. However, Floquet heating from interactions [2, 3] and losses from fine-structure collisions of $(6s6p)^3{\rm P}_2$ atoms [44] could limit lifetimes in these systems.

Appendix E. Adiabatic loading into the ground band

There are a few ways to adiabatically load into the ground band of a $\lambda/4$-spaced lattice given that one has control over $\Omega_{c1}(t)$, $\Omega_{c2}(t)$, $\Omega_p(t)$, $\phi_1(t)$, and $\phi_2(t)$. We consider here a protocol in which the time-averaged potential is grown by periodically pulsing $\Omega_c(t)$ with a slowly varying envelope $f(t)$ with a timescale much slower than the motional degree of freedom: $\tilde{\Omega}_c(t) = f(t)\Omega_c(t)$. The pulse profile for $\Omega_c(t)$ is determined by equation (7) for a given final ϵ. For pulse scheme (1), $\tilde{\Omega}_p(t)$ along the ramp is determined by $\tilde{\Omega}_p(t) = \sqrt{\beta^2 - \tilde{\Omega}_c^2(t)}$. The large and constant energy gap $\hbar\beta/2$ minimizes admixing of the dark-state channel with the bright-state channels. Under these conditions the loading is spin adiabatic because

$$\left|\frac{\partial\tilde{\alpha}(x_h,\ t)}{\partial t}\right| < |\beta r(t)| < \beta r_0, \tag{E.1}$$

for $0 < f(t) < 1$ and $\dot{f}(t) \ll 1/T$, where $\tilde{\alpha} = \tan^{-1}[\tilde{\Omega}_p(t)/\tilde{\Omega}_c(x,\ t)]$. For pulse scheme (2), we propose the protocol $\tilde{\Omega}_p(t) = (1 - f(t))\Omega_p^0$ and the pulse profile for $\Omega_{c2}(t)$ is one that creates the desired $\lambda/4$-spaced lattice for a chosen ϵ according to equation (B.1). $\tilde{\Omega}_p(t)$ is reduced from an initial large value to its final value of Ω_p^0. This ensures that the energy gap $\hbar\beta/2$ at the nodes is lower at the end of the ramp than at the start, minimizing admixing of the dark-state channel with the bright-state channels along the ramp.

ORCID iDs

S Subhankar https://orcid.org/0000-0001-8664-3098
P Bienias https://orcid.org/0000-0002-7583-7177

References

[1] Altland A and Simons B D 2010 *Response Functions* 2nd edn (Cambridge: Cambridge University Press) pp 360–408
[2] Eckardt A and Anisimovas E 2015 High-frequency approximation for periodically driven quantum systems from a Floquet-space perspective *New J. Phys.* **17** 093039
[3] Eckardt A 2017 Colloquium: Atomic quantum gases in periodically driven optical lattices *Rev. Mod. Phys.* **89** 011004
[4] Bukov M, D'Alessio L and Polkovnikov A 2015 Universal high-frequency behavior of periodically driven systems: from dynamical stabilization to floquet engineering *Adv. Phys.* **64** 139–226
[5] Holthaus M 2015 Floquet engineering with quasienergy bands of periodically driven optical lattices *J. Phys. B: At. Mol. Opt. Phys.* **49** 013001
[6] Oka T and Kitamura S 2019 Floquet engineering of quantum materials *Annu. Rev. Condens. Matter Phys.* **10** 387–408
[7] Lewenstein M, Sanpera A and Ahufinger V 2017 *Ultracold Atoms in Optical Lattices: Simulating Quantum Many-Body Systems* (Oxford: Oxford University Press)
[8] Dutta O, Gajda M, Hauke P, Lewenstein M, Lühmann D-S, Malomed B A, Sowiński T and Zakrzewski J 2015 Non-standard hubbard models in optical lattices: a review *Rep. Prog. Phys.* **78** 066001
[9] Gross C and Bloch I 2017 Quantum simulations with ultracold atoms in optical lattices *Science* **357** 995–1001
[10] Nascimbene S, Goldman N, Cooper N R and Dalibard J 2015 Dynamic optical lattices of subwavelength spacing for ultracold atoms *Phys. Rev. Lett.* **115** 140401
[11] Lewenstein M, Sanpera A, Ahufinger V, Damski B, Sen A and Sen U 2007 Ultracold atomic gases in optical lattices: mimicking condensed matter physics and beyond *Adv. Phys.* **56** 243–379
[12] Dubetsky B and Berman P R 2002 $\lambda/4$, $\lambda/8$, and higher order atom gratings via raman transitions *Laser Phys.* **12** 1161–70
[13] Anderson R P, Trypogeorgos D, Valdés-Curiel A, Liang Q Y, Tao J, Zhao M, Andrijauskas T, Juzeliūnas G and Spielman I B 2019 Realization of a fractional period adiabatic superlattice arXiv:1907.08910
[14] Ritt G, Geckeler C, Salger T, Cennini G and Weitz M 2006 Fourier synthesis of optical potentials for atomic quantum gases *Phys. Rev.* A **74** 4–7
[15] Yi W, Daley A J, Pupillo G and Zoller P 2008 State-dependent, addressable subwavelength lattices with cold atoms *New J. Phys.* **10** 073015
[16] Lundblad N, Ansari S, Guo Y and Moan E 2014 Observations of $\lambda/4$ structure in a low-loss radio-frequency-dressed optical lattice *Phys. Rev.* A **90** 053612
[17] Łacki M, Baranov M A, Pichler H and Zoller P 2016 Nanoscale 'dark State' optical potentials for cold atoms *Phys. Rev. Lett.* **117** 233001
[18] Jendrzejewski F, Eckel S, Tiecke T G, Juzeliūnas G, Campbell G K, Jiang L and Gorshkov A V 2016 Subwavelength-width optical tunnel junctions for ultracold atoms *Phys. Rev.* A **94** 063422
[19] Wang Y, Subhankar S, Bienias P, Łacki M, Tsui T C, Baranov M A, Gorshkov A V, Zoller P, Porto J V and Rolston S L 2018 Dark state optical lattice with a subwavelength spatial structure *Phys. Rev. Lett.* **120** 083601
[20] Lacki M, Zoller P and Baranov M A 2019 Stroboscopic painting of optical potentials for atoms with subwavelength resolution *Am. Phys. Soc.* **100** 033610
[21] Rahav S, Gilary I and Fishman S 2003 Effective Hamiltonians for periodically driven systems *Phys. Rev.* A **68** 013820
[22] Moody J, Shapere A D and Wilczek F 1989 Adiabatic effective Lagrangians *Report No.* IASSNS-HEP-89/13
[23] Dalibard J, Gerbier F, Juzeliūnas G and Öhberg P 2011 Colloquium: Artificial gauge potentials for neutral atoms *Rev. Mod. Phys.* **83** 1523–43
[24] Vitanov N V, Rangelov A A, Shore B W and Bergmann K 2017 Stimulated Raman adiabatic passage in physics, chemistry, and beyond *Rev. Mod. Phys.* **89** 015006
[25] Tong D M, Singh K, Kwek L C and Oh C H 2007 Sufficiency criterion for the validity of the adiabatic approximation *Phys. Rev. Lett.* **98** 150402
[26] Xiao D, Chang M-C and Niu Q 2010 Berry phase effects on electronic properties *Rev. Mod. Phys.* **82** 1959–2007
[27] Rice M J and Mele E J 1982 Elementary excitations of a linearly conjugated diatomic polymer *Phys. Rev. Lett.* **49** 1455–9
[28] Shirley J H 1965 Solution of the schrodinger equation with a Hamiltonian periodic in time *Phys. Rev.* **138** B979–87
[29] Grifoni M and Hänggi P 1998 Driven quantum tunneling *Phys. Rep.* **304** 229–354
[30] Breuer H P and Holthaus M 1989 Adiabatic processes in the ionization of highly excited hydrogen atoms *Z. Phys.* D **11** 1–14
[31] Drese K and Holthaus M 1999 Floquet theory for short laser pulses *Eur. Phys. J.* D **5** 119–34
[32] Shore B W 2017 Picturing stimulated Raman adiabatic passage: a STIRAP tutorial *Adv. Opt. Photonics* **9** 563
[33] Subhankar S, Wang Y, Tsui T-C, Rolston S L and Porto J V 2019 Nanoscale atomic density microscopy *Phys. Rev.* X **9** 021002
[34] Dahan M B, Peik E, Reichel J, Castin Y and Salomon C 1996 Bloch oscillations of atoms in an optical potential *Phys. Rev. Lett.* **76** 4508–11
[35] Kastberg A, Phillips W D, Rolston S L, Spreeuw R J C and Jessen P S 1995 Adiabatic cooling of cesium to 700 nk in an optical lattice *Phys. Rev. Lett.* **74** 1542–5
[36] Tsui T-C, Wang Y, Subhankar S, Porto J V and Rolston S L 2019 Realization of a stroboscopic optical lattice for cold atoms with subwavelength spacing arXiv:1911.00394
[37] Bienias P *et al* 2018 Coherent optical nano-tweezers for ultra-cold atoms arXiv:1808.02487
[38] Brody D C 2014 Biorthogonal quantum mechanics *J. Phys. A: Math. Theor.* **47** 035305
[39] Fleischhauer M and Marangos J P 2005 Electromagnetically induced transparency: optics in coherent media *Rev. Mod. Phys.* **77** 633–73
[40] Cheneau M, Yefsah T, Unter K J, Juzeliūnas G and Dalibard J 2008 Geometric potentials in quantum optics: a semi-classical interpretation *Europhys. Lett.* **83** 60001
[41] Goldman N, Juzeliūnas G, Öhberg P and Spielman I B 2014 Light-induced gauge fields for ultracold atoms *Rep. Prog. Phys.* (https://doi.org/10.1088/0034-4885/77/12/126401)
[42] Dykhne A M 1962 Adiabatic perturbation of discrete spectrum states *J. Exp. Theor. Phys.* **14** 941–3
[43] Vasilev G S, Kuhn A and Vitanov N V 2009 Optimum pulse shapes for stimulated Raman adiabatic passage *Phys. Rev.* A **80** 1–7
[44] Yamaguchi A, Uetake S, Hashimoto D, Doyle J M and Takahashi Y 2008 Inelastic collisions in optically trapped ultracold metastable ytterbium *Phys. Rev. Lett.* **101** 233002

Appendix E: Realization of a stroboscopic optical lattice for cold atoms with subwavelength spacing

Rapid Communications

Realization of a stroboscopic optical lattice for cold atoms with subwavelength spacing

T-C. Tsui,[*] Y. Wang,[*,†] S. Subhankar, J. V. Porto, and S. L. Rolston

Joint Quantum Institute, National Institute of Standards and Technology and the University of Maryland, College Park, Maryland 20742, USA

(Received 4 November 2019; accepted 4 March 2020; published 17 April 2020)

Optical lattices are typically created via the ac Stark shift and are limited by diffraction to periodicities $\geqslant \lambda/2$, where λ is the wavelength of light used to create them. Lattices with smaller periodicities may be useful for many-body physics with cold atoms and can be generated by stroboscopic application of a phase-shifted lattice with subwavelength features. Here we demonstrate a $\lambda/4$-spaced lattice by stroboscopically applying optical Kronig-Penney-like potentials which are generated using spatially dependent dark states. We directly probe the periodicity of the $\lambda/4$-spaced lattice by measuring the average probability density of the atoms loaded into the ground band of the lattice. We measure lifetimes of atoms in this lattice and discuss the mechanisms that limit the applicability of this stroboscopic approach.

DOI: 10.1103/PhysRevA.101.041603

I. INTRODUCTION

Ultracold atoms trapped in periodic optical potentials provide wide-ranging opportunities to study many-body physics in highly controllable systems [1,2]. In all cases, the characteristic single-particle energy scale is set by the recoil energy, $E_R = h^2/(8md^2)$, where m is the mass of the atom and d is the spatial period of the lattice. Although temperatures in such systems can be quite low, it is still challenging to reach temperatures well below the relevant many-body physics energy scales, which can be exceedingly small. Increasing the recoil energy can potentially increase both single-particle and many-body energy scales through tighter confinement, which may aid in creating systems well into the regime where many-body ground-state physics is observable. An inherent obstacle to smaller lattice spacing is the optical diffraction limit, which prevents lattice periodicities below $d = \lambda/2$, where λ is the wavelength of the light forming the lattice. Several approaches to move beyond the diffraction limit have been proposed and some realized based on multiphoton effects [3–5], rf-dressed adiabatic potentials [6–8], and trapping in near-field guided modes with nanophotonic systems [9–12].

Here we report the realization of a recently proposed Floquet-based approach [13–15] to create small-period lattices, specifically $\lambda/4$-spaced lattices, by time-averaging a modulated lattice potential that has subwavelength features. We load atoms into the ground band of this time-dependent lattice and measure their average probability density $|\psi_{\text{avg}}(x)|^2$ with nanoscale resolution [16–18], to confirm the subwavelength nature of the lattice. We study the lifetime of atoms in the lattices over a range of modulation (Floquet) frequencies $\omega_F = 2\pi/T$, where T is the period of a complete cycle, to determine the frequency range over which the time-averaged approach works.

Creating an effective time-averaged potential requires that the time dependence of the lattice be motionally diabatic [19–21], namely, that T be much smaller than the motional timescale of the atoms. Time-averaging a dynamically applied lattice potential cannot create an effective potential landscape with higher spatial Fourier components than the underlying progenitor lattice. This implies that in order to create landscapes with subwavelength periodicity, one must time-average a potential that itself has subwavelength features [13]. In this work, we make use of the Kronig-Penney-like (KP-like) potential to generate the desired potential landscapes [14,15]. Such a KP potential is implemented via the dark state associated with a three-level Λ system [22–24]. The spin adiabaticity required to maintain the dark state during the stroboscopic cycle imposes additional constraints, as discussed below.

There are multiple ways to implement time-averaging with a KP lattice [14,15]. The particular approach that we adopt, optimized for our experimental conditions, is shown in Fig. 1. Periodic potentials with $\lambda/2$ spacing but subwavelength structure are stroboscopically applied to the atoms to create the desired potential landscape. Specifically, atoms are subjected to a KP potential for half of the Floquet cycle $T/2$; the potential is then ramped down to zero and its position is shifted by half of the lattice spacing $\lambda/4$; the shifted potential is ramped on again and held for another half cycle, before being ramped off and its position is restored.

Two factors must be considered to ensure that time-averaging is an effective description of the system. First, motional diabaticity sets a lower bound on the Floquet frequency ω_F, beyond which the band structure becomes unstable and severe heating limits the lifetime. Second, the dark-state nature of the KP lattice sets an upper bound to ω_F. As the KP potential is a scalar gauge potential arising from a spatially varying dark state [22–24], switching on and off such a potential requires atoms to adiabatically follow the spatiotemporal dark state at all times. We ensure this adiabatic following by carefully designing the pulse shapes

[*]These authors contributed equally in this work.
[†]Corresponding author: wang.yang.phy@gmail.com

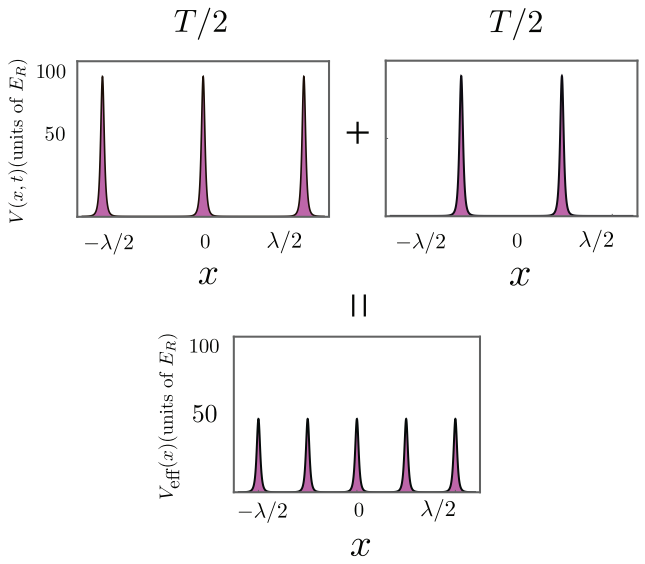

FIG. 1. The stroboscopic approach to creating a time-averaged effective potential with a lattice spacing of $\lambda/4$ by dynamically pulsing KP potentials with $\lambda/2$ spacing.

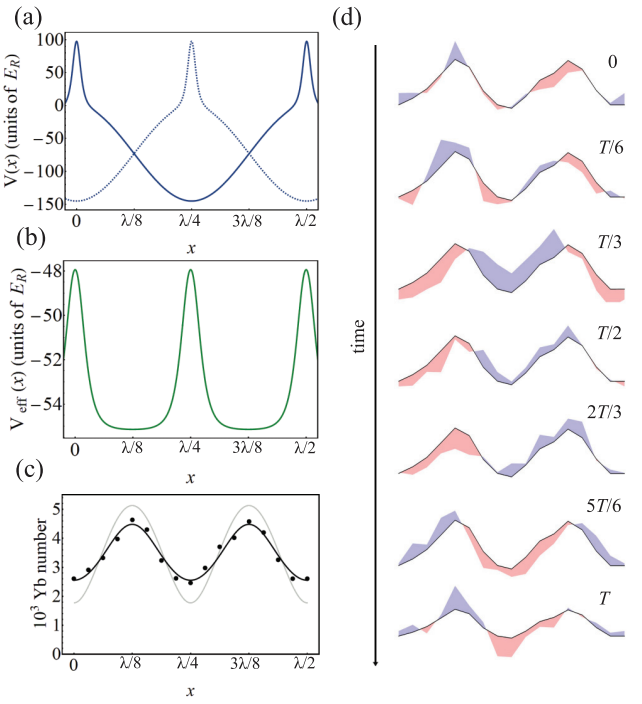

FIG. 2. (a) The stroboscopically applied potential, shown here for $\Omega_{c0} = 500\Gamma$ and $\Omega_p = 50\Gamma$, is composed of KP barriers on top of a sinusoidal potential. The dotted line represents the potential shifted by $\lambda/4$. (b) The time-averaged effective potential $V_{\text{eff}}(x)$. (c) The black points are the measured $|\psi_{\text{avg}}(x)|^2$ of atoms in $V_{\text{eff}}(x)$. Number fluctuations between realizations result in number uncertainties of 5%. The black line is the calculation based on independently measured lattice parameters. The gray line is the calculated $|\psi_{\text{avg}}(x)|^2$ in the lattice before the relaxation during the measurement. (d) The micromotion dynamics at different times within a Floquet period. The blue (red) shaded areas represent regions in which $|\psi(x,t)|^2$ is higher (lower) than $|\psi_{\text{avg}}(x)|^2$, which is shown as a solid black line.

of our light fields (Appendix C), implementing stimulated Raman adiabatic passage (STIRAP) [25]. Losses occur at high ω_F, as the atom's dark-state spin composition fails to adiabatically follow the rapid changes in the light fields. In the following sections, we show that a frequency window that simultaneously satisfies both requirements exists and that there are momentum-dependent loss channels arising from the Floquet-induced coupling with higher excited bands for particular momenta.

II. EXPERIMENT

We work with fermionic ^{171}Yb atoms that have a well-isolated Λ system (Appendix A), consisting of two ground states $|g_1\rangle$, $|g_2\rangle$ and an excited state $|e\rangle$ coupled by laser light with $\lambda = 556$ nm. We use the methods outlined in Refs. [24,26–29] to generate and optically control this well-isolated Λ system. A control field $\Omega_c(x,t) = \Omega_{c1}e^{ikx} + \Omega_{c2}(t)e^{-i[kx+\phi(t)]}$, where $k = 2\pi/\lambda$ and $\phi(t)$ is the relative phase difference between the two fields, which couples $|g_2\rangle$ and $|e\rangle$, is composed of two counterpropagating lattice beams. The maximum value of $\Omega_{c2}(t)$ is constrained to be equal to $\Omega_{c1} = \Omega_{c0}/2$, in which case it gives rise to a standing wave $\Omega_{c0}\, e^{-i\phi(t)/2} \cos[kx + \phi(t)/2]$. We control the strength and the position of the KP potential using $\Omega_{c2}(t)$ and $\phi(t)$ (Appendix C). A homogeneous probe field $\Omega_p e^{iky}$, coupling $|g_1\rangle$ and $|e\rangle$, travels perpendicular to the control beams. The resulting spatially dependent dark state gives rise to a KP lattice of narrow subwavelength barriers [22–24], plus an additional sinusoidal potential due to the light shifts caused by states outside the three-level system (Appendix A) as shown in Fig. 2(a).

Stroboscopically applying the lattice with different strengths and positions requires accurate and high bandwidth control of the amplitude and phase of the lasers coupling the three states, which we implement using dynamic control over the rf fields driving acousto-optic modulators (AOMs) [16]. We note that the spin adiabaticity condition depends significantly on the pulse shape [14] in addition to the Floquet frequency, and control of the pulse shape within a Floquet period is critical [16]. We use arbitrary waveform generators that can control the rf amplitude and phase with a resolution of 8 ns and 4 ns, respectively. However, we are limited by the bandwidth of the AOMs, which we measure to be 50 ns. This is a factor of 8 times smaller than the smallest half-period of 400 ns that we have used in this study.

For typical experimental values of $\Omega_{c0} = 500\Gamma$ and $\Omega_p = 50\Gamma$, where $\Gamma = 2\pi \times 182$ kHz is the inverse lifetime of $|e\rangle$, the KP barrier has a minimum width of 0.02 λ and a maximum height $\approx 100E_R$, where $E_R/h = h/(2m_{\text{Yb}}\lambda^2) = 3.7$ kHz, m_{Yb} is the mass of a ^{171}Yb atom, and the sinusoidal potential has a depth $\approx 145E_R$, Fig. 2(a). Time-averaging this lattice applied at two positions results in an effective potential $V_{\text{eff}}(x)$ shown in Fig. 2(b), which includes the effect of the pulse shapes, with an effective barrier height $\approx 7E_R$. (The sinusoidal component of the potential averages to a spatially invariant offset.)

III. MEASUREMENT

We apply this lattice to $\approx 2 \times 10^5$ Yb atoms at an initial temperature of 0.3 μK that has been optically pumped into $|g_1\rangle$. To load the atoms into the ground band of $V_{\text{eff}}(x)$, we adiabatically increase the depth of the stroboscopically applied lattices in 200 μs (typically ~80 Floquet cycles) described in detail in Appendix B. After the loading stage, we measure the ensemble-averaged probability density $|\psi(x,t)|^2$ of atoms in the ground band of $V_{\text{eff}}(x)$ using a nanoresolution microscopy technique [16] with FWHM resolution of 25 nm. We also measure the momentum distribution of the atoms via absorption imaging after time of flight (TOF).

A. Probing wave function density in the stroboscopic lattice

Figure 2(c) shows $|\psi(x,t)|^2$ averaged over a Floquet period $T = 2.4$ μs ($\omega_F = 2\pi \times 410$ kHz) for atoms in $V_{\text{eff}}(x)$ with a $\lambda/4$ lattice spacing, and Fig. 2(d) shows $|\psi(x,t)|^2$ at different times within a Floquet cycle. By averaging the data over a Floquet period, we eliminate the effect of micromotion and obtain the averaged wave function density $|\psi_{\text{avg}}(x)|^2$ [dotted trace in Fig. 2(c)] in the ground band of the effective potential. The black curve represents the ground-band probability density calculated from the time-averaged potential including the quasimomentum averaging, the effect of finite resolution of the microscope, and the relaxation of the wave function during the measurement. The good agreement between the data and calculation shows that time-averaging is a good description of the effective potential. The calculated wave function in the lattice before the relaxation during the measurement is plotted in gray. We resolve the micromotion in real space within a Floquet period by comparing $|\psi(x,t)|^2$ with $|\psi_{\text{avg}}(x)|^2$ [Fig. 2(d)]. The blue (red) shaded areas represents regions in which $|\psi(x,t)|^2$ is higher (lower) than $|\psi_{\text{avg}}(x)|^2$. We observe that micromotion has the same time periodicity as the Floquet drive, as expected.

B. Momentum-dependent loss channels

A characteristic feature of a Bloch-Floquet band structure is the existence of avoided crossings at particular lattice momenta arising from coupling with high-lying states [30], which for large Floquet frequency are approximately plane waves with high momenta. We measure the momentum distribution of the atoms in $V_{\text{eff}}(x)$ at different ω_F by taking an absorption image after ramping down the lattice in 100 μs followed by a TOF of 3 ms. The atomic populations at high momenta in Fig. 3(a) indicate the mixing of low-momentum and high-momentum states due to the presence of avoided crossings in our system. We use a Gaussian fit to determine the center momentum of the populations with respect to the ground band. The Floquet frequency ω_F is plotted against the center momentum [Fig. 3(b)] for the three most prominent peaks (L1: green, L2: red, R1: blue). To first order, the avoided crossings can be understood as arising from the crossing of Floquet-dressed high-lying bands, which are shifted in energy by integral multiples of ω_F, and the low-lying occupied bands of $V_{\text{eff}}(x)$, which are relatively flat. To determine the integral multiple of ω_F for the band coupling, we fit the peak positions with a quadratic function $\hbar\omega_F = (p - p_0)^2/N + \hbar\omega_0$, where

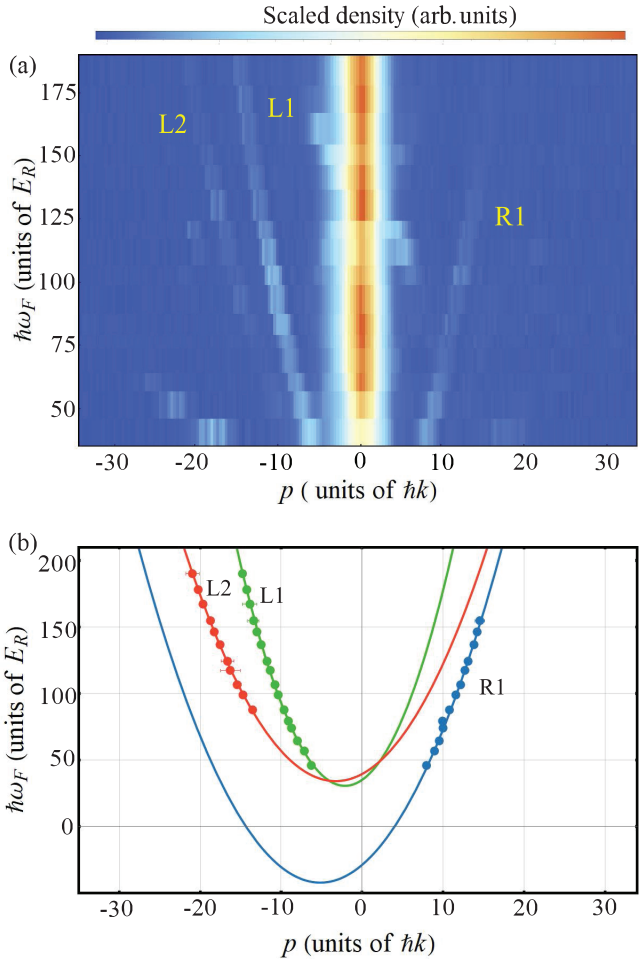

FIG. 3. (a) Integrated TOF column density at different Floquet frequencies ω_F. The atomic populations at high momenta indicate the presence of avoided crossings. The widths of the populations at avoided crossings are primarily due to the physical dimensions of the atomic cloud. (b) The Floquet frequency ω_F is plotted versus the center momentum of the populations in (a) determined using Gaussian fits. Different series of avoided crossings are labeled and colored (L1: green, L2: red, R1: blue) and their fitted quadratic functions are drawn in solid lines respectively. The error bars are one standard deviation of the Gaussian fits.

p is the momentum, N is an integer, p_0 and ω_0 are fitting parameters, and the momentum and energy are in units of $\hbar k$ and E_R. For the L1 series, a good agreement with the data is found for $N = 1$, indicating this series is due to coupling between bands with an energy difference of $\hbar\omega_F$. For the L2 and R1 series, $N = 2$ gives the best fit, indicating second-order coupling between bands that differ in energy by $2\hbar\omega_F$. (The other visible peaks do not extend over a sufficient range to accurately determine their curvatures.) The fraction of atoms in the high-momentum states decreases at higher Floquet frequency, suggesting weaker coupling to higher bands. The asymmetry in the avoided crossings with respect to $p = 0$ is due to the fact that we are driving just the Ω_{c2} control beam, which gives rise to a vector gauge potential [14].

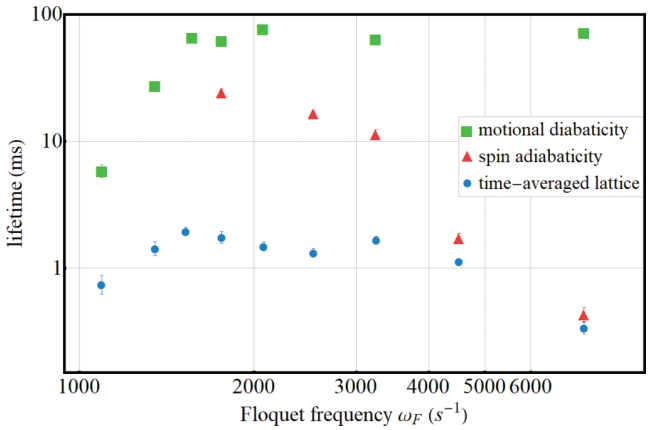

FIG. 4. Lifetimes of atoms at different ω_F under different Rabi frequency configurations. Green squares: $\Omega_{c0} = 500\Gamma$ and $\Omega_p = 0$, where the spin degree of freedom is decoupled and the loss is due solely to failure of motional diabaticity at low ω_F. Red triangles: $\Omega_{c1} = 0$, $\Omega_{c2} = 250\Gamma$, and $\Omega_p = 80\Gamma$, where the spatial potential is homogeneous and the loss is due solely to the failure of spin adiabaticity at high ω_F. Blue circles: $\Omega_{c0} = 500\Gamma$ and $\Omega_p = 80\Gamma$, where we show the lifetimes of atoms in the $\lambda/4$-spaced lattice, $V_{\text{eff}}(x)$. The error bars are one standard deviation of the exponential fits.

The ^{171}Yb atoms are nearly noninteracting (s-wave scattering length is $-3a_0$, where a_0 is the Bohr radius), so they are not likely to thermalize during the short loading and unloading sequence. However, the observed low-momentum component of the TOF distribution is consistent with the width of the ground-band Brillouin zone for the $\lambda/4$-spaced stroboscopic lattice, which is twice as large as the ground bandwidth of the progenitor $\lambda/2$ lattice. Given that the Fermi momentum at our density is of order the recoil momentum of the progenitor lattice, the filled ground band in the $\lambda/4$ lattice indicates that the effective temperature is higher than the ground bandwidth but not a significant fraction of the band spacing.

C. Lifetime study

In order to determine the range of usable Floquet frequencies for the stroboscopic scheme, we study the lifetime at different ω_F under different Rabi frequency configurations as shown in Fig. 4. We determine the lower bound on ω_F by studying the motional diabaticity of atoms in just a stroboscopically applied ac Stark shift lattice. This is done by setting $\Omega_p = 0$, which decouples the spin degree of freedom from the dynamics with $\Omega_{c1} = 250\Gamma$, while $\Omega_{c2}(t)$ is pulsed to a maximum value of 250Γ(Appendix C). At low ω_F, the atoms are affected by the turning on and off, and phase shifting of the sinusoidal ac Stark shift potential, which causes heating and loss (green squares in Fig. 4). We determine the upper bound on ω_F by studying the reduction in the fidelity of STIRAP as a function of ω_F for a spatially homogeneous dark state. This is done by setting $\Omega_{c1} = 0$, $\Omega_p = 80\Gamma$, while $\Omega_{c2}(t)$ is pulsed to a maximum value of 250Γ. The reduction in STIRAP fidelity manifests as heating and loss due to the decreasing spin adiabaticity at larger ω_F. Most importantly, we also measure the frequency-dependent lifetime of atoms loaded into $V_{\text{eff}}(x)$ for different ω_F (blue circles in Fig. 4). The reduction in spin adiabaticity accounts for the decrease in lifetime of atoms in $V_{\text{eff}}(x)$ at high ω_F.

The short lifetimes in the stroboscopically applied KP lattices are expected due to a few factors. First, couplings to the spatially and temporally dependent bright states reduce lifetimes in subwavelength-spaced lattices even for a perfect three-level system, through couplings with higher Floquet bands (as shown in Fig. 3) and off-resonant couplings with bright states [14]. In principle, these couplings can be reduced by using larger Rabi frequencies. However, lifetimes are also limited by the breakdown of the three-level approximation at large Rabi frequencies due to admixing of states outside the three-level system (Appendix A). This manifests as a dynamically varying and spatially dependent two-photon detuning (arising from $\Omega_c(x,t)$), which reduces the fidelity of STIRAP [25]. This competing requirement prevents us from benefiting from larger Rabi frequencies.

IV. CONCLUSION

In conclusion, we demonstrate the creation of a time-averaged $\lambda/4$-spaced lattice using a recently proposed stroboscopic technique [13] based on dynamically modulated dark states in a three-level system [14,15]. The subwavelength structure of the lattice is confirmed by measuring the probability density of the atoms averaged over the ground band of the lattice. We measure the loss rate of atoms in the lattice and observe high-momentum excitation due to Floquet-induced coupling to higher bands. We measure the lifetime of the atoms in the $\lambda/4$-spaced lattice to be 2 ms, which is not long enough compared to the tunneling time to allow for many-body studies in the current realization.

Further improvement of the $\lambda/4$-spaced lattice would require compensation of the two-photon detuning or the identification of other atomic systems with a more favorable (isolated) three-level system [31]. The lattice demonstrated here is limited by the off-resonant coupling to $|(6s6p)^3P_1$,

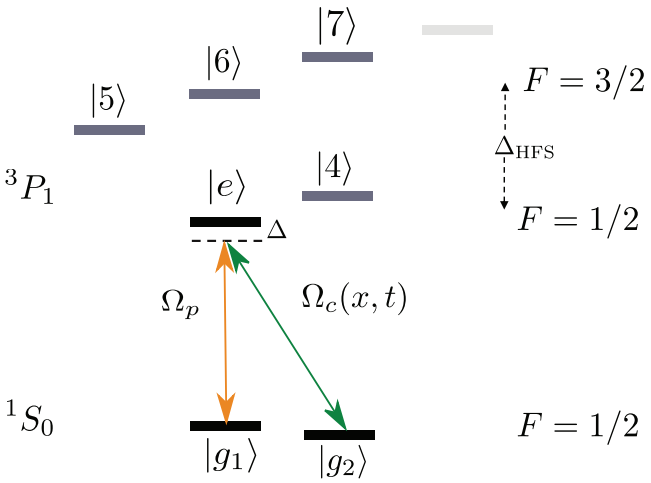

FIG. 5. Level structure of the $^1S_0$ and $^3P_1$ manifolds in ^{171}Yb: Δ is the single-photon detuning, and $\Delta_{\text{HFS}} \approx 6$ GHz is the $^3P_1$ hyperfine splitting.

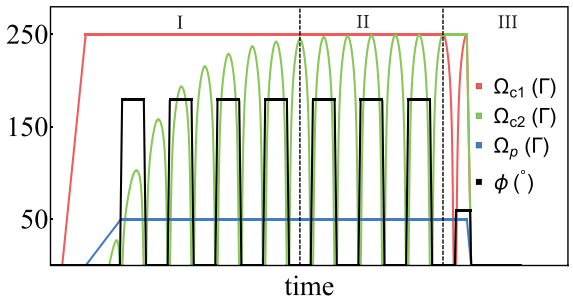

FIG. 6. Rabi frequencies of different light fields and the relative phase ϕ between Ω_{c1} and Ω_{c2} during three stages. The Floquet period is not shown to scale; the minimum number of Floquet cycles during the ramp-on of Ω_{c2} is 40.

$F = 3/2, m_F = -3/2\rangle$, which is only detuned by the hyperfine splitting from the three-level system being used. Better candidates may make use of isolated *electronic* levels, which are detuned by much larger optical separations. For example, in ^{174}Yb, the $(6s6p)^3P_0$ state and one of the states in the $(6s6p)^3P_2$ level could be used as the ground states, while one of the $(6s7s)^3S_1$ states could be used as the excited state, with appropriate choice of polarization to select the three states. In a more isolated three-level system the main limitation would be the available laser power needed to meet the Rabi frequency requirements. In addition to longer lifetimes, higher Rabi frequencies would allow for lattices with smaller spacings [14]. Our work can be extended to 2D, and additional dynamic control over the two-photon detuning—which makes subwavelength traps possible [31]—allows for construction of arbitrary time-averaged potential landscapes not limited by diffraction.

ACKNOWLEDGMENTS

We acknowledge support from NSF PFC at JQI (Grant No. PHY1430094) and ONR (Grant No. N000141712411).

APPENDIX A: ^{171}Yb ATOM LEVEL STRUCTURE

Figure 5 shows the level structure of the $^1S_0$ and $^3P_1$ manifolds in ^{171}Yb. The three hyperfine states $|g_1\rangle$, $|g_2\rangle$, and $|e\rangle$ constitute the Λ system. We use a magnetic field of 36 mT to yield a frequency separation of 1 GHz between $|e\rangle$ and $|4\rangle$. The hyperfine splitting is $\Delta_{\mathrm{HFS}} \approx 6$ GHz.

The ac Stark shifts on the ground states $|g_1\rangle$ and $|g_2\rangle$ arise due to off-resonant couplings to states outside the Λ system. The $\Omega_c(x,t)$ light field off-resonantly couples $|g_1\rangle$ with $|5\rangle$, and $|g_2\rangle$ with $|6\rangle$. The Ω_p light field off-resonantly couples $|g_2\rangle$ with $|4\rangle$, $|g_2\rangle$ with $|7\rangle$, and $|g_1\rangle$ with $|6\rangle$. The spatiotemporally dependent ac Stark shifts due to $\Omega_c(x,t)$ give rise to the dynamic sinusoidal potential mentioned in the main text.

APPENDIX B: EXPERIMENTAL SEQUENCE

Figure 6 shows the experimental sequence that we use to load atoms into the ground band of the stroboscopic lattice.

(I) We start with atoms optically pumped into $|g_1\rangle$. We then ramp on Ω_{c1} (red trace in Fig. 6) followed by Ω_p (blue trace in Fig. 6), transferring atoms into a spatially homogeneous dark state. Then, we turn on $\Omega_{c2}(t)$ (green trace in Fig. 6) in 200 μs (minimum number of Floquet cycles used during the ramp ≈ 40) to adiabatically load atoms into the ground band of the stroboscopic lattice.

(II) We pulse the stroboscopic lattice for a variable number of Floquet cycles.

(III) We measure the average probability density of the atoms in the ground band of the stroboscopic lattice using the nanoresolution microscopy technique described in Ref. [16].

The phase $\phi(t)$ of the Ω_{c2} light field, which controls the position of the stroboscopic lattice, is only changed when the dark-state spin composition is spatially homogeneous [14]. The experimental techniques used to generate the pulses are detailed in Ref. [16].

APPENDIX C: PULSE SCHEME

The functional form of $\Omega_{c2}(t)$ that we use to create the stroboscopic lattice is [14]

$$\Omega_{c2}(t) = \frac{\Omega_{c0}}{2} - \frac{\Omega_p \sin^2(\omega_F t)}{\sqrt{1+4\epsilon^2-\sin^4(\omega_F t)}},$$

$$\omega_F = \Omega_p r_0 \sqrt{1+4\epsilon^2},$$

where $\epsilon = \Omega_p/\Omega_{c0}$. In Fig. 4, changes in ω_F are parametrized using r_0. Smaller r_0 implies slower, more spin-adiabatic pulses. In our experiment, we typically use $0.02 \leqslant r_0 \leqslant 0.2$.

APPENDIX D: DETAIL OF LIFETIME STUDY

When studying lifetime for the STIRAP-only case and for the stroboscopic lattice case, we observe that ~20% of the atoms have a lifetime of ~20 ms and are insensitive to change in ω_F. We speculate that these atoms populate Floquet states that are immune to STIRAP due to the large dynamic two-photon detunings arising from the spatially dependent ac Stark shifts due to couplings to states outside the Λ system (Appendix A). The decay rates shown in the main text pertain to the major fraction of the atoms which show frequency-dependent loss rates both in the stroboscopic lattice and in the stroboscopic STIRAP case.

[1] M. Lewenstein, A. Sanpera, V. Ahufinger, B. Damski, A. Sen(De), and U. Sen, Adv. Phys. **56**, 243 (2007).

[2] I. Bloch, J. Dalibard, and W. Zwerger, Rev. Mod. Phys. **80**, 885 (2008).

[3] B. Dubetsky and P. R. Berman, Phys. Rev. A **66**, 045402 (2002).

[4] G. Ritt, C. Geckeler, T. Salger, G. Cennini, and M. Weitz, Phys. Rev. A **74**, 063622 (2006).

[5] R. P. Anderson, D. Trypogeorgos, A. Valdés-Curiel, Q.-Y. Liang, J. Tao, M. Zhao, T. Andrijauskas, G. Juzeliūnas, and I. B. Spielman, Phys. Rev. Res. **2**, 013149 (2020).
[6] W. Yi, A. J. Daley, G. Pupillo, and P. Zoller, New J. Phys. **10**, 073015 (2008).
[7] N. Lundblad, P. J. Lee, I. B. Spielman, B. L. Brown, W. D. Phillips, and J. V. Porto, Phys. Rev. Lett. **100**, 150401 (2008).
[8] N. Lundblad, S. Ansari, Y. Guo, and E. Moan, Phys. Rev. A **90**, 053612 (2014).
[9] M. Gullans, T. G. Tiecke, D. E. Chang, J. Feist, J. D. Thompson, J. I. Cirac, P. Zoller, and M. D. Lukin, Phys. Rev. Lett. **109**, 235309 (2012).
[10] J. D. Thompson, T. G. Tiecke, N. P. de Leon, J. Feist, A. V. Akimov, M. Gullans, A. S. Zibrov, V. Vuletić, and M. D. Lukin, Science **340**, 1202 (2013).
[11] O. Romero-Isart, C. Navau, A. Sanchez, P. Zoller, and J. I. Cirac, Phys. Rev. Lett. **111**, 145304 (2013).
[12] A. González-Tudela, C.-L. Hung, D. E. Chang, J. I. Cirac, and H. J. Kimble, Nat. Photonics **9**, 320 (2015).
[13] S. Nascimbene, N. Goldman, N. R. Cooper, and J. Dalibard, Phys. Rev. Lett. **115**, 140401 (2015).
[14] S. Subhankar, P. Bienias, P. Titum, T.-C. Tsui, Y. Wang, A. V. Gorshkov, S. L. Rolston, and J. V. Porto, New J. Phys. **21**, 113058 (2019).
[15] M. Lacki, P. Zoller, and M. A. Baranov, Phys. Rev. A **100**, 033610 (2019).
[16] S. Subhankar, Y. Wang, T.-C. Tsui, S. L. Rolston, and J. V. Porto, Phys. Rev. X **9**, 021002 (2019).
[17] M. McDonald, J. Trisnadi, K.-X. Yao, and C. Chin, Phys. Rev. X **9**, 021001 (2019).
[18] A. Tonyushkin and T. Sleator, Phys. Rev. A **74**, 053615 (2006).
[19] A. Eckardt, Rev. Mod. Phys. **89**, 011004 (2017).
[20] S. Rahav, I. Gilary, and S. Fishman, Phys. Rev. A **68**, 013820 (2003).
[21] M. Bukov, L. D'Alessio, and A. Polkovnikov, Adv. Phys. **64**, 139 (2015).
[22] M. Łącki, M. A. Baranov, H. Pichler, and P. Zoller, Phys. Rev. Lett. **117**, 233001 (2016).
[23] F. Jendrzejewski, S. Eckel, T. G. Tiecke, G. Juzeliūnas, G. K. Campbell, L. Jiang, and A. V. Gorshkov, Phys. Rev. A **94**, 063422 (2016).
[24] Y. Wang, S. Subhankar, P. Bienias, M. Łącki, T.-C. Tsui, M. A. Baranov, A. V. Gorshkov, P. Zoller, J. V. Porto, and S. L. Rolston, Phys. Rev. Lett. **120**, 083601 (2018).
[25] N. V. Vitanov, A. A. Rangelov, B. W. Shore, and K. Bergmann, Rev. Mod. Phys. **89**, 015006 (2017).
[26] V. D. Vaidya, J. Tiamsuphat, S. L. Rolston, and J. V. Porto, Phys. Rev. A **92**, 043604 (2015).
[27] N. C. Pisenti, A. Restelli, B. J. Reschovsky, D. S. Barker, and G. K. Campbell, Rev. Sci. Instrum. **87**, 124702 (2016).
[28] S. Subhankar, A. Restelli, Y. Wang, S. L. Rolston, and J. V. Porto, Rev. Sci. Instrum. **90**, 043115 (2019).
[29] J. Appel, A. MacRae, and A. I. Lvovsky, Meas. Sci. Technol. **20**, 055302 (2009).
[30] M. Holthaus, J. Phys. B: At., Mol. Opt. Phys. **49**, 013001 (2015).
[31] P. Bienias, S. Subhankar, Y. Wang, T.-C. Tsui, F. Jendrzejewski, T. Tiecke, G. Juzeliunas, L. Jiang, S. L. Rolston, J. V. Porto, and A. V. Gorshkov, arXiv:1808.02487.

Appendix F: Cleaning machined parts for UHV assembly

In order to clean the machined parts for UHV operation, I had asked Creston for his UHV cleaning recipe. In addition to his guidelines, I found a few resources online on the subject [112, 117, 210]. Incorporating all of these resources, I devised my own recipes to clean machined parts, which I will describe below.

Before the recipe can be executed, the workstation must be prepped. First, label four pre-cleaned beakers as "water", "acetone", "IPA", "methanol" and four pre-cleaned tongs/tweezers as "1", "2", "3", "4". Pre-cleaning involves using an ultrasonic bath to sonicate both the tongs/tweesers and the insides of the beakers with the following reagents and in that order for 15 mins each at elevated temperatures:

distilled water→acetone (HPLC grade or higher)→isopropyl alcohol (HPLC grade or higher)→ methanol (HPLC grade or higher).

Use UHV foil to define 6 zones in the work area (Fig. F.1). Each zone is dedicated to storing the cleaned parts. Parts can only go from one zone to the next, but cannot go back. This unidirectionality is indicated by the arrow in Fig. F.1. Use the pre-cleaned designated tongs/tweezers (represented as numbers in Fig. F.1) to move the cleaned parts from one zone to the next. Always use powder-free nitrile gloves for handling any cleaned part that cannot be secured using tweezers/tongs. The recipe is as follows:

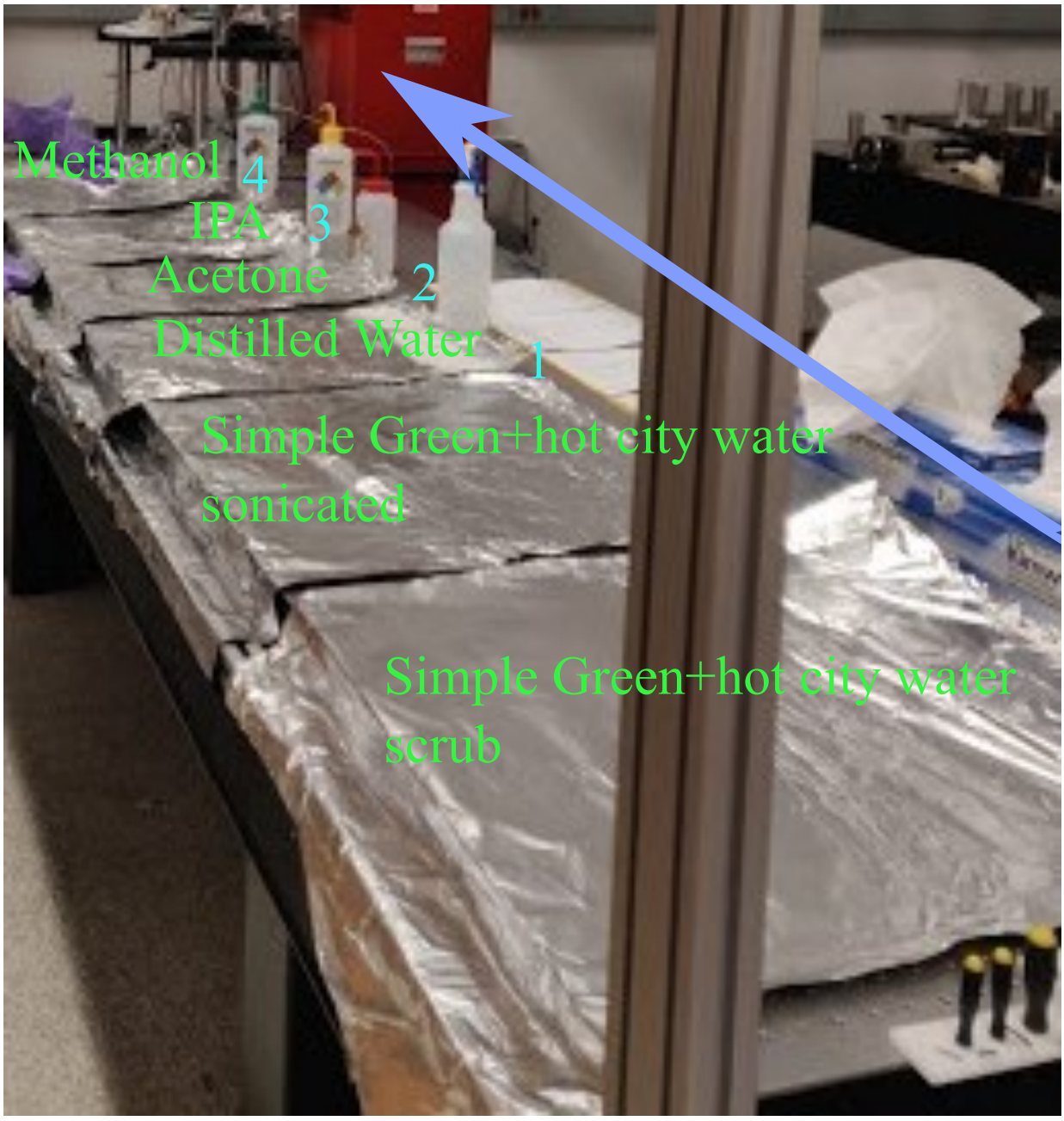

Figure F.1: The workstation for cleaning machined parts for UHV operation.

1. The ”Simple Green+hot city water scrub” zone is dedicated to parts that are scrubbed using a toothbrush (Fig. F.2) in a container filled with a solution of Simple Green and hot city water. Use a pipe brush to clean threads and holes. After the scrub, wash the part with flowing hot city water. Wipe the parts dry with Kimwipes.

2. These parts are then transferred to a beaker filled with a Simple Green (30% by volume) plus distilled water (70% by volume) solution. Sonicate the parts in an ultrasonic bath for 15 mins. Pour out the solution and then overflow the beaker with distilled water. Store the parts now in the “Simple Green+distilled water sonicated" zone.

3. Are parts visibly clean and there is no residue on the Kimwipes upon wiping the parts? If not, go to Step 1. If yes, go to the next step.

4. Use tongs/tweezers “2” to transfer parts to the “Acetone” beaker filled with HPLC grade (or higher) acetone. Sonicate the parts in an ultrasonic bath for 15 mins. Drain the beaker and dump the parts in the “Acetone” zone.

5. Use tongs/tweezers “3” to transfer parts to the “IPA” beaker filled with HPLC grade (or higher) isopropyl alcohol. Sonicate the parts in an ultrasonic bath for 15 mins. Drain the beaker and dump the parts in the “IPA” zone.

6. Use tongs/tweezers “4” to transfer parts to the “Methanol” beaker filled with HPLC grade (or higher) methanol. Sonicate the parts in an ultrasonic bath for 15 mins. Drain the beaker and dump the parts in the “Methanol” zone.

7. Allow parts to dry on the UHV foil before vacuum firing them for 48 hours at the material-dependent temperature.

Figure F.2: I am scrubbing the clamshell protectors

8. Store in UHV foil.

Appendix G: Drawings of the machined parts

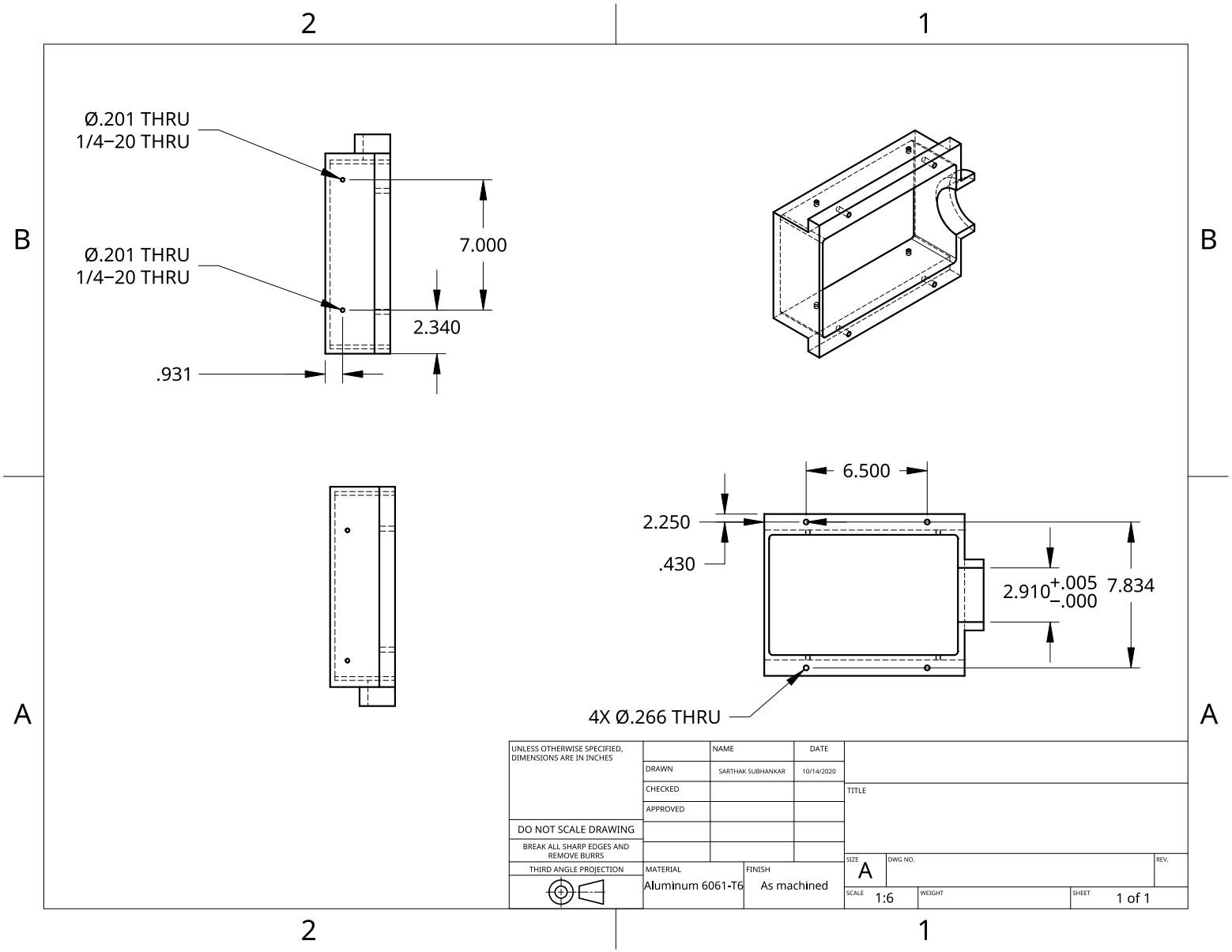

Figure G.1: Drawing of the clamshell protector for the glass cell

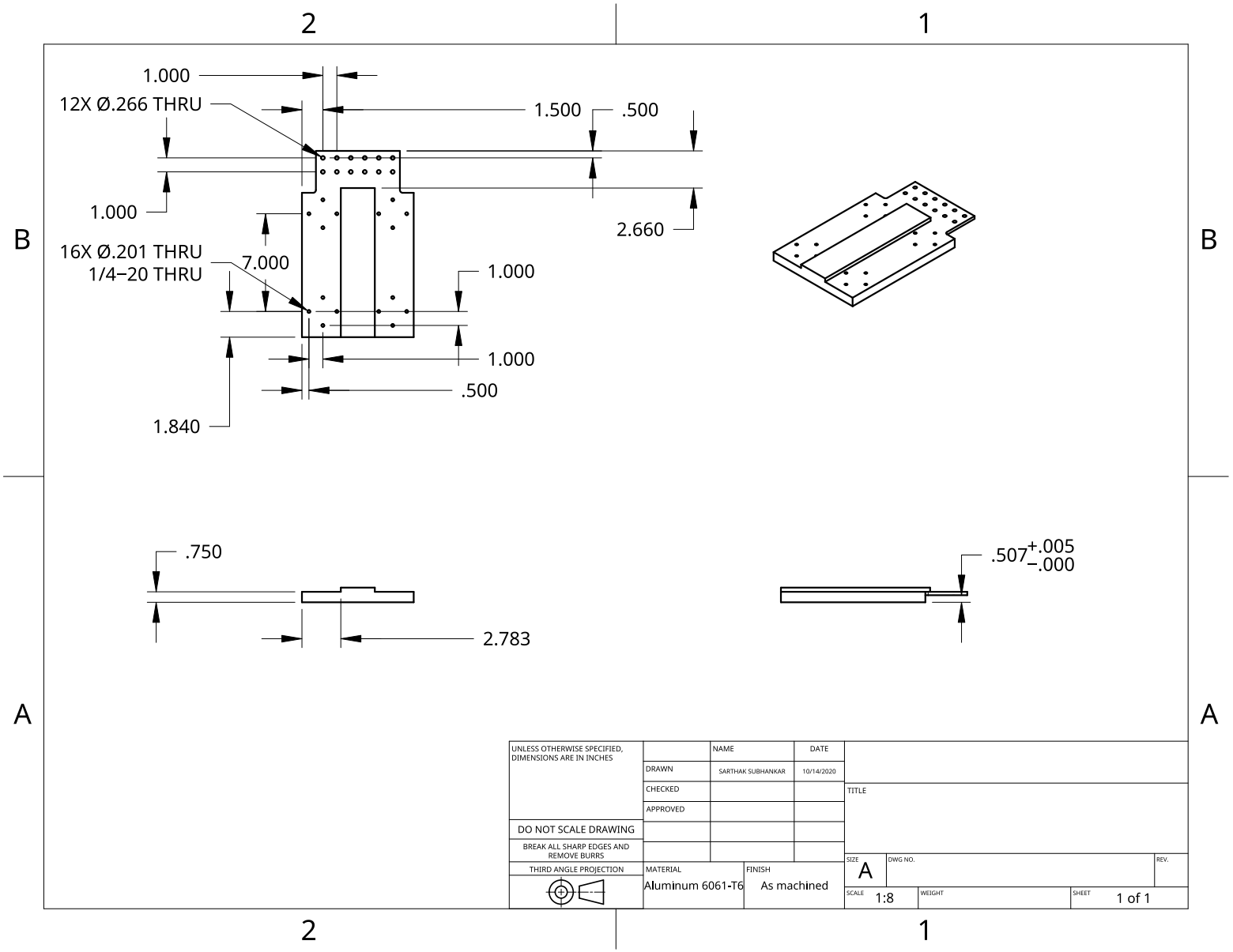

Figure G.2: Drawing of the base that supports the clamshell protectors

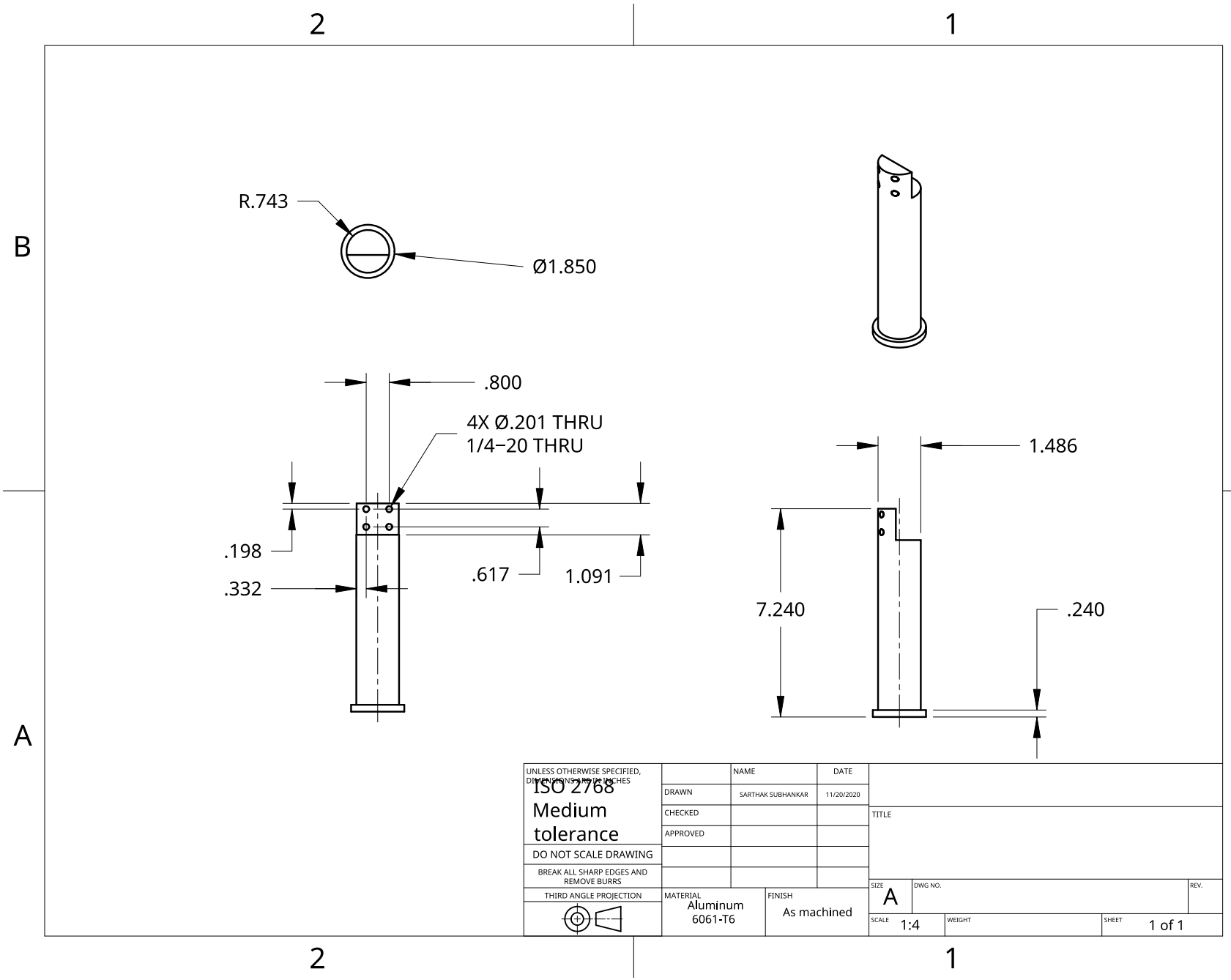

Figure G.3: Drawing of the custom post that prevents the UHV chamber from rotating about the mounting brackets

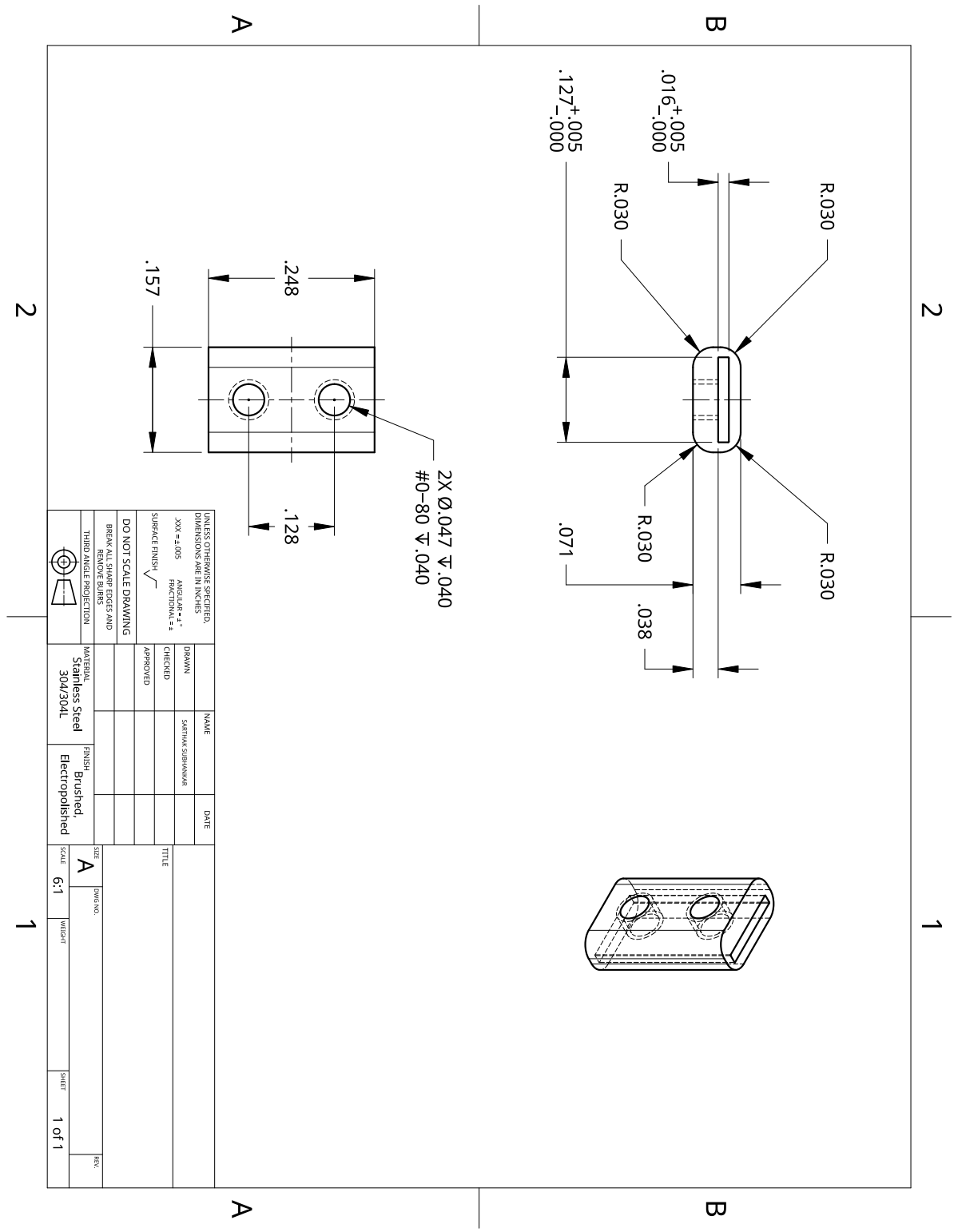

Figure G.4: Drawing of the sleeve for the Rb dispensing modules. The sleeve connects two dispensers together.

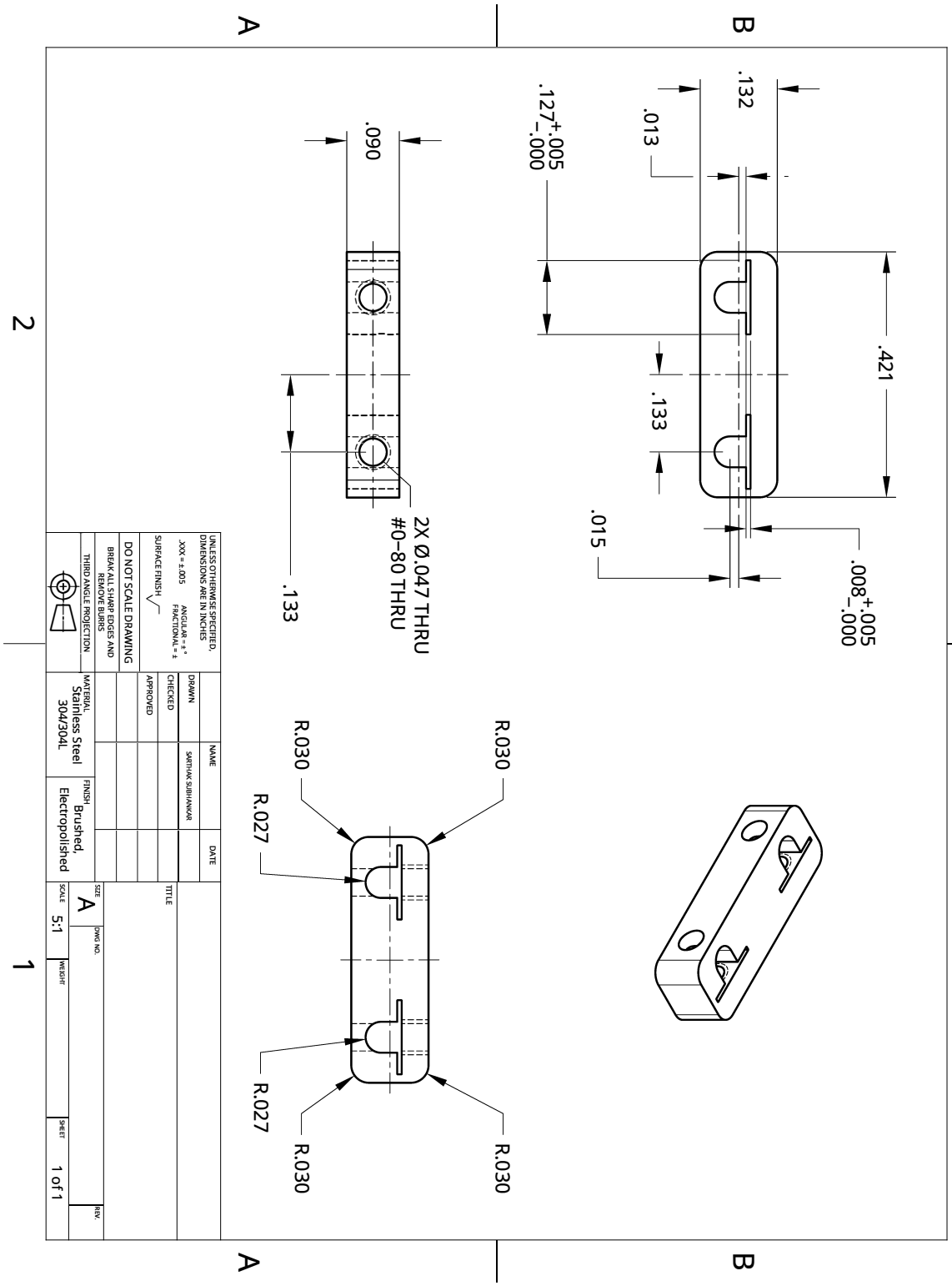

Figure G.5: Drawing of the adapter for the Rb dispensing modules. The adapter connects the dispenser to the conductors of the electrical feedthroughs.

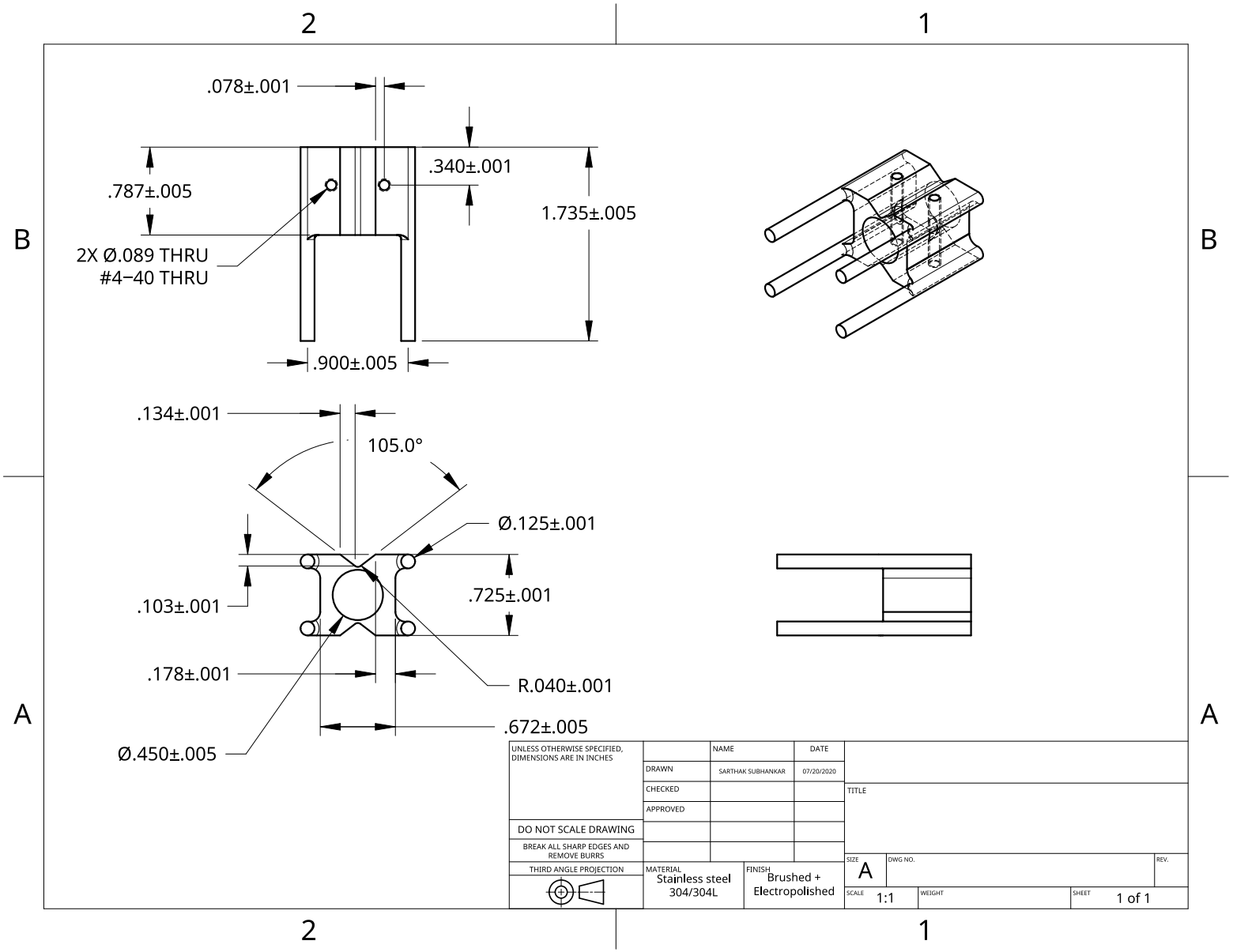

Figure G.6: Drawing of the electrode holder

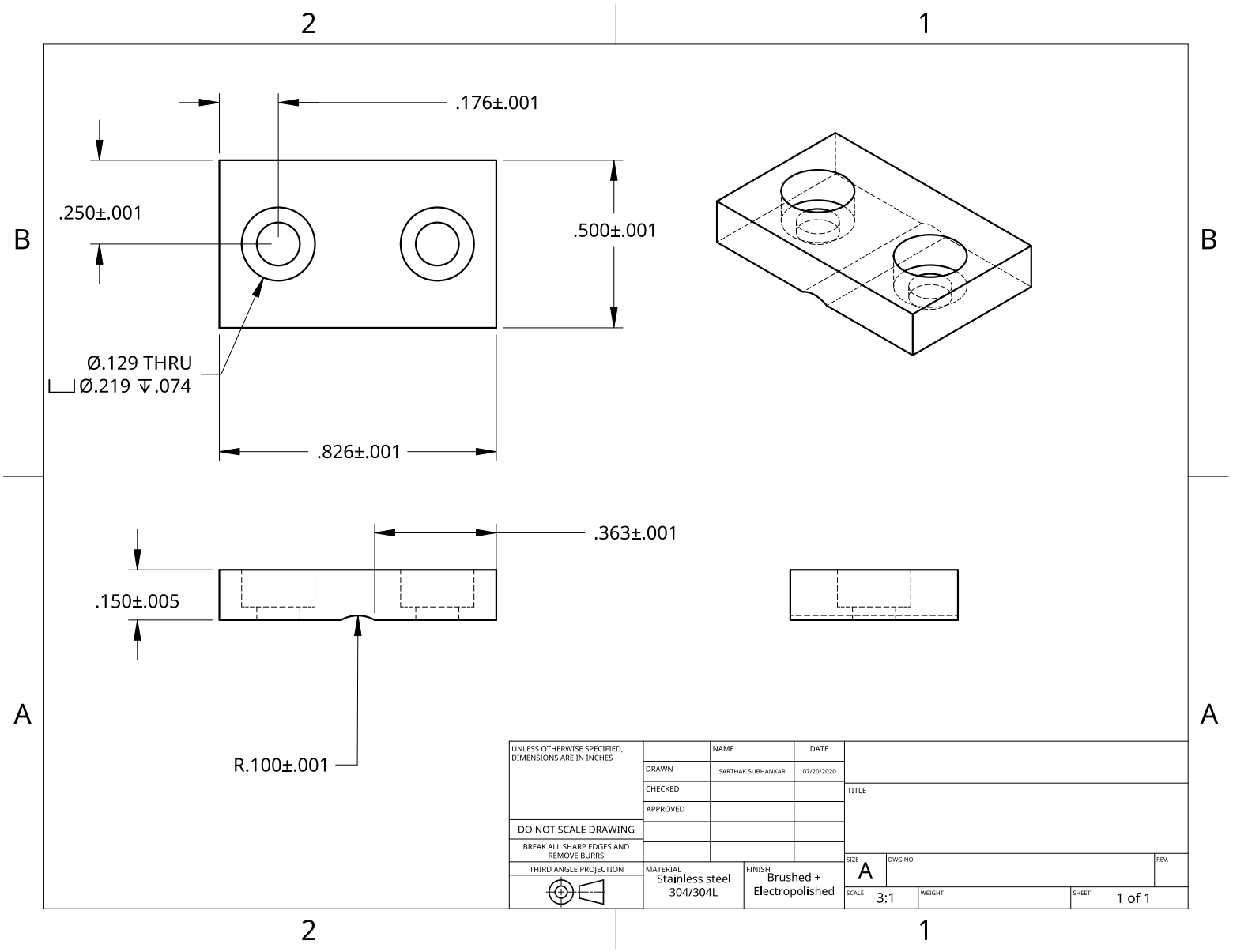

Figure G.7: Drawing of the electrode clamp

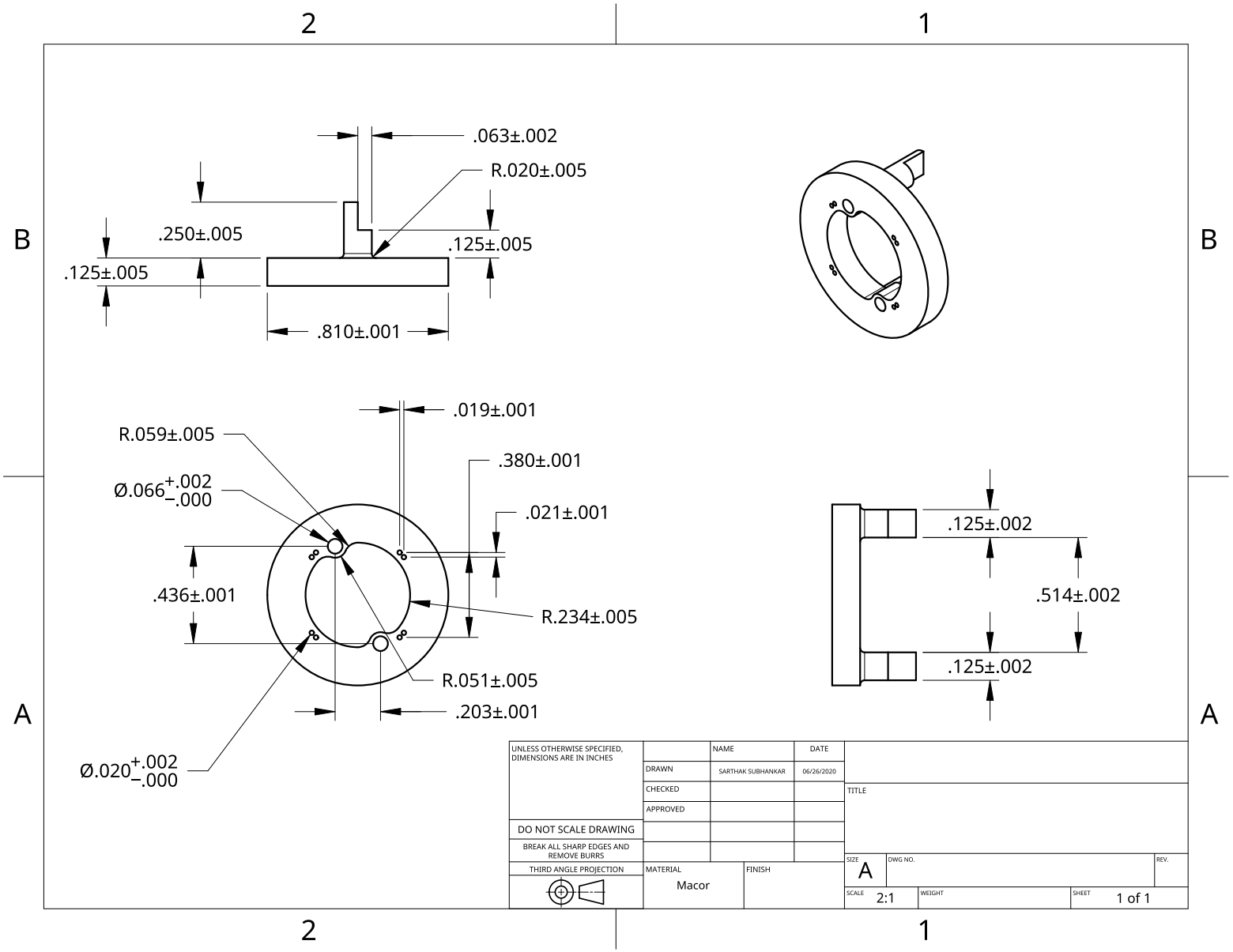

Figure G.8: Drawing of the small MACOR ring

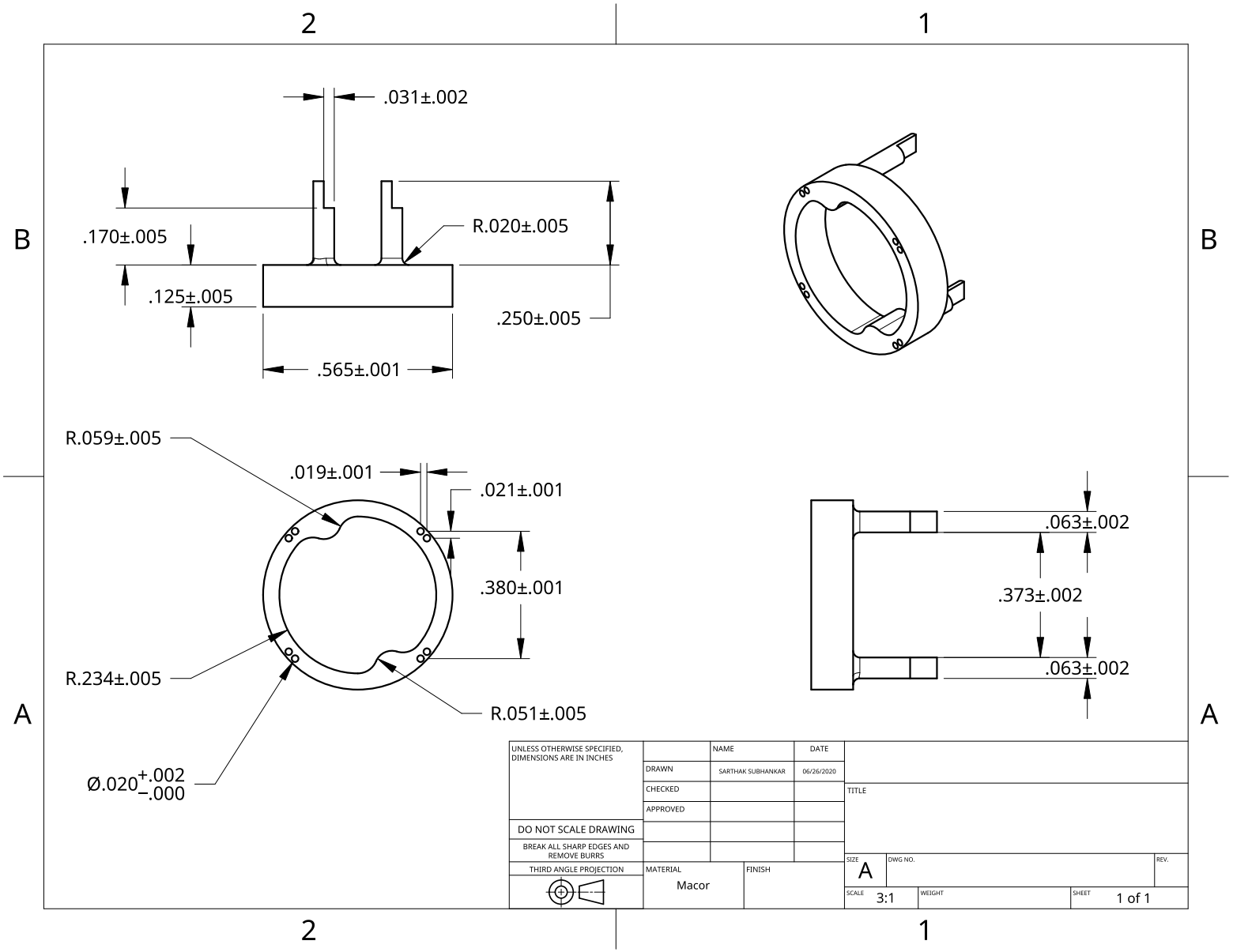

Figure G.9: Drawing of the small MACOR ring

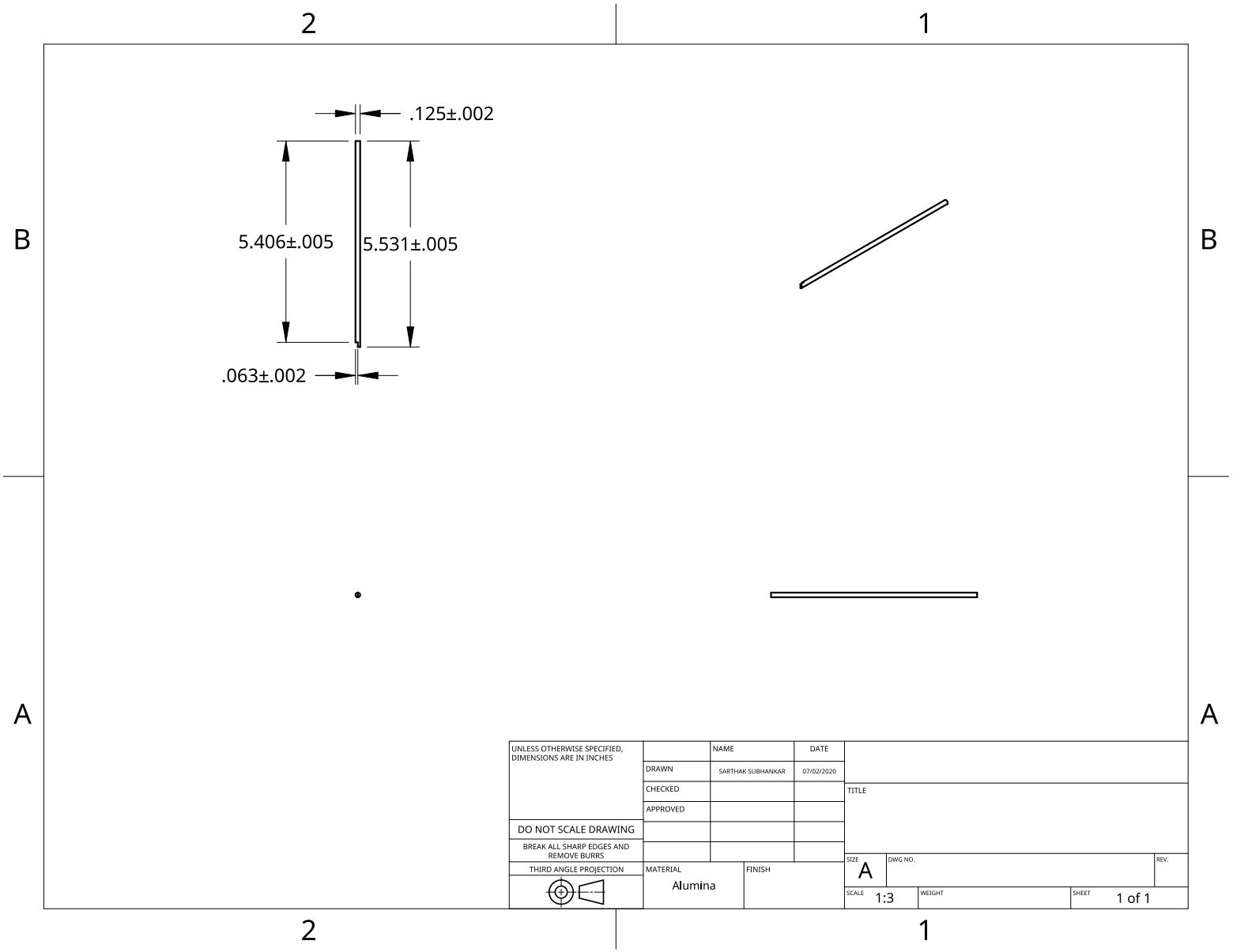

Figure G.10: Drawing of the long alumina rod

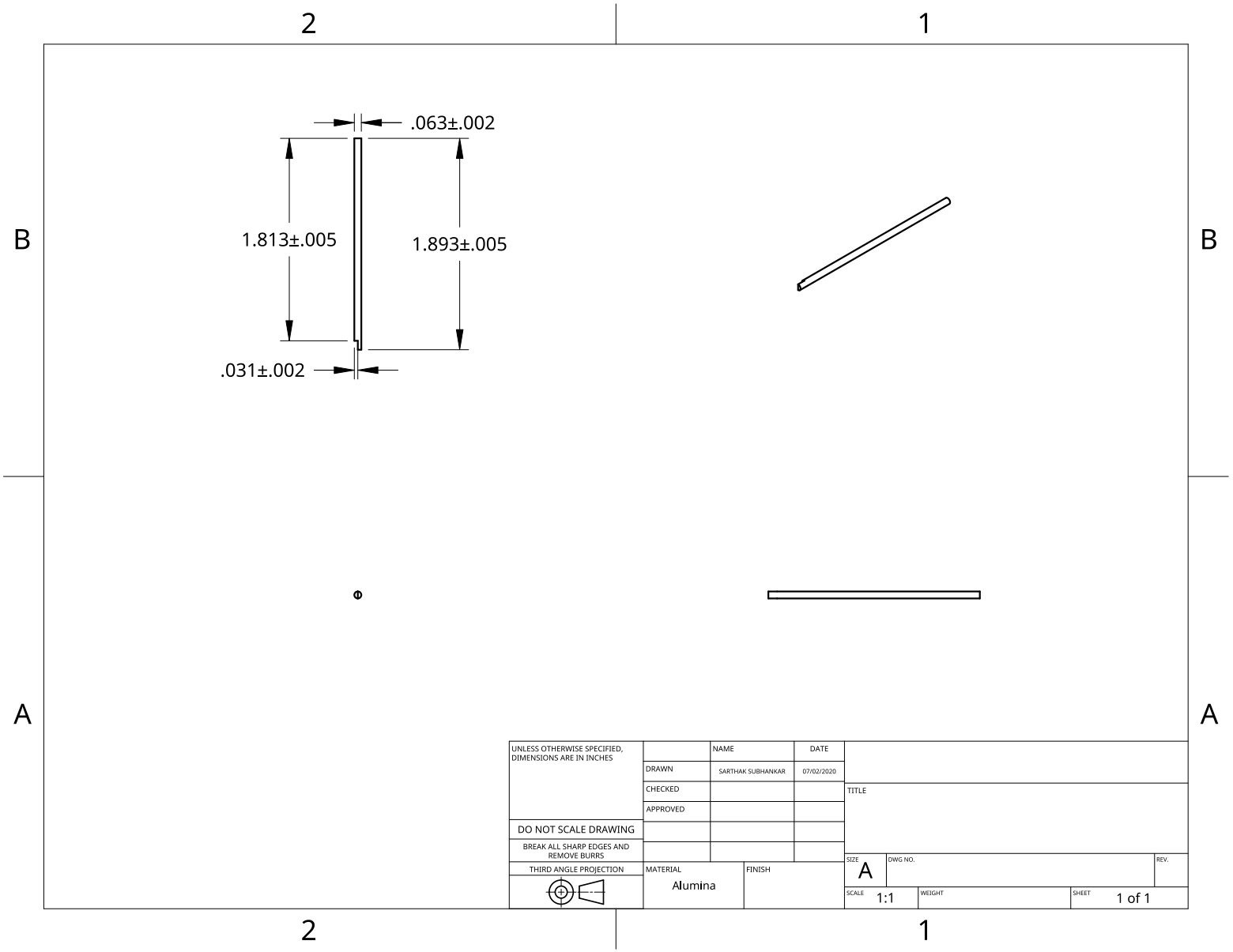

Figure G.11: Drawing of the short alumina rod

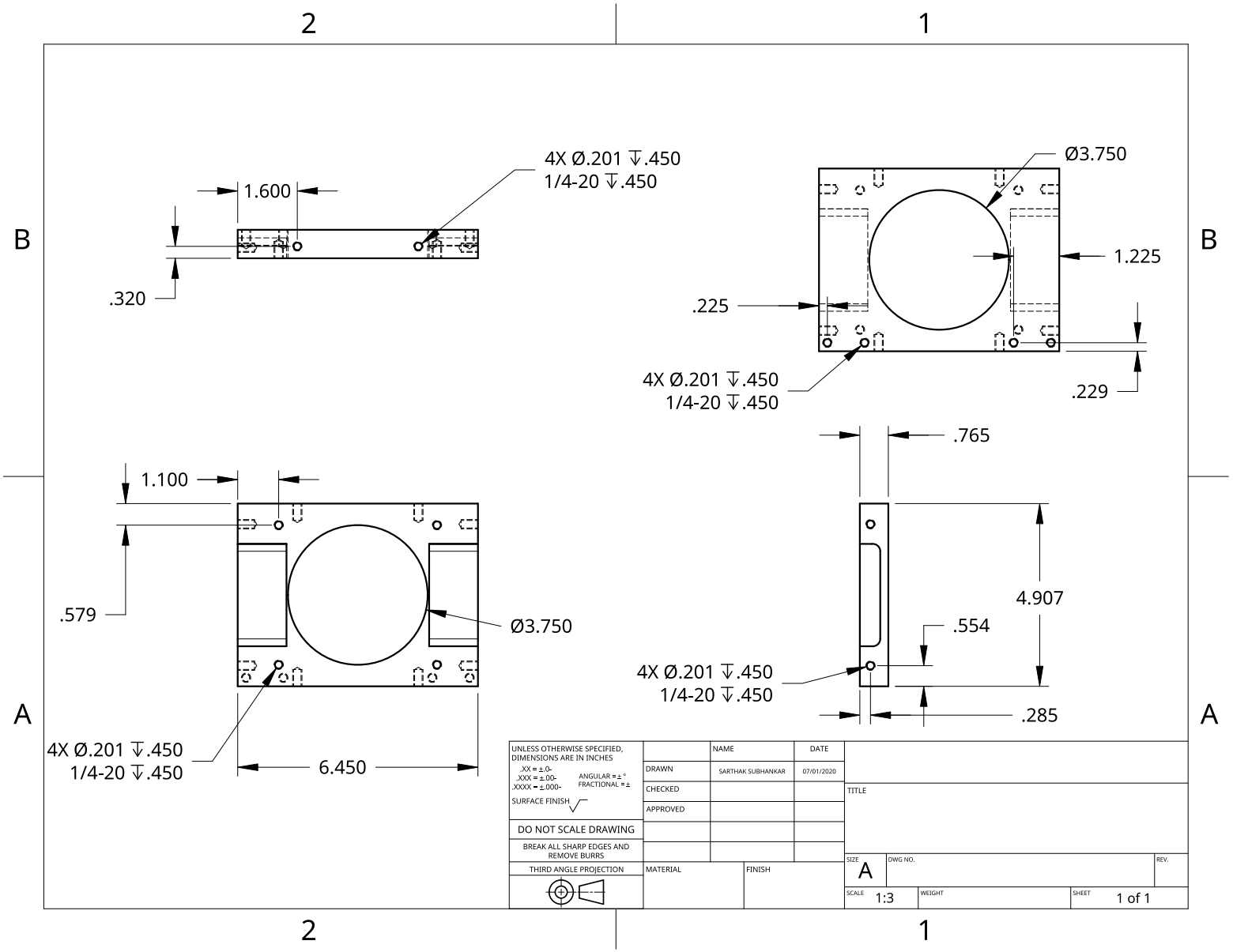

Figure G.12: Drawing of the MOT coil housing frame

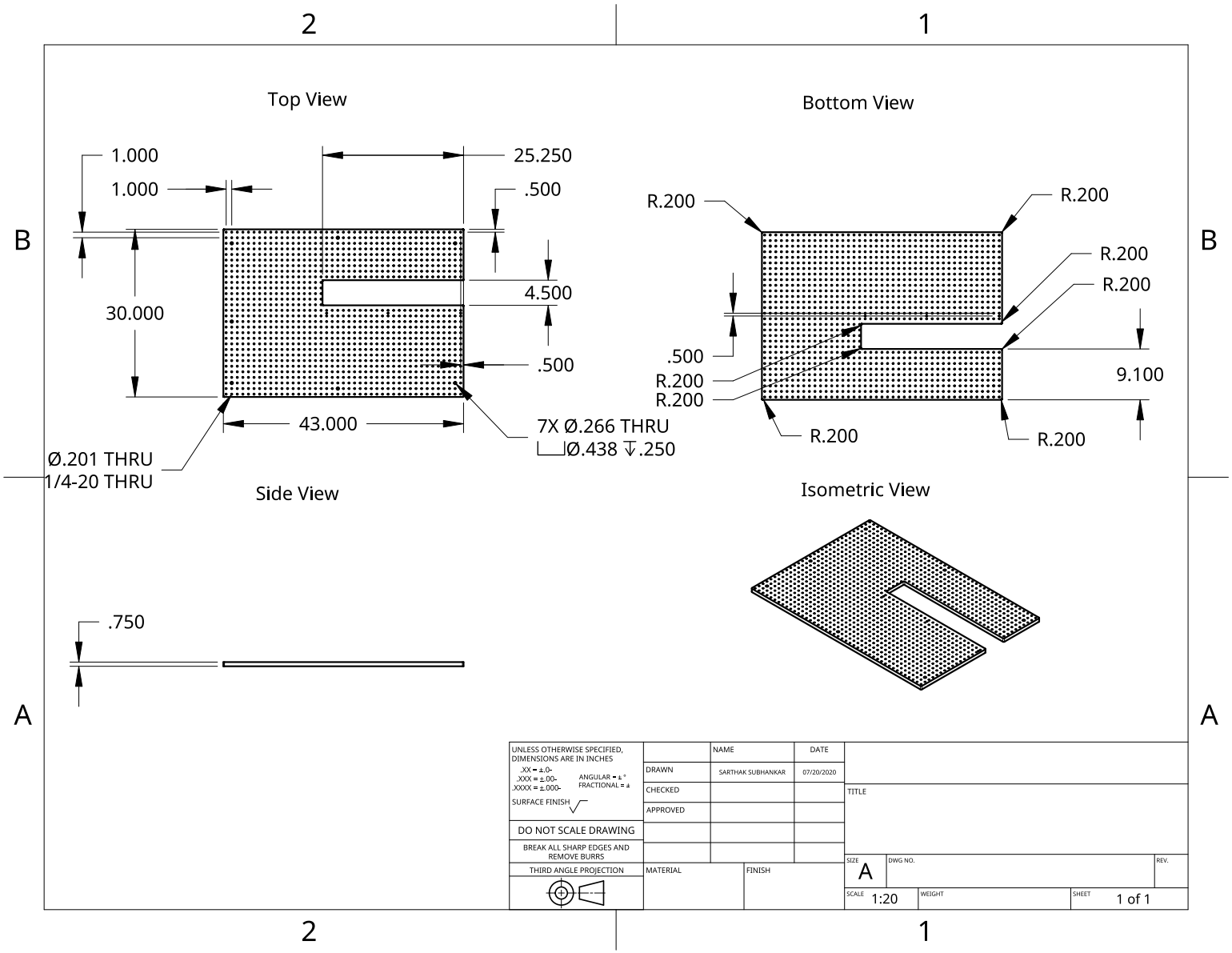

Figure G.13: Drawing of the SLM breadboard

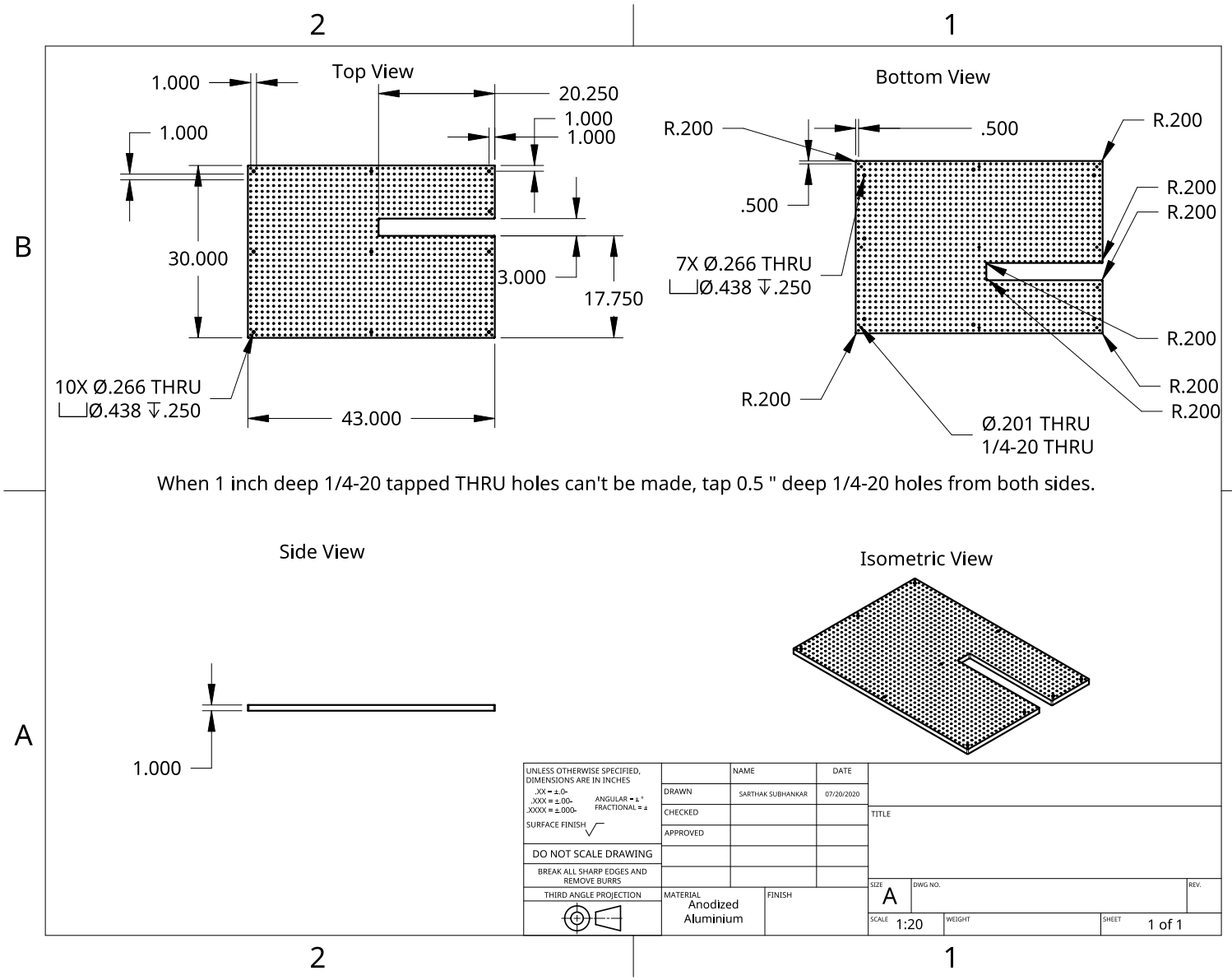

Figure G.14: Drawing of the objective breadboard

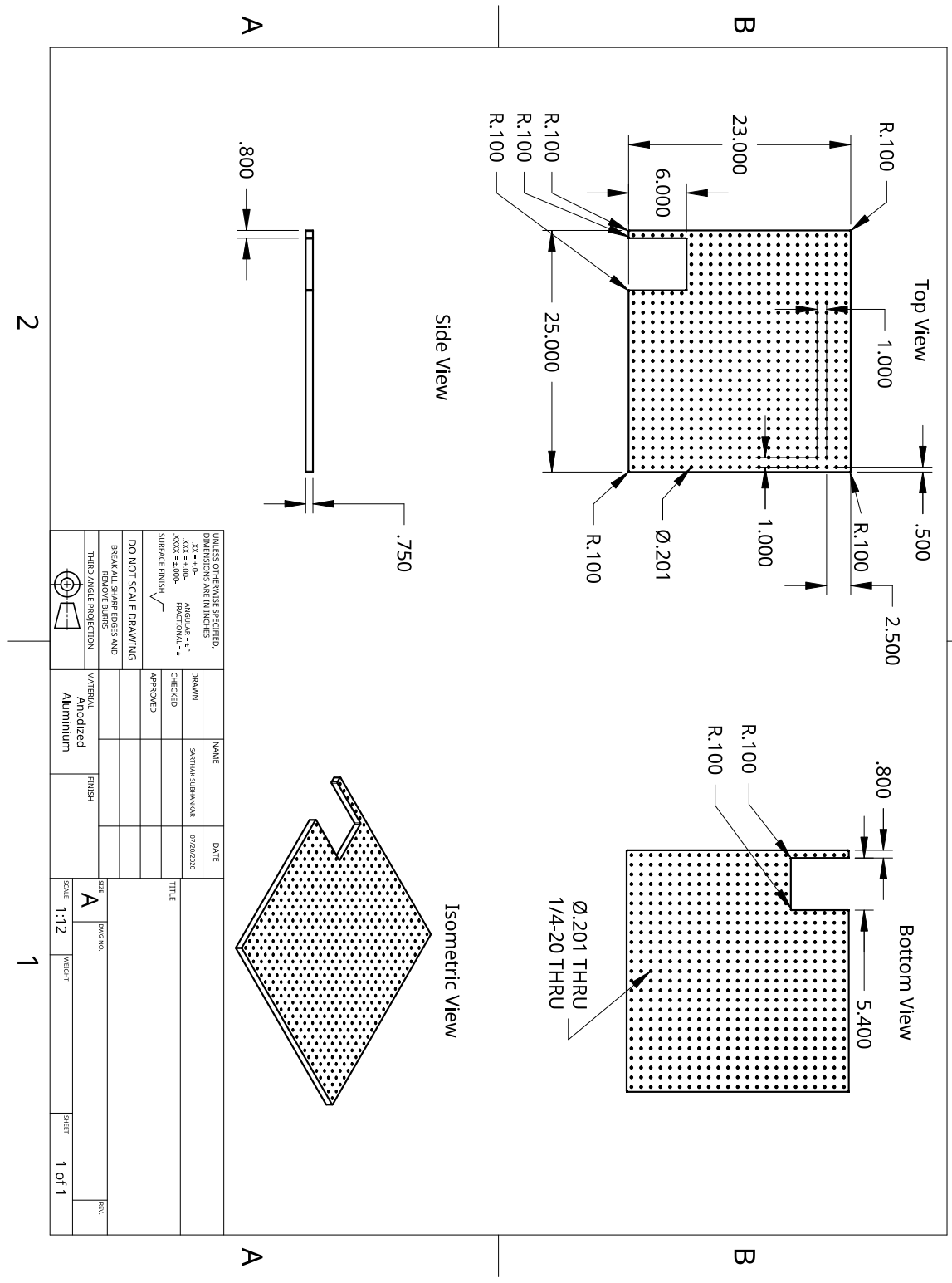

Figure G.15: Drawing of the upper vertical breadboard

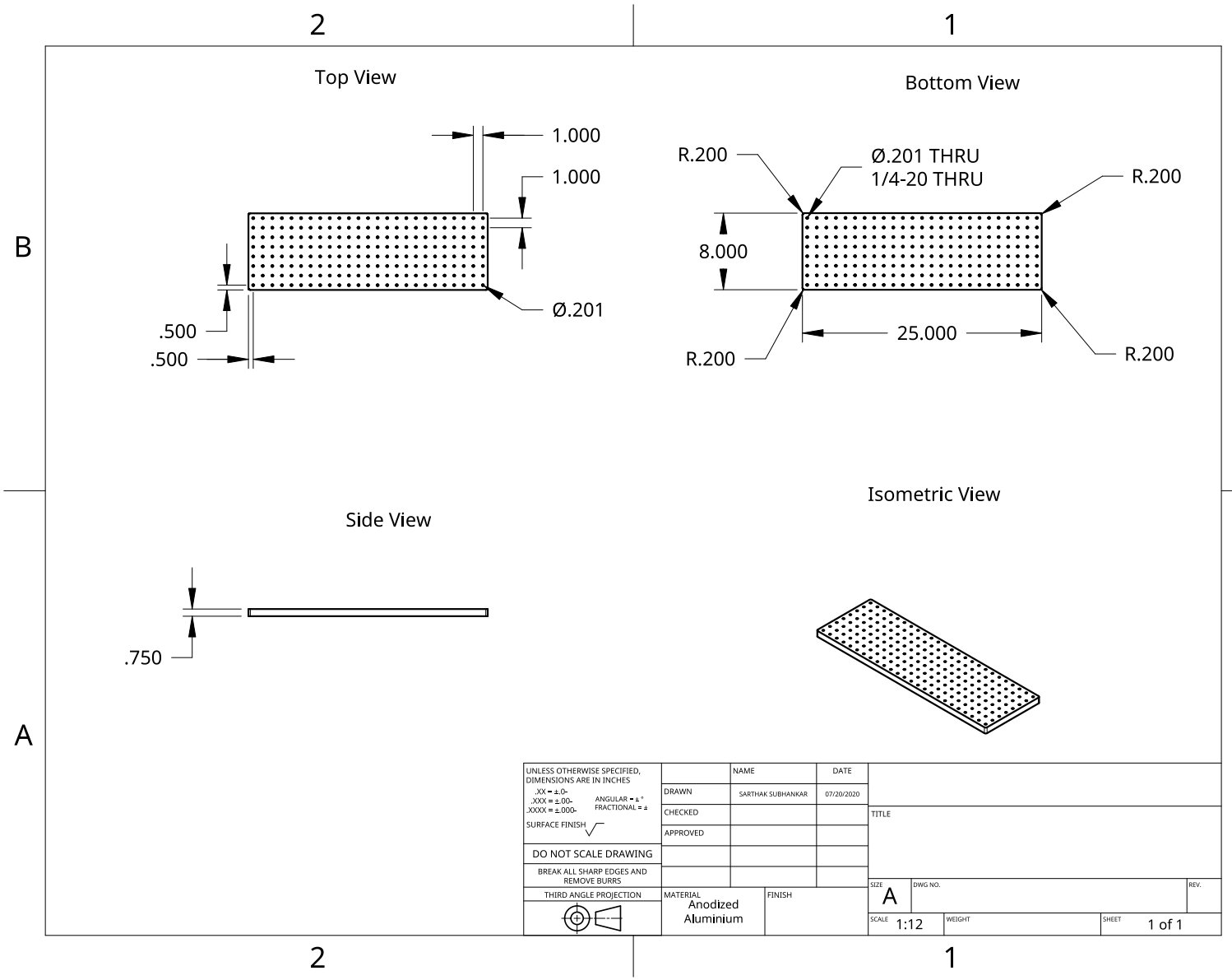

Figure G.16: Drawing of the bottom vertical breadboard

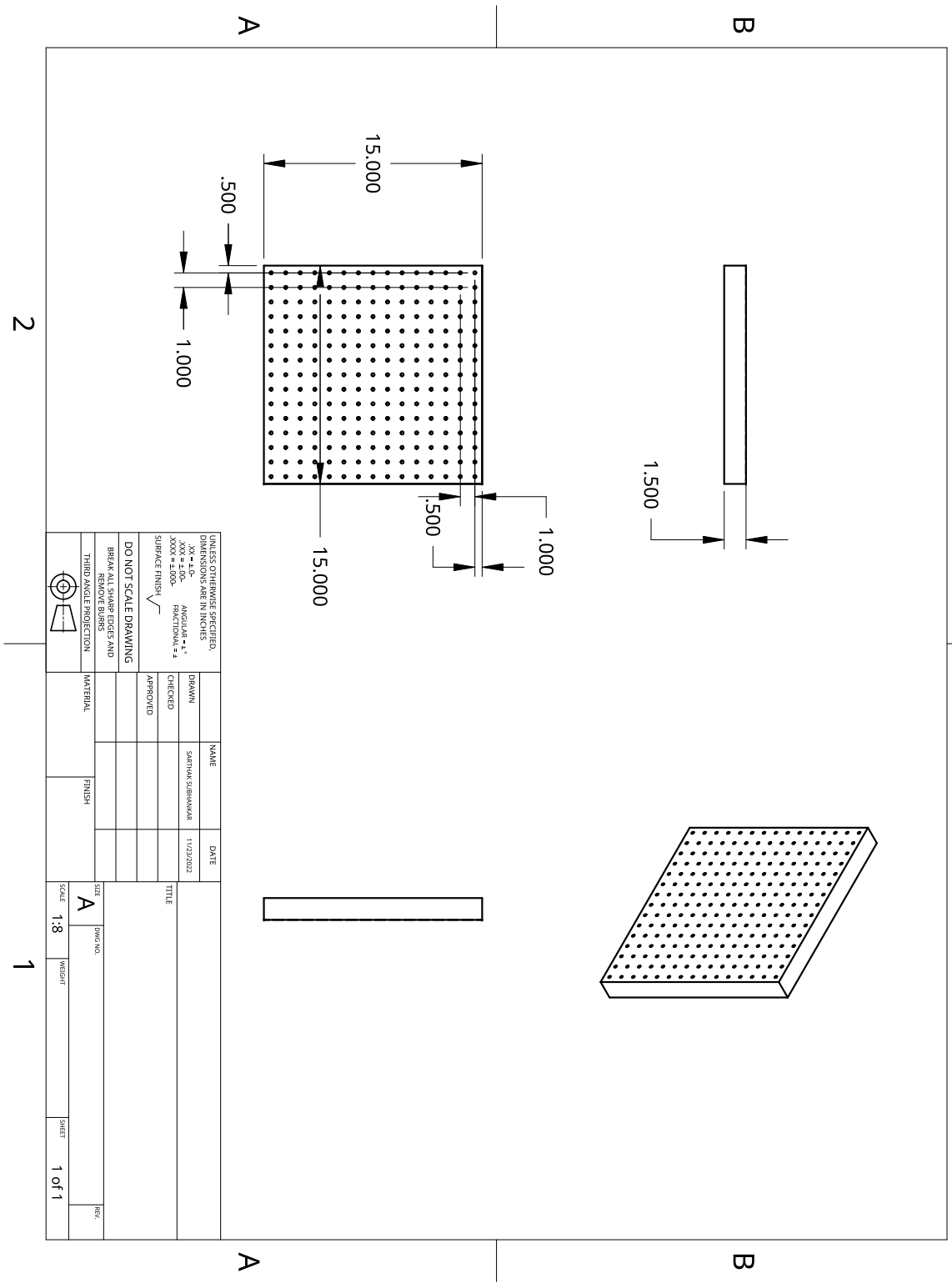

Figure G.17: Drawing of the AOD breadboard

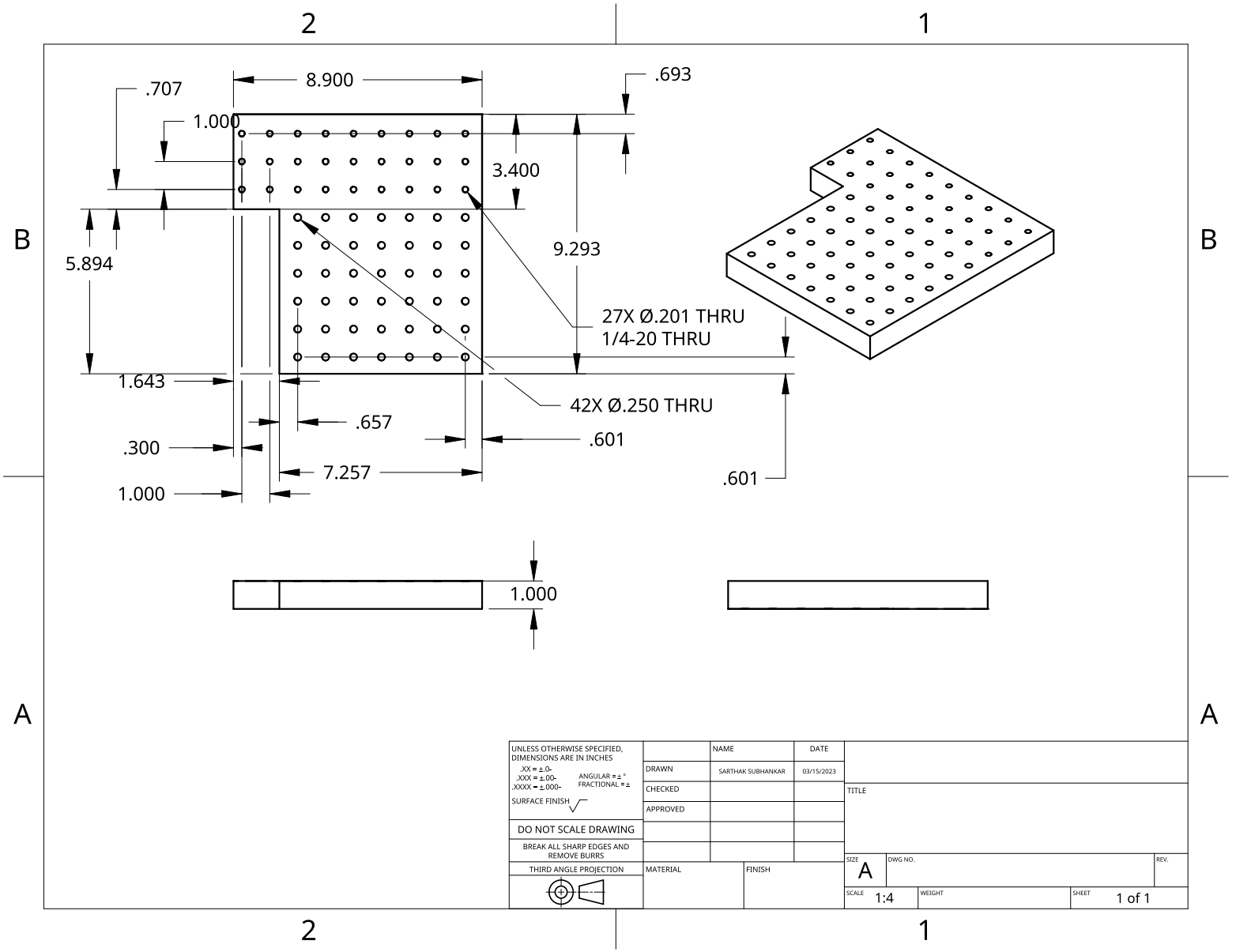

Figure G.18: Drawing of the machined shelf

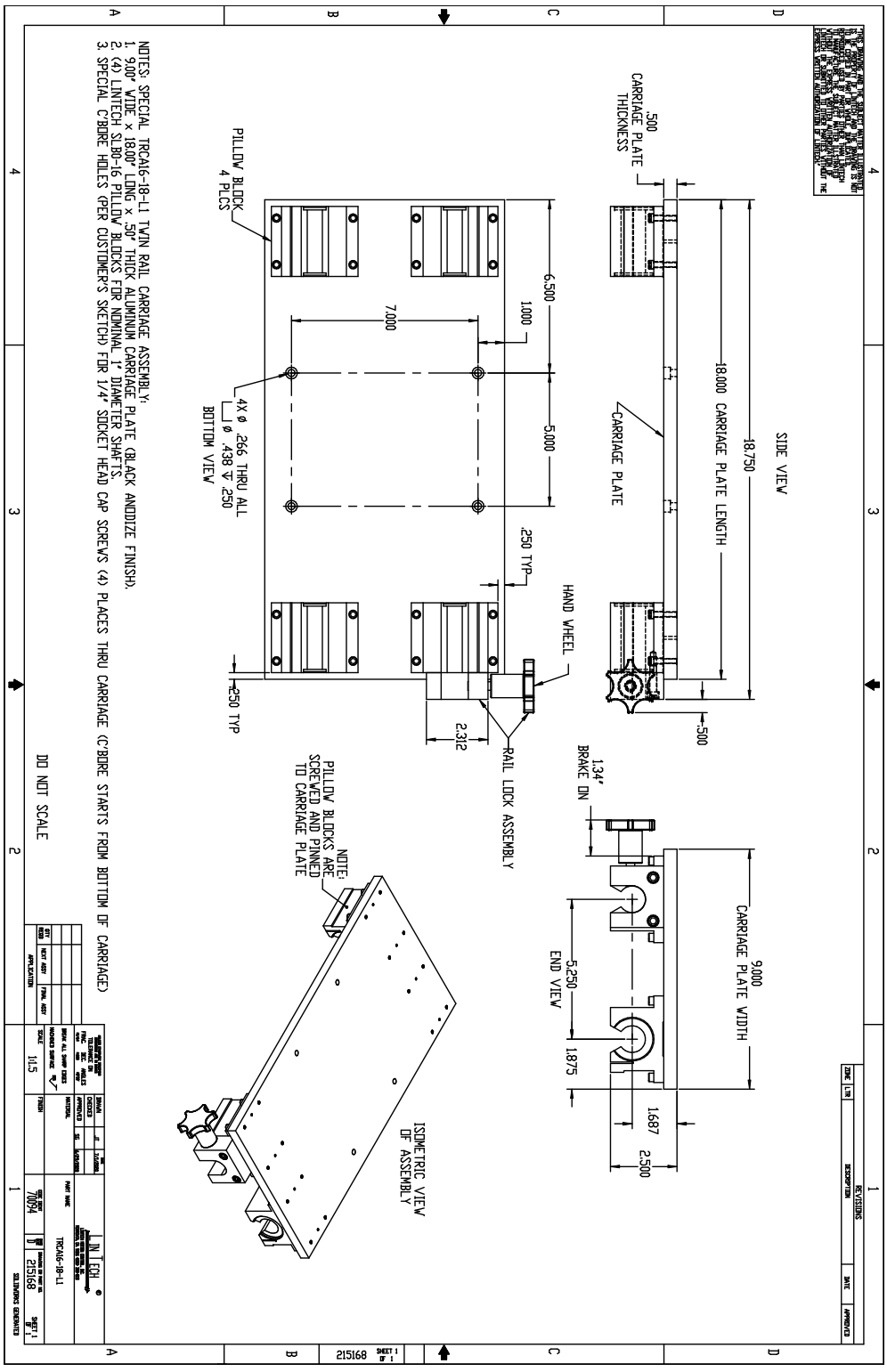

Figure G.19: Drawing of the custom pillow block carriage assembly

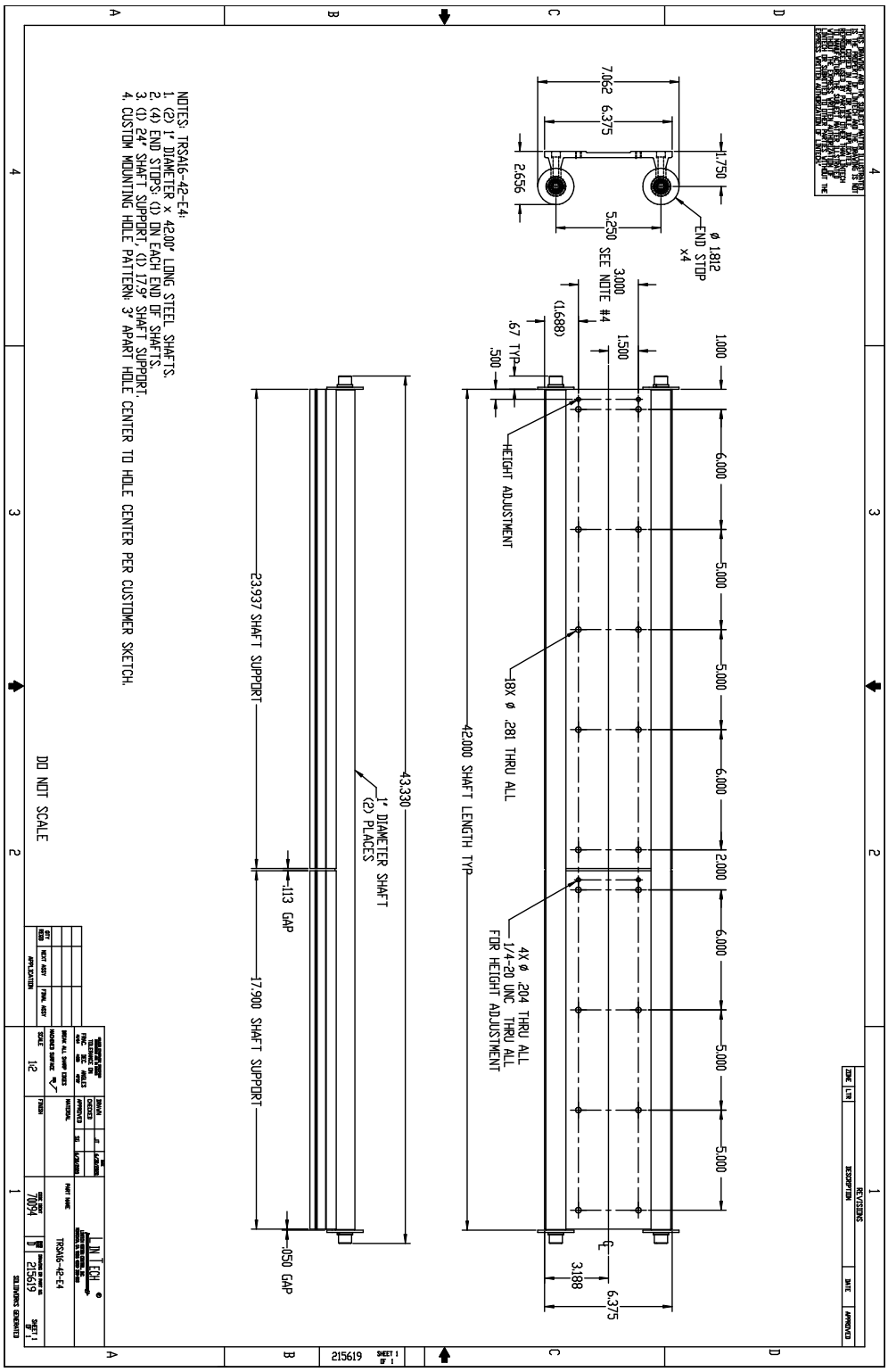

Figure G.20: Drawing of the custom pre-aligned dual shaft assembly

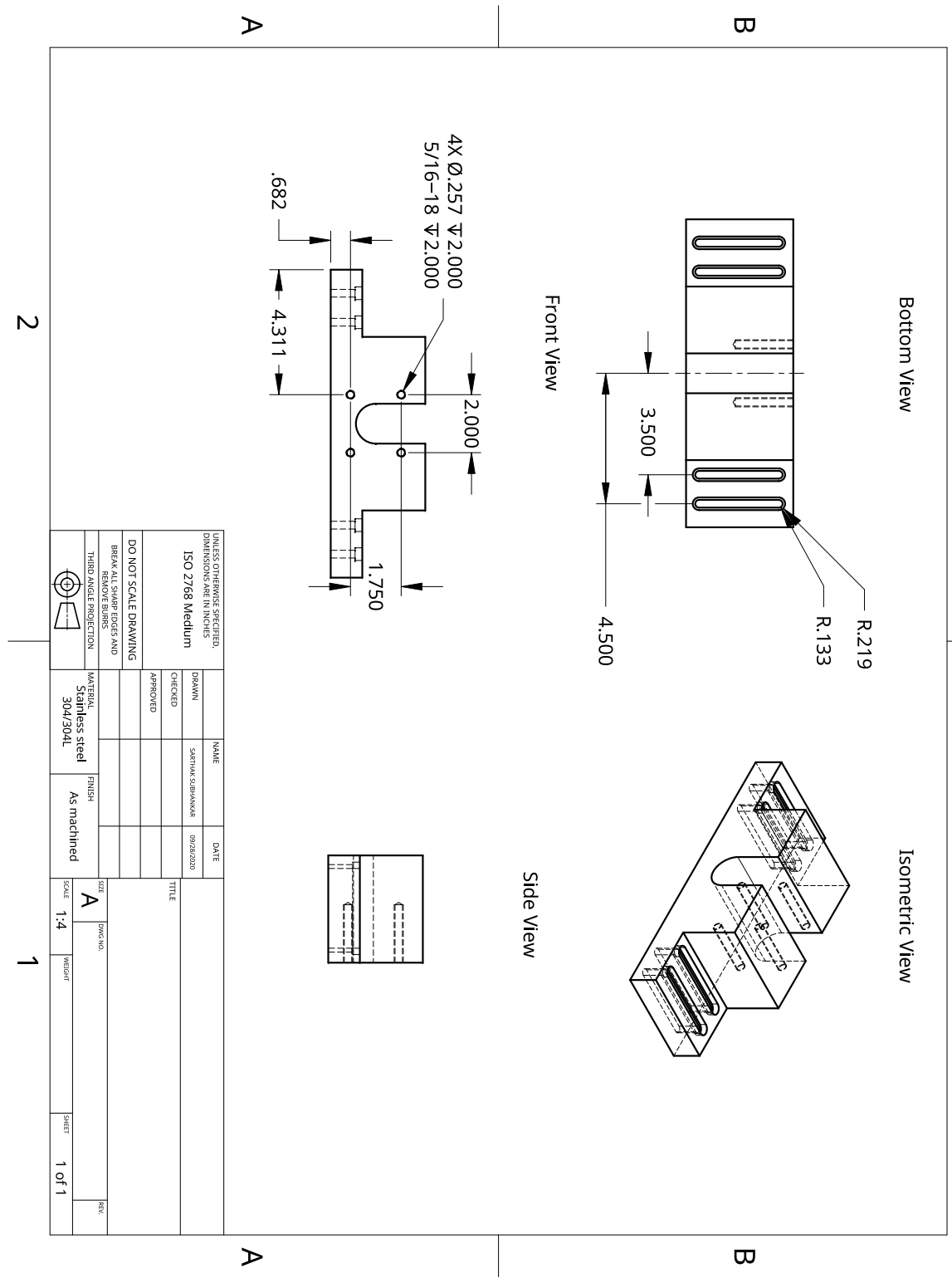

Figure G.21: Drawing of the back holder

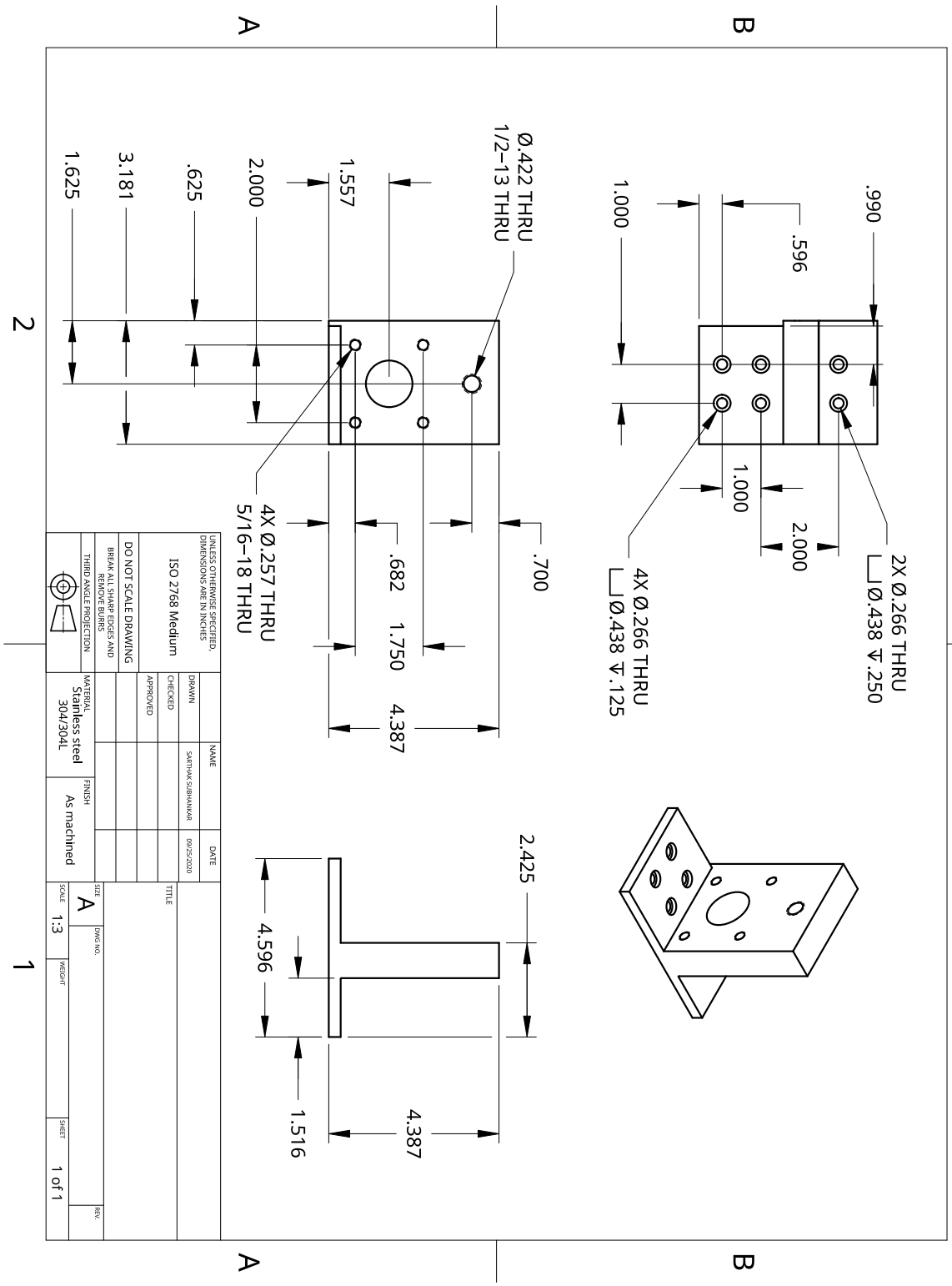

Figure G.22: Drawing of the front holder

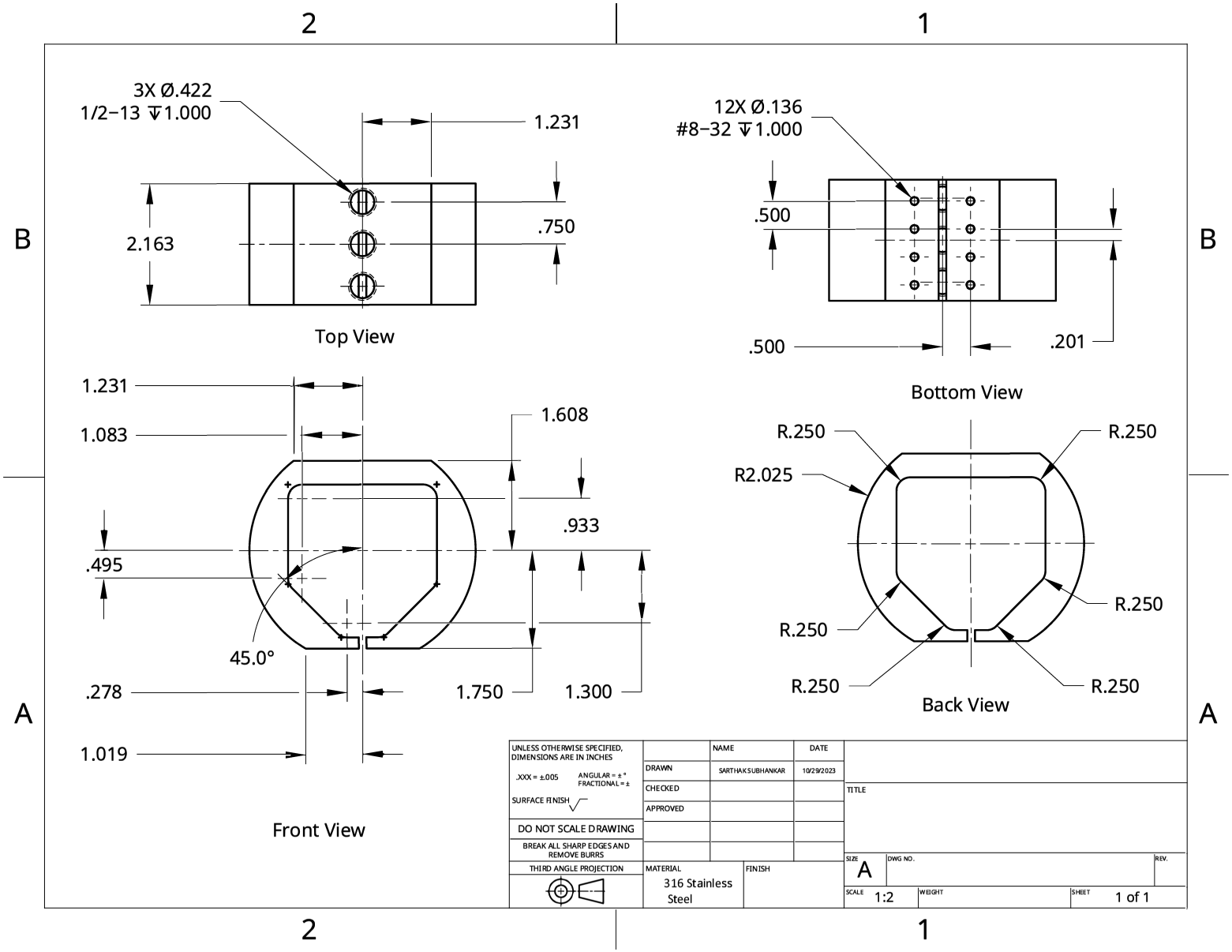

Figure G.23: Drawing of the V block mount for the objectives

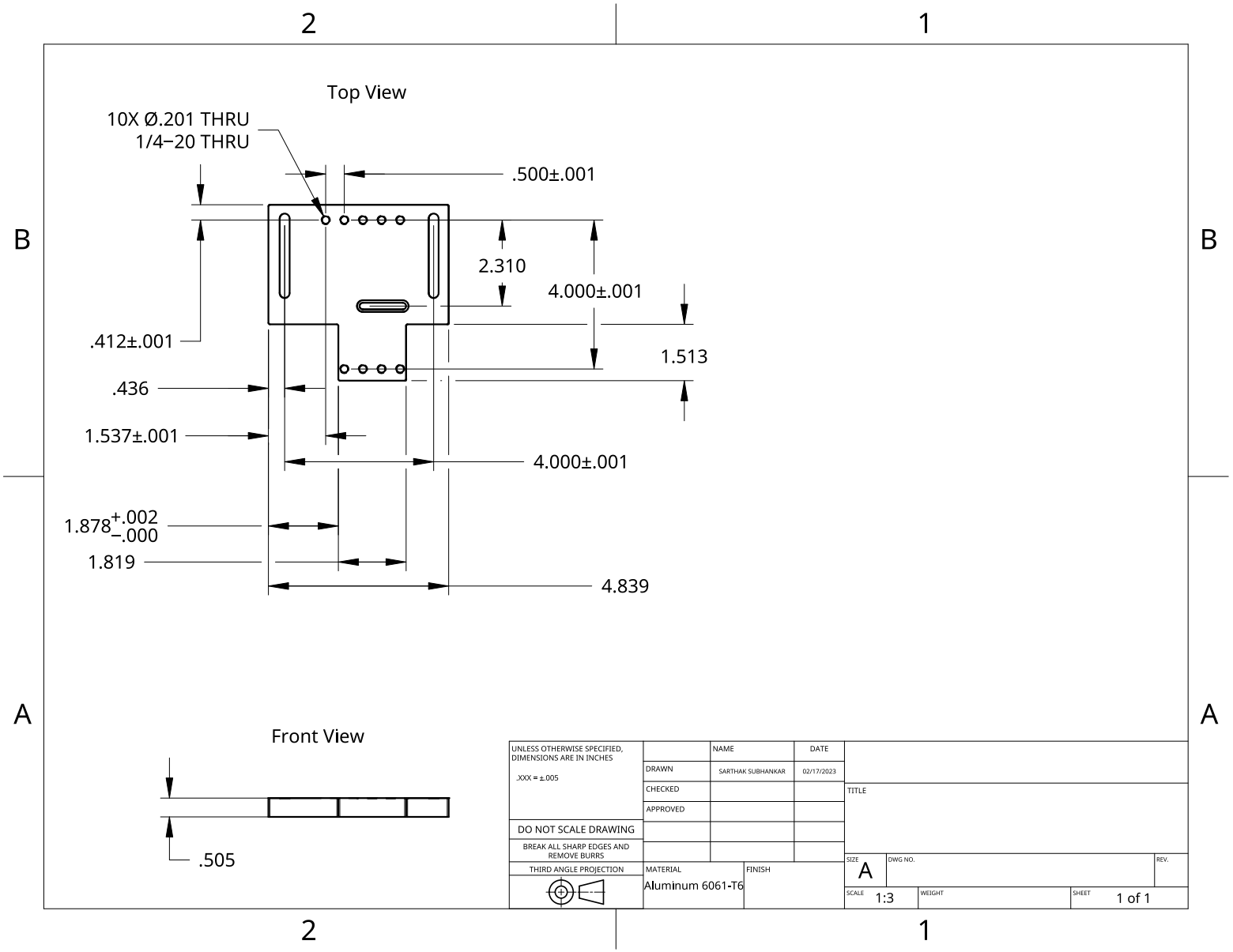

Figure G.24: Drawing of the custom mounting plate for translating the mounted objective

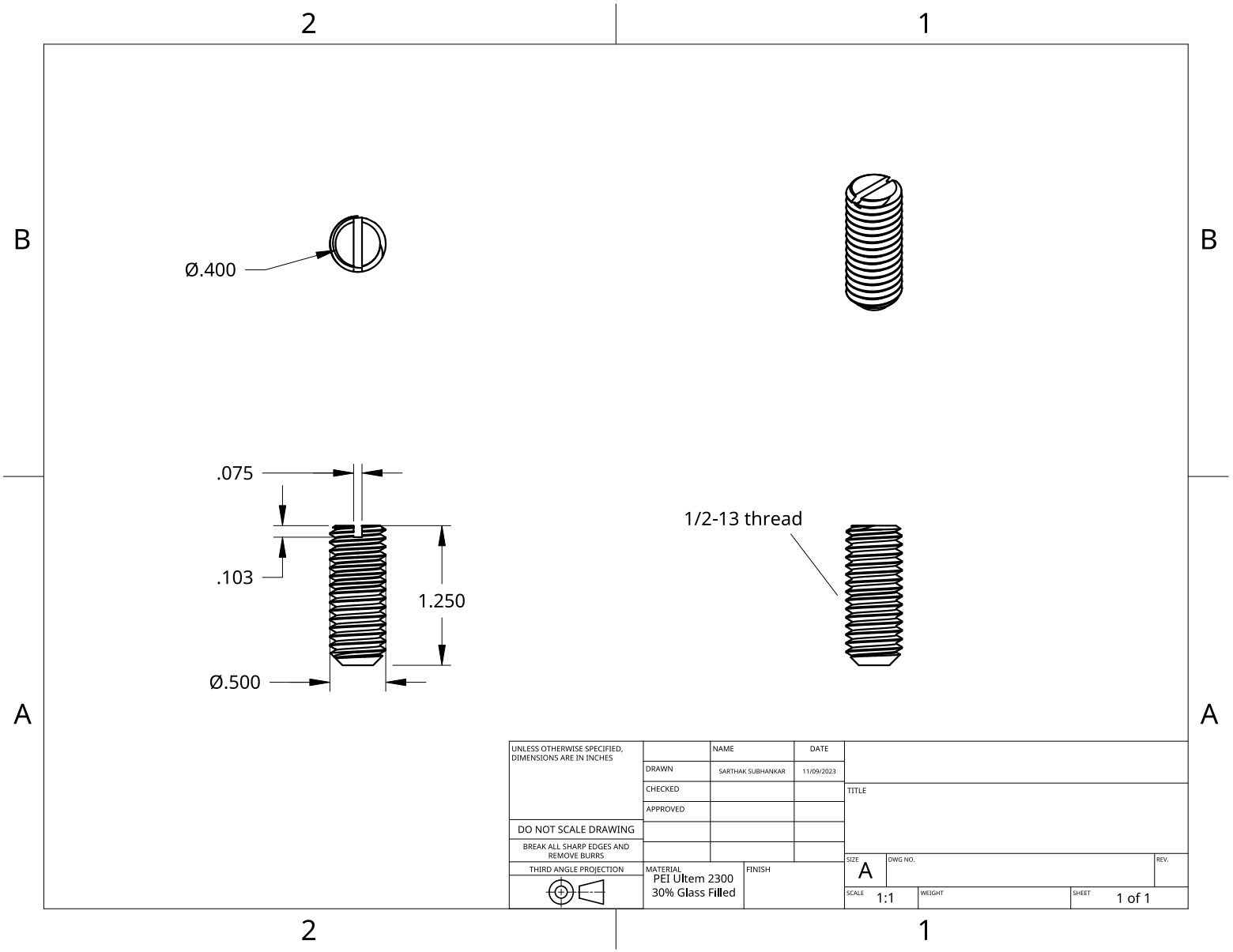

Figure G.25: Drawing of the PEI ULTEM 1/2-13 setscrews

Appendix H: Glass cell cleaning and handling

H.1 Glass cell handling instructions from Precision Glassblowing

Here are the instructions on how to handle the glass cell:

1. DO NOT TOUCH THE WINDOWS.

2. Each window has a custom made semi-rigid plastic cover that rests on the edges of the windows. These are intended to protect the window surface. Precision Glassblowing strongly recommends that the covers be left in place while working with and handling the cell. This is to prevent contact with the windows and maintain their cleanliness. Once installed, the covers can be removed. The covers will also need to be removed before bakeout as they are not made out of high-temperature plastic.

3. Retain the covers if you need to store the cell or ship it. There is always some variation in window OD (factory tolerance), so each cover is made to fit each individual window.

4. The glass cell flange is rotatable. Keep this in mind when handling the glass cell, as the ring can slide and impact the cell once it is unwrapped.

5. DO NOT TOUCH THE WINDOWS.

H.2 Cleaning the RAR nanotextured windows of the glass cell

Here are the instructions that were given to us by TelAztec (check TelAztec's Youtube channel for a video tutorial), which I layout as follows:

1. The textured surfaces of these windows require special attention when cleaning. Conventional cleaning techniques used for thin-film coatings—such as the drop-and-drag method or physical wiping or cleaning using polymer films—should be avoided since this can result in further contamination from solvent residues and debris from wipes being forced deeper into the valleys of the textures.

2. RAR surface textured laser optics are most effectively cleaned by solvent rinsing first with methanol (UHPLC grade or higher) or isopropyl alcohol (HPLC plus grade or higher), or by immersion in an ammonia solution or a simple soap and water bath. Highly contaminated textures can be cleaned very aggressively by immersion in acid solutions such as a mix of sulfuric acid and hydrogen peroxide. The cleaning of the textured optics should be completed by rinsing with isopropyl alcohol followed by drying with filtered dry nitrogen.

As we had already installed our glass cell by the time we decided to clean it, any form of aggressive cleaning was out of the picture. First, we sprayed dry nitrogen from a pressurized tank ($\sim$ 75 PSI) on the windows several times to eliminate any contaminants. The pressurized dry nitrogen was filtered through a nozzle to achieve a particulate size of less than 750 nm. Then we sprayed UHPLC grade Methanol and HPLC plus grade acetone on the windows. We immediately followed this by spraying filtered dry nitrogen in the direction of gravity to push the sprayed reagents toward the bottom of the window.

Appendix I: Aligning the tweezer projection systems

The optical layouts for both the AOD-based and SLM-based tweezer projection systems (see Fig. 7.48 and Fig. 7.49) are similar, and hence their alignment strategies are also similar. Here, I will detail how the AOD-based tweezer projection system was aligned using the nomenclature introduced in Fig. 7.47.

1. The first step is to ensure that the input beam to the tweezer-projection system is both level and mechanically aligned to the center of the optical rails in its entirety. This must be done prior to assembling or aligning the optical system. While lenses in the optical mounts mounted on rail carriages/plates can be readily centered transversely with respect to the rails via mechanical constraints, fine-tuning of this alignment is only possible by using the aligned input beam as the reference. To that end, two similar irises are each mounted mechanically centered to a rail carriage. One such iris-carriage assembly is placed close to the input beam launch and the other iris-carriage assembly is placed far away from the launch, but before the folding mirror. We placed a beam profiler or a camera after both irises and ensured that transmitted beam clipping was radially symmetric around the intensity center when each iris was closed individually. We used the hexagonal edges of the input beam collimated from a PCF fiber as the reference for this radially symmetric clipping iris centration.

2. We then moved the two irises to after the folding mirror. Translate the mirror on the first rail to center the input beam on the near iris, and change the tip and tilt of the mirror mount to center the beam on the far iris.

3. Now the input beam to the tweezer projection system is centered to the two optical rails. The next step is to center all the lenses and remove any tip or tilt error with respect to the aligned input beam. We use five-axis mounts for this purpose (Newport LP-2A, 9081 stage). As all the lenses in the optical layouts have one flat side, the back-reflection of the input beam from the flat surface was used as a guide to remove tip and tilt errors i.e. the back reflection must pass through both alignment irises. The input beam must first interface with the flat surface of the lens to get a collimated back-reflection. Once the tip and tilt alignment errors were corrected, we locked the tip and tilt knobs on the mount.

4. In order to remove decentration errors, the curved surface of the lens was used as it also provides a back reflection, which increases in size with increasing distance from the lens. By moving the decenter x and decenter y knobs on the five-axis mounts, the back reflection halo from the curved surface can be centered to the collimated back-reflection from the flat surface. This is typically easier for lenses that have larger radius of curvature i.e. less optical power. The other method is to screw a threaded iris onto the five-axis lens mount, and center the lens to the input beam by closing the iris while monitoring the radially symmetric clipping of the transmitted beam profile. Lastly, we locked the decenter x and decenter y knobs of the lens mount.

5. Steps 3 and 4 must be repeated for each lens to remove all decentration and tip/tilt error. We are now in a position to correct the defocus/despace errors. Given that our optical

systems can be broken down to afocal systems, we used shearing interferometry to correct for defocus/despace errors. For instance, lens 0 and lens 1 constitute a Keplerian telescope, lens 1 and lens 2 constitute a Keplerian telescope, lens 2 and lens 3 constitute a Galilean telescope, and lens 4 and lens 5 constitute a Keplerian telescope. The out-of-order alignment facilitated by the use of optical rails will be very relevant now. As the tip, tilt, and decentration of the lenses are all corrected and the lenses mounted on rail carriages recover near perfect alignment when you remove and reinstall them, the defocus/despace alignment errors between the lenses can be isolated and corrected.

6. In the layout, the flat mirror is placed $4f$ away from the AOD for historical reasons. Initially, I had thought about adding (and actually installed) a deformable mirror $4f$ away from the AOD to adaptively correct for aberrations, but switched it out for the flat mirror later. One can see that the flat mirror is at the simultaneous focus of lens 2 and lens 1. We start by placing lens 1 upstream from the mirror and at a distance f_1 away from it. The shearing interferometer sets the location of lens 2 downstream from the mirror as lens 1 and lens 2 constitute a Keplerian telescope. Now the location of lens 0 can be defined with respect to lens 1 as they constitute a Keplerian telescope. We used the shearing interferometer before the mirror to determine the location of lens 0 with respect to lens 1. Now we can determine the location of lens 3 with respect to lens 2 by using a shearing interferometer as they together constitute a Galilean telescope. Lastly, lenses 4 and 5 can be placed with respect to each other as they constitute a Keplerian telescope by using a shearing interferometer. If not for the rails, this out-of-order alignment would be hard. The tip/tilt-corrected-lenses are now all placed appropriately with respect to each other i.e.

defocus/despace errors corrected as well. The last step is determining d_1 and the location of the AOD with respect to lens 0.

7. The correct position of the AOD with respect to the lens 0 is where all the AOD diffracted orders coalesce at the mirror, as enforced by the $4f$ imaging of the AOD plane on to the mirror. Shrinking the beam entering the AOD prior to being diffracted helps in better resolving the appropriate AOD position. As the AOD is mounted on a rail carriage, we just slide the AOD-carriage assembly on the rails to determine the appropriate position. The diffraction efficiency of the 2-axis AOD (is typically 55% after diffracting twice) is hardly affected while sliding the AOD carriage when the carriage is properly justified with respect to the rails. We drive both axes of the AOD with a multi-tone waveform generated by a commercial arbitrary waveform generator M4i.6622-x8 from Spectrum Instrumentation.

8. The AOD diffraction order coalescing method for determining its position was used to determine d_1 (and therefore d_2) as well. The AOD diffraction orders must coalesce at the entrance aperture of the objective. However, this time lens 4 and lens 5 must be moved simultaneously by exactly the same amount to avoid defocus/errors in this Keplerian telescope.

9. Last but not least, the tweezer projection system must now be aligned to the objectives. To do that, we drive the AOD to generate a single diffracted beam that is centered on all the optics in the tweezer projection system. This diffracted order traverses both objectives and makes it way to the Twyman-Green-Fizeau interferometer setup (see Fig. 7.56). The folding mirrors after lens 5 and before the objectives are now used to overlap the beam from the tweezer projection system with the reference beam from the short interferometer

arm (see Fig. 7.48).

In order to align the SLMs, the center of intensity of the beam illuminating the SLM must be aligned with the SLM pixel array. To that end, I recommend using a vortex pattern on the SLM for proper centration of the input beam intensity to the SLM pixel array. Lastly, we use lead shot filled sea bags to suppress vibrations in some of our optical setups, as suggested by Nathan.

Bibliography

[1] José Sasián. Aberration coefficients. In *Introduction to Aberrations in Optical Imaging Systems*, page 132–146. Cambridge University Press, 2012.

[2] Warren J Smith. *Modern Optical Engineering: The Design of Optical Systems*. McGraw-Hill Education, New York, 4th editio edition, 2008. ISBN 9780071476874. URL https://www.accessengineeringlibrary.com/content/book/9780071476874.

[3] James Wyant and Katherine Creath. Basic Wavefront Aberration Theory for Optical Metrology. *Appl Optics Optical Eng*, 11, 1992.

[4] Joseph Braat. Analytical expressions for the wave-front aberration coefficients of a tilted plane-parallel plate. *Applied Optics*, 36(32):8459, 1997. ISSN 0003-6935. doi: 10.1364/ao.36.008459.

[5] Christian Gross and Immanuel Bloch. Quantum simulations with ultracold atoms in optical lattices. *Science*, 357(6355):995–1001, 2017. ISSN 10959203. doi: 10.1126/science.aal3837.

[6] C. Javaux, I. G. Hughes, G. Lochead, J. Millen, and M. P.A. Jones. Modulation-free pump-probe spectroscopy of strontium atoms. *European Physical Journal D*, 57(2):151–154, 2010. ISSN 14346060. doi: 10.1140/epjd/e2010-00029-4.

[7] Shaobing Zhu, Tao Chen, Xiaolin Li, and Yuzhu Wang. Polarization spectroscopy of 1S01P1 transition of neutral ytterbium isotopes in hollow cathode lamp. *Journal of the Optical Society of America B*, 31(10):2302, 2014. ISSN 0740-3224. doi: 10.1364/josab.31.002302.

[8] Varun Vaidya. *DEGENERATE MIXTURES OF RUBIDIUM AND YTTERBIUM FOR ENGINEERING OPEN QUANTUM SYSTEMS*. PhD thesis, 2015. URL https://drum.lib.umd.edu/items/b7808239-7244-43ae-9a77-40e44d73d0f5.

[9] Creston David Herold. *Ultracold Mixtures of Rubidium and Ytterbium for Open Quantum System Engineering*. PhD thesis, 2014. URL http://hdl.handle.net/1903/15714.

[10] Andrew MacRae J¨ urgen Appel and A I Lvovsky. A versatile digital GHz phase lock for external cavity diode lasers. *Meas. Sci. Technol. Meas. Sci. Technol*, 18753(20):206–55302, 2009. doi: 10.1088/0957-0233/20/5/055302. URL http://iopscience.iop.org/0957-0233/20/5/055302.

[11] N. C. Pisenti, A. Restelli, B. J. Reschovsky, D. S. Barker, and G. K. Campbell. An ultra-low noise, high-voltage piezo-driver. *Review of Scientific Instruments*, 87(12), 2016. ISSN 10897623. doi: 10.1063/1.4969059. URL http://dx.doi.org/10.1063/1.4969059.

[12] G. Binnig and H. Rohrer. Scanning tunneling microscopy. *Surface Science*, 126(1-3): 236–244, 3 1983. ISSN 0039-6028. doi: 10.1016/0039-6028(83)90716-1.

[13] Stefan W. Hell. Far-field optical nanoscopy. *Science*, 316(5828):1153–1158, 2007. ISSN 00368075. doi: 10.1126/science.1137395.

[14] Suzanne J. Matthews, Tia Newhall, and Kevin C. Webb. *Dive Into Systems: A Gentle Introduction to Computer Systems*. No Starch Press, 2022. ISBN 9781718501362.

[15] Alexander Altland and Ben D Simons. Response functions. In *Condensed Matter Field Theory*, page 360–408. Cambridge University Press, 2010.

[16] André Eckardt and Egidijus Anisimovas. High-frequency approximation for periodically driven quantum systems from a Floquet-space perspective. *New Journal of Physics*, 17(9), 2015. ISSN 13672630. doi: 10.1088/1367-2630/17/9/093039.

[17] André Eckardt. Colloquium: Atomic quantum gases in periodically driven optical lattices. *Reviews of Modern Physics*, 89(1):1–30, 2017. ISSN 15390756. doi: 10.1103/RevModPhys.89.011004.

[18] Marin Bukov, Luca D'Alessio, and Anatoli Polkovnikov. Universal high-frequency behavior of periodically driven systems: From dynamical stabilization to Floquet engineering. *Advances in Physics*, 64(2):139–226, 2015. ISSN 14606976. doi: 10.1080/00018732.2015.1055918. URL http://arxiv.org/abs/1407.4803%5Cnhttp://www.arxiv.org/pdf/1407.4803.pdf.

[19] Martin Holthaus. Floquet engineering with quasienergy bands oferiodically driven optical lattices. *Journal of Physics B: Atomic, Molecular and Optical Physics*, 49(1):013001, 2015. ISSN 13616455. doi: 10.1088/0953-4075/49/1/013001.

[20] Takashi Oka and Sota Kitamura. Floquet Engineering of Quantum Materials. *Annual Review of Condensed Matter Physics*, 10(1):387–408, 2019. ISSN 1947-5454. doi: 10.1146/annurev-conmatphys-031218-013423. URL http://arxiv.org/abs/1804.03212%0Ahttp://dx.doi.org/10.1146/annurev-conmatphys-031218-013423.

[21] Maciej Lewenstein, Anna Sanpera, and Ver‘ onica Ahufinge. *Ultracold Atoms in Optical Lattices Simulating quantum many-body systems*, volume 1. 2015. ISBN 9788578110796. doi: 10.1017/CBO9781107415324.004.

[22] Omjyoti Dutta, Mariusz Gajda, Philipp Hauke, Maciej Lewenstein, Dirk Sören Lühmann, Boris A. Malomed, Tomasz Sowiński, and Jakub Zakrzewski. Non-standard Hubbard models in optical lattices: a review. *Reports on Progress in Physics*, 78(6), 2015. ISSN 00344885. doi: 10.1088/0034-4885/78/6/066001.

[23] Sylvain Nascimbene, Nathan Goldman, Nigel R. Cooper, and Jean Dalibard. Dynamic Optical Lattices of Subwavelength Spacing for Ultracold Atoms. *Physical Review Letters*, 115(14):1–5, 2015. ISSN 10797114. doi: 10.1103/PhysRevLett.115.140401.

[24] Maciej Lewenstein, Anna Sanpera, Veronica Ahufinger, Bogdan Damski, Aditi Sen, and Ujjwal Sen. Ultracold atomic gases in optical lattices: Mimicking condensed matter physics and beyond. *Advances in Physics*, 56(2):243–379, 2007. ISSN 00018732. doi: 10.1080/00018730701223200.

[25] Antoine Browaeys and Thierry Lahaye. Many-body physics with individually controlled Rydberg atoms. *Nature Physics*, 16(2):132–142, 2020. ISSN 17452481. doi: 10.1038/s41567-019-0733-z. URL http://dx.doi.org/10.1038/s41567-019-0733-z.

[26] Xiaoling Wu, Xinhui Liang, Yaoqi Tian, Fan Yang, Cheng Chen, Yong Chun Liu, Meng Khoon Tey, and Li You. A concise review of Rydberg atom based quantum computation and quantum simulation. *Chinese Physics B*, 30(2), 2021. ISSN 20583834. doi: 10.1088/1674-1056/abd76f.

[27] M. Saffman, T. G. Walker, and K. Mølmer. Quantum information with Rydberg atoms. *Reviews of Modern Physics*, 82(3):2313–2363, 2010. ISSN 00346861. doi: 10.1103/RevModPhys.82.2313.

[28] M. Morgado and S. Whitlock. Quantum simulation and computing with Rydberg-interacting qubits. *AVS Quantum Science*, 3(2), 2021. ISSN 26390213. doi: 10.1116/5.0036562.

[29] Nicolò Defenu, Tobias Donner, Tommaso Macrì, Guido Pagano, Stefano Ruffo, and Andrea Trombettoni. Long-range interacting quantum systems. *Reviews of Modern Physics*, 95(3):35002, 2023. ISSN 0034-6861. doi: 10.1103/revmodphys.95.035002. URL https://doi.org/10.1103/RevModPhys.95.035002.

[30] M. Saffman. Quantum computing with atomic qubits and Rydberg interactions: Progress and challenges. *Journal of Physics B: Atomic, Molecular and Optical Physics*, 49(20), 2016. ISSN 13616455. doi: 10.1088/0953-4075/49/20/202001.

[31] Loïc Henriet, Lucas Beguin, Adrien Signoles, Thierry Lahaye, Antoine Browaeys, Georges Olivier Reymond, and Christophe Jurczak. Quantum computing with neutral atoms. *Quantum*, 4:1–34, 2020. ISSN 2521327X. doi: 10.22331/Q-2020-09-21-327.

[32] Adam M. Kaufman and Kang Kuen Ni. Quantum science with optical tweezer arrays of ultracold atoms and molecules. *Nature Physics*, 17(12):1324–1333, 2021. ISSN 17452481. doi: 10.1038/s41567-021-01357-2.

[33] Xiao Feng Shi. Quantum logic and entanglement by neutral Rydberg atoms: Methods and fidelity. *Quantum Science and Technology*, 7(2), 2022. ISSN 20589565. doi: 10.1088/2058-9565/ac18b8.

[34] N Schlosser, G Reymond, I.˜Protsenko, and P Grangier. Subpoissonian loading of a microscopic dipole trap. *Nature*, 411(June):1024, 2001.

[35] M. A. Norcia, A. W. Young, and A. M. Kaufman. Microscopic Control and Detection of Ultracold Strontium in Optical-Tweezer Arrays. *Physical Review X*, 8(4):41054, 2018. ISSN 21603308. doi: 10.1103/PhysRevX.8.041054. URL https://doi.org/10.1103/PhysRevX.8.041054.

[36] Alexandre Cooper, Jacob P. Covey, Ivaylo S. Madjarov, Sergey G. Porsev, Marianna S. Safronova, and Manuel Endres. Alkaline-Earth Atoms in Optical Tweezers. *Physical Review X*, 8(4):41055, 2018. ISSN 21603308. doi: 10.1103/PhysRevX.8.041055. URL https://doi.org/10.1103/PhysRevX.8.041055.

[37] S. Saskin, J. T. Wilson, B. Grinkemeyer, and J. D. Thompson. Narrow-line cooling and imaging of Ytterbium atoms in an optical tweezer array. *Physical Review Letters*, 122(14):143002, 2019. ISSN 10797114. doi: 10.1103/PhysRevLett.122.143002. URL https://doi.org/10.1103/PhysRevLett.122.143002.

[38] Damien Bloch, Britton Hofer, Sam R. Cohen, Antoine Browaeys, and Igor Ferrier-Barbut. Trapping and Imaging Single Dysprosium Atoms in Optical Tweezer Arrays. *Physical Review Letters*, 131(20):203401, 2023. ISSN 0031-9007. doi: 10.1103/physrevlett.131.203401. URL https://doi.org/10.1103/PhysRevLett.131.203401.

[39] Daniel Barredo, Sylvain De Léséleuc, Vincent Lienhard, Thierry Lahaye, and Antoine Browaeys. An atom-by-atom assembler of defect-free arbitrary two-dimensional atomic arrays. *Science*, 354(6315):1021–1024, 2016.

[40] T. M. Graham, Y. Song, J. Scott, C. Poole, L. Phuttitarn, K. Jooya, P. Eichler, X. Jiang, A. Marra, B. Grinkemeyer, M. Kwon, M. Ebert, J. Cherek, M. T. Lichtman, M. Gillette, J. Gilbert, D. Bowman, T. Ballance, C. Campbell, E. D. Dahl, O. Crawford, N. S. Blunt, B. Rogers, T. Noel, and M. Saffman. Multi-qubit entanglement and algorithms on a neutral-atom quantum computer. *Nature*, 604(7906):457–462, 2022. ISSN 14764687. doi: 10.1038/s41586-022-04603-6.

[41] Shraddha Anand, Conor E. Bradley, Ryan White, Vikram Ramesh, Kevin Singh, and Hannes Bernien. A dual-species Rydberg array. pages 1–24, 2024. URL http://arxiv.org/abs/2401.10325.

[42] Kevin Singh, Shraddha Anand, Andrew Pocklington, Jordan T. Kemp, and Hannes Bernien. Dual-Element, Two-Dimensional Atom Array with Continuous-Mode Operation. *Physical Review X*, 12(1):11040, 2022. ISSN 21603308. doi: 10.1103/PhysRevX.12.011040. URL https://doi.org/10.1103/PhysRevX.12.011040.

[43] Jeremy T. Young, Przemyslaw Bienias, Ron Belyansky, Adam M. Kaufman, and Alexey V. Gorshkov. Asymmetric blockade and multi-qubit gates via dipole-dipole interactions. 2020. URL http://arxiv.org/abs/2006.02486.

[44] I. I. Beterov and M. Saffman. Rydberg blockade, Förster resonances, and quantum state measurements with different atomic species. *Physical Review A - Atomic, Molecular, and Optical Physics*, 92(4):1–10, 2015. ISSN 10941622. doi: 10.1103/PhysRevA.92.042710.

[45] K. Singh, C. E. Bradley, S. Anand, V. Ramesh, R. White, and H. Bernien. Mid-circuit correction of correlated phase errors using an array of spectator qubits. *Science*, 380(6651): 1265–1269, 2023. ISSN 10959203. doi: 10.1126/science.ade5337.

[46] Mohan Sarovar, Timothy Proctor, Kenneth Rudinger, Kevin Young, Erik Nielsen, and Robin Blume-Kohout. Detecting crosstalk errors in quantum information processors. *Quantum*, 4, 2020. ISSN 2521327X. doi: 10.22331/Q-2020-09-11-321.

[47] Dolev Bluvstein, Simon J. Evered, Alexandra A. Geim, Sophie H. Li, Hengyun Zhou, Tom Manovitz, Sepehr Ebadi, Madelyn Cain, Marcin Kalinowski, Dominik Hangleiter, J. Pablo Bonilla Ataides, Nishad Maskara, Iris Cong, Xun Gao, Pedro Sales Rodriguez, Thomas Karolyshyn, Giulia Semeghini, Michael J. Gullans, Markus Greiner, Vladan Vuletić, and Mikhail D. Lukin. Logical quantum processor based on reconfigurable atom arrays. *Nature*, 626(7997):58–65, 2024. ISSN 14764687. doi: 10.1038/s41586-023-06927-3.

[48] Joanna W. Lis, Aruku Senoo, William F. McGrew, Felix Rönchen, Alec Jenkins, and Adam M. Kaufman. Midcircuit Operations Using the omg Architecture in Neutral Atom Arrays. *Physical Review X*, 13(4):41035, 2023. ISSN 21603308. doi: 10.1103/PhysRevX.13.041035. URL https://doi.org/10.1103/PhysRevX.13.041035.

[49] M. A. Norcia, W. B. Cairncross, K. Barnes, P. Battaglino, A. Brown, M. O. Brown, K. Cassella, C. A. Chen, R. Coxe, D. Crow, J. Epstein, C. Griger, A. M.W. Jones, H. Kim, J. M. Kindem, J. King, S. S. Kondov, K. Kotru, J. Lauigan, M. Li, M. Lu, E. Megidish, J. Marjanovic, M. McDonald, T. Mittiga, J. A. Muniz, S. Narayanaswami, C. Nishiguchi, R. Notermans, T. Paule, K. A. Pawlak, L. S. Peng, A. Ryou, A. Smull, D. Stack, M. Stone, A. Sucich, M. Urbanek, R. J.M. Van De Veerdonk, Z. Vendeiro, T. Wilkason, T. Y. Wu, X. Xie, X. Zhang, and B. J. Bloom. Midcircuit Qubit Measurement and Rearrangement in a Yb 171 Atomic Array. *Physical Review X*, 13(4):41034, 2023. ISSN 21603308. doi: 10.1103/PhysRevX.13.041034. URL https://doi.org/10.1103/PhysRevX.13.041034.

[50] Shuo Ma, Genyue Liu, Pai Peng, Bichen Zhang, Sven Jandura, Jahan Claes, Alex P. Burgers, Guido Pupillo, Shruti Puri, and Jeff D. Thompson. High-fidelity gates and mid-circuit erasure conversion in an atomic qubit. *Nature*, 622(7982):279–284, 2023. ISSN 14764687. doi: 10.1038/s41586-023-06438-1.

[51] Emma Deist, Yue Hui Lu, Jacquelyn Ho, Mary Kate Pasha, Johannes Zeiher, Zhenjie Yan, and Dan M. Stamper-Kurn. Mid-Circuit Cavity Measurement in a Neutral Atom Array. *Physical Review Letters*, 129(20):203602, 2022. ISSN 10797114. doi: 10.1103/

PhysRevLett.129.203602. URL https://doi.org/10.1103/PhysRevLett.129.203602.

[52] Jonathan M. Baker, Andrew Litteken, Casey Duckering, Henry Hoffmann, Hannes Bernien, and Frederic T. Chong. Exploiting long-distance interactions and tolerating atom loss in neutral atom quantum architectures. *Proceedings - International Symposium on Computer Architecture*, 2021-June:818–831, 2021. ISSN 10636897. doi: 10.1109/ISCA52012.2021.00069.

[53] Ahmed M. Farouk, Ilya I. Beterov, Peng Xu , Silvia Bergamini , and Igor I. Ryabtsev . Parallel Implementation of CNOTN and C2NOT2 Gates via Homonuclear and Heteronuclear Förster Interactions of Rydberg Atoms. *Photonics*, 10(11), 2023. ISSN 23046732. doi: 10.3390/photonics10111280.

[54] M. Morgado and S. Whitlock. Quantum simulation and computing with Rydberg-interacting qubits. *AVS Quantum Science*, 3(2):023501, 2021. doi: 10.1116/5.0036562.

[55] C. L. Vaillant, M. P.A. Jones, and R. M. Potvliege. Long-range RydbergRydberg interactions in calcium, strontium and ytterbium. *Journal of Physics B: Atomic, Molecular and Optical Physics*, 45(13), 2012. ISSN 09534075. doi: 10.1088/0953-4075/45/13/135004.

[56] Christophe L Vaillant. Long-Range Interactions in One- and Two-Electron Rydberg Atoms. 2014. URL http://etheses.dur.ac.uk/10594/.

[57] R Grimm, M Weidemüller, and Y Ovchinnikov. Optical dipole trap for neutral atoms. *Adv. At. Mol. Opt. Phys.*, 42:95, 2000. ISSN 0065-2199. doi: 10.1016/S1049-250X(08)60186-X.

[58] Giuseppe Pesce, Philip H. Jones, Onofrio M. Maragò, and Giovanni Volpe. *Optical tweezers: theory and practice*, volume 135. Springer Berlin Heidelberg, 2020. ISBN 0123456789. doi: 10.1140/epjp/s13360-020-00843-5. URL https://doi.org/10.1140/epjp/s13360-020-00843-5.

[59] Herbert Gross, Wolfgang Singer, and Michael Totzeck. *Handbook of Optical Systems*, volume 2. 2006. ISBN 9783527403783. doi: 10.1002/3527606688.

[60] Y. R.P. Sortais, H. Marion, C. Tuchendler, A. M. Lance, M. Lamare, P. Fournet, C. Armellin, R. Mercier, G. Messin, A. Browaeys, and P. Grangier. Diffraction-limited optics for single-atom manipulation. *Physical Review A - Atomic, Molecular, and Optical Physics*, 75(1):1–7, 2007. ISSN 10502947. doi: 10.1103/PhysRevA.75.013406.

[61] José Sasián. *Introduction to aberrations in optical imaging systems*, volume 9781107006. 2011. ISBN 9780511795183. doi: 10.1017/CBO9780511795183.

[62] William D. Phillips. Laser cooling and trapping of neutral atoms. *Reviews of Modern Physics*, 70(3):721–741, 1998. ISSN 00346861. doi: 10.1103/revmodphys.70.721.

[63] Harold J. Metcalf and Peter van der Straten. *Laser Cooling and Trapping*, volume 4. Springer, 1999. ISBN 978-0-387-98728-6. doi: 10.1007/978-1-4612-1470-0. URL https://books.google.ie/books?id=jzbY4NisxckC&printsec=frontcover&source=gbs_ge_summary_r&cad=0#v=onepage&q&f=false%0Ahttp://link.springer.com/10.1007/978-1-4612-1470-0.

[64] M. Saffman. Quantum computing with atomic qubits and Rydberg interactions: Progress and challenges. *Journal of Physics B: Atomic, Molecular and Optical Physics*, 49(20), 2016. ISSN 13616455. doi: 10.1088/0953-4075/49/20/202001.

[65] Kai Niklas Schymik, Sara Pancaldi, Florence Nogrette, Daniel Barredo, Julien Paris, Antoine Browaeys, and Thierry Lahaye. Single Atoms with 6000-Second Trapping Lifetimes in Optical-Tweezer Arrays at Cryogenic Temperatures. *Physical Review Applied*, 16(3):1, 2021. ISSN 23317019. doi: 10.1103/PhysRevApplied.16.034013. URL https://doi.org/10.1103/PhysRevApplied.16.034013.

[66] M. Morgado and S. Whitlock. Quantum simulation and computing with Rydberg qubits. (November), 2020. URL http://arxiv.org/abs/2011.03031.

[67] Simon J. Evered, Dolev Bluvstein, Marcin Kalinowski, Sepehr Ebadi, Tom Manovitz, Hengyun Zhou, Sophie H. Li, Alexandra A. Geim, Tout T. Wang, Nishad Maskara, Harry Levine, Giulia Semeghini, Markus Greiner, Vladan Vuletić, and Mikhail D. Lukin. High-fidelity parallel entangling gates on a neutral-atom quantum computer. *Nature*, 622(7982): 268–272, 2023. ISSN 14764687. doi: 10.1038/s41586-023-06481-y.

[68] Harry Levine, Alexander Keesling, Giulia Semeghini, Ahmed Omran, Tout T. Wang, Sepehr Ebadi, Hannes Bernien, Markus Greiner, Vladan Vuletić, Hannes Pichler, and Mikhail D. Lukin. Parallel Implementation of High-Fidelity Multiqubit Gates with Neutral Atoms. *Physical Review Letters*, 123(17):1–6, 2019. ISSN 10797114. doi: 10.1103/PhysRevLett.123.170503.

[69] Eric D. Black. An introduction to Pound–Drever–Hall laser frequency stabilization. *American Journal of Physics*, 69(1):79–87, 1 2001. ISSN 0002-9505, 1943-2909. doi: 10.1119/1.1286663. URL http://scitation.aip.org/content/aapt/journal/ajp/69/1/10.1119/1.1286663http://scitation.aip.org/deliver/fulltext/aapt/journal/ajp/69/1/1.1286663.pdf;jsessionid=2tsth6dxi8nup.x-aip-live-03?itemId=/content/aapt/journal/ajp/69/1/10.1119/1.1286663&mimeType=.

[70] Warren Nagourney. *Quantum Electronics for Atomic Physics and Telecommunication*. Oxford University Press, 2014. doi: 10.1093/acprof:oso/9780199665488.001.0001.

[71] Remy Legaie, Craig J. Picken, and Jonathan D. Pritchard. Sub-kilohertz excitation lasers for quantum information processing with Rydberg atoms. *Journal of the Optical Society of America B*, 35(4):892, 2018. ISSN 0740-3224. doi: 10.1364/josab.35.000892.

[72] N. Schlosser, G. Reymond, and P. Grangier. Collisional Blockade in Microscopic Optical Dipole Traps. *Physical Review Letters*, 89(2):1–4, 2002. ISSN 10797114. doi: 10.1103/PhysRevLett.89.023005.

[73] Yin Fung, Pimonpan Sompet, and Mikkel Andersen. Single Atoms Preparation Using Light-Assisted Collisions. *Technologies*, 4(1):4, 2016. doi: 10.3390/technologies4010004.

[74] M. O. Brown, T. Thiele, C. Kiehl, T. W. Hsu, and C. A. Regal. Gray-Molasses Optical-Tweezer Loading: Controlling Collisions for Scaling Atom-Array Assembly. *Physical Review X*, 9(2):11057, 2019. ISSN 21603308. doi: 10.1103/PhysRevX.9.011057. URL https://doi.org/10.1103/PhysRevX.9.011057.

[75] Hyosub Kim, Woojun Lee, Han Gyeol Lee, Hanlae Jo, Yunheung Song, and Jaewook Ahn. In situ single-atom array synthesis using dynamic holographic optical tweezers. *Nature Communications*, 7(January), 2016. ISSN 20411723. doi: 10.1038/ncomms13317.

[76] Manuel Endres, Hannes Bernien, Alexander Keesling, Harry Levine, Eric R Anschuetz, Alexandre Krajenbrink, Crystal Senko, Vladan Vuletic, Markus Greiner, and Mikhail D Lukin. Atom-by-atom assembly of defect-free one-dimensional cold atom arrays. *Science*, 354(6315):1024–1027, 2016. ISSN 10959203. doi: 10.1126/science.aah3752.

[77] Connor M. Holland, Yukai Lu, and Lawrence W. Cheuk. On-demand entanglement of molecules in a reconfigurable optical tweezer array. *Science*, 382(6675):1143–1148, 2023. ISSN 10959203. doi: 10.1126/science.adf4272.

[78] Yicheng Bao, Scarlett S. Yu, Loïc Anderegg, Eunmi Chae, Wolfgang Ketterle, Kang Kuen Ni, and John M. Doyle. Dipolar spin-exchange and entanglement between molecules in an optical tweezer array. *Science*, 382(6675):1138–1144, 2023. ISSN 10959203. doi: 10.1126/science.adf8999.

[79] Alexander Keesling, Ahmed Omran, Harry Levine, Hannes Bernien, Hannes Pichler, Soonwon Choi, Rhine Samajdar, Sylvain Schwartz, Pietro Silvi, Subir Sachdev, Peter Zoller, Manuel Endres, Markus Greiner, Vladan Vuletić, and Mikhail D. Lukin. Quantum Kibble–Zurek mechanism and critical dynamics on a programmable Rydberg simulator. *Nature*, 568(7751):207–211, 2019. ISSN 14764687. doi: 10.1038/s41586-019-1070-1.

[80] William J. Eckner, Nelson Darkwah Oppong, Alec Cao, Aaron W. Young, William R. Milner, John M. Robinson, Jun Ye, and Adam M. Kaufman. Realizing spin squeezing with Rydberg interactions in an optical clock. *Nature*, 621(7980):734–739, 2023. ISSN 14764687. doi: 10.1038/s41586-023-06360-6.

[81] G. Semeghini, H. Levine, A. Keesling, S. Ebadi, T. T. Wang, D. Bluvstein, R. Verresen, H. Pichler, M. Kalinowski, R. Samajdar, A. Omran, S. Sachdev, A. Vishwanath, M. Greiner, V. Vuletić, and M. D. Lukin. Probing topological spin liquids on a programmable quantum simulator. *Science*, 374(6572):1242–1247, 2021. ISSN 10959203. doi: 10.1126/science.abi8794.

[82] Dolev Bluvstein, Harry Levine, Giulia Semeghini, Tout T. Wang, Sepehr Ebadi, Marcin Kalinowski, Alexander Keesling, Nishad Maskara, Hannes Pichler, Markus Greiner, Vladan Vuletić, and Mikhail D. Lukin. A quantum processor based on coherent transport of entangled atom arrays. *Nature*, 604(7906):451–456, 2022. ISSN 14764687. doi: 10.1038/s41586-022-04592-6.

[83] Juntian Tu and Sarthak Subhankar. Fast real-time arbitrary waveform generation using graphic processing units. 2024. URL http://arxiv.org/abs/2403.15582.

[84] Harry Levine, Alexander Keesling, Ahmed Omran, Hannes Bernien, Sylvain Schwartz, Alexander S. Zibrov, Manuel Endres, Markus Greiner, Vladan Vuletić, and Mikhail D. Lukin. High-Fidelity Control and Entanglement of Rydberg-Atom Qubits. *Physical Review Letters*, 121(12):1–6, 2018. ISSN 10797114. doi: 10.1103/PhysRevLett.121.123603.

[85] Bahtiyar Mamat, Cheng Sheng, Xiaodong He, Jiayi Hou, Peng Xu, Kunpeng Wang, Jun Zhuang, Mingrui Wei, Min Liu, Jin Wang, and Mingsheng Zhan. Mitigating noise of residual electric fields for single Rydberg atoms with electron photodesorption. pages 1–8, 2023. URL http://arxiv.org/abs/2312.02597.

[86] K Afrousheh, P Bohlouli-Zanjani, D Vagale, A Mugford, M Fedorov, and J D D Martin. Spectroscopic Observation of Resonant Electric Dipole-Dipole Interactions between Cold Rydberg Atoms. *Phys. Rev. Lett.*, 93(23):233001, 11 2004. doi: 10.1103/PhysRevLett.93.233001. URL https://link.aps.org/doi/10.1103/PhysRevLett.93.233001.

[87] P Bohlouli-Zanjani, J A Petrus, and J D D Martin. Enhancement of Rydberg Atom Interactions Using ac Stark Shifts. *Phys. Rev. Lett.*, 98(20):203005, 5 2007. doi: 10.1103/PhysRevLett.98.203005. URL https://link.aps.org/doi/10.1103/PhysRevLett.98.203005.

[88] Asaf Paris-Mandoki, Hannes Gorniaczyk, Christoph Tresp, Ivan Mirgorodskiy, and Sebastian Hofferberth. Tailoring Rydberg interactions via Förster resonances: State combinations, hopping and angular dependence. *Journal of Physics B: Atomic, Molecular and Optical Physics*, 49(16), 2016. ISSN 13616455. doi: 10.1088/0953-4075/49/16/164001.

[89] J. Susanne Otto, Niels Kjærgaard, and Amita B. Deb. Strong zero-field Förster resonances in K-Rb Rydberg systems. *Physical Review Research*, 2(3), 2020. ISSN 26431564. doi: 10.1103/PhysRevResearch.2.033474.

[90] Alec Jenkins, Joanna W. Lis, Aruku Senoo, William F. McGrew, and Adam M. Kaufman. Ytterbium Nuclear-Spin Qubits in an Optical Tweezer Array. *Physical Review X*, 12(2):21027, 2022. ISSN 21603308. doi: 10.1103/PhysRevX.12.021027. URL https://doi.org/10.1103/PhysRevX.12.021027.

[91] Shuo Ma, Alex P. Burgers, Genyue Liu, Jack Wilson, Bichen Zhang, and Jeff D. Thompson. Universal Gate Operations on Nuclear Spin Qubits in an Optical Tweezer

Array of Yb 171 Atoms. *Physical Review X*, 12(2):1–12, 2022. ISSN 21603308. doi: 10.1103/PhysRevX.12.021028.

[92] Harry Levine, Dolev Bluvstein, Alexander Keesling, Tout T. Wang, Sepehr Ebadi, Giulia Semeghini, Ahmed Omran, Markus Greiner, Vladan Vuletić, and Mikhail D. Lukin. Dispersive optical systems for scalable Raman driving of hyperfine qubits. *Physical Review A*, 105(3):1–13, 2022. ISSN 24699934. doi: 10.1103/PhysRevA.105.032618.

[93] William Huie, Lintao Li, Neville Chen, Xiye Hu, Zhubing Jia, Won Kyu Calvin Sun, and Jacob P. Covey. Repetitive Readout and Real-Time Control of Nuclear Spin Qubits in 171Yb Atoms. *PRX Quantum*, 4(3):1, 2023. ISSN 26913399. doi: 10.1103/PRXQuantum.4.030337. URL https://doi.org/10.1103/PRXQuantum.4.030337.

[94] Robert D. Fiete and Bradley D. Paul. Modeling the optical transfer function in the imaging chain. *Optical Engineering*, 53(08):1, 2014. doi: 10.1117/1.oe.53.8.083103.

[95] Julie Bentley and Craig Olson. *Field Guide to Lens Design*. 2013. ISBN 9780819491640. doi: 10.1117/3.934997.

[96] John E. Greivenkamp. *Field Guide to Geometrical Optics*. 2009. ISBN 9780819478160. doi: 10.1117/3.547461.

[97] Charles S. Adams and Ifan G. Hughes. *Optics f2f: From Fourier to Fresnel*. 2018. ISBN 9780198786788. doi: 10.1093/oso/9780198786788.001.0001. URL https://academic.oup.com/book/43688.

[98] Keith J. Kasunic. *Optical Systems Engineering*. 2019. ISBN 978-0-07-175441-5.

[99] Keith J. Kasunic. *Optomechanical Systems Engineering*, volume 59. 2015. ISBN 9781118809860. doi: 10.1002/9781118809860.

[100] Douglas S. Hobbs, Bruce D. MacLeod, and Ernest Sabatino. Continued advancement of laser damage resistant optically functional microstructures. *Laser-Induced Damage in Optical Materials: 2012*, 8530:85300O, 2012. ISSN 1996756X. doi: 10.1117/12.976909.

[101] Douglas S. Hobbs, Bruce D. MacLeod, Ernest Sabatino, Jerald A. Britten, and Christopher J. Stolz. Contamination resistant antireflection nano-textures in fused silica for laser optics. *Laser-Induced Damage in Optical Materials: 2013*, 8885:88850J, 2013. ISSN 1996756X. doi: 10.1117/12.2042888.

[102] Keith J Kasunic. *Optical Systems Engineering*. McGraw-Hill Education, New York, 1st editio edition, 2011. ISBN 9780071754408. URL https://www.accessengineeringlibrary.com/content/book/9780071754408.

[103] Stuart A. Boden and Darren M. Bagnall. *Moth-Eye Antireflective Structures*. 2015. ISBN 978-94-007-6178-0. doi: 10.1007/978-94-007-6178-0{_}262-2.

[104] Hisao Kikuta, Hiroshi Toyota, and Wanji Yu. Optical elements with subwavelength structured surfaces. *Optical Review*, 10(2):63–73, 2003. ISSN 13406000. doi: 10.1007/s10043-003-0063-2.

[105] Douglas S. Hobbs, Bruce D. MacLeod, and Juanita R. Riccobono. Update on the development of high performance anti-reflecting surface relief micro-structures. *Window and Dome Technologies and Materials X*, 6545:65450Y, 2007. ISSN 0277786X. doi: 10.1117/12.720672.

[106] Tomasz S. Tkaczyk. *Field Guide to Microscopy*. 2010. ISBN 9780819472465. doi: 10.1117/3.798239.

[107] Alexander Egner and Stefan W Hell. Aberrations in Confocal and Multi-Photon Fluorescence Microscopy Induced by Refractive Index Mismatch. In James B Pawley, editor, *Handbook Of Biological Confocal Microscopy*, pages 404–413. Springer US, Boston, MA, 2006. ISBN 978-0-387-45524-2. doi: 10.1007/978-0-387-45524-2{_}20. URL https://doi.org/10.1007/978-0-387-45524-2_20.

[108] H Ernst Keller. Objective Lenses for Confocal Microscopy. In James B Pawley, editor, *Handbook Of Biological Confocal Microscopy*, pages 145–161. Springer US, Boston, MA, 2006. ISBN 978-0-387-45524-2. doi: 10.1007/978-0-387-45524-2{_}7. URL https://doi.org/10.1007/978-0-387-45524-2_7.

[109] Warren C Young, Richard G Budynas, and Ali M Sadegh. *Roark's Formulas for Stress and Strain, Eighth Edition*. McGraw-Hill Education, New York, 8th ed. / edition, 2012. ISBN 9780071742474. URL https://www.accessengineeringlibrary.com/content/book/9780071742474.

[110] Karl Jousten. *Handbook of Vacuum Technology*. 2016. ISBN 9783527413386. doi: 10.1002/9783527688265.

[111] LIGO. LIGO Vacuum Compatible Materials List. *Laser Interferometer Gravitational Wave Observatory*, pages 1–24, 2014. URL https://dcc.ligo.org/LIGO-E960050-v12/public.

[112] M Filippova, Y Papaphilippou, D Rivoiron, H Schmickler, and F Tecker. Proceedings of the 2017 course on Vacuum for Particle Accelerators. (June):6–16, 2017. URL https://cds.cern.ch/record/2646487/files/CERN-ACC-2020-0009.pdf.

[113] Agilent Technologies. High and Ultra-High Vacuum for Science Research. *Seminar on High and Ultra-High Vacuum for Science Research*, pages 1–132, 2011. URL https://www.agilent.com/cs/library/training/Public/UHV_Seminar_Handbook.pdf.

[114] Pfeiffer Vacuum. *The Vacuum Technology Book, Volume II, Know how book*. URL https://www.pfeiffer-vacuum.com/filepool/file/literature/vacuum-technology-book-ii-part-2.pdf?request_locale=en_US.

[115] Makfir Sefa, James A. Fedchak, and Julia Scherschligt. Investigations of medium-temperature heat treatments to achieve low outgassing rates in stainless steel ultrahigh vacuum chambers. *Journal of Vacuum Science & Technology A: Vacuum, Surfaces, and Films*, 35(4), 2017. ISSN 0734-2101. doi: 10.1116/1.4983211.

[116] James A. Fedchak, Julia Scherschligt, Daniel Barker, Stephen Eckel, Alex P. Farrell, and Makfir Sefa. Vacuum furnace for degassing stainless-steel vacuum components. *Journal of Vacuum Science & Technology A: Vacuum, Surfaces, and Films*, 36(2), 2018. ISSN 0734-2101. doi: 10.1116/1.5016181.

[117] Kevin M Birnbaum. Cavity QED with Multilevel Atoms. *Caltech thesis*, 2005, 2005. URL http://citeseerx.ist.psu.edu/viewdoc/download?doi=10.1.1.136.7188&rep=rep1&type=pdf.

[118] Damien Robertson. An improved vacuum system for storing highly charged ions in a Penning trap. 2011. URL https://titan.triumf.ca/intern/documents/report_DRobertson.pdf.

[119] Yulin Li and Xianghong Liu. Vacuum Science and Technology for Accelerator Vacuum Systems: Vacuum Components/Hardware. 2015. URL https://uspas.fnal.gov/materials/17UCDavis/Vacuum/USPAS2017VacuumSession5_4Fab_and_Clean.pdf.

[120] M. AUDI, C. PAOLINI, and C. MACCARRONE. The phenomenon of leakage current in ION Pumps. URL https://www.scanwel.com/wp-content/uploads/2021/04/Agilient-The-Phenomenon-of-Leakage-Current.pdf.

[121] Paolo Manassero. How to Optimize Ion Pump Performance by Selecting the Correct Operating Voltage. URL https://www.agilent.com/cs/library/technicaloverviews/public/Copyoftechnical-overview-how-to-optimize-ion-pump-performance-by-sele
pdf.

[122] P. T. Starkey, C. J. Billington, S. P. Johnstone, M. Jasperse, K. Helmerson, L. D. Turner, and R. P. Anderson. A scripted control system for autonomous hardware-timed experiments. *Review of Scientific Instruments*, 84(8), 2013. ISSN 00346748. doi: 10.1063/1.4817213.

[123] Magnus Haw, Nathan Evetts, Will Gunton, Janelle Van Dongen, James L. Booth, and Kirk W. Madison. Magneto-optical trap loading rate dependence on trap depth and vapor density. *Journal of the Optical Society of America B*, 29(3):475, 2012. ISSN 0740-3224. doi: 10.1364/josab.29.000475.

[124] Jürgen Hagedorn, Florian Sell-Le Blanc, and Jürgen Fleischer. *Handbook of coil winding: Technologies for efficient electrical wound products and their automated production*. 2017. ISBN 9783662544020. doi: 10.1007/978-3-662-54402-0.

[125] FAUSTO FIORILLO. *Measurement and Characterization of Magnetic Materials*. Elsevier. ISBN 9780122572517. doi: 10.1002/3527603409.ch4.

[126] Weinan Zhao, Hanxu Wu, Yang Fu, Jun Ge, Honglei Yang, and Shengkang Zhang. Design of a transportable miniaturized optical reference cavity with flexibly tunable thermal expansion properties. *Frontiers in Physics*, 10(January):1–10, 2023. ISSN 2296424X. doi: 10.3389/fphy.2022.1080196.

[127] Thomas Legero, Thomas Kessler, and Uwe Sterr. Tuning the thermal expansion properties of optical reference cavities with fused silica mirrors. *Journal of the Optical Society of America B*, 27(5):914, 2010. ISSN 0740-3224. doi: 10.1364/josab.27.000914.

[128] Alexandre Didier, Jacques Millo, Clément Lacroûte, Morvan Ouisse, Jérôme Delporte, Vincent Giordano, Enrico Rubiola, and Yann Kersalé. Design of an ultra-compact reference ULE cavity. *Journal of Physics: Conference Series*, 723(1), 2016. ISSN 17426596. doi: 10.1088/1742-6596/723/1/012029.

[129] N O Zhadnov, K S Kudeyarov, D S Kryuchkov, G A Vishnyakova, and K Yu Khabarova. Long 48-cm ULE cavities in vertical and horizontal orientations for Sr optical clock.

[130] Jamie A. Boyd and Thierry Lahaye. A basic introduction to ultrastable optical cavities for laser stabilization. *American Journal of Physics*, 92(1):50–58, 2024. ISSN 0002-9505. doi: 10.1119/5.0161369.

[131] J. I. Thorpe, K. Numata, and J. Livas. Laser frequency stabilization and control through offset sideband locking to optical cavities. *Optics Express*, 16(20):15980, 2008. ISSN 1094-4087. doi: 10.1364/oe.16.015980.

[132] T. Rabga, K. G. Bailey, M. Bishof, D. W. Booth, M. R. Dietrich, J. P. Greene, P. Mueller, T. P. O'Connor, and J. T. Singh. Implementing an electronic sideband offset lock for isotope shift spectroscopy in radium. *Optics Express*, 31(25):41326, 2023. ISSN 10944087. doi: 10.1364/oe.500578.

[133] Jiandong Bai, Jieying Wang, Jun He, and Junmin Wang. Electronic sideband locking of a broadly tunable 318.6 nm ultraviolet laser to an ultra-stable optical cavity. *Journal of Optics (United Kingdom)*, 19(4), 2017. ISSN 20408986. doi: 10.1088/2040-8986/aa5a8c.

[134] L. Hanzo, S. X. Ng, T. Keller, and W. Webb. Quadrature amplitude modulation: From basics to adaptive trellis-coded, turbo-equalised and space-time coded OFDM, CDMA and MC-CDMA systems second edition. *Quadrature Amplitude Modulation: From Basics to Adaptive Trellis-Coded, Turbo-Equalised and Space-Time Coded OFDM, CDMA and MC-CDMA Systems*, pages 1–1105, 2011. doi: 10.1109/9780470010594.

[135] Marcelo Sampaio de Alencar. *Modulation Theory*, volume 192. 1st edition, 2018. ISBN 9788770220262. doi: 10.1201/9781003338864.

[136] Oded Mor and Ady Arie. Performance analysis of Drever-Hall laser frequency stabilization using a proportional + integral servo. *IEEE Journal of Quantum Electronics*, 33(4):532–540, 1997. ISSN 00189197. doi: 10.1109/3.563380.

[137] Timothy Day, Eric K. Gustafson, and Robert L. Byer. Sub-Hertz Relative Frequency Stabilization of Two-Diode Laser-Pumped Nd: YAG Lasers Locked to a Fabry-Perot Interferometer. *IEEE Journal of Quantum Electronics*, 28(4):1106–1117, 1992. ISSN 15581713. doi: 10.1109/3.135234.

[138] Gianni Di Domenico, Stéphane Schilt, and Pierre Thomann. Simple approach to the relation between laser frequency noise and laser line shape. *Applied Optics*, 49(25):4801–4807, 2010. ISSN 15394522. doi: 10.1364/AO.49.004801.

[139] Fritz Riehle. *Frequency Standards: Basics and Applications*. 2005. ISBN 9783527605996. doi: 10.1002/3527605991.

[140] D. S. Elliott, Rajarshi Roy, and S. J. Smith. Extracavity laser band-shape and bandwidth modification. *Physical Review A*, 26(1):12–18, 1982.

[141] Michael J. Martin and Jun Ye. *High-precision laser stabilization via optical cavities*, volume 9781107003. 2012. ISBN 9780511762314. doi: 10.1017/CBO9780511762314.017.

[142] John L Hall, Matthew S Taubman, and Jun Ye. LASER STABILIZATION. In Michael Bass, editor, *Handbook of Optics: Volume II - Design, Fabrication, and Testing; Sources and Detectors; Radiometry and Photometry*. McGraw-Hill Education, New York, 3rd editio edition, 2010. ISBN 9780071498906. URL https://www.accessengineeringlibrary.com/content/book/9780071498906/chapter/chapter22.

[143] A. D. Ludlow, X. Huang, M. Notcutt, T. Zanon-Willette, S. M. Foreman, M. M. Boyd, S. Blatt, and J. Ye. Compact, thermal-noise-limited optical cavity for diode laser stabilization at 1×10ˆ15. *Optics Letters*, 32(6):641, 2007. ISSN 0146-9592. doi: 10.1364/ol.32.000641.

[144] N. Poli, M. G. Tarallo, M. Schioppo, C. W. Oates, and G. M. Tino. A simplified optical lattice clock. *Applied Physics B: Lasers and Optics*, 97(1):27–33, 2009. ISSN 09462171. doi: 10.1007/s00340-009-3488-x.

[145] Gregory Bonaguide and Neil Jarvis. *The VNA Applications Handbook*. ARTECH HOUSE, 2019. ISBN 9781630816001.

[146] Michael Tröbs, Luigi d'Arcio, Gerhard Heinzel, and Karsten Danzmann. Frequency stabilization and actuator characterization of an ytterbium-doped distributed-feedback fiber laser for LISA. *Journal of the Optical Society of America B*, 26(5):1137, 2009. ISSN 0740-3224. doi: 10.1364/josab.26.001137.

[147] John Bechhoefer. Kramers–Kronig, Bode, and the meaning of zero. *American Journal of Physics*, 79(10):1053–1059, 2011. ISSN 0002-9505. doi: 10.1119/1.3614039.

[148] Jürgen Appel, Andrew MacRae, and A. I. Lvovsky. A versatile digital GHz phase lock for external cavity diode lasers. *Measurement Science and Technology*, 20(5):206–55302, 2009. ISSN 09570233. doi: 10.1088/0957-0233/20/5/055302. URL http://iopscience.iop.org/0957-0233/20/5/055302.

[149] Daniel Adam Steck. Quantum and Atom Optics. *Book*.

[150] C. D. Herold, V. D. Vaidya, X. Li, S. L. Rolston, J. V. Porto, and M. S. Safronova. Precision measurement of transition matrix elements via light shift cancellation. *Physical Review Letters*, 109(24):1–5, 2012. ISSN 00319007. doi: 10.1103/PhysRevLett.109.243003.

[151] W. Ketterle, D. S. Durfee, and D. M. Stamper-Kurn. Making, probing and understanding Bose-Einstein condensates. 1999. URL http://arxiv.org/abs/cond-mat/9904034.

[152] Wolfgang Ketterle and Martin W Zwierlein. Making, probing and understanding ultracold Fermi gases. 2008.

[153] Daniel Adams and Shelby Ament. Understanding Aspheric Lenses. *Optik & Photonik*, 13 (4):60–63, 2018. doi: 10.1002/opph.201800033.

[154] Joseph W.Goodman. *Introduction to Fourier Optics*. Roberts and Company Publishers, 3rd edition. ISBN 978-0974707723.

[155] Daniel G. Smith. *Field Guide to Physical Optics*. 2013. ISBN 9780819485489. doi: 10.1117/3.883971.

[156] Norbert Lindlein and Gerd Leuchs. Wave Optics. In Frank Träger, editor, *Springer Handbook of Lasers and Optics*, pages 87–156. Springer New York, New York, NY, 2007. ISBN 978-0-387-30420-5. doi: 10.1007/978-0-387-30420-5{_}3. URL https://doi.org/10.1007/978-0-387-30420-5_3.

[157] J. Scott Tyo and Andrey Alenin. Field Guide to Linear Systems in Optics. *Field Guide to Linear Systems in Optics*, 31(1):35–37, 2015. doi: 10.1117/3.1002932.

[158] Herbert Gross. *Handbook of Optical Systems*, volume 1. Wiley, 1 2005. ISBN 9783527699223. doi: 10.1002/9783527699223. URL https://onlinelibrary.wiley.com/doi/book/10.1002/9783527699223.

[159] Herbert Gross, Hannfried Zügge, Martin Peschka, and Fritz Blechinger. *Handbook of Optical Systems, Aberration Theory and Correction of Optical Systems*, volume 3. 2015. ISBN 9783527699254. doi: 10.1002/9783527699254.

[160] Virendra N. Mahajan. *Optical imaging and aberrations: Part II: Wave diffraction optics: Second edition*. 2001. ISBN 9780819487001. doi: 10.1117/3.898443.

[161] Virendra N. Mahajan. *Optical Imaging and Aberrations: Part I: Ray geometrical optics*. 1998. ISBN 081942515X. doi: 10.1117/3.265735.

[162] Noah Bareket. Second moment of the diffraction point spread function as an image quality criterion. *Journal of the Optical Society of America*, 69(9):1311, 1979. ISSN 0030-3941. doi: 10.1364/josa.69.001311.

[163] Yueqian Zhang and Herbert Gross. Systematic design of microscope objectives. Part I: System review and analysis. *Advanced Optical Technologies*, 8(5):313–347, 2019. ISSN 21928584.

[164] Michael J. Kidger. *Fundamental Optical Design*. SPIE—The International Society for Optical Engineering, 2009. ISBN 0-8194-3915-0. doi: 10.1117/3.397107.

[165] MASUD MANSURIPUR. Abbe's Sine Condition. *Optics and Photonics News*, 9(2):56, 1998. ISSN 1047-6938. doi: 10.1364/opn.9.2.000056.

[166] Alex Small. Spherical aberration, coma, and the Abbe sine condition for physicists who don't design lenses. *American Journal of Physics*, 86(7):487–494, 2018. ISSN 0002-9505. doi: 10.1119/1.5036939. URL http://dx.doi.org/10.1119/1.5036939.

[167] Yueqian Zhang and Herbert Gross. Systematic design of microscope objectives. Part II: Lens modules and design principles. *Advanced Optical Technologies*, 8(5):349–384, 2019. ISSN 21928584.

[168] Yueqian Zhang and Herbert Gross. Systematic design of microscope objectives. Part III: Miscellaneous design principles and system synthesis: Systematic design of microscope objectives. Part I/II/III. *Advanced Optical Technologies*, 8(5):385–402, 2019. ISSN 21928584. doi: 10.1515/aot-2019-0014.

[169] Herbert Gross, Fritz Blechinger, and Bertram Achtner. *Handbook of Optical Systems*, volume 4. 2015. ISBN 9783527699247. doi: 10.1002/9783527699247. URL http://eu.wiley.com/WileyCDA/WileyTitle/productCd-3527403809.html.

[170] V. E. Karpus and V. A. Ivanov. Locating accuracy of shafts in V-blocks. *Russian Engineering Research*, 32(2):144–150, 2012. ISSN 1068798X. doi: 10.3103/S1068798X1202013X.

[171] R Kingslake. *Lens design fundamentals Second Edition*, volume 26. 1978. ISBN 9780819479396.

[172] Michael Bass, editor. *Handbook of Optics: Volume I - Geometrical and Physical Optics, Polarized Light, Components and Instruments*. McGraw-Hill Education, New York, 3rd editio edition, 2010. ISBN 9780071498890. URL https://www.accessengineeringlibrary.com/content/book/9780071498890.

[173] José Sasián. *Introduction to lens design*. 2019. ISBN 9781108625388. doi: 10.1017/9781108625388.

[174] José Sasián. Structural aberration coefficients. In *Introduction to Aberrations in Optical Imaging Systems*, page 147–161. Cambridge University Press, 2012.

[175] Daniel A Steck. Classical and Modern Optics. pages 1–354, 2015. URL papers3://publication/uuid/9FF1EF6D-3B33-4340-8565-DC8A4C76252C.

[176] R. V. Brooks, S. Spence, A. Guttridge, A. Alampounti, A. Rakonjac, L. A. McArd, Jeremy M. Hutson, and Simon L. Cornish. Preparation of one 87Rb and one 133Cs atom in a single optical tweezer. *New Journal of Physics*, 23(6), 2021. ISSN 13672630. doi: 10.1088/1367-2630/ac0000.

[177] ZEMAX. Optical Design Program, User's Manual. 2011. URL www.zemax.com.

[178] Hyosub Kim, Minhyuk Kim, Woojun Lee, and Jaewook Ahn. Gerchberg-Saxton algorithm for fast and efficient atom rearrangement in optical tweezer traps. *Optics Express*, 27(3): 2184, 2019. ISSN 1094-4087. doi: 10.1364/oe.27.002184.

[179] Eric P. Goodwin and James C. Wyant. *Field Guide to Interferometric Optical Testing*. 2009. ISBN 0819465100. doi: 10.1117/3.702897.p22.

[180] Danial Malacara. *Optical Shop Testing: Third Edition*, volume 11. 2006. ISBN 9780470135976. doi: 10.1002/9780470135976.

[181] Jörg S. Eismann, Martin Neugebauer, Klaus Mantel, and Peter Banzer. Absolute characterization of high numerical aperture microscope objectives utilizing a dipole scatterer. *Light: Science and Applications*, 10(1), 2021. ISSN 20477538. doi: 10.1038/s41377-021-00663-x.

[182] Shuming Yang and Guofeng Zhang. A review of interferometry for geometric measurement. *Measurement Science and Technology*, 29(10), 2018. ISSN 13616501. doi: 10.1088/1361-6501/aad732.

[183] Herbert Gross, Bernd Dörband, and Henriette Müller. Handbook of Optical Systems, Metrology of Optical Components and Systems, 2015.

[184] Robert Smythe. Practical aspects of modern interferometry for optical manufacturing quality control: Part 1. *Advanced Optical Technologies*, 1(1-2):59–64, 2012. ISSN 21928584. doi: 10.1515/AOT-2011-0007.

[185] Robert Smythe. Practical aspects of modern interferometry for optical manufacturing quality control: Part 2. *Advanced Optical Technologies*, 1(3):203–212, 2012. ISSN 21928584. doi: 10.1515/aot-2012-0026.

[186] H. A. Buchdahl. Optical Aberration Coefficients. IX. Theory of Reversible Optical Systems. *Journal of the Optical Society of America*, 57(4):517–522, 1967. ISSN 00303941. doi: 10.1364/JOSA.57.000517.

[187] J. B. Houston, C. J. Buccini, and P. K. O'Neill. A Laser Unequal Path Interferometer for the Optical Shop. *Applied Optics*, 6(7):1237, 1967. ISSN 0003-6935. doi: 10.1364/ao.6.001237.

[188] Peter J. De Groot. A review of selected topics in interferometric optical metrology. *Reports on Progress in Physics*, 82(5):ab092d, 2019. ISSN 00344885. doi: 10.1088/1361-6633/ab092d. URL https://doi.org/10.1088/1361-6633/ab092d.

[189] Daniel Malacara, Manuel Servín, and Zacarias Malacara. *Interferogram for Optical Analysis Testing*, volume 31. 2006. ISBN 9781574446821. doi: 10.1139/H06-080.

[190] Katie Schwertz and James H Burge. *Field Guide to Optomechanical Design and Analysis*. 2012. ISBN 9780819491619.

[191] Ian T Young, Rick Zagers, and Lucas J Van Vliet. Depth-of-Focus in Microscopy. (January), 1993.

[192] Hanshin Lee. Optimal collimation of misaligned optical systems by concentering primary field aberrations. *Optics Express*, 18(18):19249, 2010. ISSN 10944087. doi: 10.1364/oe.18.019249.

[193] Ulrich Kubitscheck. *Fluorescence Microscopy: From Principles to Biological Applications: Second Edition*. 2017. ISBN 9783527687732. doi: 10.1002/9783527687732.

[194] Douglas B. Murphy and Michael W. Davidson. *Fundamentals of Light Microscopy and Electronic Imaging: Second Edition*. 2012. ISBN 9780471692140. doi: 10.1002/9781118382905.

[195] James B. Pawley. Points, pixels, and gray levels: Digitizing image data. *Handbook of Biological Confocal Microscopy: Third Edition*, pages 59–79, 2006. doi: 10.1007/978-0-387-45524-2{_}4.

[196] S. J.M. Kuppens, K. L. Corwin, K. W. Miller, T. E. Chupp, and C. E. Wieman. Loading an optical dipole trap. *Physical Review A*, 62(1):13, 2000. ISSN 10941622. doi: 10.1103/PhysRevA.62.013406.

[197] Loïc Anderegg, Lawrence W. Cheuk, Yicheng Bao, Sean Burchesky, Wolfgang Ketterle, Kang Kuen Ni, and John M. Doyle. An optical tweezer array of ultracold molecules. *Science*, 365(6458):1156–1158, 2019. ISSN 10959203. doi: 10.1126/science.aax1265.

[198] Harry Jay Levine. *Quantum Information Processing and Quantum Simulation with Programmable Rydberg Atom Arrays*. PhD thesis, Harvard University, 2021. URL https://nrs.harvard.edu/URN-3:HUL.INSTREPOS:37368420.

[199] Ivaylo Sashkov Madjarov. *Entangling, Controlling, and Detecting Individual Strontium Atoms in Optical Tweezer Arrays*. PhD thesis, California Institute of Technology, 1 2021. URL https://resolver.caltech.edu/CaltechTHESIS:01292021-001639979.

[200] Kai-Niklas Schymik. *Scaling-up the Tweezer Platform - Trapping Arrays of Single Atoms in a Cryogenic Environment*. PhD thesis, Université Paris-Saclay, 3 2022. URL https://pastel.hal.science/tel-03643133.

[201] Pierre-Alexandre J. Blanche. *Field Guide to Holography*. 2014. ISBN 9780819499578. doi: 10.1117/3.1002325.

[202] Tieyu Zhao and Yingying Chi. Modified gerchberg–saxton (G-s) algorithm and its application. *Entropy*, 22(12):1–26, 2020. ISSN 10994300. doi: 10.3390/e22121354.

[203] Peter J. Christopher, George S. D. Gordon, and Timothy D. Wilkinson. Benchmarking the Gerchberg-Saxton Algorithm. 2020. URL http://arxiv.org/abs/2005.08623.

[204] Stefan Rothe, Philipp Daferner, Sebastian Heide, David Krause, Felix Schmieder, Nektarios Koukourakis, and Jürgen W. Czarske. Benchmarking analysis of computer generated holograms for complex wavefront shaping using pixelated phase modulators. *Optics Express*, 29(23):37602, 2021. ISSN 10944087. doi: 10.1364/oe.434842.

[205] Akio Kawasaki, Boris Braverman, Qinqin Yu, and Vladan Vuletic. Two-color magneto-optical trap with small magnetic field for ytterbium. *Journal of Physics B: Atomic, Molecular and Optical Physics*, 48(15), 2015. ISSN 13616455. doi: 10.1088/0953-4075/48/15/155302.

[206] Stephen Eckel, Daniel S. Barker, Eric B. Norrgard, and Julia Scherschligt. PyLCP: A Python package for computing laser cooling physics. *Computer Physics Communications*, 270, 2022. ISSN 00104655. doi: 10.1016/j.cpc.2021.108166.

[207] M. Müller, I. Lesanovsky, H. Weimer, H. P. Büchler, and P. Zoller. Mesoscopic rydberg gate based on electromagnetically induced transparency. *Physical Review Letters*, 102 (17):1–4, 2009. ISSN 00319007. doi: 10.1103/PhysRevLett.102.170502.

[208] K. McDonnell, L. F. Keary, and J. D. Pritchard. Demonstration of a Quantum Gate Using Electromagnetically Induced Transparency. *Physical Review Letters*, 129(20): 200501, 2022. ISSN 10797114. doi: 10.1103/PhysRevLett.129.200501. URL https://doi.org/10.1103/PhysRevLett.129.200501.

[209] Ruben Verresen, Nathanan Tantivasadakarn, and Ashvin Vishwanath. Efficiently preparing Schr\"odinger's cat, fractons and non-Abelian topological order in quantum devices. (1): 23–26, 2021. URL http://arxiv.org/abs/2112.03061.

[210] Betsy Bland, Dennis Coyne, and Jodi Fauver. LIGO Clean and Bake Methods and Procedures. LIGO-E9600(LIGO-E960022-v25), 2010.